

AD-A248 420



①

Aerospace Sponsored Research

SUMMARY REPORT

DTIC
ELECTE
APR 13 1992
S D

1 December 1990

Scientific and
Engineering Research

92-09268



THE AEROSPACE CORPORATION



APPROVED FOR PUBLIC RELEASE,
DISTRIBUTION UNLIMITED

To provide architect-engineering support to national security space missions, Aerospace must be at the scientific and technological forefront of those missions. Aerospace Sponsored Research therefore concentrates on problems of long-range importance and potentially high payoff in future space system architectures.

A handwritten signature in black ink, appearing to read "Samuel M. Tennant". The signature is fluid and cursive, with a prominent initial "S" and a stylized "T".


Samuel M. Tennant
President
The Aerospace Corporation

Aerospace Sponsored Research

SUMMARY REPORT

1 December 1990

**Scientific and
Engineering Research**

THE AEROSPACE CORPORATION 

Composed on Sun Microsystems using Interleaf Technical
Publishing Software Text is in 11 point Times Display
lines are in Swiss

Foreword

This report presents brief summaries of the results and progress achieved by the Aerospace Sponsored Research program during the period 1 October 1989 through 30 September 1990. More detailed accounts are given in Aerospace Technical Reports (ATRs), published as particular milestones are reached, as well as in journal publications.

Management responsibility for the program is assigned to the Group Vice President, Development. He is supported by the Aerospace Sponsored Research Advisory Committee, which is responsible for reviewing, evaluating, and recommending projects for funding, as well as for periodic reviews of ongoing projects. The dedicated efforts of the committee members are gratefully acknowledged. The committee members were

J. D. Gilchrist	Chairman, Engineering Group
S. Rubin	Member, Engineering Group
A. C. Liang	Member, Engineering Group
L. T. Greenberg	Member, Programs Group
R. J. DeLorenzo	Member, Programs Group
H. R. Rugge	Member, Development Group
A. N. Sorensen	Member, Development Group
J. R. LaFrieda	Member, Development Group
J. L. Kirschner	Secretary, Development Group
D. J. Evans	Advisor
J. M. Straus	Advisor
W. P. Thompson	Advisor

Edward M. Lassiter

Edward M. Lassiter
Group Vice President, Development

Accession For	
NTIS	<input checked="" type="checkbox"/>
CRA&I	<input type="checkbox"/>
DTIC	<input type="checkbox"/>
TAB	<input type="checkbox"/>
Unannounced	<input type="checkbox"/>
Justification	
By	
Distribution /	
Availability Codes	
Dist	Availability / or Special
A-1	

Contents

Foreword	iii
Introduction	1
ELECTRONICS	5
High Temperature Superconducting Electronics (R. C. Lacoe, J. P. Hurrell, and J. P. Wendt)	5
Novel Approaches to GaAs Growth (D. M. Speckman and J. P. Wendt)	9
Superlattice Plasmon Excitations for EHF Devices (W. L. Bloss and B. K. Janousek)	13
Transition Dynamics and Guest-Host Interactions in Laser Materials (T. S. Rose)	17
Deposition of High- T_c Superconducting Oxides (M. S. Leung, R. A. Lipeles, D. J. Coleman, J. F. Kirshman and R. C. Lacoe)	20
Characterization of Radiation Damage in Solids (R. A. Fields)	23
Indium Phosphide Photovoltaic Technology (L. F. Halle and D. C. Marvin) ...	26
OPTICS	31
Magnesium Atomic Filter for Submarine Laser Communications (J. A. Gelbwachs and Y. C. Chan)	31
Analysis of Infrared Detector Materials (C. J. Selvey, P. A. Dafesh, R. P. Wright, and P. M. Adams)	35
Picosecond Studies of Space Optical Materials (S. C. Moss)	39
Novel Short-Wavelength Lasers (J. M. Herbelin)	45
Stimulated Brillouin Scattering Phase Conjugation (S. T. Amimoto and R. F. W. Gross)	50
Microparticle Linear and Nonlinear Optics (D. E. Masturzo and A. Pluchino)	54
High-Energy Laser Particle Interaction (D. W. Pack, A. Pluchino, and D. E. Lake)	59
CHEMISTRY AND PHYSICS	67
Laser Surface Photolyzed Chemistry (H. Helvajian, H.-S. Kim, and L. H. Wiedeman)	67
Ultraviolet-Visible Plume Chemistry and Spectroscopy (R. F. Heidner, D. G. Sutton, R. B. Cohen, J. F. Bott, J. Steadman, J. B. Koffend, and J. A. Syage)	72
Flame Front Kinetics (T. A. Spiglanin, J. A. Syage, and R. B. Cohen)	74
High-Resolution Chemical Dynamics (J. E. Pollard, L. K. Johnson, D. A. Lichtin, and R. B. Cohen)	79
Picosecond State-Specific Reaction Dynamics (J. A. Syage and J. Steadman) ..	82
Mechanism of Diamond Film Growth (L. R. Martin)	86
Propulsion Diagnostics Program (S. W. Janson, R. P. Welle, T. A. Spiglanin, and R. B. Cohen)	89
Reacting Flow Field Kinetics (N. Cohen and J. F. Bott)	94
Chemically Reacting Flows (J. C. T. Wang and G. F. Widhopf)	96
Extended X-ray Absorption Fine Structure of Metal Dichalcogenides (J. R. Lince, M. R. Hilton, and J. L. Childs)	99

<i>Ab Initio</i> Calculations of Solid Lubricants (T. B. Stewart)	102
Scanning Tunneling Microscope Studies of Nickel Oxyhydroxides (A. H. Zimmerman, M. V. Quinzio, and N. A. Ives)	106
Metallic Cluster Ions—Electronic Structure and Stability (N. D. Bhaskar and C. M. Klimcak)	110
Vibrational Chemiluminescence in Gas-Solid Reactions (G. S. Arnold and D. J. Coleman)	113
Chaotic Dynamics of Atoms (J. C. Camparo)	116
Semiclassical Analysis of Two-Electron Atoms (B. R. Johnson)	120
Physics and Chemistry of Metal-Semiconductor Clusters (S. M. Beck)	123
Spin Effects In Electron-Atom Collisions (B. Jaduszliwer and Y. C. Chan) ...	126
 ATMOSPHERIC PHYSICS AND ASTRONOMY	135
High-Resolution Infrared Technology and Applications (R. W. Russell, J. A. Hackwell, D. K. Lynch, G. S. Rossano, and R. J. Rudy)	135
Atmosphere Dynamics and Coupling (R. L. Walterscheid, L. R. Lyons, M. N. Ross, and G. Schubert)	141
Aeronomy of Auroral/Airglow Emission (J. H. Hecht and A. B. Christensen)	145
Ionospheric Processes (F. T. Djuth)	149
Infrared Studies of Star-Forming Regions (J. A. Hackwell, R. W. Canterna, D. J. Edelson, L. M. Friesen, J. H. Hecht, J. Kepner, D. K. Lynch, R. W. Russell, and E. A. Walkup)	153
Auroral Energization and Geomagnetic Disturbances (L. R. Lyons and J. F. Fennell)	157
Trends in Middle Atmosphere Ozone (M. N. Ross)	161
Solar-Terrestrial Physics and Astrophysics (R. J. Rudy, J. B. Blake, M. C. McNab, M. Schulz, and J. H. Hecht)	164
 INFORMATION SCIENCE	171
Applications of Logic to Computer Verification (L. G. Marcus, J. V. Cook, J. E. Doner, I. V. Filippenko, and T. K. Menas)	171
Neural Network Architectures (M. P. Plonski, W. K. Peter, and R. P. Ma)	173
Software Application Generators (R. R. Razouk)	176
Classification Tree Optimization by Simulated Annealing (R. S. Bucy and R. S. Di Esposti)	180
Fractals and Image Processing (D. J. Evans, L. A. Campbell, and M. Jankins)	184
Linear Algebra with Symbolic Interface (D. M. Nystrom, R. S. Beezley, H. E. Kim, B. H. Sako, and W. K. Yeung)	187
On-Line Parameter Estimation (L. A. Campbell)	189
 Bibliography of Journal Publications	193
Author Index	203

Introduction

The Aerospace Corporation provides architect-engineer services for military space and launch systems, and for other projects related to national security. Aerospace performs engineering, planning, analysis, and research for constantly evolving advanced systems. Aerospace's work is primarily under contract to the Space Systems Division of the Air Force Systems Command, providing support in the planning, design, development, and operations of complex space systems. To carry out this mission it is necessary for the Corporation to engage in a vigorous and continuing research and development program.

Aerospace's research and development efforts advance critical technologies needed for present and future military space systems. They contribute directly to Aerospace's missions: conceptual design, systems engineering, launch readiness verification, on-orbit diagnostics, and anomaly analysis; and to the assessment of mission performance and cost and schedule risks.

To support military space programs most effectively, Aerospace must contribute in those advanced technologies and analytical fields critical to the timely acquisition and operation of cost-effective military space systems. To do so requires a research and development program that provides insight into probable advances in science and technology, likely new missions, and the evolution of present military space systems that will help accomplish those missions.

The structure and mission of The Aerospace Corporation's research and development program is coordinated with, and complementary to, that of the Air Force laboratories and other organizations actively working in space system-related technology.

In line with these objectives, broad guidelines for the direction and emphasis of the overall research and development activities at Aerospace are periodically developed to assess in detail the trends in relevant technologies and their application to military space systems. The major fields of endeavor now being pursued are

- Electronics and Optics
- Materials Properties and Processing
- Information Sciences and Data Processing
- Space and Atmospheric Environment
- Space Communication and Navigation
- Surveillance from Space
- Spacecraft and Launch Vehicle Design and Operation
- Spacecraft Survivability
- Systems Architecture, Planning, and Analysis

As part of its overall research and development program, the Corporation engages in an Aerospace Sponsored Research (ASR) program, consisting primarily, but not exclusively, of long-term research. Many individual research and development projects, supported by corporate resources, comprise the ASR program.

Because the ASR program is of great importance to the long-term objectives of the Corporation, and because it uses corporate assets, the overall program and projects are reviewed annually by the Technical Committee of the Board of Trustees, and their recommendation is acted on by the full Board of Trustees. Since the inception of the Corporation, the Board of Trustees has vigorously endorsed the ASR program and allocated to it a substantial share of corporate resources.

This ASR Summary Report for FY 1990 contains summary reports of the Scientific and Engineering Research projects carried out under the ASR program. The reports are grouped into the following technical areas:

- Electronics
- Optics
- Chemistry and Physics
- Atmospheric Physics and Astronomy
- Information Science

References (numbered) and a bibliography appear at the end of each report. For further details on any of the individual projects, please refer to the listed Aerospace reports or contact the authors.

Electronics

ELECTRONICS

High Temperature Superconducting Electronics

R. C. Lacoë, J. P. Hurrell, and J. P. Wendt,
Research Laboratory

The overall objective of this project is to demonstrate and evaluate applications of high temperature superconductors (HTS) to satellite electronic systems. The specific objectives involve the fabrication and evaluation of thin-film-based far-infrared detectors, passive microwave/millimeter-wave structures, and weak-link structures.

During the past year, we continued our studies of flicker $1/f$ noise in thin HTS films in order to assess the impact of this excess noise on the ultimate sensitivity of proposed infrared detectors. Although thermal noise establishes the minimum noise level in these films, excess $1/f$ noise can limit the sensitivity of infrared detectors because of their long integration times.

Our investigation into the noise properties of HTS thin films was aided through collaboration with superconductivity research groups at Los Alamos and TRW. Los Alamos films were prepared by coevaporation of yttrium (Y), copper (Cu), and barium fluoride (BaF_2) on (100) strontium titanate (SrTiO_3) substrates. The $0.5\text{ }\mu\text{m}$ thick films displayed a broad superconducting transition, with onset (T_{co}) and final (T_{cf} , $R = 0$) temperatures of 78 and 69 K, respectively. TRW films were prepared *in-situ* by off-axis radio-frequency sputtering from a yttrium barium copper oxide ($\text{YBa}_2\text{Cu}_3\text{O}_7$) target on (100) lanthanum aluminate (LaAlO_3). The $0.4\text{ }\mu\text{m}$ thick films were patterned into cross-bridges of varying widths and lengths, and displayed a sharp superconducting transition with $T_{co} = 91\text{ K}$ and $T_{cf} = 87\text{ K}$. The broad superconducting transition (Los Alamos) films were designed to show a nonequilibrium response. These films would be applicable as infrared detectors that use the change in nonequilibrium properties of the film with temperature. The sharp superconducting transition (TRW) films would be more appli-

cable as bolometric detectors, in which changes in resistance due to infrared heating are sensed.

The square root of the noise spectral density at 10 Hz , $S_v^{1/2}(f = 10\text{ Hz})$ for both types of samples is shown in Figure 1. The general temperature dependence is similar, but the absolute magnitude of the noise is different in the two films. We found that the $1/f$ noise spectral power density, normalized by the square of the average dc voltage V , can be expressed in the form where both the magni-

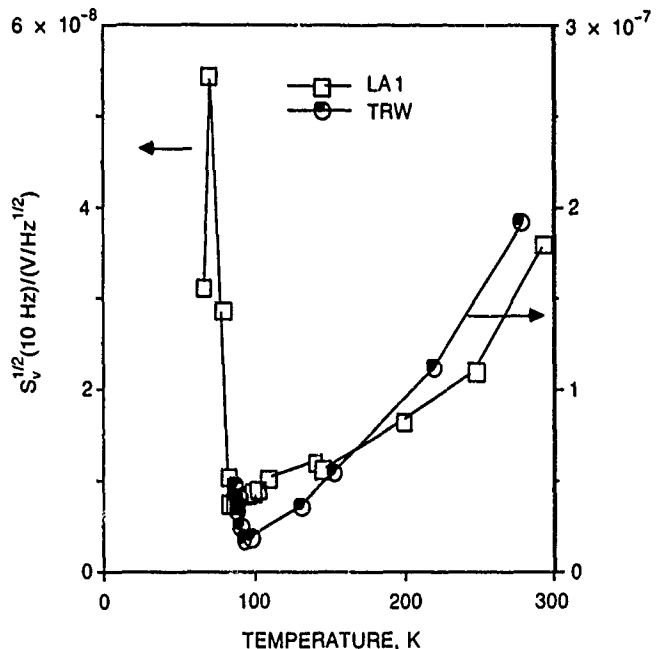


Figure 1. $S_v^{1/2}(10\text{ Hz})$ vs T for Los Alamos sample (\square) and TRW sample (\bullet). The solid lines are to guide the eye.

tude coefficient K and the $1/f$ exponent α are temperature dependent. This agrees with the relationship

$$\frac{S_v}{V^2} = \frac{K(T)}{A} \left(\frac{1}{f} \right)^{\alpha(T)}, \quad (1)$$

first expressed by Hooge [1], where $K(T)/A = \alpha_H/(N_c) = \alpha_H/(nAt)$; here α_H is the Hooge constant, N_c is the number of carriers, n is the carrier density, A is the film area, and t is the film thickness. Although it is no longer believed that the value of $\alpha_H \sim 2 \times 10^{-3}$ is a universal constant for semiconductors and metals, it is nevertheless useful to compare the magnitude of the $1/f$ noise of different films by comparing the Hooge parameter of different films. Extracting the effective room-temperature Hooge parameter for the Los Alamos and TRW films, we find $\alpha_{LA} \sim 1 \times 10^{-1}$ and $\alpha_{TRW} \sim 4 \times 10^{-2}$. These values are much smaller than those as large as 10^6 reported by other investigators [2,3]. The factor of 2.5 reduction in the noise of the TRW film over the Los Alamos film is accompanied by a reduced superconductivity transition width from 20 to 4 K.

The areal dependence of the noise was confirmed by measuring structures of different active area on the same film (TRW) (Figure 2). The normalized noise voltage at fixed frequency was determined to scale inversely with the active film area (Figure 3). This result is consistent with the interpretation of the $1/f$ noise as resistance fluctuations. Although the measured resistivity varied by 20% over the film surface, the noise voltage follows an $A^{-1/2}$ dependence very closely, indicating that the measured noise represented an intrinsic property of the film. The areal dependence of the flicker noise in these films implies that this noise term will predominate in small detectors unless the film quality is extremely high.

In Figure 4, $S_v^{1/2}(f)/V$ versus temperature is plotted for the Los Alamos sample. $S_v^{1/2}(f)/V$ is weakly temperature-dependent above the transition. At the transition, however, $S_v^{1/2}(f)/V$ increases dramatically by more than three orders of magnitude. The striking difference in appearance between Figures 1 and 4 reflects the fact that the rapid increase in $S_v^{1/2}(f)/V$ is due mostly to the rapid decrease in V at the superconducting transition rather than the moderate increase in $S_v(f)$. The resistance fluctuations represent a larger fraction of the average resistance not because the resistance fluctuations are rapidly increasing, but because the average resistance is rapidly dropping toward zero. The insert in Figure 4 shows that the crossover from a weakly temperature-dependent to a highly temperature-dependent normalized noise occurs about 5 K below the resistive transition, as defined by the knee in the temperature versus $\beta \equiv (1/R)(dR/dT)$ curve.

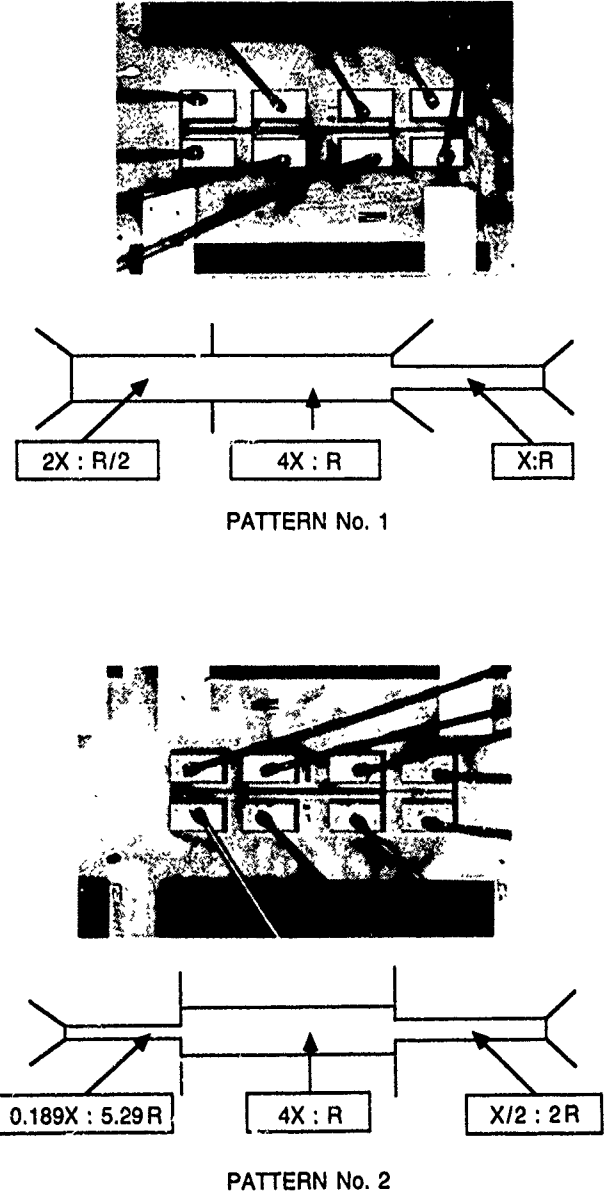


Figure 2. Schematic of the mask set and photographs of the patterned and bonded films used to measure the areal dependence of the noise. R represents arbitrary resistance units, X represents arbitrary area units.

Clearly, there are two temperature regimes that separate a comparatively temperature-dependent normalized noise level from one that is highly temperature-dependent. In these structures, the separation occurs at a temperature where the resistance has already dropped significantly and β is large. Consequently, it is attractive to consider the thermal fluctuation model of Voss and Clarke [4] to understand this strong temperature dependence in the vicinity of $R \rightarrow 0$. In this model, $S_v^{1/2}(f)/V$ is proportional to $\beta T' C_v^{1/2}$, where C_v is the heat capacity of

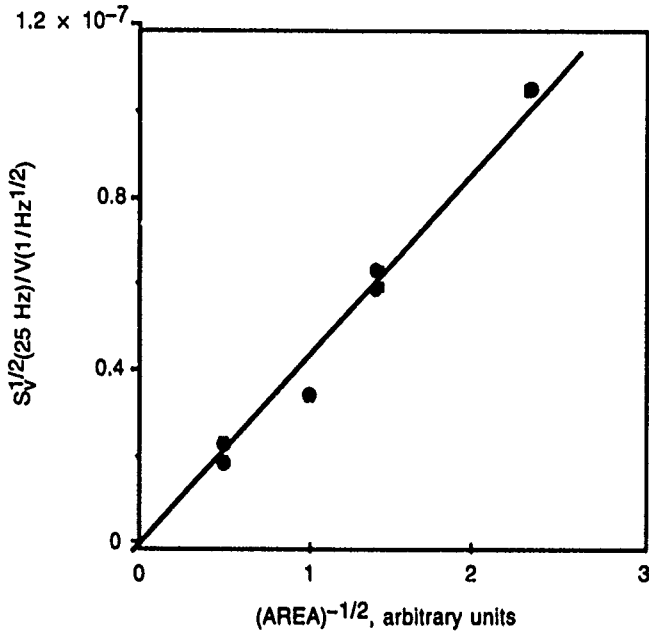


Figure 3. The normalized noise voltage $S_V^{1/2}$ vs $(\text{area})^{-1/2}$ measured at 25 Hz. The solid line is to guide the eye.

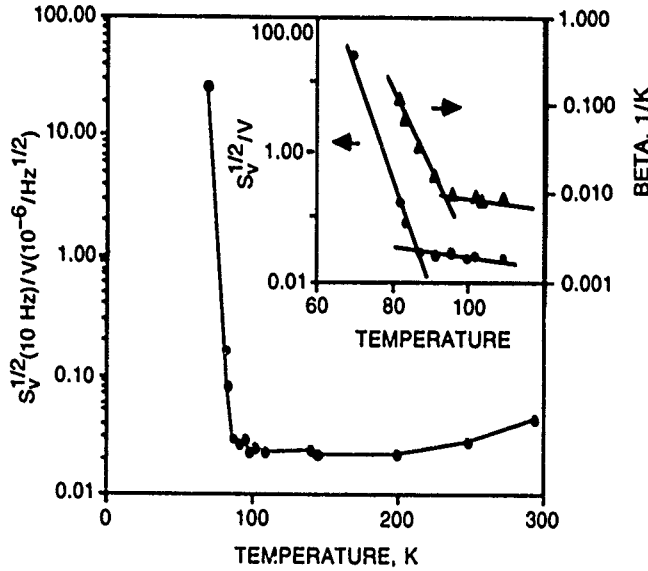


Figure 4. $S_V^{1/2}(10 \text{ Hz})/V$ vs T for sample LA1. The insert shows $S_V^{1/2}/V$ vs T and β vs T at the superconducting transition. The solid lines are to guide the eye.

the sample. Figure 5 presents the data for both samples in this form, where the weak temperature dependence of bulk $\text{YBa}_2\text{Cu}_3\text{O}_7$ has been assumed for C_V [5]. For all samples measured, it was found near the onset of superconductivity that $S_V^{1/2}/V \sim \beta^n$, where $0.8 < n < 1.4$. We have observed no evidence of the dramatic dependence on β as reported by other investigators, who have reported n -values in excess of 15 [6]. The modest dependence on β suggests that thermal fluctuations are contributing near $R \rightarrow 0$ in these bridges.

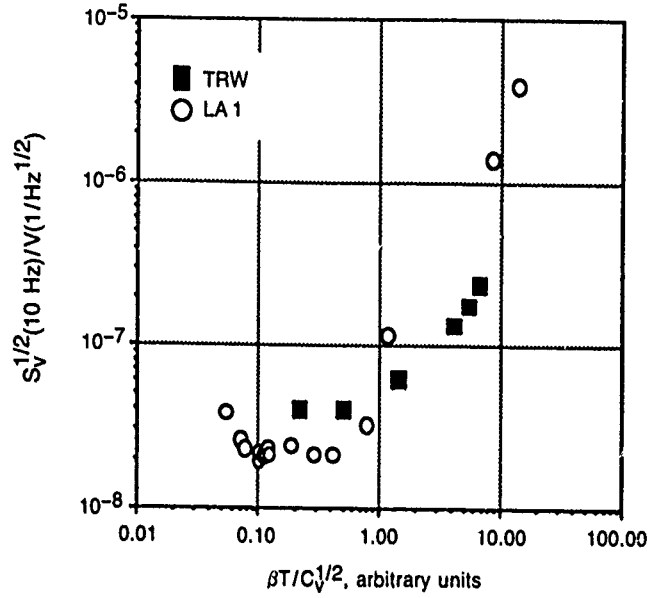


Figure 5. $S_V^{1/2}(20 \text{ Hz})/V$ vs $\beta T/C_V^{1/2}$ (arbitrary units) for LA1 sample (○) and the TRW sample (■).

More interesting is the absolute independence of the noise level on $\beta T/C_V^{1/2}$ from room temperature to below the knee of the R versus T curve. In this regime, where $\beta T/C_V^{1/2}$ changes by more than an order of magnitude, the resistance fluctuations are clearly not produced by thermal fluctuations and reflect more intrinsic noise processes occurring within the films. Although the approximately linear dependence of R on T above T_c compresses the temperature scale in Figure 5, there remains a clear temperature range near the onset of superconductivity where β is changing rapidly ($0.1 < \beta T/C_V^{1/2} < 1$) but the noise is constant. The alternative trapping-detrapping models [7,8] of $1/f$ noise generation lead to a weak dependence on temperature, but require the presence of a specific distribution of trap energies and scattering times. The lack of exact stoichiometry in $\text{YBa}_2\text{Cu}_3\text{O}_7$, which produces a large number of defect sites in the bulk of the material, at the grain boundaries, and at the surfaces, provides the opportunity for the occurrence of such trap-induced noise. The concept that there are two independent sources of $1/f$ noise, one that dominates above the superconducting transition and is only weakly dependent on temperature, and one that is dominant below the transition and is roughly proportional to β , is supported by examining the temperature dependence of the resistance and noise near T_c . The Figure 4 insert, which shows that the resistive transition occurs above 5 K above the knee in the $S_V^{1/2}/V$ versus T curve, is consistent with this interpretation. The temperature-dependent noise term dominates only when it has been sufficiently enhanced by a large β value.

To enhance our capabilities for studying the properties of high-temperature superconducting films, we have constructed a thin-film deposition system. A single-target ion beam sputtering (IBS) thin-film deposition technique was chosen with the use of an ion gun to provide high-energy argon atoms, which sputter the target material onto a substrate. This approach provides flexible target selection and potentially good target-substrate isolation. A problem experienced in the deposition of HTS thin-films from a single target by conventional sputtering techniques is a lack of electrical isolation between the sputtering electronics and the substrates. Negative ions sputtered off the target are accelerated toward the substrate and in turn preferentially sputter material off the substrates, resulting in nonstoichiometric thin films. The solution to this problem has been to use an off-axis technique to deposit stoichiometric films, but this geometry results in very slow deposition rates. The excellent isolation between the target and the substrate in the IBS technique should result in high-quality on-stoichiometric thin films deposited at relatively high deposition rates.

A schematic of the IBS technique implemented at Aerospace is shown in Figure 6. A controlled oxygen leak near the substrate and a heated substrate platform that can reach temperatures of 700°C have been designed, built, and integrated into the deposition system, allowing control over the oxygen stoichiometry and *in-situ* creation of the $\text{YBa}_2\text{Cu}_3\text{O}_7$ phase.

Film deposition has begun on SrTiO_3 and magnesium oxide (MgO) substrates. By optimizing the deposition geometric and sputtering parameters, we have been able to obtain on-stoichiometric films within 2%. This is the first report of on-stoichiometric *in-situ* HTS films by the IBS method. X-ray diffraction results indicate that our films are primarily *c*-axis oriented. Scanning electron micrographs shows that our film are smooth on the scale of approximately 1 μm . The best films displayed metallic conductivity in the normal state and a sharp superconducting onset at approximately 80 K.

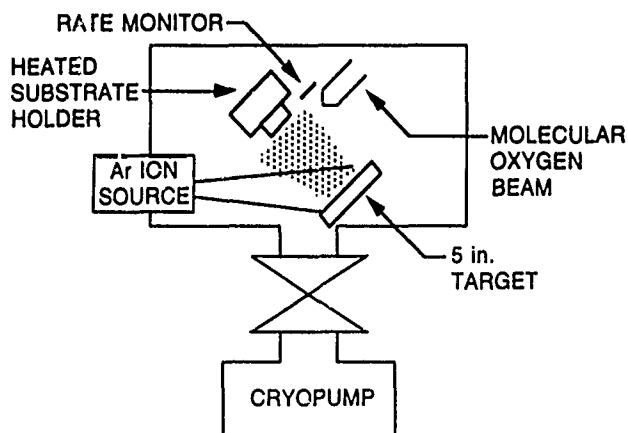


Figure 6. Schematic of the ion-beam sputtering system.

In summary, we have reported measurements of the temperature-dependent excess $1/f$ noise in $\text{YBa}_2\text{Cu}_3\text{O}_7$ thin films. The *ohmic* dependence of the noise voltage on current strongly suggests that the noise is due to resistance fluctuations. We have shown that S_V/V^2 is inversely proportional to the active film area. By comparing the properly normalized noise (Hooge parameter), we have seen that the film with the sharper superconducting transition had less noise than that of a film with a relatively broad superconducting transition. The normalized noise power S_V/V^2 is proportional to T^2 in the normal state before leveling off near the onset of superconductivity and is clearly not produced by thermal fluctuations except near $R \rightarrow 0$. Elimination of this excess noise will help to improve the performance of HTS thin-film bolometers. Aerospace capabilities have been established for depositing HTS thin films and for adequately characterizing them. Stoichiometric HTS superconducting thin films were deposited. Future work will be directed toward film deposition, extension of the noise measurements, and the development of techniques to produce controlled film granularity.

* * * * *

1. F. N. Hooge and A. M. H. Hoppenbrouwers, "1/f Noise in Continuous Thin Gold Films, *Physica* 45, 386 (1969).
2. A. Maedal et al., "Conductance Fluctuation of Bi-Sr-Ca-Cu-O System," *Physica C* 162-164, 1203 (1989).
3. J. A. Testa et al., "Noise Power Spectrum of Copper Oxide Superconductors in the Normal State," *Phys. Rev. B* 38, 2922 (1988).
4. R. F. Voss and J. Clarke, "Flicker (1/f) Noise: Equilibrium Temperature and Resistance Fluctuations," *Phys. Rev. B* 13, 556 (1976).
5. J. C. Van Miltenburg et al., "Specific Heat Measurements of High-T Superconductor $\text{YBa}_2\text{Cu}_3\text{O}_7$ Between 78K and 260K," *Physica B* 146, 319 (1987).
6. R. Rosenthal et al., "Low Frequency Resistance Fluctuations in Films of High Temperature Superconductors," *IEEE Trans. Magn.* 25, 973 (1989).
7. A. van der Ziel, "On the Noise Spectra of Semiconductor Noise and of Flicker Effect," *Physica* 16, 359 (1950).
8. P. Dutta, P. Dimon, and P. M. Horn, "Energy Scales for Noise Processes in Metals," *Phys. Rev. Lett.* 43, 646 (1979).

Lacoe, R. C., et al., "Flicker 1/f Noise in YBa₂Cu₃O₇ Thin Films," *Bull. Am. Phys. Soc.* **35**, 425 (1990).

Lacoe, R. C., et al., "Low Frequency 1/f Noise Measurements in YBa₂Cu₃O₇ Thin Films and the Implications for HTS IR Detectors," *IEEE Trans. Magn.* **27**, 2832 (1991).

Novel Approaches to GaAs Growth

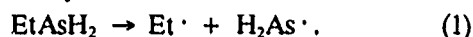
D. M. Speckman and J. P. Wendt,
Electronics Research Laboratory

Organometallic chemical vapor deposition (OMCVD) is an important process in the semiconductor industry for the growth of high-purity GaAs epilayers and related semiconductor materials, for their use in high speed electronic devices and in high-efficiency solar cells. The OMCVD process for GaAs film growth has traditionally used arsine (AsH₃) and trimethylgallium (Me₃Ga) as the organometallic precursor reagents. In this process, the arsenic and gallium reagents are typically flowed past a heated substrate (~ 650°-800°C), which causes the reagents to pyrolyze and deposit as a crystalline GaAs epilayer. Arsine is a prohibitively toxic gas however, and the development of new arsenic reagents to replace arsine is an urgent goal of the OMCVD community.

Organoarsines show promise as safer alternatives to the use of arsine in OMCVD processes because of their lower toxicities and lower vapor pressures. A variety of organoarsines have been examined for their potential to grow high-purity GaAs by OMCVD, but many of those tested as precursors produce films with high levels of carbon impurities [1]. It was proposed that this carbon doping was likely related to the inherent growth chemistry of the organoarsenic reagents [2,3]; however, the manner in which this doping might occur was poorly understood, because of the scarcity of data on growth mechanisms for these reagents. Thus, during the first year of this project, we examined the decomposition chemistry of a series of ethylarsines (mono-, di-, and triethylarsenic, plus a mixture of triethylarsenic and arsine), correlated the decomposition data with purity data obtained for GaAs epilayers grown from these precursors during preliminary growth experiments, and identified those pyrolysis intermediates that appeared to be essential for the formation of high-purity GaAs films. These studies suggested that the formation of an arsenic dihydride intermediate such as H₂As· is probably responsible for the growth of high-purity GaAs films [4-6]. Such an intermediate could participate in GaAs growth without introducing any carbon contamination from arsenic-bound organic ligands, and could also supply hydride ligands to the growing GaAs surface. These surface hydrides could aid in the removal of other carbon-containing fragments on the GaAs sur-

face by means of reductive-elimination [5]. Organoarsine reagents of the general form RAsH₂ (where R = alkyl, aryl) are the most likely to decompose in such a way as to generate AsH₂ radicals, and these compounds were thus identified as the best candidates for further study as arsine replacements. Our objective this past year was to carry out an in-depth study of GaAs epilayer growth using promising organoarsine precursors of the form RAsH₂, first by performing an extensive series of growth experiments using reagents of this type, and then by characterizing the purity of the resulting films in detail.

The most exhaustive GaAs growth and characterization studies carried out this past year involved monoethylarsine (EtAsH₂) as the arsenic precursor. This precursor was initially selected for in-depth growth studies because our earlier mechanism experiments involving this reagent indicated that this species decomposes under very mild conditions by means of homolytic cleavage to give H₂As· and an ethyl radical,



The dihydridoarsenic radical intermediate thus produced should aid in the growth of very high-purity GaAs films. The few early growth experiments carried out using this compound (in the course of our mechanism/purity correlations) also supported this hypothesis. In addition, monoethylarsine exhibits physical and toxicological properties that make it an ideal arsine substitute. It has the advantage of being a liquid at room temperature (unlike arsine, which must be stored as a compressed gas), yet exhibits an appreciable vapor pressure (~ 145 Torr at -7°C). Since monoethylarsine is transported to the growth chamber in the vapor phase by means of a carrier gas that is bubbled through the liquid reagent, this high-vapor pressure eases the transport of the reagent to the growth chamber. Monoethylarsine is also reported to be less toxic than arsine.

All of the growth experiments carried out using this monoethylarsine reagent used trimethylgallium as the gallium source. The gallium arsenide films grown using these two reagents were deposited on undoped GaAs substrates in a custom built, atmospheric pressure, vertical

reactor. Palladium diffused hydrogen was used as the carrier gas. Two different lots of EtAsH_2 were used for this study, designated as Lot 1 and Lot 2. Lot 1, which contained significant quantities of silicon, was far less pure than Lot 2. Two different bottles of Lot 1 were also used, identified as Lot 1A and 1B. Lot 1A was used for our initial growth experiments. Lot 1B was used for our most recent growth experiments and provided the most reproducible results and the best epilayer uniformities. These latter results reflect improvements we made in reagent gas flow uniformity. We discovered that the presence of any localized surface gas turbulence caused a significant increase in epilayer carbon contamination in these areas, as indicated by secondary ion mass spectroscopy (SIMS) measurements. This contamination apparently results from the incorporation of carbon-containing fragments produced by reagent decomposition. Improved gas flow uniformity reduced surface turbulence and subsequent impurity incorporation. Lot 2 was evaluated during our initial phase of growth studies, prior to any flow uniformity adjustments, and it is therefore anticipated that the

results reported for this lot provide only a conservative estimate of the GaAs purity that can be obtained using EtAsH_2 .

All films grown using EtAsH_2 in this laboratory were *n*-type, and the epilayer surfaces were mirror-like in appearance, with some fine structure visible at high magnification (500 \times). The optimum growth temperatures appeared to be in the range of 575° to 600°C, and in all cases, GaAs epilayer purity increased with increasing V/III (arsenic reagent/gallium reagent) molar ratio. The influence of V/III molar ratio on 77 K mobility for films grown at 575°C and 600°C is illustrated in Figures 1(a) and 1(b), respectively. It is noteworthy that good quality GaAs films could be grown from EtAsH_2 at V/III ratios as low as 5, and these epilayers are superior to those grown from $\text{AsH}_3/\text{Me}_3\text{Ga}$ under similar conditions. The highest purity epilayers were obtained using EtAsH_2 from Lot 2, as might be expected based on the purity of the reagent material. At a V/III ratio of 30, a GaAs film with a 77 K mobility as high as 55,300 $\text{cm}^2/\text{V-s}$, a room-temperature mobility as great as 7200 $\text{cm}^2/\text{V-s}$, and a net carrier concentration of $6 \times 10^{14} \text{cm}^{-3}$ was grown using Lot 2 EtAsH_2 . These mobility values are among the highest ever reported for initial evaluation studies of a new organoarsine source. In addition, since reactor flow uniformity for our system was improved subsequent to our Lot 2 growths, it is expected that even higher-purity films should be obtainable from similar source batches.

The most common impurity usually found in organoarsine-grown GaAs films is carbon, and this impurity generally results from the inherent decomposition chemistry of the organoarsine precursor. Significant concentrations of alkyl- or alkylarsenic-radical species are often produced during organoarsine decomposition, and these species can react with the growing GaAs epilayer surface and become incorporated into the epilayer as carbon. However, our decomposition studies on EtAsH_2 indicate that this reagent should be less likely to exhibit carbon contamination, since it appears that the $\text{H}_2\text{As}^\cdot$ species is the dominant decomposition product of EtAsH_2 . In order to identify the impurity types in EtAsH_2 -grown GaAs films, and to determine their possible origins, several films were subjected to analysis by SIMS and low-temperature photoluminescence (PL). For these analyses, epilayers were grown from EtAsH_2 at V/III ratios of 5 and 40, using our optimized reactor flow conditions. These films exhibited 77 K mobility values of 31,400 $\text{cm}^2/\text{V-s}$ and 44,100 $\text{cm}^2/\text{V-s}$, respectively. For comparison, an epilayer was grown in the same modified reactor from arsine/ Me_3Ga using growth parameters that had previously been optimized for high-purity GaAs deposition from these reagents. This film exhibited a 77 K mobility of 80,900 $\text{cm}^2/\text{V-s}$. Analysis of each of these films by SIMS measurements was carried out by Charles Evans & Associates. Each sample was depth-profiled for the presence of car-

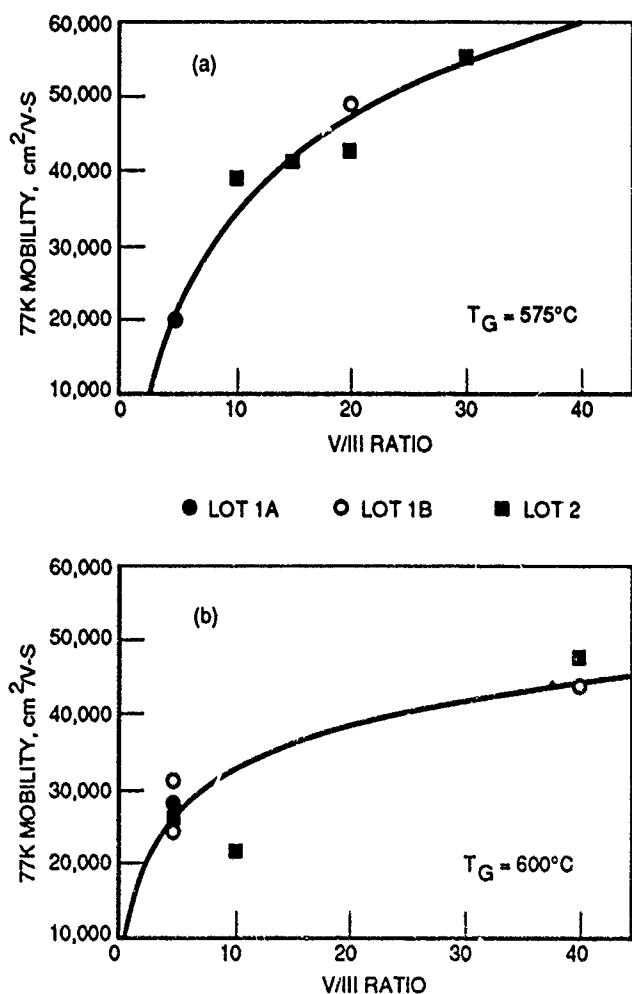


Figure 1. Influence of V/III ratio on 77 K mobility for GaAs films grown using EtAsH_2 and Me_3Ga . (a) Growth temperature, 575°C, (b) growth temperature, 600°C.

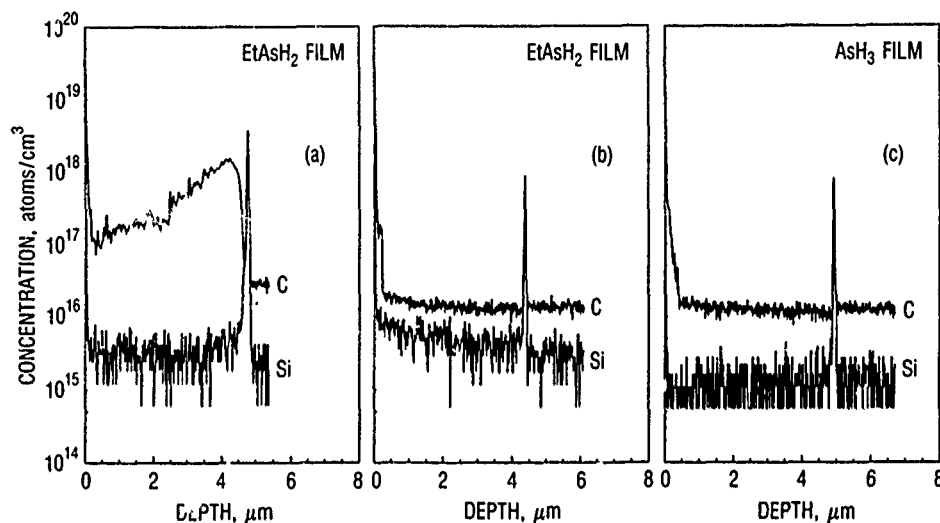


Figure 2. SIMS measurements of carbon and silicon in GaAs films grown at 600°C using Me_3Ga and (a) EtAsH_2 (V/III ratio = 5), (b) EtAsH_2 (V/III ratio = 40), (c) AsH_3 (V/III ratio = 27).

bon and silicon, since these species were expected to be the most dominant epilayer contaminants (SIMS analysis of earlier EtAsH_2 samples showed no evidence for contamination by O, S, Se, Ge, Te, B, Mg, Al, Cr, Fe, Mn, Cu, or Na); the results of these analyses are illustrated in Figure 2. At a V/III ratio as low as 5, the GaAs epilayer sample grown from EtAsH_2 was heavily contaminated with carbon (10^{17} – 10^{18}cm^{-3}), but for a sample grown under similar conditions with a V/III ratio of 40, the epilayer carbon was at the background carbon level of the SIMS instrument (as determined by comparison with the carbon level found in a liquid encapsulated Czochralski GaAs substrate wafer). Silicon was slightly higher than the SIMS detection limit in both of these epilayers (5 – $8 \times 10^{15}\text{cm}^{-3}$). As expected, the arsine-grown film exhibited carbon and silicon levels at the detection limit of the SIMS instrument. It is interesting to note that despite an extremely high carbon content in the EtAsH_2 -film grown at a V/III ratio of 5, the epilayer was still n -type and exhibited a reasonably good 77 K mobility. This may indicate that the carbon in this film is not electrically active.

Low-temperature (17 K) photoluminescence spectra were also obtained for these three GaAs films (courtesy of V. Sundaram at Boeing); an overlay of the resulting spectra is shown in Figure 3. Essentially identical conditions were used for obtaining each of these spectra. The GaAs epilayer grown using EtAsH_2 at a V/III ratio of 5 exhibits a very large acceptor peak corresponding to epilayer carbon (and possibly silicon), which is consistent with the SIMS results. It is possible that, at this low V/III ratio, the concentration of surface arsenic-hydride species is also low, which in turn could limit the removal of gallium-bound methyl groups by reductive-elimination. The GaAs film grown from EtAsH_2 at a V/III ratio of 40 exhibits a PL spectrum similar to that of our arsine-grown film, which is also consistent with the corresponding SIMS data. Both the latter EtAsH_2 -grown film and the arsine-

grown film exhibit photoluminescence peaks at 1.494 and 1.490 eV, which are consistent with carbon acceptors in the epilayers (free electron to neutral acceptor ($e-A^0$) and neutral donor to neutral acceptor (D^0-A^0) transitions, respectively). The high V/III ratio EtAsH_2 -grown GaAs film exhibits stronger peak intensities, and a higher intensity ratio for the (D^0-A^0) to ($e-A^0$) luminescence peaks, than is observed for the arsine-grown films however, which is consistent with the higher compensation ratio for the EtAsH_2 -grown film [7] (compensation ratio = N_A/N_D^+ , where N_D and N_A are the concentrations of ionized donors and acceptors, respectively). Some of the luminescence intensity for the peak at 1.490 eV may also be due to ($e-A^0$) transitions related to other acceptor

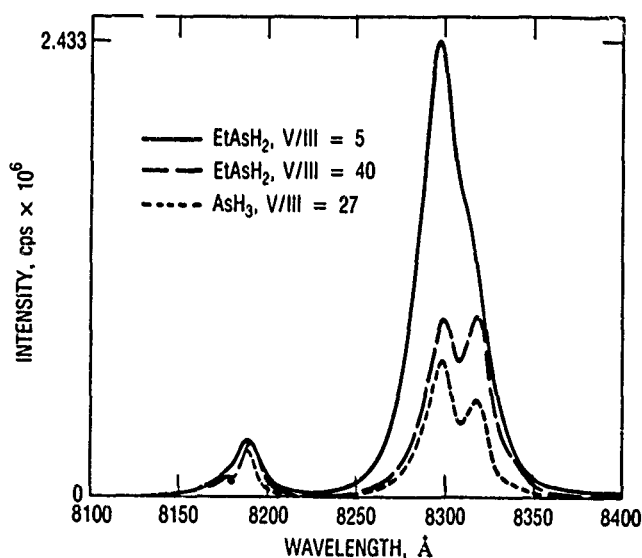


Figure 3. Photoluminescence spectra at 17 K of GaAs films grown at 600°C using Me_3Ga and either EtAsH_2 (V/III ratio = 5: solid line; V/III ratio = 40: dashed line) or AsH_3 (V/III ratio = 27: dotted line).

impurities in the film; i.e., Zn, Mg. Both films (in particular the EtAsH₂-grown film) also exhibit a third peak as a shoulder at 1.485 eV, which corresponds to the presence of silicon acceptors in these films. If silicon is present as an acceptor in these films, it is likely that its presence as a donor is even greater. Further reduction in epilayer contamination is anticipated with subsequent improvements in reactor flow conditions and in reagent purity. However, these data demonstrate that high-quality GaAs can be grown using the novel organoarsine source, EtAsH₂.

A series of OMCVD growth experiments have also been carried out using the novel organoarsine precursor phenylarsine (C₆H₅AsH₂). Phenylarsine was of interest as part of our study on organoarsines for comparison with our monoethylarsine results, since it is also anticipated to decompose by means of homolysis to give the crucial H₂As· intermediate species and a resonance-stabilized phenyl radical (C₆H₅·). Growth experiments using this new reagent were thus carried out to determine whether or not phenylarsine is capable of growing high-purity GaAs films. Successful GaAs growth would suggest that this reagent exhibits a chemical reactivity similar to that of monoethylarsine, and such information should aid in the design of new and better organoarsine reagents. Trimethylgallium was used as the gallium source for the phenylarsine growth experiments, and the growth parameters selected for our first experiments were typical for OMCVD growth experiments: V/III ratio = 10, growth temperature = 600° to 650°C, growth rate ~ 2.5 μm/h. The first few epilayers grown using the phenylarsine/trimethylgallium combination exhibited promising characteristics. The films were *n*-type, had reasonably good surface morphology, and had room temperature and 77 K mobility values of 4500 to 5000 and 10,000 to 13,000 cm²/V-s, respectively. However, as additional growth experiments were carried out, the quality of each successive GaAs film degraded until only highly compensated, *p*-type films could be obtained under any growth conditions. These data suggest that the phenylarsine reagent source probably contains some high boiling impurity. Over time, the phenylarsine would preferentially distill from the bubbler, causing a corresponding increase in the relative impurity concentration. Because of the severe reagent contamination, no valid conclusions could be reached concerning the viability of PhAsH₂ as an arsine replacement source.

In summary, from the results of our earlier organoarsine decomposition studies, which suggested that an ideal arsine substitute reagent should decompose to primarily produce a dihydridoarsenic radical species (H₂As·), the use of EtAsH₂ was expected to produce high-purity, low-carbon GaAs films. In general, our growth studies support this hypothesis. Good-quality, *n*-type GaAs films were grown from EtAsH₂ and Me₃Ga in an atmospheric pressure OMCVD vertical reactor.

Film quality depended on V/III ratio, growth temperature, and reagent purity. Film purity was also a function of reagent gas flow uniformity, with turbulence apparently increasing impurity levels of carbon in the epilayers. SIMS and low-temperature PL analysis of epilayers grown under optimized flow conditions from EtAsH₂ at high V/III ratios demonstrate that these films exhibit very little carbon contamination when compared with high-purity arsine-grown epilayers produced under similar reaction conditions, as anticipated by the earlier mechanism studies. The EtAsH₂ reagent is thus expected to be a very good source for use as a substitute for arsine in all CVD applications. Unfortunately, studies carried out to determine the viability of phenylarsine as an arsine replacement source were inconclusive because of an apparently severe contamination of the source material.

* * * * *

1. G. B. Stringfellow, "Non-hydride Group V sources for OMVPE," *J. Electron. Mater.* **17**, 327 (1988); G. B. Muhr et al., "Recent Advances in the Development of Arsine Substitutes for use In Metal Organic Vapour Phase Epitaxy of GaAs," *Chemtronics* **4**, 26 (1989).
2. R. M. Lum, J. K. Klingert, and D. W. Kisker, "¹³C Isotopic Labeling Studies of Growth Mechanisms in the Metalorganic Vapor Phase Epitaxy of GaAs," *J. Cryst. Growth* **93**, 120 (1988).
3. D. M. Speckman and J. P. Wendt, "Atmospheric pressure OMCVD Growth of GaAs Using Triethylarsenic and Alkylgallium Organometallic Precursors," *Proc. Mater. Res. Soc. Symp.* **102**, 187 (1988); "Triethylarsenic and Arsine as Co-Reagents: The Novel Manipulation of in-situ GaAs OMCVD Growth Chemistry to Improve Growth Efficiency and Safety," *J. Cryst. Growth* **93**, 29 (1988); "The Role of Arsine in Reducing Carbon in Triethylarsenic Grown GaAs Films," *Proc. Mater. Res. Soc. Symp.* **145**, 193 (1989).
4. D. M. Speckman and J. P. Wendt, "Novel Approaches to GaAs Growth," *Aerospace Sponsored Research Summary Report, Scientific and Engineering Research*, ATR-89(8498)-1, The Aerospace Corp. (1 December 1989), p. 60.
5. D. M. Speckman and J. P. Wendt, "Carbon Reduction in Triethylarsenic-Grown GaAs Films Using Chemically Activated Arsine as a Co-Reagent," *J. Electron. Mater.* **19**, 495 (1990).
6. D. M. Speckman and J. P. Wendt, "Monoethylarsine as a Novel Replacement for Arsine in the Vapor Deposition of GaAs," *J. Cryst. Growth* **105**, 275 (1990).

7. K. Nagata et al., "Effects of Hydrogen on Growth Mechanism of GaAs in Chemical Beam Epitaxy," *J. Cryst. Growth* **93**, 265 (1988).

_____, "Vapor Deposition of High Purity GaAs Epilayers Using Monoethylarsine," *Appl. Phys. Lett.* **56**, 1134 (1990).

_____, "Process for Growing GaAs Epitaxial Layers," U.S. Patent No. 4,935,381 (19 June 1990).

Speckman, D. M., and J. P. Wendt, "The Role of Arsine in Reducing Carbon in Triethylarsenic Grown GaAs Films," *Proc. Mater. Res. Soc. Symp.* **145**, 193 (1989).

Superlattice Plasmon Excitations for EHF Devices

W. L. Bloss and B. K. Janousek,
Electronics Research Laboratory

With the advent of the precise crystal growth techniques of molecular beam epitaxy (MBE) and metal-organic chemical vapor deposition (MOCVD), structures can now be grown with tailored band gap profiles and with many layers, ranging from a single monolayer to hundreds of angstroms. These growth methods open up new possibilities in fabricating novel structures with unique physical and electronic properties, leading to the development of new classes of devices, based on quantum wells, tunneling, and ballistic transport. New structures and phenomena, derived from quantum confinement and reduced dimensionality, include the quantum confined Stark effect (QCSE) for optical modulation [1,2], negative differential conductivity tunneling devices for high-frequency microwave/millimeter wavelength oscillators and mixers [3], a number of nonlinear optical devices [4,5] involving enhanced x^2 and x^3 , and infrared detectors based on intersubband absorption [6,7].

In this project, we are investigating a new physical phenomenon, made possible by these new growth processes for fabricating structures with dimensions on the atomic scale. This new phenomenon is called *superlattice plasmon excitation* and arises from the coupling of the plasmon oscillations of electrons between the individual quantum wells in a periodic array, by the long-range Coulomb interaction. These oscillations were first theoretically proposed by Bloss and Brody [8] and Das Sarma and Quinn [9], and it was suggested that the GaAlAs/GaAs system was an ideal structure to investigate these unique coupled electronic excitations. In those investigations [8,9], it was shown that a periodic superlattice of quantum wells has a band of Bloch-like plasmon excitations propagating along the superlattice axis. The electrons never physically move along this direction, but are confined in the plane perpendicular to the superlattice axis (the exci-

tation is transverse to the superlattice axis); energy, however, is transported along the superlattice axis. These oscillations are unique in that their energy dispersion relation, including properties such as bandwidth and group velocity, can be varied widely by the appropriate selection of parameters during the MBE growth process (i. e., doping and well separation) and can be tailored to fit a particular device application. In the case of a semi-infinite superlattice, Guilian and Quinn [10] investigated the possibility of surface plasmon modes. They predicted the existence of surface plasmons between a semi-infinite superlattice and an adjoining bulk material if the dielectric constants of the two were different. Surface plasmons were found to exist only for wavevectors larger than some critical wavevector depending on the ratio of the dielectric constants [10]. In this work, we investigate localized interface plasmon modes in a number of different superlattice structures.

Another major focus of this research is to investigate possible drift instabilities of plasmons in heterojunction superlattices and quantum wells. These instabilities occur if there is a low-lying acoustic plasmon mode (energy directly proportional to the velocity) in this system. If the drift velocity of the electrons is larger than the characteristic velocity of the acoustic plasmon, energy transfer from the drifted electrons to the plasmon modes will occur. The required critical velocity for the drift instability to occur in the GaAs-AlGaAs superlattice structure is close to the electron saturation velocity in GaAs ($\approx 2 \times 10^7$ cm/s). It is desirable to lower the velocities of the acoustic plasmons in order to make drift instability more favorable. Because of the flexibility available in designing the plasmon energy bands and the possibility of wave amplification, these structures offer the possibility of creating oscillators and amplifiers with frequencies in

the infrared, millimeter, and microwave regions of the spectrum.

During the past year, we investigated the interface plasmon modes for three different superlattice structures. The objective of this effort was to find localized acoustic plasmons with characteristic velocities significantly less than the electron velocity in GaAs in order to obtain plasmon amplification. The first superlattice structure studied consists of a one-dimensional infinite periodic array of quantum wells with periodicity a , as shown in Figure 1. The quantum wells are uniformly doped with an equivalent two-dimensional electron density n , except for the well at $z = 0$, which is doped to a density of n_0 . This breaks the symmetry of the infinite periodic array. In analogy with the local phonon modes of a vibrational lattice having all atoms with identical mass m except for one with mass m_0 , we find the existence of local plasmon modes. Exact solutions are found for these local modes. Contrary to the surface plasmon modes of the semi-infinite superlattice [10], these local modes are found to exist for all values of qa , where q is the wavevector perpendicular to the superlattice axis.

In the second superlattice structure, we investigated the local interface plasmon modes of two semi-infinite semiconductor superlattices separated by a distance d (Figure 2). In general, the two superlattices can have different periodicities, densities, and dielectric constants. In Figure 2, two semi-infinite superlattices are shown. The one on the left (labeled 1 in region 1) has periodicity b ; the one on the right (labeled 3 in region 3) has periodicity a . The two superlattices are separated by a distance d . The quantum wells of each superlattice are uniformly doped and have an equivalent two-dimensional electron density (three-dimensional dopant density times the well width) n_1 for superlattice 1 and n_3 for superlattice 3. In region 1, dielectric constant is ϵ_1 ; in region 2, ϵ_2 ; and in region 3, ϵ_3 . The quantum wells are labeled with the index j . The formalism that we derive pertains to the general case, although we specialize the results here to the case where the dielectric constants and the periodicities of the two superlattices are the same, but the superlattices have different densities. In this limit, we have obtained exact solutions for the interface plasmon modes. The different densities of the superlattices give rise to two distinctly different continuum plasmon bands for the individual

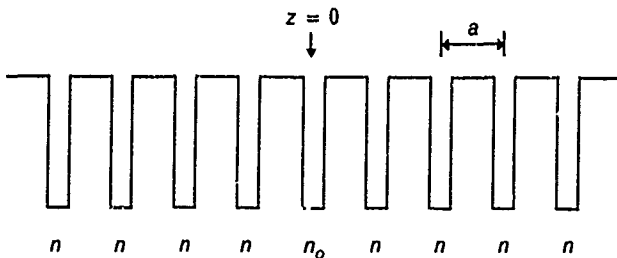


Figure 1 A superlattice of doped quantum wells with density n except for the well at $z = 0$, which has density n_0 .

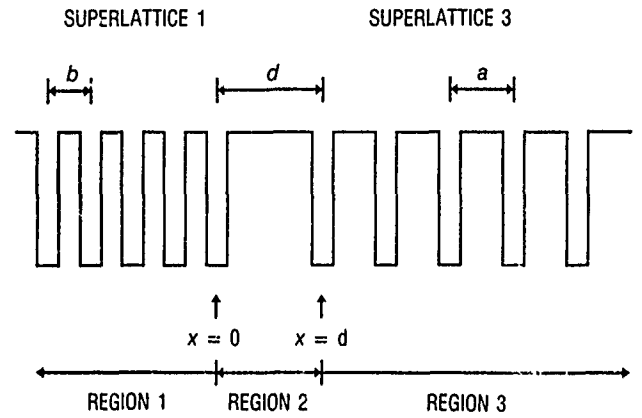


Figure 2 Two superlattices of quantum wells with periodicities a and b separated by a distance d .

superlattices. The coupling of plasmon excitations of the superlattices results in a newly discovered set of interface plasmon modes. In the case considered here with equivalent dielectric constants, the isolated semi-infinite superlattices do not have Guiliiani-Quinn [10] type surface plasmon modes that require dielectric discontinuities.

In the third superlattice structure, we investigated the local interface plasmon modes of a semi-infinite semiconductor superlattice coupled to the surface plasmon mode of a doped layer (Figure 3). In the figure, a semi-infinite superlattice is shown on the right side with periodicity a . On the left side, region 1, is a semi-infinite doped layer with electron density n_1 . The semi-infinite superlattice and doped layer are separated by a distance d in region 2. In region 3, the quantum wells of the superlattice are uniformly doped and have an equivalent two-dimensional electron density n_3 . The doped overlayer is treated classically and has a dielectric constant $\epsilon_1(\omega)$, which is explicitly a function of ω ; regions 2 and 3 have static dielectric constants ϵ_2 and ϵ_3 , respectively. In the following analysis, the superlattice, doped layer, and intervening region are assumed to have the same static dielectric constant. Again, there is no Guiliiani-Quinn [10] type surface mode.

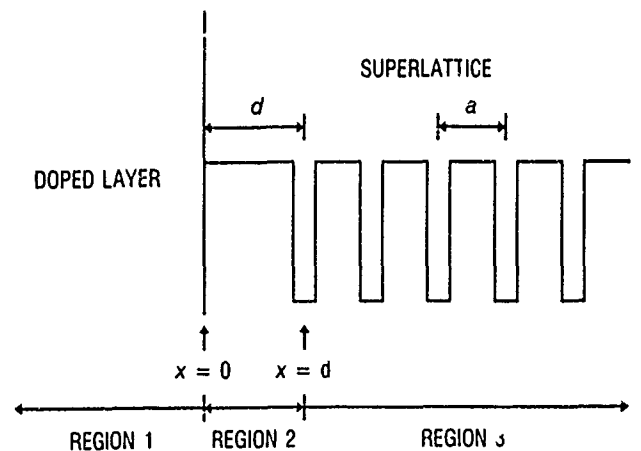


Figure 3 Superlattice of quantum wells with periodicity a separated by distance d from a doped layer.

However, because of the dynamic dielectric constant associated with the doped overlayer, interface plasmon modes can exist. In the theory and analysis given here, these local and interface plasmon modes are investigated for the three structures studied and demonstrate the rich plasmon energy dispersion that is obtainable.

In all cases, the wells are assumed to be far enough apart that wave function overlap is negligible. In addition, we specialize the model to the case where the quantum well widths go to zero, giving rise to an array of two-dimensional plasmon sheets. This model has been successfully used in the past for the eigenmodes of the infinite superlattice and semi-infinite superlattices [8-10]. The effect of finite well thickness on the plasmon dispersion relation of the superlattice was considered [11] and shown to be only a few percent correction to the zero-width results.

To find the interface plasmon excitations, one solves Maxwell's equations coupled to the density response of the two-dimensional electron sheets. The formalism outlined here is for the more general case of two superlattices, as shown in Figure 2. The other cases (Figures 1 and 3) follow directly from this approach. The density response to an applied potential is treated within the framework of linear response theory. For a p -polarized electromagnetic wave, the solution for the electric field in region 3 ($z > d$) must be of the following form in order to satisfy Maxwell's equations:

$$E_x = 0, E_y = e^{i(qy - \omega t)} (E_{3j}^+ e^{\beta_{3j} z} + E_{3j}^- e^{-\beta_{3j} z}), \quad (1)$$

$$E_z = -q\beta_{3j}^{-1} e^{i(qy - \omega t)} (E_{3j}^+ e^{\beta_{3j} z} - E_{3j}^- e^{-\beta_{3j} z}).$$

Similar equations apply in regions 1 and 2. Here, β_n is related to q by $\beta_n^2 = \epsilon_n \omega^2 / c^2 - q^2$, n refers to the specific region, and j labels the quantum well. The z -direction is along the superlattice; the x - and y -directions are perpendicular to the superlattice (along the quantum wells).

To solve for the interface plasmon modes of the coupled semi-infinite superlattices, we make the assumption of decaying solutions in regions 1 and 3 of the form

$$E_{1j}^+ = E_{1j}^{+*} e^{-\alpha_{1j} z}, \quad (2)$$

$$E_{3j}^{+*} = E_{3j}^{+*} e^{-\alpha_{3j} z}, \quad (3)$$

where α_1 and α_3 are the inverse decay lengths in the respective superlattices. Applying the continuity of the tangential component of the electric field and discontinuity of the normal component of the displacement vector by $4\pi\rho$ in region 3, where $\rho(j)$ is determined from linear response theory to be

$$\rho_3(j) = \frac{ie^2 \chi_3^0(q, \omega) (E_{3j}^+ + E_{3j}^-)}{q} \quad (4)$$

$\rho_3(j)$ and $\chi_3^0(q, \omega)$ is the susceptibility of the two-dimensional electron gas, results in eight equations that must be

solved simultaneously. In the random phase approximation (RPA) [12] and for $\omega \gg qv_F$, $\chi_3^0(q, \omega)$ is given by

$$\chi_3^0(q, \omega) = 2 \sum_p \frac{f_p + - f_p}{\epsilon_p + q - \epsilon_p - \omega} \equiv \frac{n_3 q^2}{m \omega^2}, \quad (5)$$

where the subindex on x refers to the specific semi-infinite superlattice and v_F is the Fermi velocity. The solution of these equations results in fourth-order equation for $x_3 = e^{\alpha_3 a}$, the inverse decay factor into the superlattice. The equation that results is too lengthy to be presented here. After obtaining x_3 , substituting into Eq. (6) gives the energy of the localized plasmon excitation. It is also necessary to solve for x_1 , since to have a physically acceptable solution (a decaying solution), one must show that both x_1 and x_3 are larger than +1 or less than -1:

$$\begin{aligned} \omega^2 &= (\omega_{p,3}^{2D})^2 \frac{\sinh(qa)}{\cosh(qa) - \cosh(\alpha_3 a)} \\ &= (\omega_{p,3}^{2D})^2 \frac{\sinh(qa)}{\cosh(qa) - \frac{1}{2}(x_3 + \frac{1}{x_3})}, \end{aligned} \quad (6)$$

where $\omega_{p,3}^{2D}$ is the single-well two-dimensional plasmon dispersion energy [12]

$$(\omega_{p,3}^{2D})^2 = \frac{2\pi n_3 e^2 q}{\epsilon_3 m}, \quad (7)$$

where n_3 is the two-dimensional density of the quantum well and q is directed along the superlattice axis (the z -direction). Identical equations are obtained for the superlattice plasmon 1, where every equation with subscript 3 is replaced with subscript 1. For the physically relevant case in which the dielectric constants are equal, the quartic equation can be simplified. In this limit, the quartic equation has two unphysical solutions for x_3 ; $x_3 = e^{qa}$ and $x_3 = e^{-qa}$. The quadratic equation that results can then be solved for x_3 , and subsequently, x_1 . Although the solution to the quadratic equation is trivial, the final equation for the roots is rather involved and is not explicitly given here. It is important to realize, however, that this constitutes an exact solution for these newly predicted localized excitations. In the following discussion, we present results for the localized and interface modes for the cases shown in Figures 1 through 3.

For the situation given in Figure 1, where one well has a different density n_0 , we plot in Figure 4 the local plasmon energy dispersion versus qa for n_0/n less than 1. Here, $n_0/n = 0.9, 0.5$, and 0.1 . In Figures 4 and 5 the regions between the dashed lines correspond to the energies of the continuum of the bulk plasmon states of the infinite superlattice. The energies are measured in reduced units of $\omega_0 = [4\pi(n/a)e^2/m\epsilon]^{1/2}$. The energies start at zero and increase in value asymptotically approaching the two-dimensional plasmon for the isolated well with density n_0 for large qa . The plasmon mode

is acoustic-like for small qa with velocity proportional to $(n_0/n)^{1/2}$. Localized plasmon modes are found that are centered at the $z = 0$ well, where the density discontinuity occurs. For the local plasmon mode, there is no critical value of qa below which it does not exist, as in the case for the surface plasmons of a semi-infinite superlattice.

For the situation given in Figure 2, where there are two distinct superlattices separated by a distance d , we plot in Figure 5 the plasmon dispersion for $\beta = n_3/n_1 = 2$ (the density of superlattice 3 is two times that of superlattice 1) versus qa for the separations $d = 0.01a$ and $0.4a$. We find the existence of two interface plasmon modes corresponding to the symmetric (higher-energy) and anti-symmetric (lower-energy) combination of plasmon eigenstates associated with each individual superlattice. The lower-energy mode is acoustic-like for small qa . The higher-energy mode does not exist for qa less than a critical value. The critical value for qa , below which the higher-energy mode ceases to exist, is $(qa)_{\text{crit}} = 0.97$ for $d = 0.01a$ and $(qa)_{\text{crit}} = 2.07$ for $d = 0.4a$. It should be noted that, as the separation d increases, so does the critical value of qa . For $d < 0.5a$ (not shown), both the upper- and lower-energy modes are very close to the continuum. For $d \approx 0.5a$, the upper mode ceases to exist. The lower mode ceases to exist for $d > 0.65a$. Similar low-lying acoustic modes are found for the situation given in Figure 3.

In all the preceding cases, we find a low-lying acoustic plasmon mode whose velocity can be significantly less than the electron saturation velocity. This indicates that these systems with localized/interface plasmons are excellent candidates to observe plasmon amplification. For example, for the localized plasmon mode of Figures 1 and 4, we find that the characteristic velocity of the acoustic mode is approximately $(n_0/n)^{1/2}$ times the electron saturation velocity. For $n_0 = 1 \times 10^{11} \text{ cm}^{-2}$ and $n = 1 \times 10^{12} \text{ cm}^{-2}$, this gives a plasmon velocity of $\approx 1/3$ the electron saturation velocity. In the GaAs system, it is experimentally easy to achieve drift velocities of this magnitude and, consequently, reach the critical velocity required for plasmon amplification.

In conclusion, we have predicted the existence of new localized and interface plasmon excitations in superlattice structures. These structures will allow plasmon amplification to occur. This was one of the major objectives established at the start of this project. The results of the past year's work coupled with those of the first 2 years of this project on the physics of electrons in quantum-confined structures constitute a major advancement in improving our understanding of plasmon excitations in superlattices [13-21]. This 3-year effort has established the theoretical base for plasmon excitations; this theoretical analysis proves the feasibility of obtaining plasmon instability and amplification of the plasmon modes in systems that exhibit localized acoustic plasmon modes.

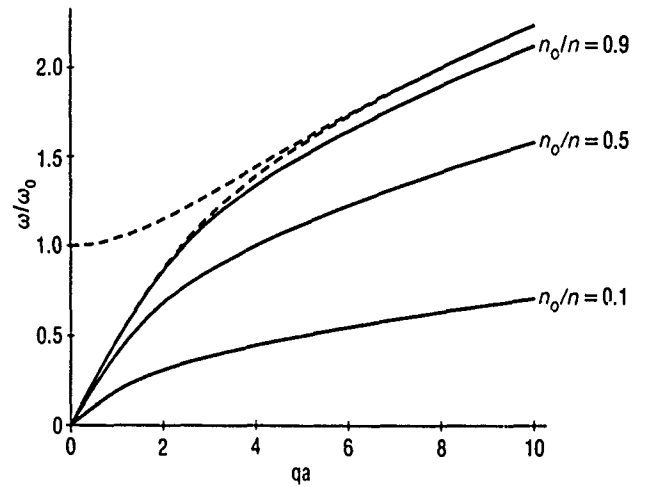


Figure 4. Local plasmon energy plotted vs qa for $n_0/n = 0.9, 0.5$, and 0.1 . The dashed lines correspond to the energies of the continuum of the bulk plasmon states of the infinite superlattice.

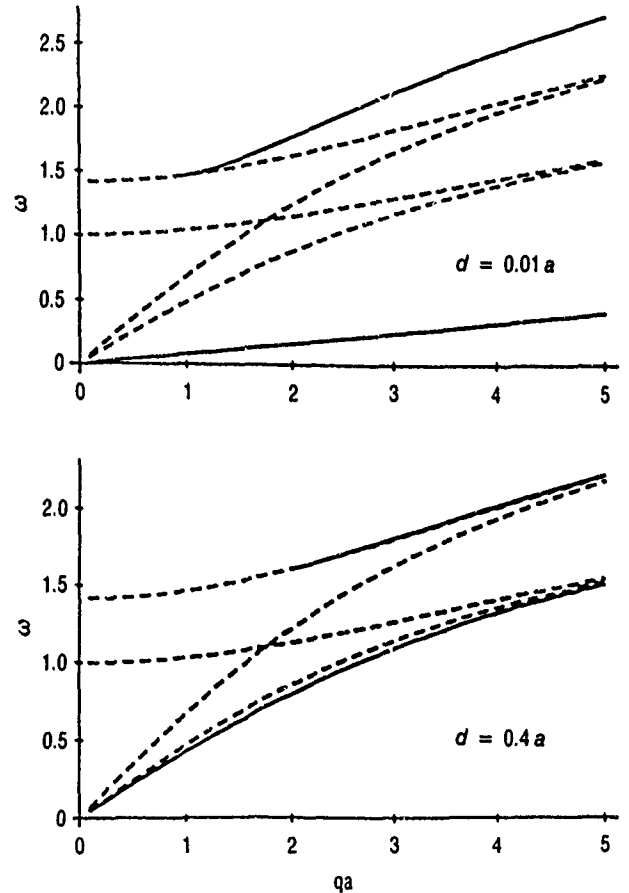


Figure 5. Interface plasmon energies plotted vs qa for $b = 2$ and separations $d = 0.01a$ and $d = 0.4a$. The dashed lines correspond to the energies of the continuum of the bulk plasmon states of the infinite superlattice.

1. D. A. B. Miller et al., "Electric Field Dependence of Optical Absorption Near the Band Gap of Quantum Well Structures," *Phys. Rev. B* **32**, 1043 (1985).
2. D. A. B. Miller, J. S. Weiner, and D. S. Chemla, "Electric Field Dependence of Linear Optical Properties in Quantum Well Structures: Wave-Guide Electroabsorption and Sum Rules," *IEEE J. Quantum Electron.* **QE-22**, 1816 (1986).
3. T. C. L. G. Sollner et al., "Resonant Tunneling Through Quantum Wells at Frequencies up to 2.5 THz," *Appl. Phys. Lett.* **43**, 588 (1983).
4. J. Khurgin, "Second-Order Susceptibility of Asymmetric Coupled Quantum Well Structures," *Appl. Phys. Lett.* **51**, 201 (1987).
5. W. L. Bloss and L. Friedman, "Theory of Optical Mixing by Mobile Carriers in Superlattices," *Appl. Phys. Lett.* **41**, 1023 (1982).
6. L. C. West and S. J. Eglash, *Appl. Phys. Lett.* **46**, 1156 (1985).
7. B. F. Levine et al., "New 10 mm Infrared Detector Using Intersubband Absorption in Resonant Tunneling GaAlAs Superlattices," *Appl. Phys. Lett.* **50**, 1092 (1987).
8. W. L. Bloss and E. M. Brody, "Collective Modes of a Superlattice - Plasmons, LO-Plasmons, and Magnetoplasmons," *Solid State Commun.* **43**, 523 (1982).
9. S. Das Sarma and J. J. Quinn, "Collective Excitations in Semiconductor Superlattices," *Phys. Rev. B* **25**, 7603 (1982).
10. G. F. Giuliani and J. J. Quinn, "Charge Density Excitations at the Surface of a Semiconductor Superlattice," *Phys. Rev. Lett.* **51**, 919 (1983).
11. W. L. Bloss, "Effects of Finite Layer Thickness on Superlattice Plasmons," *Surf. Sci.* **136**, 594 (1984).
12. F. Stern, "Polarizability of a Two-Dimensional Electron Gas," *Phys. Rev. Lett.* **18**, 546 (1967).
13. W. L. Bloss, "Electric Field Dependence of Quantum Well Eigenstates," *J. Appl. Phys.* **65**, 4789 (1989).
14. W. L. Bloss, "Density of States and Linewidths of Quantum Wells with Applied Electric Fields," *J. Appl. Phys.* **66**, 1240 (1989).
15. W. L. Bloss, "Resonant Enhancement of Quantum Well Linewidths by Pseudo-Barrier Energy Levels," *J. Appl. Phys.* **66**, 2481 (1989).
16. W. L. Bloss, "Energy Resonances of a Single Quantum Barrier," *Superlattices Microstruct.* **6**, 129 (1989).
17. W. L. Bloss, "Effects of Hartree, Exchange, and Correlation Energy on Intersubband Transitions," *J. Appl. Phys.* **66**, 3639 (1989).
18. W. L. Bloss, "Linewidths of Quantum Wells with Finite Barriers," *Superlattices Microstruct.* **7**, 63 (1990).
19. W. L. Bloss, "Electric Field Dependence of the Eigenstates of Coupled Quantum Wells," *J. Appl. Phys.* **67**, 1421 (1990).
20. W. L. Bloss, "Local Plasma Modes of a Semiconductor Superlattice," *J. Appl. Phys.* **69**, 3068 (1991).
21. W. L. Bloss, "Coupled Interface-Plasma Modes of a Superlattice and Doped Overlayer," *Phys. Rev. B* **43**, 4034 (in press).

Transition Dynamics and Guest-Host Interactions in Laser Materials

T. S. Rose,
Electronics Research Laboratory

Tunable solid-state laser devices will play an increasingly important role in the future areas of communication and remote sensing. For example, tunable communication sources will permit wavelength multiplexing for increased data rates; in the area of remote sensing, wavelength tunability will allow monitoring of specific atmospheric constituents. In general, for all space applications, solid-state lasers offer high peak and average powers, high efficiency, compactness, and the capability for generating short optical pulses. Consequently, there is a need for the development and improvement of solid-

state laser materials. The performance of these materials depends on the intrinsic properties of the active laser ions and the interaction between the ions and their crystal host environment. An understanding of these interactions is not only interesting from a scientific point of view, but is also crucial for the development of new laser media that will exhibit desirable characteristics such as long excited-state lifetimes, broad tunability, thermal stability, and resistance to external radiation damage. The objective of this research is to investigate potential tunable solid-state laser materials by studying dynamical processes and inter-

actions between laser ions ($\text{Ti}^{2+,3+}$, $\text{V}^{3+,4+}$, Cr^{3+}) and various host crystals (sapphire, YAG, and Forsterite). Time-resolved spectroscopic techniques will be used to study pertinent energy relaxation and transport processes in the materials of interest.

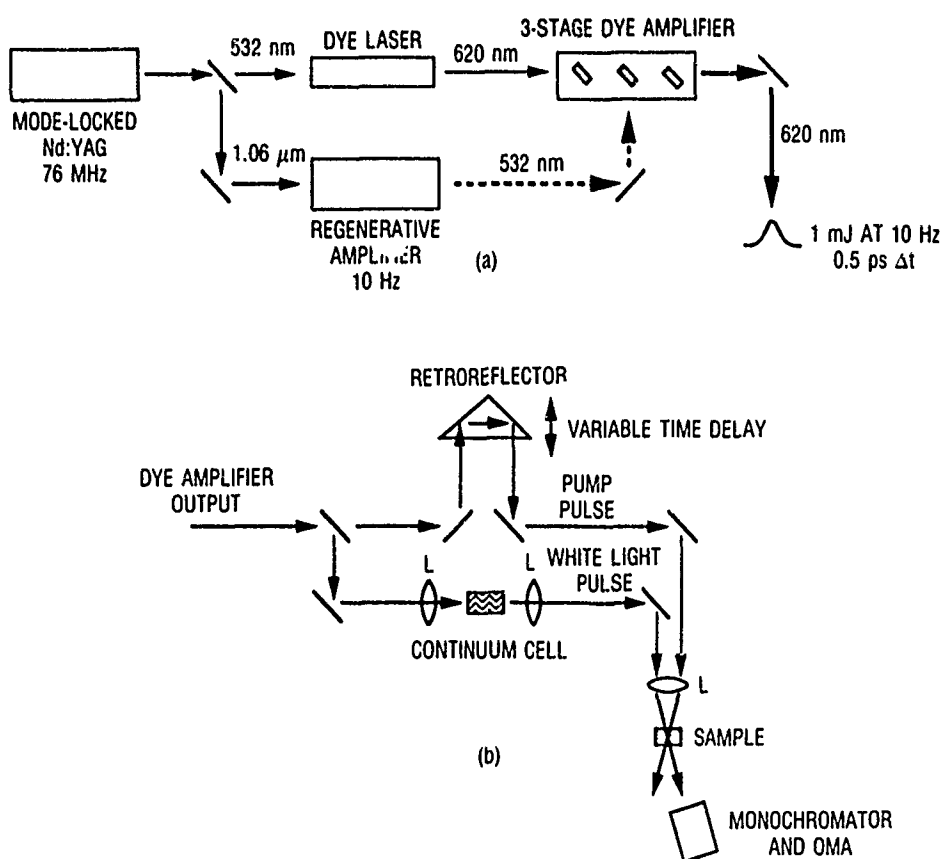
As part of this work, we are developing the capability to measure energy dynamics of laser materials in the time domain using a tunable laser system that will yield ultrashort (~ 100 fs) pulses. While this laser was being assembled, experiments were pursued with Dr. H. Lee at the Lawrence Livermore Laboratories. Dr. Lee's research efforts involve the study of divalent rare earth ions (such as Sm^{2+}) doped in fluoride crystals or glasses. Interest in these materials stems from the interaction between the 4f and 5d orbitals of the lowest excited-state manifold [1,2]. This mixing of states increases the oscillator strength between the ground state (which has a 4f electronic configuration) and the lowest excited-state manifold, thereby increasing the absorption of pump light that is resonant with this transition. In comparison, the absorption strengths of transition metal ions such as Nd^{3+} and Cr^{3+} are much weaker because the same relevant transitions are symmetry forbidden. Consequently, the potential efficiency of a divalent rare-earth ion laser systems may be greater than commercially available transition metal systems by virtue of their higher absorption.

The absorption strength of the laser material at the pump wavelength is not the only criterion for an efficient laser. A problem common to many laser systems is the

loss of laser emission through the depopulation of emitting states by nonradiative (phonon) processes or the absorption of laser photons by excited-state species. Our experimental efforts this past year have concentrated on exploring the latter effect. In particular, we have studied the time dependence of the excited-state absorption in $\text{Sm}^{2+}:\text{CaF}_2$, a system that has been shown to lase but has not been optimized [3,4]. This work allowed us to view the temporal characteristics of the absorption spectrum and provided insight regarding the time required to populate the upper metastable state of a lasing transition.

Subpicosecond transient absorption experiments are now being used to measure the excited-state dynamics of $\text{Sm}^{2+}:\text{CaF}_2$ as a function of the pump wavelength. The experimental arrangement is shown schematically in Figure 1. Pulses from a mode-locked Nd:YAG laser are used to pump a dye laser and (after amplification) a dye amplifier. The output pulses from the dye amplifier are then split into pump and probe pulses for the experiment, as indicated by Figure 1(b). The probe pulse is tightly focused into a D_2O cell in order to generate a broadband continuum (i.e., a white light source), whereas the pump pulse is directed along a variable delay line. The probe pulse has a fixed delay (not indicated in the figure) to ensure that it follows the pump pulse. Both pulses are recombined and focused into the sample, which is maintained at a fixed temperature in a liquid helium refrigerator. The transmission of the continuum pulse is measured as a function of the delay time between the pump and probe pulses. At

Figure 1. Experimental arrangement. (a) Schematic for the generation of short high-power tunable pulses. The doubling crystals for the conversion of the $1.06\text{ }\mu\text{m}$ fundamental to 532 nm have been omitted from the diagram; (b) schematic of the transient absorption experiment. The output pulses generated from the dye amplifier are split to form the pump and continuum pulses. Lenses (denoted by L) are used to focus the pulses into the D_2O continuum cell and for focusing the pump and probe continuum into the sample.



each given delay time, the entire transmission spectrum, over the wavelength range of the continuum, is recorded in a single shot with a monochromator and an optical multichannel analyzer (OMA). Typically, 200 shots are averaged together for each delay point.

Preliminary results for the transient absorption experiments at 13.6 K are given in Figure 2. In this particular experiment, the transmission intensity of the continuum pulse is detected with and without the presence of a pump pulse (I_p and I_u , respectively) that is tuned to 620 nm. In order to normalize for the spectral profile of the continuum and explicitly emphasize the difference between the excited-state and ground-state absorptions, the quantity $-\ln[(I_u - I_p)/I_u]$ is plotted as a function of wavelength. It can be readily shown that this quantity is related to the difference between the ground- and excited-state optical densities,

$$-\ln\left[\frac{I_u - I_p}{I_u}\right] = (\sigma_g^1 - \sigma_e^1)N_e^1(t)L + \sum_i \sigma_e^i N_e^i(t)L,$$

where σ_g and σ_e are the ground- and excited-state absorption cross sections, $N_e(t)$ is the time-dependent excited-state number density, and L is the length of the crystal. The superscripts 1 and i denote the initially pumped excited level and all other excited levels, respectively. Thus, the positive features in the spectra shown in Figure 2 result from excited absorption of the initial state 1 and from the other excited states i , whereas the negative features result from ground-state absorption.

The spectra in Figure 2 show the difference between the excited-state and ground-state optical densities for delays of 1 and 650 ps. At short times (on the order

of a few picoseconds), it is expected that only the initially excited level is populated. As the delay time between the pump and the probe continuum is increased (i.e., the probe arrives later in time), relaxation processes transfer population from the initial excited-state to other levels in the excited-state manifold. In the case of $\text{Sm}^{2+}:\text{CaF}_2$, the 620 nm pump excites the samarium ions from the 7F_0 ground-state (Figure 3) to $\sim 2000 \text{ cm}^{-1}$ above the upper metastable state of the lasing transition (708 nm). The broad excited-state absorption (positive feature in Figure 2) most likely results from transition to an upper-level conduction band. The overall decrease in intensity of the excited-state absorption in going from 1 ps to 650 ps of delay is indicative of the relaxation rate(s) of the system. The final destination of the excited-state population is the bottom of the d -band (i.e., the upper metastable lasing level), which has a radiant lifetime on the order of 2 μs .

Our efforts this past year have resulted in the development of a valuable analytic tool, a wavelength tunable laser capable of emitting ultrashort pulses. This system, coupled with the collaboration that has been established, should eventually lead to the optimization of tunable solid-state laser materials for use in practical laser systems. The experiments reported here have allowed us to observe relaxation of the population into the upper metastable lasing level of $\text{Sm}^{2+}:\text{CaF}_2$. Further experiments and theoretical modeling in this area are continuing in order to relate the time dependence of the excited-state population densities to the experimental results. Studies of the effects of the pump wavelength and temperature on the dynamics as well as comparative experiments with $\text{Sm}^{2+}:\text{SrF}_2$ are in progress.

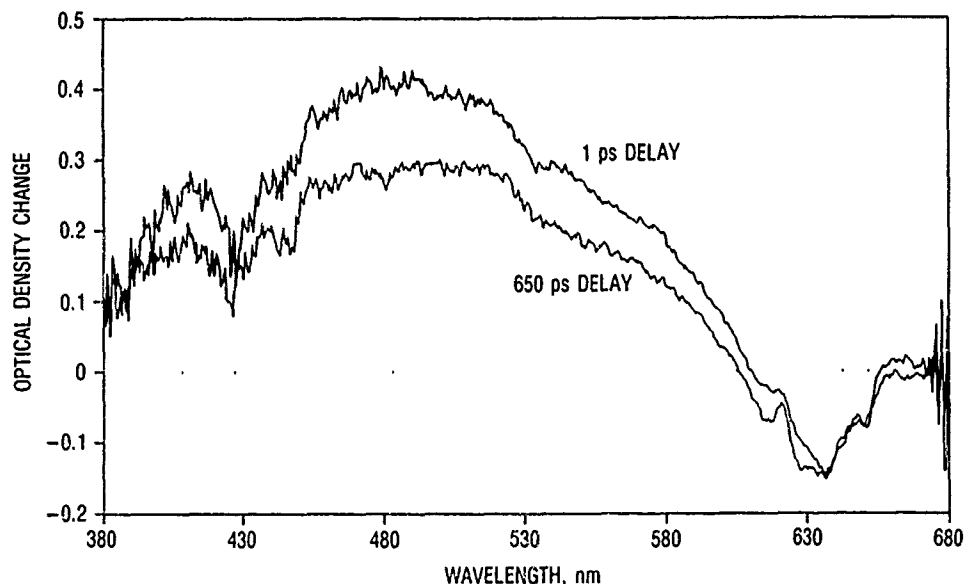


Figure 2. The normalized optical density change, $-\ln[(I_u - I_p)/I_u]$, vs wavelength for delay times of 1 and 650 ps.

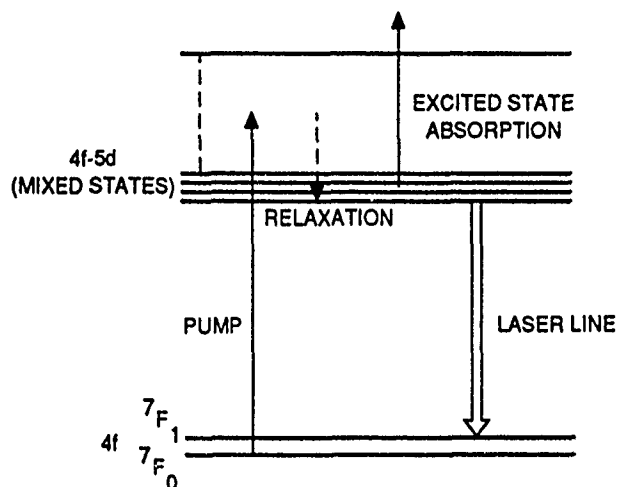


Figure 3. Simplified energy level diagram for $\text{Sm}^{2+}:\text{CaF}_2$. Absorption of the 620 nm pump creates population in some initial level of 4f-5d manifold. Fast relaxation processes put population into lower lying states resulting in a change in the excited absorption spectrum.

1. D. L. Wood and W. Kaiser, "Absorption and Fluorescence of Sm^{2+} in CaF_2 , SrF_2 , and BaF_2 ," *Phys. Rev.* **126**, 2079 (1962).
2. S. A. Payne, L. L. Chase, and W. F. Krupke, "Excited State Absorption of Sm^{2+} in SrF_2 and SrCl_2 ," *J. Chem. Phys.* **88**, 6751 (1988) and references therein.
3. P. P. Sorokin and M. J. Stevenson, "Solid State Optical Maser Using Divalent Samarium in Calcium Fluoride," *IBM J. Res. Dev.* **5**, 56 (1961).
4. W. Kaiser, C. G. B. Garret, and D. L. Wood, "Fluorescence and Optical Maser Effects in $\text{CaF}_2:\text{Sm}^{++}$," *Phys. Rev.* **123**, 766 (1961).

Deposition of High- T_c Superconducting Oxides

M. S. Leung, R. A. Lipeles, D. J. Coleman, and J. F. Kirshman,
Chemistry and Physics Laboratory;
R. C. Lacoë,
Electronics Research Laboratory

The objective of this project is to develop the knowledge and expertise needed to support the development of high-temperature superconducting devices for use in Space Systems Division programs. Our work focuses on two areas of investigation: the development of diffusion barrier layers for the high- T_c materials, and the preparation of device-quality high- T_c thin films.

The objective of our barrier layer work is to gain an understanding of the reactions of substrates and barrier layers with $\text{Y}_1\text{Ba}_2\text{Cu}_3\text{O}_{7-x}$ (YBC) leading to the integration of high-quality YBC films with semiconductor devices. Dielectric films, such as silicon dioxide (silica), and high thermal conductivity substrates, such as sapphire, are used in low-temperature, thin-film semiconductor devices. One of the challenges of making high-speed superconductor-semiconductor devices is the reactivity of YBC with those materials [1]. Simple barrier layers (such as zirconium dioxide films) have been used to decrease diffusion of barium into the substrate from the YBC film [2]. However, these films are not thermodynamically stable with respect to YBC, and diffusion can occur during subsequent high-temperature processing. This past year, we investigated barium silicate and barium aluminate barrier films on fused silica and sapphire substrates. Barium silicate forms glassy films, and barium

aluminate forms crystalline films. We examined the consequence of this difference on the morphology of the barrier film and its ability to restrict diffusion and reaction during the processing of YBC films using sol-gel processing.

Dense, compositionally uniform barrier layers and YBC films were made using sol-gel processing. In the sol-gel technique, a viscous coating solution is prepared through the formation of mixed metal oxide-organic polymers of yttrium, barium, and copper atoms linked together by metal-oxygen-metal bonds [3,4]. The coating solution is spin-coated onto a substrate and thermally annealed (from 500° to 900°C) to drive off the solvent and organics and form an oxide film. The results of our extensive work on the chemistry of the barrier layers and the substrate are summarized in Table 1.

YBC films were deposited by the sol-gel technique and annealed at high temperatures on barrier-layer coated substrates to compare crystalline (barium aluminate) and amorphous (barium silicate) boundary layers. Due to the poor adhesion of the barium aluminate film on silica and the reactivity of barium silicate on silica, extensive barium diffusion occurred from YBC films deposited on coated silica. The YBC films on both the barium sili-

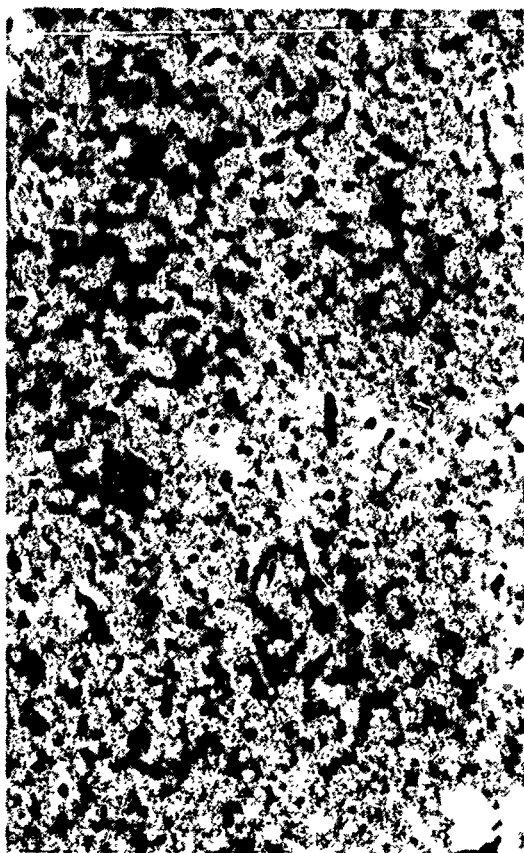
Table 1. Barrier Layer Films [4]

Substrate	Barrier Layer	Morphology/Structure	Interface
Sapphire	Barium aluminate	Smooth/oriented	Abrupt
Sapphire	Barium silicate	Smooth/amorphous	Abrupt
Silica	Barium aluminate	Spalling/crystalline	
Silica	Barium silicate	Smooth/amorphous	Diffused

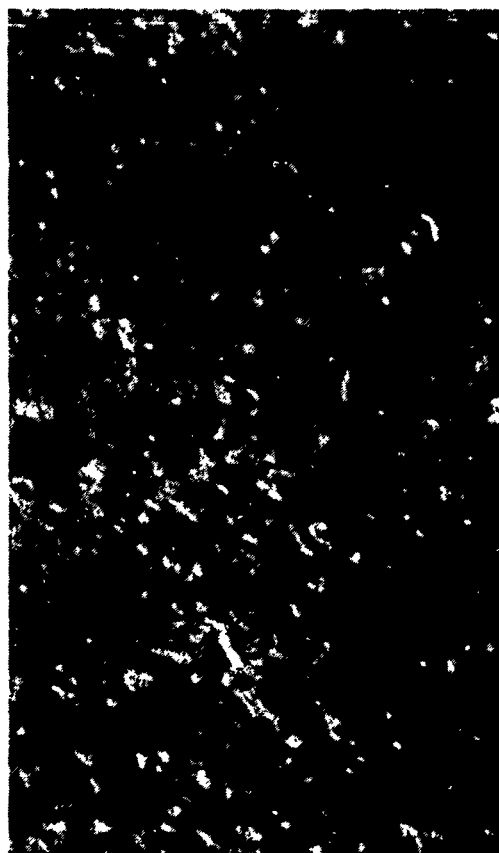
cate-on-sapphire and barium aluminate-on-sapphire had similar morphology (Figure 1). Both films were porous and fine-grained and had the *c*-axis oriented parallel to the substrate. However, the structure of the interface was different for the two barrier layers (Figure 2). The barium silicate layer reacted with YBC, forming several barium-

deficient silicate compositions that are more stable than YBC. The formation of these silicates changed the stoichiometry of the YBC layer, as shown by the nonuniform stoichiometry of the YBC layer in the depth profiles of the barium and yttrium in Figure 2(a).

The oriented, crystalline barium aluminate was effective in reducing barium diffusion into the substrate and in providing a uniform YBC film. The elemental depth profiles plotted in Figure 2(b) show a uniform stoichiometry of barium and yttrium in the YBC layer, demonstrating the suppression of barium and yttrium diffusion out of the YBC. The stoichiometry of the YBC film was the same as that found for YBC deposited on the non-reactive strontium titanate substrates. The proper stoichiometry of both the metals and oxygen is essential for superconductivity. Although the proper stoichiometry of the metals was obtained, the YBC film on the barium aluminate layer did not superconduct because the thermal processing was not optimized for the proper oxygen stoichiometry and crystal orientation. These samples were intentionally heated to high temperatures (at least 900°C)



(a)



(b)

1 μm

Figure 1. Electron micrographs of YBC films with similar morphology deposited on (a) barium silicate-on-sapphire and (b) barium aluminate-on-sapphire.

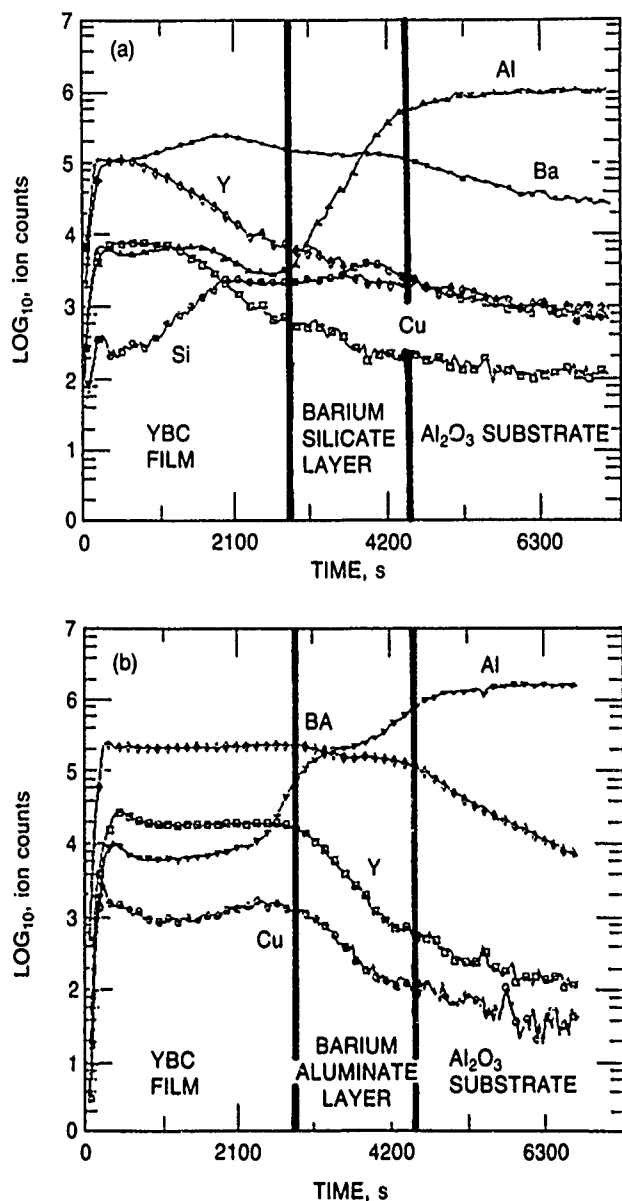


Figure 2. Depth profiles obtained of a nonstoichiometric YBC layer (a) when YBC is deposited on barium silicate-on-sapphire and a uniform layer of YBC with the proper stoichiometry (b) when YBC is coated on barium aluminate-on-sapphire.

as a severe test of the diffusion barrier. Optimization of the oxygen stoichiometry and thermal annealing will result in high-quality superconducting films. The development of the barrier layer is a key element in the integration of high-temperature superconducting materials with the present semiconductor technologies.

Substantial progress has been made in the fabrication of device-quality high- T_c thin films by the laser deposition technique. A series of experiments was conducted to examine systematically the effects of various deposition parameters such as laser power, residual oxygen pressure, and substrate temperature on film quality. Results of our

work indicate that laser power and oxygen pressure in the deposition chamber affect the smoothness of the films. High laser power and low oxygen pressure produce films that are rough. Under these conditions, large clusters of the YBC material are ablated from the target and deposited on the substrate. Lowering the laser power and increasing the oxygen pressure reduces the size of the clusters formed, and the resultant films are smooth. Our results further indicate that the substrate temperature has the strongest influence on the crystal structure and the electrical properties of the films.

The crystal structure of the YBC superconducting oxide is orthorhombic. As a result, superconducting YBC thin films tend to nucleate into two distinct morphologies: one with the c -axis of the orthorhombic crystal oriented perpendicular to the substrate surface, and the other with the c -axis parallel to the surface, which is called the a - b phase. The former gives rise to highly oriented films with electrical properties (high superconducting transition temperatures) superior to those of the a - b phase-dominated films. The highly c -axis-oriented films are the most desirable for device fabrication. Scanning electron microscopy and x-ray diffraction analysis of films deposited at substrate temperatures below 600°C show large amounts of the undesirable a - b phase. The transition temperatures of these films are low, about 75 K. Starting at a substrate temperature above 600°C, the c -axis-oriented phase begins to dominate and the transition temperature increases. Our work also showed that uniform heating of the substrate during deposition is critical to achieving high-quality superconducting thin films. Several materials were investigated for promoting heat transfer from the heating block to the substrate. Silver paste was found to be the most promising. The best films we made were deposited at a substrate temperature of 650°C with silver paste as the heat transfer coupling material. The resistance-versus-temperature plot shows a sharp transition temperature onset at about 91 K and a very narrow transition region with zero resistance at 88 K (Figure 3). These results compare favorably with the best reported in the literature. Scanning electron microscope examination of these films revealed the films to be mostly c -axis-oriented with only a small amount of a - b phase, which, we believe, can be eliminated by the use of better-quality substrate materials and more uniform heating of the substrate.

In summary, we have achieved our project objective to develop an understanding and expertise to support the deployment of devices based on the high-temperature superconducting materials. The barrier layers we developed will be useful for the integration of the high- T_c materials with existing semiconductor technologies. The films we made by laser ablative deposition are of a quality suitable for device fabrication.

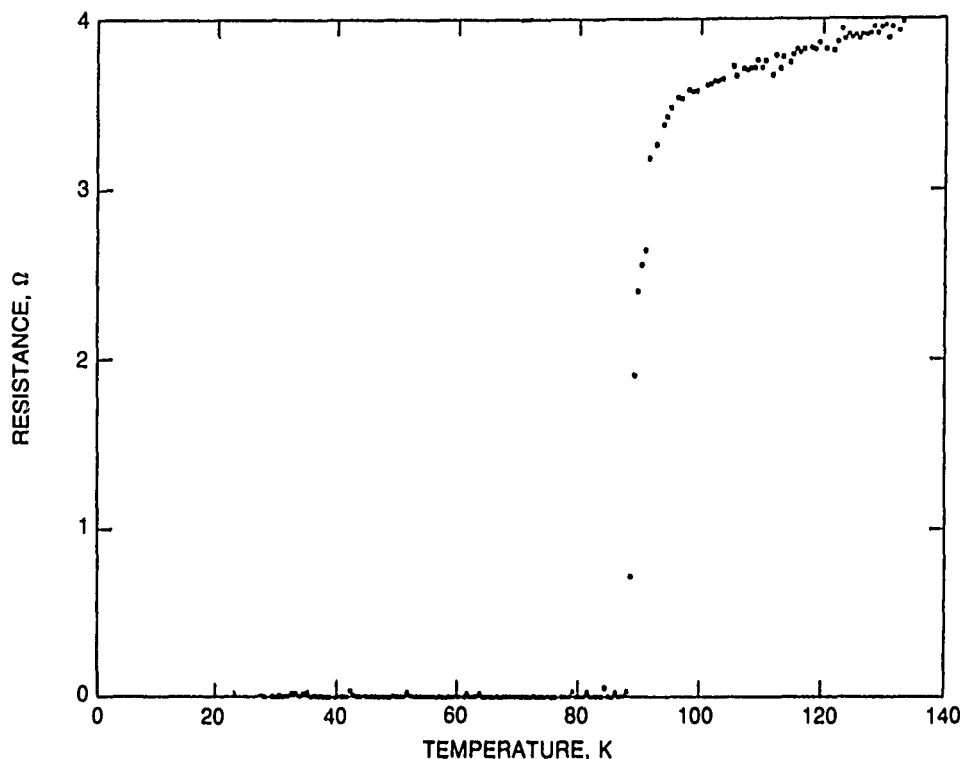


Figure 3. Resistance vs temperature plot of an Aerospace device-quality film prepared by laser ablative deposition. A sharp transition temperature onset at about 91 K is shown, as well as a narrow transition region of about 3 K and zero resistance at 88 K.

* * * * *

1. T. Komatsu et al., "On the Reaction of Quenched BaYCuO Powders with Various Materials," *Jpn. J. Appl. Phys.* **27** (6), L1025-L1028 (1988).
2. A. Mogro-Campero and L. G. Turner, "Thin films of Y-Ba-Cu-O on Polycrystalline Sapphire," *Supercon. Sci. Technol.* **1**, 269 (1989).
3. R. A. Lipeles et al., "Hydrolysis of Methoxyethoxide Coating Solutions for $Y_1Ba_2Cu_3O_{7-x}$ Films," *J. Non-Cryst. Mater.* (in press).
4. R. A. Lipeles, D. A. Thiede, and M. S. Leung, "Barium diffusion in Metallo-Organic Solution Deposited Barrier Layers and $Y_1Ba_2Cu_3O_{7-x}$ Films," *Proc. SPIE* **1287**, 206 (1990).

Characterization of Radiation Damage in Solids

R. A. Fields,
Electronics Research Laboratory

The growth of space applications for optical devices has generated a renewed interest in their radiation sensitivity. Several early studies [1,2] carried out on a flashlamp-pumped neodymium doped yttrium aluminum garnet (Nd:YAG) solid-state laser suggested that its performance could be significantly affected by the radiation environment encountered in orbit. More recently, a similar investigation conducted in the Electronics Research Laboratory on the radiation sensitivity of a semiconductor diode-laser-pumped Nd:YAG laser revealed that the laser was only moderately affected. The ambiguity raised by these two studies is indicative of the complex ways in which radiation effects can impact a system's overall per-

formance. More specifically, in the case of Nd:YAG, it is unresolved whether radiation-induced performance effects result from gain depletion, pump absorption loss, or increased optical loss at the lasing wavelength. It is also unclear whether or not flashlamp pumping photochemically enhances the creation of deleterious effects through excited-state absorption in the irradiated laser crystal. This new research program segments the problem into more elemental steps. The past year's study concentrated on developing a combined optical and magnetic capability for spectroscopically characterizing radiation-induced defect sites in the isolated laser crystal. Subsequent

efforts will correlate performance observables to the systematically created and assigned radiation defects.

The Nd:YAG laser crystal is an appropriate material for initiating such a detailed study. Nd:YAG is the most widely used solid-state laser material and is currently baselined for several long-term space missions. The optical properties of the material have been well-characterized by several research groups. The material is naturally prone to a number of nonequivalent crystal field (NCF) sites, depending on the crystal growth process. Through years of development, growth processes have been refined to produce crystals with Nd^{3+} predominantly confined to the high quantum efficiency lasing site. The f electronic transitions of rare earth ions, such as Nd^{3+} , are weakly coupled to the lattice and strongly spin-orbit split compared with the transition metal ions. Thus, the Nd^{3+} optical transitions in crystals are sharp line-like spectra. At low temperatures, the natural NCF sites of Nd:YAG give distinctly resolved fluorescence lines, as demonstrated by Devor, DeShazer, and Pastor [3]. In addition, the highly localized magnetic moment of the ion can be used as a probe of the local environment through dipole-dipole interactions with yttrium, aluminum, or contaminant protons [4].

The initial phase of this study has focused on gaining an understanding of the susceptibility of diode-laser-pumped Nd:YAG lasers to radiation performance degradation. Diode-laser-pumped Nd:YAG lasers have evolved as the system of choice for space-based lasers because of their high efficiency. The diode lasers can confine the pump wavelengths to a 4-nm bandwidth centered around the 808.5-nm absorption line of Nd^{3+} . We have observed that, at room temperature, a typical Nd:YAG (1.0 at. % Nd^{3+}) crystal will have an absorption coefficient of 5.1 cm^{-1} for a laser diode. An energy level diagram for the Nd:YAG crystal with the relevant processes is shown in Figure 1. The diode laser excites the Nd^{3+} ions into the $4F_{5/2}$ multiplet, from which they rapidly and efficiently relax into the lower energy $4F_{3/2}$ state. From this metastable state, the laser ion will emit preferentially from R_2 to the various $4I$ multiplets; the strongest transition is to one of the $4I_{11/2}$ sublevels at $1.064 \text{ }\mu\text{m}$.

This past year, our principal effort focused on developing an experimental capability for variable temperature (1.5–300 K), high resolution optical and magnetic spectroscopy. The excitation source for these experiments is a narrow-linewidth ($< 0.02 \text{ nm}$) Ti:sapphire laser, which is capable of simulating a diode laser pump, but with more spectral control. This laser is computer-controlled and can either be locked to a specific wavelength or scanned as required. The sample space is contained within a helium cryostat at the center of a highly homogeneous split-pair superconducting magnet (0–6 T) (inhomogeneity of order 1 part in 10^4 over 1 cm). The detection system consists of a high-resolution ($\Delta\lambda = 0.02 \text{ nm}$) spectrometer and a photon counting system.

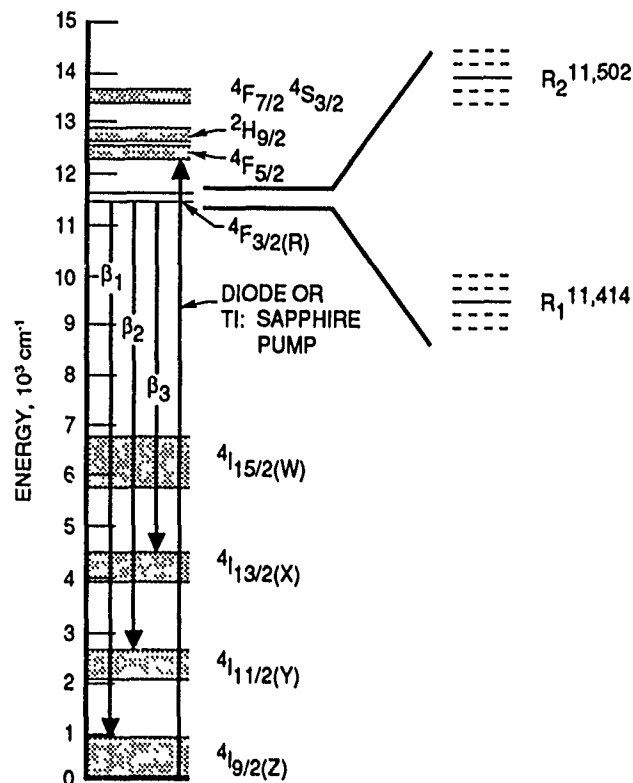


Figure 1. Nd:YAG energy levels. Overall Stark splitting of the various levels is labeled by their J quantum numbers. The transitions labeled β_i refer to the principal laser transitions at 0.95, 1.06, and $1.31 \text{ }\mu\text{m}$, respectively. The metastable R_i levels are ideally single-energy levels at zero magnetic field. The dashed levels refer to defect sites.

As a precursor to spectroscopic identification of radiation defect sites, one must first characterize the naturally occurring defects. Devor, DeShazer, and Pastor [3] observed a variety of spectral defects that could be correlated to particular crystal growth methods. The various defect sites are a result of local impurities (contaminant ions or missing ions) in the crystal lattice. The radiative efficiencies can vary greatly depending on the nature of the defect site. The most resolved transitions in Nd:YAG are those from the metastable $4F_{5/2}$ (R_i) to the ground $4I_{9/2}$ multiplet (Z_i). With the Ti:sapphire laser tuned to the maximum absorption (808.5 nm) in the $4F_{5/2}$ state of a Czochralski-grown Nd:YAG (1 at. %) crystal, we measured the low-temperature $R_1 \rightarrow Z_1$ fluorescence spectrum shown in Figure 2. Except for the main feature at 874.98 nm (this line corresponds to the site in the crystal at which the principal efficient lasing occurs), our spectrum differed considerably from that of Devor, DeShazer, and Pastor [3]. By changing the excitation wavelength, the spectrum in Figure 2 can be modified in two ways: by adding or subtracting spectral lines, or by changing the relative spectral intensities. Additional spectral lines correspond to different sites for Nd^{3+} in the host. Their spectral appearance depends both on their relative absorption wavelengths and radiative efficiencies. It has become

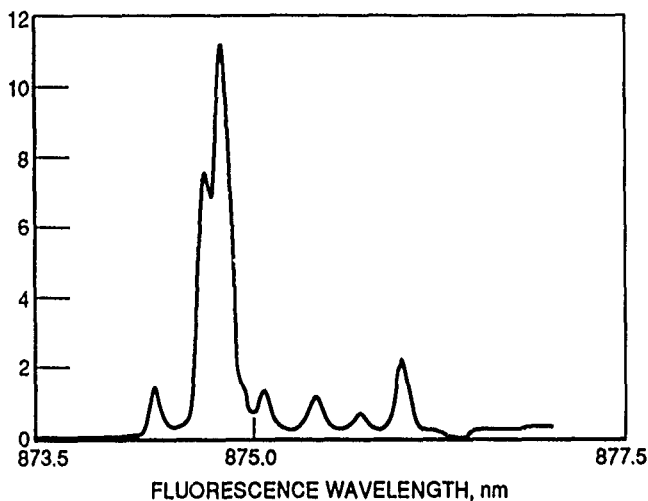


Figure 2. Fluorescence spectrum of $R_1 \rightarrow Z_1$ transitions in Nd:YAG at 2 K with a Ti:sapphire pump wavelength of 808.65 nm.

clear from this preliminary study that a more effective defect characterization for a particular sample would entail a series of fluorescence spectra as a function of pump source wavelength (preferably a broadband source such as a laser diode that emits simultaneously over several spectral lines). The three-dimensional spectrum that results could be correlated to laser efficiency comparisons.

To gain some preliminary experimental experience and insight into the nature of radiation defects in Nd:YAG, we subjected the aforementioned crystal to 600 krad gamma radiation from a ^{60}Co source. Our earlier study indicated that diode-laser-pumped Nd:YAG laser performance is degraded by 37% under identical irradiation conditions. Spectral modification of the sample is not clearly evident from the $R_1 \rightarrow Z_1$ spectrum of the irradiated sample displayed in Figure 2. Except for the disappearance of a small line at 875.7 nm the spectra are nearly identical. A somewhat more illuminating experiment is a comparison of the $R_1 \rightarrow Z_1$ transition spectrum at high magnetic field (3.62 T) both before and after irradiation. The magnetic field lifts the combined \pm spin degeneracies for the F_1 and Z_1 states. This Zeeman splitting is clearly resolved in the high-field unirradiated spectrum in Figure 3(a). In contrast, the spectrum of the high field irradiated sample, Figure 3(b), shows considerable intensity at 878.5 nm. A change in the spectrum such as this indicates that some of the sites have experienced a reorientation of the anisotropic Zeeman interaction or a change in its magnitude. This could result from subtle local distortions, which modify the principal axes of the spin-spin interactions of the high-efficiency laser ion site without substantially modifying the transition energy. Such an effect could impact the emission cross section by affecting the transition strength. This preliminary result will require additional investigation in order to make a more definitive conclusion, but it clearly indicates

that the techniques are promising tools for developing an understanding of the underlying causes of radiation damage.

In summary, we have demonstrated high-resolution fluorescence spectra from Nd:YAG at 1.5 K and 3.62 T. The high-field Zeeman spectra indicate some laser ion site distortions that result from irradiation with 600 krad gamma irradiation. Next year, we will attempt to substantiate some of these early results by still more detailed experiments. More resolution can be obtained in the optical spectra by using a fluorescence line-narrowing technique developed in earlier company-sponsored work [5]. The development of the optically detected electron paramagnetic resonance capability will permit unequivocal assignment of defect centers within the main optical band and also provide insight into the environments of the naturally

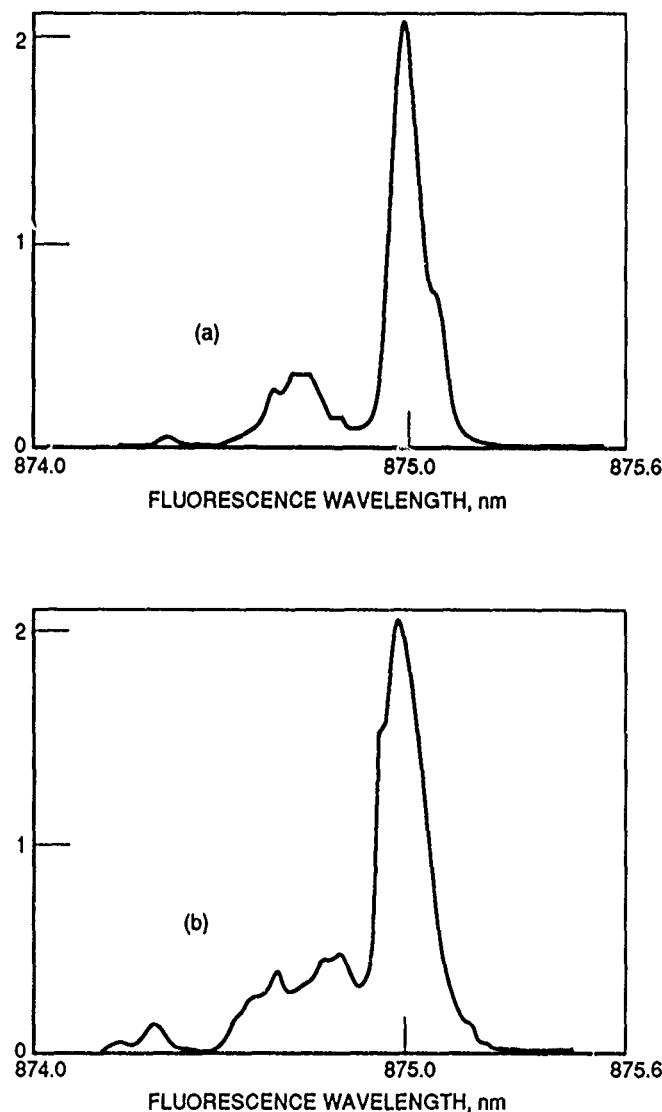


Figure 3. Fluorescence spectrum of $R_1 \rightarrow Z_1$ transitions in Nd:YAG at 2 K with a Ti:sapphire pump wavelength of 808.65 nm and in a magnetic field of 3.62 T. (a) Before irradiation; (b) after irradiation with 600 krad ^{60}Co gamma rays.

occurring defects. The spectroscopic identification process will be correlated to a variety of end pump laser observables, such as absorption, loss, and slope efficiency.

* * * * *

1. J. Halpin, *The Transient Radiation Effects on Laser Materials*, NRL-MR-2155, AD 511181, Naval Research Laboratories, Washington, D.C.
2. D. Compton and R. A. Cessna, *Mechanisms of Radiation Effects on Lasers*, *IEEE Trans. Nucl. Sci.* **NS-14**, 55 (1976).

3. D. P. Devor, L. G. DeShazer, and R. C. Pastor, "Nd:YAG Quantum Efficiency and Related Radiative Properties," *IEEE J. Quantum Electron.* **25**, 1863 (1989).
4. C. A. Hutchison, Jr., and D. B. McKay, "The Determination of Hydrogen Coordinates in Lanthanum Nicotinate Dihydrate Crystals by Nd^{3+} -proton Double Resonance," *J. Chem. Phys.* **66**, 3311 (1977).
5. R. A. Fields, "Investigations of Ti^{3+} in Laser Hosts," *Aerospace Sponsored Research Summary Report, Scientific and Engineering Research*, ATR-88(8498)-1, The Aerospace Corp. (1 December 1988), p. 47.

Indium Phosphide Photovoltaic Technology

L. F. Halle and D. C. Marvin,
Chemistry and Physics Laboratory

Two of the more important factors in sizing a solar array for a spacecraft are the efficiency of the solar cells used and their tolerance to irradiation by the electrons and protons of the natural environment. Typical silicon cells have efficiencies of about 13 to 14%, whereas the efficiencies of more advanced cells made of III-V materials such as GaAs and InP are in the 20% range. An additional, important advantage of InP technology is that solar cells made of this material have been shown not only to be more resistant to radiation damage, but that the damage that is incurred has been reported to anneal at low temperatures. The objective of this study is to develop an understanding of the radiation damage and annealing processes that occur in InP by studying the induced defects by electronic and spectroscopic means.

We have been using deep-level transient spectroscopy (DLTS) to measure the energy levels and concentrations of defects in electron-irradiated InP. InP diodes with a unique type of crystalline organic contact were fabricated at the University of Southern California. These contacts permit probing of defects in the bulk material without complications that can arise from a diffused or metal Schottky junction [1]. Both *n*-type and *p*-type diodes were irradiated at the Jet Propulsion Laboratory. Figure 1 shows a typical DLTS spectrum for the first *n*-type chip, which was irradiated with a fluence of 1×10^{16} electrons/cm² at an energy of 1 MeV. Four trap levels are observed. Energy levels, concentrations, and cross sections are given in Table 1. In general, the literature reports six traps [2,3]. The lesser number we detect may be due to the nonperturbing nature of the organic contact. The traps at 0.65 and 0.42 eV have been noted

previously in the literature for both Schottky and junction diodes.

Because only one diode on this chip survived the repeated probing necessary for the DLTS data, a second *n*-type chip was prepared to enable us to make annealing measurements. Four traps were also noted on these samples, and a comparison of the DLTS spectra at the same conditions is shown in Figure 2. The energy and concentrations of these traps differed somewhat from the first sample for unknown reasons, since both were made from the same lot of InP. Due to equipment problems, the second chip had to be reworked twice before the final diodes were processed. It may be that the surface of the InP is very sensitive to the surface preparation techniques and that the changes in trap states reflect this. This will be further investigated with a third set of samples to be processed. The samples now on hand will be used for annealing studies.

The first *p*-type sample, like the *n*-type samples, was irradiated with a fluence of 1×10^{16} electrons/cm². Current versus voltage characteristics of the device were measured before and after irradiation. The irradiated device no longer shows diode behavior, but rather looks almost like a resistor of very high resistance ($\sim 10^8 \Omega$). No meaningful DLTS data can be obtained with such a device. This diode was annealed at 60°C and checked after a number of time intervals. After 5 h, no change was noted, but after 7 h, the diode characteristics had returned. DLTS measurements were taken on the annealed devices, but no trap levels were observed. This might be because all the traps had now been annealed, although from literature reports, this appears unlikely. Annealing

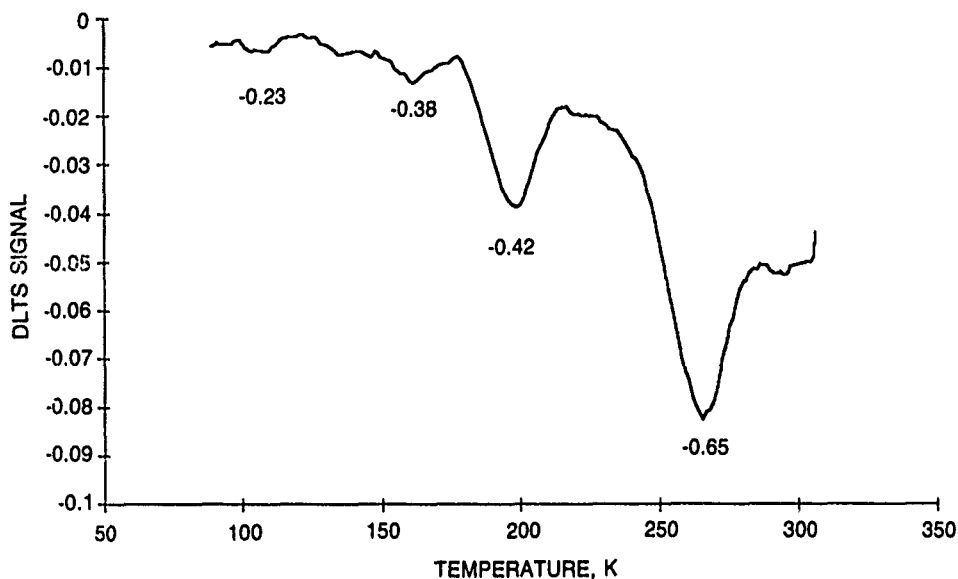


Figure 1. Typical DLTS spectrum of first set of n-type diodes. Rate window is 21.5 ms.

Table 1. Results of Irradiation of n-Type InP Diodes

Energy, ev	Concentration, cm^{-3}	Cross Section, cm^2
-0.23	5×10^{12}	5.4×10^{-13}
-0.38	6×10^{12}	1.2×10^{-12}
-0.42	2×10^{13}	5.4×10^{-13}
-0.65	6×10^{13}	1.1×10^{-13}

studies of *p*-InP solar cells do not show a complete recovery of the device, but rather a saturation of the power gain at long annealing times [4]. This *p*-type sample was then reirradiated with a much lower fluence level of 1×10^{15} electrons/ cm^2 . Once again, after irradiation the diode characteristics disappeared and a resistor-like behavior was observed. This was unexpected, since prior studies

noted only moderate damage at this fluence with samples that had a background concentration similar to our samples [4]. It is unclear if the behavior we observe is due to the presence of the organic contact, and if so, whether the contact itself is degrading or whether it is inducing changes in the InP surface, which then heal. These devices will be annealed again, but with shorter time intervals to determine if a state can be found in which traps can be observed. If this is not successful, we will fabricate samples with a metal Schottky junction to investigate whether we observe the same problems on diodes made with a different type of contact.

These unexpected results have delayed our studies of the annealing behavior of the radiation-induced defects under heating or current injection, or both. We wish to compare the changes in defect concentration observed by DLTS with changes in minority carrier lifetimes that will be measured with transient photoluminescence (TPL).

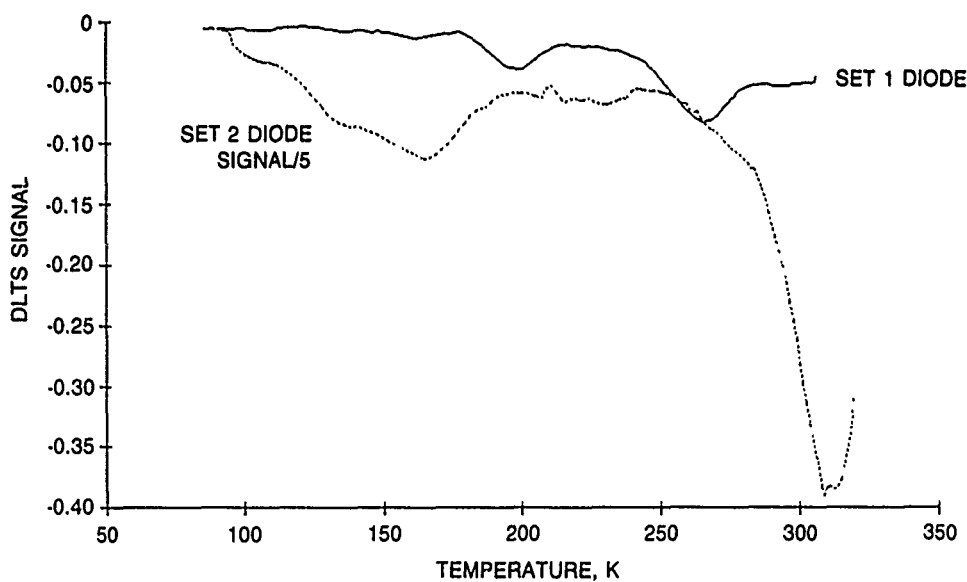


Figure 2. Comparison of DLTS spectra of first set (solid curve) and second set (dashed curve) of n-type diodes. The signal for the diode from the second set of samples has been reduced by a factor of 5. The rate window in both cases is 21.5 ms.

For the TPL measurements, a high resolution monochromator and a fast infrared detector have been integrated into our TPL facility.

In summary, we have irradiated both *n*-type and *p*-type InP diodes. DLTS spectra have been obtained for the *n*-type diodes, but the *p*-type devices lose their diode characteristics, even after mild irradiation. The diode characteristics return upon annealing. These results are not what had been expected and we are investigating their causes. In the meantime, annealing studies of the *n*-type diodes and TPL measurements will begin.

* * * * *

1. S. R. Forrest et al., "Evaluation of III-V Semiconductor Wafers Using Non-Destructive Organic-on-Inorganic Contact Barriers," *J. Appl. Phys.* **57**, 2892 (1985).
2. P. R. Tapster, P. J. Dean, and M. S. Skolnick, "Deep Levels Introduced by Electron Irradiation of InP," *J. Phys. C: Solid State Phys.* **15**, L1007 (1982).
3. M. Levinson et al., "Defect States in Electron Bombarded n-InP," *Appl. Phys. Lett.* **40**, 990 (1982).
4. M. Yamaguchi and K. Ando, "Mechanism of Radiation Resistance of InP Solar Cells," *J. Appl. Phys.* **63**, 5555 (1988).

Optics

OPTICS

Magnesium Atomic Filter for Submarine Laser Communications

J. A. Gelbwachs and Y. C. Chan,
Chemistry and Physics Laboratory

The Navy has a strong interest in the development of a satellite-based submarine laser communications (SLC) system. The system will use laser transmitters emitting in the blue-green spectral region for maximum ocean penetration. However, sunlight interferes with detection of the narrowband signal light. To discriminate against the solar background, ultranarrowband (0.01 Å) filters at the receivers are required. Atomic resonance filters [1] have been recognized by the Navy as a promising technology for solar background rejection.

Atomic filters operate at numerous discrete wavelengths throughout the near ultraviolet, visible, and infrared spectral regions [1]. Laboratory exploration of atomic filtering action has been conducted on cesium [2] and rubidium ground-state species, and optically pumped transitions in rubidium [3], thallium-cesium [4], and potassium [5].

In this project, we are developing atomic filters that transmit less sunlight than any other known atomic filters. The superior performance arises due to an overlap of the filter's passband with a Fraunhofer dip. Fraunhofer dips are solar background minima due to absorption in the outer layer of the sun by atomic species. They form natural low-background passbands for atmospheric laser communications.

In previous work in this project, we demonstrated the first Fraunhofer-wavelength atomic filter [6]. It was based on the spectroscopy of the triplet levels in magnesium and operated at three wavelengths near 518 nm. Our objective for this past year, the final year of this activity, was to develop Fraunhofer-wavelength atomic filters at different blue-green wavelengths in order to expand the wavelength options for underwater communications.

The energy-level diagram for a typical atomic vapor is shown in Figure 1. Signal photons at λ_s are absorbed between levels 1 and 2. The population is then trans-

ferred to another level depicted as level 3 in the diagram. This wavelength-shifting process is shown by the broken arrow. Emitted light at λ_0 serves to monitor the absorption of signal photons. The absorption of signal light may originate from the ground level or an excited state. If an excited state is used, as depicted in Figure 1, a low-power laser at λ_p is present to create the required population in level 1 in order to absorb signal photons.

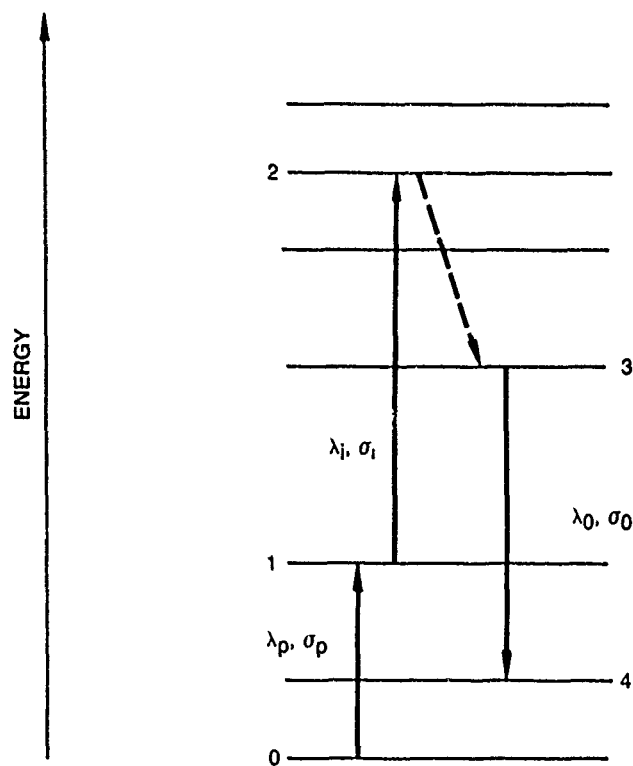


Figure 1 Energy-level diagram for a typical atomic vapor used for atomic filtering.

Table 1. Promising Blue-Green Atomic Filter Concepts

Property	Active	Passive	Metastable
Signal wavelength, nm	422.7	422.7	534.9
Output wavelength, nm	272	657	423, 586
Internal photon conversion efficiency, %	90	25-100	65
Response time	60 ns	~1 ms	15 ns
Doppler width, Å	0.012	0.012	0.015
Fraunhofer advantage, dB	16	16	5
Pump wavelength, nm	672		458

A systematic study was undertaken to discover new atomic filters. First, we identified methods that could be used to shift signal light into a different spectral band suitable for detection. Then, we developed photophysical models for these techniques that allowed quantitative assessment of the efficiency of the internal photon conversion process. Finally, we applied the models to real atomic systems to identify promising atomic filtering concepts.

It was determined that collisional energy transfer with an inert buffer gas was useful for population transfer between levels that were separated by less than 1000 cm^{-1} . Above 1000 cm^{-1} , optical pumping with low-power continuous-wave lasers could be used. Furthermore, both processes could be applied simultaneously to achieve greater wavelength-shifting flexibility.

Our photophysical models identified three spectroscopic parameters that govern the efficiency of conversion of signal photons to output photons, $\eta\phi$:

- The ratio of the Einstein A coefficient of the emitting level to that of the signal level.
- The degeneracy ratio of the two levels.
- The energy separation between levels that are collisionally coupled.

Our models indicate that in order to maximize $\eta\phi$, one seeks a large Einstein A coefficient ratio, a large degeneracy ratio, and exoergic collisional energy transfer.

Three new Fraunhofer-wavelength atomic filter concepts in the blue-green spectral region were developed during the past year. All three use atomic transitions in neutral calcium vapor. The properties of these new filter concepts are given in Table 1. The internal photon conversion efficiency measures the ratio of output photons to absorbed signal photons. The Fraunhofer Advantage measures the reduction of the solar background at the dip center; i.e., a 50% reduction corresponds to a Fraunhofer Advantage of 3 dB. The active and passive filters overlap an intense Fraunhofer line at 422.7 nm. The transmission at the center of this Fraunhofer dip is only 2.4% of the continuum solar background. The active filter emits in the ultraviolet, a spectral region in

which high-sensitivity, large-area, low-noise photomultiplier tubes are available.

The passive filter requires no pump laser; therefore, it is the filter of choice for high-reliability, low-cost operation. The metastable calcium filter exactly matches the output of the well-developed frequency-doubled Nd:BEL laser. It is the first atomic filter that matches a fixed-frequency laser source and overlaps a Fraunhofer line. Two photons are emitted upon absorption of signal light. Hence, the filter offers the unique potential for greater-than-unity internal photon conversion.

A final accomplishment of the past year's work was the laboratory demonstration of the passive calcium filter [7]. A patent disclosure has been filed on this new atomic filter. Let us identify the levels of this filter with those shown in Figure 1. Because the passive filter requires no pump source, levels 0, 1, and 4 coalesce to form the ground 1S_0 level. The signal transition is the resonance line ($^1P-^1S$) at 422.7 nm. Thus, level 2 in Figure 1 corresponds to the 1P level. Collisions with xenon buffer gas transfer population with the 3P level, corresponding to level 3 in Figure 1. The 3P level decays to the ground level by the emission of a 657 nm photon.

The experimental arrangement used in this study is shown in Figure 2. A cross-shaped stainless steel cell with sapphire viewports contained the calcium vapor. The cell was electrically heated by external heating tapes. The temperature of the cell was monitored by thermocouples placed at various locations outside the cell. The temperature reading of a thermocouple inserted inside the center of the cell was 430°C and was assumed to be equal to the equilibrium temperature of the Xe-Ca system. Research-grade calcium metal chips (99% pure) were loaded into a side-arm attachment of the cell, which was independently heated to 385°C, which corresponded to an equilibrium calcium vapor concentration of $\sim 10^{11} \text{ cm}^{-3}$. Window temperature was maintained 50°C above the calcium sidearm temperature to avoid metal vapor condensation. A simple vacuum and gas handling system, incorporating a capacitance-type pressure gauge, allowed xenon gas at pressures of up to 1000 Torr to be introduced into the calcium cell.

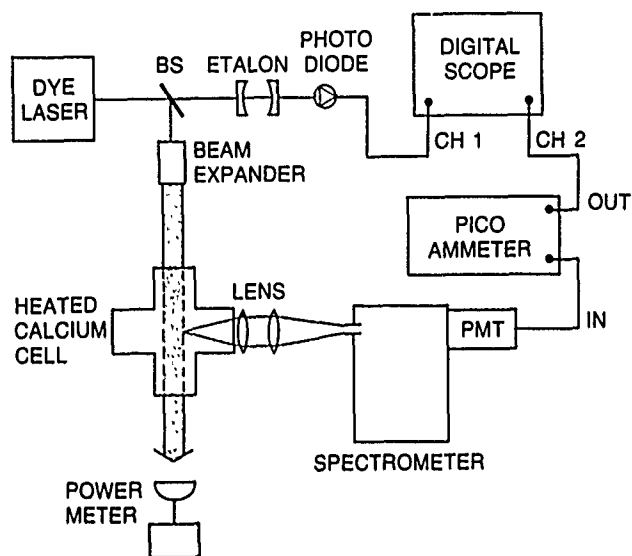


Figure 2. Schematic representation of experimental apparatus used for demonstration of passive calcium atomic filter.

A continuous-wave single-mode ring dye laser with Stilbene 3 dye pumped by the ultraviolet lines of an Ar ion laser excited the calcium atoms. The laser beam was expanded and collimated into a 1.5-cm diam beam before entering the cell. Typical laser power used was 30 mW. Laser-induced emissions were collected perpendicular to the laser beam and were focused into a 0.25-m spectrometer by a pair of converging lenses. A GaAs photomultiplier tube was used to detect the spectrally resolved signals, and the photocurrents that resulted were amplified by a picoammeter. The spectral response of the entire optical system was calibrated with a blackbody irradiance standard.

During the conversion efficiency measurement, the laser was first tuned to the $4p^1P_1 - 4s^1S_0$ transition. Then, photocurrents were recorded at the 422.7-nm and 657.3-nm settings of the spectrometer. The laser was then detuned from the resonance line and photocurrents at the two spectrometer settings were again recorded. The latter readings measured the background contributions due to the laser scattering and the dark current of the photomultiplier tube. The difference between the signals with the laser on-resonance and off-resonance represents the net emission signal. The measurements were repeated at least five times at various laser powers, ranging from 0.02 to 30 mW. The cell was then evacuated and refilled with xenon gas for the next pressure measurement. To ensure complete thermal equilibrium in the Ca-Xe system, we allowed a stabilization period of at least 2 h after each xenon gas pressure change.

For the pressure-broadened absorption linewidth measurements, the laser wavelength was scanned 0.006 nm across the resonance line. Emission profiles of the 422.7-nm fluorescence signal were recorded and sig-

nal-averaged with a digital oscilloscope. A small portion of the laser beam was transferred into a Fabry-Perot etalon. The free spectral range of the etalon was 0.001 nm and the transmission signals of the etalon were used as wavelength markers. To avoid power broadening of the resonance line, we reduced the laser intensity by a calibrated neutral density filter before it entered the oven.

Figure 3 shows the experimental data expressed in terms of the internal photon conversion efficiency. A monotonic increase of the conversion efficiency is shown up to 25% at 650 Torr. The solid line was calculated using a least-squares analysis. Experimental errors for the conversion efficiency as inferred from the standard deviations of the individual sets of measurements are less than 10% of the conversion efficiency values. The systematic errors due to the spectral response calibration, the fluctuations of the cell temperature, the gas pressure, and laser intensity are less than the aforementioned error.

Also shown in Figure 3 is the full width at half maximum of the collisionally broadened $4p^1P_1 - 4s^1S_0$ resonance emission as a function of xenon gas concentration. The measured pressure-broadening coefficient for the resonance line is 13.9 ± 0.2 MHz/Torr. The ability to broaden the filter bandwidth to 10 GHz is useful for the reception of Doppler-shifted laser signals from rapidly moving transmitters such as those encountered onboard spacecraft. It should be noted that a 1 km/s Doppler shift corresponds to 2 GHz at this wavelength.

During this four-year project, we have achieved the following accomplishments:

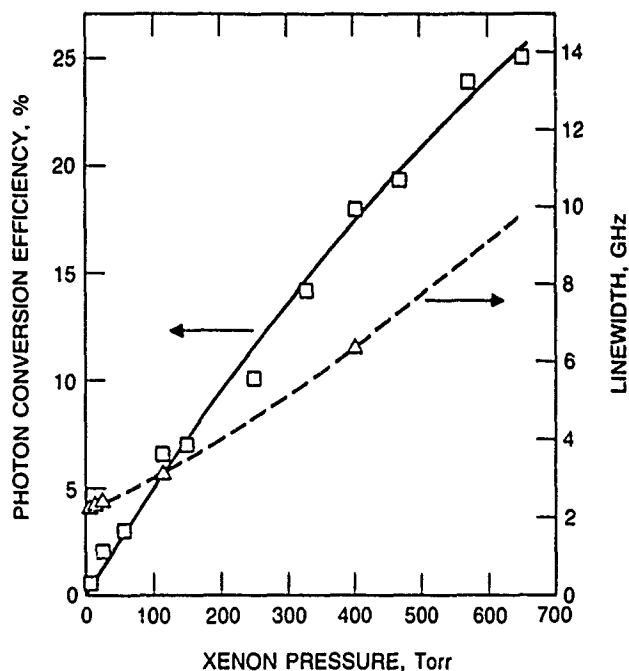


Figure 3. Internal photon conversion efficiency and filter linewidth of the passive calcium atomic filter plotted as a function of xenon pressure.

- The concept of atomic filters operating at Fraunhofer wavelengths was proposed.
- The theory of atomic filters and wavelength shifting was developed, followed by the development of photophysical models to identify promising atomic filtering schemes.
- The feasibility of two Fraunhofer-wavelength atomic filters was experimentally demonstrated.
- Atomic filtering schemes were proposed at several other blue-green wavelengths to expand the wavelength range for SLC.
- The project yielded three patent disclosures, nine journal articles, and four invited presentations.

* * * * *

1. J. A. Gelbwachs, "Atomic Resonance Filters," *IEEE J. Quantum Electron.* **24**, 1266(1988); also, ATR-86A(8534)-1, The Aerospace Corp. (15 November 1988).
2. J. B. Marling, "An Ultrahigh Q Isotopically Sensitive Optical Filter Employing Atomic Resonance Transitions," *J. Appl. Phys.* **50**, 610 (1979).
3. Y. C. Chung and T. M. Shay, "Experimental Demonstration of a Diode Laser-Excited Optical Filter in Atomic Rb Vapor," *IEEE J. Quantum Electron.* **24**, 709 (1988).
4. C. S. Liu, P. J. Chantry, and C. L. Chen, "A 535 nm Active Atomic Line Filter Employing the Thallium Metastable State as an Absorbing Medium," *Proc. SPIE* **709**, 132 (1986).
5. T. M. Shay, "Ultra-High Resolution K Laser-Excited Optical Filter for Doubled Nd Lasers," *Proceedings of the Lasers and Electro-Optics Society*, IEEE (1988), p. 243.
6. Y. C. Chan, M. D. Tabat, and J. A. Gelbwachs, "Experimental Demonstration of Internal Conversion in the Magnesium Atomic Filter," *Opt. Lett.* **14**, 722 (1989); also, ATR-89(8434)-4, The Aerospace Corp. (1 November 1989).

7. J. A. Gelbwachs and Y. C. Chan, "Passive Fraunhofer-Wavelength Atomic Filter at 422.7 nm," *Opt. Lett.* **16**, 336 (1 March 1991).

Gelbwachs, J. A., "An Atomic Resonance Filter Operating at Fraunhofer Wavelengths," *Laser Spectroscopy VIII*, Springer-Verlag, Berlin (1987), p. 409.

_____, "Recent Developments in the Fraunhofer-Wavelength Atomic Filter," *Proceedings of the 1988 Lasers and Electro-Optics Society*, IEEE (1988), p. 240.

_____, "Broadening and Shift of the Mg Intercombination Line and First Triplet Line due to the Presence of Noble Gases," *Phys. Rev. A* **39**, 3343 (1989); also, ATR-89(8434)-1, The Aerospace Corp. (15 June 1989).

Gelbwachs, J. A., and M. D. Tabat, "Solar Background Rejection in the Pressure Broadened Fraunhofer Wavelength Atomic Resonance Filter," *Opt. Lett.* **14**, 211 (1989); also, ATR-89(8434)-2 The Aerospace Corp. (7 September 1989).

Gelbwachs, J. A., and Y. C. Chan, "CW Laser Spectroscopy of the Triplet Manifold of Magnesium," *Laser Spectroscopy IX*, Academic Press, Boston (1989), p. 113.

Gelbwachs, J. A., "A 422.7 nm Atomic Filter with Superior Solar Background Rejection," *Opt. Lett.* **15**, 236 (1990); also ATR-90(8534)-1, The Aerospace Corp. (1 April 1990).

_____, "Sunlight Suppression by Fraunhofer-Wavelength Atomic Resonance Filters," *Proceedings of the International Conference on Lasers '90*, D. G. Hanes and T. M. Shay, eds., STS Press, McClean, Virginia (1990), p. 928.

_____, "Active Wavelength-Shifting in Atomic Resonance Filters," *IEEE J. Quantum Electron.* **26**, 1140 (1990).

_____, "A Proposed Fraunhofer-Wavelength Atomic Filter at 534.9 nm," *Opt. Lett.* **15**, 1165 (1990).

Analysis of Infrared Detector Materials

C. J. Selvey, P. A. Dafesh, and R. P. Wright,
Chemistry and Physics Laboratory;
P. M. Adams,
Materials Sciences Laboratory

The passive detection of cold bodies (e.g., satellites and reentry vehicles) from orbit requires the use of high-performance detectors capable of detecting long-wavelength infrared (LWIR) radiation ($> 8 \mu\text{m}$). The development of high performance LWIR detectors is impeded by poor quality of the detector materials. Impurities and defects decrease carrier lifetime and mobility in HgCdTe detectors and the quantum efficiency of Si impurity band conduction (IBC) detectors, thus degrading the performance of two major classes of detectors developed for this wavelength region. Advances in solid-state materials growth technology now allow the fabrication of multilayer superlattice and quantum well detectors with cutoff wavelengths tunable into the LWIR region. These superlattice detectors comprise this third major class of LWIR detectors, proposed by a community frustrated with the materials problems in HgCdTe and the extreme cooling requirements for Si IBC detectors. However, recent results [1] indicate that photocarrier lifetime in these structures is not transit-time limited, but depends on the quality of the detector material. Thus, poor material quality also degrades the performance of this third major class of LWIR detectors. The superlattice detectors are in such an early stage of development that all the mechanisms for degradation of performance due to inadequate material quality have not yet been identified.

Our work has focused on determining relevant materials parameters that affect detector performance, through the optical characterization of selected superlattice materials that have optical transitions in the LWIR region. We have used various spectroscopic techniques, including photoreflectance (PR), x-ray diffraction, Raman light scattering and transmission electron microscopy. Photoreflectance modulation spectroscopy [2], our main analytical tool, has been used to study materials parameters (e.g., electronic structure, composition, crystalline quality and carrier lifetime [3-6]) from the measurement of changes in reflectance on the photon-induced modulation of a semiconductor's built-in electric field.

This past year we augmented our experimental capability, particularly our ability to identify the role of impurities and defects in LWIR detector performance, by adding the capability for LWIR photoluminescence (PL) spectroscopy. Because it can identify contaminant impurities and defects, PL has been instrumental in the devel-

opment of wide-bandgap semiconductor materials, but its ability to analyze LWIR detector materials has been impeded by the lack of sufficiently sensitive detectors. The unique sensitivity of our proposed LWIR PL spectrometer is due to the recently developed solid-state photomultiplier (SSPM) [7] we plan to use as the spectrometer's detector. The SSPM has the unprecedented ability to count individual LWIR photons.

For materials characterization, the AlGaAs/GaAs multiple quantum well (MQW) system has generated the most interest for use as a LWIR detector material [8-10]. However, in previous company-sponsored work, we have identified other candidate systems for LWIR detectors, in particular Si/SiGe superlattices. Even though the latter system is difficult to grow, because strain is introduced into the layers by the lattice mismatch between Si and Ge, it has a technological advantage in that it is based on Si technology. With the use of advanced Si processing technology, it may be possible to fabricate monolithic detector arrays that contain both sensor and readout electronics [11]. Unlike AlGaAs/GaAs MQW detectors, it is possible to design Si/SiGe superlattice detectors that can couple radiation at normal incidence [11]. Furthermore, the mixed Si and Ge materials are interesting because they give promise of synthesizing a direct gap material that has strong absorption, from two indirect gap materials, Si and Ge, that have weak absorption [12].

The most exciting scientific result we obtained this past year is the first measurement and interpretation of the PR spectra of a strain-symmetrized [3] Si/Ge strained-layer superlattice (SLS). The measured PR spectra of a Ge-rich $\text{Si}_{10}\text{Ge}_{32}$ (made from unit cells composed of 8 Si and 32 Ge monatomic layers) SLS at 87, 200, and 295 K are plotted in Figure 1. The measured transitions (dotted curve) are identified as E_0^1 (1), from the heavy hole to the conduction band, and E_0^1 (2), from the light hole to conduction band; the transitions are split by strain and confinement [4]. The solid line is the fit to a third derivative Lorentzian line shape function [2]. The measured PR spectra have also been fit to the first derivative of a complex Gaussian dielectric function believed to be appropriate for phonon-broadened excitonic spectra [2], but no appreciable changes were observed in the transition energies or the relative values of the PR amplitude.

The measured temperature dependences of the E_0^1 (1) and E_0^1 (2) interband transitions (solid points) are

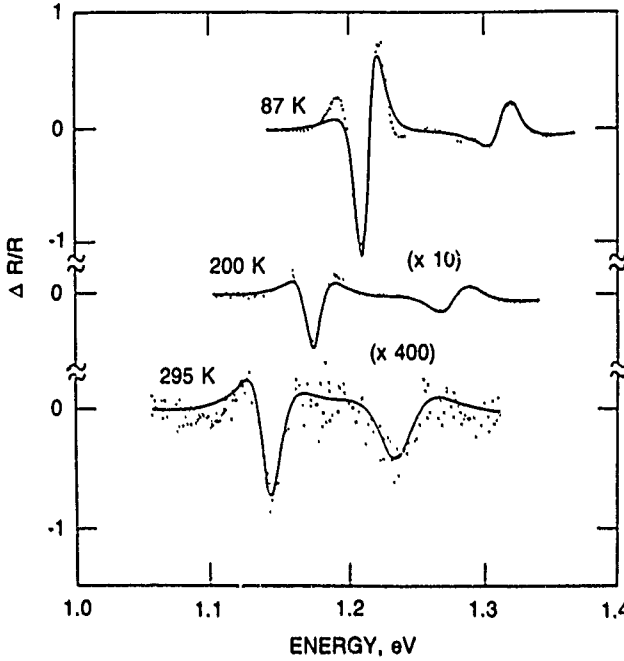


Figure 1. Measured photoreflectance spectra (dotted curve) from a strain-symmetrized $\text{Si}_8\text{Ge}_{32}$ superlattice at 87, 200 and 295 K. Each spectrum was normalized to the measured value of $\Delta R/R_{\text{max}}$ at 87 K. The solid curve is a nonlinear least-squares fit to Aspnes' line shape function for two-dimensional critical points.

plotted in Figures 2(a) and 2(b). These are shown to fit well to the Varshni relation (solid curve) for the temperature dependence of bulk critical points [13],

$$E = E_0 - \alpha T^2 / (T + \beta),$$

where E_0 is the transition energy at 0 K, and α and β are constants.

The temperature dependence of the E_0 transition in bulk Ge was also measured and used for comparison. For the measured $E_0(\text{Ge})$ temperature dependence, we find good agreement with prior results [13], where α , β and $E_0(\text{Ge})$ were measured as 0.889 eV, 6.84×10^{-4} eV/K, and 398 K, respectively. The results of these fits are summarized in Table 1.

The difference between $E_0(\text{Ge})$, and $E_0^1(1)$ and $E_0^1(2)$ can be attributed to both confinement effects and to strain in the SLS not present in bulk Ge. In addition to

Table 1. Results of Fits to the Varshni Relation: $E = E_0 - \alpha T^2 / (T + \beta)$

Transition	E_0 , eV	α , eV/K	β , K
$E_0^1(1)$	1.23	4.35×10^{-4}	147
$E_0^1(2)$	1.33	9.56×10^{-4}	598
$E_0(\text{Ge})$	0.892	7.25×10^{-4}	433

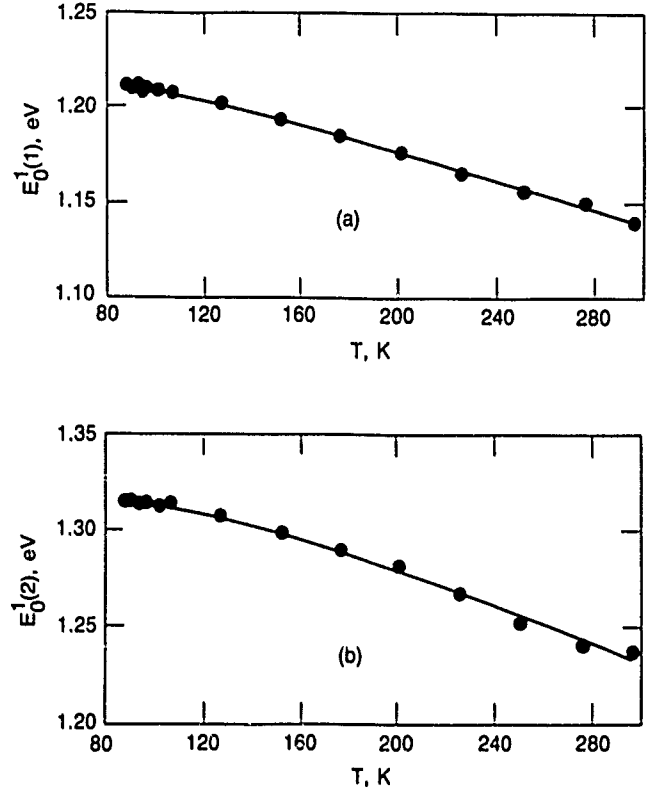


Figure 2. (a) Measured temperature dependence of the $n = 1$ heavy hole-to-electron miniband transition (solid points) in the $\text{Si}_8\text{Ge}_{32}$ superlattice sample. (b) Measured temperature dependence of the $n = 1$ light hole-to-electron miniband transition (solid points) in the $\text{Si}_8\text{Ge}_{32}$ superlattice sample. The solid curves are a fit to the Varshni relation given in Table 1.

differences in the transition energies, our results illustrate a noticeable difference between the temperature dependence of the $E_0(\text{Ge})$, $E_0^1(1)$, and $E_0^1(2)$ transitions. The temperature dependence of transition energies is due to shifts associated with the electron-phonon interaction and, to a smaller extent, changes in the lattice dilation. Differences in the temperature dependence of transition energies between bulk and superlattice systems have not been observed in unstrained systems, so we believe that the difference we observe may arise from strain in the $\text{Si}_8\text{Ge}_{32}$ superlattice. Furthermore, we observe a notable difference in the temperature dependence of the PR amplitude between bulk and superlattice systems. The much more rapid decrease in amplitude with temperature observed for the E_0 transitions in the SLS is believed to be associated with the dependence of the PR amplitude on minority carrier lifetime [2, 14].

In addition to experimental studies of the Si/Ge system, PR studies have been used to assess the composition and uniformity of $\text{Al}_x\text{Ga}_{1-x}\text{As}/\text{GaAs}$ -based MQW infrared detector structures [8,9]. By probing a given sam-

ple at different positions, variations in the PR transition energies indicate variation in layer thickness. In the discussion that follows, the position of the probe is denoted by *I*, *C*, and *O* for regions at the inside, the center, and outside of the wafer, respectively.

Figure 3 shows the measured PR spectrum at position *I* for a sample designed for $x = 0.2$. The main features are a structure near 1.42 eV, due to the GaAs band gap transition (from some residual GaAs not removed in the etch); a structure near 1.5 eV, due to heavy and light hole-to-conduction-band transitions, a structure at 1.66 eV, due to the AlGaAs band gap E_0 transition, and a structure near 1.76 eV, due to the $n = 1$ subband transition from the split-off to conduction bands in the GaAs well regions. The fine structure just beyond 1.43 eV is due to Franz Keldysh oscillations from the residual GaAs. These oscillations may be observed in the PR spectra of heavily doped semiconductors [2]. The spectra at positions *C* and *O* are similar.

In Table 2, we show the variations in the $\text{Al}_x\text{Ga}_{1-x}\text{As}$ direct band transitions E_0 at the three different positions and the aluminum fractions calculated from these transition energies. The composition of the $\text{Al}_x\text{Ga}_{1-x}\text{As}$ barrier region is shown to vary negligibly across the sample. The variation in line width, which is believed to be the result of variation in defect density across the sample in the barrier region, is appreciable.

The measured transition energies agree well with the calculated energies only at position *I*. The large increase in energies toward the outer edge of the wafer is an indication of a narrowing of the GaAs well regions, as would be expected from a simple square well model. Even

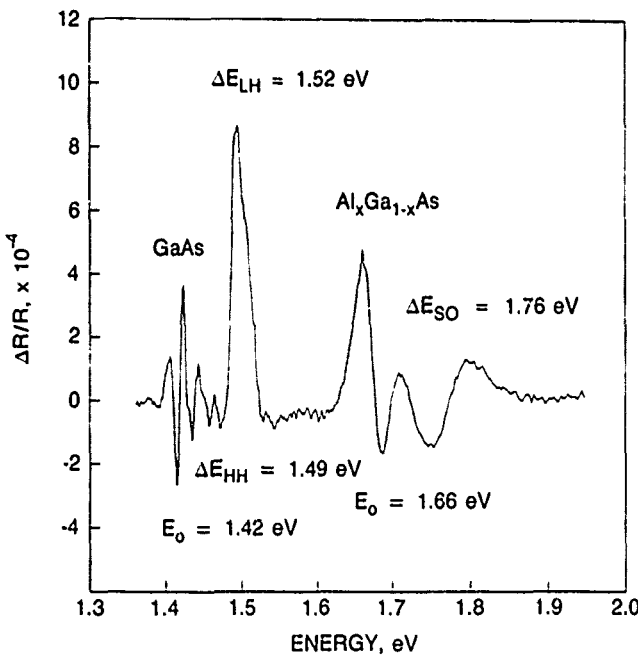


Figure 3. PR spectrum from the $\text{Al}_x\text{Ga}_{1-x}\text{As}$ sample ($x = 0.20$) taken at position *I*.

Table 2. Measured Bulk $\text{Al}_x\text{Ga}_{1-x}\text{As}$ ($x = 0.2$) Direct Band Gap Transitions E_0 at Three Different Sample Positions

Location of Probe	Line Width, meV	Measured Energy, eV	Aluminum Fraction, % Al
<i>I</i>	31	1.664	17.2 ± 0.5
<i>C</i>	47	1.662	17.2 ± 0.5
<i>O</i>	37	1.663	17.2 ± 0.5

variations of several millielectron volts could have a drastic effect on the response characteristics of a 10 μm MQW detector. The observed variations in line widths, the result of the nonuniformities due to defects, also greatly affect the response of an infrared MQW.

The uniformity of the MQW region, especially uniformity of the well widths, is indicated by variations in the heavy hole and light hole interband transition energies across the sample. Comparison with theory yields well widths that would give rise to the observed transition energies. The model we used to predict these energies was an envelope function calculation [15, 16]. A comparison of these calculations to the measured $n = 1$ interband transitions (excluding the split-off hole to electron transition) is given in Table 3.

The need for low photon backgrounds required for SSPM operation makes designing and constructing the PL spectrometer a considerable technical challenge. All of the optics in the spectrometer must be kept at cryogenic temperatures to reduce the thermal photon background, and photons not originating from PL must be rejected. Our cryogenic spectrometer design is shown in Figure 4. The SSPM, the cold sample, cold optics, and the cold circular variable filter (CVF) will be housed in a liquid He dewar. The CVF, used to resolve the spectral lines, is

Table 3. Measured $n = 1$ Heavy and Light Hole-to-Electron Interband Transitions at Three Different Sample Positions

Location of Probe	Line Width, meV	Measured Energy, eV	Calculated Energy, eV
<i>Heavy Hole-to-Electron Interband Transition</i>			
<i>I</i>	7	1.487	1.490
<i>C</i>	8	1.519	1.490
<i>O</i>	7	1.524	1.490
<i>Light Hole-to-Electron Interband Transition</i>			
<i>I</i>	15	1.515	1.515
<i>C</i>	14	1.519	1.515
<i>O</i>	16	1.525	1.515

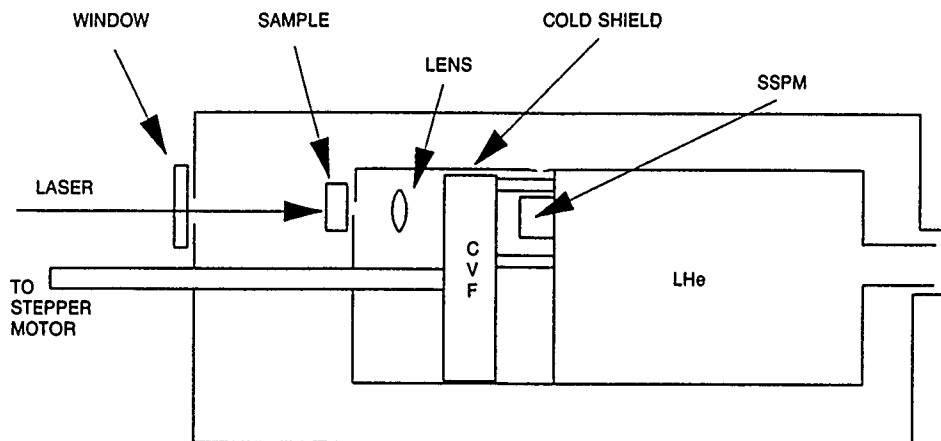


Figure 4. LWIR photoluminescence spectrometer design. The sample and optics are held in contact with a plate at liquid He (LHe) temperature. Photoexcitation is accomplished with an external laser.

capable of spectral resolution out to 14 μm . Luminescence excitation will be accomplished by a laser external to the spectrometer. To prevent laser emission from impinging on the detector, we place the sample between the laser and the detector. Since most of the samples of interest are epitaxial material grown on substrates (CdTe, Si, or GaAs) opaque to the excitation laser light, but transparent to the luminescence, the luminescence is detected after it passes through the substrate, and the substrate filters out the incoming laser light. Our SSPM is backside-illuminated, and the detector substrate acts to further filter out the laser light from the detector.

We have achieved operation of the SSPM in the photon-counting mode. The extreme sensitivity of the SSPM makes such operation difficult to achieve, because the photon backgrounds in conventional dewars are large enough to cause saturation of the SSPM detector. Our measurements show that the gain of the SSPM decreases with signal level, which indicates that the SSPM is near saturation and that the background photon level in the test dewar is still much higher than anticipated or desired. We are now trying to eliminate the photon background in our test dewar and will apply the successful techniques used in the design of the dewar to house the spectrometer.

The objective of these studies is to characterize several superlattice systems to determine their feasibility for LWIR detector materials. We have obtained and interpreted the first PR spectrum of a Ge/Si superlattice. The experimentally determined transition energies agree well with those theoretically predicted, thereby verifying the ability to synthesize a new Si/Ge superlattice material with electronic transitions very different from the constituent layers that comprise the structure. Confirmation of the theoretically predicted optical properties of the detector material is a necessary first step in the design of a detector. To our knowledge, we are the first to use PR to measure a difference in the temperature dependence of the transition energies between bulk and superlattice systems, an effect we attribute to strain in the Si/Ge superlattice. The temperature dependence of the transition amplitude indicates that lifetime may be an important factor

limiting the performance of Si/Ge superlattice detectors. We have also determined that uniformity may be a problem in growing AlGaAs/GaAs superlattice detector material. We have also started construction of a LWIR PL spectrometer, which, when completed, will permit the identification of impurities and defects in LWIR detector materials. We have completed an initial spectrometer design based on measurements of the performance of our SSPM detector made during the past year. Next year, we will concentrate on completing construction of the PL spectrometer.

* * * * *

1. G. Hasnain et al., "Large Photoconductive Gain in Quantum Well Infrared Photodetectors," *Appl. Phys. Lett.* **57**, 608 (1990).
2. F. H. Pollak and O. J. Glembocki, "Modulation Spectroscopy of Semiconductor Microstructures: An Overview," *Proc. SPIE* **946**, 2 (1988).
3. P. A. Dafesh, V. Arbet, and K. L. Wang, "Electronic Transitions in a Si_mGe_n Strained Monolayer Superlattice Measured by Photoreflectance," *Appl. Phys. Lett.* **56**, 1498 (1990).
4. P. A. Dafesh, V. Arbet, and K. L. Wang, "Electronic Transitions in a Ge-Rich Strain-Symmetrized $\text{Si}_8\text{Ge}_{32}$ Strained Monolayer Superlattice Measured by Photoreflectance Spectroscopy," *Proc. SPIE* **1286**, 308 (1990).
5. Michael Snyder et al., "Photoreflectance of $\text{Al}_x\text{Ga}_{1-x}\text{As}$ and $\text{Al}_x\text{Ga}_{1-x}\text{As}/\text{GaAs}$ Interfaces and High-Electron-Mobility Transistors," *J. Appl. Phys.* **67**, 7423 (1990).
6. R. C. Bowman, Jr., et al., "Effects of Helium Ion Implantation on the Optical and Crystal Properties of GaAs," *Proc. Mater. Res. Soc. Symp.* **147**, 303 (1989).
7. M. D. Petroff, M. G. Stapelbroek, and W. A. Kleinhaus, "Detection of Individual 0.4-28 μm wave-

- length Photons via Impurity-Impact Ionization in a Solid-State Photomultiplier," *Appl. Phys. Lett.* **51**, 406 (1987).
8. B. F. Levine et al., "High-Detectivity $D^* = 1.0 \times 10^{10} \text{ cm}^2/\text{Hz/W}$ GaAs/AlGaAs Multiquantum Well $\lambda = 8.3 \text{ } \mu\text{m}$ Infrared Detector," *Appl. Phys. Lett.* **53**, 296 (1988).
 9. B. K. Janousek et al., "High Detectivity GaAs Quantum Well IR Detectors with Peak Responsivity at $8.2 \text{ } \mu\text{m}$," *J. Appl. Phys.* **67**, 7608 (1990).
 10. B. F. Levine, "Comment on Performance Limitations of GaAs/AlGaAs Infrared Superlattices," *Appl. Phys. Lett.* **56**, 2354 (1990).
 11. E. Kasper et al., "Strained Layer Si/SiGe Superlattices," *Superlattices and Microstructures* **3**, 141 (1987).
 12. M. A. Gell, "Direct-Gap Si/Ge Superlattices," *Phys. Rev. B* **40**, 1966 (1989).
 13. Y. P. Varshni, "Temperature Dependence of the Energy Gap in Semiconductors," *Physica* **34**, 149 (1967).
 14. H. Shen et al., "Photoreflectance of GaAs and $\text{Ga}_{0.82}\text{Al}_{0.18}$ at Elevated Temperatures Up to 600°C ," *Appl. Phys. Lett.* **53**, 1080 (1988).
 15. G. Bastard, "Electronic Energy Levels in Quantum Wells and Superlattices," *Superlattices Microstructures* **1**, 265 (1985).
 16. L. L. Chang and B. C. Grossen, *Synthetic Modulated Structures*, Academic Press, New York (1985).
-
- Adams, P. M., et al., "Double-Crystal X-ray Diffraction Studies of Si Ion-implanted and Pulsed Laser Annealed GaAs," *Advan. X-Ray Anal.* **34**, 531 (1991).
- Bowman, R. C., et al., "Structural Characterization of Symmetrically Strained Si_mGe_n Superlattices," *Proc. Mater. Res. Soc. Sym.* **160**, 101 (1990).
- Bowman, R. C., Jr., et al., "Structural Characterization of $\alpha\text{-Sn}$ and $\alpha\text{-Sn}_{1-x}\text{Ge}_x$ Alloys Grown by Molecular Beam Epitaxy on CdTe and InSb," *J. Vac. Sci. Technol. A* **8**, 1577 (1990); also, ATR-89(8459)-13, The Aerospace Corp. (17 July 1990).
- Bowman, R. C., Jr., et al., "X-ray and Topographic Studies of GaAs Implanted with $^{28}\text{Si}^+$ and Pulsed Laser Annealed," *Proc. Mater. Res. Soc. Symp.* **157**, 157 (1990).
- Bowman, R. C., Jr., J. F. Knudsen, and R. G. Downing, "Neutron Depth Profiles of Boron Implanted Semiconductors," *Proc. Mater. Res. Soc. Symp.*, **166**, 331 (1990).
- Campaan, A., R. C. Bowman, Jr., and D. E. Cooper, "Raman Studies of Composition and Structural Ordering in $\text{Hg}_{1-x}\text{Cd}_x\text{Te}$," *Semicond. Sci. Technol.* **5**, S73 (1990).
- Chang, S. J., et al., "Study of Ultra-thin Ge/Si Strained Layer Superlattices," *J. Cryst. Growth* **95**, 451 (1989).
- Chang, S. J., et al., "Studies of Interdiffusion in Ge_mSi_n Strained Layer Superlattices," *J. Electron. Mater.* **19**, 125 (1990); also, ATR-89(8459)-10, The Aerospace Corp. (1 July 1990).
- Dafesh, P. A., "Characterization of GaAs/ $\text{Al}_x\text{Ga}_{1-x}\text{As}$ Multiple Quantum Well IR Detector Structures Using Photoreflectance," *J. Appl. Phys.* (in press).
- Hochst, H., M. A. Engelhardt, and R. C. Bowman, Jr., "Characterization of MBE-Grown $\alpha\text{-Sn}$ Films and $\alpha\text{-Sn}_{1-x}\text{Ge}_x$ Alloys," *Semicond. Sci. Technol.* **5**, S240 (1990); also, ATR-89(8459)-8, The Aerospace Corp. (6 July 1990).

Picosecond Studies of Space Optical Materials

S. C. Moss,
Chemistry and Physics Laboratory

Present and future space satellite systems require optical components that exceed the capabilities of present optical manufacturers in terms of quality, size, and reliability. Optical components now being developed for use in future space satellite systems include passive elements (e.g., mirrors, filters, beam splitters, and lenses) as well as active elements (e.g., diode lasers, electro-optical and acousto-optical devices, focal plane arrays, and solar

cells). Many of these components incorporate multilayer thin film dielectric coatings. In this project, we are developing laser-based diagnostic techniques that allow nondestructive evaluation of the quality and reliability of optical components for space optical systems. The fundamental physical phenomena governing the reliability of these components are intimately related to their response to optically induced energy deposition, energy transfer, and

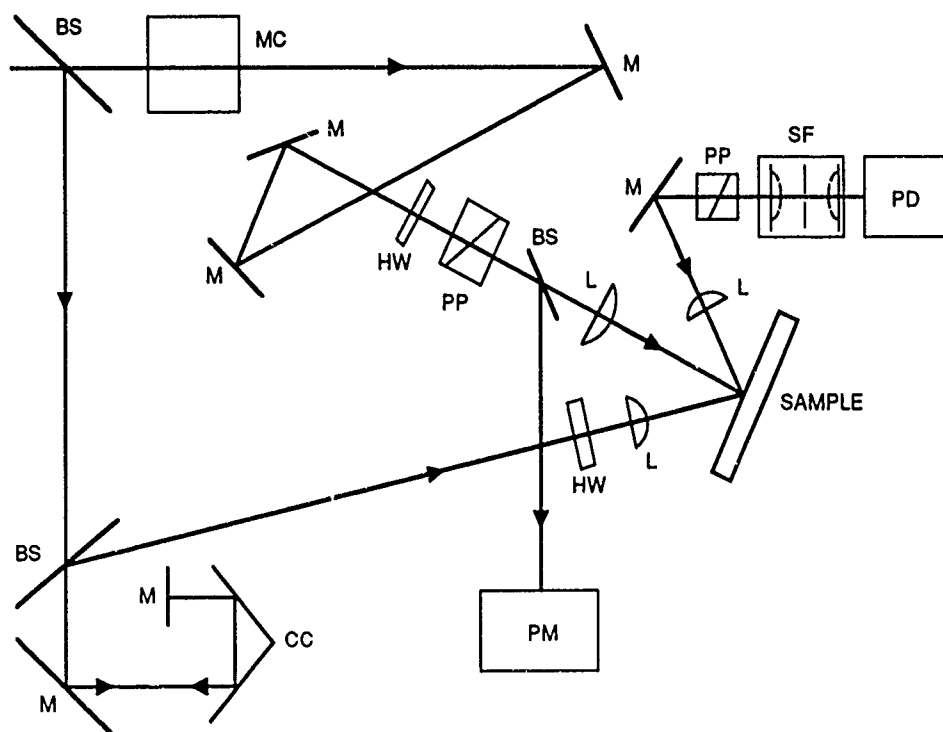
energy dissipation. Because of the geometry of many of these thin film structures and because of the short absorption depth within these materials, thermophysical phenomena that dominate the temperature rise within these structures occur on the picosecond time scale, even for continuous illumination. We propose to develop and exploit powerful picosecond, and subpicosecond, stimulus-response techniques to measure ultrafast optical properties of thin film optical components and substrates commonly used in space satellite systems. Picosecond optical techniques offer the only methods for measuring the fundamental phenomena that drive thermal loading because these are the only techniques with the temporal resolution capable of unambiguously separating various energy transport effects that occur in these materials. Consequently, a rigorous investigation of these processes leads to a better understanding of the precursors to optically induced thermal damage. These techniques also allow nondestructive evaluation of the quality of buried interfaces for both optical coatings and substrates that could identify manufacturing processes that yield higher quality thin film optics that are more damage resistant.

We have developed transient photoreflectance (TPR) techniques [1] as a tool for monitoring the thermo-optical properties of materials commonly used in space systems as a function of the damage encountered in on-orbit environments. Measurements were performed for materials damaged to various levels (up to amorphization) by ion implantation. Characteristics of the implants were selected after simulation using the TRIM-88 Monte-Carlo code [2]. Damage levels are representative of those inflicted on components over various lifetimes in space.

We have measured the TPR induced by picosecond optical pulses in samples of bulk silicon, a multilayer silicon structure incorporating a buried oxide layer (SIMOX), gallium arsenide (GaAs), and heavily carbon-implanted silicon. Bulk silicon is used as a substrate material for mirrors in space systems. The SIMOX structure has properties similar to coatings on a bulk substrate and to infrared edge filters. Narrowband rugate filters for the infrared have been fabricated from GaAs-based materials. SiC is used as a substrate material for reflective optical components. These laser-based diagnostic techniques are non-destructive and allow sensitive measurement of modification of near-surface properties, even at relatively low ion implant fluences. We have also assessed ion-induced damage effects using various characterization techniques such as Rutherford backscattering spectrometry (RBS) and Raman spectroscopy and compared these assessments with results of picosecond TPR measurements.

The apparatus used to perform picosecond TPR measurements is based on a cavity-dumped dye laser synchronously pumped by an actively mode-locked frequency-doubled Nd:YAG laser. Dye laser parameters were as follows: temporal pulse width, 12 ps; repetition rate, 1 MHz; and average power, 100 mW. The dye laser beam was split into a pump beam and a probe beam, as shown in Figure 1. The pump beam, polarized perpendicular to the plane of incidence, traveled a fixed path through a mechanical chopper, was focused onto the sample at near normal incidence, and was intense enough to alter the sample's reflectivity through a combination of photocarrier and photothermal phenomena. The probe beam,

Figure 1. Picosecond pump-probe apparatus: M, mirror; L, lens; CC, corner cube; BS, beam splitter; MC, mechanical chopper; PP, polarizing prism; SF, spatial filter; PD, photodetector.



polarized parallel to the plane of incidence, traveled a path of variable length controlled by a mechanical translation stage. The probe beam (1% of the pump beam intensity) was incident on the sample at an angle of 45 deg relative to normal. The probe pulse, spatially coincident with the sample surface region illuminated by the pump-pulse, experiences altered reflectivity that depends on the temporal separation between the two pulses. After reflection from the sample, probe beam light was collected, passed through a polarization analyzer, focused through a spatial filter, and detected with a photodiode. The signal from the photodiode was transmitted through signal processing electronics to a microcomputer, where it was stored and processed as a function of delay stage position, yielding a sensitive measurement of the transient's temporal duration. Measurements of the rise and decay of TPR signals thus, in principle, permit extrapolation of photocarrier and photothermal phenomena.

We have used this picosecond TPR technique to characterize damage induced by multiple energy $^{28}\text{Si}^+$ implants into SIMOX and bulk silicon wafers. We have correlated these results with other materials characterization techniques such as Raman spectroscopy and RBS. The SIMOX wafers had a superficial layer of 220 nm of Si with a 350-nm buried oxide layer. Subsequently, the superficial layer was intentionally damaged by a triple-energy implant of 25/75/125 keV $^{28}\text{Si}^+$, each at $1 \times 10^{14} \text{ cm}^{-2}$ (type-A implant) or $3 \times 10^{14} \text{ cm}^{-2}$ (type-B implant). These implants were designed to produce uniform damage throughout the superficial layer with little induced damage in the oxide layer. These same implant conditions were used to damage bulk silicon wafers so that effects of implantation-induced damage could be compared with those in the more complex SIMOX structure. RBS data for bulk silicon wafers show that type-B implants fully amorphize the near-surface region to a depth of 200 nm, whereas type-A implants show significantly less damage indicating that the near-surface region is not amorphized. RBS data for the SIMOX wafers show that type-B implants fully amorphize the superficial layer, whereas type-A implants show significantly less damage, indicating that the near-surface region is not amorphized. These implants produce similar damage profiles in bulk silicon or SIMOX.

In Figure 2(a), we show TPR data for unimplanted bulk Si, bulk Si with the A implant, and bulk Si with the B implant. In Figure 2(b), TPR data are shown for unimplanted SIMOX, SIMOX with the A implant, and SIMOX with the B implant. In each case, the transient reflectivity decay time is shortest for unimplanted samples. Damage levels ranged up to complete amorphization of the near-surface region and, in the SIMOX material, included some damage of the buried oxide. Slowing of the transient response with increasing ion-induced damage was consistent with longer thermal diffusion times expected for disrupted lattices.

Raman scattering measurements were performed in the usual backscattering geometry for both bulk silicon wafers and SIMOX wafers with excitation at the 514.5-nm Ar^+ laser line. At this wavelength, the Raman technique is sensitive to depths of about 600 nm in crystalline silicon, but only about 50 nm in amorphous silicon. The longitudinal optical (LO) phonon spectra at 521 cm^{-1} for the as-received SIMOX wafer and the unimplanted silicon wafer are identical. With increasing implant dose, the intensity of the LO peak decreases dramatically and vanishes for the B implant. Heavier doses also show no observable spectra. The vanishing of the LO peak at the B implant dosage is consistent with the complete amorphization of the superficial layer in the SIMOX and bulk silicon.

The short transient reflectivity times in the unimplanted SIMOX and bulk silicon are consistent with the evolution of the photogenerated carriers in these samples, indicating that their photoreflectance transients are dominated by photocarrier phenomena. From other measurements on heavily damaged silicon, the carrier lifetime is known to be subpicosecond in material amorphized by high dose implants [3]. However, decay times of TPR signals in samples damaged by high dose implants are longer than 1 ns. Because the Raman data just described indicate that the superficial layer is amorphized by the triple $3 \times 10^{14} \text{ cm}^{-2}$ implant, we conclude that these decay times are too long to be accounted for completely by reflectance changes due to photocarrier phenomena alone, and most likely indicate that the TPR signals are dominated by photothermal effects. Damaging the material substantially increases thermal diffusion times because of disruption of the lattice. Although ion-implantation-induced amorphization substantially reduces the absorption depth of these samples, which produces larger thermal gradients, we note that these increased thermal gradients are not enough to offset the reduction in the thermal diffusion coefficient. Thermal diffusion is further complicated in the SIMOX by the thermal barrier presented by the buried oxide layer. The Raman and RBS data all agree that the threshold for amorphization is greater than the type A implant and less than the type-B implant. Optical components based on SIMOX and silicon structures must take these amorphization effects into consideration. Bulk silicon is used as a substrate material for mirrors in space systems. The SIMOX structure has properties similar to coatings on a bulk substrate and to infrared edge filters. It is possible that the damage induced by a type A implant in a SIMOX structure can be removed by annealing with complete recrystallization. However, it is unlikely that the damage produced by a type B implant in a SIMOX structure can be removed by annealing because of the lack of a seed.

We have also used this picosecond TPR technique to measure the near-surface characteristics of ion-implanted GaAs. This nondestructive laser-based diag-

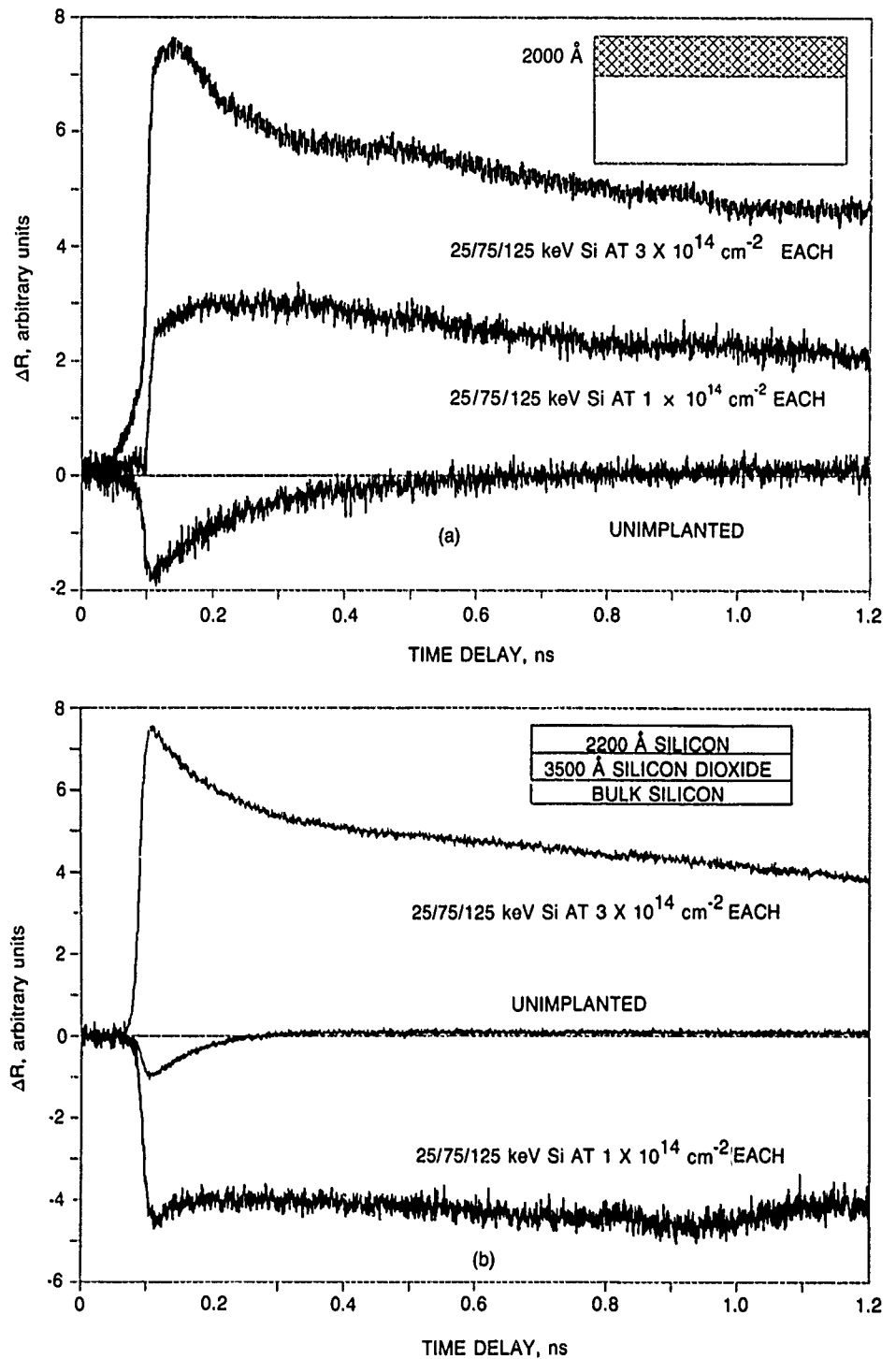


Figure 2. Picosecond transient photoreflectance measurements of (a) bulk silicon and (b) SIMOX. Each graph shows results for the as-received wafer and wafers with the type-A and type-B implants.

nostic technique permits the measurement of the modification of near-surface properties at relatively low implant fluences. We observe picosecond TPR signals for unimplanted and implanted GaAs and relate differences in the observed response to ion-implantation induced material modification. Other picosecond TPR measurements of GaAs have been previously reported but were in wavelength or fluence regimes where only photocarrier phenomena were important [1]. However, TPR measurements are sensitive to changes in crystal temperature as

well as changes in photocarrier population. Photothermal phenomena dominate our new results and yield important information concerning the extent of implant-induced modification.

Semi-insulating (100)-GaAs wafers were implanted with $^4\text{He}^+$ ions with beam currents sufficiently low to avoid significant heating above room temperature. Damage was induced by a quadruple energy implant of 20/50/100/200 keV $^4\text{He}^+$ resulting in total dosages of 7×10^{12} , 7×10^{13} , 7×10^{14} , or 7×10^{15} ions/cm². The

200 keV implant dose was half that of the other implants. The implants were designed to produce fairly uniform damage to a depth of near 1 μm . This depth corresponds to five absorption depths of the 600 nm light used for the picosecond measurements.

The results of these measurements for the five samples described here are shown in Figure 3. In each case, the TPR signal rises to a maximum (normalized to unity) and then decays rapidly away. The rise time (10-90%) is 18 ps, approximately the amount of time expected for an integration effect, given these optical pulse widths. The decay of the TPR signal is not a single exponential for any of these samples. The signal from the unimplanted sample has a signal of one polarity followed after approximately 1 ns by a signal of the opposite polarity. In general, the transient photoresponse decays more slowly with increased ion-induced damage consistent with longer photothermal diffusion times associated with lattice disruption. One measurement, at the highest damage level, had a faster decay time than the crystal with the next highest level of ion-induced damage. These results are shown here to be consistent with the combined results of photocarrier generation and photothermal effects produced by the absorption of the pump pulse. In the measurements shown in Figure 3, the decay time of the TPR signal increases with increasing implant dose. However, disruption of the lattice produced by implantation works to reduce the photocarrier lifetime. Thus, if the response were dominated by photocarrier phenomena, we would expect to see the decay time of the TPR signal decrease with increasing dose. As previously described, slowed thermal diffusion processes in implanted samples would yield a longer decay time for the TPR signal, if it were

dominated by photothermal effects. Consequently, we conclude that these TPR measurements are dominated by photothermal phenomena. For the highest dose implant, it is possible that other conduction mechanisms may come into play. Other measurements show a reduced resistivity in heavily implanted GaAs that may result from an enhanced hopping conduction mechanism [4]. This could alter the relative strengths of the photocarrier and photothermal contributions to the TPR signal and yield the anomalous result we observe for the heaviest dose implant. Space-based optical components such as narrowband rugate filters based on multilayer GaAs structures should account for these effects in their design to efficiently eliminate anomalous optically induced heating due to transient exposure to sunlight or laser action on areas subject to ion-induced damage in space.

Previously, we reported results of Raman scattering measurements to examine GaAs samples after $^4\text{He}^+$ ion implants [5]. Even though $^4\text{He}^+$ ions have low mass, substantial disorder and lattice strain are found in (100)-GaAs after room-temperature implants. The Raman spectra indicate that near-surface material is not totally structurally disordered, even for the 7×10^{15} ion cm^{-2} total dose. Picosecond TPR measurements are strongly influenced by implant damage at low ion fluences that produce little or no observable effect on the Raman studies.

SiC has substantial interest to the optics community because of its hardness and thermal properties. Recent picosecond optical studies using transient-induced absorption [6] or degenerate four-wave mixing [7] have been performed on Si-C alloy materials formed by plasma-enhanced chemical vapor deposition. Those picosec-

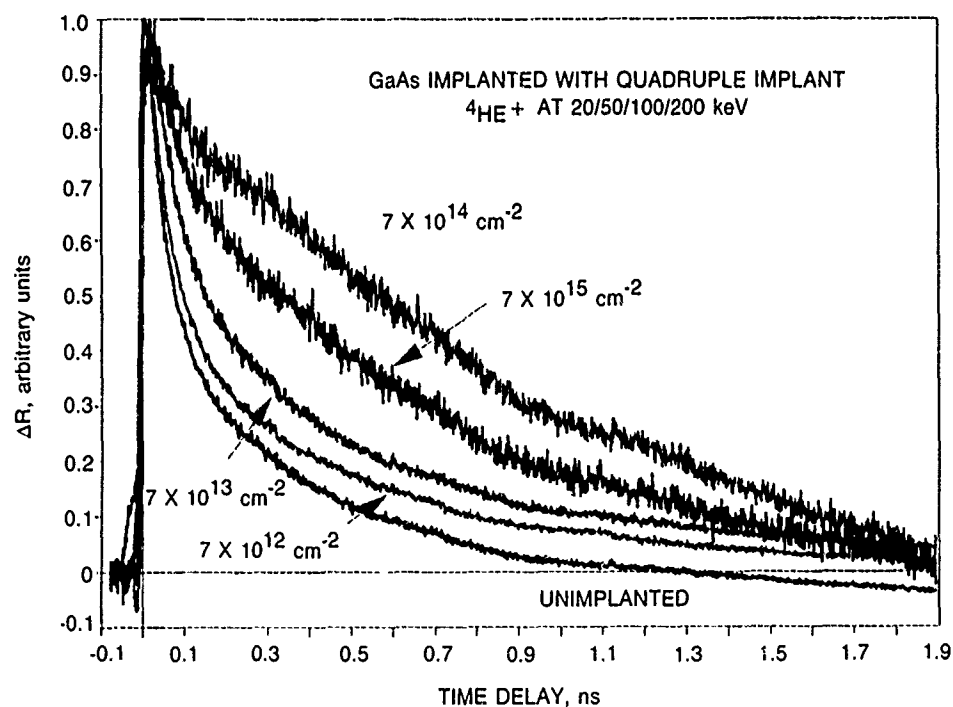


Figure 3. Picosecond transient reflectance signals from an unimplanted GaAs sample and four implanted GaAs samples.

ond techniques are very sensitive to bulk phenomena but are not so sensitive to near-surface phenomena. Consequently, they are not the technique of choice to study phenomena in the near surface layers produced by ion implantation.

We have used picosecond TPR techniques to measure the near-surface characteristics of silicon heavily implanted with carbon, unimplanted silicon, and sintered alpha SiC. Photothermal phenomena dominate these results and yield important information concerning the extent of implant-induced materials modification. We have compared these results before and after annealing of the implantation-induced damage and have correlated these measurements with those of Raman spectroscopy.

The samples were initially *p*-type (boron doped) silicon wafers [7-10 ohm-cm resistivity, (100 orientation)]. Two samples, SC1 and SC2, were implanted with 220 keV $C_2H_5^+$ ions to doses of $1 \times 10^{15} \text{ cm}^{-2}$ and $1 \times 10^{16} \text{ cm}^{-2}$, respectively. Sample SC3 was implanted with 240 keV $C_2H_5^+$ ions to a dose of $1 \times 10^{17} \text{ cm}^{-2}$. The wafers were heated to 400°C during the implant. TRIM-88 results implied that these implants would yield a buried region of heavily carbon-implanted silicon and that, at high implant doses, a buried SiC layer could be formed with annealing subsequent to the implant.

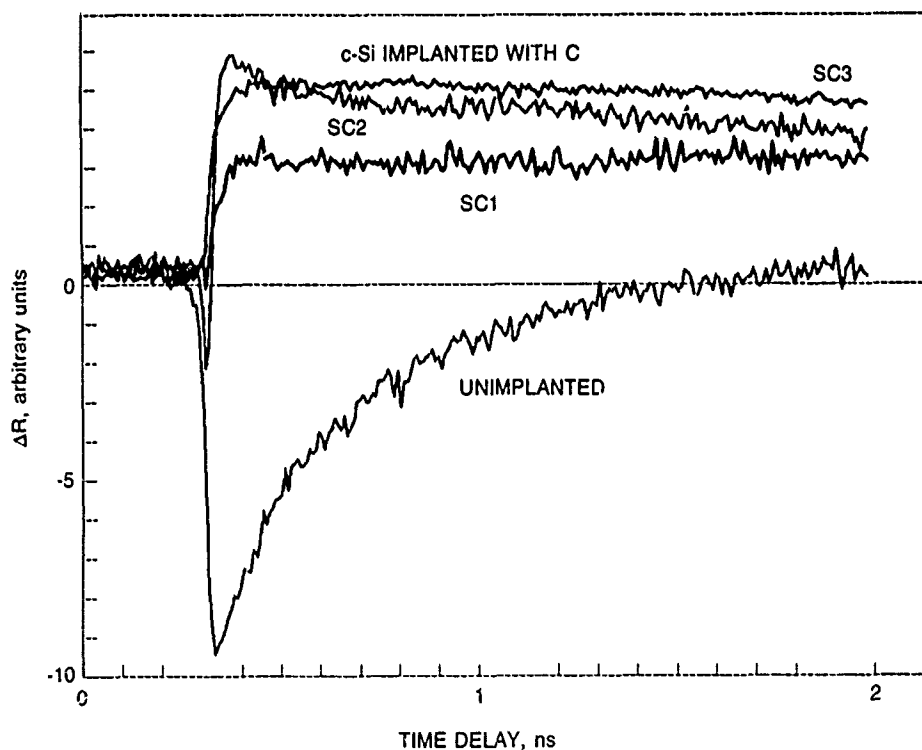
Results of measurements for the as-implanted samples previously described are shown in Figure 4 together with results for the unimplanted silicon wafer. The polarity of the change in reflectivity is opposite for the unimplanted sample and for the heaviest dose implant SC3. The rise time (10-90%), in each case, is 18 ps, approxi-

mately the amount of time expected for an integration effect, given these optical pulsewidths. The TPR signal decay for the unimplanted sample is approximately a single exponential with a decay time of 400 ps. The TPR decay on sample SC3 is much longer. TPR measurements on samples SC1 and SC2 show some characteristics of both the unimplanted sample and sample SC3. The signal first decreases, as in the unimplanted sample, then rapidly increases to a positive value with a much longer decay time, as in sample SC3.

In the measurements shown in Figure 4, the decay time of the TPR signal increases with increasing implant dose. However, the disruption of the lattice produced by implantation works to reduce the photocarrier lifetime. Thus, if the response were dominated by photocarrier phenomena, we would expect to see the decay time of the transient signal decrease with increasing dose. As previously described, the slowed thermal diffusion processes in the implanted samples would yield a longer decay time for the transient reflectance signal, if it were dominated by photothermal effects. Consequently, we conclude that these TPR measurements are dominated by photothermal phenomena.

We have developed picosecond TPR techniques that are powerful tools for nondestructive evaluation of the thermo-optical properties of both crystalline and amorphous materials commonly used in space satellite systems. These techniques also yield important information concerning the extent of irradiation induced damage in these materials and the effects of the damage on their thermo-optical properties. Further measurements are

Figure 4. Picosecond transient reflectance signals from an unimplanted silicon sample, three carbon-implanted silicon samples, and sintered alpha silicon carbide.



under way, as well as an initial effort to model the transport processes that affect these measurements. Our ability to develop laser-based materials diagnostic techniques is significantly enhanced by the ready availability at Aerospace of materials modification facilities (e.g., the ion implanter) and the materials analysis capabilities such as those described herein.

* * * * *

1. S. M. Beck and J. E. Wessel, *Appl. Phys. Lett.* **50**, 149 (1989).
2. J. P. Biersack and L. G. Haggmark, *Nucl. Instrum. Meth.* **174**, 257 (1980).
3. F. E. Doany, D. Grischkowsky, and C.-C. Chi, *Pico-second Electronics and Optoelectronics II*, F. J. Leonberger, C.-H. Lee, and H. Morkoc, eds., Springer-Verlag, New York (1987), p. 228.
4. J. P. Donnelly and F. J. Leonberger, *Solid-State Electron.* **20**, 183 (1977); K. Steeples, G. Dearnaley, and A. M. Stoneham, *Appl. Phys. Lett.* **36**, 981 (1980).
5. R. C. Bowman et al., *Ion Beam Processing of Advanced Electronic Materials*, N. W. Cheung, A. D. Marwick, J. B. Roberto, eds., Materials Research Society, Pittsburgh (1989), p. 303.
6. U. Eicker et al., *Phys. Rev. B* **39**, 3664 (1989).
7. A. Darzi et al., *J. Appl. Phys.* **67**, 443 (1990).

Novel Short-Wavelength Lasers

J. M. Herbellin,
Aerophysics Laboratory

The nitrogen fluoride/bismuth fluoride reaction system continues to be under intensive investigation as an energy source to power a short-wavelength (visible blue) laser. Most of our past work has focused on the development of an extensive kinetic database and the successful scaling of the NF and BiF excited states to the densities required for laser operation. Meanwhile, very little is known about the ground-state properties of BiF, in particular the distribution of the population in the vibrational levels. This work has been directed toward the characterization of this distribution by analyzing the emission from a high- Q resonator surrounding a 1.5-m pin discharge facility. The results from this study show that the lower-state vibrational levels are not fully relaxed and, if one attempts to fit them to a Boltzmann distribution, the resulting temperature, $T_{\text{vib}} = 1800$ K, is substantially higher than the excited-state vibrational temperature, $T_{\text{vib}}^* = 950$ K. Moreover, intracavity absorption measurements show that the system is very close to gain threshold on the 0-3 transition, and that operation of the reaction system at lower temperature and pressure, such as can be achieved in a supersonic flow medium, may be sufficient to produce lasing.

We recently reported [1] the production of high concentrations (4×10^{11} mol cm $^{-3}$) of electronically excited BiF(AO^+) by the injection of trimethylbismuthine (TMB) into a supersonic flow of electronically excited nitrogen fluoride, NF($a^1\Delta$). Winker, Benard, and Seder [2] reported the successful scaling of BiF(AO^+) to still higher concentrations in a pulse mode using the dissociation of fluorine azide as the source of NF($a^1\Delta$), and

they provided preliminary evidence of inversion and perhaps even gain. The question then arises as to whether or not the lower concentrations and temperature regimes associated with the supersonic flow experiments could likewise support an inversion resulting in sufficient gain to sustain lasing.

Due to the low gains associated with shorter-wavelength laser systems, very long gain lengths as well as very high Q cavities are required to achieve threshold. Warren and Schneider [3] presented an attractive method for developing such a long gain length in a supersonic flow—the use of a blowdown facility. However, because such an approach requires a substantial investment of both time and equipment, we decided to use a long-pulse discharge as the medium generator. This approach is quicker, much less expensive, and can be used to determine if the ground-state vibrational distribution is indeed a Boltzmann distribution and to determine its temperature.

We constructed a 1.5-m 500-pin discharge facility (Figure 1) into which various mixtures of hydrogen (H_2), trimethylbismuthine (TMB), tetrafluorohydrazine (N_2F_4), sulfur hexafluoride (SF_6), and helium (He) diluent were introduced in order to produce BiF in the electronically excited (AO^+) and ground (XO^+) states, respectively. The excited-state BiF densities were monitored using the ($A-X$) spontaneous emission, which also provided information about the temperature and vibrational distribution of the excited state. These measurements and the associated analysis are quite straightforward and have been discussed in considerable detail elsewhere [1-3]. However, measurement of the ground elec-

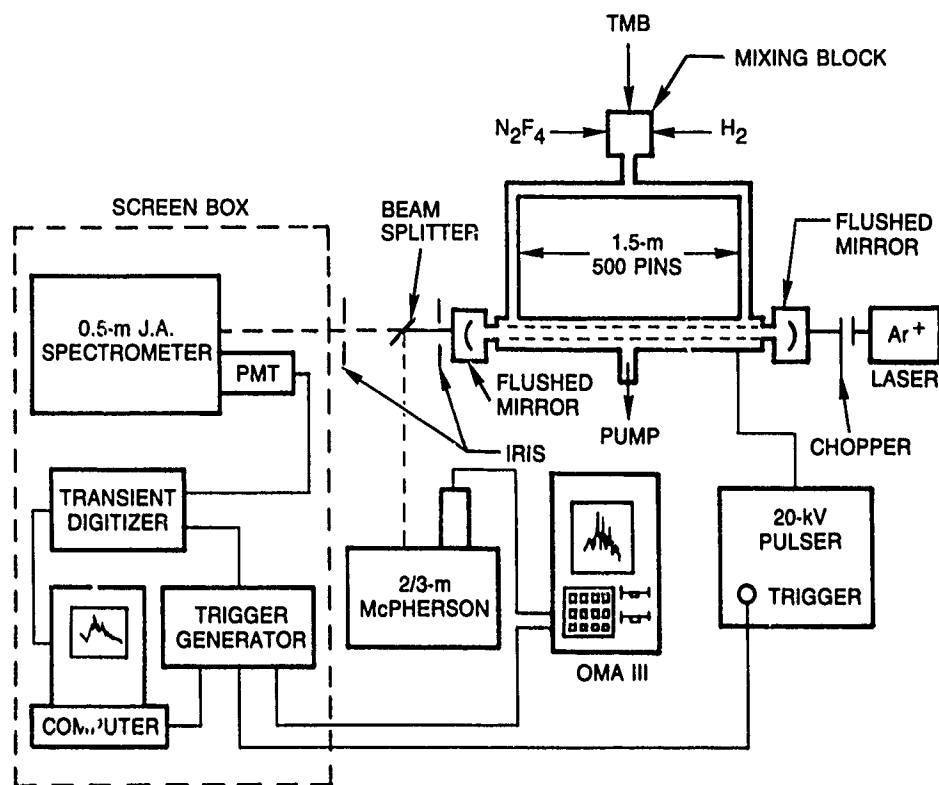


Figure 1. Schematic overview of absorption and cavity emission experiment.

tronic state presents a somewhat greater challenge; for this, we applied two complementary techniques. The first involved the use of a single-frequency continuous-wave (CW) ring dye laser with a 1-MHz bandwidth tuned to a single vibrational-rotational transition of the ($A, \nu' = 1; X, \nu'' = 0$) band. The dye laser was positioned at line center by observation of the laser-induced fluorescence generated in a separate facility. For mixtures containing only SF₆, TMB, and He, BiF(X) densities as high as 1×10^{13} mol cm⁻³ were observed, corresponding to an absorption of nearly 50% over the 1.5-m path length. A detailed comparison to the pulsed, optically pumped laser experiments of Davis and co-workers [4] suggests that this is more than sufficient absorption to produce a pulsed, optically pumped BiF laser, an experiment that is now in progress in another laboratory.

Meanwhile, the mixtures that contained both H₂ and N₂F₄, in addition to TMB and He (SF₆ optional), did not show any ground-state absorption down to our detection limit of approximately 2%/pass, which corresponds to a ground-state BiF($X, \nu'' = 0$) concentration of 2×10^{12} mol cm⁻³. This result was very encouraging, since these same mixtures were optimized to yield excited-state BiF(A) densities on the order of $\sim 1 \times 10^{12}$ mol cm⁻³. It is reasonable to expect that the higher vibrational levels of the ground state have smaller populations and, therefore, there is the definite possibility of chemically pumped inversion and gain on the transitions to these levels.

Subsequently, high-quality mirrors were purchased and placed into the cavity. It was our hope that we might

observe laser action; however, the temperatures achieved in the pulse facility were too hot to permit lasing.

The very-high-reflectivity mirrors were obtained by the application of a special-order dielectric coating from Ojai Corporation on substrates polished to 1 Å equivalent scattering roughness by General Optics. A reflectance of 0.9999 was verified by direct measurement using the cavity-attenuated phase-shift (CAPS) technique [5] at the 488-nm line of an argon ion laser. The CAPS approach is strictly a CW technique and, in order to measure the effective cavity lifetime during the actual discharge and subsequent reaction period, which lasts on the order of 50 μs, we used the alternative ring-down procedure [6]. We measured a 19.5-μs lifetime for the photons in the cavity which, for the 2.2-m separation of the mirrors, computes to 1333 round trips or a single-pass loss of 375 ppm. The difference between this and the 100-ppm reflectance loss is attributed to a combination of mode mismatching with the probe laser and scattering losses in the medium.

With the high- Q cavity established, we investigated the effect of this cavity on the band emissions. Figure 2(a) shows a typical BiF($A-X$) emission spectrum (no cavity) as recorded using an optical multichannel analyzer (OMA III) through a 0.67-m McPherson spectrometer. Figure 2(b) shows the relative emissions of these same bands as measured at the peak of the emission pulse ($t \sim 20$ μs) using a 0.50-m Jarrell-Ash spectrometer/LeCroy transient digitizer combination (JAL). Figure 2(c) shows the relative emissions (with cavity) as measured with the JAL.

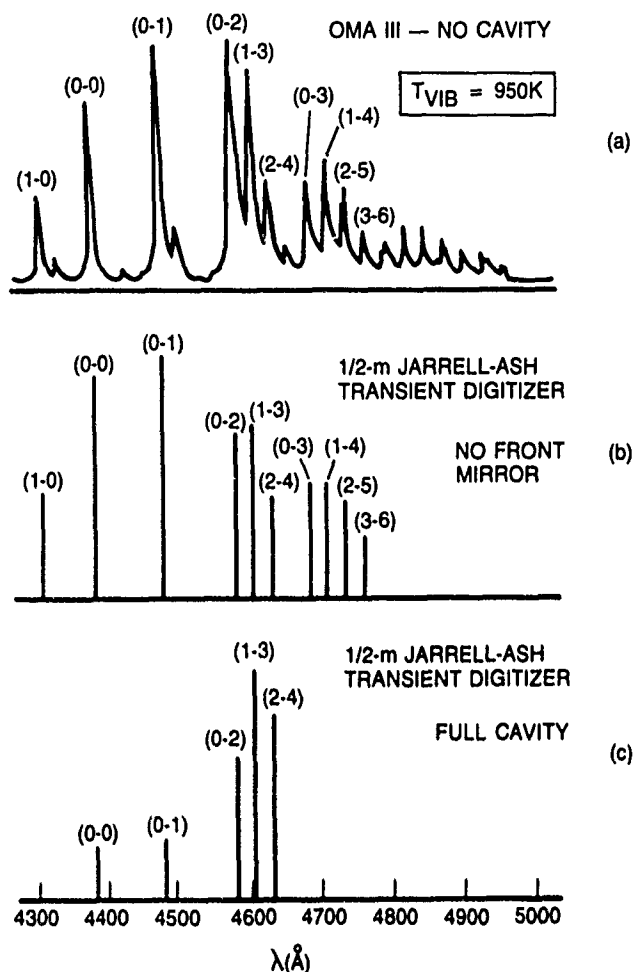


Figure 2. (a) Emission spectra (no cavity) as measured using the OMA III/0.67-m McPherson spectrometer system; (b) the relative band emission (no cavity) as measured using the 0.50-m Jarrell-Ash/LeCroy transient digitizer system; (c) the relative band emissions (with cavity) as measured using the Jarrell-Ash/LeCroy system.

The JAL technique was necessary due to the very low signal with the front mirror in place (it is in effect a 1×10^{-4} transmitting filter). That we observed any light out at all supports the fact that the single-pass absorption was quite small, even on the bands terminating on $v'' = 0$. Moreover, the strong distortion of the relative emissions confirms our previous expectations that this absorption would decrease for the bands terminating on the higher-ground-state vibrational levels.

We now show how the ratio of these emissions, for the front mirror on and off, leads to a determination of the population of these vibrational levels. With the back mirror only, the observed emission, $I(\text{no cavity})$, is given by the simple expression μ

$$I(\text{no cavity}) = GI_{sp}(1 + R), \quad (1)$$

where G is a geometric factor, R is the mirror reflectance, and I_{sp} is the spontaneous emission. When the front mirror is in place, the expression for the external emission, $I(\text{cavity})$, is given by

$$I(\text{cavity}) = 2GI_{sp} \sum_{n=0}^{\infty} (Re^{-\alpha\ell})^{2n}, \quad (2)$$

$$I(\text{cavity}) = 2GTI_{sp}/(1 - R^2e^{-2\alpha\ell}), \quad (3)$$

where T represents the transmission of the mirror, and ℓ is the length of the active medium: 1.5 m.

Assuming that $R \sim 1$ and the single-pass absorption α is < 1 , we can arrive at the simple expression for population density difference ΔN between the upper (u) and lower (l) levels for each of the different bands. The expression involves the ratio of $I(\text{no cavity})$ and $I(\text{cavity})$ and the effective stimulated absorption cross section for the band system, σ_{lu} :

$$\Delta N = N_l - N_u = T[I(\text{no cavity})/I(\text{cavity})]/2\sigma_{lu} \quad (4)$$

Since the populations of the vibrational levels of the upper, electronically excited $\text{BiF}(A, v')$ can all be determined from analysis of the spontaneous emission, the population of each of the vibrational levels of the ground state $\text{BiF}(X, v'')$ can be computed using Eq. (4).

The resulting deduced populations for the different ground-state vibrational levels are shown in Figure 3 as a function of the N_2F_4 flow rate. We have assumed that the effective stimulated absorption cross section for each of the respective bands can be approximated as ~ 0.5 of the value for the peak rotational transition. This accounts for the fact that we are measuring an average absorption over a portion ($\sim 10 \text{ \AA}$) of the band rather than of a single line.

Note first that the absolute value of the $v'' = 0$ population is consistent with the previous dye-laser absorption measurements. This supports the validity of this approach and the foregoing approximations for those transitions that are clearly absorbing (we will return to this point later). The next important feature is that the vibrational levels seem to be separated into two groups: levels $v'' = 0, 2, 3$ and $v'' = 1, 4$. One expects the $\text{BiF}(X, v'')$ to increase with increasing N_2F_4 (and $\text{NF}(a^1\Delta)$), but it is unclear why there appears to be such a variation within the ground state.

The deduced ground-state vibrational-level population is plotted in Figure 4 as a function of the vibration quantum number v'' ; only for the 100- $\mu\text{mole/s}$ flow rate does the distribution approach a Boltzmann distribution. If we attempt to assign a Boltzmann temperature, we find that $T_{\text{vib}} = 1800 \text{ K}$, or nearly twice the temperature deduced for the excited state from its emission spectrum (lower dashed curve). Indeed, this unrelaxed distribution closely resembles the distribution that can be predicted from Franck-Condon radiation from the excited state (upper dot-dash curve). However, this Franck-Condon distribution is for the most part independent of the vibrational temperature of the excited state and, therefore, independent of the N_2F_4 or $\text{NF}(a^1\Delta)$, which is not consistent with our observations.

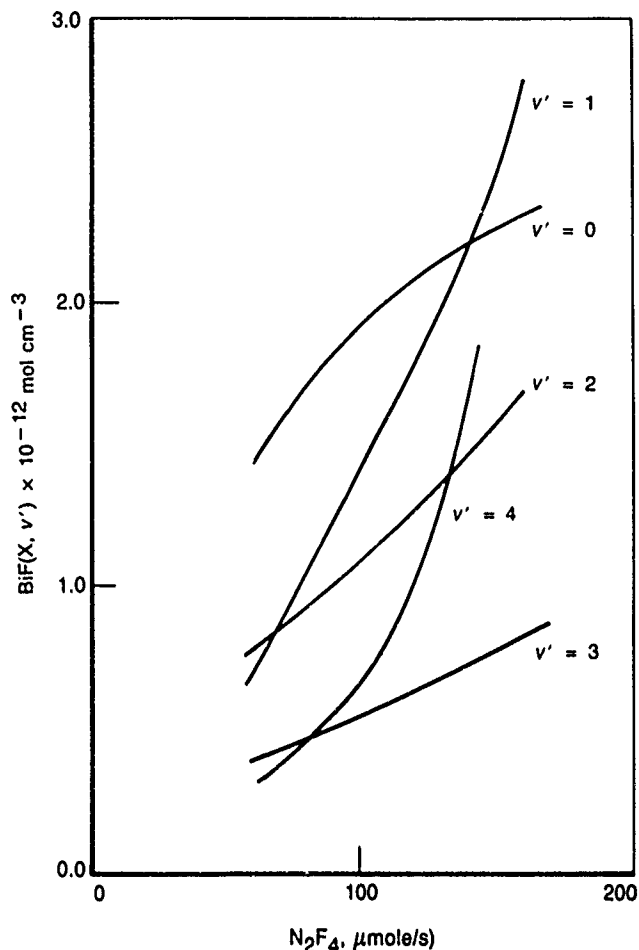


Figure 3. Deduced $\text{BiF}(X, v')$ ground vibrational-state populations as a function of the N_2F_4 flow rate.

An alternative explanation for the anomalous hot vibrational distribution of the ground state is that it results from quenching processes on the BiF dark states that could be feeding the $\text{BiF}(X, v')$ levels. Ever since the discovery of this reaction system, these dark states have been suspected to be involved in the generation of the excited-state $\text{BiF}(4)$ by collisions with $\text{NF}(a^1\Delta)$ [7,8], although to date this remains an open question; the more recent studies appear to support the original mechanism [9].

However, any kinetic models that might be conceived to explain the unusual distribution all suffer from one fundamental inconsistency: the excited state, with a $1.4\text{-}\mu\text{s}$ radiative lifetime, shows a Boltzmann $T_{\text{vib}} = 950\text{ K}$ distribution, whereas the ground state, with a much longer lifetime, hundreds of milliseconds, is not Boltzmann. Any kinetic argument would have to assume that the vibrational relaxation of the ground state is orders of magnitude slower than for the excited state, and this is extremely difficult to believe since the vibrational spacing is comparable.

One explanation, however, circumvents this dilemma. The anomalous, non Boltzmann distribution is really the first indication of gain. This follows from the fact that

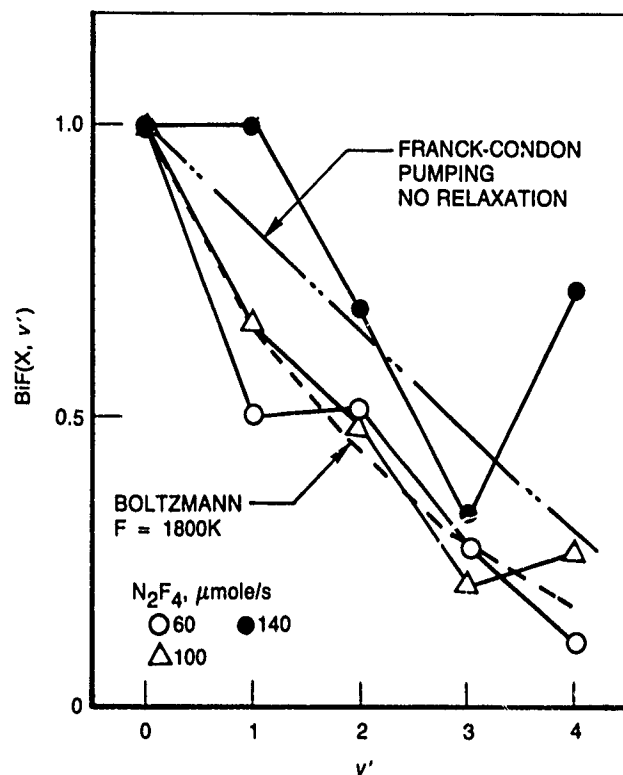


Figure 4. Deduced $\text{BiF}(X, v')$ ground vibrational-state populations as a function of the ground-state vibrational quantum number v' for various N_2F_4 flow rates.

the preceding analysis basically involves an integration in time over the cavity lifetime ($\sim 20\text{ }\mu\text{s}$), during which time the medium is assumed to be absorbing. If, on the other hand, the medium actually produced gain during some portion of this time, then an increased signal would be emitted from the cavity, which would be interpreted as an anomalously low population. The population difference ΔN that was measured for the various transitions is shown in Figure 5 together with the absolute density of the $v' = 0, 1$, and 2 levels of the excited state. It is important to note that deduced population differences for the 0-2 and 1-3 transitions are less than the absolute populations of the corresponding excited-state level, $v' = 0$ and $v' = 1$, respectively, whereas for the 0-1 and 2-4 transitions, the deduced population differences are greater than the corresponding excited-state level, $v' = 0$ and $v' = 2$, respectively.

In other words, for the 0-2 and 1-3 transitions, the generation of an inversion, and thus gain, for a few microseconds is very likely to have occurred, given that the deduced population difference, which is an average, is less than the excited-state population. Meanwhile, for the 0-0, 0-1, and 2-4 transitions, this is not the case and normal behavior is anticipated.

As a final piece of evidence, we have reproduced, in Figure 6, the deduced ground-state vibrational distribution that was obtained in an earlier study in which a simi-

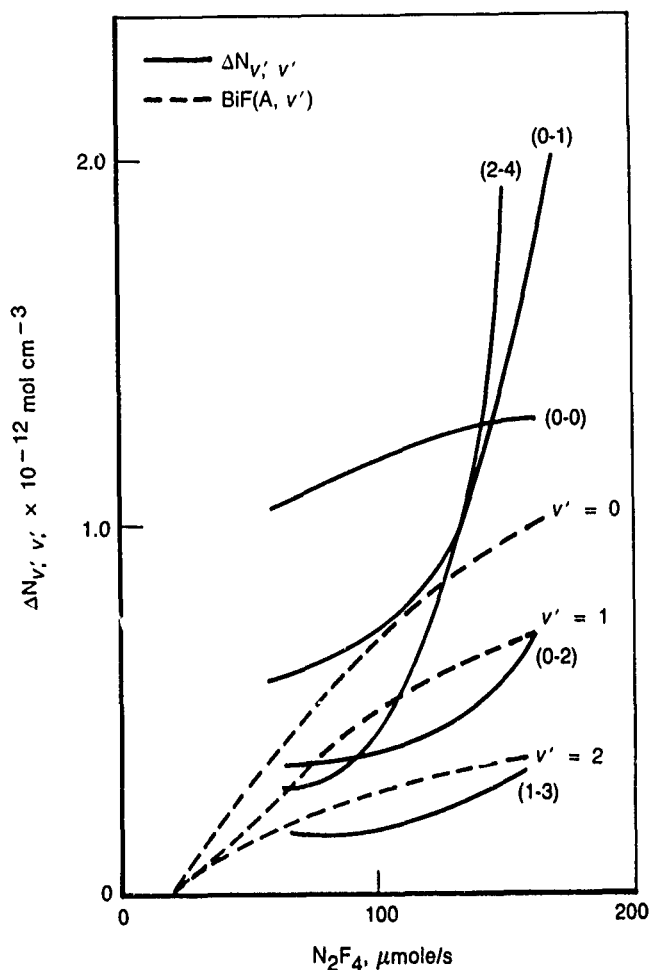


Figure 5. Deduced population differences $N_{v', v''}$ for the relevant transitions (solid lines) and absolute populations of the excited-state vibrational levels, $\text{BiF}(A, v')$ (dashed lines).

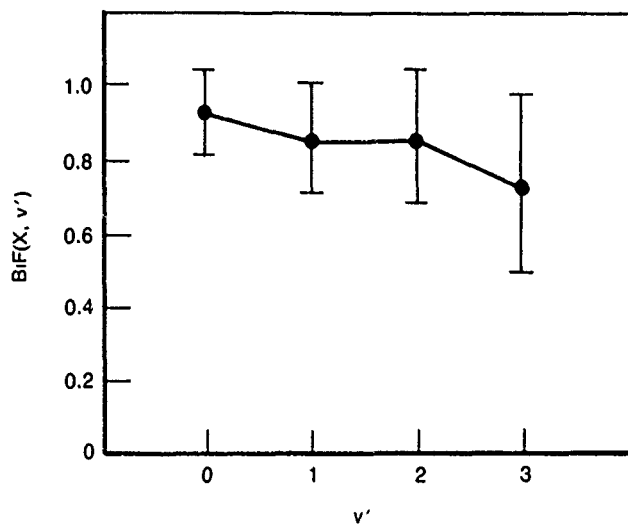


Figure 6. Deduced ground-state vibrational-level population distribution from a prior study (see text).

lar, but not identical, pulse discharge facility was used [10]. Somewhat higher densities of both $\text{BiF}(\text{AO}^+)$ and $\text{BiF}(\text{XO}^+)$ were generated, so that single-pass absorption was sufficient to determine the ground-state distribution by comparing the emission with and without the back mirror. As can be seen, the distribution is quite hot, and the $v'' = 2$ and 3 levels are behaving as expected. Although this is far from conclusive proof, it is nevertheless a most encouraging result. It strongly suggests that if the static temperature is reduced from the 950 K region of this experiment to < 700 K, which was already accomplished using a supersonic flow [1], then inversions, gain, and lasing should occur on the 0-3 and 1-4 transitions.

* * * * *

1. J. M. Herbelin and M. A. Kwok, "Production of $\text{Bi}(^2\text{D})$ and $\text{BiF}(\text{AO}^+)$ in a Supersonic Flow," *Proceedings of the International Society for Optical Engineering-High Power Gas Lasers*, 1225, Avizonis et al., eds. (January 1990), p. 560.
2. B. K. Winker, D. J. Benard, and T. A. Seder, "Chemical Pumping of Potential Visible Laser Transitions in Bismuth Monofluoride by Thermal Dissociation of Fluorine Azide," *ibid.*, p. 543.
3. W. R. Warren, Jr. and L. B. Schneider, "New Fluid Dynamic Experimental Techniques in Chemical Laser Research," *ibid.*, p. 571.
4. S. J. Davis, L. Hanko, and R. F. Shea, "Iodine Monofluoride B-X Lasing from Collisionally Pumped States," *J. Chem. Phys.* **78** (1), 172 (1983).
5. J. M. Herbelin and J. A. McKay, "Development of Laser Mirrors of Very High Reflectivity Using the Cavity-Attenuated Phase-Shift Method," *Appl. Opt.* **20** (19), 3341 (1981).
6. A. O'Keefe and D. Deacon, "Cavity Ring Down for Optical Measurements," *Rev. Sci. Instrum.* **59**, 2544 (1988).
7. J. M. Herbelin and R. A. Klingberg, "Efficient Production of Electronically Excited $\text{BiF}(\text{AO}^+)$ via Collisions with $\text{NF}(a^1\Delta)$," *Int. J. Chem. Kinet.* **16** (7), 849 (1984).
8. K. Balasubramanian, "On the Low-Lying Electronics State of BiF ," *Chem. Phys. Lett.* **127** (4), 324 (1986).
9. J. S. Holloway, "Kinetics of the $\text{Bi}(^2\text{D})$ and $\text{BiF}(\text{XO}^+)$ in the $\text{NF}(a^1\Delta)/\text{BiF}$ Laser System," *Proceedings of the International Conference on Lasers '90*, STS Press (1991).
10. J. M. Herbelin, "Scaling of a Blue-Green Chemical Laser Candidate," paper 1391, AIAA 19th Fluid

Herbelin, J. M., "Electronic Energy Transfer Between NF(b) and IF(X)," *Chem. Phys. Lett.* **133** (4), (1988).

_____, "Short-Wavelength Laser Development," *Proceedings of the International Conference on Lasers '87*, STS Press (1987), p. 218.

_____, "Short-Wavelength Chemical Laser Development," *Proceedings of the International Conference on Lasers '89*, STS Press (1989), p. 241.

_____, "High-Power Gas Lasers," *Proc. SPIE* **1225** (1990).

Stimulated Brillouin Scattering Phase Conjugation

S. T. Amimoto and R. F. W. Gross,
Aerophysics Laboratory

The role of space surveillance is undergoing rapid expansion to reflect recent changes in U.S.-Soviet political relations, military incursions in the Middle East, and a strong desire to monitor environmental changes or pollutants. To meet the challenge posed by these changes, we are investigating a new class of ultrasensitive coherent detectors (USCDs) that will enable new missions that reflect these recent developments. These detectors have remarkable capabilities. In the future, we envision a space-based capability to look through clouds at optical frequencies, to detect objects submersed in the seas, and to detect and identify trace molecular constituents in the atmosphere. The detector is also able to correct an image distorted by its passage through an aberrating medium (i.e., turbulent atmosphere or poor optics) in a single pass on a time scale limited only by the speed of light.

The performance of these new detectors and the feasibility of these new missions are based on measurements performed by Pasmanik [1], who reported gains of 10^{12} [2], noise levels of one photon/pixel [3,4], and narrow bandwidths of 30 to 700 MHz at 1060 nm. The capability of this detector is limited only by its extremely narrow bandwidth, which serves to exclude background noise, and the low noise level comparable to a quantum-limited detector.

In this project, USCDs under investigation are based on the use of laser amplifiers rods and a four-wave Brillouin mirror (FWBM). Typically, USCDs would be used in a surveillance system to detect a scattered return of a whole or partial image that is produced by active illumination of a target. The FWBM is a dynamic mirror formed when three light beams, one of which is the signal to be detected, are temporally and spatially overlapped in a Brillouin medium to generate a fourth (return) beam. Generally, a high pressure gas or a liquid may be used for the Brillouin medium. The advantage of a FWBM is that the phase conjugation process may be made thresholdless

with the result that the mirror can be used to conjugate extremely weak input signals.

The overall objective of this work is to study and develop USCDs for surveillance applications. Three general areas of research will be addressed:

- The study of a laboratory bench-top USCD as a function of parameters that affect its efficiency and conjugation ability; i.e., phase matching, bandwidth, spatial resolution, gain, and noise level. During the past year, we emphasized the investigation of a FWBM without the laser amplifier and measured its sensitivity, noise level, and spatial resolution. Studies of the USCD have been postponed until the required laser amplifiers now on order are delivered.
- Investigation of a technique for single-pass image correction using FWBMs. A method that uses a special optical filter to isolate aberration information was identified for further study [5]. The question of how well correction may be effected will be answered by investigating the spatial resolution ability, the field of regard, and the number of optical modes of the FWBM used in the corrective process.
- The use of nonlinear frequency mixing methods to provide frequency-agile tuning of the detector from 200 to 12,000 nm. The fidelity and resolution of the image are affected by phase matching bandwidths determined by geometric and nonlinear crystal choices. A goal is the measurement and development of theoretical limits that govern resolution requirements for imaging in the frequency-agile tuners.

Some experiments have been performed on a high-pressure methane FWBM to investigate the phase conjugation performance of a FWBM with the experimental arrangement shown in Figure 1. These results will be published in detail later. These results are needed to guide

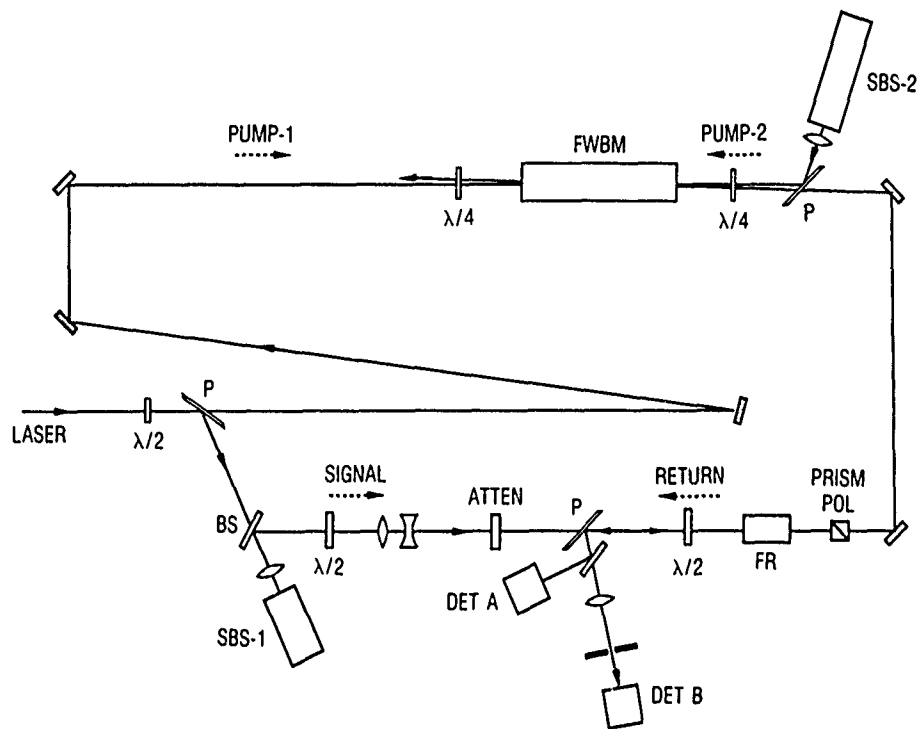


Figure 1. Experimental layout of a four-wave Brillouin mirror experiment. A single-frequency (mode) laser is used to provide the signal and pump beams. The major portion of the main laser beam passes through the polarizer and traverses the FWM. It is deflected into the cell, SBS-2, and is returned to the FWM as a frequency-shifted beam, pump 2. The $\lambda/4$ waveplates on each end of FWM ensure that pump-1 and pump-2 are circularly polarized in opposite polarizations to reduce noise leakage into the phase conjugate return beam. The minor portion of the main laser beam is split off by the use of a $\lambda/2$ waveplate and the polarizer P and is converted to the signal frequency within the cell, SBS-1. It is diverted by the beam splitter

BS to the rest of the signal beam train. The $\lambda/2$ waveplate, the polarizer, and absorbing glass filters are used to adjust the intensity of the signal beam. The signal beam passes through the $\lambda/2$ waveplate, the Faraday rotator FR and the prism polarizer, which are used to ensure that only the properly polarized return from the FWM is reflected by the polarizer near the detectors. The signal beam passes through the polarizer near cell SBS-2 into the FWM, where it is reflected as a phase-conjugated return beam. This return beam is detected by detectors A and B (which has a lens and pinhole aperture placed before it). The Strehl ratio is proportional to the ratio of responses of detector B to detector A.

future experiments in which laser amplifiers will be added to form the USCD. Although the experiment and its layout are complex, the physics of the FWM can be explained in a simplified manner. A high-energy beam (pump 1) and a frequency-shifted signal beam enter the FWM; the electric fields of the beams act on the molecules or atoms of the Brillouin medium by means of electrostrictive forces to form an acoustic-wave interference pattern. The high-energy pump beam traverses the cell and enters a stimulated Brillouin scattering (SBS) cell, where it is phase-conjugated, converted to a slightly different frequency, and returned back into the FWM. This returned second high-energy beam (pump 2) is used to read the acoustic interference pattern. The signal beam in this experiment is generated in another SBS cell, SBS-1, and the returned phase-conjugated beam is detected by DET B.

In the experiment, input (signal) and phase-conjugated (returned) energies are measured and the ratio (shown as reflectivity) is plotted for three values of pump energy (Figure 2). The data indicate that the reflectivity is constant over six orders of magnitude in signal intensity.

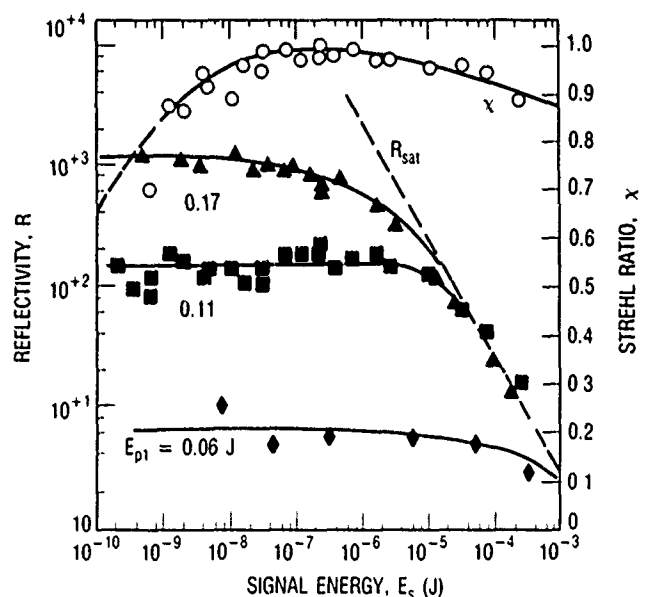


Figure 2. Reflectivity and Strehl ratios of a methane-based FWM. Pump energies E_{p1} were varied from 0.06 to 0.17 J/pulse.

As the pump intensity is increased, the gain or reflectivity of the FWBM also increases. For large input signal energy the amplification reaches a saturation value that produces a return beam of 1.8 mJ/pulse independent of the pump energy. As the pump energy is increased, the saturation level is reached at lower signal input levels due to higher gain from the larger pump level. As the signal intensity is decreased, a limit is reached where the return beam energy is dominated by spontaneous Brillouin noise caused by scattering from thermal phonons in the medium. Strehl ratio measurements, which are a measure of the goodness of beam quality, are also shown in Figure 2. (A beam of perfect beam quality has a Strehl ratio of 1.0.) Strehl ratios of 0.9 or more were observed above 10^{-9} J. When noise is equal to the return signal, the Strehl ratio is 0.5, a level at which the phase conjugation ability of the FWBM is degraded by the thermal noise. From independent estimates of total noise [6] we can infer the quantum efficiency (0.012) and the number of transverse spatial modes (67) that are related to the spatial resolution of the FWBM. These measured noise-limited sensitivity and spatial resolution values would apply to a USCD using this methane-based FWBM.

Correction of aberrations in single-pass and two-way pass configurations, as shown in Figure 3, have also been studied. Single pass refers to a configuration in which the signal is passed through the aberrator into the FWBM, and the return beam is detected without passage through the same aberrator. The two-way pass refers to a configuration in which the signal is passed through the aberrator into the FWBM, and the return is sent back

through the aberrator before it is detected. Despite the preliminary nature of the experiments, the results have been highly encouraging. Resolution and phase correction ability of a combined lens and FWBM are measured. Preliminary measurements using a standard resolution target show that resolution is limited by the effective f -number of the lens and by the Fresnel parameter of the Brillouin mirror. The Fresnel parameter, the ratio of the transverse extent of an image or imaging system divided by the resolution, is calculated using $D*d/(\lambda*L)$, where d is the transverse extent of the image, D is the aperture of a lens, λ is the wavelength of light, and L is the length of the gain medium or distance from the lens to image. Resolution of $30\text{ }\mu\text{m}$ was observed using a 20-cm focal length lens.

Experiments to test aberration correction using two different aberrators have been performed. When a beam is passed through an aberrator and then phase-conjugated upon reflection from the FWBM, the second pass through the aberrator *undoes* the beam degradation, restoring the original image quality. Unaberrated and aberrated images returned from the methane FWBM are shown in Figures 4(a) and 4(b) for a double-pass experiment. The aberrator was a resealable plastic bag used for storage. Differences due to the presence of the aberrator are not discernible, which implies good correction. Correction of fog-induced aberrations was also attempted using an ultrasonic humidifier to produce a water aerosol cloud with average particle diameter of $5\text{ }\mu\text{m}$, Figure 4(c). Calculations show that following a single pass of a whole beam through a cloud, the transmitted beam experiences optical smooth-

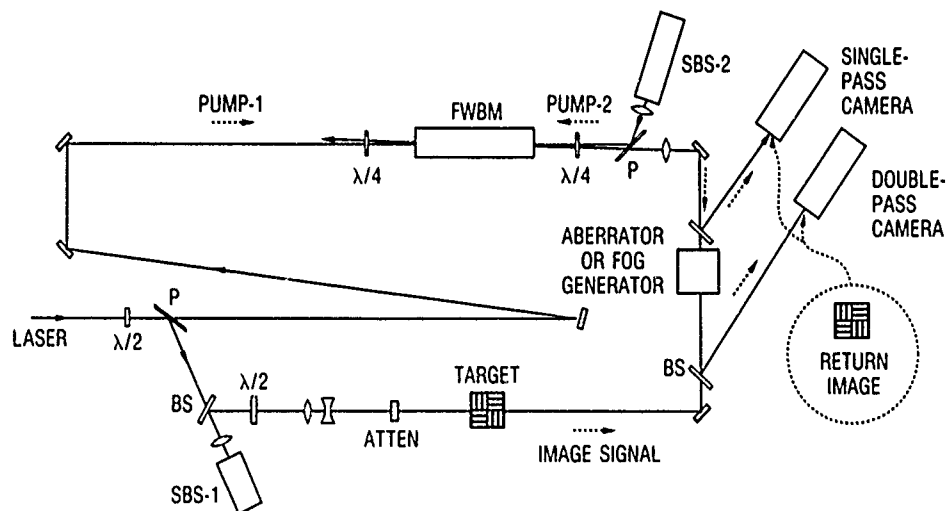
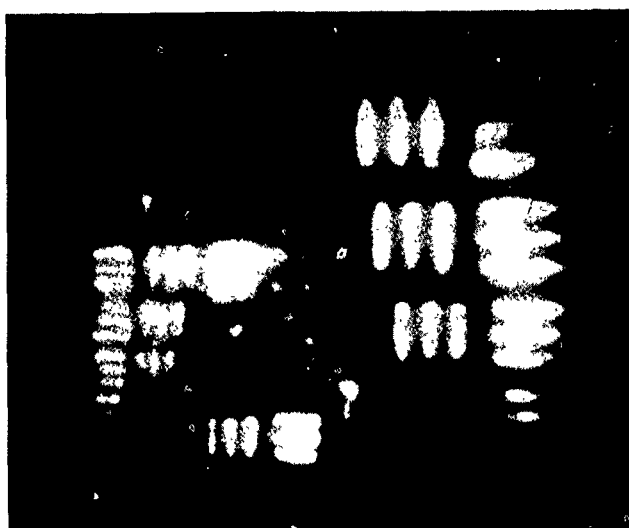


Figure 3. This layout is similar to Figure 1, but has been modified to accept images. A resolution target is inserted just after the attenuator in the signal beam train to investigate the phase conjugation of images. A lens located near the polarizer between cell SBS 2 and the FWBM (in the signal beam train) is used to relay the image of the target into the FWBM and to focus the return image to the CCD cameras after reflection by the beam splitter. An aberrator or fog gen-

erator is placed midway between the beam splitter and lens. Pump-1 and pump-2 portions of the beam train are identical to those of Figure 1. The single-pass camera sees the phase-conjugated image returned from the FWBM that has traversed the aberrator only once. The double-pass camera sees the phase-conjugated image returning from the FWBM after it has passed back through the aberrator or fog cell.



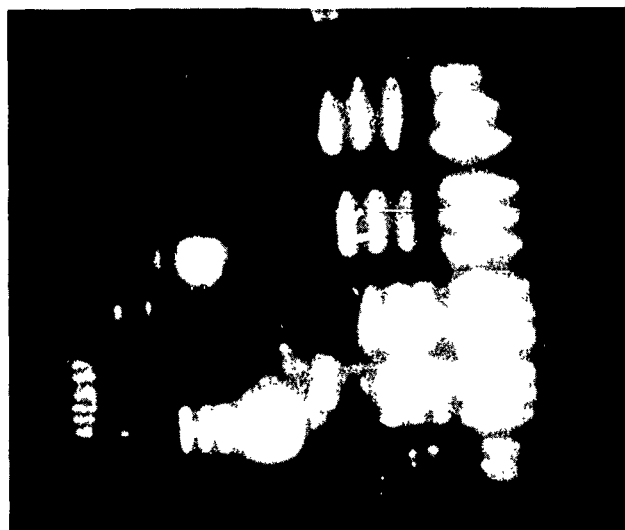
(a)



(b)



(c)



(d)

Figure 4. Conjugated images returned from a FWBM based on methane. A standard Air Force resolution target was used in these experiments to estimate image resolution. (a) Unaberrated target in a double-pass configuration. The smallest triplet of lines is 14 line pairs/mm; (b) the identical target and condition as in (a), but a flat

plastic bag inserted near the imaging lens was used to aberrate the image; (c) a double-pass image through a water aerosol cloud of transmission 10^{-2} ; (d) a single-pass image through the water cloud aerosol of transmission 10^{-2} . The resolution target in (c) was inadvertently placed upside-down relative to the others.

ing (averaging of optical path differences along the transverse direction) but is attenuated by Mie scattering. This incoherently scattered beam is predominantly in the forward direction but is several orders of magnitude smaller than the coherently transmitted beam. They become approximately equal when the cloud transmission is 10^{-7} . This number is dependent on the geometry of the beam, the number and size of scatterers, and the observation geometry. In general, the transverse resolution necessary to conjugate the incoherent beam is on the order of the dimensions of the wavelength of light λ , too high for successful conjugation in this limit. However, it is expected that for the coherently transmitted beam, even in the double-pass case, good imaging will be possible. In-

deed, good double-pass images could be obtained down to one-way cloud transmissions of 10^{-2} , where total cloud losses experienced by the signal and return beams were 10^{-4} . Single-pass detection through clouds was also successfully observed for cloud transmission down to 10^{-2} [Figure 4(d)]. These results imply that observation through many types of clouds may be readily achieved at optical frequencies. Up to now, the limit on how much attenuation can be handled by the FWBM based on the coherent-to-incoherent content of the input signal beam has not been verified and will be further investigated.

In summary, we have investigated a FWBM for use in an ultrasensitive detector. The noise, reflectivity or gain, quantum efficiency, and resolution capability were

characterized. The phase conjugation ability of a FWBM using simple aberrators has been demonstrated. For a water aerosol cloud used as an aberrator, images of targets were successfully detected through optically thick clouds. We will add the necessary laser amplifiers to convert the FWBM into an ultrasensitive detector for study next year. A liquid Brillouin medium will likely be used to reduce Brillouin noise further. Single-pass image correction and frequency mixing methods will also be pursued in a parallel course when the new laser system is delivered.

* * * * *

1. V. I. Bespalov and G. A. Pasmanik, "Nelineynaya Optika i Adaptivnyye Sistemy," (*Nonlinear Optics and Adaptive Systems*) (in Russian), Moscow (1986).
2. N. F. Andreev et al. "Wave-front Inversion of Weak Optical Signal with a Large Reflection Coefficient," *JETP Lett.* **32**, 625 (1980).
3. A. Z. Matveev, "Noise of Four-Wave Hypersonic Wavefront-Reversing Mirrors Under Absolute Instability Conditions," *Sov. J. Quantum Electron.* **15**, 783 (1985).

4. V. I. Bespalov, A. Z. Matveev, and G. A. Pasmanik, "Limiting Sensitivity of a Stimulated-Brillouin-Scattering Amplifier and a Four-Wave Hypersonic Phase Conjugating Mirror," *Izvestia Vyssh. Ucheb. zaved. Radiofiz.* **19**, 1080 (1986).
5. G. O. Reynolds, D. E. Yansen, and J. L. Zuckerman, "Time Varying Random Media Compensation with Holography," in *Developments in Holography*, J. B. DeVelis and B. J. Thompson, eds., *Proc. SPIE* **25**, 183 (1971).

Amimoto, S. T., R. W. F. Gross, and L. Garman-DuVall, "Phase Conjugation of Transient Pulses by a SBS Oscillator-Amplifier System," Paper PD49, Conference Proceedings, CLEO, Baltimore, 24-28 April 1989.

_____, "Gain and Phase Conjugation Fidelity of a Four-Wave Brillouin Mirror Based on Methane. Phase Conjugation Through Dense Fog," Paper QDP36, Conference Proceedings, IQEC/CLEO '90, Anaheim, California, 21-25 May 1990.

Microparticle Linear and Nonlinear Optics

D. E. Masturzo and A. Pluchino,
Chemistry and Physics Laboratory

The fundamental objective of this project is to improve our understanding of the emissivity of aluminum oxide microparticles. The relevance of this objective to the correct prediction of infrared signatures from aluminumized solid propellant rockets has been discussed previously [1]. Significant progress has been made recently in the development of our measurement system.

Measurement of the emissivity of a single aluminum oxide particle involves levitating the particle in an evacuated chamber, heating it with a laser, shutting off the laser, and observing the decay of the particle's thermal radiation with an InSb detector. From the thermal radiation decay curve, particle temperature and emissivity values can be calculated. Critical to this type of measurement are control of the irradiating laser beam, the particle environment, and the particle stability both during and after pumpdown. For this reason, various improvements were made in the apparatus during the past year.

Our new optical layout is shown in Figure 1. The main improvement is the use of a coated zinc selenide beam splitter to divide the beam into two approximately equal components that are then symmetrically lens-

focused onto the particle. In our earlier arrangement, an upward-going beam was focused on the particle with a lens; the beam exited the levitator, and a concave mirror refocused this light on the particle. Achieving upward and downward beams of equal intensity with this system was difficult. The new arrangement ensures equal laser irradiation from above and below. Confidence in the equality of upward and downward irradiances is important when estimating total particle irradiance and when aligning the beams on the particle using either photophoresis-induced motion or observation of laser scatter by means of a HgCdTe detector. The installation of an electro-optic modulator in our CO₂ laser cavity has further added to our control over the laser irradiation by enabling exposure times ranging from microseconds to tens of seconds.

Particle environment is another concern in our measurement. Previously, with the use of liquid nitrogen-cooled sorption pumps, the ultimate levitator chamber pressure was in the mid 10⁻⁴/Torr range. The vacuum system has now been upgraded by the addition of a cryopump, which allows pressures of about 2 × 10⁻⁵/Torr to be achieved. This increased operating range provides the

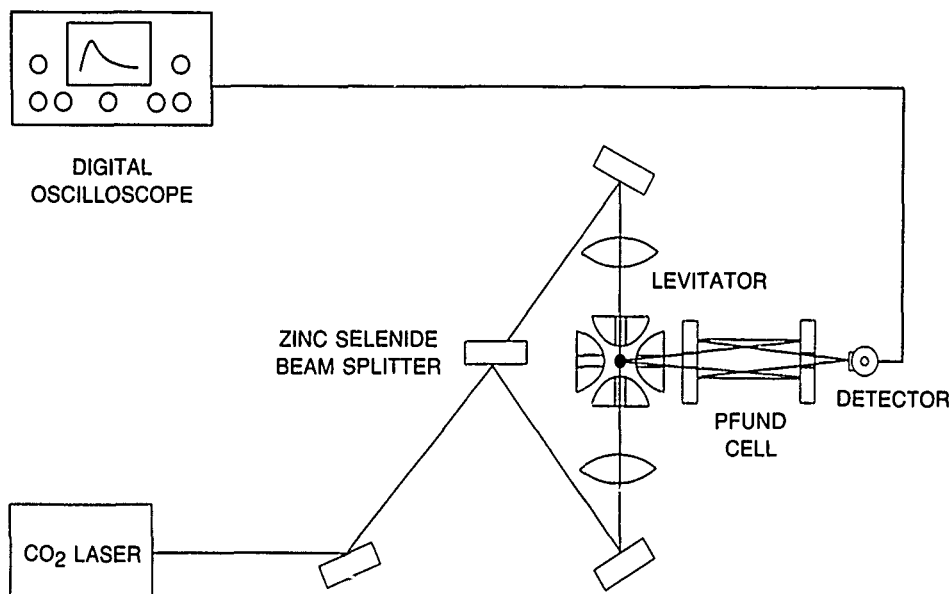


Figure 1. Single-particle emissivity measurement apparatus.

freedom to test for any pressure effects associated with the emissivity measurement.

During installation of the cryopump, the vacuum system was redesigned to provide more control over pumpdown. At the same time, the levitator electronics were changed so that the electrodynamic trap became more symmetric and stable. With these improvements came the ability to keep a single particle trapped during an entire pumpdown/irradiate/repressurize cycle. This ability allows spring point measurements to be made before and after the particle has been irradiated. Spring point measurements are done at atmospheric pressure and involve increasing the amplitude of the ac field in the levitator until the particle trapping becomes unstable. By noting the dc voltage on the levitator endcaps and the ac voltage and frequency on the levitator's center ring when the instability occurs, one can calculate both the net charge on the particle and the particle size. In the past, particles had to be trapped by pulling them off the levitator walls while under vacuum. Under these circumstances, no spring point measurement could be made, and particle size had to be determined using a microscope. The microscope measurements were difficult and presented large uncertainties compared to the spring point method. Although the fitting routine used to determine the particle temperature and emissivity allows for some uncertainty in the particle size, a precise value should result in more accuracy in the calculations. A further benefit is that any significant size change in the particle due to irradiation can be detected.

As the apparatus has been improved, the problem of particle motion has become increasingly important. There are two types of particle motion that need to be considered. One is that due to the loss of viscous damping. As the pressure in the levitator is reduced, the viscous

damping of the particle by the surrounding gas decreases. In the 10^{-4} /Torr regime, particle damping is still evident, and a levitated particle on the order of $20\text{ }\mu\text{m}$ in diameter rarely moves more than a diameter or so. In the 10^{-5} /Torr regime, damping becomes less and less effective. If not well isolated from vibrations, the particle can oscillate wildly, the swing of these oscillations increasing as the pressure is reduced. In the worst observed cases, particle orbits have reached at least 2 mm in diameter. Such motion in and out of a tightly focused laser beam can result in erratic heating. More important, the imaging of the particle onto the InSb detector is currently 1:1, and the detector diameter is approximately 1 mm. If a wildly moving particle is successfully heated by the laser beam, observing the particle's thermal decay becomes difficult, since the radiating particle is not always in the detector field of view. An example of this behavior is shown in Figure 2, where the thermal radiation signal from a carbon particle is plotted versus time during a 500-ms exposure. This problem can be overcome by imaging a larger area onto the detector. Our present approach is to take great care during the pumpdown process not to disturb the particle. If a transient disturbance sets the particle in motion, it can be calmed by briefly increasing the pressure in the chamber and then repumping. In most cases, such a procedure is successful up to the time that the particle is irradiated.

The second cause of particle motion is due to the particle changing its net charge during irradiation. In all experiments carried out so far, the trapped particles have had a net positive charge. Left in air, these particles will naturally lose charge at a very slow rate, and, with infrequent adjustment of the dc potential on the levitator endcaps, one can keep a particle trapped for days. Under vacuum, the change in charge with time is even slower. However, it is found that irradiating the particle either in

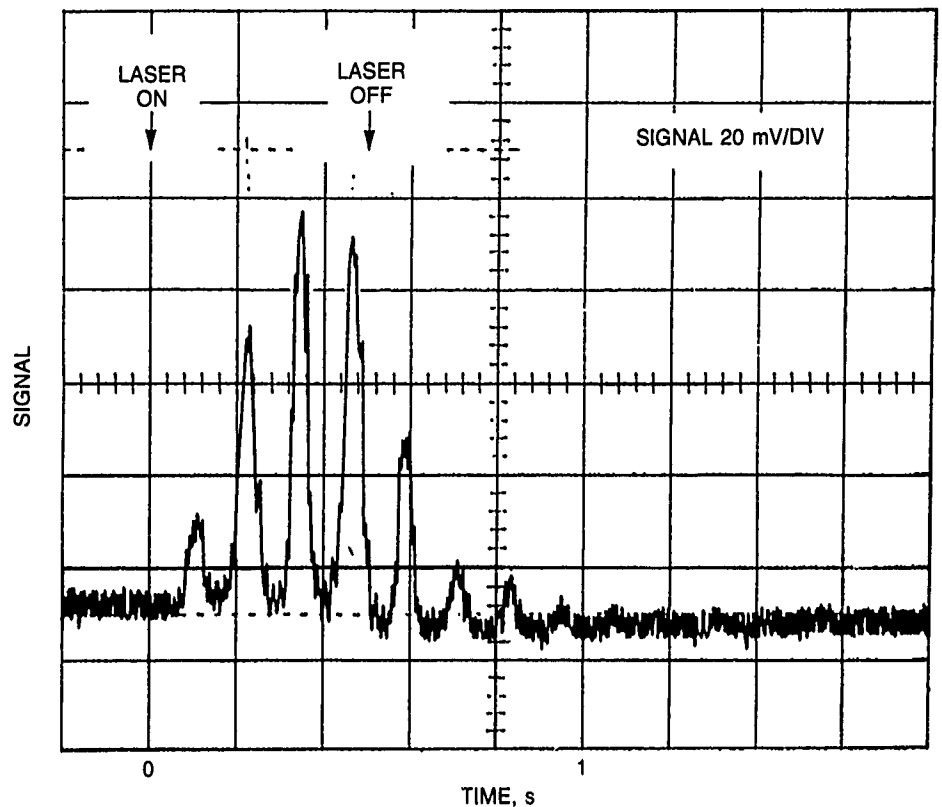


Figure 2. Oscilloscope trace of infrared thermal decay signal from carbon particle in vacuum. The particle is shown moving outside the detector field of view.

air or vacuum with CO₂ laser light of high enough intensity results in rapid charge change. As the particle is irradiated, it is observed to lose positive charge and move downward in the levitator; i.e., toward the positive end-cap. At low pressure, where there is little or no damping, this motion is abrupt and usually results in the particle escaping the levitator. Similar charge loss during irradiation has been reported by other investigators in the field [2,3]. From their discussions and our observations, it appears more likely that the change is due to the loss of positive charge from the particle rather than the gain of negative charge from the environment. We are currently investigating this behavior in order to minimize its effects. This will allow us to obtain higher particle temperatures and thus expand the domain of our emissivity measurements.

The experimental apparatus has been used to make the radiative decay measurements shown in Figures 3 through 5. The measurements are in the 1.3- to 5.5- μm waveband. All three of the particles were on the order of 10 μm in radius and were exposed to an irradiance of $\sim 26 \text{ W/cm}^2$ for $\sim 500 \text{ ms}$. Nonlinear least-squares fits of the data are currently being performed, but a few preliminary observations can be made. Figure 3 shows the thermal signal from a carbon sphere of 9.6 μm radius. Note that the signal levels off during the exposure, indicating that the particle has reached equilibrium with the laser. The peak temperature for the particle is estimated to be $\sim 1000 \text{ K}$. Figure 4 shows the thermal signal from an aluminum oxide sphere of 10 μm radius under the same conditions.

Note that equilibrium is never reached during the exposure and that the signal is much smaller than for the carbon particle. Figure 5 shows the barely visible thermal signal from another aluminum oxide particle, with a radius of 9.1 μm . One can understand qualitatively the differences between the carbon and aluminum oxide signals. The carbon particle will approach equilibrium more quickly because the product of its density and specific heat (i.e., its thermal inertia) is smaller. Further, on the basis of room-temperature index of refraction data from the literature [4,5], Mie calculations at the CO₂ laser wavelength show that the carbon particle's absorption cross section should be three or four times larger than that of the aluminum oxide particles. Finally, the carbon particle should show a higher emissivity in the wavelength region observed. However, it is another matter to explain the large difference in signal between the two aluminum oxide particles. Both particles came from the same sample bottle supplied by Tafa Industries. Both were about the same size, and Mie calculations yield room-temperature absorption cross sections for the first and second particles of $\sim 97 \mu\text{m}^2$ and $\sim 77 \mu\text{m}^2$, respectively. This small variation is certainly not enough to explain a factor of ~ 6 difference in peak signal. Perhaps what is indicated is the large variation in the radiative properties of the individual particles in the sample under test. Figure 6 shows a scanning electron microscope image of some of the Tafa aluminum oxide particles. Clearly, there are surface variations from particle to particle; some are fairly smooth, others have convoluted surfaces. Also found in the sample but not

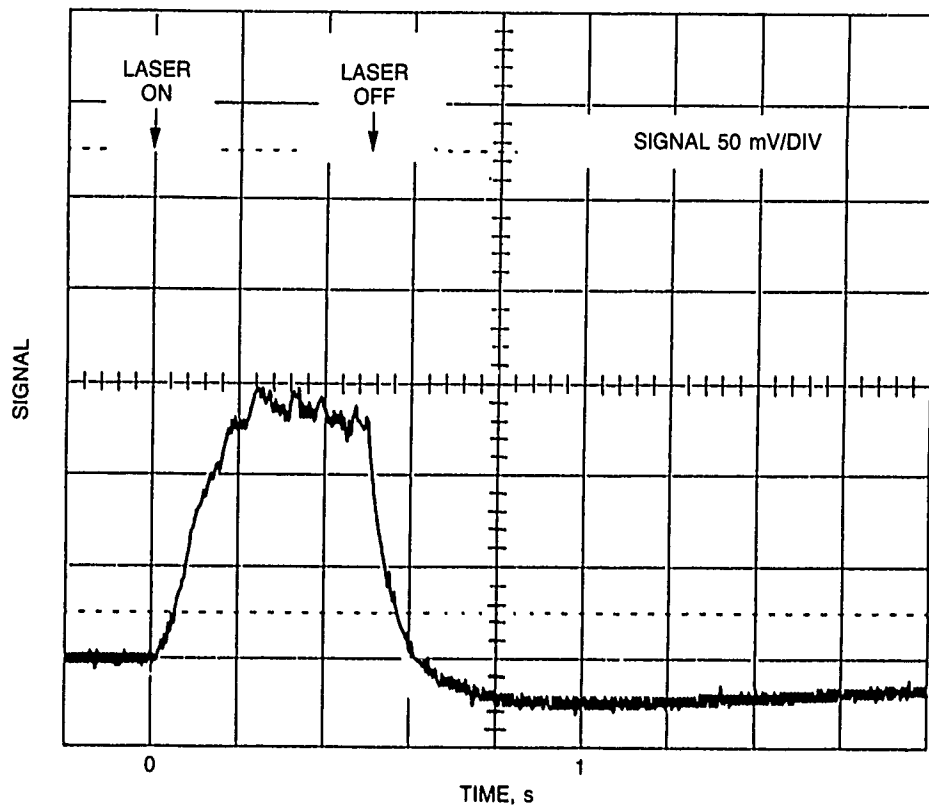


Figure 3. Oscilloscope trace of infrared thermal decay signal from 9.6-μm radius carbon particle in vacuum (1 exposure).

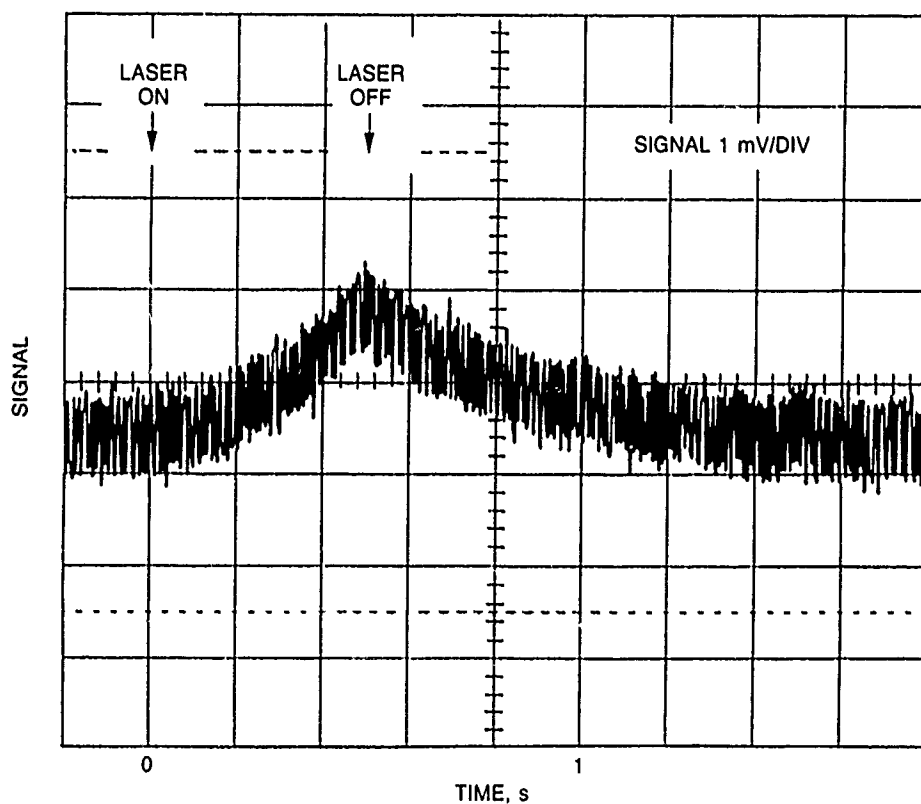


Figure 4. Oscilloscope trace of infrared thermal decay signal from 10-μm radius aluminum oxide particle in vacuum (average of 20 exposures).

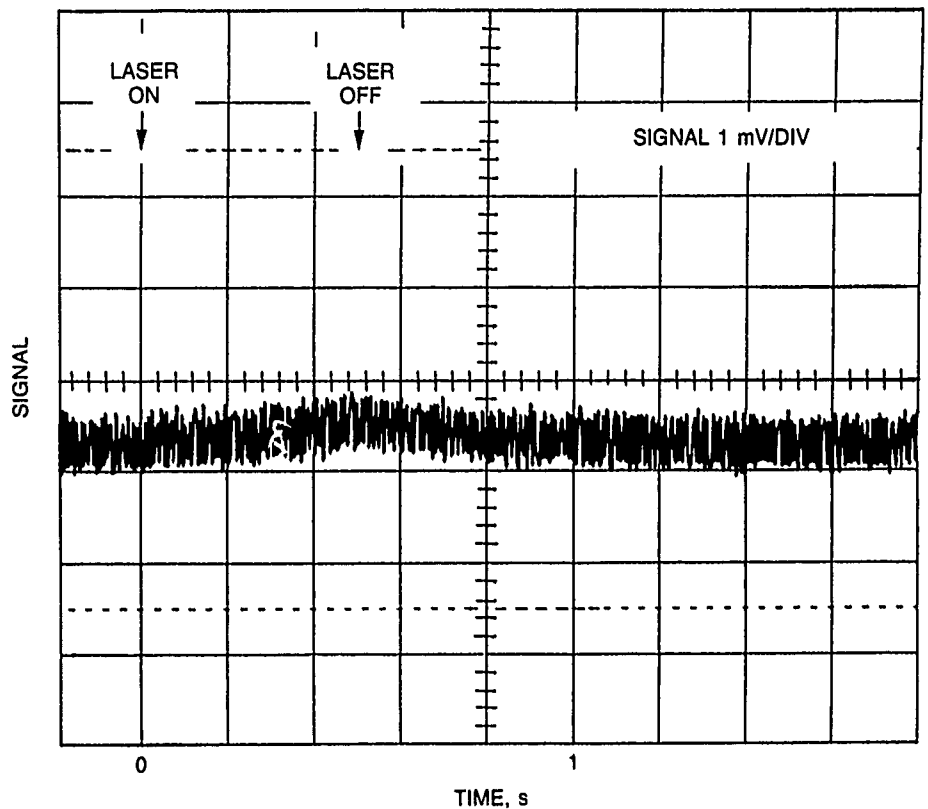


Figure 5. Oscilloscope trace of infrared thermal decay signal from 9.1- μm radius aluminum oxide particle in vacuum (average of 50 exposures).

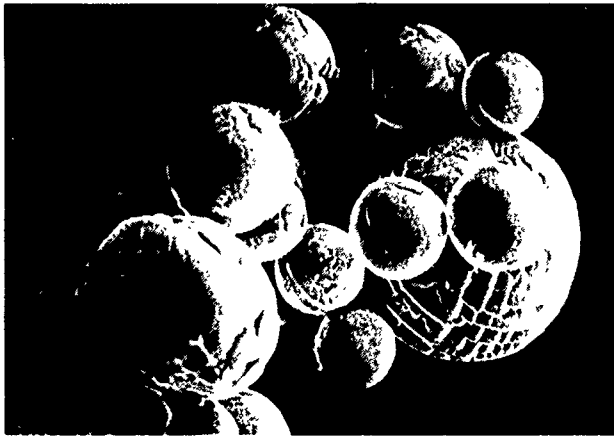


Figure 6. Scanning electron microscope image of Tafa Industries aluminum oxide particles used in experiment.

shown are spheres that look like complex balls of string. Further, under the microscope, some of the particles appear shiny, whereas others are dull. As discussed previously [1], the condition of the surface of the aluminum oxide particle has an enormous effect on the particle's radiating properties. It comes as no surprise, then, that the aluminum oxide particles from this sample would display variations in emissivity. In order to characterize the radiative properties of the Tafa particles, it may be more meaningful to determine the emissivity distribution function for the particles rather than a single emissivity value. In

the larger scope of our experimental objectives, these results indicate that the apparatus has developed to a point where it is now appropriate to pay serious attention to the purity of the aluminum oxide particles under test. The question of particle purity may also be relevant to the problem of charge loss mentioned earlier. At the present time, we are determining the maximum temperatures we can achieve without the escape of the Tafa particles due to charge loss. It will be interesting to see how these temperature limits compare with those of aluminum oxide particles from other sources.

In summary, the major achievements in the single-particle emissivity experiment involve control. We now have the capability to control the particle during the various phases of the experiment. Also, we can now control the heating of the particle to the point that results are reproducible and, when necessary, signal averaging can be used.

* * * * *

1. A. Pluchino, D. E. Masturzo, and D. E. Lake, "Microparticle Linear and Nonlinear Optics," *Aerospace Sponsored Research Summary Report, Scientific and Engineering Research*, ATR-89(8498)-1, The Aerospace Corp. (1 December 1989), p. 67.
2. R. E. Spjut et al., "Electrodynamic Thermogravimetric Analyzer," *Rev. Sci. Instrum.* **57**, 1604 (1986).

3. R. W. Weeks and W. W. Duley, "Interaction of TEA CO₂ Laser Radiation with Aerosol Particles," *Appl. Opt.* **15**, 2917 (1976).
4. A. P. Lenham and D. M. Treherne, "The Optical Constants of Graphite," *Observ.* **86**, 36 (1966).
5. O. B. Toon et al., "The Optical Constants of Several Atmospheric Aerosol Species: Ammonium Sulfate, Aluminum Oxide, and Sodium Chloride," *J. Geophys. Res.* **81**, 5733 (1976).

Arnold, S., et al., "Optical Bistability of an Aqueous Aerosol Particle Detected Through Light Scattering: Theory and Experiment," *Appl. Opt.* **29**, 3473 (1990).

Pluchino, A., "Nonlinear Optical Properties of CdS Microspheres," *J. Aerosol Sci.* **20**, 1083 (1990).

High-Energy Laser Particle Interaction

D. W. Pack, A. Pluchino, and D. E. Lake,
Chemistry and Physics Laboratory

The potential use of high-power lasers for communication, remote sensing, and strategic defense has stimulated increased research in the nonlinear optics of the atmosphere. A great deal of work on atmospheric propagation has been done on topics such as self focusing, air breakdown, and stimulated Raman scattering. Recently, more attention has been given to aerosols. Depending on visibility, micron-size aerosol particles can be the single most important atmospheric component in determining the state of a laser beam traversing an atmospheric path. At high-power levels, nonlinear effects become important and give rise to a variety of detectable signals. Such phenomena include plasma emission, multiorder stimulated Raman scattering (SRS), and stimulated Brillouin scattering. In the Chemistry and Physics Laboratory, we have completed preliminary experiments on imaging and studied the power dependences of SRS and breakdown-induced plasma emission in micron-size water aerosols.

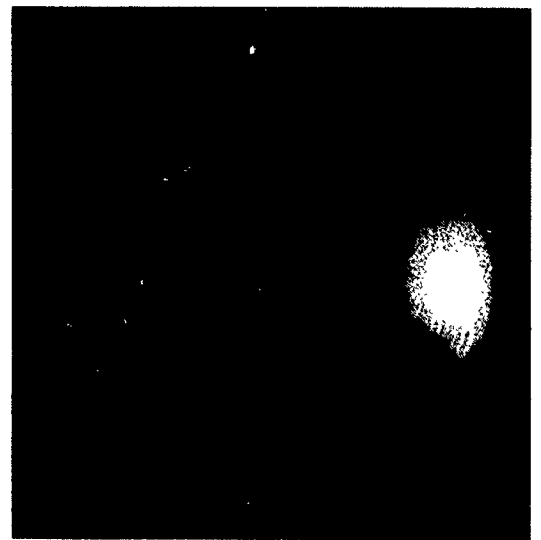
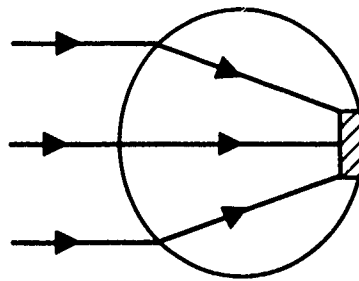
A unique aspect of the study of nonlinear optics in liquid microdroplets is the effect of their restricted spherical geometry. Spherical droplets in the micron-size range (radius $a >$ laser wavelength λ) act as high- Q optical cavities for visible light, with resonant modes referred to as MDRs (morphology-dependent resonances) [1]. Two conditions may occur when a laser interacts with a spherical system. In the first case, Figure 1(a), the off-resonance case, the droplet acts as a lens, and internal intensity is increased by a factor of about 100. In the second case, Figure 1(b), the laser frequency is on resonance, and the internal field has many peaks of comparable intensity confined near the circumference of the droplet. Both peak and average intensities are greatly increased, with important consequences for nonlinear optical behavior [2]. A manifestation of these high- Q spherical modes is

enhanced stimulated Raman scattering relative to bulk fluids. This may be understood qualitatively as enhancement from the strong internal fields and many orders of total internal reflection in the droplet. The amplification of SRS is exponential [3]:

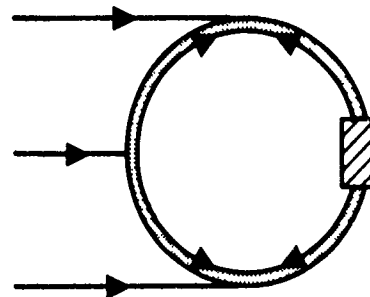
$$I_s(z) = I_s(0) \exp(gIz), \quad (1)$$

where I_s is the intensity of the Stokes shifted light, g is the Raman gain factor, I is the intensity of the incident laser radiation, and z is the interaction length. The cavity effect of a spherical droplet increases I and z , resulting in significant signal increases relative to bulk conditions. Enhancement occurs when either the input (laser) or output (Raman) wavelengths match a mode resonance.

The Chemistry and Physics Laboratory has a long-standing effort in the levitation, trapping, and optical study of small particles [4]. This capability has recently been expanded with the construction of pulsed sources of micron-size aerosols to study volatile samples such as water microdroplets. The experimental apparatus in Figure 2 is used to study water aerosol-laser interactions. The aerosol beam uses piezo-ceramic transducers to force a droplet through one of a set of interchangeable micron-size orifices. The droplets emerge with a velocity of approximately 200 cm/s. The size and number of the individual droplets per transducer pulse are determined by the orifice diameter and the driving pulse voltage and duration. The device is similar to an ink-jet printer nozzle [5-7]. A pulse generator triggers the transducers and fires the laser after a delay to synchronize the laser with the droplet train. Laser alignment and safe observation and recording of images are aided by viewing the magnified image of the aerosol droplets and their emissions through a microscope video system protected by an appropriate fil-



(a)



(b)

Figure 1. The effect of spherical geometry. (a) The internal field distribution when the incident wavelength does not correspond to an MDR. The internal field is enhanced by ~ 100 ; (b) the case when the incident wavelength does correspond to an MDR. The internal field is enhanced by factors between ~ 100 and 10^5 . The photographs are of SRS mapping out the regions of high intensity in single water droplets ($a = 60 \mu\text{m}$) following excitation by a single 7-ns, 532-nm laser pulse. Resonant 532-nm laser scatter is filtered out. In practice, for droplets in the tens of microns size range, the mode density is such that a laser always overlaps broad, low- Q resonances. Greater enhancement occurs when the laser matches a narrow, high- Q MDR. From Ref. 2.

ter. A 35-mm camera is attached to the microscope to obtain photographs such as those in Figure 1. An additional aid to droplet-laser alignment is provided by projecting the laser on a weakly fluorescent screen after it passes through the droplet. This arrangement provides an image of the overlap between the beam area and the microdroplet, allowing the beam to be centered accurately. In both the camera and projected views, radiation from the YAG laser is synchronized with the pulsed droplets at 10 Hz, producing a stroboscopic image.

Our first experimental efforts have focused on studying the spectrum and power-dependent intensity of stimulated Raman scattering and breakdown-induced plasma emission with 532-nm light from the Q -switched Nd:YAG second harmonic. The first samples studied were water aerosols in the size range of 20 to 65 μm

(radius). Figure 3 shows a stimulated Raman scattering spectrum, centered at 650 nm, of a single water droplet of 60 μm radius. Also shown in Figure 3 is the linear scattering signal of a continuous-wave HeNe laser (at 633 nm) that intersects 100 droplets from the same beam train. The Raman shift of approximately 3400 cm^{-1} to the red of the 532-nm exciting energy corresponds to one quantum of the ν_1 stretch vibration of H_2O . The 13 peaks in the spectrum result from the enhancement of the stimulated scattering at specific wavelengths within the wide spontaneous Raman bandwidth, wavelengths that correspond to morphological resonances of the spherical water droplets [8]. The contour of the band is roughly a convolution of the broad spontaneous Raman spectrum of water with the discrete morphological resonances observed in linear scattering and predicted by Mie theory [8]. From the reso-

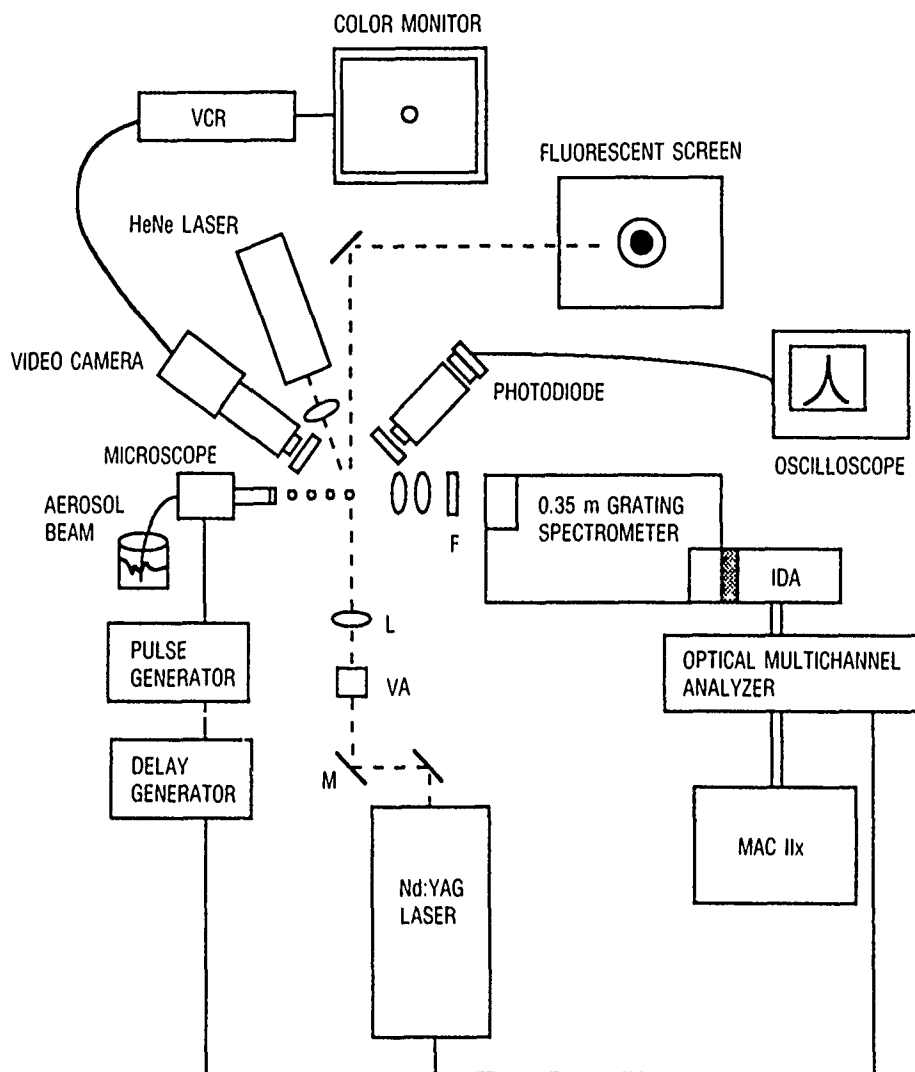


Figure 2. High-energy laser particle interaction experimental arrangement. M = mirror, VA = variable attenuator, L = lens, F = filter, IDA = intensified diode array. Spectrometer resolution was 0.36 nm.

nant peak spacings, the microdroplets can be sized through the use of the approximate formula [1]:

$$\Delta\lambda = \frac{\tan^{-1}(m^2 - 1)^{1/2}}{(m^2 - 1)^{1/2}} \frac{\lambda^2}{2\pi a}. \quad (2)$$

The refractive index of water is $m = 1.33$ at 532 nm. From the 0.87-nm spacing $\Delta\lambda$ of the peaks in Figure 3, a radius of 63 μm is calculated from Eq. (2) for the water droplet, in close agreement with microscopic measurements.

From the integrated intensities of the linear scattering signal and the stimulated Raman scattering signal, and from knowledge of the relevant laser parameters such as power and spot size, a value can be calculated for the efficiency of SRS relative to linear scattering. For the data in Figure 3, the collection optics gather light at an angle of approximately 90 deg relative to the collinear HeNe and YAG laser beams. From several series of measurements of water droplets of 60- μm radius, $I_{\text{SRS}}/I_{\text{LS}} = 1$ to 6% was found (I_{SRS} and I_{LS} are the integrated scattering signal intensities for SRS and linear scattering, respectively.) These I s contain all of the physical parameters such as Raman cross section, but are normalized for the number

of incident laser photons. The range of values found is in agreement with the only published measurement, $I_{\text{SRS}}/I_{\text{LS}} = 0.2$ to 2.0% at 90 deg [9]. The intensity of the SRS signal increases when the laser input matches a high- Q MDR. This makes the size stability of an aerosol source important when comparing averaged results from different laboratories. The size stability of the Aerospace source is at least 0.1% and often much better. A study of the amount of variation in SRS intensity from input resonance effects is continuing.

Figure 4 shows the effect of size on the water droplet SRS spectrum for radii varying from 29 to 65 μm . The smaller particles show more widely spaced morphological resonances, as predicted by Mie theory. Sizes from Eq. (2) agree closely with optically measured ones. The spectrum in Figure 4 of the $a = 29 \mu\text{m}$ droplet shows two different mode orders appearing, both spaced by 1.96 nm. The range of particle sizes for these particular four spectra was obtained by varying the impulse driving the transducers on the aerosol beam. At low transducer voltages, only one droplet per pulse is emitted. At higher voltages, the stronger impulse produces smaller satellite droplets in

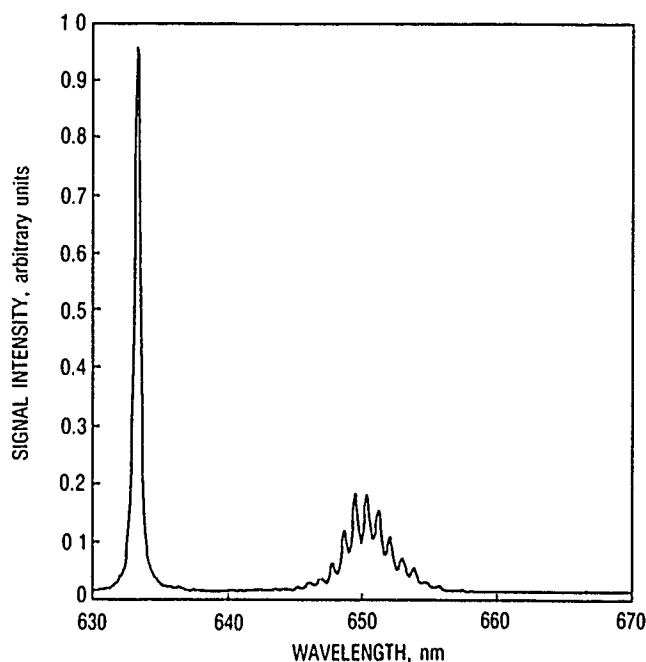


Figure 3. Linear and nonlinear laser scattering from $60\text{ }\mu\text{m}$ radius water droplets. OMA spectrum from exposure to HeNe laser resonant scattering at 633 nm from 100 droplets and Nd:YAG 532-nm stimulated Raman scatter from a single droplet at approximately 650 nm . The 13 equally spaced peaks are from enhanced SRS at wavelengths corresponding to spherical cavity resonances.

addition to the larger primary one. Satellite droplets are closely spaced but have sufficiently different velocities that a focused laser beam triggered at varying time delays can select them out individually. This technique provides a new method to generate and size precisely controlled multidroplet sprays. This method of generating and sizing individual particles and sprays could find use in combustion studies.

As laser power is increased above the SRS threshold in water droplets, the intensity of the signal increases until, possibly, a saturation level is reached. At higher power densities, laser-induced breakdown occurs and generates a broad continuum spectrum. The continuum is from the recombination and radiative energy losses of the laser-induced plasma. The breakdown process involves initial multiphoton ionization followed by rapidly multiplying cascade ionization and subsequent laser heating of the absorbing plasma [10]. A power study of this progression from SRS to plasma emission in approximately $60\text{ }\mu\text{m}$ water droplets is shown in Figure 5. Spectrum (a) shows SRS only at a power level of about 3.0 GW/cm^2 . As the droplets are pumped harder, Figure 5(b), 3.5 GW/cm^2 , SRS intensity increases and more modes appear around 642 nm . These are from a lower gain shoulder in the hydrogen bond symmetric stretch region of water. In Figure 5(c), the breakdown threshold has been exceeded and the SRS intensity is decreasing ($\sim 6\text{ GW/cm}^2$). As a point of reference, air breaks down at about 80 GW/cm^2 .

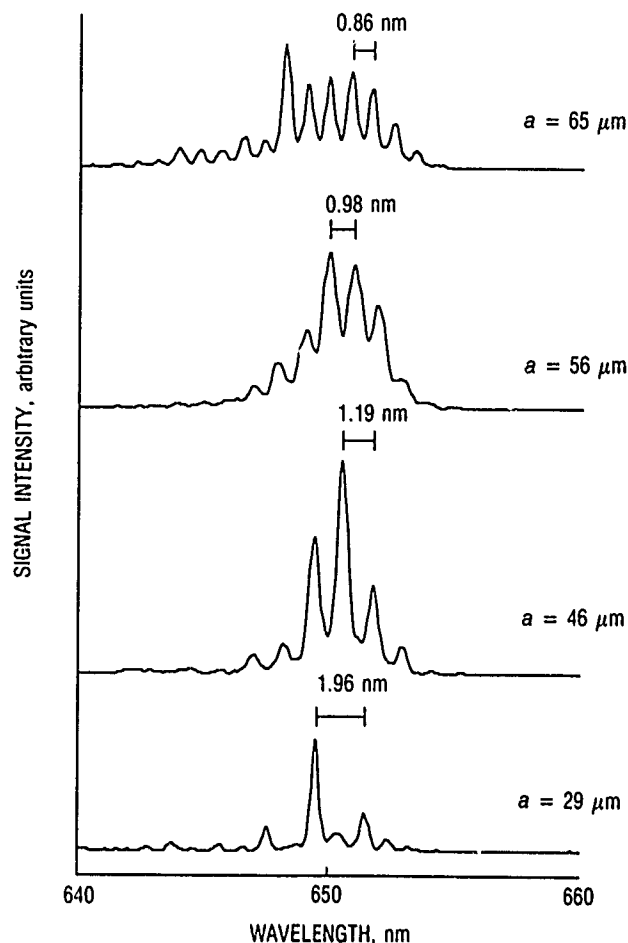


Figure 4. The effect of changing droplet size on stimulated Raman scattering spectra from single water droplets interacting with a single 7-ns , 532-nm laser pulse. a is the droplet radius. Spacings of peaks from spherical cavity resonances are inversely proportional to droplet size.

In 5(d), the laser intensity is $\sim 8\text{ GW/cm}^2$, SRS appears totally quenched, and the spectrum is dominated by continuum plasma emission. This quenching of SRS is attributed to lowering of the Q -factor of the spherical cavity resonances from absorptive loss in the plasma region. Additional data are being collected to fully map out the gain curve for SRS in water microdroplets.

In the initial work reported here, we have measured the efficiency of SRS relative to resonant scattering and studied the emission from water droplets around the breakdown power threshold. The quenching of SRS from plasma formation within droplets has been observed. Ongoing and planned experimental work includes the following:

- The study of other types of samples, such as highly concentrated sulfate solutions similar to sulfate aerosols.
- The measurement of higher-order Raman shifts, including anti-Stokes shifts.

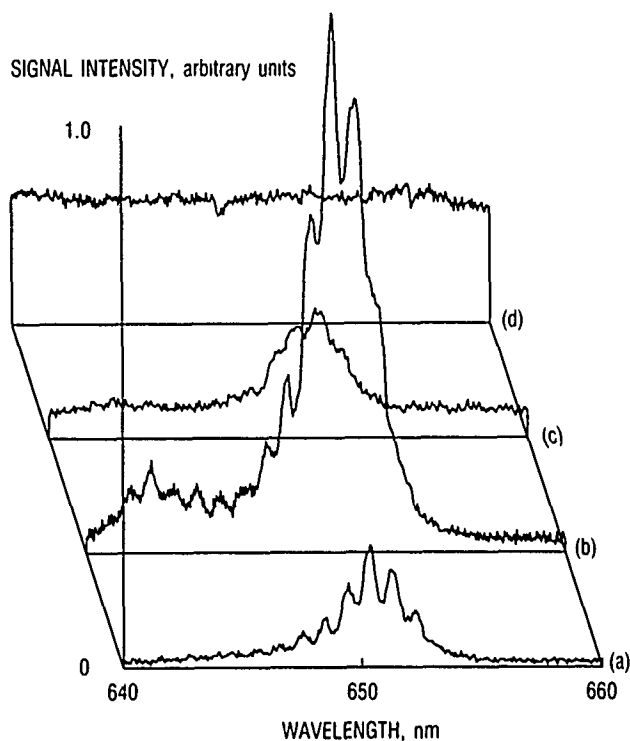


Figure 5. The effect of increasing laser power on the nonlinear signal from 60 μm radius water droplets. Spectra are accumulations of 500 laser-droplet interactions. Laser power density is approximately 3.0, 3.5, 6.4, and 8.4 GW/cm^2 in the sequence (a) through (d). (a) SRS only. The mode structure is broadened by small size variation among the 500 droplets; (b) increasing SRS intensity and the appearance of the lower gain component of the symmetric stretch band at approximately 642 nm (-3220 cm^{-1}). Some breakdown-induced plasma emission is beginning to occur; (c) increasing plasma continuum signal accompanied by the reduction of SRS; (d) SRS is essentially quenched and signal is mostly from continuum emission.

- The use of different laser wavelengths.
- The study of the angular behavior of SRS.

These efforts will help increase our understanding of high-energy laser-particle phenomenology.

* * * * *

1. S. C. Hill and R. E. Benner, "Morphology Dependent Resonances," *Optical Effects Associated with Small Particles*, P. W. Barber and R. K. Chang, eds., World Scientific Publishing Co. (1988), p. 4.

2. S. X. Quian, J. B. Snow, and R. K. Chang, "Nonlinear Optical Processes in "Micron-sized Droplets," *Laser Spectroscopy VII*, T. W. Hänsch and Y. R. Shen, eds., Springer Verlag (1985), p. 204.
3. A. Yariv, *Quantum Electronics*, John Wiley and Sons, Inc. (1975), p. 477.
4. S. A. Arnold et al., "Optical Bistability of an Aqueous Particle Detected Through Light Scattering: Theory and Experiment," *Appl. Opt.* **29**, 3473, (1990); A. B. Pluchino, "Observation of Halo Scattering From Single Ice Crystals," *Opt. Lett.* **11**, 276 (1986); A. B. Pluchino and S. A. Arnold, "Comprehensive Model of the Photophoretic Force on a Spherical Particle," *Opt. Lett.* **10**, 261 (1985); A. B. Pluchino, "Radiometric Levitation of Spherical Carbon Aerosol Particles Using a Nd:YAG Laser," *Appl. Opt.* **22**, 1861 (1983).
5. S. Arnold and L. Folan, "Fluorescence Spectrometer for a Single Electrodynamically Levitated Microparticle," *Rev. Sci. Instrum.* **57**, 2250 (1986).
6. W. T. Pimbley and H. C. Lee, "Satellite Droplet Formation in a Liquid Jet," *IBM J. Res. Dev.* **21**, (1977).
7. D. B. Bogoy and F. E. Tälke, "Experimental and Theoretical Study of Wave Propagation Phenomena in Drop on Demand Ink Jet Devices," *IBM J. Res. Dev.* **28**, 314 (1984).
8. J. B. Snow, S.-X. Quian, and R. K. Chang, "Stimulated Raman Scattering From Individual Water and Ethanol Droplets at Morphology Dependent Resonances," *Opt. Lett.* **10**, 37 (1985).
9. R. G. Pinnick et al., "Stimulated Raman Scattering in Micrometer-Sized Droplets: Measurements of Angular Scattering Characteristics," *Opt. Lett.* **13**, 1099 (1988).
10. J. H. Eickmans, W.-F. Hsieh, and R. K. Chang, "Laser-Induced Explosion of H_2O Droplets: Spatially Resolved Spectra," *Opt. Lett.* **12**, 22 (1987).

Chemistry and Physics

CHEMISTRY AND PHYSICS

Laser Surface Photolyzed Chemistry

H. Helvajian, H.-S. Kim, and L. H. Wiedeman,
Aerophysics Laboratory

Three years ago we succeeded in measuring the nascent photoejected kinetic energy distributions from pulsed ultraviolet laser excitation of a crystalline silver metal [1-2]. This was achieved by maintaining the laser fluence near the threshold for particle ejection, thereby isolating, at the molecular level, the fundamental process in the laser/surface interaction. The data established for the first time that the threshold excitation proceeds not through thermal initiation as previously believed, but by means of an electronic excitation in the solid. These results are measurable only when the laser fluence is well below the threshold for substrate evaporation and laser-induced plasma formation. Since that initial observation, we have observed similar phenomena in the threshold-fluence laser ablation of crystalline aluminum, copper (110), and polycrystalline $\text{YBa}_2\text{Cu}_3\text{O}_{x+6}$ [3-4]. Our experimental results show that cationic species are ejected with high kinetic energy (KE) (3-10 eV), and that the energy value is specific to the target atomic composition.

This past year, we conducted experiments to determine the following:

- The effect of adsorbates on the laser ablation of oxidized Al (111).
- The effect of the $\text{YBa}_2\text{Cu}_3\text{O}_{x+6}$ bulk target temperature on the photoejected species KE.
- The anion (O^- , O_2^-) KE distribution from the laser ablation of $\text{YBa}_2\text{Cu}_3\text{O}_{x+6}$.

Only the results from the first two experiments are presented here.

Two experimental facilities were used for studying the threshold-fluence laser ablation process. The first experiment was conducted in an ultrahigh vacuum (10^{-10} Torr) apparatus. The other two experiments were conducted in a different apparatus, maintaining only high vacuum (10^{-9} Torr). The experimental arrangement is shown

schematically in Figure 1. For simplicity, we have integrated both experimental facilities using an idealized experimental chamber. In reality, the ultrahigh vacuum apparatus incorporates a time-of-flight (TOF) mass spectrometer and measures the nascent photoejected ions; a quadrupole (QP) mass spectrometer mounted on the high-vacuum apparatus measures both neutrals and ions.

The TOF technique is well suited for the study of adsorbate ablation, since the measurement does not disturb the chemical composition of the target surface. An Auger spectrometer, mounted near the TOF spectrometer, is used to characterize the surface. An additional difference between the two chambers is the sample holder. The one installed in the ultrahigh vacuum chamber can be heated (1173 K, max); the one in the high-vacuum chamber is designed for cooling only (10 K, min). Apart from these differences, both experimental arrangements are the same. Figure 1 also shows the pulsed lasers used in these experiments. An excimer laser operating at 193, 248, and 351 nm wavelengths was used to photoablate the Perovskite $\text{YBa}_2\text{Cu}_3\text{O}_{x+6}$ ceramic; the third harmonic (355 nm) of a Nd:YAG laser was used in the Al (111) threshold ablation studies. The excimer laser radiation is randomly polarized, whereas that from the Nd:YAG laser is rotated to s polarization (electric field normal to the plane of incidence). The output from both lasers is spatially filtered to provide a uniform intensity distribution on the target. In addition, a Raman cell is used to temporarily smooth the laser pulse through optical nonlinear mixing in H_2 gas. The incident laser beam is focused ($f = 50$ cm) on the target in the latter two experiments. The laser fluence used in all the experiments is maintained at the threshold for product ejection. The measured threshold fluence value is approximately 30 mJ/cm^2 for the adsorbate/aluminum studies and 100 to 200 mJ/cm^2 for the $\text{YBa}_2\text{Cu}_3\text{O}_{x+6}$ bulk target ablation.

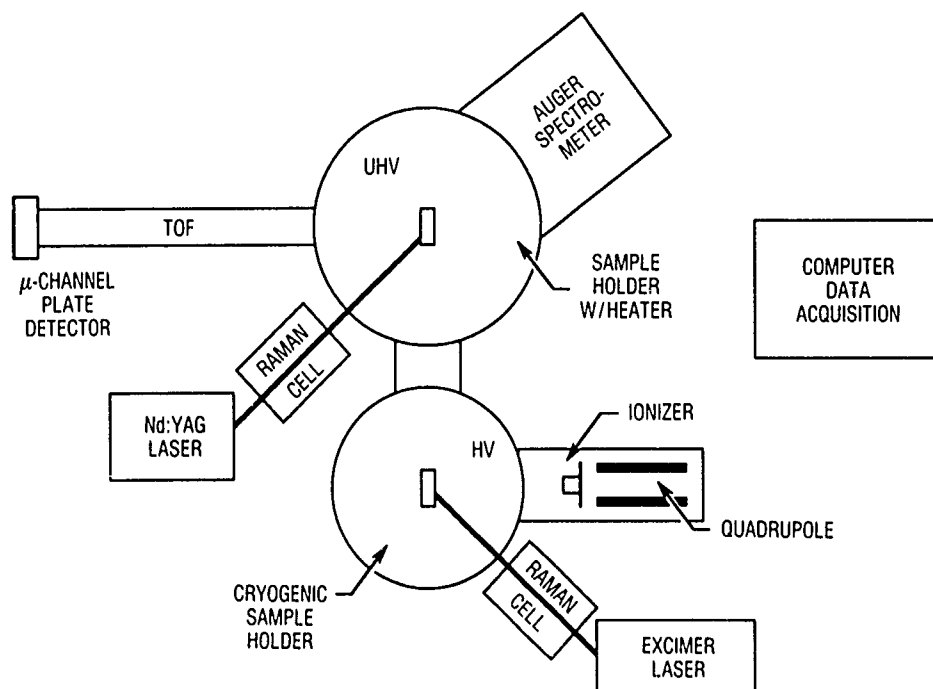


Figure 1. Experimental apparatus schematic integrating two facilities used in threshold fluence laser ablation studies.

The photoablation of oxidized crystalline aluminum displays a sharp threshold in the laser fluence for ion product formation. Figure 2 shows this result for the photoejected Al^+ ions. If the data are fit to an equation of the form $Y = C(\text{ion signal})^n$, $n \geq 6$ is deduced. This result identifies the photoejection process as a multiphoton absorption event requiring approximately 21 eV for Al^+ ion photoejection. Unlike the result from the silver target experiment [1], the KE of the photoejected Al^+ shows two distinct distributions. Furthermore, these distributions appear at laser fluences that do not overlap. At the

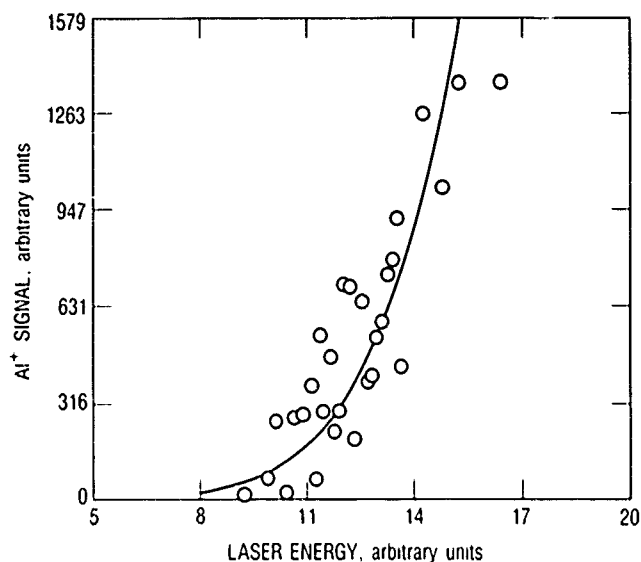


Figure 2. Dependence of the photoejection Al^+ ion signal on the laser fluence near the threshold for product formation. The 355 nm wavelength laser was not focused. Each point is an individual laser shot.

lower laser fluences, and for a room-temperature oxidized crystal, we measured the nascent ion KE distribution of the substrate and the adsorbate species to be the same. Figure 3 shows a high-resolution TOF mass spectrum of the potassium (K^+) adsorbate and the Al^+ substrate ions. The upper scale represents the nascent photoejected KE. The data show that, regardless of mass, both ejected species have a mean KE, $\langle \text{KE} \rangle$, of approximately 4 eV with a 3 ± 1 eV full width at half maximum. However, after a large number of laser shots, we measured an abrupt increase (50%) in the laser fluences required to eject Al^+ species. Also, the KE distribution measured for the substrate (Al^+) species broadens ($\langle \text{KE} \rangle$ 5-6 eV), whereas that for the adsorbates (K^+ , Na^+) remains the same. This result is shown in Figures 4 and 5. Figure 4 shows a TOF mass spectrum following many laser shots. The data show that the Al^+ TOF distribution is much broader than that of the adsorbates (K^+ and Na^+). In Figure 5, the Al^+ TOF signal is plotted with the calibrated energy axis. The broadening in the KE distribution relative to that shown in Figure 3 is apparent. In addition, there is a distinct asymmetry to the Figure 5 TOF shape. As a function of the laser shot number, two aluminum ion KE distributions appear independently. This discontinuous change in the monomer ion KE distribution is shown in a contour plot representation (Figure 6), which shows two 300 laser shot sequences, each plotted as a function of the laser fluence. The contour plot basically displays a cut in the three-dimensional TOF mass spectrum. The cross-sectional area shown in Figure 6 is a slice just above the noise amplitude level and identifies the arrival of the fastest and slowest ions for a particular species. Figure 6(a) represents the data taken after the

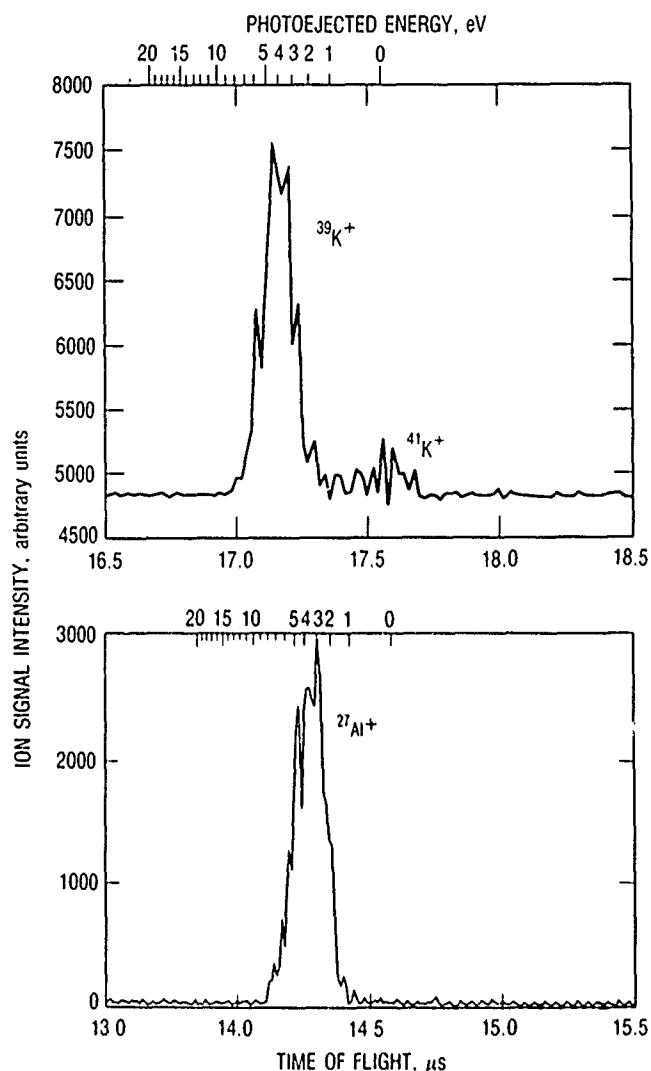


Figure 3. Sum of 300 TOF mass spectra of K^+ contaminant and Al^+ substrate ions ejected from an aluminum crystal surface under high mass resolution (10 ns/point digitization). The laser fluence was maintained near the threshold for product formation.

target was exposed to only a few thousand laser shots; Figure 6(b) shows the data after many thousand laser shots with the surface contaminant level reduced significantly. In comparing Figures 6(a) and 6(b), the laser fluence in the transition region should be noted. Within this laser fluence transition region, the data in 6(a) show the Al^+ TOF cross-sectional width to be the same as that measured at the lower laser fluences. However, in 6(b), no signal appears. At higher laser fluences, a new channel for Al^+ ablation appears with a larger variance in the TOF arrival times relative to that measured in 6(a). This broadening in the Al^+ TOF arrival time signals is not the result of an above-surface plasma acceleration process. This is evident in Figure 6(b), where the arrival time width does not appreciably change with increase in the laser fluence. In an above-surface plasma acceleration process,

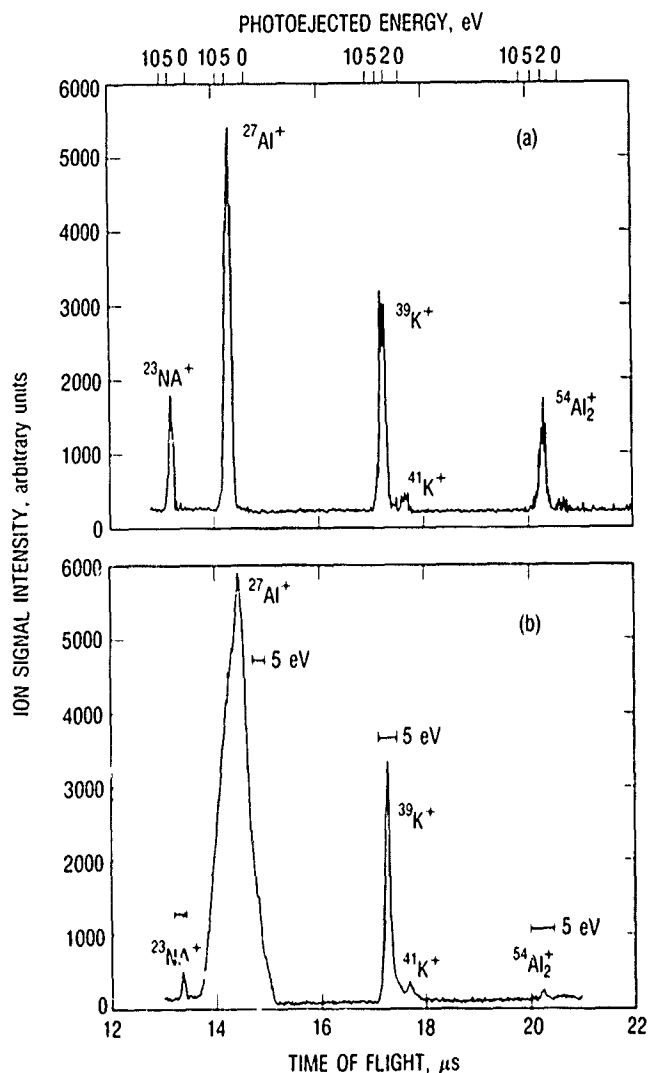


Figure 4. Sum of 300 TOF mass spectra taken with low mass resolution. (a) Near threshold fluence ($I_h = 30 \text{ mJ/cm}^2$), (b) above the initial threshold fluence.

the broadening in the ion KE distributions is a continuous function of the laser fluence. In Figure 6(b), the laser fluence is varied over a range of 40%, which, for a plasma-process, would have resulted in a measurable change in the fastest ion TOF. The broad Al^+ KE distribution (Figure 5) may be the result of a laser-induced Coulombic explosion process at the surface. This occurs by the photo-generation of excess surface charge, which reduces the Madelung potential and allows the positive species ejection. At the present time we believe this enhancement in excess surface charge to be due to the increase of crystalline defects caused by the laser ablation process. Preliminary experimental evidence in this laboratory shows that, after annealing the crystal, the measured Al^+ KE distributions revert to the narrow profile shown in Figure 3. We are preparing a systematic study to identify the physical basis for the measured broad Al^+ KE distribution.

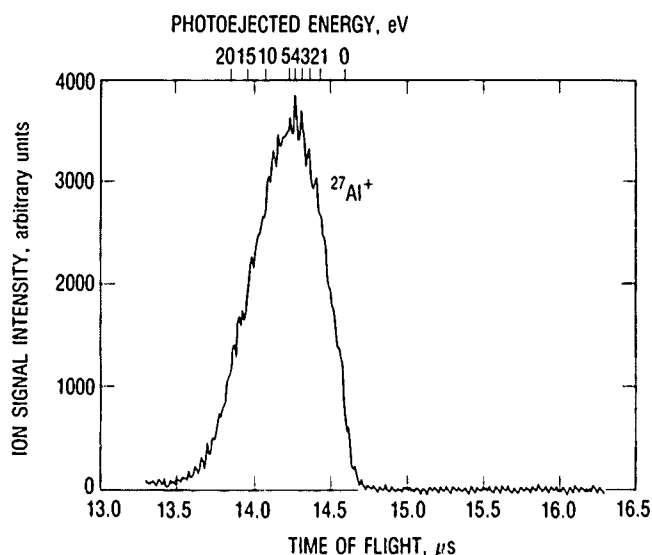


Figure 5. Sum of 300 TOF mass spectra taken with high mass resolution (10 ns/point digitization). The laser fluence is at product formation threshold ($I = 1.5 I_h$).

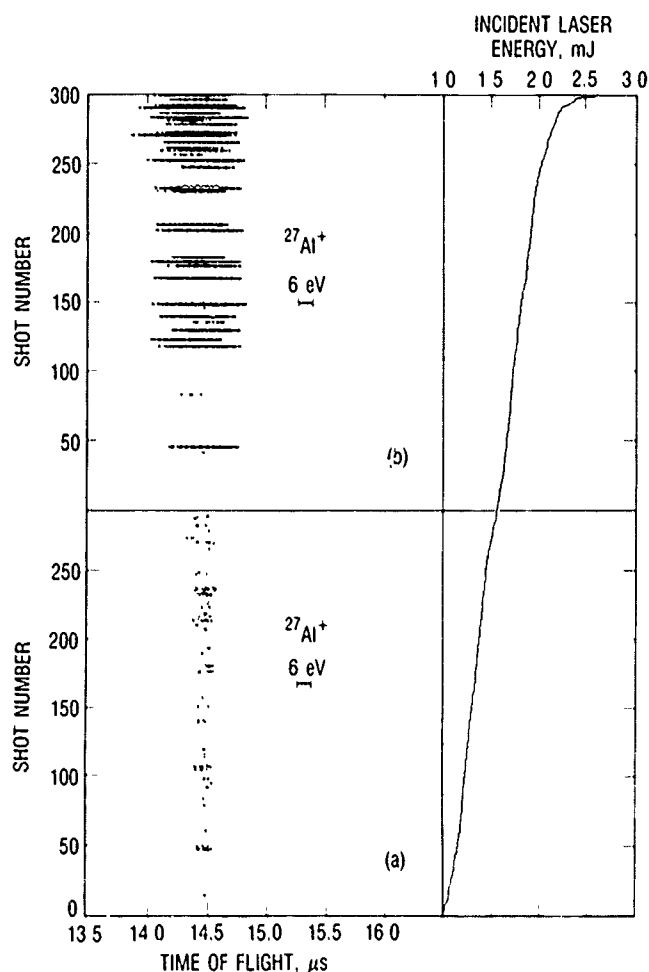


Figure 6. Contour plot representation of the Al^+ TOF mass spectrum vs incident laser energy. (a) Target after initial threshold laser fluence surface cleaning, (b) after 10 K shots with laser fluence maintained near threshold.

We believe that the narrow KE distribution (Figure 3) is the result of a direct multiphoton excitation to excited electronic states of the adsorbate/substrate system. We have measured a similar narrow ion KE distribution from the ultraviolet laser ablation of a crystalline silver target. In this experiment, the excitation energy correlated with a core electronic state of the substrate. Also, our result is comparable with those from ESD (electron stimulated desorption) and PSD (photon stimulated desorption) studies, where high-KE ions with narrow KE distributions have also been reported [5,6]. The mechanism for ESD and PSD is believed to be by means of electronic excitation of the adsorbate/substrate system. The results in this experiment confirm that, for laser fluences near ion product formation thresholds, the ablation process ejects species with high KE, which cannot be explained by the thermal excitation mechanism. Our results further show that surface oxidation and contamination do not seem to inhibit the ejection of the high-KE ion species.

Our experimental results show that, for both crystalline (aluminum, copper, and silver) and polycrystalline ($\text{Y}_1\text{Ba}_2\text{Cu}_3\text{O}_{x+6}$) samples, we measure photoejected cation species with high KE [1-4]. The mean KE for these species is in excess of 2 eV and cannot be explained by either a plasma acceleration or a thermionic emission mechanism. At present, there is no theory for explaining the photoejection of hyperkinetic energy species. In our first experiment [1], we observed that the KE of the ejected species corresponded to the free-electron metal plasmon frequency of the silver substrate. To first order, the plasmon frequency, in centimeter-gram-seconds, is given by

$$\omega_p = [4\pi n(T)e^2/m]^{1/2}, \quad (1)$$

where $n(T)$ is the electron concentration in the conduction band, T is the temperature, e is the electron charge, and m is the electron mass. The free-electron plasmon energy in silver is 9.0 eV [7], which agrees with the value we measured for the mean Ag^+ ion KE [1]. If the plasmon oscillations are somehow coupled to nuclear motion, one should be able to observe a temperature dependence in the ion KE [Eq. (1)]. For pure metals, $n(T)$ does not change much with T ; therefore, a weak temperature dependence of the ion KE would be expected. However, for narrow band gap semiconductors or semimetals, there is a strong temperature dependence of the carrier concentration. The $\text{Y}_1\text{Ba}_2\text{Cu}_3\text{O}_{x+6}$ material is one such semimetal. For x between 0.9 and 1.0, the compound has the orthorhombic (o) structure with superconducting properties below 93 K. However, for x much less than 0.9, the lattice structure converts to the tetragonal (t) form, which acts more like a semiconductor. Figure 7 shows the results of our temperature-dependence studies using sintered $\text{Y}_1\text{Ba}_2\text{Cu}_3\text{O}_{x+6}$ targets. Shown are two TOF mass spectra taken using 308-nm laser ablation of $\text{Y}_1\text{Ba}_2\text{Cu}_3\text{O}_{x+6}$ at the target temperatures of 30 K and

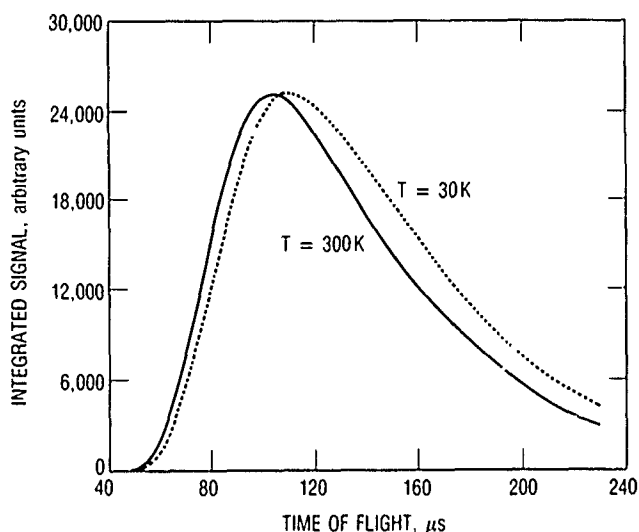


Figure 7 TOF mass spectra of photoejected Cu^+ species for the bulk $\text{Y}_1\text{Ba}_2\text{Cu}_3\text{O}_{x+6}$ target temperatures of 300 and 30 K. The TOF was taken with the quadrupole mass spectrometer configured for TOF detection.

300 K. For both spectra, the laser fluence is maintained near the threshold for Cu^+ ejection. The data show that there is a 4 eV change in the Cu^+ KE for a 22-meV change in the bulk target energy kT (where k is Boltzmann's constant). This strong temperature dependence in the ion KE cannot be due to optical excitation differences resulting from hotband absorption. Our experiments on $\text{Y}_1\text{Ba}_2\text{Cu}_3\text{O}_{x+6}$ show no wavelength dependence of the photoejected-ion KE distribution and, as shown in Figure 2 for the aluminum target, we also have measured a multiphoton excitation process for $\text{Y}_1\text{Ba}_2\text{Cu}_3\text{O}_{x+6}$. Therefore, any temperature dependence in the initial electronic-state distribution is not expected to strongly influence the access to different dissociative electronic states. We therefore believe that the large change measured in the ion KE cannot result from the small changes in the initial and final state distributions. However, the charge carrier density, in some semimetals and semiconductors, is strongly affected by a relatively small change in the substrate temperature. The question is whether or not the measured maximum KE of the photoejected ions depends on the substrate carrier concentration. It is possible to calculate the intrinsic carrier concentration $n(T)$ if the Fermi energy e_f and the bandgap energy E_g between the valence and conduction bands are known. The concentration of electrons in the conduction band is given by

$$n(T) = \int D_c(e) f_c(e) de, \quad (2)$$

where $D_c(e)$ is the electron density of states, and $f_c(e)$ is the Fermi-Dirac distribution function [7]. Making a first-order calculation of $n(T)$ and inserting the result in Eq. (1) yields the plasmon frequency $[\omega_p(T = 300 \text{ K})/\omega_p(T = 30 \text{ K})]$ ratio, R_{calc} , of 1.3. We selected the $(e_f - E_g)$ band over-

lap energy difference to be 80 cm^{-1} for the $\text{Y}_1\text{Ba}_2\text{Cu}_3\text{O}_{x+6}$ semimetal. On comparison with our data, the ratio of the maximum photoablated ion KE at 30 K and 300 K is 1.4 [$R_{\text{meas}} = \omega_p(T = 300 \text{ K})/\omega_p(T = 30 \text{ K}) = 14 \text{ eV}/10 \text{ eV}$]. The measured ratio ($R_{\text{meas}} = 1.4$) is close to that calculated ($R_{\text{calc}} = 1.3$) by using Eqs. (1) and (2). An additional comparison can be made with the published values of the intrinsic carrier concentration measured by the Hall effect. Karpe and co-workers [8] have measured the carrier concentration $[n(T)]$ for both the orthorhombic and tetragonal forms of $\text{Y}_1\text{Ba}_2\text{Cu}_3\text{O}_{x+6}$ as a function of temperature (90–300 K). Using their values for $\text{oY}_1\text{Ba}_2\text{Cu}_3\text{O}_{x+6}$ and extrapolating their curve to $T = 30 \text{ K}$ yields a ratio [$R_{\text{Karpe}} = \omega_p(T = 300 \text{ K})/\omega_p(T = 30 \text{ K})$] of 1.6.

In summary, the ratio of our measured ion kinetic energies, taken at 30 K and 300 K, yields a value of 1.4. When the ratio of the plasmon energies is calculated at the two temperatures using a reasonable band overlap energy, a value of 1.3 is obtained. When the carrier concentration of Karpe and co-workers is used (extrapolated to 30 K), a value of 1.6 is obtained. The results of Karpe and co-workers and the preceding calculation both predict large changes in the plasmon energy, with the ratios surprisingly close to our measured ratio of the maximum ion KE. The fact that the results from our initial experiment also show a correlation between the measured Ag^+ KE and the free-metal plasmon energy further supports our hypothesis. We believe that the substrate charge carrier density is involved in promoting nuclear motion during the threshold-fluence laser ablation process. The mechanism by which this nuclear motion is initiated may be through the normal mode oscillations (plasmons) of the free carrier density. We have not yet determined how this coupling can be effected. A similar set of experiments is being prepared using single-crystal semiconductors (germanium) where both (e_f) and E_g are well known.

* * * * *

1. H. Helvajian and R. P. Welle, "Threshold Level Laser Photoablation of Crystalline Silver: Ejected Ion Translational Energy Distributions," *J. Chem. Phys.* **91**, 2616 (1989).
2. H. Helvajian and R. P. Welle, "Ejected Product Energy Distributions from Laser Ablated Solids," *Proc. Mater. Res. Soc. Symp.* **129**, 359 (1989).
3. L. Wiedeman and H. Helvajian, "Threshold Level Laser Ablation of $\text{Y}_1\text{Ba}_2\text{Cu}_3\text{O}_{x+6}$ at 351 nm, 248 nm and 193 nm; Ejected Product Population and Kinetic Energy Distributions," *Proc. Mater. Res. Soc. Symp.* **191** (1990).
4. L. Wiedeman and H. Helvajian, "UV Tunable Laser Ablation of $\text{Y}_1\text{Ba}_2\text{Cu}_3\text{O}_{x+6}$: Changes in the Product Population and Kinetic Energy Distribu-

- tions as a Function of the Laser Wavelength and Target Bulk Temperature," *Proc. Mater. Res. Soc. Symp.* **191** (1990).
5. M. L. Yu, "Observations of Positive and Negative Oxygen Ions During Electron Bombardment of Oxygen Covered Mo (100) Surfaces," *Phys. Rev. B* **19**, 5995 (1979).
 6. J. A. Yarmoff and S. A. Joyce, "Photon-Stimulated Desorption of Fluorine from Silicon via Substrate Core Excitations," *Phys. Rev. B* **40**, 343 (1989).
 7. C. Kittel, *Introduction to Solid State Physics*, 5th ed., J. Wiley and Sons, New York (1976).
 8. N. Karpe et al., "Carrier Concentration and High T_c Superconductivity," *Proc. Mater. Res. Soc. Symp.* **99**, 483 (1988).

Ultraviolet-Visible Plume Chemistry and Spectroscopy

R. F. Heidner, D. G. Sutton, R. B. Cohen, J. F. Bott,
J. Steadman, J. B. Koffend, and J. A. Syage,
Aerophysics Laboratory

Information on the processes that give rise to ultraviolet-visible (UV-VIS) signatures supports critical Air Force missions involving surveillance, launch detection, and battle management, although the information has a much wider audience. UV-VIS spectroscopy and radiation rate constants comprise vital inputs to plume phenomenology codes. Despite the pivotal role served by hydrazine fuels for a broad range of space vehicle activities, the collective body of known spectroscopic and chemical dynamic properties of these molecules is surprisingly sparse. The plume signature effort in the Aerophysics Laboratory focuses on the elucidation of the complex chemical physics of the plume environment.

The emphasis during the past year was on the development of new molecular beam spectroscopic techniques to improve our understanding of propellant spectroscopy and dissociation. Toward this end, the spectroscopy and dynamics of fuels such as ammonia (NH_3), hydrazine (N_2H_4), and substituted hydrazine [1,2] were studied by supersonic jet vacuum ultraviolet (VUV) spectroscopy and by molecular beam multiphoton ionization (MPI) spectroscopy. We are progressively developing the VUV supersonic jet spectrometer to improve performance and enhance capabilities.

The objectives of the past year's work were to obtain spectroscopic data to provide information on electronic states and geometries, and to provide the information needed to undertake dynamical studies. The most challenging experiments involving the VUV jet spectrometer are direct absorption measurements. The difficulty arises because of the low molecular densities (about 10^{16} molecules/cm³) and short path length (< 1 cm) in the jet. For small absorption cross sections (e.g., $< 10^{-18}$ cm²), the attenuation of the light beam crossing the absorbing vol-

ume will typically be less than 1%. The weak absorption demands a very stable light source and elimination of noise sources. We have recently replaced our analog detection system with a photon counting system and have achieved the statistical photon noise limit. An example of a recorded VUV spectrum is shown in Figure 1 for NH_3 . To our knowledge, this is the first single-photon VUV absorption spectrum recorded for a supersonic jet-cooled molecule [3]. We have also recorded spectra for CH_3I and NF_3 . The absorption cross section for N_2H_4 is sufficiently

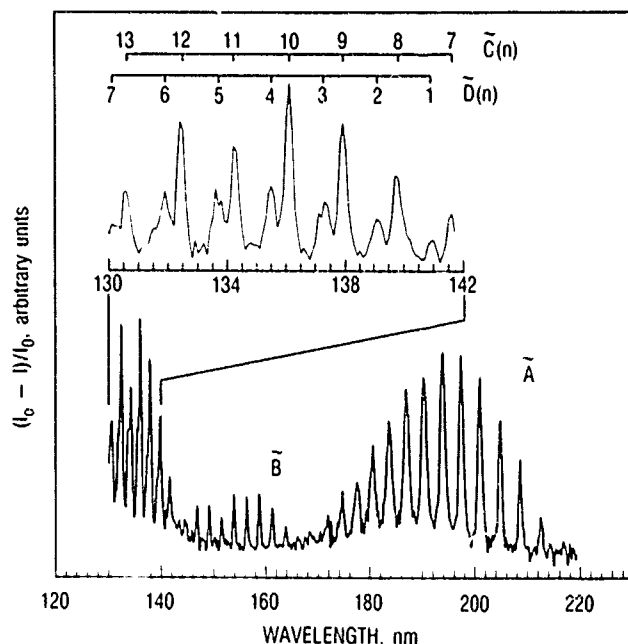


Figure 1 Supersonic-jet VUV absorption spectrum of NH_3 . The overlapping \tilde{C} and \tilde{D} branches are expanded in the upper portion of the figure to show the individual rovibrational lines

weak that we could not obtain reliable jet-cooled absorption spectra using our prototype apparatus. Instead, VUV spectra were recorded (Figure 2) for room-temperature-hydrazine, methyl hydrazine (MMH), and unsymmetrical dimethyl hydrazine (UDMH) reaching to energies (wavelengths) exceeding the ionization potential. Very distinct spectra were recorded; however, the features were broad for all three molecules. This contrasts with observations for ammonia, which has well-resolved absorption lines, even under ambient conditions. The jet spectrometer is undergoing a number of other improvements that will enhance sensitivity by more than an order of magnitude and make possible the future recording of direct absorption spectra of weak absorbers such as the hydrazines.

The VUV jet spectrometer was configured for two other experiments: single-photon ionization, and product chemiluminescence detection. Excellent sensitivity was obtained for the ionization threshold measurements leading to values for the vertical ionization potential of 8.70 eV (hydrazine), 8.45 eV (MMH), and 8.11 eV (UDMH).

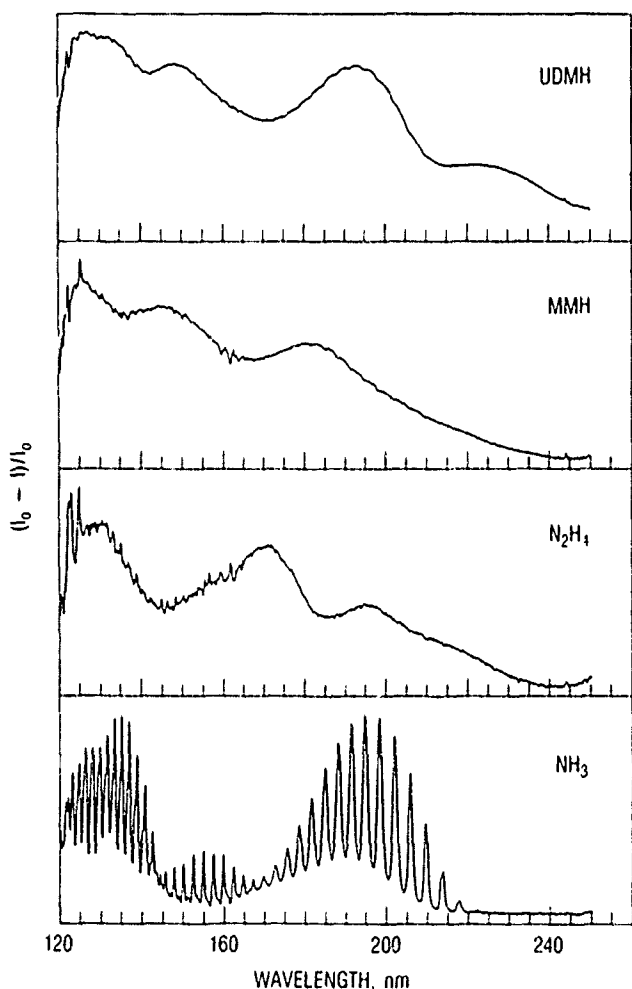


Figure 2 Ambient temperature VUV absorption spectra of NH_3 , hydrazine (N_2H_4), monomethyl hydrazine (MMH), and unsymmetrical dimethyl hydrazine (UDMH).

The recorded photoionization efficiency curves in Figure 3 reveal a very sharp threshold for NH_3 , but diffuse thresholds for the series of hydrazine molecules. This behavior is typical of molecules that have geometries that are very different in their neutral and ionic forms. The product chemiluminescence excitation spectrum of hydrazine was recorded and showed a strong onset at 145 nm. From energetic considerations, the fluorescing species must be a product other than the hydrogen atom, which has been invoked as the primary photoproduct at 193 nm [4,5]. Either N_2H_3 fluoresces or a different dissociation mechanism occurs at higher energy. Electron-impact excitation has been shown to lead to chemiluminescence in NH fragments [6,7].

A crossed electron-molecular beam mass spectrometer apparatus [8,9] was used to study the energy-dependent single-collision electron ionization/dissociation of hydrazine. Dissociative ionization in the electron energy range of 20 to 100 eV leads primarily to products of the form N_2H_n , where values of $n = 0$ to 3 were formed in nearly equal abundance.

In conclusion, we have developed a versatile VUV supersonic-jet spectrometer capable of recording direct absorption spectra, single-photon photoionization efficiency curves, and product chemiluminescence excitation spectra. Next year, we will focus on the study of unimolecular photoreactions to establish the primary photodissociation pathways among the energetically likely candidates. Previous investigators suggested that only the higher-energy hydrogen atom dissociation occurs by a collisionless mechanism; however, this work was conducted in a colli-

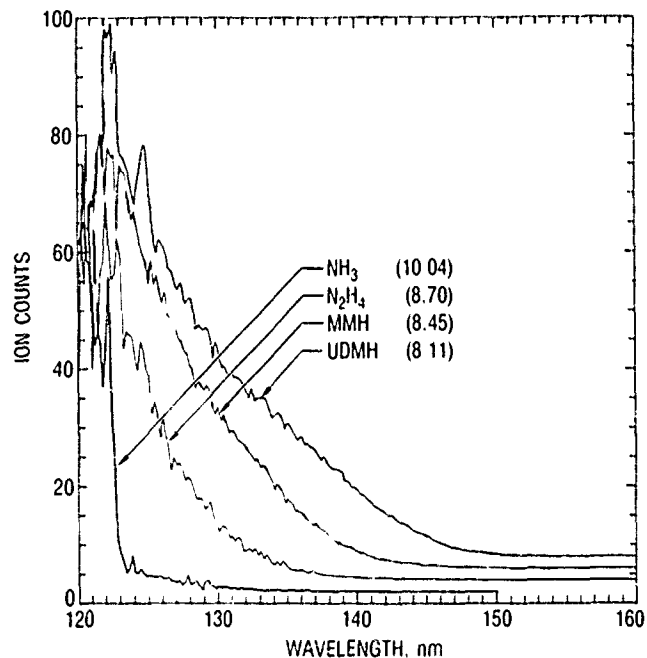


Figure 3. Single-photon photoionization efficiency curves for jet-cooled NH_3 , N_2H_4 , MMH, and UDMH. Ionization thresholds are given in electron volts.

sional low-pressure cell [4,5]. We plan to validate the correct mechanism by using the collisionless conditions of a molecular beam. We will extend our understanding by measuring product branching ratios and state distributions by nanosecond probing, and reaction rates by picosecond probing. A new tunable source of far-ultraviolet laser pulses and a scanning autotracking system have been developed that will enable the convenient detection of hydrogen atoms resulting from anticipated hydrazine chemistry. This capability will complement our methods for detecting other reactive intermediates such as OH, NH, and NH₂.

* * * * *

1. P. Lindberg et al., "The Production of Electronically Excited Species from the Photolysis of N₂H₄ and N₂D₄ at 193 nm," *Mol. Phys.* **62**, 1297 (1987).
2. C. Willis and R. A. Back, "Di-imide: Some Physical and Chemical Properties and the Kinetics and Stoichiometry of the Gas-Phase Decomposition," *Can. J. Chem.* **51**, 3605 (1973).
3. E. W. Fournier et al., "A Vacuum Ultraviolet, Supersonic Jet Absorption Spectrometer," *Appl. Spectrosc.* (in press).
4. W. G. Hawkins and P. L. Houston, "Hydrazine Photochemistry Induced by an ArF Laser," *J. Phys. Chem.* **86**, 704 (1982).

5. M. Arvis et al., "Isothermal Flash Photolysis of Hydrazine," *J. Phys. Chem.* **78**, 1356 (1974).
6. I. Tokue, A. Fujimaki, and T. Ito, "Formation and Internal Energy Distribution of the NH(A,c) Radicals by Electron-Impact Dissociation of Hydrazine and Methylamine," *J. Phys. Chem.* **88**, 6250 (1984).
7. K. Fukui, I. Fujita, and K. Kuwata, "Formation of the NH(A,c) Radicals by Electron Impact Near Threshold," *J. Phys. Chem.* **81**, 1252 (1977).
8. J. A. Syage, "Measurements of Electron-Impact Ionization and Dissociation Cross Sections in a Crossed Electron-Supersonic Molecular Beam," *Chem. Phys. Lett.* **143**, 19 (1988); also, ATR-88(8366)-1, The Aerospace Corp. (31 May 1988).
9. J. A. Syage, J. E. Pollard, and J. Steadman, "Resonance Ion Dissociation Spectroscopy of CH₃I⁺ Produced by Molecular Beam Electron-Impact Ionization," *Chem. Phys. Lett.* **161**, 103 (1989); also, ATR-90(8538)-1, The Aerospace Corp. (15 January 1990).

Bott, J. F., et al., *Electronic Energy Transfer from N₂(A) to NO*, ATR-89(8438)-1, The Aerospace Corp. (15 September 1989).

Flame Front Kinetics

T. A. Spiglanin, J. A. Syage, and R. B. Cohen,
Aerophysics Laboratory

The microscopic details of the chemical and dynamical processes that produce ignition are important to the future of high-performance rocket motors and airbreathing engines. Although the literature is laden with reports on stationary flames, few detailed studies exist of the ignition and flame propagation processes [1-12]. A number of obstacles impede study on this subject, notably that the time scale for observation is extremely short and reproducibility from one event to another is poor due to the statistical nature of the process. Theoretical studies are likewise restricted, primarily by the innate complexity of the process, but also by an incomplete knowledge of all chemical reaction rates that may be important over the wide temperature range that encompasses ignition.

As a result, we focus our efforts on making very detailed experimental measurements of species concentrations as a function of time and space following

attempted ignition. These experiments must provide a great deal of information on each attempted ignition, since averaging between separated ignition events may blur or obscure important information. These measurements must meet two important goals: they must provide information that can be immediately used to understand ignition so we may better optimize our combustion systems, and they must supply data critical to improving theoretical modeling. In the process, we expect to fit a simple parametric ignition model to the results from our experiments. Although it is not as accurate or intuitive as a comprehensive computer simulation, the parametric model will allow us to predict important events such as ignition/nonignition, a capability that is greatly needed.

Very few experimental studies have focused on the microscopic details of ignition and flame formation resulting from point ignition, where energy is deposited into a

small region of an otherwise cold gas mixture in a short period of time [13–20]. Point ignition begins with the deposition of energy into the gas, energy that can convert to heat, rupture chemical bonds, or ionize the gas. The excited kernel of gas then begins to react, liberating more heat in the process by producing species that are chemically more stable than either the fuel or the oxidizer. The immediate result of the reactions is an expansion of the flame kernel. Depending on the amount of energy deposited, the time to deposit the ignition energy, and the time to ignition, energy may be lost from the region in the form of a shock wave or may dissipate through conduction and diffusion. The kernel of hot gas will continue to react and to expand to a point where the flame will clearly form or extinguish. Because the initial flame is relatively small, the ratio of the initial surface area to the initial volume is greater than at any other time. The rate of heat lost from this region may be considered to scale with the surface area, leading us to conclude that the greatest heat loss per unit volume occurs during the early critical stages of ignition.

Our approach for studying flame formation and propagation is based on pulsed-laser ignition and several

state-of-the-art laser-based diagnostic techniques to make specific, detailed measurements within the forming flame. The important aspects are presented here with reference to the diagram in Figure 1(a). The ignition sequence begins with a pulse from a passively Q-switched Nd:YAG laser (the *spark* laser), radiating at 1024 nm. This infrared pulse is expanded with a diverging spherical quartz lens, then focused with a converging quartz lens to produce a small spark at the center of a flowing flammable gas mixture immediately above a sintered bronze burner assembly. Perpendicular to the direction of gas flow and to the direction of propagation of the spark laser, all-quartz optics collect light from the plane containing the spark, imaging this region onto the focal plane of our customized charge-coupled device (CCD) camera system (described later). At a selected time following the spark laser pulse, the probe laser fires. Its beam is formed into a sheet and directed along a path that eventually intersects the region where the spark had occurred, crossing as near as possible to 180 deg relative to the spark laser beam. This beam illuminates the region of the spark and its immediate surroundings for approximately 7 ns. The frequency of this probe laser is tuned to coincide exactly

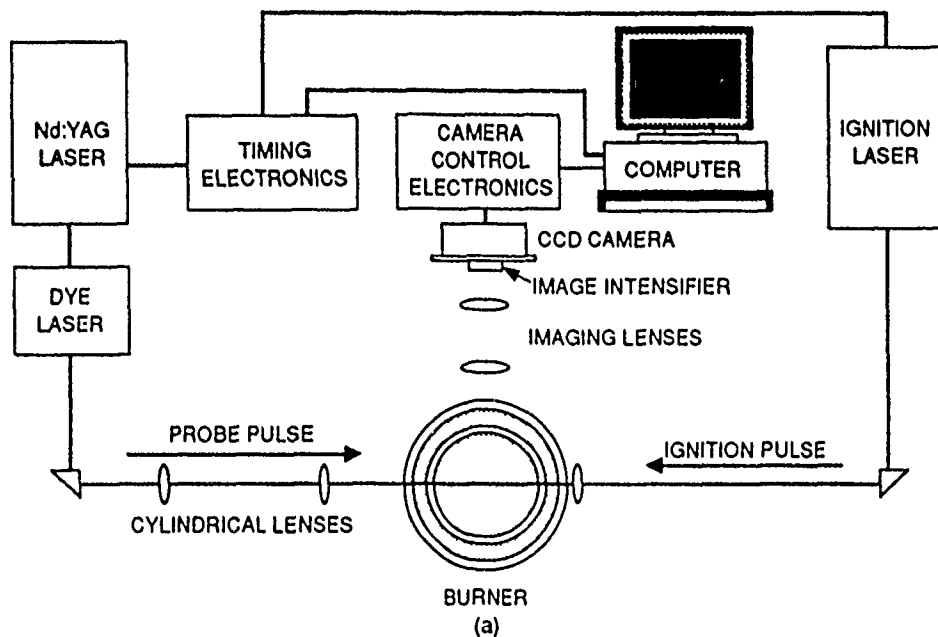
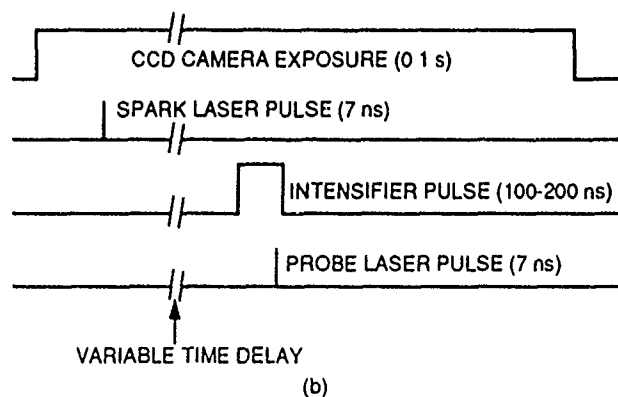


Figure 1. Experimental arrangement for planar laser-induced fluorescence (PLIF) imaging of species in nascent flames following laser ignition (a) Key components of the system; (b) the basic timing sequence. The delay between the spark laser and the probe laser can be continuously varied from 0 to 10 ms.



with a molecular or atomic absorption transition. If these selected molecules or atoms are present in the illuminated volume, they are excited by the laser pulse. As these excited states decay by fluorescence, this emission is captured by the camera collection optics and recorded by the CCD camera. The result is a 7-ns, species-specific snapshot of the spark as it forms into a flame at a well-specified time in its evolution. The all-important timing that is used to capture data with this system is illustrated in Figure 1(b).

The CCD camera system was developed specifically to support this work. It uses a highly sensitive image intensifier tube as the ultraviolet sensor, which doubles as an electronic shutter. The intensifier tube pulses on to permit the flow of photoelectrons generated at the photo-sensitive surface through the image-quality electron multiplier system. When off, this intensifier tube very effectively blocks light from entering the camera system; when on it amplifies its intensity (measured in electron flux), thus making extremely low-light exposures possible. Without the intensifier, the CCD camera itself would be incapable of producing these short-duration exposures of the nascent flames.

Last year, we reported initial measurements made with this system. These measurements revealed the system to be capable of amplifying the emission of a single photon to a level significantly above the background current generated within the CCD detector. We experimented with several optical designs for optimally collecting emission and maintaining adequate image fidelity at the focal plane of the camera system. We then examined in detail the nature of the laser-induced sparks we use routinely as our ignition source. This information is vital both for planning new experiments and for analyzing their results.

The single most important achievement during this past year was the capability of making routine planar laser-induced fluorescence (PLIF) measurements of the OH radical in evolving flame fronts. This is significant for several reasons:

- Our experiments effectively prove the performance of the timing system and demonstrate dramatically the performance of the camera system.
- We determined limitations in the apparatus, particularly in the timing mechanism that sets the time delay between the two lasers, and can now plan modifications for future generations of the experiments to overcome these shortcomings.
- The OH radical is one of the more important radicals in the formation and propagation of a hydrogen/air flame and is also a key species in reaction mechanisms for virtually all hydrocarbon combustion. Our ability to map relative concentrations of OH in developing flames with a 10-ns exposure is therefore extremely important.

Figure 2 shows a series of images of an igniting hydrogen/air mixture following laser-induced sparks recorded at several times following the spark. These images are photographs of OH luminescence excited by the sheet of light from the probe laser, effectively *slices* through the three-dimensional developing flame. The images point up several interesting effects of laser-ignited gases. Most notable is the nonspherical nature of the expansion. As early as 20 μ s following the initial spark, the forming flame front is approximately toroidal in shape, expanding radially about the axis defined by the spark laser beam, resulting in the image shown in Figure 2(b). Planar laser-induced fluorescence imaging of OH in flames that develop following laser-induced sparks had been used only once before, by Seitzman, Paul, and Hanson at Stanford University, who observed similar structure in the development of a methane/air flame with subtle differences [20]. First, the development of the flame in the direction toward the spark laser was less pronounced relative to the radial spreading of the nascent flame. Second, the time required to achieve the *closure* of the flame around the leading edge of the spark region seen clearly in Figure 2(f) at 242 μ s, required approximately 1200 μ s.

The unique shape of the ignition kernel results from several effects. The initial toroidal expansion appears likely to result from the shock of the laser-induced spark that imparts initial momentum to the flame gases in the radial direction. Propagation of the flame in the direction of the spark laser arises from some preheating caused by the original ignition laser beam. We do not know at this point whether this preheating is truly thermal, aided by radical production within the converging ignition laser beam, or some other artifact of the laser-induced plasma that started the flame. We then made a series of chemical kinetics calculations based on the CHEMKIN [21-22] packages that clearly show that a small difference in temperature between the front and back of the ignition kernel can lead to significant differences in thermal ignition times.

We have also started a study of the ignition processes as a function of the fuel/oxidizer ratio. In these studies, the ratio of hydrogen fuel to the oxidizer/inert gas mixture is varied and PLIF images of the OH spatial distribution are captured as a function of time following attempted laser-ignition. It is clear that the initial development of the nascent flame that extinguishes spatially mimics the development of a nascent flame that at longer times ignites, the principal differences being the intensity of the flame kernel as a function of time and the longer time behavior where dynamics attributable to the initial spark are less important and flame propagation dynamics intrinsic to the gas mixture are more important. These studies are under way, but the results have shown that we need to better control and measure both the intensity of

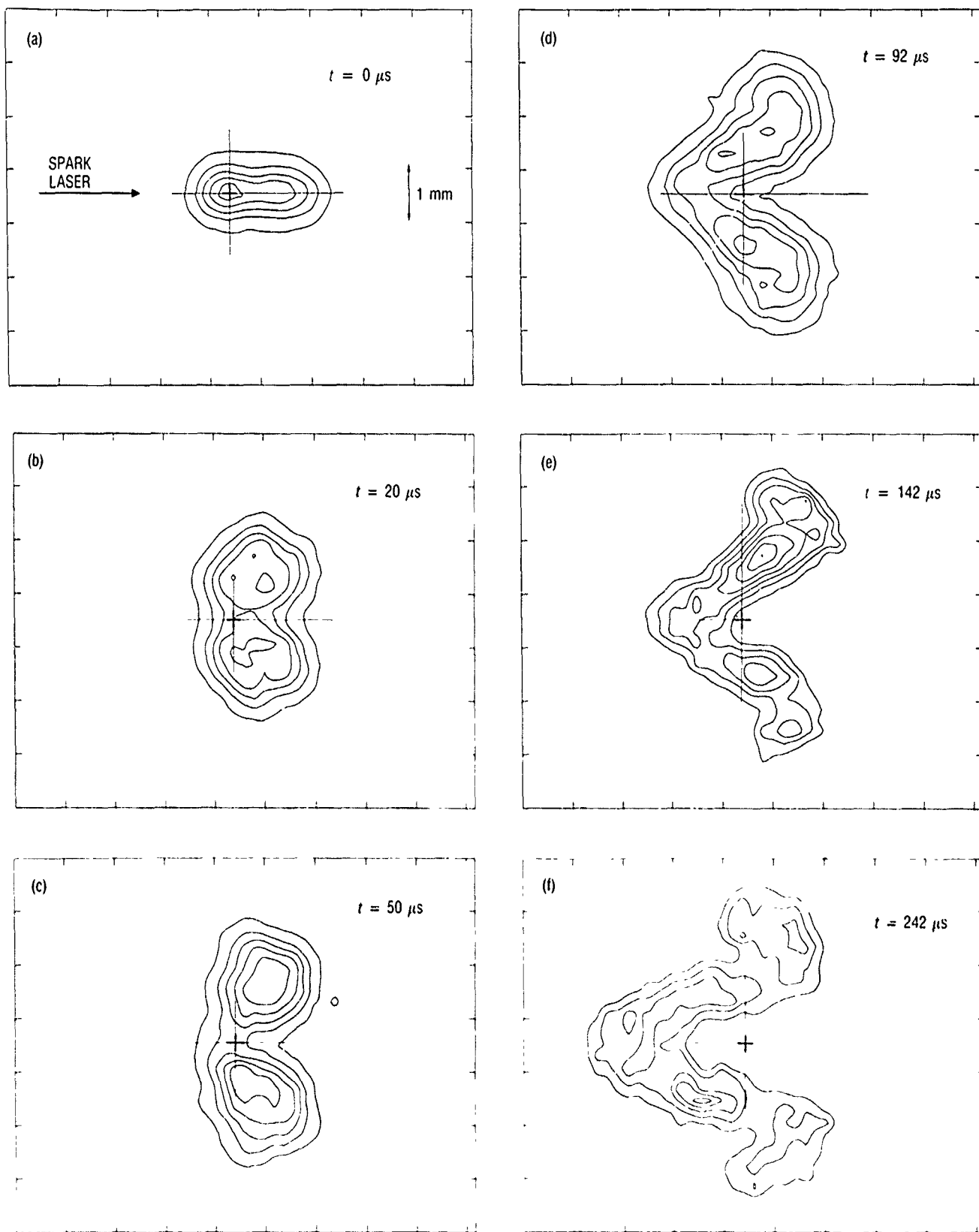


Figure 2 Contour plots of OH PLIF intensities for hydrogen/air flames at several times following laser induced spark ignition. The images are recorded using the apparatus shown in Figure 1 and the spark laser passes from left to right. The time delay between the igni-

tion pulse and the probe pulse is indicated in the upper right of each frame. The tick spacing on each plot represents 1 mm at the flame. The + symbol represents the location of the initial spark emission peak.

the laser-induced spark and the flux of our probe laser beam. We have identified solutions to our difficulties and are continuing to improve the techniques.

Future studies will follow three well-defined paths:

- We will continue to study ignition of hydrogen/air mixtures and develop the diagnostic capabilities required to spatially image H and O atoms. These species are key to almost all oxygen-sustained combustion and are extremely important in the propagation of the flame front. The high concentration and mobility of H atoms in a hydrogen-fueled flame is believed responsible for its extraordinarily high velocity. These two species also happen to be very difficult to image using PLIF techniques and require a somewhat different strategy involving two-photon spectroscopy.
- We will concentrate on determining the flame initiation and propagation dynamics for other fuels. These include methane and propane (candidates for supersonic combustor fuels) and NH_x -containing fuels that are used for satellite propulsion and some large boosters.
- We will also continue to study the dynamics of flame formation, assuming the 100 μs time as the end of the period where measurements are dominated by the dynamics of spark formation. These studies will clarify the mechanism that leads to ignition and extinction of flames.

We are also pursuing the laser-facilitated flame propagation implied by the growth of the flame kernel in the direction of the spark laser beam. This growth, backed by our chemical kinetics calculations, is strong evidence that a laser can greatly reduce the ignition time in flammable gases. This technology has applications for future launch vehicle ignition processes and for the National Aerospace Plane, where flame holding at supersonic velocities is extremely important.

* * * * *

1. R. A. Strehlow, *Combustion Fundamentals*, McGraw-Hill, New York (1985).
2. B. Lewis and G. Von Elbe, *Combustion, Flames, and Explosion of Gases*, 2nd ed., Academic Press, New York (1967).
3. K. Kohse-Hoinghaus, R. Heidenreich, and Th. Just, "Determination of Absolute OH and CH Concentrations in a Low Pressure Flame by Laser-Induced Saturated Fluorescence," *20th International Symposium on Combustion*, Combustion Institute, Pittsburgh (1984), p. 1177.
4. J. T. Salmon et al., "Laser-Saturated Fluorescence Measurements of NH in a Premixed Subatmospheric $\text{CH}_4/\text{N}_2\text{O}/\text{Ar}$ Flame," *ibid.*, p. 1187.
5. G. Kychakoff, R. K. Hanson, and R. D. Howe, "Simultaneous Multiple-Point Measurements of OH in Combustion Gases Using Planar Laser-Induced Fluorescence," *ibid.*, p. 1265.
6. R. J. Cattolica and S. R. Vosen, "Two-Dimensional Measurements of the [OH] in a Constant Volume Combustion Chamber," *ibid.*, p. 1273.
7. J. A. Vanderhoff et al., "Raman and Fluorescence Spectroscopy in a Methane-Nitrous Oxide Laminar Flame," *ibid.*, p. 1299.
8. K. Kohse-Hoinghaus, P. Koczar, and Th. Just, "Absolute Concentration Measurements of OH in Low-Pressure Hydrogen-Oxygen, Methane-Oxygen, and Acetylene-Oxygen Flames," *21st International Symposium on Combustion*, Combustion Institute, Pittsburgh (1986), p. 1719.
9. R. J. Hennessy, C. Robinson, and D. B. Smith, "A Comparative Study of Methane and Ethane Flame Chemistry by Experiment and Detailed Modelling," *ibid.*, p. 761.
10. R. G. Joklik, J. W. Daily, and W. J. Pitz, "Measurements of CH Radical Concentrations in an Acetylene/Oxygen Flame and Comparisons to Modeling Calculations," *ibid.*, p. 895.
11. J. Bian, J. Vandooren, and P. J. Van Tigglen, "Experimental Study of the Structure of an Ammonia-Oxygen Flame," *ibid.*, p. 953.
12. L. R. Thorne et al., "Hydrocarbon/Nitric Oxide Interactions in Low-Pressure Flames," *ibid.*, p. 965.
13. G. Dixon-Lewis and I. G. Shepherd, "Some Aspects of Ignition by Localized Sources, and of Cylindrical and Spherical Flames," *15th International Symposium on Combustion*, Combustion Institute, Pittsburgh (1974), p. 1483.
14. R. Maly and M. Vogel, "Initiation and Propagation of Flame Fronts in Lean CH_4 -Air Mixtures by Three Models of the Ignition Spark," *17th International Symposium on Combustion*, Combustion Institute, Pittsburgh (1978), p. 821.
15. R. Atkinson, D. C. Bull, and P. J. Shuff, "Initiation of Spherical Detonation in Hydrogen/Air," *Combust. Flame* **39**, 287 (1980).
16. R. A. Hill and G. A. Laguna, "Laser-Initiated Combustion of $\text{CH}_4 + \text{O}_2$ Mixtures," *Opt. Commun.* **32**, 435 (1980).
17. R. Maly, "Ignition Model for Spark Discharges and the Early Phase of Flame Growth," *18th International Symposium on Combustion*, Combustion Institute, Pittsburgh (1980), p. 1747.
18. J. A. Syage et al., "Dynamics of Flame Propagation Using Laser-Induced Spark Initiation: Ignition Energy Measurements," *J. Appl. Phys.* **64**, 1499

- (1988); also, ATR-89(8407)-7, The Aerospace Corp. (15 November 1988).
19. B. E. Forch and A. W. Miziolek, "Ultraviolet Laser Ignition of Premixed Gases by Efficient and Resonant Multiphoton Photochemical Formation of Microplasmas," *Combust. Sci. Technol.* **52**, 151 (1988).
 20. J. M. Seitzman, P. H. Paul, and R. K. Hanson, "Digital Imaging of Laser-Ignited Combustion," Paper 88-2775, AIAA Thermophysics, Plasmadynamics and Lasers Conference, San Antonio, June 1988.
 21. R. J. Kee, J. A. Miller, and T. H. Jefferson, *CHEMKIN: A General Purpose, Problem-Independent, Transportable, Fortran Chemical Kinetics Code Package*, SAND80-8003, Sandia National Laboratories (March 1980).
 22. A. E. Lutz et al., *SENKIN: A Fortran Program for Predicting Homogeneous Gas Phase Chemical Kinetics with Sensitivity Analysis*, SAND87-8248, Sandia National Laboratories (February 1988).

Syage, J. A., et al., "Minimum Ignition Energy Measurements Using Laser-Induced Spark Initiation," *Proceedings of the JANNAF Combustion Meeting*, CPIA Press, Baltimore (1988); also, ATR-89(8407)-1, The Aerospace Corp. (15 November 1988).

High-Resolution Chemical Dynamics

J. E. Pollard, L. K. Johnson, D. A. Lichtin, and R. B. Cohen,
Aerophysics Laboratory

The investigation of bimolecular reactive scattering under single-collision conditions gives direct insight into the forces that control chemical reactivity. Basic research in this area is closely tied to progress in propulsion and combustion science, atmospheric chemistry, and chemical laser development. Scattering experiments can identify whether a reaction proceeds by a direct mechanism or through a long-lived intermediate, and whether it involves head-on or glancing collisions. Also revealed are the effects of reactant translational and internal energy and the distribution of energy release to the products.

The ion-neutral reaction $H_2^+ + H_2$ continues to challenge the understanding of chemical dynamicists, due primarily to the participation of competing product channels whose relative contributions are strongly dependent on collision energy and on reactant vibrational excitation. $H_2^+ + H_2$ is of fundamental interest because of the opportunity for meaningful comparisons between experiment and theory in a system where calculation of the potential energy surface is tractable. The 1.72 eV exoergic product channel, $H_2^+ + H_2 \rightarrow H_3^+ + H$, predominates at center-of-mass translational energies (E_{cm}) less than 2 eV. The process can occur either by proton (H^+) transfer or by atom (H) transfer, but proton transfer is expected to be the more likely route due to the weaker bond energy of H_2^+ ($D_0 = 2.65$ eV) compared with H_2 ($D_0 = 4.48$ eV). Isotopic substitution experiments indicate that charge equilibration (by multiple electron transfers between H_2^+ and H_2) scrambles the original identities of

the ion and neutral at $E_{cm} < 3$ eV. Net electron transfer ($H_2^+ + H_2 \rightarrow H_2 + H_2^+$) is the major product channel for $E_{cm} \geq 2$ eV, and the cross section is not strongly dependent on collision energy. Collision-induced dissociation ($H_2^+ + H_2 \rightarrow H^+ + H + H_2$) becomes a more probable outcome than H_3^+ formation at $E_{cm} \geq 5$ eV and is substantially enhanced by reactant vibrational excitation.

The integral cross section for $H_2^+ + H_2 \rightarrow H_3^+ + H$ has been measured previously using the guided-beam method for $E_{cm} = 0.1$ to 100 eV [1,2]. Experiments with crossed ion and neutral beams have recorded product angular and energy distributions (relative differential cross sections) for $E_{cm} = 1$ –4 eV without reactant state selection [3]. The merged-beam method has been used to measure absolute integral cross sections and axial energy distributions for $E_{cm} = 0.002$ to 10 eV [4]. The experiments have been interpreted with a direct reaction mechanism that does not involve a long-lived complex. The near-Langevin dependence of the cross section ($\sigma \propto E_{cm}^{-1/2}$) indicates that reaction occurs primarily at large impact parameter with no significant energy barrier. Surface-hopping trajectory calculations have been applied to electron transfer, to H_3^+ formation, and to collision-induced dissociation in $H_2^+ + H_2$ [5]. The results are generally in good agreement with the measured integral cross sections, but a quantitative comparison with measured differential cross sections has been not been possible. Crossed-beam and merged-beam experiments tradition-

ally rely on electron-bombardment ion sources that produce H_2^+ in a broad distribution of vibrational states, allowing for less definitive tests of theory.

We have developed a technique to measure ion-neutral differential cross sections (Figure 1) in which vibrationally state-selected H_2^+ reactant ions are produced within a collimated molecular beam by resonantly enhanced multiphoton ionization of H_2 . The ions are accelerated by a variable-angle impulsive electric field and collide with neutral H_2 molecules in the beam. Velocity distributions for the H_3^+ product ions are determined from time-of-arrival spectra with a quadrupole mass spectrometer. Angular distributions are measured by rotating the reactant ion velocity vector relative to the fixed axes of the detector and neutral beam. The scattering data are transformed from the laboratory frame to the center-of-mass frame for subsequent manipulation. Coverage of product velocity space is sufficiently complete for the results to be put on an absolute scale by normalizing to the known integral cross sections [2]. The ability to obtain differential cross sections for state-selected reactions by this method is a significant advance in the field of experimental chemical dynamics.

During the past year, we investigated $H_2^+ + H_2 \rightarrow H_3^+ + H$ at collision energies of $E_{cm} = 1.5, 2.3, 3.5$, and 5.3 eV with H_2^+ in the vibrational states $v = 0, v = 1$, and $v = 2$. Figures 2 and 3 show examples of the differential

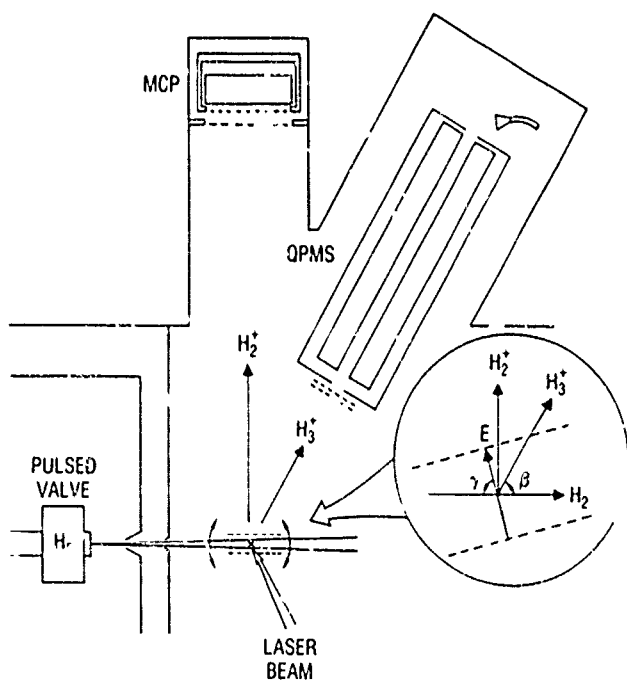


Figure 1. Schematic of the apparatus showing the laser beam and molecular beam intersecting at the center of the rotating grid assembly. Reactant ions are detected by a microchannel plate (MCP), and product ions are detected by a quadrupole mass spectrometer (QPMS). E denotes the direction of the impulsive electric field.

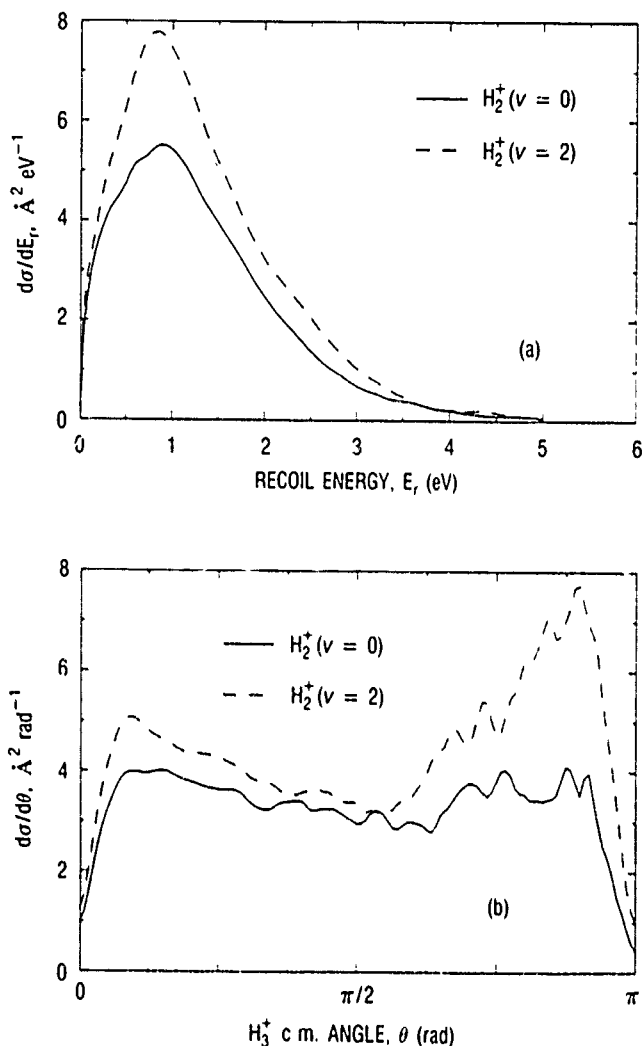


Figure 2. Differential cross section, measured with respect to product recoil energy and scattering angle for $H_2^+ + H_2 \rightarrow H_3^+ + H$ at a collision energy of $E_{cm} = 2.3$ eV. The incident H_2^+ velocity vector is at $\theta = 0$; the incident H_2 velocity vector is at $\theta = \pi$. Product ions are described as forward scattered for the range $0 \leq \theta \leq \pi/2$ and backward scattered for the range $\pi/2 \leq \theta \leq \pi$.

cross sections, $d\sigma/dE_r$ and $d\sigma/d\theta$, measured with respect to product recoil energy E_r and center of mass scattering angle θ .

The reaction cross section decreases with increasing collision energy but is enhanced by H_2^+ vibrational excitation. The recoil energy distribution is determined mainly by the collision energy and to a lesser extent by H_2^+ vibration. The fraction of the available energy (total reactant energy plus 1.72 eV exoergicity) that appears as product translation is in the range of 27 to 41% for all cases studied. Hence, the major portion of the available energy goes into product internal excitation, as is often observed for exoergic reactions. In fact, at higher E_{cm} , we find evidence for product ions with internal energies substantially

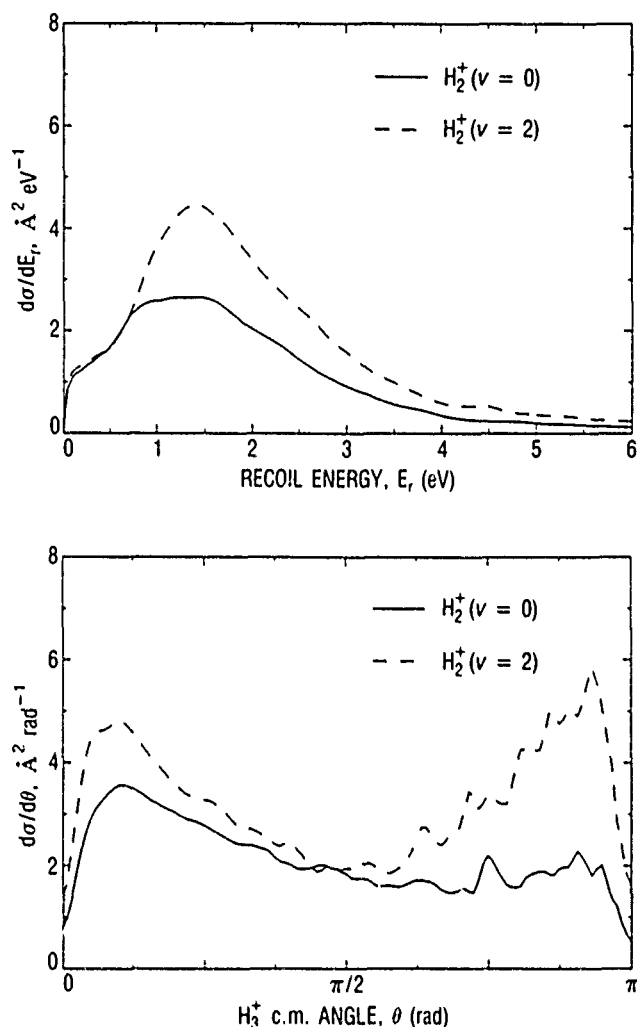


Figure 3. Differential cross sections measured with respect to product recoil energy and scattering angle for $\text{H}_2^+ + \text{H}_2 \rightarrow \text{H}_3^+ + \text{H}$ at a collision energy of $E_{\text{cm}} = 3.5 \text{ eV}$.

in excess of the dissociation limit. Theoretical results [6] support the possibility that metastable H_3^+ in states of high angular momentum could survive long enough to be detected in this experiment.

For $\text{H}_2^+ (v = 0)$ reactant at low collision energy, the H_3^+ product ions are scattered almost isotropically with respect to θ ($d\sigma/d\theta = \text{constant}$), but as E_{cm} increases, there is greater depletion of the backward-scattered product than the forward-scattered product. Reactant vibrational excitation preferentially enhances backward scattering and gives an angular distribution more strongly peaked near $\theta = 0$ and $\theta = \pi$. The angular distribution also provides clues about the competition between H_3^+ formation and electron transfer at low E_{cm} and between H_3^+ formation and collision-induced dissociation at higher E_{cm} . Trends in the angular and energy distributions are

in good agreement with the predictions of surface-hopping trajectory calculations [5]. An analysis of the complete data set and a quantitative comparison with theory are given in a paper to be published later.

A search for scattering resonances in the theoretically important endoergic reaction $\text{H}_2^+ + \text{He} \rightarrow \text{HeH}^+ + \text{H}$ [7] is now under way. This search involves measuring the product ion velocity distribution at $\theta = 0$ and $\theta = \pi$ as a function of collision energy. If successful, the experiment will provide a uniquely sensitive probe of the potential energy surface for comparison with theory.

* * * * *

1. S. L. Anderson et al., "The Effect of Vibration and Translational Energy on the Reaction Dynamics of the $\text{H}_2^+ + \text{H}_2$ System," *J. Chem. Phys.* **75**, 2153 (1981).
2. J. D. Shao and C. Y. Ng, "A Vibrational State-Selected Study of the Reaction $\text{H}_2^+ + \text{H}_2 \rightarrow \text{H}_3^+ + \text{H}$ Using the Tandem Photoionization Mass Spectrometry and Radio Frequency Ion Guide Methods," *J. Chem. Phys.* **84**, 4317 (1986).
3. J. R. Krenos et al., "Crossed-Beam Study of the Reactions of H_2^+ with D_2 and D_2^+ with H_2 ," *Chem. Phys.* **16**, 109 (1976).
4. C. H. Douglass, D. J. McClure, and W. R. Gentry, "The Dynamics of the Reaction $\text{H}_2^+ + \text{H}_2 \rightarrow \text{H}_3^+ + \text{H}$, with Isotopic Variations," *J. Chem. Phys.* **67**, 4931 (1977).
5. C. W. Eaker and G. C. Schatz, "A Quasiclassical Trajectory Study of the $\text{H}_2^+ + \text{H}_2 \rightarrow \text{H}_3^+ + \text{H}$ Reaction," *J. Phys. Chem.* **89**, 2612 (1985).
6. E. Pollak, "Total Angular Momentum Barriers for Triatomic Systems," *J. Chem. Phys.* **86**, 1645 (1987).
7. N. Sathyamurthy, M. Baer, and T. Joseph, "Resonances in Collinear $\text{He} + \text{H}_2^+$ Collisions," *Chem. Phys.* **114**, 73 (1987).

Pollard, J. E., and R. B. Cohen, "Electron-Impact Ionization Time-of-Flight Mass Spectrometer for Molecular Beams," *Rev. Sci. Instrum.* **58**, 32 (1987).

Pollard, J. E., D. A. Lichtin, and R. B. Cohen, "Differential Cross Sections for State-Selected Reactions in the $\text{H}_2^+ + \text{H}_2$ System," *Chem. Phys. Lett.* **152**, 171 (1988).

Picosecond State-Specific Reaction Dynamics

J. A. Syage and J. Steadman,
Aerophysics Laboratory

One of the fundamental issues in chemical dynamics is understanding how solvent molecules influence the properties of chemical reactions. This has traditionally been investigated by comparing the kinetics of gas phase reactions with that in solvents of varying viscosity [1-3]. Our approach in this work is to examine how a gas phase reaction is modified by the stepwise addition of single solvent molecules [4-9]. Important topics include learning how unimolecular and bimolecular gas phase reactions are influenced by stepwise solvation, or how large a solvent shell must be to make a bulk solution phase reaction energetically favorable in a small cluster. Molecules seeded in solvent clusters have great appeal because they represent an environment that is intermediate between the gas phase and the condensed phase.

The most noteworthy achievement of the past year involves our success in obtaining picosecond measurements of intermolecular reaction rates in molecular clusters [5-9]. The experiment is based on a two-pulse picosecond pump-probe sequence in which the first pulse excites the cluster and initiates a chemical reaction, and the second pulse, delayed in time, ionizes either reactant, product, or reactive intermediate. The time evolution of each species of interest is obtained by scanning the pump-probe delay time. The molecular clusters are formed in a molecular beam expansion, and the ions are formed by resonance-enhanced multiphoton ionization. The ion masses are identified in a time-of-flight (TOF) mass spectrometer.

In one study, we chose as a prototype for excited-state proton transfer [10,11] the molecule phenol bonded to a selected number ($n = 1-20$) of solvent molecules of various basicity; e.g., NH_3 , CH_3OH , H_2O , N_2H_4 , and $\text{N}(\text{CH}_3)_3$ [7-9]. This model system forms the basis for understanding the evolution of acid-base chemistry as we systematically solvate a gas-phase reaction, one molecule at a time, to approach the condensed phase. Our work has revealed striking solvent-cluster effects that depend strongly on the cluster size and basicity. For the relatively basic solvent NH_3 , we observed a striking onset to proton transfer as we increased the solvent cluster size. The addition of a single solvent molecule from size $n = 4$ to $n = 5$ increased the rate of proton transfer by at least two orders of magnitude to $(60 \text{ ps})^{-1}$, as illustrated in Figure 1,

which shows time-dependent measurements of the parent ion signals. An important result that confirms the proton transfer mechanism is the measurement of the kinetics of formation of product, which is detected by monitoring the protonated solvent signal in the mass spectrum. As illustrated in Figure 2, the 60-ps time constant for decay of reactant is matched by the formation of product. The product formation channel, quite interestingly, revealed a sequential double time dependence that can be explained by a rapid (60 ps) proton transfer from phenol to the $(\text{NH}_3)_n$ solvent cluster followed by a slower (0.3 ns) rearrangement of the solvent cluster about the proton; i.e., rate of solvation. Finally, time-dependent measurements of reactant phenol seeded in the less basic solvent clusters $(\text{CH}_3\text{OH})_n$ and $(\text{H}_2\text{O})_n$ show that no proton transfer occurs for the same solvent sizes that reacted in $(\text{NH}_3)_n$ solvent [9].

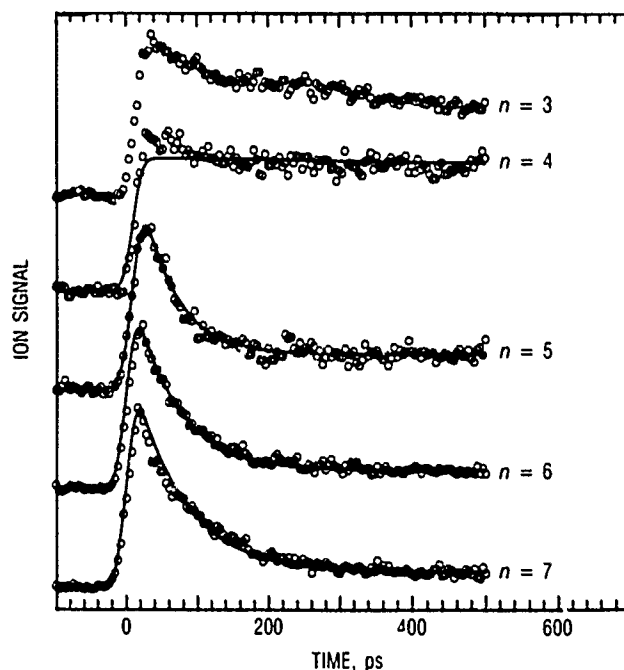


Figure 1 Time-resolved measurements of reactant cluster $\text{ROH}^*(\text{NH}_3)_n$ as detected by the ion signal $\text{ROH}^+(\text{NH}_3)_n$, with onset to reaction at $n=5$ shown. The calculated curves, based on a simple model [7-9], are included for clarity.

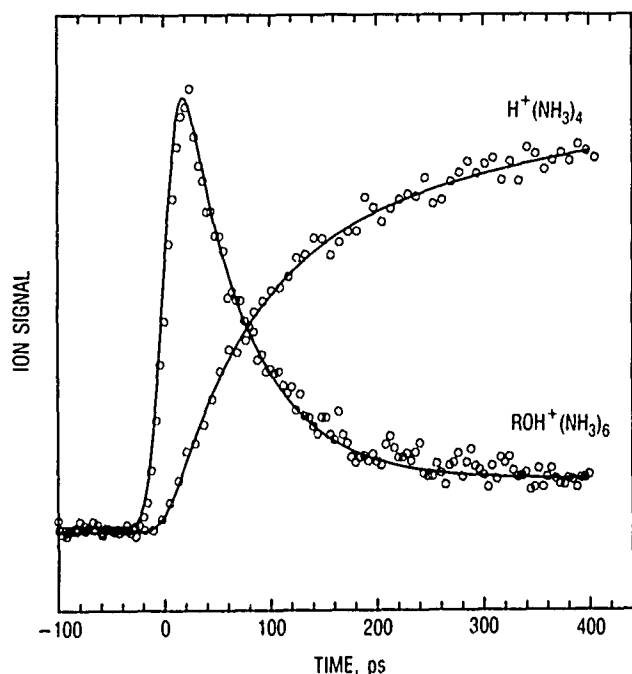


Figure 2. Representative traces for reactant cluster $ROH^+(NH_3)_n$, as detected by the ion signal $ROH^+(NH_3)_n$, and product $RO^+H^+(NH_3)_n$, as detected by the ion signal $H^+(NH_3)_n$, with the same 65 ± 10 ps time-constant for proton transfer shown.

In another picosecond molecular beam study, we investigated the properties of free-radical chemistry in molecular clusters [6,8]. Our system of choice was CH_3I clusters. With 266-nm excitation, a single molecule in the cluster undergoes very rapid (< 1 ps) dissociation [12] to produce very energetic (1–2 eV) and reactive methyl CH_3 radicals. The partner iodine atom is formed at very low kinetic energy due to the very different masses of the fragments and therefore acts as a spectator on the short measurement time scales of the experiment. The *hot* methyl radical, on the other hand, can induce a chain mechanism, much like that encountered in combustion processes. Indeed, our picosecond measurements revealed very complex and rapid sequential chemistry in the clusters. Short-lived reactive intermediates are evident by the complex time-dependences measured for many fragment

species (Figure 3). The cluster dynamics and geometries allow for sequential loss of CH_3 radicals and substantial caging of fragment I atoms and recombined I_2 molecules. Loss of up to five CH_3 radicals for cluster sizes $n \geq 8$ occurs within the 25-ps excitation pulse duration, as indicated by the presence of ion signals such as $I_5(CH_3I)_3^+$. The evidence suggests that the extensive demethylation in the larger clusters is driven in part by the energy of intracluster recombination of two CH_3 radicals and elimination of ethane [6].

In other developments, we have further refined our TOF low-mass filter technique for mass-selective ion and cluster ion photodissociation studies. We have reported on the metastable dissociation of aniline cation in solvent clusters and the photodissociation of methyl iodide cluster ions and have presented a full description of the technique [5,8,13]. The importance of ion dissociation measurements to the picosecond study of neutral cluster reactions is illustrated in Figure 4 for $(CH_3I)_n$ clusters. The electron-impact cluster mass spectrum in Figure 4(a) shows ion fragment signals that occur exclusively by ion dissociation mechanisms. In Figure 4(b), the TOF low-mass filter is activated to reject all noncluster species. In 4(c), subsequent resonant photodissociation of the cluster ions reveals only van der Waals dissociation. Picosecond resonance-enhanced multiphoton ionization excitation of $(CH_3I)_n$ through the dissociative *A*-state gives a distinctly different mass spectrum in Figure 4(d). These additional signals can be unambiguously assigned to ionization of neutral products [8].

In summary, we have made considerable progress in developing methods toward gaining a better understanding of the microscopic properties of chemical reactions as they evolve from the gas phase to the condensed phase on a single molecule basis. The next series of experiments will probe the energy dependence of reaction for specific cluster sizes in an effort to model the changes that occur in the potential energy surface by stepwise addition of solvent molecules. We hope that this effort will enable classical chemistry to be understood on a more quantum mechanical level.

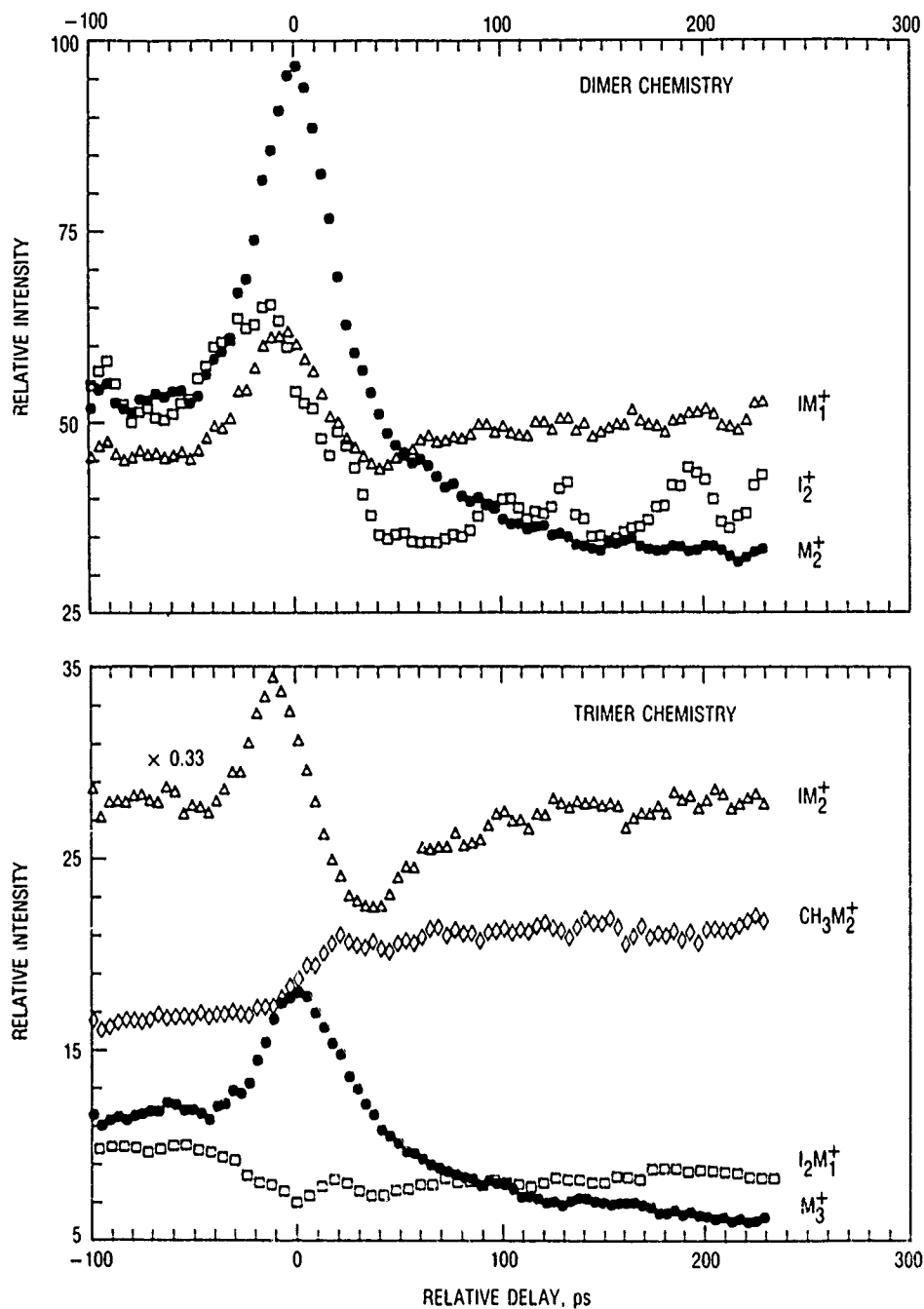


Figure 3. Picosecond measurements for $(CH_3I)_n$ cluster A-state excitation using 266 nm pump and 532 nm probe excitation. Reactant parent decays M_n , as measured by M_n^+ , and fragment intermediates are noted where $M = CH_3I$.

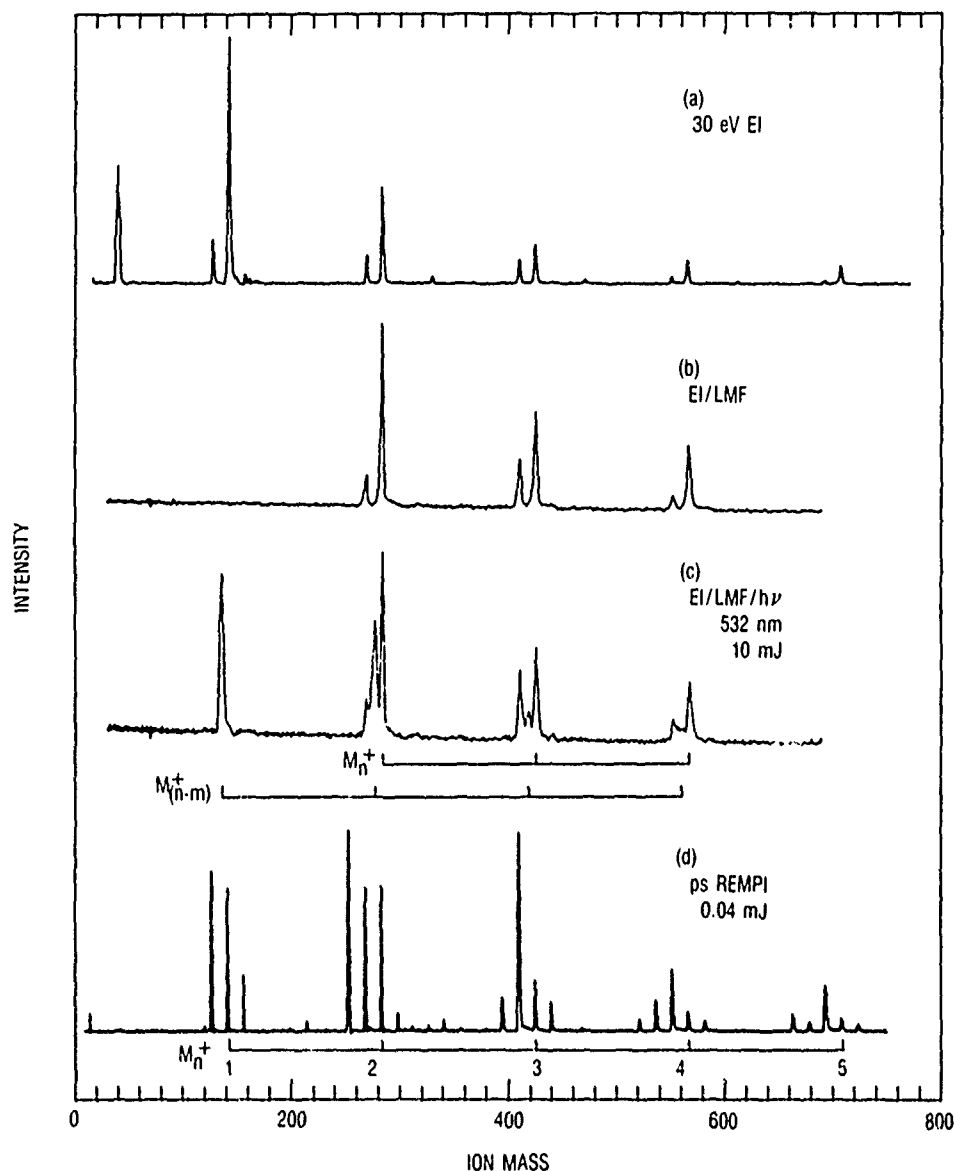


Figure 4. $(\text{CH}_3\text{I})_n$ cluster ionization mass spectra ($M = \text{CH}_3\text{I}$). (a) Direct ionization by electron impact excitation at 30 eV; (b) electron impact ionization and low-mass filter (LMF); (c) same as (b), but with resonant photodissociation of cluster ions; (d) picosecond A-state REMPI.

1. M. Maroncelli, J. MacInnis, and G. R. Fleming, "Polar Solvent Dynamics and Electron-Transfer Reactions," *Science* **243**, 1674 (1989).

2. J. A. Syage, P. M. Felker, and A. H. Zewail, "Picosecond Dynamics and Isomerization of Stilbene in Supersonic Beams: II. Reaction Rates and the Potential Energy Surface," *J. Chem. Phys.* **81**, 4706 (1984).

3. G. Rothenberger, D. K. Negus, and R. M. Hochstrasser, "Solvent Influence on Photoisomerization Dynamics," *J. Chem. Phys.* **79**, 5360 (1983).

4. J. A. Syage, "Reactivity of Aniline Cation to Stepwise Solvation in Hydrogen-Bonded Molecular Clusters," *J. Phys. Chem.* **93**, 170 (1989); also, ATR-89(8413)-1, The Aerospace Corp. (20 April 1989).

5. J. A. Syage, "Photodissociation and Metastable Decay of Solvated Cluster Ions," *J. Chem. Phys.* **92**, 1804 (1990); also, ATR-90(8513)-1, The Aerospace Corp. (15 April 1990).

6. J. A. Syage and J. Steadman, "Picosecond Mass-Selective Measurements of Molecular Cluster Reactions: $(\text{CH}_3\text{I})_n$ A State Excitation," *Chem. Phys. Lett.* **166**, 159 (1990); also, ATR-90(8513)-2, The Aerospace Corp. (15 April 1990).

7. J. Steadman and J. A. Syage, "Picosecond Mass-Selective Measurements of Phenol- $(\text{NH}_3)_n$ Acid-Base Chemistry in Clusters," *J. Chem. Phys.* **92**, 4630 (1990); also, ATR-90(8513)-3, The Aerospace Corp. (1 May 1988).

8. J. Steadman, E. W. Fournier, and J. A. Syage, "Detection of Neutral and Ionic Reaction Mechanisms in Molecular Clusters," *Appl. Opt.* **29**, 4962 (1990).

9. J. A. Syage, "Picosecond Photochemistry in Molecular Clusters," *Proc. SPIE* **1209**, 64 (1990).
 10. J. J. Breen et al., "Real-Time Probing of Reactions in Clusters," *J. Chem. Phys.* **92**, 805 (1990).
 11. O. Cheshnovsky and S. Leutwyler, "Proton Transfer in Neutral Gas-Phase Clusters: Naphthol-(NH₃)_n," *J. Chem. Phys.* **88**, 4127 (1988).
 12. J. L. Knee, L. R. Khundkar, and A. H. Zewail, "Picosecond Monitoring of a Chemical Reaction in Molecular Beams: Photofragmentation of R-I → R[#] + I," *J. Chem. Phys.* **83**, 1996 (1985).
 13. J. A. Syage and J. Steadman, "A Time-of-Flight Mass Filter for Ion and Cluster Ions Photodissociation Studies," *Rev. Sci. Instrum.* **61**, 1204 (1990); also, ATR-90(8513)-4, The Aerospace Corp. (10 May 1988).
-
- Syage, J. A., "Measurements of Electron-Impact Ionization and Dissociation Cross Sections in a Crossed Electron-Supersonic Molecular Beam," *Chem. Phys. Lett.* **143**, 19 (1988); also, ATR-88(8366)-1, The Aerospace Corp. (31 May 1988).
- _____, "On the Direct Vibrational Spectroscopy of Transition States," *Chem. Phys. Lett.* **158**, 122 (1989); also, ATR-89(8413)-2, The Aerospace Corp. (15 September 1989).
- _____, "Radiative Trapping of a Direct Photodissociation," *Bull. Am. Phys. Soc.* **34**, 1534 (1989).
- Syage, J. A., and J. Steadman, "Photodissociation Spectroscopy of Cold Molecular Ions and Cluster Ions," *Laser Spectroscopy IX*, M. S. Feld, J. E. Thomas, and A. Mooradian, eds., Academic Press (1989), p. 418.
- Syage, J. A., "New Developments in Molecular Detection by Supersonic Molecular Beam Laser Mass Spectrometry," *Lasers and Mass Spectrometry*, D. M. Lubman, ed., Oxford University Press (1990), p. 468.
- Syage, J. A., and J. Steadman, "Strong Field Effects in the Spectroscopy of the B State of CH₃I," *J. Phys. Chem.* **94**, 7343 (1990); also, ATR-91(8313)-1, The Aerospace Corp. (1 December 1990).

Mechanism of Diamond Film Growth

L. R. Martin,
Aerophysics Laboratory

The new field of diamond film synthesis at low pressures is continuing to develop with extraordinary speed. Some of the recent technological advances include heteroepitaxy of diamond on cubic boron nitride, and the production of carbon-12 enriched diamonds. Homoepitaxy of diamond on high-pressure diamond substrates was achieved last year, but heteroepitaxy is believed to be essential for the practical production of single-crystal semiconducting devices. The carbon-12 enriched diamonds were produced at General Electric by first making enriched diamond films using a new low-pressure technique and then recrystallizing the diamonds at high pressure. This approach yielded approximately 1 carat gem quality diamonds with a heat conductivity 50% higher than natural diamonds. Since natural diamonds have the highest heat conductivity known—five times that of silver—this improvement is very significant. Further purification of the carbon-12 diamonds is expected to yield even better performance.

Our own work has now shown conclusively that methyl radicals and hydrogen atoms are the essential pre-

cursors for diamond film growth at low pressure, although results also indicate that acetylene molecules will yield a small growth rate. We have further shown that nucleation of the diamond microcrystals is inhibited by the presence of oxygen-containing molecules. Since growth rates are enhanced by oxygen-containing molecules, it appears that nucleation and growth kinetics will have conflicting optimal conditions.

Our experiments are carried out on the rudimentary apparatus shown in Figure 1. A flowtube made entirely of quartz is passivated to prevent wall loss of atoms and molecules. A hydrogen/argon gas mixture passes through a microwave discharge to generate hydrogen atoms in the flow. After going through a 90-degree bend to keep out most of the ultraviolet light, the flowing gas enters a tube furnace, where organic material is injected into the flow. Diamonds crystallize on single-crystal silicon substrates near the point of injection and for a short distance downstream. Since the system is at uniform temperature and flow speed, and since the chemistry is simplified, the system lends itself to computer modeling.

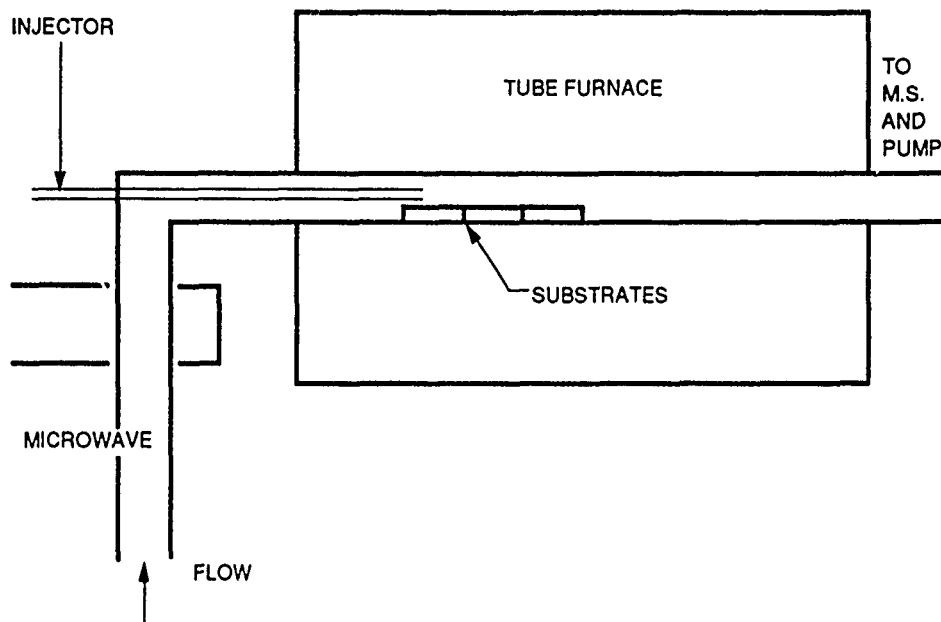


Figure 1. Schematic diagram of quartz flowtube (MS denotes mass spectrometer).

The most important improvement in the apparatus this past year was the addition of a probe for hydrogen atoms. This probe consists of two thermocouples, one shielded with a quartz thimble, the other wrapped with platinum wire. Hydrogen atom recombination on the platinum wire produces a large temperature difference between the two thermocouples. By titrating the hydrogen atoms with nitrosyl chloride (NOCl), we have been able to calibrate this detector and used it to measure sticking coefficients for hydrogen atoms on quartz, silicon, and diamond. These numbers are very useful for the modeling. The probe also contributed to our discovery of a problem with the wall passivation in the microwave discharge region; the elimination of this has tripled the diamond growth rate.

Since our apparatus keeps the organic material out of the microwave plasma, and shields it from the ultraviolet light, it allows us to operate in a *kinetic* rather than a *thermodynamic* regime [1]. In other words, the maximum temperature seen by the organic molecule is not so great that it decomposes into an equilibrium mixture of carbon species. Rather, it retains its structural integrity, and reaction kinetics govern the system's behavior. With this capability, we have been able to compare the reactivity of different carbon-containing species directly, as shown in Figure 2, which shows the diamond growth rates for methane injection and acetylene injection. Prior to this work, theoretical calculations had indicated that acetylene was the most likely precursor for diamond formation, and this view was widely accepted. It is clear from the results of our studies that growth from methane injection is about 10 times faster than that for acetylene. We also found that the quality of the methane-derived diamonds,

as determined by Raman spectroscopy, is much superior [2] to the acetylene-derived diamonds. We believe that, in the case of methane injection, the diamond comes from methyl radicals generated by the reaction of hydrogen atoms with the methane.

The results of a modeling study, conducted jointly with S. J. Harris of General Motors Research Laboratories, have increased our knowledge of this system. The results show that secondary chemical reactions produce very little *interference* between the two experiments; i.e., very little acetylene is generated in the methane system and very little methyl radical is generated in the acetylene system. Hence, we can say with confidence that the two reactivities are very different. Also, the calculated concentrations of the chemical species allow us to estimate heterogeneous reactivities for diamond formation. The sticking coefficients are about 10^{-3} for methyl radical and 10^{-5} for acetylene.

The modeling results indicate further that the temporal profile of diamond formation follows the product of the hydrogen atom and the methyl radical concentrations. This result is consistent with the most recent theories of the mechanism of diamond film growth.

We have used our knowledge of the mechanism to design several new synthesis routes for diamond, including methyl bromide and methyl alcohol as the organic reactants. Methyl alcohol appears to be particularly efficient. We have also used molecules that decompose to give methyl radical directly, rather than by reaction with hydrogen atoms. The most successful of these is biacetyl, $(\text{CH}_3\text{CO})_2$, which readily decomposes to methyl radicals and carbon monoxide at the temperature of the tube furnace.

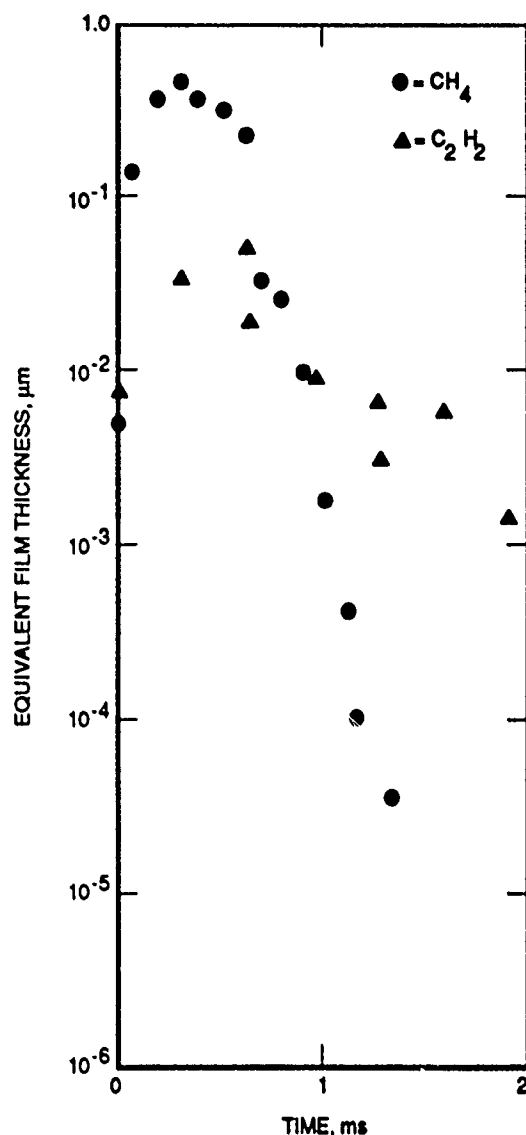


Figure 2. Equivalent film thickness of diamond in microns as a function of time after mixing in flow. Dot symbols represent methane injection, triangles represent acetylene injection.

In a different type of experiment, we were able to disprove a recent theory about the chemistry of diamond formation. The theory, which was based on thermodynamic analysis of diamond formation at high temperature and low pressure, predicted that the presence of aromatic molecules would poison the formation of diamond and would lead to increased formation of graphite [3]. Several experiments were conducted in which we added increasing amounts of benzene to the methane used for growing the diamonds. The presence of benzene in the flowtube was confirmed by mass spectrometry. In no case did we observe an effect on the growth rate, purity, or morphology of the diamonds. Thus, the aromatic inhibition theory is without merit.

In conclusion, we believe that this past year's work has been highly successful:

- Two key theories of diamond growth were tested and found to be in error.
- Information about nucleation of diamond was obtained that is distinct from the mechanism of growth.
- Our understanding of our apparatus was increased and its capabilities and performance greatly improved.
- New synthetic methods for diamond were developed based on the new mechanistic knowledge.

* * * * *

1. L. R. Martin and M. W. Hill, "Diamond Film Synthesis in a Chemically Simplified System," *Appl. Phys. Lett.* **55** 2248 (1989).
2. L. R. Martin and M. W. Hill, "A Flowtube Study of Diamond Film Growth: Methane versus Acetylene," *J. Mater. Sci. Lett.* **9**, 621 (1990).
3. M. Frenklach, "The Role of Hydrogen in Vapor Deposition of Diamond," *J. Appl. Phys.* **65**, 5142 (1989).

Harris, S. J., and L. R. Martin, "Methyl vs Acetylene as Diamond Growth Species," *J. Mater. Res.* **5**, 2313 (1990).

Martin, L. R., and A. R. Calloway, "Some Experiments on the Mechanism of Diamond Film Growth," *Proceedings of the 197th ACS National Meeting*, Vol. 34, No. 2 (1989), p. 535.

Martin, L. R., and M. W. Hill, "Methyl Regeneration: An Important Role for Hydrogen Atoms in Diamond Film Synthesis," *Proceedings of the First International Symposium on Diamond and Diamond-Like Films*, J. P. Dismukes et al., eds., Electrochem. Soc. (1989).

_____, "Experiments with a Flowtube for the Study of Diamond Formation Kinetics," Paper T11, *Proceedings of the SDIO/IST-ONR Diamond Technology Initiative Symposium*, Crystal City, Virginia, July 1989.

_____, "Flowtube Experiments on Diamond Formation: Separating the Growth and Nucleation Kinetics," Paper 1325-11, *Proceedings of the SPIE 1990 International Symposium on Optical and Optoelectronic Applied Science and Engineering*, San Diego, July 1990.

Propulsion Diagnostics Program

S. W. Janson, R. P. Welle, T. A. Spiglanin, and R. B. Cohen,
Aerophysics Laboratory

Advances in propulsion technology are needed to support cost-effective development of military and commercial space-based assets. The complexity and cost of modern satellites and their launch systems require that the propulsion system used for orbit transfer, on-orbit maneuvering, or stationkeeping, be mass efficient, power efficient, and have minimum impact on other satellite systems. Mass efficiency is characterized by the thruster's specific impulse I_{sp} , the ratio of thrust produced to propellant flow rate; power efficiency, or thrust efficiency, is determined by the directed kinetic energy in the exhaust plume divided by the input energy. Conventional chemical thrusters are inherently power efficient, since thrust power is produced by propellant chemical reactions, but the I_{sp} is limited by the thermochemistry of the propellants to a maximum of ~ 470 s for a well-designed hydrogen/oxygen thruster. Electric thrusters use energy added to a propellant stream from an external power source, either a solar array or a nuclear reactor, to generate exhaust velocities that lead to I_{sp} between 500 and 10,000 s with power efficiency between 30 and 75%. The dramatic increase in specific impulse offered by electric propulsion enables larger payloads, increased maneuvering capability, or increased lifetime on-station for existing and future satellite systems due to lower propellant mass requirements.

For an ideal thruster, the propellant chemical energy plus any added energy is converted into directed kinetic energy in the exhaust plume, antiparallel to the thrust vector. In real thrusters, a fraction of this energy is converted into internal energy and nonaxial velocity of the plume species, thereby reducing the energy available for thrust generation. By analyzing the species velocities V_i and internal energy present in the plume (i.e., the ionization fraction, dissociation fractions, electronic state E_i distributions, and vibration-rotation v_i, j_i distributions), the energy losses for a given thruster can be evaluated. Our objective is to develop the species, velocity, and state-resolved (V_i, E_i, v_i, j_i) diagnostic techniques necessary to obtain a scientific and engineering understanding of thruster operation. This *microscopic* characterization of thruster plumes can contribute to the development of thrusters with improved performance, reliability, and reduced potential for contamination. The application of these advanced diagnostic techniques will also enable performance and contamination codes to be validated and improved with a minimum of ground test time, thereby expediting thruster development.

Optical diagnostic techniques that can yield limited species state-resolved (E_i, v_i, j_i) data for electric thrusters

have been used since 1963 [1]. These methods have generally been limited to emission and absorption measurements using filters [2,3], spectrographs [1,4], and a scanning Fabry-Perot interferometer used for Doppler velocimetry [5]. These techniques have been used to measure line-integrated electron densities, electron temperatures, and excited species number densities and velocities.

With the introduction of high-power pulsed tunable dye lasers, new diagnostic techniques are now available. Laser-induced fluorescence (LIF) and planar laser-induced fluorescence (PLIF) have been used to measure two-dimensional species resolved vibrational and rotational distributions v_i, j_i for NO [6,7], OH [8,9], O₂ [10,11], CH [12,13], and NH [14,15] in flames. For probing high-density flows, where LIF techniques become difficult due to temperature-dependent quenching effects, coherent anti-Stokes Raman spectroscopy (CARS) has been used [16]. After almost two decades of neglect, diagnostic approaches and instrumentation available for electric thruster development are beginning to match the state-of-the-art in chemical thruster combustion diagnostics.

The Aerophysics Laboratory has already developed a mass/velocity analyzer (MVA) that is capable of measuring, in real-time, the velocity distributions of up to six masses (species), simultaneously, with a temporal resolution of 20 μ s [17]. We used this device to measure the mass distributions and axial N₂ velocity distributions in the plume of a 1-kW ammonia arcjet [18]. Although the MVA measures the kinetic energy component of plume species which in turn provides information on species translational temperatures and Mach numbers, it cannot measure species internal energy distributions. Our focus is on the development and application of state-resolved diagnostic techniques, as well as techniques to characterize the electron component of these flows, to complement the capabilities of the MVA.

For plume flowfield studies, thrusters must be operated in a vacuum with pressures below 1 Torr and preferably below 10^{-3} to 10^{-4} Torr, depending on the thruster and degree of full plume expansion required. Our overall experimental arrangement, based on our 2.4-m diam \times 5.8-m long vacuum chamber and MVA, is shown schematically in Figure 1. The vacuum pumping rate of our chamber with all pumps functioning is sufficient to allow 1-kW ammonia arcjet or 10-kW xenon ion engine operation at pressures below 5×10^{-4} Torr. By relaxing the vacuum requirement to 1 to 10^{-2} Torr, our diagnostic techniques may be extended to thrusters ranging from small bipropellant thrusters to 30-kW electrothermal thrusters.

Figure 1. Schematic of basic experimental configuration. Spatially resolved emission spectra are recorded throughout the thruster plume using an optical multichannel analyzer, and focused lasers will be used to probe various parts of the thruster plume for LIF and CARS measurements. A mass/velocity analyzer directly samples the far-field plume; Langmuir probes and microwave interferometry are used to measure electron temperature and density.

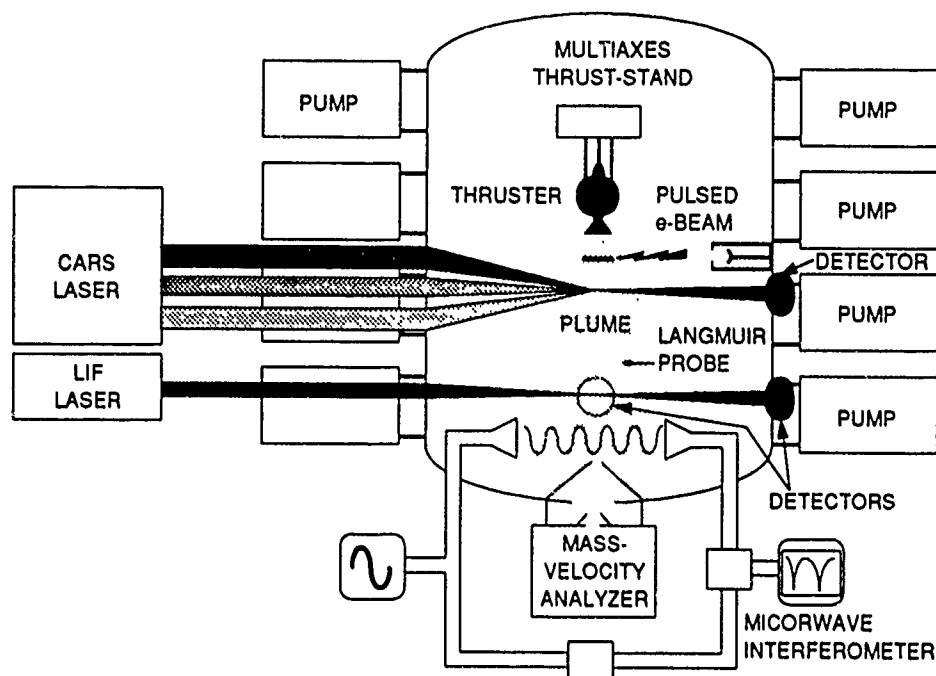
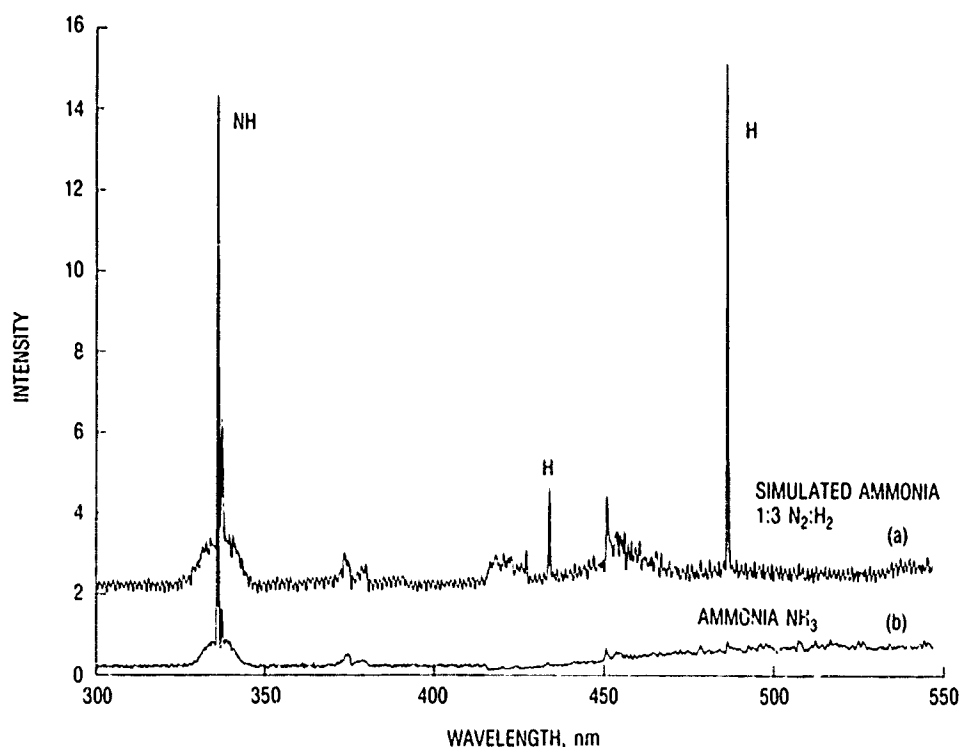


Figure 2. Emission spectra for the 300 to 550 nm wavelength range from an ammonia arcjet with a mass flow rate of 38 mg/s at a power level of 1.05 kW. (a) Operation with a 1:3 nitrogen:hydrogen mixture used to simulate ammonia; (b) Operation with neat ammonia.



The first step toward determining the frozen-flow loss mechanisms for chemical and electric thrusters is the measurement of optical emission spectra from the plume. We have obtained emission spectra for the near-ultraviolet through visible range from a 1 kW class ammonia arcjet operating at a power level of 1.05 kW with a mass flow rate of 38 mg/s [19]. The spectrum produced by a 1:3 N_2/H_2 propellant mixture used to simulate ammonia is shown in Figure 2(a), Figure 2(b) shows the equivalent spectrum produced by neat ammonia. Both spectra are

dominated by NH emission between 330 and 344 nm due to $A^1\Pi \rightarrow X^1\Sigma^-$ electronic transitions, but additional structure due to hydrogen Balmer emission at 434 and 486 nm also exists in the simulated ammonia spectrum.

By moving the arcjet axially and obtaining emission spectra at a number of radial locations, we obtained two-dimensional images of the plume over selected wavelength ranges. Figure 3 is a contour plot of emission intensity integrated between 330 and 345 nm for arcjet operation with simulated ammonia. The nozzle exit plane

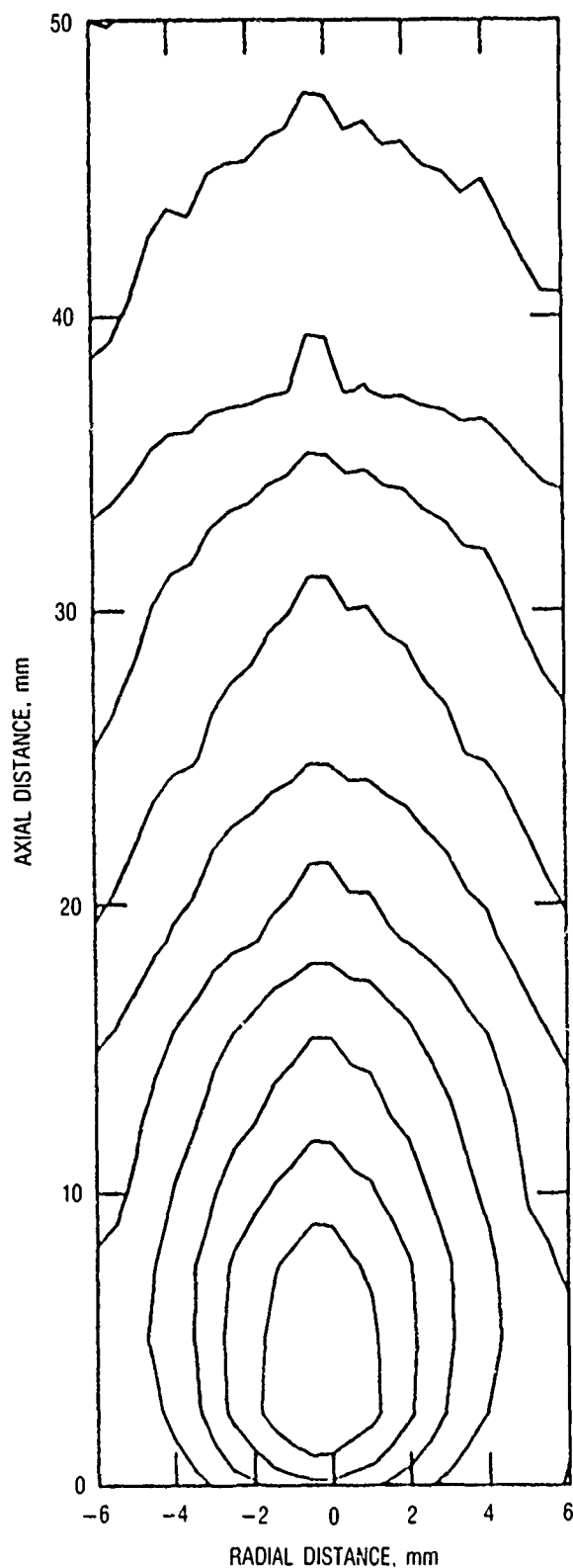


Figure 3. Emission contours for the NH emission between 328 and 345 nm. The nozzle exit plane is at the axial distance of 0 mm, and the contour spacing is $1/e$.

is at an axial distance of 0 mm, the contour lines are spaced $1/e$ apart in emission intensity, and the most intense emission occurs on axis 3 mm downstream of the nozzle. Velocity measurements obtained with our MVA indicated that exhaust velocities of ~ 5 km/s occur under these operating conditions [18]. When combined with the $0.5 \mu\text{s}$ lifetime of the $A^3\Pi$ state [20], the $1/e$ emission decay distance should be 2.5 mm. Since the measured $1/e$ emission decay distance was 6 mm, active repopulation of the NH $A^3\Pi$ state must occur during plume expansion.

A high-resolution spectrum of the 330- to 344-nm NH emission is shown in Figure 4. This rovibrational signature is due to the 0-0 and 1-1 bands of the NH $A^3\Pi \rightarrow X^3\Sigma^-$ system. The strong peak centered at 336 nm is the 0-0 Q branch, the smaller peak centered at 337.2 nm is the 1-1 Q branch, and the rotational bands to the right and left of these peaks are the P and R branches, respectively.

Sufficient structure exists in Figure 4 to obtain a lower bound on the rotational temperatures for the $A^3\Pi$ state of NH. Comparison of our spectra with previously published spectra reveals that our rotational temperatures, as determined by analysis of the Q -branch intensity distributions, are greater than 4300 K. We are now developing software that calculates emission spectra as a function of rotational temperature to enable more accurate temperature determinations.

To measure the electron temperature and density in the plume, we used a Langmuir double probe on a two-dimensional positioning system. A surface plot of plume electron density for a 1-kW arcjet operating with N_2 as propellant is shown in Figure 5. The measured electron density peaked at $3 \times 10^{10} \text{ cm}^{-3}$ at locations closest to the nozzle and decayed in a roughly inverse square manner with distance from the nozzle exit plane. Electron temperature was nearly constant at 0.4 eV over this spatial range, indicating that little collisional cooling occurs within this plume.

Our objective is to determine the best techniques for measuring the species-specific state-resolved number densities of atomic, molecular, and charged species throughout the plume flowfield. Active probing with LIF or CARS is required in order to obtain v_i, j_i distributions in the molecular ground electronic state. LIF is especially well suited for determining atomic and molecular state distributions in the low-density external plume, where quenching interferences are minimized, whereas CARS, a three-wave mixing process, is best suited for the rovibrational distribution measurement in high-density and high-luminosity regions.

From our emission data, we obtained excited-state information on NH and N_2 , making these molecules prime candidates for our initial LIF testing. At the present time, we are preparing a one-photon LIF experiment

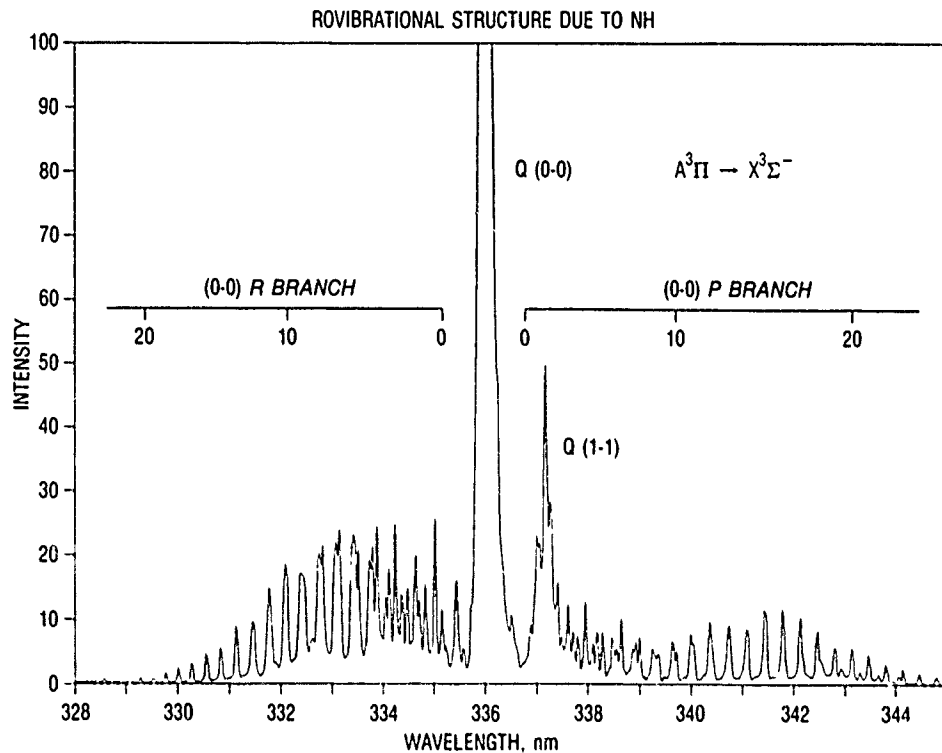


Figure 4. High-resolution spectrum of NH emission from an ammonia arcjet.

that uses 337-nm radiation to excite ground-state NH molecules to the $A^3\Pi$ state, which subsequently fluoresces back down to the ground state. Excitation of N_2 out of its ground state will be more challenging because of the higher energies involved, which necessitate a two-photon process.

Next year, we plan to optimize our diagnostic techniques for hydrogen arcjets, ammonia arcjets, xenon ion engines, krypton ion engines, and microwave thrusters. Development of diagnostic techniques will continue, based on emission spectroscopy, LIF, and Langmuir probes, with an emphasis on microcomputer-based data acquisition and processing to reduce the time required for complete thruster characterization. We will experiment with CARS, mass-spectrometric techniques, and electron beam fluorescence to determine which techniques are the most cost-effective for a given application. We will also develop models of thruster operation based on the improved database generated by our diagnostic experiments. From these models, improved thrusters may be developed.

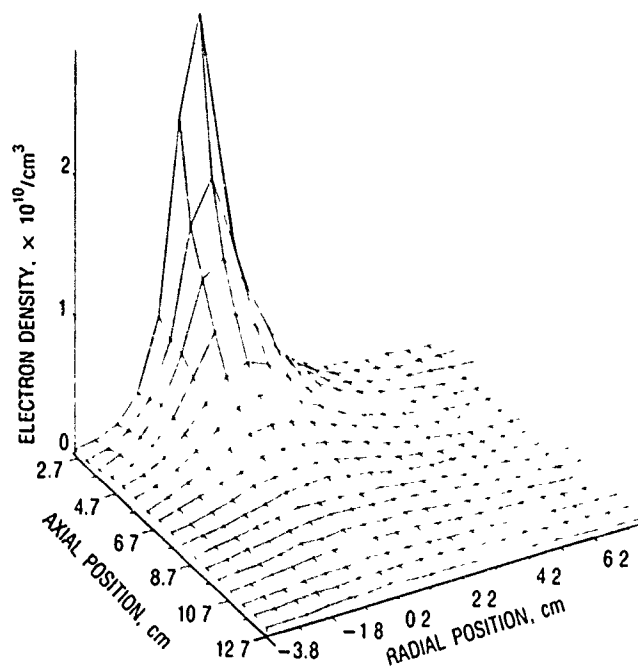


Figure 5. Plume electron density vs position for a nitrogen arcjet operating at 0.8 kW with a mass flow rate of 42 mg/s.

1. F. Robben, W. B. Kunkel, and L. Talbot, "Spectroscopic Study of electron Recombination With Monatomic Ions in a Helium Plasma," *Phys. Rev.* **132** (6), 2363 (1963).
2. A. C. Ducati et al., "1-kW Arcjet-Engine System-Performance Test," *J. Spacecraft Rockets* **1** (3), 327 (1964).
3. K. Rahman and R. Meyers, Filter Photography of a Steady-State Magnetoplasma-dynamic Thruster, Progress Report, Electric Propulsion Laboratory, Princeton University (September/October 1987).
4. D. J. Merfeld, A. J. Kelly, and R. G. Jahn, "MPD Thruster Performance: Propellant Distribution and Species Effects," *J. Prop. Power* **2** (4), 317 (1986).
5. T. J. Pivrotto and W. D. Deininger, Velocity Measurements in the Plume of an Arcjet Engine, Paper 87-1063, AIAA (1987).
6. G. Kychakoff et al., "Flow Visualization in Combustion Gases Using Nitric Oxide Fluorescence," *AIAA J.* **22**, 153 (1984).
7. J. M. Seitzman, G. Kychakoff, and R. K. Hanson, "Instantaneous Temperature Field Measurements Using Planar Laser-Induced Fluorescence," *Opt. Lett.* **10**, 439 (1985).
8. G. Kychakoff, R. K. Hanson, and R. D. Howe, "Simultaneous Multiple-Point Measurements of OH in Combustion Gases Using Planar Laser-Induced Fluorescence," *20th (International) Symposium on Combustion*, The Combustion Institute, Pittsburgh (1985), p. 1265.
9. R. J. Cattolica and S. R. Vosen, "Two-Dimensional Measurements of The [OH] in a Constant Volume Combustion Chamber," *20th International Symposium on Combustion*, The Combustion Institute, Pittsburgh (1985), p. 1273.
10. J. E. M. Goldsmith and R. J. M. Anderson, "Laser-Induced Fluorescence Spectroscopy and Imaging of Molecular Oxygen in Flames," *Opt. Lett.* **11**, 67 (1986).
11. M. P. Lee, P. H. Paul, and R. K. Hanson, "Laser-Fluorescence Imaging of O₂ in Combustion Flows Using an ArF Laser," *Opt. Lett.* **11**, 7 (1986).
12. M. J. Dyer and D. R. Crosley, "Fluorescence Imaging for Flame Chemistry," *Proceedings of the International Conference on Lasers '84* STS Press, McLean, Virginia (1985), p. 211.
13. M. G. Allen, R. D. Howe, and R. K. Hanson, "Digital Imaging of Reaction Zones in Hydrocarbon-Air Flames Using Planar Laser-Induced Fluorescence of CH and C₂," *Opt. Lett.* **11**, 126 (1986).
14. R. P. Lucht, R. C. Peterson, and N. M. Laurendeau, *Fundamentals of Absorption Spectroscopy for Selected Diatomic Flame Radicals*, PURDU CL-78-06, Purdue University (1978).
15. W. R. Anderson, L. J. Decker, and A. J. Kotlar, "Concentration Profiles of NH and OH in a Stoichiometric CH₄/N₂O Flame by Laser Excited Fluorescence and Absorption," *Combust. Flame* **48**, 179 (1982).
16. R. L. Farrow et al., "Coherent Anti-Stokes Raman Spectroscopic Measurements of Temperature and Acetylene Spectra in a Sooting Diffusion Flame," *20th International Symposium on Combustion*, The Combustion Institute, Pittsburgh (1985), p. 1307.
17. J. E. Pollard et al., "Time-Resolved Mass and Energy Analysis by Position-Sensitive Time-Of-Flight Detection," *Rev. Sci. Instrum.* **60** (10), 3171 (1989).
18. D. A. Lichtin et al., "Arcjet Plume Characterization Part I: Mass/Velocity Analyzer Results," Paper 90-2642, 21st AIAA/DGLR/JSASS International Electric Propulsion Conference, Orlando, Florida, July 1990.
19. S. W. Janson et al., "Arcjet Plume Characterization Part II: Optical Diagnostic Results," Paper 90-2643, 21st AIAA/DGLR/JSASS International Electric Propulsion Conference, Orlando, Florida, July 1990.
20. H. K. Haak and F. Stuhl, "ArF (193 nm) Laser Photolysis of HN₃, CH₃NH₂, and N₂H₄: Formation of Excited NH Radicals," *J. Phys. Chem.* **88**, 3527 (1984).

Reacting Flow Field Kinetics

N. Cohen and J. F. Bott,
Aerophysics Laboratory

Several current Air Force programs are affected by the chemistry and fluid dynamics of high-temperature reacting flowfields. Typical applications include (1) the hydrocarbon-oxygen thermochemistry and kinetics of combustors for both ground vehicles and advanced launch systems, (2) the high-temperature clean air (HTCA) re-entry flowfield associated with the national aerospace plane (NASP), and (3) the hydrogen-air combustion chemistry (HAC) of a scramjet engine.

This project's long-term objectives are

- To survey existing reacting flowfield kinetics models.
- To reevaluate critically the required kinetic and thermochemical parameters.
- To conduct exploratory calculations to identify critical reactions and rate parameters.
- To identify and execute appropriate experiments and calculations to provide the requisite data.

A major undertaking during the past year was a critical and extensive review of the thermochemistry of alkane and cycloalkane compounds [1]. The primary objective of the study was to survey, update, and extend semiempirical techniques for estimating fundamental thermochemical properties (heat capacities, entropies, and enthalpies) for this large body of hydrocarbons. The review describes important data sources and experimental techniques, critiques the reliability of the database, and discusses in detail methods for calculating or estimating thermochemical properties at temperatures from 298 to 1500 K for gaseous and liquid phase species that have not been studied in the laboratory. The compounds under review (alkanes and cycloalkanes) include many hydrocarbons that are of interest as fuels and propellants, such as methane, ethane, propane, butane, the octanes, and cetane (hexadecane). In addition to being used as fuels by themselves, alkanes are among the major constituents of kerosene, diesel oil, and jet fuel. Hydrocarbon fuels are being used (or considered) for advanced launch systems.

Two extensive kinetics data reviews were carried out and published [2,3]. The first, a survey of HTCA kinetics, evaluated 87 reactions involving nitrogen, oxygen, their compounds, ions, and excited states, with recommended rate coefficients for each. This survey revealed that many of the reactions have not been studied at sufficiently high temperatures to provide a reliable database for all conditions likely to be of interest in reentry flowfield applications. In particular, many reactions involving ionic species are studied at high electron temperatures of the ions but ambient kinetic temperatures of the neutral species,

theories are not always adequate to predict how rate coefficients determined under such conditions will extrapolate to the conditions of interest in reentry flowfields (for which ion and neutral temperatures are generally equilibrated, but at very high values).

This broad survey revealed that the five principal neutral species reactions in the N_2 - O_2 system, $NO + N \leftrightarrow N_2 + O$ (1), $O_2 + N \leftrightarrow NO + O$ (2), $2N + M \leftrightarrow N_2 + M$ (3), $2O + M \leftrightarrow O_2 + M$ (4), and $N + O + M \leftrightarrow NO + M$ (5), required more detailed analysis, which was done in a separate report to be published later. This critical study revealed considerable scatter in the experimental record for reaction (1): a factor of 1.8 at high temperatures (> 2000 K), a factor of 5 at 700 K, and a factor of 3 at 300 K. With such a database, an accurate temperature dependence of k_1 is difficult to discern, and it was only with the support of transition state theory calculations that we had any assurance of the temperature behavior of the rate coefficient. Reaction (2) seems to be much better established; the scatter over the entire temperature range of 300 to 5000 K is no worse than a factor of 2. The three three-body combination reactions (3-5) all exhibit large scatter. Furthermore, in all cases the consensus of the high-temperature studies (generally on the reaction in the reverse direction) is in poor accord with low-temperature measurements (on the reaction in the forward direction). In some studies, early high-temperature measurements, made in the presence of more than one third body M , were interpreted with an assumed, rather than deduced, temperature dependence, and this may account for some of the discrepancies. Similarly, it was often assumed that different third bodies had the same temperature dependences. All of these reactions deserve reinvestigation, if possible, under conditions where these questionable assumptions need not be made.

The second review consisted of an evaluation of 57 reactions of hydrogen and oxygen and their compounds, ions, and electronically excited states. Rate coefficient expressions, with particular attention to the temperature regime above 1000 K, were recommended. One consistent shortcoming noted was the absence of rate coefficient data for ion-molecule reactions above 300 K. This can seriously impede modeling efforts at high temperatures because theoretical models for predicting rates of such reactions are not nearly so reliable as for reactions involving neutral species.

In the course of evaluating reaction rate coefficients and endeavoring to provide best estimates for modeling applications, it became apparent that there was a

need for a simple method to predict the temperature dependence of a rate coefficient. It is common to express rate coefficients in a three-parameter modified Arrhenius form, $k(T) = A T^n \exp(-B/T)$. The constant B is essentially a measure of the energy barrier that must be surmounted for the reaction to occur; it must be known accurately, but is very difficult to calculate from first principles. However, it can be estimated from a measurement of the rate coefficient at a single temperature. Formerly, it was common to assume that the exponent n is 0 or, at most 1/2, (the latter is a consequence of simple hard-sphere kinetic theory). For many purposes, particularly if one is interested only in a small temperature range, it is sufficiently accurate to assume that $n = 0$. However, for combustion applications, or for the chemistry of a reentry vehicle that can pass from the low temperatures of ambient outer space to the high temperatures of an ablation-induced boundary layer, the value of n can be critical. Rate coefficients estimated at 2000 K can underpredict actual values by an order of magnitude if it is assumed that $n = 0$. A more detailed analysis was undertaken in order to develop simple rules for predicting the value of n with greater accuracy than that of the earlier crude assumptions. The results of this study were presented in technical meetings and subsequently published [4]. It was found that n can be evaluated explicitly for each type of reaction (atom + diatom, diatom + linear polyatom ...) if the harmonic oscillator-rigid free rotor approximation is valid for the reagents and activated complex (the transitory intermediate that separates reagents from products), and if the contribution from quantum mechanical tunneling is small. When allowances are made for more realistic molecular parameters, n can be defined within a small range of values. Various reaction types were examined, and the range of n was computed for each one.

A preliminary survey of various computer codes for chemical and fluid dynamic modeling presently available in the Aerophysics Laboratory was conducted. A simple test case was run on both the CHEMKIN program, obtained from Sandia National Laboratories, and on the Aerospace NEST (N-Element System) program. Agreement between the two calculations was satisfactory except for minor concentration species. On some of these, CHEMKIN allowed concentrations to go negative.

A series of constant-temperature calculations was carried out to determine the sensitivity of a model used by Widhopf and Wang [5] to differences in the incorporated chemistry and kinetics. These sensitivity analysis calculations showed that reactions involved in plume radiation phenomena are particularly sensitive to uncertainties in the database, and point out the need for more experimental data.

Initial model calculations for reactions in the HTCA system at 10,000 and 20,000 K were carried out using the Acuchem code, a program suitable for use on an IBM personal computer, recently obtained from the

National Bureau of Standards. The models included 76 separate reactions (in both forward and reverse directions). The calculations revealed that, at such high temperatures, the concentrations of ionic species and electronically excited states are considerable, illustrating the importance of these constituents in the overall chemistry. Although the chemistry of the neutral ground-state species (N_2 , O_2 , N , O , and NO) is well-characterized up to 3000 K, very little is known about ionic species chemistry, and electronically excited-state chemistry is very poorly understood. These calculations illustrate the necessity of sensitivity studies to establish which ionic and excited-state processes are important in determining species concentrations and affecting fluid-dynamic parameters.

A chemical kinetic bibliographic database was set up for future application to this and other projects involving the use of kinetic data. The entries in the database are citations of articles in the current scientific literature that contain rate coefficient data for the several chemical systems enumerated herein. The entries are indexed by reagents, authors, and selected keywords. At present, the database contains over 750 bibliographic entries from 1986 to 1990.

This past year was the third and final year of our work on this project. Substantial progress was made on all of our major objectives related to the HTCA, the HAC, and the hydrocarbon-oxygen system. Less focus was given the other systems that were scheduled for similar investigation, in particular, hydrazine/UDMH/MMH chemical systems. The importance of these chemical systems to a variety of Air Force programs suggests that the kinds of studies carried out under this project should be continued.

* * * * *

1. N. Cohen and S. W. Benson, "The Thermochemistry of Alkanes and Cycloalkanes," *The Chemistry of Alkanes and Cycloalkanes*, S. Patai and Z. Rappaport, eds., Wiley (to be published).
2. N. Cohen, *A Survey of High-Temperature Clean Air (N_2 - O_2) Kinetics*, ATR-89(8412)-1, The Aerospace Corp. (15 September 1989).
3. N. Cohen, *A Brief Review of the Kinetics of H_2 - O_2 Reactions*, The Aerospace Corp. ATR-89(8412)-2 (15 September 1989).
4. N. Cohen, "Predicting the Preexponential Temperature Dependence of Bimolecular Metathesis Reaction Rate Coefficients using Transition State Theory," *Int. J. Chem. Kinet.* **21**, 909 (1989).
5. G. F. Widhopf and J. C. T. Wang, "A TVD Finite-Volume Technique for Nonequilibrium Chemically Reacting Flows," paper 88-2711, AIAA Thermophysics, Plasmadynamics, and Lasers Conference, San Antonio June 1988.

Cohen, N., *Revised Group Additivity Values of Enthalpies for Linear Alkanes and Alkyl Radicals*, ATR-88(7073)-2, The Aerospace Corp. (15 June 1988).

Cohen, N., and K. R. Westberg, *Chemical Kinetic Data Sheets For High-Temperature Chemical Reactions, Vol. II*, ATR-88(7073)-3, The Aerospace Corp. (14 November 1988).

Foster, K. L., *The Aerospace Thermodynamic Library Tapes Data Generation Program and Maintenance Programs*, ATR-89(8412)-1, The Aerospace Corp. (1 March 1989).

Vaghjiani, G. L., A. R. Ravishankara, and N. Cohen, "Reactions of OH and OD with H₂O₂ and D₂O₂," *J. Phys. Chem.* **93**, 7833 (1989).

Chemically Reacting Flows

J. C. T. Wang and G. F. Widhopf,
Vehicle and Control Systems Division

The overall objective of this project is to develop a versatile three-dimensional viscous chemically reacting flow analysis tool for broad application to geometrically complex problems of interest in space and launch vehicle systems. During the first year of this work, an efficient and accurate numerical algorithm for solving general multispecies chemically reacting inviscid flows was developed and tested by simulating one-dimensional hypersonic shocked flows. The algorithm eliminated the chemical stiffness introduced by multiple chemical time scales. Strong shocks were accurately resolved in a few computational cells. During the second year, the work was extended to the solution of the viscous two-dimensional/axisymmetric time-dependent Navier-Stokes equations, including multispecies finite-rate chemical reactions. Solution of the viscous reacting flow over a spherical forebody at Mach 29.5 demonstrated the accuracy and utility of the numerical model. During the third year, the work was extended to three dimensions and to developing efficient implicit numerical techniques capable of obtaining steady-state solutions that are orders of magnitude faster than previous explicit schemes. Various three-dimensional inviscid solutions were obtained using the derived code and compared to available data, which verified the solution technique. During the past year, the emphasis was on extending the work to complex three-dimensional multibody viscous problems and to coupling the multicomponent reacting chemistry into this final version.

The governing Navier-Stokes equations can be written in the form where U is the vector of the chemical

$$\frac{\partial U}{\partial t} + \frac{\partial(F_1 + G_1)}{\partial x} + \frac{\partial(F_2 + G_2)}{\partial y} + \frac{\partial(F_3 + G_3)}{\partial z} = S, \quad (1)$$

species mass fractions and the conserved mixture flow quantities (mass, momentum, and total energy), F and G are vectors representing convective and diffusive flux of these quantities, and S represents the time-rate of production of individual species due to chemical reactions as well as other source terms. These terms have been detailed in previous reports [1-3] and are not repeated here.

A finite-volume numerical algorithm using general transformed grids was previously developed to solve these equations, either in a time-consistent manner or by relaxing the solution quickly to a steady state. Detailed descriptions of these numerical techniques are contained in [4-7].

During the past year, our work focused on optimizing the implicit relaxation techniques and validating the numerical procedures by solving complex three-dimensional multibody viscous turbulent flow problems. The primary example was the solution of the Mach 1.6 flow over a Titan IV launch vehicle configuration (Figure 1). Flow over the solid rocket motors interacts with that over the core vehicle. Very complex flow patterns define the flow and pressure environment in this region. Shocks formed in front of the solid rocket motor (SRM) nosetip interact with the separated region behind the core boattail and, as a result of the three dimensionality of the geometry, the flow over the core, between the SRMs, becomes a spiraling vortex. This example was selected because of its importance to Titan dynamic loads and because wind tunnel pressure data are available that can be used to validate the code results.

Because of the multibody three-dimensional configuration and the resulting complex flowfield, a large number of cells were needed to obtain a proper numerical resolution. An innovative three-dimensional grid was designed by Dr. P. Than that consists of a highly stretched

grid in all three spatial directions using approximately 370,000 cells. Because of this large number of cells and corresponding large computer memory requirements, the Cray-2 at The Air Force Weapons Laboratory (AFWL) was needed to perform the calculations. The converged results are shown in Figure 1 in three orthogonal color contour perspective views of the pressure environment. Shown in Figure 2 are sample comparisons with wind tunnel test data to demonstrate the quantitative accuracy of the computation. It should be noted that these are the first available detailed three-dimensional viscous solu-

tions for the flow environment about a multibody expendable launch vehicle. They will be described in detail in a forthcoming report. The previously developed multicomponent chemistry model has been incorporated into the implicit three-dimensional line relaxation code and will be validated during the next year.

All of the past year's objectives were accomplished and the project is on schedule. These codes have already proved invaluable in solving a number of SRM and launch vehicle problems and are being used extensively throughout Aerospace.

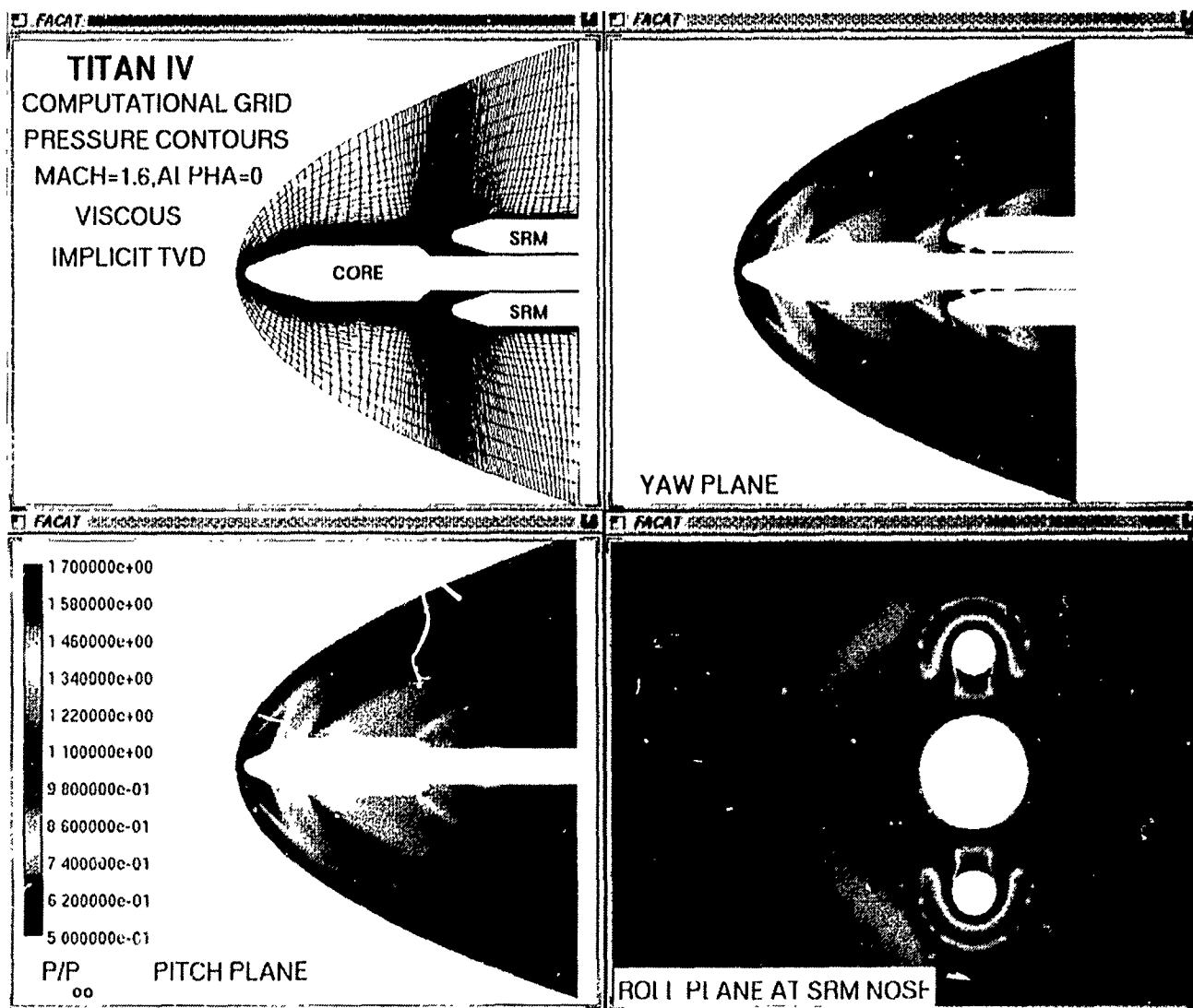


Figure 1 The computed pressure field (normalized with the free stream pressure) about the depicted Titan IV expendable launch vehicle configuration at a Mach number of 1.6 is shown in three

orthogonal views. The newly developed implicit TVD code was used to obtain these results.

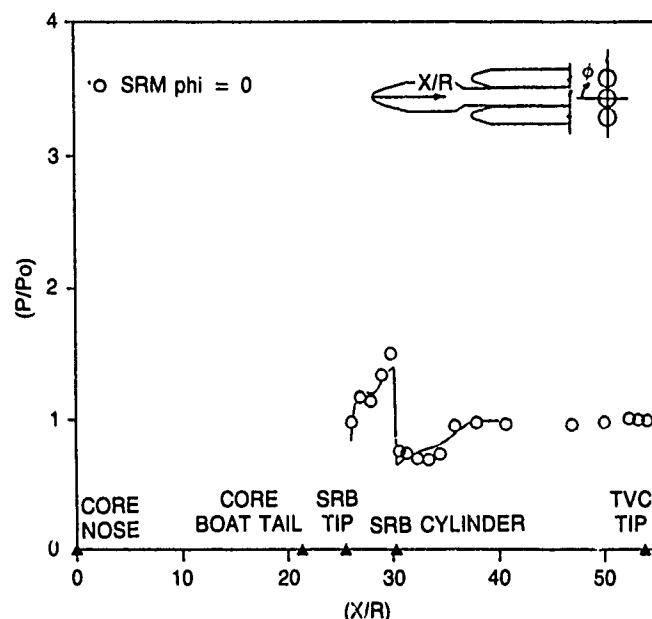
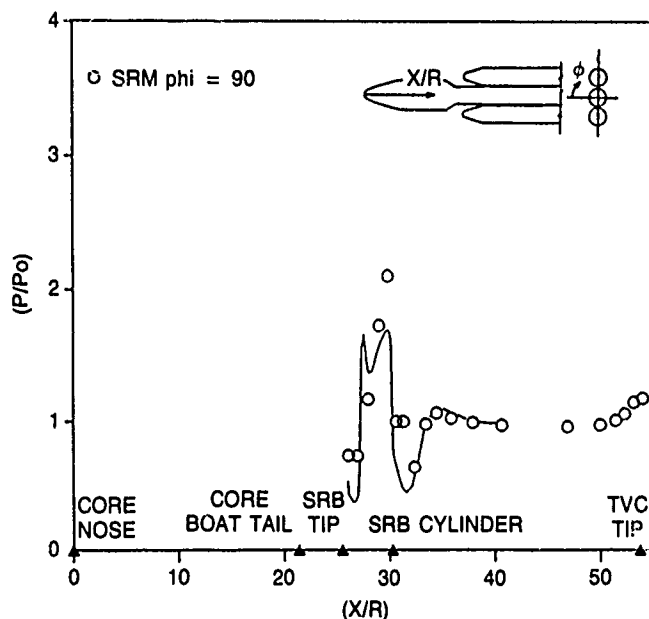
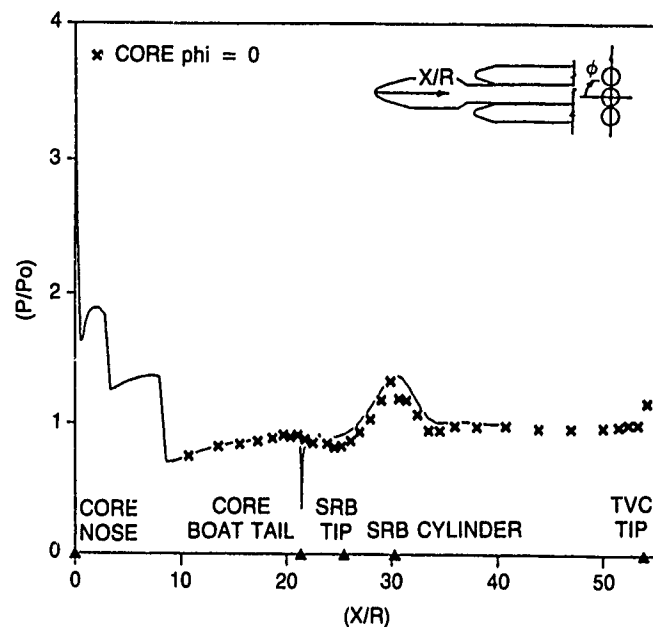
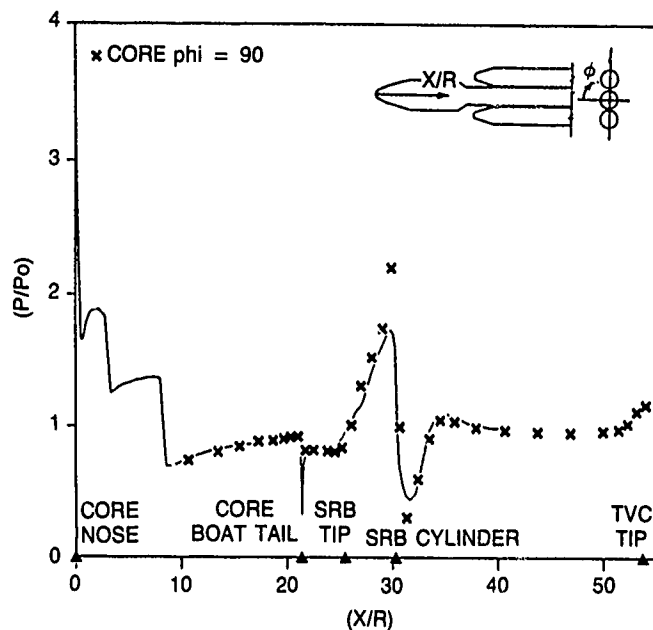


Figure 2. The computed normalized pressure (p/p_X) on the surface of the core section of the Titan IV, between the core and SRM and 90 deg from this plane, is compared to wind tunnel measurements.

Similar comparisons are also depicted for the surface of the SRM, as indicated.

* * * * *

1. G. F. Widhopf and J. C. T. Wang, "Chemically Reacting Flows," *Aerospace Sponsored Research Summary Report, Scientific and Engineering Research*, ATR-86A(8498)-1, The Aerospace Corp. (1 December 1987), p. 68.
2. G. F. Widhopf and J. C. T. Wang, "Chemically Reacting Flows," *Aerospace Sponsored Research Summary Report, Scientific and Engineering Research*, ATR-88(8498)-1, The Aerospace Corp. (1 December 1988), p. 74.
3. J. C. T. Wang and G. F. Widhopf, "Chemically Reacting Flows," *Aerospace Sponsored Research Summary Report, Scientific and Engineering Research*, ATR-89(8498)-1, The Aerospace Corp. (1 December 1989), p. 64.
4. J. C. T. Wang and G. F. Widhopf, "A High Resolution TVD Finite Volume Scheme for the Euler Equations in Conservation Form," *J. Comput. Phys.* **84**, 145 (1989).
5. J. C. T. Wang and G. F. Widhopf, "Numerical Simulation of Blast Flowfields Using a High Resolution

TVD Finite Volume Scheme," *Int. J. Comput. Fluids* 18, 103 (1990).

6. G. F. Widhopf and J. C. T. Wang, "A TVD Finite-Volume Technique for Non-Equilibrium Chemically Reacting Flows," Paper 88-2711, AIAA Thermophysics, Plasmadynamics, and Lasers Conference, San Antonio, June 1988.

7. J. C. T. Wang and G. F. Widhopf, "An Efficient Finite Volume TVD Scheme for Steady State Solutions of the 3-D Compressible Euler/Navier-Stokes Equations." Paper 90-1523, AIAA 21st Fluid Dynamics, Plasma Dynamics and Lasers Conference, Seattle, 18-20 June 1990.

Extended X-ray Absorption Fine Structure of Metal Dichalcogenides

J. R. Lince, M. R. Hilton, and J. L. Childs,
Chemistry and Physics Laboratory

Co-sputtering agents such as oxygen [1,2] and nickel [3,4] can cause densification of sputter-deposited MoS₂ films. Under certain conditions, the doped films give considerably longer wear lives for high-load applications such as gimbal bearings in satellite pointing-and-tracking mechanisms. However, there is much confusion over the role of the additives in these films, and no mechanism of densification has been determined. In addition, the effects of the dopants on nanostructure and local (short-range) order have not been assessed. Consequently, film production has been rather arbitrary with poor quality control.

In previous years, we conducted extended x-ray absorption fine structure (EXAFS) and x-ray photoelectron spectroscopy (XPS) studies on sputter-deposited MoS₂ films [2]. Our results indicated that oxygen commonly becomes incorporated in these films (from small amounts of background O₂ and H₂O in the sputtering ambient), resulting in the production of a MoS_{2-x}O_x phase (with the MoS₂ crystal structure) coexisting with a relatively pure MoS₂ phase. The results illustrate the utility of EXAFS in this area of materials science, since it can probe short range order, obtaining information on poorly crystalline phases within these films that would elude other techniques [5].

Recently, we extended these studies to MoS₂ films that were co-sputtered with Ni, SbO_x, and Au. In our second and third experimental runs at the National Synchrotron Light Source (NSLS) at Brookhaven National Laboratory, we concentrated on MoS₂ films co-sputtered with 9% and 3% Ni, and with SbO_x (produced at Hohman Plating and Manufacturing) and two multilayer MoS₂ films with layers separated by thin films of Ni and Au, respectively (produced at Ovonic, Inc.). The results of data analysis performed for the Hohman Ni-doped films are reported here.

X-ray absorption spectra (i.e., plots of the x-ray absorption coefficient μ versus photon energy $h\nu$) were taken of the films for both the Ni-K and Mo-K edges, rep-

resenting the local environment around the Ni and Mo atoms, respectively. Data reduction has been discussed elsewhere [2,5] but will be briefly described here. After the absorption edge is removed from the data (only data 30 eV above the absorption edge and higher are used for analysis), a smooth background is fitted to the data using a spline-fitting technique. This background is subtracted from μ , which is then divided by the x-ray absorption edge height μ_0 to normalize the data. The result is defined as χ . The χ data are then multiplied by a factor k^3 (k is the wavevector) to enhance the lower-amplitude oscillations at high k values and are plotted as a function of k (instead of energy). The resultant Ni-K EXAFS (or $k^3 \cdot \chi$) for the MoS₂ (9% Ni) film is shown in Figure 1.

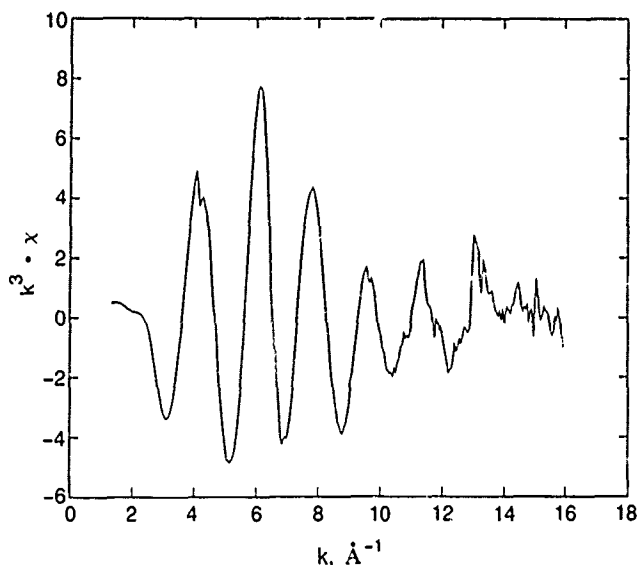


Figure 1. EXAFS for a Ni-doped (9%) sputter-deposited MoS₂ film after removal of a smooth background from the raw data. The data were taken at the Ni-K x-ray absorption edge at 8.3 keV photon energy. The data are plotted here vs the wavenumber k and are weighted by a factor of k^3 in preparation for Fourier analysis.

The magnitude of the Fourier transform of the EXAFS data is a qualitative radial distribution function (RDF). This RDF describes the local order around the element whose absorption spectrum was taken. Results of our previous studies have shown that these plots, when compared with those produced for appropriate standards (i.e., pure MoS_2 and MoO_2 powders in the earlier study), can allow the identification of phases present in the films [2].

The RDF for Ni in the MoS_2 (9% Ni) film is shown in Figure 2(b) and displays only one peak (nonzero data below 1.5 \AA are generally neglected in analysis, since this is due to difficulties in background subtraction). In Figure 2, curves (a) and (c) represent similarly produced RDFs for Ni and NiO powders, respectively. Comparison of the RDF for the MoS_2 (9% Ni) film with that for the NiO powder indicates that the peak in Figure 2(b) represents an Ni-O bond. (The presence of oxygen in the film has been corroborated by XPS.) That the Ni in the MoS_2 (9% Ni) film is not in the elemental form is shown by comparison with the RDF for the Ni powder [Figure 2(a)], which exhibits a first nearest-neighbor peak (representing the Ni-Ni bond length) that is considerably higher than for the film. In addition, Ni bonding to S or Mo can be ruled out, since a Ni-S or Ni-Mo bond would occur in other locations. The lack of additional peaks in Figure 2(b) indicates that the Ni is present in a finely dispersed, amorphous form, and is probably present in particles only a few angstroms in diameter, resulting in the lack of second and

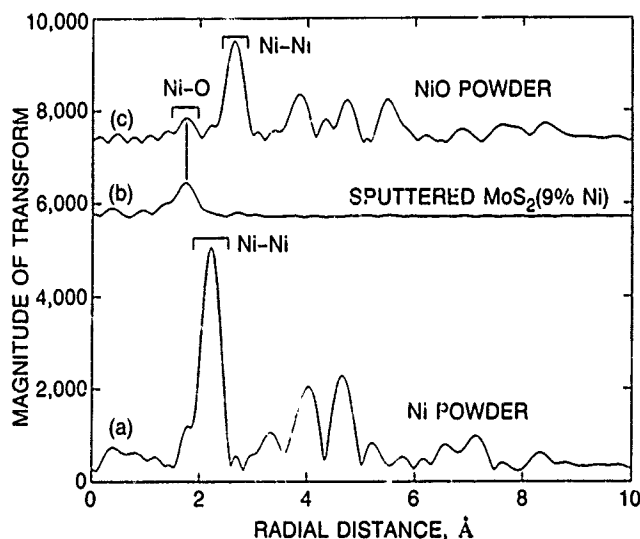


Figure 2. Radial distribution functions (RDFs) produced by Fourier transformation of EXAFS data at the Ni-K absorption edge. Spectra are for (a) a pure Ni standard, (b) the sputter-deposited MoS_2 (9% Ni) film, and (c) a pure NiO standard. The peak positions in the curves correspond to interatomic distances (minus a correction factor due to phase shift effect). The intensity below $\sim 1.5 \text{ \AA}$ is due to background subtraction effects and does not represent interatomic distances.

higher neighbors. This result is also similar to that for a sputter-deposited MoS_2 (3% Ni) film (data not reproduced here).

The RDF produced from the Mo-K x-ray absorption spectrum of the sputter-deposited MoS_2 (9% Ni) film is shown in Figure 3(b), together with one for a sputter-deposited film that was not co-sputtered with Ni [Figure 3(a)] and one for a pure MoS_2 powder standard [Figure 3(c)]. XPS and x-ray diffraction results show that the films exist as small, somewhat disordered crystallites of MoS_2 -like phases whose lattice constants depend on oxygen concentration [2]. Comparison of the RDF for the pure MoS_2 film with the MoS_2 standard [Figures 3(a) and 3(c), respectively] indicates the presence of the two phases, $\text{MoS}_{2-x}\text{O}_x$ and MoS_2 . This is shown by the presence of two Mo-Mo(1) distances in the RDF [Figure 3(a)] for the film, the shorter one corresponding to the $\text{MoS}_{2-x}\text{O}_x$ phase.

Comparison of Figures 3(a) and 3(b) indicates that sputter-deposited MoS_2 films have similar short-range order, regardless of the presence or absence of Ni in the films. However, transmission electron microscopy (TEM) shows that the microstructure of Ni-doped MoS_2 films is quite different than that for undoped films. Specifically, addition of Ni causes a large reduction in the crystallite size (of either the MoS_2 or $\text{MoS}_{2-x}\text{O}_x$ phases) in the films, resulting in a less porous film with a resultant increase in density.

The Ni-K and Mo-K EXAFS results for the Ni-doped MoS_2 films suggest that when Ni is co-sputtered with MoS_2 , no reaction occurs between the Ni and the $\text{MoS}_2/\text{MoS}_{2-x}\text{O}_x$ phases. However, the Ni causes inter-

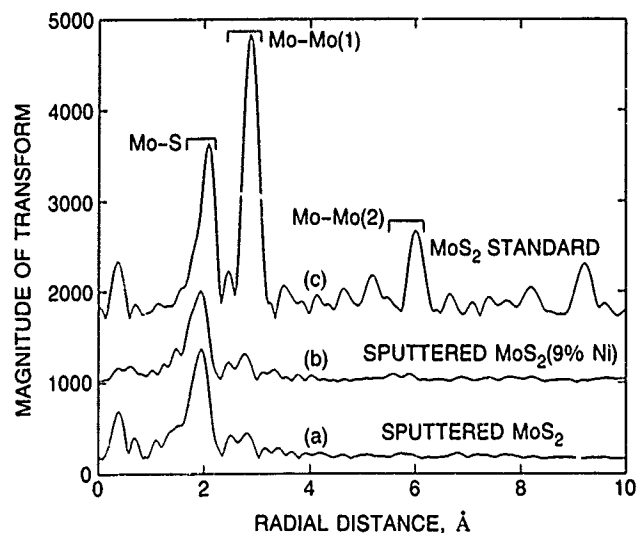


Figure 3. Radial distribution functions (RDFs) produced by Fourier transformation of EXAFS data at the Mo-K absorption edge. Spectra are for (a) an undoped sputter-deposited MoS_2 (i.e., with both $\text{MoS}_{2-x}\text{O}_x$ and MoS_2 phases present), (b) the sputter-deposited MoS_2 (9% Ni) film, and (c) a pure MoS_2 standard.

ruption of crystallite growth of these phases, resulting in a large size reduction and reorientation of the platelets in the films. The Ni probably affects this rearrangement by forming a monolayer-thick nucleation barrier on the edges of the growing crystallites. Although there is such a large change in the microstructure of the film, the local order of the film does not change appreciably; hence, the basic lubricating MoS₂ crystal structure is preserved. During exposure of the film to the sputtering ambient or after exposure to atmosphere (or both), the Ni becomes oxidized, giving rise to the Ni-O bond length observed in the Ni-K EXAFS.

Although the RDF gives a qualitative picture of the phases present in the film, significant errors can result from attempts to determine the bond lengths in these phases simply by measuring where the peak maxima occur. This difficulty arises because the Fourier transform (FT) of the EXAFS data has both real and imaginary parts, whereas the RDF represents only the *magnitude* of the complex transform. One way of overcoming this difficulty is to perform a least-squares (LS) fit of the data to the theoretical EXAFS $\chi(k)$ equation. In practice, R can be determined with $\pm 0.02 \text{ \AA}$ accuracy. We have performed a preliminary fit of the first- and second-shell Mo-K EXAFS and the Ni-K EXAFS to give values for $R_{\text{Mo-S}}$, $R_{\text{Mo-Mo}}$, and $R_{\text{Ni-O}}$; the results are given in Table 1.

Table 1. EXAFS Fitting Results for Sputter-Deposited MoS₂ Films^a

Material	$R_{\text{Mo-S}}, \text{ \AA}$	$R_{\text{Mo-Mo}}, \text{ \AA}$	$R_{\text{Ni-O}}, \text{ \AA}$
Sputtered MoS ₂	2.32	2.79	
		3.08	
Sputtered MoS ₂ (9%Ni)	2.32	2.77	2.07
		3.04	
Standards:			
MoS ₂	2.41	3.16	
NiO			2.08

^aUncertainty in R values is $\sim \pm 0.02 \text{ \AA}$

Two coordination shells were used in the LS fit to simulate the two Mo-Mo(1) distances in each of the phases MoS_{2-x}O_x and MoS₂ in the sputter-deposited films. For these preliminary calculations, only one coordination shell was used to fit the Mo-S peak in the FT magnitude. Even though the presence of two phases might give rise to two slightly different Mo-S bond lengths, the difference in these lengths is expected to be much smaller than for the Mo-Mo(1) distances. In general, the similar-

ity in bond lengths between the two films confirms the qualitative observations just discussed, that the MoS₂-like phases in the Ni-doped and undoped films have similar local orders.

The MoS_{2-x}O_x phase gave rise to a Mo-Mo(1) distance of $\sim 2.78 \text{ \AA}$ in each of the two films, the MoS₂ phase gave rise to a Mo-Mo(1) distance of $\sim 3.06 \text{ \AA}$ in each of the two films. The Mo-Mo(1) distance for the MoS_{2-x}O_x phase in the films is 12% smaller than for the pure MoS₂ standard. This considerable contraction of the crystal lattice in the (1 0 0) and (1 1 0) (or *edge plane*) directions has been discussed previously in terms of the molecular orbital (MO) structure of MoS₂ [6]. Briefly, the higher electronegativity of O, as compared with S, causes removal of electron density from the Mo atom, resulting in lower electrostatic repulsion between Mo atoms and contraction in that direction in the lattice.

A surprising result is that the Mo-Mo(1) distance for the MoS₂ phase in the films is actually $\sim 3\%$ smaller than for the MoS₂ standard. This small contraction may be caused by the presence of S vacancy defects in this phase. There is some support for this interpretation, since the MO model discussed previously indicates that lattice contraction in the edge plane directions can occur for S vacancies in addition to O substitution [6].

In summary, EXAFS has been used to investigate the effect of adding Ni during growth of sputter-deposited MoS₂ films. Because EXAFS is a local, or short-range order probe, it provides information on these films that other techniques cannot. Specifically, it was shown that Ni did not form a compound with the MoS₂-like phases within the film, but formed very finely dispersed Ni that became oxidized during growth and after exposure to atmosphere (or both). The ability of Ni to cause such a large reduction in crystallite size is probably due to its action as a nucleation barrier to growing MoS_{2-x}O_x and MoS₂ crystallites in the film, whereas the retention of the lubricating properties of the film is due to the unreactivity of Ni with these MoS₂-like phases.

Continuing studies will involve more detailed LS fitting of the EXAFS spectra to determine if two Mo-S bond lengths can be deconvoluted from the data, or even if the Mo-O bond length (from the MoS_{2-x}O_x phase) can be separated from the Mo-S peak. The LS analysis will also be applied to previous EXAFS data taken for a number of samples that were sputter-deposited at our laboratory and at several other laboratories [2]. The overall objective is to determine if a systematic correlation can be developed between the bond lengths, the chemical composition (as determined by XPS), the long-range order (as determined by x-ray diffraction), and the micro-/nanos-structure (as determined by transmission electron microscopy) in the doped and undoped films so that this information can be used ultimately to interpret film performance.

1. J. R. Lince, "MoS_{2-x}O_x Solid Solutions in Thin Films Produced by Rf-Sputtering," *J. Mater. Res.* **5**, 218 (1990); also, ATR-89(8461)-1, The Aerospace Corp. (1 April 1990).
2. J. R. Lince, M. R. Hilton, and A. S. Bommannavar, "Oxygen Substitution in Sputter-Deposited MoS₂ Films Studied by EXAFS, XPS, and X-ray Diffraction," *Surf. Coat. Techn.* **43/44**, 640 (1990); also, ATR-90(8561)-1, The Aerospace Corp. (to be published); also, J. R. Lince, M. R. Hilton, and J. L. Childs, *Aerospace Sponsored Research Summary Report, Scientific and Engineering Research*, ATR-89(8498)-1, The Aerospace Corp. (1 December 1989), p. 69.
3. P. D. Fleischauer, M. R. Hilton, and R. Bauer, "Effects of Microstructure and Adhesion on Performance of Sputter-Deposited MoS₂ Solid Lubri-

cant Coatings," *Proceedings of the 16th Leeds-Lyon Conference Mechanics of Coatings, Tribology Series* Vol. 17, D. Dowson, C.M. Taylor, and M. Godet, eds., Elsevier, London (1990), p. 121.

4. B. C. Stupp, "Performance of Conventionally Sputtered MoS₂ versus Co-sputtered MoS₂ and Nickel," *Proceedings of the Third International Conference on Solid Lubrication*, ASLE Special Publication, Vol. 14, (1984), p. 217.
5. D. E. Sayers and B. A. Bunker, "Data Analysis," *X-ray Absorption: Principles, Applications, Techniques of EXAFS, SEXAFS, and XANES*, Chemical Analysis, D. C. Konigsberger and R. Prins, eds., John Wiley and Sons (1988), Chap. 6.
6. P. D. Fleischauer et al., "Electronic Structure and Lubrication Properties of MoS₂: A Qualitative Molecular Orbital Approach," *Langmuir* **5**, 1009 (1989).

Ab Initio Calculations of Solid Lubricants

T. B. Stewart,
Chemistry and Physics Laboratory

Metal dichalcogenides such as molybdenum disulfide are becoming an important class of compounds for use as solid lubricants for spacecraft applications. The electronic structure and chemical bonding of transition metal dichalcogenides are fundamentally important to an understanding of the properties of these materials as they relate to their use as solid lubricants. These compounds are of interest because of their unusual chemical structure, which consists of *atomic sandwiches* stacked in layers with transition-metal atoms between two layers of chalcogen atoms (Figure 1). A qualitative model in which molecular orbital description of the electronic structure of MoS₂, for example, has been proposed to explain the source of its lubricating properties and the difference in the properties of MoS₂ and NbSe₂ [1]. This model suggests that the energy and occupancy of the transition-metal 4d orbitals are responsible for the inherent difference in the lubricating properties of MoS₂ and NbSe₂. The former is considered a good lubricant because of a filled 4d orbital which leads to a repulsive interaction between layers; the latter is an abrasive because of a partially filled 4d orbital, which leads to a bonding interaction between layers (Figure 2).

Experimental studies by means of valence level photoelectron spectroscopy (VLPS) and electron energy loss spectroscopy (EELS) have been made to determine

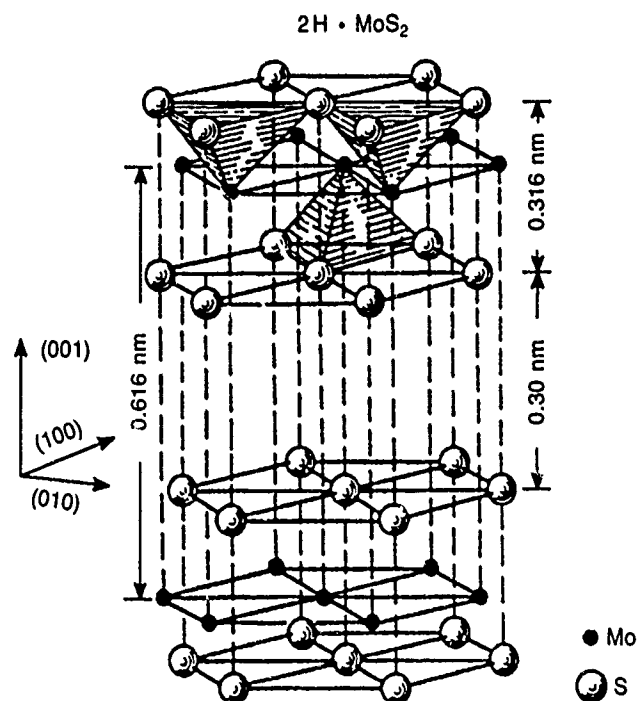
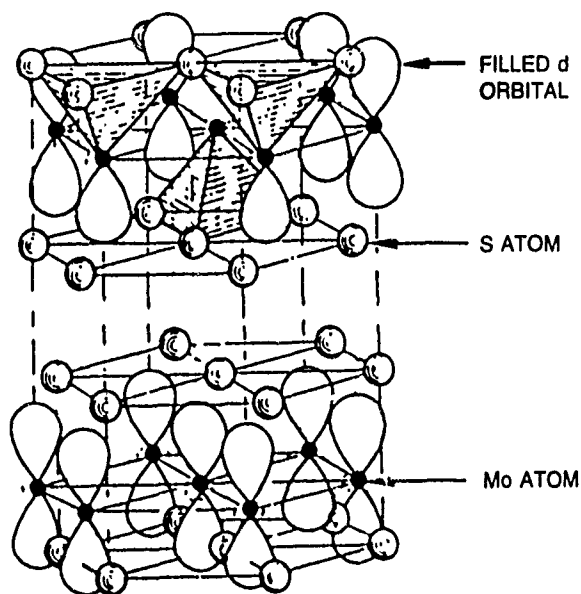


Figure 1. Crystal structure of 2H-MoS₂ with primary crystallographic directions and dimensions shown.

GOOD LUBRICANT

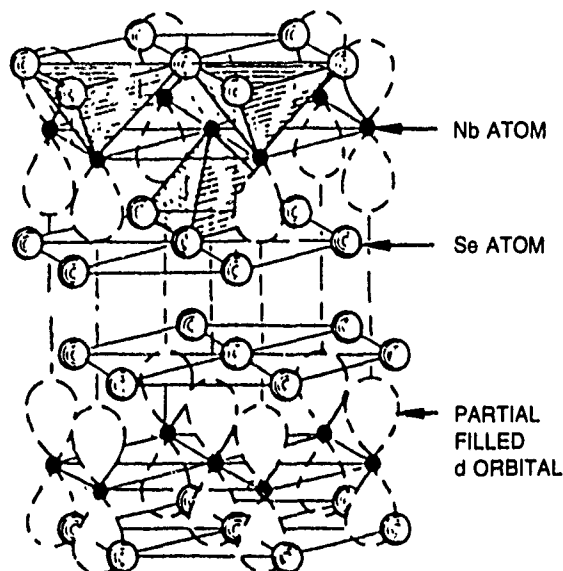
MoS₂



- FILLED d ORBITAL
- METAL ATOMS STAGGERED
- NO LONG-RANGE BONDING
- LOW SHEAR STRENGTH

POOR LUBRICANT

NbSe₂



- HALF-FILLED d ORBITAL
- METAL ATOMS ALIGNED
- LONG-RANGE d ORBITAL BONDS
- HIGH SHEAR STRENGTH

Figure 2. Influence of d orbitals in the structures and lubrication properties of MoS₂ and NbSe₂.

the electronic structure of MoS₂ and the nature of the atomic orbitals involved in bonding that gives rise to lubricant performance. The exact assignment has not yet been made. *Ab initio* calculations were undertaken to determine the electronic structure of MoS₂, make quantitative atomic orbital assignments to the molecular orbitals, and correlate the computed orbital energies to experimental measurements. A knowledge of the electronic structure will allow prediction of the effect that structural and chemical modifications such as doping or intercalation will have on lubricant performance and will enable design of solid lubricants for particular applications. These calculations were done in collaboration with Dr. N. W. Winter at the Lawrence Livermore National Laboratory.

The approach consisted of carrying out Hartree-Fock self-consistent field (SCF) calculations on the moiety MoS₆ (Figure 3). The essence of the Hartree-Fock approximation is to replace the complicated N electron-electron repulsion problem in the cluster by a one-electron problem in which the energy of one electron is solved in the presence of an average field V^{HF} produced by $N-1$ electrons. This average potential depends on the spin orbitals of the other $N-1$ electrons and must be solved iteratively. This iteration procedure is called the *self-consistent field* method.

The size and complexity of these calculations are determined by the number of electrons in the cluster. For example, in the case of MoS₆, there are 146 electrons that must be considered in order to do an all-electron calculation for this cluster. This number of electrons is too large for most computers; therefore, the size is reduced to a 58-electron problem by using effective core potentials to replace the 1s, 2s, 3s, and 3p core electrons on molybdenum and 1s, 2s, and 2p electrons on sulfur. Such replacements are considered valid because the chemistry of atoms occurs mainly with the valence electrons, which for these calculations are the 4s, 4p, 5s, and 4d electrons on molybdenum and 3s and 3p on sulfur. The effective core potentials and Gaussian analytical functions used to describe the valence atomic orbitals were taken from LaJohn and co-workers [2] and Pacios and Christiansen [3].

The energy assignments, atomic orbital contributions to the molecular orbitals of MoS₂, and the electron densities of the atoms have been computed for the moiety MoS₆. The results of the Hartree-Fock calculations are displayed in Figure 4, an energy-level diagram for the various molecular orbitals. In Table 1, the orbital energies and the Mulliken population analysis are given for selected molecular orbitals that have prominent bands in EELS and the VLPS of MoS₂. The Mulliken population

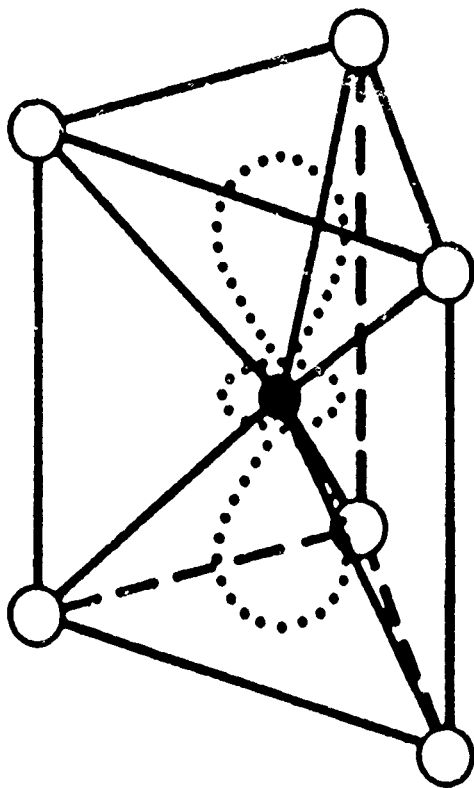


Figure 3. Moiety MoS_6 cluster used for calculations with the principal Mo 4d atomic orbitals shown.

is obtained from the solution to the Hartree-Fock calculations, from which one obtains a set of molecular orbitals that is used to determine the electron density of the atoms in the cluster and the atomic orbital contributions to the molecular orbitals. The orbital energies are referenced to the Fermi Level, which is composed of sulfur 3p orbitals.

A comparison of the theoretical and experimental excitation energies from VLPS and EELS measurements for the molecular orbitals of MoS_2 is given in Table 2. The correlation diagram for the band assignments is shown in Figure 5.

The calculation shows fair agreement between the theoretical results and experimentally measured excitation energies; however, the position of the sulfur 3p orbital as the highest occupied molecular orbital does not agree with previous assumptions [4], which place one non-bonding molybdenum 4d atomic orbital as the highest occupied molecular orbital.

Using the MoS_6 results, one can make definitive assignments of the observed contributions. The highest a_1 molecular orbital at 2.7 eV (2.5 eV, VLPS; 3.5 eV, EELS) is composed of sulfur 3p and molybdenum 4d atomic orbitals. The calculations do show that the sulfur 3p is a major contributor to the highest a_1 molecular orbital with significant molybdenum 4d contribution. This particular molybdenum 4d orbital is oriented in a direc-

tion perpendicular to the molybdenum plane of the crystal and directed between the sulfur atoms (Figure 3). This observation agrees with the result of an x-ray photoelectron spectroscopy (XPS) study of MoS_2 by Haycock, Urch, and Wiech [5], who found that the Mo 4d character is extensively present in the sulfur 3p band, and that the sulfur 3p character is present in the *tight* Mo 4d orbital. This result disagrees, however, with a resonance photoemission study of MoS_2 by Lince and Didizulis [6], who found that a_1 is composed primarily of one of the molybdenum 4d orbitals with no contributions from the sulfur 3p orbital. The disagreement may result from the inadequate description of the MoS_2 crystal by the MoS_6 cluster. This point will be covered later. The next peak at 5.5 eV of a_1' symmetry is mainly S 3p with some contributions from Mo 4p and 5p atomic orbitals. The peak at 6.5 eV is assigned to e' , which is composed of S 3p and Mo 4d, and Mo (4p + 5p) atomic orbitals. The 7.4 eV peak is assigned to e'' and consists of S 3p and Mo 4d atomic orbitals. Our assignments of the e' and e'' peaks are the reverse of the published assignments [4]. The peak at 8.6 eV is a_1' and consists of Mo 4d and S 3p atomic orbitals. The results of the calculation do show some Mo 5p contributions to the 5.5 and 6.5 eV peaks in the photoelectron spectrum. Evidence for such contributions from the Mo 5p has been observed in the valence level photoelectron spectra of MoS_2 .

The calculated orbital energies appear to agree more closely with EELS measurements. This is not surprising when one considers that EELS measures the molecular orbital energies by scattering electrons off the surface atoms and exciting electronic transitions of these orbitals. The surface atoms are in an environment much like the MoS_6 cluster approximation. The XPS measurements, however, are detecting photoelectrons from atoms in the *bulk*, which are a few atoms below the surface and are exposed to a different electrostatic environment.

The results of the calculation place formal charges of +0.4 and -1.3 on the molybdenum and sulfur atoms, respectively. The presence of the -1.3 charge on the sulfur atoms in positions in the crystal lattice would lead to a large repulsive interaction between *sandwich* layers and, in concert with the repulsive interactions of the Mo 4d orbitals, provide low shear strength between layers.

The results of the calculations produce too large an electron density on the molybdenum atom. The problem arises from electrons being transferred from the sulfur atoms to the molybdenum atom. Although the computed orbital energies are in agreement with experiment, the excessive charge on the molybdenum atom and the reduced S 3p orbital population indicate that the S 3p orbitals are not being properly coordinated in this cluster model.

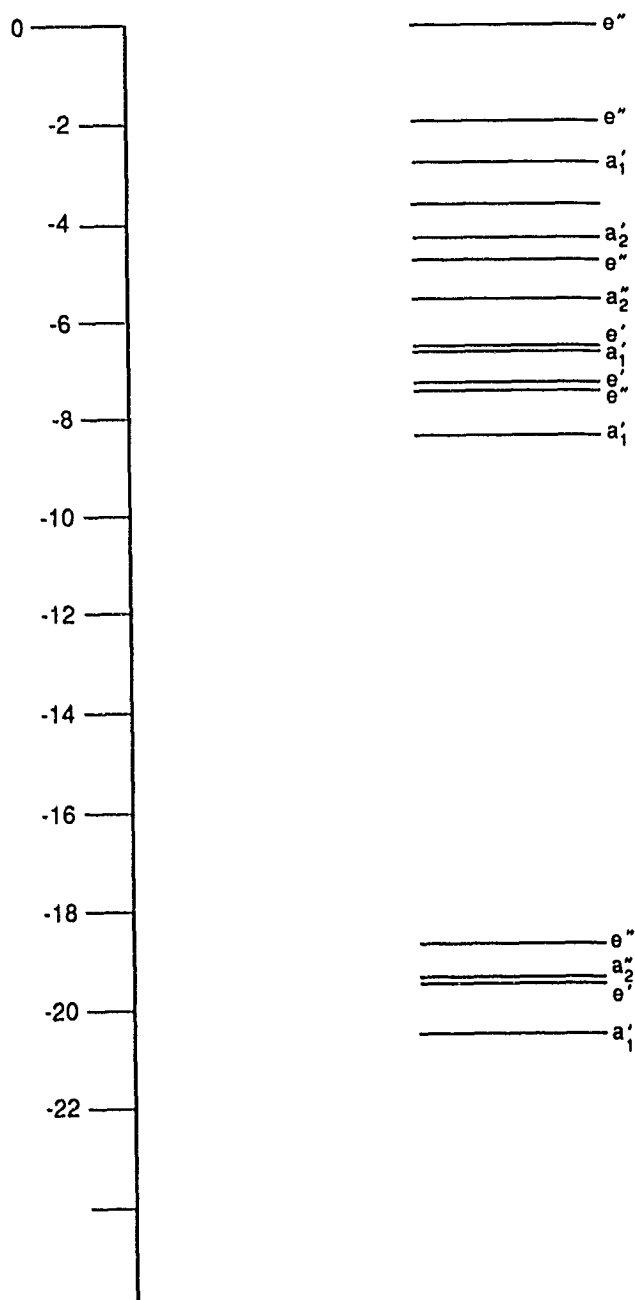


Figure 4. Molecular orbital energy levels for the moiety MoS_6 .

An effort was made to stabilize the $3p$ electrons on the sulfur atom by placing a lattice consisting of 42 Mo + 4 and 56 S - 2 point charges to approximate a Madelung potential around the MoS_6 cluster (Figure 6). The results produced an excessive amount of electron density on the molybdenum atom. The problem arises from the excessive repulsive interaction between the unbound sulfur $3p$ electrons in the cluster and the -2 negative charge at position of the sulfur ions in the adjacent layers. This repulsive interaction is forcing electrons from the S $3p$ orbitals into the Mo $4d$ and higher-energy $5s$ and $5p$ atomic orbitals. The presence of the Mo + 4 point charge in the same plane as the cluster is not enough to stabilize the sulfur $3p$

Table 1. Computed Molecular Orbital Energies and Mulliken Population Analysis for MoS_6

Molecular Orbital	Orbital Energy, eV	Mulliken Population Analysis with Atomic Orbital Character
a_1'	-2.7	63% S $3p$ + 37% Mo $4d$
a_2''	-5.5	82% S $3p$ + 18% Mo ($4p$ and $5p$)
e'	-6.5	70% S $3p$ + 27% Mo $4d$ + 3% Mo ($4p$ + $5p$)
e''	-7.4	59% S $3p$ + 3% S $3s$ + 37% Mo $4d$
a_1'	-8.6	55% Mo $4d$ + 45% S 3

Table 2. Theoretical and Experimental Excitation Energies

M. O.	VLPS, eV	EELS, eV	Theory, eV
a_1'	2.5	3.5	2.7
a_2''	3.8	5.3	5.5
e'	5.1		6.5
e''	5.8	7.5	7.4
a_1'	7.1	8.5	8.6

electrons. Further work must be done to vary the point charges and refine the Madelung potential and determine the effect on populations and orbital energies in the cluster.

The *ab initio* calculations of MoS_6 have been completed and have produced an energy correlation diagram for MoS_2 . Orbital energies have been calculated that are in reasonably good agreement with the experimental measurements. The results of the calculation show considerable mixing of the S $3p$ and Mo $4d$ atomic orbitals and that the highest molecular orbital in the XPS measurements is of a_1' symmetry. The computed negative charge on the sulfur atoms and the fact that the highest-energy-occupied molecular orbital has some Mo $4d$ character would give rise to a repulsive interaction between sulfur atoms on adjacent layers, thus enhanced lubricity. The calculations do, however, place an excessive electron population on the molybdenum atom, and placement of the sulfur $3p$ orbital as the highest occupied molecular orbital does not agree with published assignments. It is believed that this is due to the incomplete coordination of sulfur $3p$ orbitals in the MoS_6 cluster approximation. Calculations are in progress in which the sulfur $3p$ orbitals are formally bonded to molybdenum atoms in a Mo_7S_6 cluster. The results from the MoS_6 cluster are being used to assist this phase of the calculations.

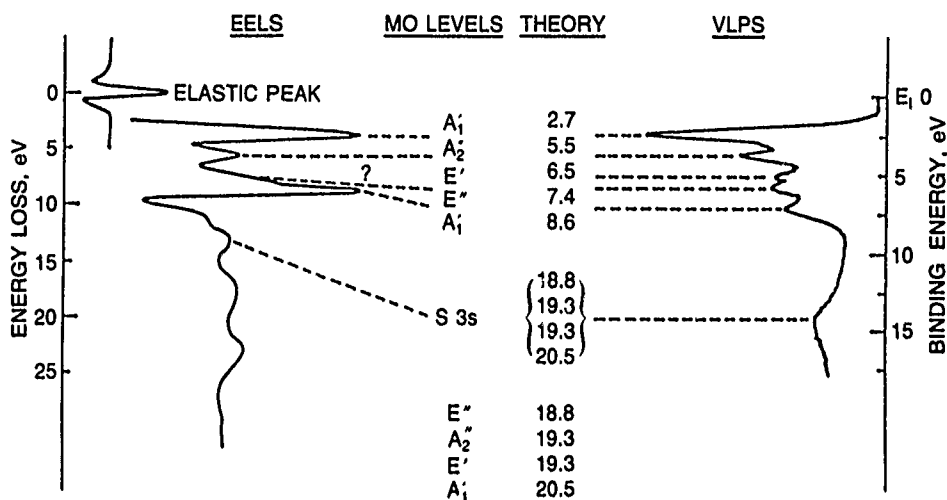


Figure 5. Energy correlation diagram for MoS₂.

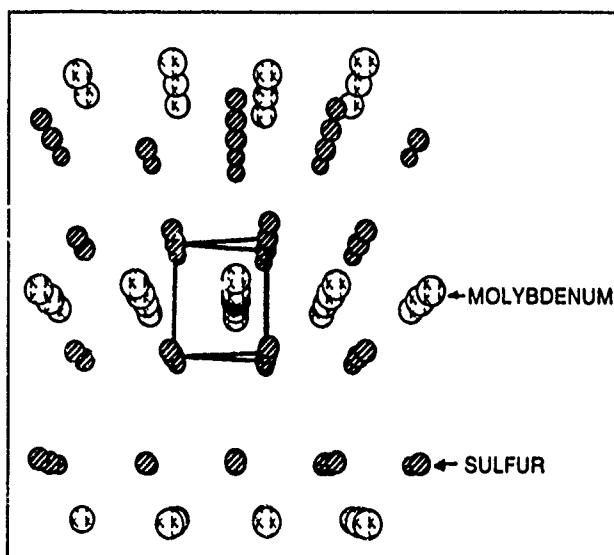


Figure 6. Lattice of point charges around MoS₆ cluster.

1. P. D. Fleischauer, "Fundamental Aspects of the Electronic Structure, Material Properties and Lubrication Performance of Sputtered MoS₂ Films," *Thin Solid Films* **154**, 309 (1987).
2. L. A. LaJohn et al., "ab initio Relativistic Effective Potentials with Spin-Orbit Operators. III. Rb Through Xe," *J. Chem. Phys.* **87**, 2812 (1987).
3. L. F. Pacios and P. A. Christiansen, "ab initio Relativistic Effective Potentials with Spin-Orbit Operators. I. Li Through Ar," *J. Chem. Phys.* **82**(6), 2664 (1985).
4. P. D. Fleischauer et al., "Electronic Structure and Lubrication Properties of MoS₂: A Qualitative Molecular Orbital Approach," *Langmuir* **5**, 1009 (1989).
5. D. E. Haycock, D. S. Urch, and G. Wiech, "The Electronic Structure of Molybdenum Disulfide," *J. Chem. Soc. Faraday Trans. II* **75**(12), 1692 (1979).

Scanning Tunneling Microscope Studies of Nickel Oxyhydroxides

A. H. Zimmerman, M. V. Quinzio, and N. A. Ives,
Chemistry and Physics Laboratory

The development of the scanning tunneling microscope (STM) within the past 5 years has made it possible for the first time to routinely obtain images of surfaces with a resolution equal to or better than the sizes of the individual atoms making up the surface. In the STM method, a fine metal tip is allowed to approach the surface being imaged. The electron tunneling current that flows between the surface and the metal tip is monitored as the tip is scanned across the surface. The method is capable of

extremely high resolution because the electron tunneling current is extraordinarily sensitive to distance variations on the order of several angstroms or less; i.e., atomic dimensions. Because the STM measures electron tunneling current from the surface, it actually measures the density of electrons available for conduction at the surface. Thus, assuming that the surface is conductive, the STM senses the electron clouds around each of the atoms that make up the surface.

In recent years, STM has been widely used to examine the structure of highly ordered surfaces such as single crystals at the atomic level or to examine the morphology of solid surfaces with a resolution much better than is attainable by means of scanning electron microscopy or other methods. The use of STM for studying the poorly ordered surfaces typically found for many oxides, particularly at the atomic level, has generally been more difficult. A major objective of this project is to evaluate the capability of STM to provide atomic-level structural data for oxyhydroxide compounds of nickel. These compounds, when properly doped with foreign elements, have technical applications ranging from battery electrode materials to electrochromic elements. Initial STM studies of these materials are reported here for pure nickel oxyhydroxides. An additional future objective is to use STM to evaluate the electronic and structural mechanisms by which commonly used dopants alter the characteristics of the oxyhydroxides.

Nickel oxyhydroxide compounds, which are the energy storage materials used in nickel electrodes for battery cells, tend to have only short-range crystallinity. In addition, they are typically nonstoichiometric compounds, able to accommodate wide ranges of nickel oxidation states and intercalated components within a single crystalline habit. Atomic-level imaging of these materials offers promise for direct observation of defect structures, grain sizes, and variations in electronic density either at localized charge transfer sites or delocalized through individual crystal grains. Correlation of the local structural characteristics with the electrochemical performance of these materials should provide major advances in understanding how they work most effectively in battery electrodes, as well as general data for modeling the relationships between solid-state structure and electrochemical activity.

Nickel oxyhydroxide samples were prepared as thin films on both single-crystal (111) and polycrystalline nickel metal surfaces. The nickel metal surfaces were polished, annealed, and cleaned prior to electrochemical deposition of a thin film of nickel hydroxide from a nickel nitrate solution. Subsequent oxidation of the film in alkaline electrolyte produced the nickel oxyhydroxide at any desired oxidation state. This method was used to produce films that ranged from 0.66 to 1000 Å in average thickness. STM images of the thin film surfaces were obtained using existing STM facilities previously developed in this laboratory in other company-sponsored work.

The bare nickel substrates, on which the oxyhydroxides were deposited for imaging, were examined to determine the native oxide structure upon which the films were deposited. Nickel metal reacts with atmospheric oxygen to produce a thin (6.1 Å, as deduced by ion microprobe sputtering, or several monolayers) layer of native oxide. Figure 1 shows the native oxide layer at atomic resolution.

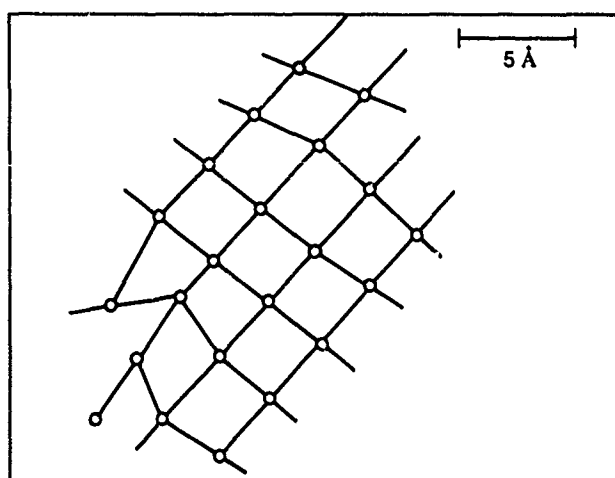
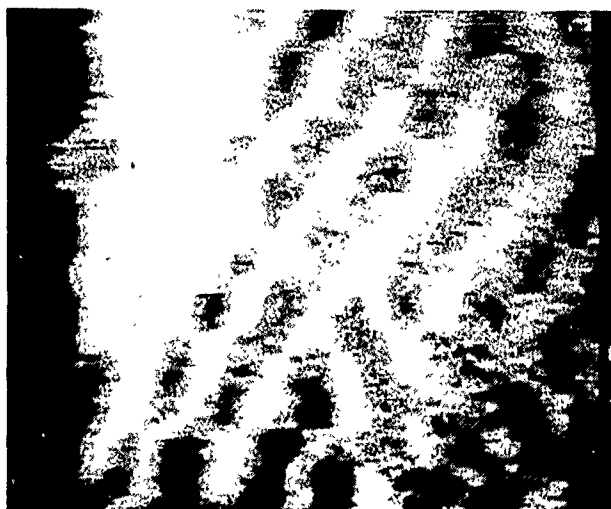


Figure 1. STM image of bare nickel substrate covered with native oxide at atomic resolution. Lattice image is consistent with a strained nickel oxide layer.

Regions of high electron density (such as atoms) are light; regions of low electron density are dark. To our knowledge, this is the first published report of atomic level imaging of oxygen (as oxide) on nickel. The oxide layer in Figure 1 has a highly strained cubic NiO structure. The strained and defect-filled structure is to be expected because of the lattice mismatch between the cubic nickel metal, which has a 3.53 Å unit cell, and the NiO, which has a 4.18 Å unit cell. Figure 1 shows the typical lattice defect to be an interstitial NiO species that is forced into the NiO lattice as it forms from the more compact Ni metal lattice. It is apparent from the figure that each light area is not an individual atom, since the light spots are not symmetric. The length of each light area is about 1.9 Å, corresponding quite well to typical transition metal/oxygen bond lengths.

A submonolayer film (0.66 Å average thickness) was produced in a fully oxidized state, for which the nickel atoms typically have an average oxidation state in excess of +3. STM images of this film revealed islands of crys-

tals (typically 25–30 Å in diameter) spread over the nickel substrate. These islands covered about 15 to 20% of the substrate. This suggests that the nickel hydroxide deposition initiated at nucleation sites that then grew in size to form crystalline islands that are strictly two-dimensional. Images of one of these flat crystalline islands are shown in Figures 2 and 3. The hexagonal structure of the nickel oxyhydroxide is clearly shown. Measurement of the angles and bond lengths in the two-dimensional crystallite of Figures 2 and 3 indicates a somewhat distorted hexagonal structure with a nickel hydroxide bond length in one direction and a significantly expanded bond length in the other direction. Further studies are under way to compare the electrochemistry of these two-dimensional crystallites with that of thicker three-dimensional materials.

Sufficient oxidation can force the hexagonal nickel oxyhydroxide structure to reorganize into a rhombohedral superstructure [1] that has a unit cell extending through multiple sheets of the type shown in Figure 2. The size of the unit cell in this case is 23.6 Å. For an oxidized film with an average thickness of about 100 Å, a region was located that exhibited ridges of higher electronic density with a 23.8 Å separation, and extending over about 100 Å. It is likely that this crystallite has reorganized into the rhombohedral structure as a result of electrochemical oxidation.

Nickel oxyhydroxides in layers about 100 Å thick typically yielded surface images such as that shown in Figure 4 for a 50 × 50 Å area. In Figure 4, the hexagonal lattice structure of the oxyhydroxide is clearly shown. However, the film also contains a region approximately 10 to 20 Å across on the right-center of the image, which stands out noticeably from the surface. The raised area in the figure appears to be the beginning of the growth of another layer of hexagonal cells on top of the underlying layer. Thus, the film growth mode encountered here appears to be similar to that of Figure 2; i.e., single molecular layer growth prior to nucleation of the next layer.

Closer examination of a thick oxyhydroxide film (100-Å thick) after oxidation reveals an image such as that in Figure 5. A hexagonal lattice pattern is observed; however, the lattice is significantly distorted and less regular than that of the thin layer in Figure 2. The hexagonal unit cells in Figure 5 are much more distorted than those in Figure 2. This distortion appears to result largely from lattice dislocations. In Figure 5, a lattice dislocation runs diagonally through the center of the structure and is indicated by the cross marks.

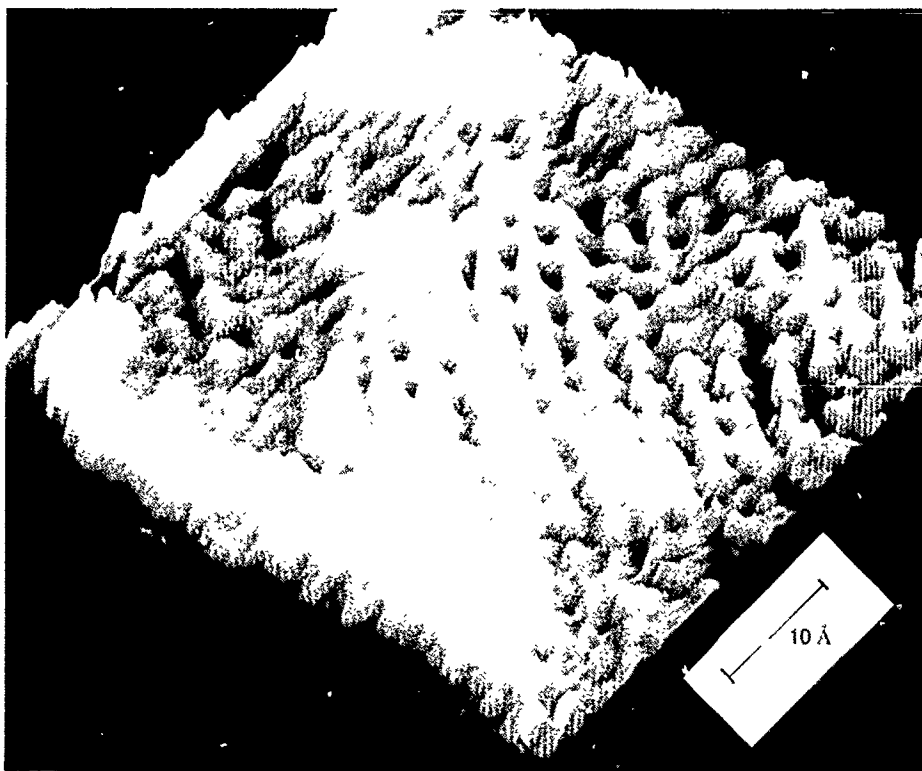


Figure 2. STM image of a small crystallite of nickel oxyhydroxide at atomic resolution. This crystallite has a distorted hexagonal struc-

ture and appears to be a two-dimensional crystallite formed from a submonolayer film.

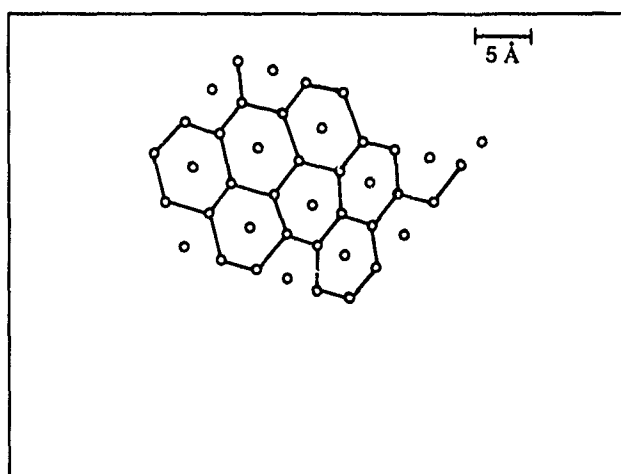
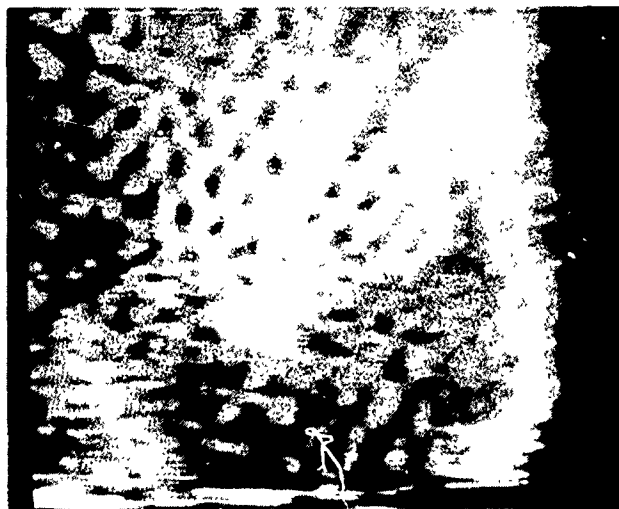


Figure 3. Top-down STM view of the crystallite of Figure 2. The hexagonal ordering of the lattice is illustrated. The full size of this crystallite is only 10 to 20 Å across and was part of a submonolayer film.

The morphology of the oxyhydroxide crystallites was found to be highly dependent on the film deposition rate. Quite low deposition rates yielded highly crystalline films, intermediate deposition rates yielded films with crystalline order extending up to 100 Å, and quite high deposition rates yielded films with relatively short-range atomic order but large variations in surface morphology several hundred angstroms across. Since electron delocalization appears to be primarily within individual layers of hexagonal cells, it is quite possible that the disorder created by the high deposition rates is important in maintaining good electronic conductivity through thick layers and is thus critical in maintaining electrochemical activity. Studies are continuing to determine how morphology variations influence the electrochemical properties of oxyhydroxide layers.

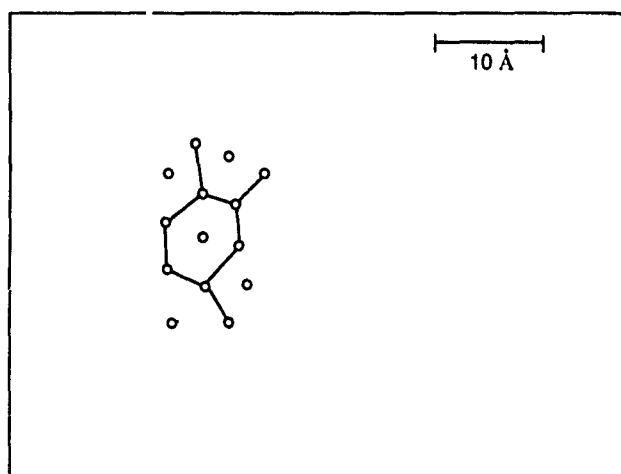
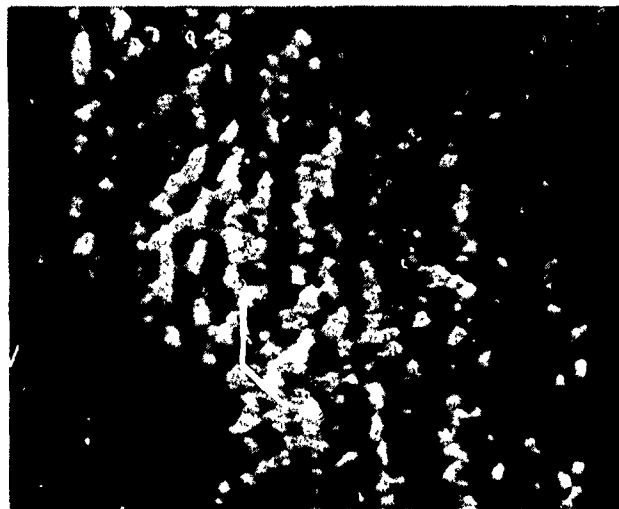


Figure 4. STM image of a 100-Å-thick nickel oxyhydroxide film indicating atomic level resolution of the molecules in the film. The raised structure in the left center of the image, which is sketched in the lower view, appears to be an overlayer that had just begun to form during the film deposition.

The results of STM imaging of pure nickel oxyhydroxides reported here clearly illustrate the usefulness of this method for measuring the structure and morphology of these types of materials with atomic level resolution. As stated earlier, we believe these measurements are the first reported atomic imaging in the nickel oxide and oxyhydroxide classes of materials and suggest a number of factors expected to be important in maintaining the function of these materials in battery electrodes. The results reported here provide a good baseline for undoped nickel oxyhydroxide, thus enabling further studies that are planned to examine the effect of various dopants on the atomic level structures in the nickel oxyhydroxide lattice. Since a number of dopants, materials such as cobalt, silicon, and platinum, have been found to have a significant effect on nickel electrode performance in batteries used

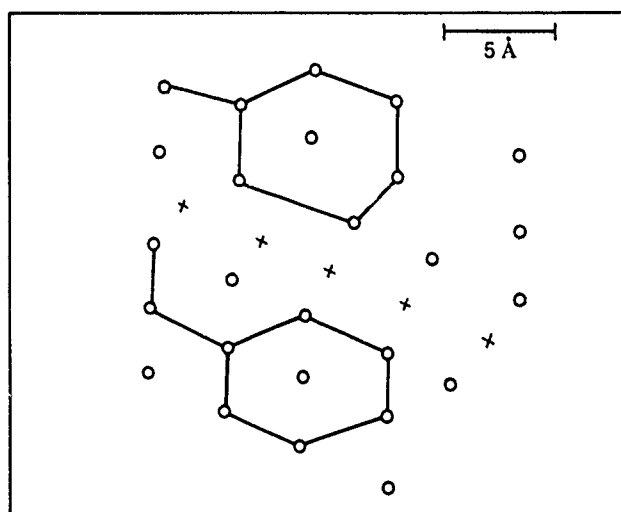
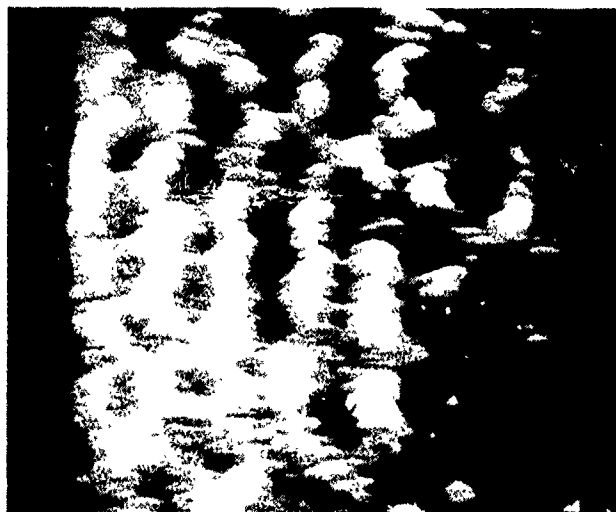


Figure 5. STM image of nickel oxyhydroxide in a 100-Å thick film at atomic level resolution. The positions of the molecules in this image are sketched in the lower view. A dislocation, marked by crosses, appears to run diagonally through the lattice in this region.

in satellite programs, this future work will enable a direct transfer of results from these studies to answering battery performance questions. The results from this work will also be used in modeling the active material in nickel electrodes as part of a program to model the nickel hydrogen battery cell.

* * * * *

1. A. H. Zimmerman and V. E. Johnson, *Electrochemical Reactions of Mixed Cobalt/Nickel Oxide Hydroxides in Alkaline Solution*, ATR-86(9561)-4, The Aerospace Corp. (15 July 1987).

Metallic Cluster Ions – Electronic Structure and Stability

N. D. Bhaskar and C. M. Klimcak,
Chemistry and Physics Laboratory

When metals or semiconductors are shrunk down to *clumps* only 10 to 100 atoms or molecules in size, they become a totally new class of materials with potentially valuable applications. These clumps are called *clusters*. They have many unique physical and chemical properties governed by their size and the explicit nature of their binding forces. Clusters form a natural bridge between iso-

lated atoms or molecules and extended solids. Our present understanding of their fundamental properties still remains fragmentary. They represent a new frontier, exploration of which will undoubtedly answer many questions that are posed by a variety of scientific disciplines. Astrophysicists speculating on interstellar grains, chemists and materials scientists concerned with catalysis and

the properties of nanophase materials, and even solid-state theorists who design novel quantum devices—all are ultimately concerned with the properties and behavior of clusters.

The elucidation of the structures of clusters is one of the principal goals of research in this field [1–4]. The structures are governed by the internal binding forces. For example, geometric structure plays a dominant role in covalently bonded species such as semiconductor clusters (Si_n , C_n ...). On the other hand, clusters of simple metals that have a highly delocalized valence shell of electrons (Na_n , Au_n ...) are species for which electronic structure effects become dominant [5,6]. In this case, the details of the geometrical arrangement play only a minor role. With this sensitivity to both geometric and electronic effects, clusters exhibit a very rich spectrum of properties.

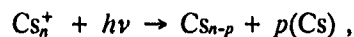
In the Chemistry and Physics Laboratory, we are investigating the electronic properties of cluster ions of simple metals (alkali metals). Our earlier efforts concentrated on studying the structure and stability of small cluster ions Rb_n^+ and Cs_n^+ [7,8]. We observed *magic numbers* corresponding to $n = 9, 19, 21$. This was explained using the electronic shell model of simple metal clusters developed by Knight and co-workers [3]. The magic numbers correspond to enhanced intrinsic stability of certain cluster sizes resulting from a closed electronic shell structure. At the present time, we are investigating the optical properties of these clusters to gain further insight into their electronic properties. This is a nascent field with vast unexplored areas.

Our experimental apparatus is shown schematically in Figure 1. We use a liquid metal ion source (LMIS) [9] to generate the clusters. Cluster ions are extracted from a tungsten capillary needle by applying a strong electric field (on the order of volts/angstrom) to the tip. The capillary is filled with the liquid metal of interest. The cluster ion beam is collimated by an electrostatic lens assembly. With the use of two pairs of deflecting plates (A and B), a mass-selected pulsed cluster ion beam is produced. A col-

linear counter-propagating pulsed laser beam approximately 1 ms in duration interacts with the pulsed ion beam at the entrance of a 2-m long time-of-flight (TOF) drift tube. Very good spatial and temporal overlap of the two beams is essential to obtaining a reliable measurement of the cross sections. An off-axis electron multiplier (CEM2) fitted with an energy analyzer/retarder assembly is used for the detection of cluster ions.

Here, we present new results regarding the interaction of the cluster ions with light produced by a laser. The TOF mass spectra of the cluster ions are shown in Figure 2 with the laser beam off and on. In this case, the laser beam causes a large depletion in the cluster beam strength for sizes in the range of $n = 4$ to 9. Because of the laser beam's narrow temporal width, only a limited range of cluster sizes interact with the laser beam at one time. However, by adjusting the time delay between the pulsed ion beam and the laser pulse, any desired mass range for the laser interaction can be obtained. The foregoing data were obtained for 600-nm laser wavelength.

The sharp reduction in the cluster beam intensity when the laser beam is present arises due to photofragmentation. Absorption of a photon leads to internal excitation of the cluster. The increase in the internal energy of the cluster ion is rapidly redistributed among the numerous vibrational modes of the cluster leading to evaporative cooling. The process can be represented by



where p is approximately proportional to the photon energy. The laser excitation occurs in an electric-field-free region. The energy required for fragmentation is typically several electron volts, which is much smaller than the kinetic energy of the cluster ions (a few kiloelectron volts). Therefore, in the fragmentation process, the kinetic energy is partitioned in inverse proportion of the masses of the fragments; although the parent and the fragment ion kinetic energies are different, they travel with essentially the same speed. However, the fragments

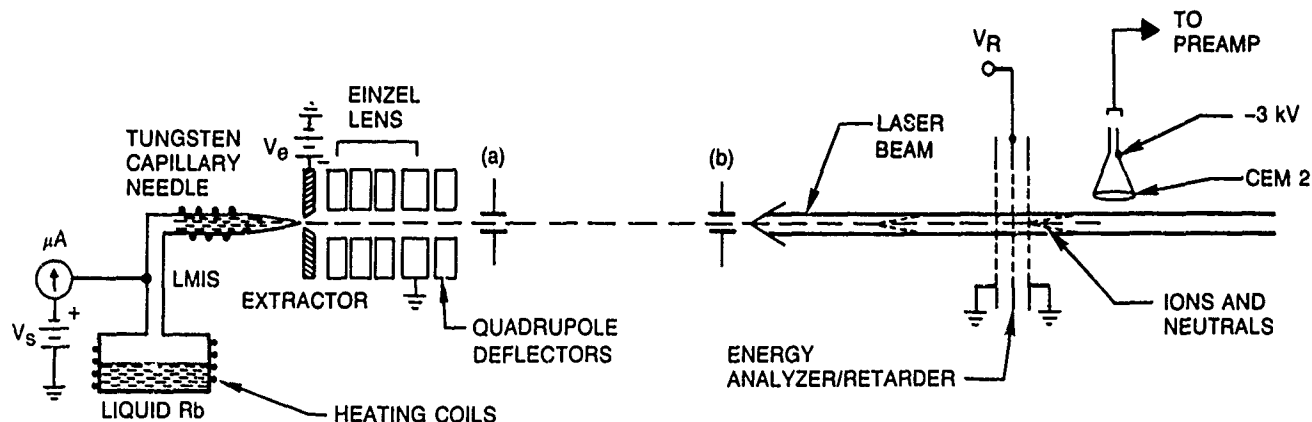


Figure 1. Schematic of the cluster ion beam apparatus.

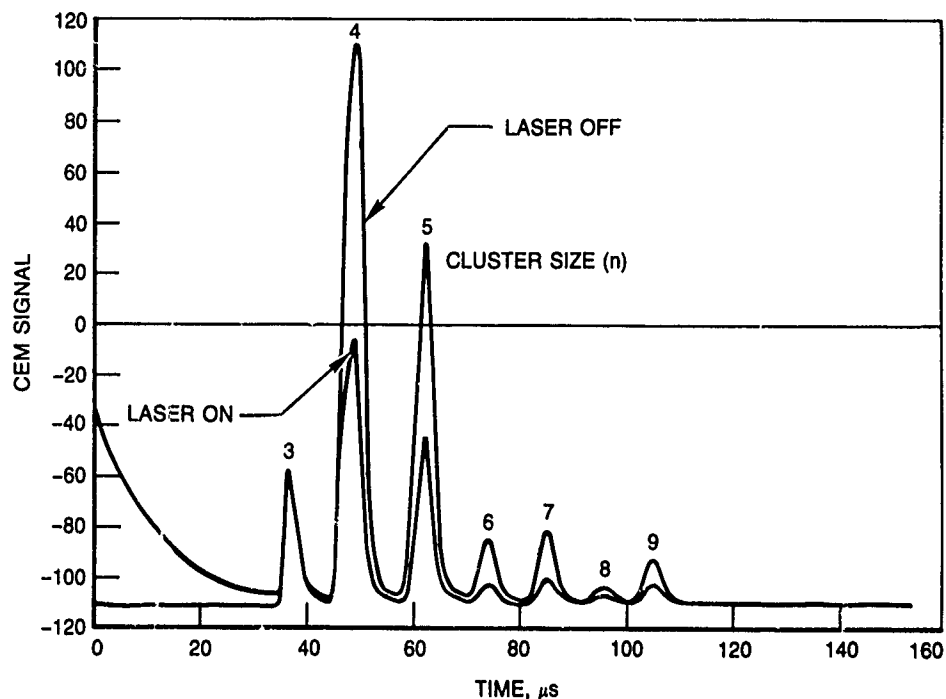


Figure 2. Mass spectrum of Cs_n^+ with and without the laser beam for cluster sizes $n = 3 - 9$. The average power per laser pulse is 4 mJ. The kinetic energy of the cluster ion beam is 2.8 keV and the electrostatic retarder is set at 2.7 kV.

will have a much larger angular divergence than the parents and therefore some of the fragments will miss the detector. In our experiments, we use the energy retarder very effectively to isolate the fragment ions from reaching the detector without relying on the differential divergence. The electrostatic energy retarder is set to transmit only the parent ions. Although the neutral fragments are not affected by the retarder, they do not reach the off-axis ion detector. This enables us to obtain a reliable measurement of the fractional loss in the parent ion signal due to the photofragmentation process.

For a particular parent cluster ion size n , let N_n^0 denote the cluster beam signals for laser on and off, respectively. Then,

$$N_n = N_n^0 \exp(-\sigma\Phi),$$

where σ is the single-photon absorption cross section and Φ is the number of photons per unit area per laser pulse. This relationship is valid only when the observed photofragmentation results from a single-photon absorption process, a condition we have experimentally verified. From our experimental results, we then determine the absorption cross sections.

In Figure 3, the experimentally measured photoabsorption cross section is shown as a function of the size of the cesium cluster ion. These measurements were made at a laser wavelength of 600 nm. We have made a limited scan of the laser wavelength. Our preliminary observation is that the absorption features are fairly broad. 100 nm is the typical spectral width. Similar observations have been reported in Na_n [10] and in K_n^+ [11]. Our results may be explained as follows: If we treat these clusters as small metal particles, we can use the classical Mie theory for absorption results in collective excitation of the calculating

the photoabsorption cross section. The photovalence electrons in the cluster, which are relatively free in metallic clusters and can be treated as an electron gas. The displacement by an electromagnetic field of the electron gas, as a whole, with respect to the fixed positive background of the ions, which provide the restoring force, gives rise to a collective plasma excitation. Our estimates for the cross section using this approach are in qualitative agreement with the measured values. The damping of the plasma oscillation into a localized vibration then fragments the cluster.

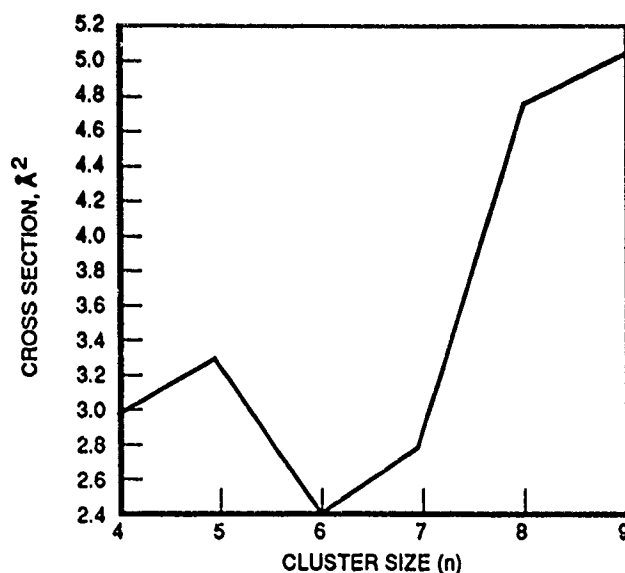


Figure 3. Measured total photoabsorption cross section as a function of cluster size for laser wavelength of 600 nm.

Experiments are in progress to measure carefully the cross section as a function of the wavelength of the laser radiation. This will enable us to accurately obtain the width of the absorption curve and also locate the resonance maxima in the absorption curves. The width is a measure of the damping of the collective plasma oscillation. These studies will give us further insight into the electronic structure of simple metal clusters.

* * * * *

1. A. W. Castleman, Jr., and R. W. Keesee, "Clusters: Properties and Formation," *Ann. Rev. Phys. Chem.* **37**, 525 (1986).
2. J. Koutecky and P. Fantucci, "Theoretical Aspects of Metal Atom Clusters," *Chem. Rev.* **86**, 536 (1986).
3. W. A. de Heer et al., "Electronic Shell Structure and Metal Clusters," *Solid State Phys.* **40**, 93 (1987).
4. M. Kappes, "Experimental Studies of Gas Phase Main Group Metal Clusters," *Chem. Rev.* **88**, 369 (1988).
5. W. D. Knight et al., "Electronic Shell Structure and Abundances of Sodium Clusters," *Phys. Rev. Lett.* **52**, 2141 (1984).
6. W. D. Knight et al., "Electronic Shell Structure in Potassium Clusters," *Solid State Commun.* **53**, 445 (1985).
7. N. D. Bhaskar et al., "Evidence of Electronic Shell Structure in Rb_N^+ ($N = 1-100$) Produced in a Liquid Metal Ion Source," *Phys. Rev.* **36B**, 4418 (1987).
8. N. D. Bhaskar, C. M. Klimcak, and R. A. Cook, "Electronic Shell Structures Effects in Cs_n^+ ," *Phys. Rev. B* **42** (14), 9147 (1990).
9. N. D. Bhaskar, C. M. Klimcak, and R. P. Frueholz, "Liquid Metal Ion Source for Cluster Ions of Metals and Alloys: Design and Characteristics," *Rev. Sci. Instrum.* **61**, 366 (1990).
10. K. Selby et al., "Surface Plasma Resonances in Free Metal Clusters," *Phys. Rev.* **40B**, 5417 (1989).
11. C. Brechignac et al., "Collective Excitation in Closed-Shell Potassium Cluster Ions," *Chem. Phys. Lett.* **164**, 433 (1989).

Bhaskar, N. D., et al., "Production of Mass-Selected Neutral Clusters of Rubidium," *Chem. Phys. Lett.* **154**, 175 (1989).

Vibrational Chemiluminescence in Gas-Solid Reactions

G. S. Arnold and D. J. Coleman,
Chemistry and Physics Laboratory

It has become well known that a spacecraft in low earth orbit *glows* as a result of some chemical or physical interaction between vehicle surfaces and the earth's residual atmosphere [1]. Although observations of vehicle glows have been limited to the visible [1] and (perhaps) vacuum ultraviolet [2], there is a legitimate concern that gas-surface interactions of the type that cause visible glows may also contribute to the infrared environment of a space vehicle in the thermosphere, a matter of significant systems concern [3-5].

The overall objective of this project is to enhance the understanding of the partitioning of chemical energy into molecular vibrations of gas-phase products of surface reactions, so that the impact of these processes on a vehicle's environment may be more nearly quantitatively predicted. The specific tasks for last year were to review the existing literature base, to estimate the potential impact of such phenomena on a vehicle environment, and to examine the feasibility of performing laboratory research in this field with the facilities of the Chemistry and Physics

Laboratory. This work has already found application in enhancing the understanding of the performance of space systems [6].

The objective for the past year was to begin the experimental portion of the project. Laboratory measurements were performed to enhance our confidence that low-probability surface reactions actually could be detected in the face of potentially interfering gas-phase reactions. Laboratory facility modifications were initiated so that infrared chemiluminescence and modulated beam scattering techniques could be used to study vibrational excitations in gas-solid reactions.

The approach proposed in this work was to study vibrational excitation by direct infrared chemiluminescence measurements from molecular beam-solid interactions, ultimately from O atom surface reactions [6]. Furthermore, it was decided to use essentially continuous-wave beams, rather than the pulsed-beam approaches used in other laboratories [7] in order that the reactions observed might be representative of those that would

occur in low earth orbit. This approach requires an experiment sensitive to surface reactions, not gas-phase reaction. Our confidence in this approach was based, to some degree, on our earlier studies of visible chemiluminescence from the surface-mediated reaction of O and NO, which produces electronically excited NO₂ [8].

Additional examination of the results of those studies raised the concern that we had not actually observed a primary surface process, but rather the results of a gas-phase reaction on NO with excited molecular oxygen (O₂) produced by surface recombination of O atoms. Since one objective of this effort is to examine vibrational excitation in this reaction system, it was important to resolve this question.

To help distinguish whether the chemiluminescence we had observed came from a surface reaction of O and NO or a gas phase reaction of NO with O₂, we measured the luminescence while NO source temperature was varied from 308 to 413 K. This measurement was intended to examine whether there was any *activation energy* in NO velocity, which would be indicative of a gas-phase reaction, not a surface reaction. A *decrease* in visible chemiluminescence with increasing source temperature was observed. One might imagine that this shows an inverse translational energy dependence for the NO + O₂ reaction, indicating an exoergic reaction without a barrier [9]. However, examination of the results and procedures reveals this is not the case.

The NO source temperature was varied by first heating the source, allowing the NO flow to stabilize, starting the O atom beam, and then recording the chemiluminescent intensity as the NO source cooled. It was observed that the magnitude of the apparent inverse source temperature effect was not reproducible; it depended on the length of time spent at high temperature. Figure 1 shows Arrhenius plots, in source temperature, recorded after two different dwell times at high temperature. In fact, the effect observed could be explained by radiant heating of the catalyst surface by the NO source, as seen in Figure 2, which shows Arrhenius plots (in substrate temperature) of the metal catalyzed luminescence. The diamonds and rectangles on the main plot were obtained in two of the NO source heating experiments (using much the same source temperature range) with a nickel catalyst. When plotted against NO source temperature, these two measurements show strikingly different behaviors. The inset compares these results to those measured by intentionally varying the substrate temperature. These plots show that there is no discernible dynamic effect of NO source temperature (velocity) on the rate of chemiluminescence.

The negative Arrhenius behavior (in surface temperature) of the metal-catalyzed chemiluminescent reaction of O and NO is characteristic of a surface process, controlled by the concentration of some transiently

adsorbed reagent. The O + NO and O + O chemiluminescent reactions both proceed most rapidly on nickel and nickel-containing substrates [10,11]. This indicates that an adsorbed O atom is involved in the O + NO reaction.

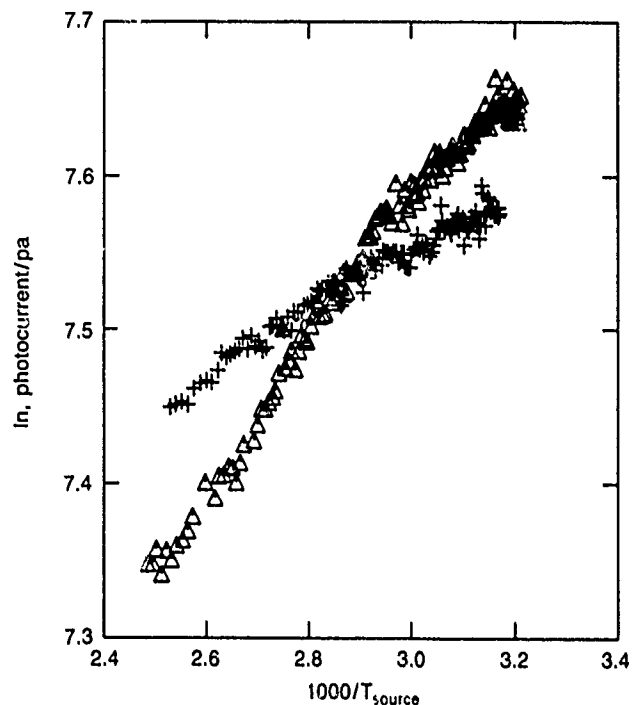


Figure 1. Arrhenius plot (in substrate temperature) of the rate of chemiluminescence from the nickel catalyzed reaction of O and NO. That these results are not reproducible indicates the observed effect is an experimental artifact, not a dynamic effect of NO velocity. See text for details.

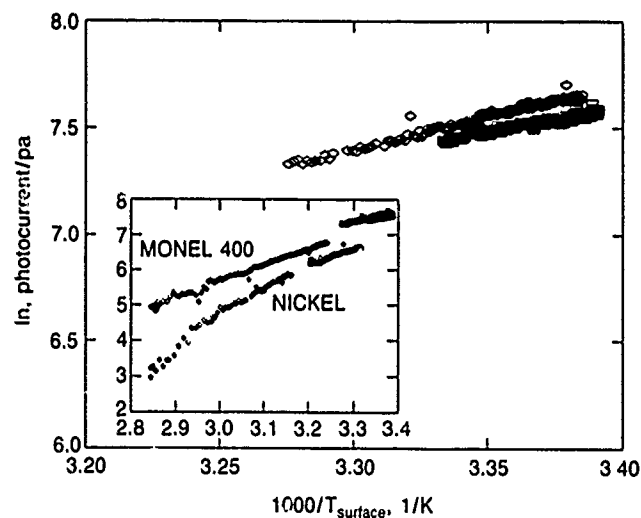


Figure 2. Arrhenius plot (in substrate temperature) of the rate of chemiluminescence from the metal catalyzed reaction of O and NO. The diamonds and rectangles in the main plot are the results of varying the NO source temperature, which radiantly heats the substrate (Figure 1). The inset compares these results with the Arrhenius plots for nickel and a nickel-containing alloy, Monel 400, for a constant NO source temperature. (Compare only the slopes.)

Results obtained earlier argue strongly that the rate of chemiluminescence we observe is controlled by the flux of NO striking the surface, not the number density of NO near the surface [11]. Therefore, a surface reaction of O and NO is indicated. Recently, Caledonia and co-workers have shown that similar $O + O +$ surface luminescence can be produced by directing atomic oxygen at a surface previously exposed to NO [12]. It can be concluded, therefore, that the most likely mechanism for the metal-mediated chemiluminescent reaction of O and NO is the reaction of adsorbed O and NO, to produce excited gas-phase NO_2 . With confidence restored in the ability (with some effort) to separate gas-phase from surface processes, we proceeded with the apparatus modifications necessary for infrared chemiluminescence and mass spectrometric vibrational excitation experiments. These modifications involved construction of a new, high-temperature supersonic molecular beam source, a liquid-nitrogen cooled shroud in the detection chamber to provide a low infrared background, and building differential pumping

for mass-spectrometric detection of surface reaction products and velocities. All of these elements have been designed and built or are under construction. Figure 3 presents schematic views of the detection chamber of the molecular beam apparatus configured for the two types of experiments. An InSb infrared detector with a cooled filter wheel for wavelength selection has been obtained and tested.

In summary, we have confirmed that the surface-mediated chemiluminescent reaction of O and NO is, indeed, a surface process. With this confirmation, we have supported the validity of our approach to studying energy disposal in surface chemical reactions with gas-phase products. Assembly of the experimental facilities for direct infrared luminescence and mass spectrometric detection of vibrational excitation in surface processes is well advanced. These facilities will be tested in studies of excitation of ammonia and carbon dioxide in collision with an inert surface, lithium fluoride.

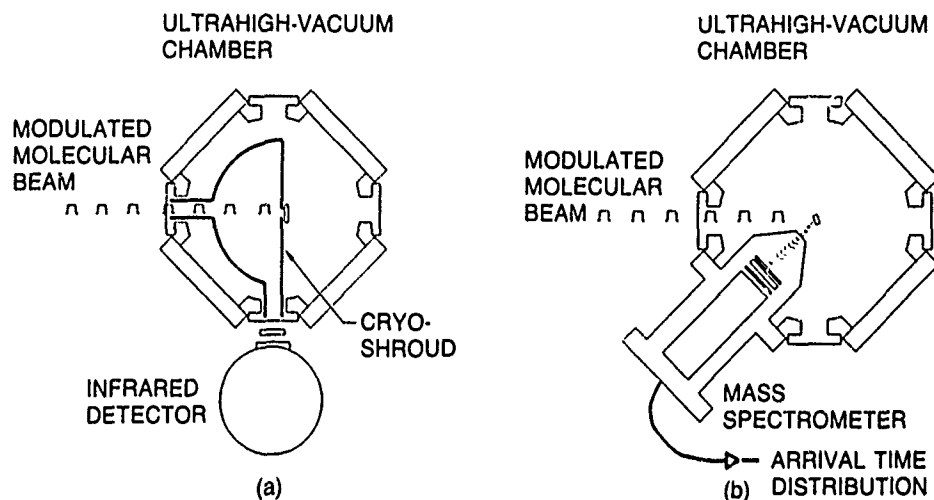


Figure 3. (a) Apparatus configured for photometric measurements; (b) apparatus configured for mass spectrometric observations.

* * * * *

1. J. H. Waite and T. W. Moorehead, *Second Workshop on Spacecraft Glow*, NASA CP 2391, NASA Marshall Space Flight Center (September 1985).
2. R. R. Conway et al., "The Far Ultraviolet Vehicle Glow of the S3-4 Satellite," *Geophys. Res. Lett.* **14**, 628 (1987).
3. J. P. Simpson and F. C. Witteborne, "Effect of the Shuttle Contamination Environment on a Sensitive Infrared Telescope," *App. Opt.* **16**, 2051 (1977).
4. S. J. Young and R. R. Herm, "Model for Radiation Contamination by Outgassing from Space Platforms," *J. Spacecraft Rockets* **25**, 413 (1988).
5. M. E. Fraser et al., "Calculation of Space Station Infrared Irradiance from Atmosphere-Induced Emissions," *A Study of Space Station Contamination*

Effects, NASA CP 3002, NASA Marshall Space Flight Center (May 1988), p. 61.

6. G. S. Arnold, "Vibrational Chemiluminescence in Gas-Solid Reactions," *Aerospace Sponsored Research Summary Report, Scientific and Engineering Research*, ATR-89 (8498)-1, The Aerospace Corp. (1 December 1989), p. 30.
7. G. E. Caledonia, "Laboratory Simulations of Energetic Atom Interactions Occurring in Low Earth Orbit," *Rarefied Gas Dynamics: Space Related Studies*, Vol. 116, AIAA, Washington, D.C. (1989).
8. G. S. Arnold and D. J. Coleman, "Surface-Mediated Radical Recombination Luminescence: $O + NO + Ni$," *J. Chem. Phys.* **88**, 7147 (1988).
9. R. D. Levine and R. B. Bernstein, *Molecular Reaction Dynamics*, Oxford (1974).

10. R. L. Sharpless, L. E. Jusinski, and T. G. Slanger, *J. Chem. Phys.* **91**, 7936 (1989).
 11. G. S. Arnold and D. J. Coleman, "Surface-Mediated Chemiluminescent Reaction of O and NO," *Chem. Phys. Lett.* **177** (3), 279 (1991).
 12. G. E. Caledonia et al., "Laboratory Investigation of Shuttle Glow Mechanisms," *Geophys. Res. Lett.* (in press).
- Arnold, G. S., and D. J. Coleman, "Gas-Solid Chemistry in Low Earth Orbit," *Proceedings of the 4th Annual AFOSR Workshop on Surface Reactions in the Space Environment*, Northwestern University, September 1989, Lt. Col. L. Burgraaf, Air Force Office of Scientific Research, ed. (in press).

Chaotic Dynamics of Atoms

J. C. Camparo,
Chemistry and Physics Laboratory

In recent years, a new branch of both classical and quantum mechanics called *chaos* has emerged, which deals with simple, nonlinear systems in regimes where the dynamics exhibit *random-like* behavior [1]. For example, although the few simple equations governing the general behavior of masers and lasers are completely deterministic, the intensity output of such devices will become very erratic under certain conditions [2,3]. This random-like behavior is not due to any noise process, but arises because certain maser and laser operating conditions lead to exceedingly complicated dynamics; i.e., chaos. In atomic physics, theoretical calculations have indicated that simple quantum systems, similar to those used in atomic clocks, may exhibit chaotic behavior when they are subjected to quasiperiodic perturbations. The objective of this project is to investigate experimentally and computationally the complicated dynamical behavior that can arise in atomic systems when they interact with quasiperiodic electromagnetic fields. Since very little is known about the actual chaotic behavior of quantum systems, often referred to as *quantum chaos*, experimental results are needed to indicate the strengths and limitations of various theoretical calculations. In addition, even though many new techniques have been developed, their application to other problems of complicated, but not necessarily chaotic, dynamics has been limited. An additional objective of the present study, therefore, is to develop the analytical tools of chaos in the Aerospace laboratories, so that they may be applied to more general problems of complicated dynamics. Space programs where complicated dynamics often arise include lasers, atomic clocks, orbital mechanics, and meteorology.

Chaotic behavior is analyzed in the phase space of the dynamical system [4] and, as a result of dissipative forces, dynamical systems will move toward a steady-state orbit in phase space called the *attractor*. Cross-sectional slices of this attractor are called *Poincaré sections*. During the past year, we developed many of the numerical algo-

rithms that are required to analyze the geometrical characteristics of phase space attractors as follows:

- To construct Poincaré sections for multidimensional dynamical systems.
- To reconstruct multidimensional attractors from one-dimensional time-series signals.
- To calculate an important characteristic of the attractor, its Hausdorff (scaling) dimension.

Although geometrical dimensions are commonly found to be integer (e.g., one-dimensional line and two-dimensional surface), the Hausdorff dimension of an entity can be fractional. When an object has a noninteger Hausdorff dimension, it is called a *fractal* [5], and attractors that are fractal entities are said to be *strange attractors* [4]. Strange attractors are often used as evidence for an underlying nonlinearity in the dynamical system.

Since our primary interest is in the chaotic dynamics of atoms, these analytical tools were initially applied to the computational problem of an idealized two-level atom interacting with a resonant field whose phase θ varies in a quasiperiodic fashion:

$$\theta(t) = \pi \{ \sin(\omega_s t) + H(t) \}, \quad (1)$$

where $H(t)$ represents a square wave varying between 0 and 1 with a period of T_{sq} . Although the idealized two-level atom does not exist in nature, it is the standard model system for studying the field-atom interaction. Further, this particular quasiperiodic phase variation was chosen because of its relevance to previous studies performed in this laboratory [6]. To describe the atom's response to the field, we used the optical Bloch equations [7]. Oscillations in the population imbalance between the two quantum states Z result from a coherent superposition of ground and excited-state wavefunctions called *atomic coherence*, represented by the complex quantity $X + iY$. The strength of the field-atom interaction is characterized by a quantity Ω called the *Rabi frequency*. Essentially,

when $\Omega \gg \omega_s$, the atom-field interaction is adiabatic, and the atom easily follows all the rapid phase variations of the field. However, when $\Omega \ll \omega_s$, the atom-field interaction is nonadiabatic, and the atom averages the field fluctuations. It is important to note that the system of equations describing the atom-field interaction is linear, and that the attractor exists in a four-dimensional phase space consisting of X , Y , Z , and θ coordinates.

Figure 1 is an example of Poincare sections for the atomic system's attractor [4]. The Poincare sections are formed by plotting all (X, Y) attractor coordinates that are associated with some specific value of the pair $[Z, \text{sign}(dZ/dt)]$. (In actuality, the Poincare sections of Figure 1 represent a family of Poincare sections, obtained by summing individual Poincare sections over all values of θ .) The triplet (X, Y, Z) forms a vector called the *Bloch vector*, which contains complete information on the state of an ensemble of two-level atoms. Hence, the Poincare sections of Figure 1 provide a cross-sectional slice of the Bloch vector's trajectory in what could be called an *atomic-state space*.

Three separate Poincare sections are illustrated in Figure 1 for three different values of the Rabi frequency. Figure 1(a) corresponds to $\Omega = 17,772$, the adiabatic regime of dynamics; (b) corresponds to $\Omega = 1200$, an intermediate regime of dynamics; and (c) corresponds to $\Omega = 300$, the nonadiabatic regime of dynamics. From a study of these Poincare sections, it can be argued that, even though the temporal evolution of the atomic dynamics is quite complicated, the attractor geometry typically falls into one of two limiting categories. There is a geometrical category for adiabatic dynamics and a geometrical category for nonadiabatic dynamics. (We will not consider the possibility of a third category associated with the transition from nonadiabatic to adiabatic dynamics.) Thus, by analyzing the atomic dynamics graphically with Poincare sections, we find that the attractor geometry is controlled to a large extent by a single parameter, adiabaticity.

To describe the attractor of the atomic dynamics in a more quantitative fashion, we used another analytical tool, the Grassberger-Procaccia correlation integral $C(r)$ [8], which, basically, is defined as the probability of finding two points on the attractor within a distance r of each other, where r is the *scaling length*. In many, but not all, cases, $C(r)$ displays a power-law dependence on r with exponent ν :

$$C(r) \sim r^\nu. \quad (2)$$

The usefulness of ν as a measure of attractor geometry is that it is a lower bound on the Hausdorff dimension of the attractor, and in the case of a uniformly covered attractor, it is equal to the Hausdorff dimension.

An example of the dependence of the correlation integral on scaling length is shown in Figure 2(a), where two different correlation dimensions are apparent. For

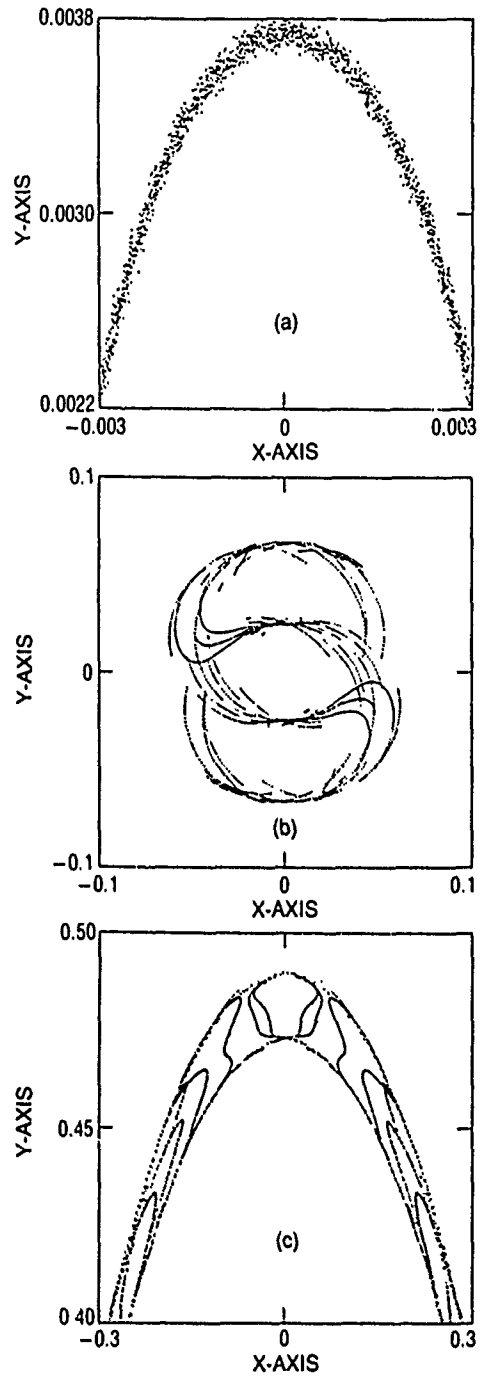


Figure 1 Poincare sections of the Bloch vector's motion through the xy plane [$\text{sign}(dZ/dt) > 0$]. The xy plane cuts the z -axis at the average value of Z , which varies between -1 and 0 as Ω increases. (a) Partial section of adiabatic regime with $\Omega = 17,772$; (b) intermediate regime with $\Omega = 1200$; (c) partial section of nonadiabatic regime with $\Omega = 300$.

small scaling lengths, the attractor geometry yields $\nu_s \sim 3$, whereas for larger scaling lengths, it is described by $\nu_a = 1$. This large scaling behavior of the attractor is dominated by θ variations, implying that the small scaling behavior is primarily associated with the atomic popula-

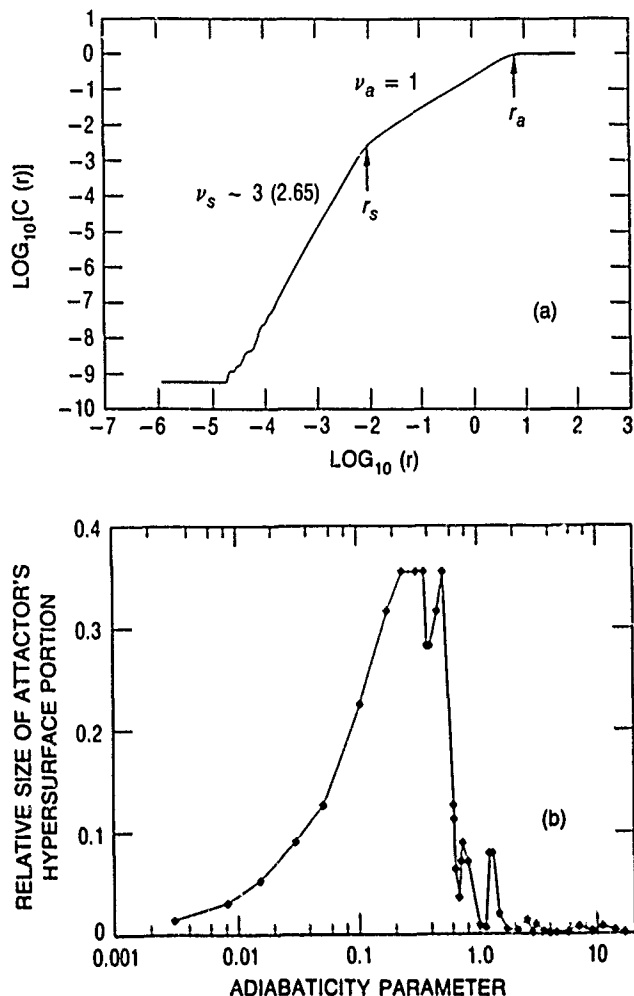


Figure 2. (a) Logarithm of the correlation integral $C(r)$ vs the logarithm of the scaling length r for the case of $\Omega = 17,772$. Note the two different scaling regions with $\nu_s \sim 3$, and $\nu_a = 1$. The actual value of ν_s obtained by a least-squares fit to the curve is shown in parentheses. r_s and r_a are related to the size of the attractor's hypersurface portion and size of the whole attractor, respectively; (b) variation in the relative size of the attractor's hypersurface portion (r_s/r_a) with adiabaticity parameter η .

tion (i.e., Bloch vector) dynamics. We therefore see the attractor as a geometrical entity that looks macroscopically like a curve, but on closer examination is actually a hypersurface; i.e., a three-dimensional entity existing in a four-dimensional space.

Note that the scaling length r_a indicates the maximum size of the attractor, and that r_s is related to the maximum extent of the attractor's hypersurface portion. The ratio r_s/r_a is thus a measure of the relative size of the attractor's hypersurface portion, and this ratio is plotted in Figure 2(b) as a function of an adiabaticity parameter η , the ratio of Ω to ω_s . As the figure clearly shows, there is a large increase in r_s/r_a near $\eta \sim 1$, and near this maximum there are resonance-like features. In other calculations, we have found that these resonant increases in the attractor's hypersurface portion are correlated with enhance-

ments in the amplitude of field-induced population oscillations. Such enhancements in the transient response of a quantum system to a train of radiation field changes are called *Rabi-resonances* [6].

Since the hypersurface portion of the attractor is associated with the Bloch vector's motion, it can be argued that the attractor's geometrical change results from changes in the hypersurface. It should therefore be possible to quantify the change in attractor geometry by calculating ν_s as a function of η . Unfortunately, the determination of ν_s is not always straightforward. In the nonadiabatic and transition regimes of the dynamics, the small scaling length behavior of $C(r)$ does not obey a simple power-law scaling relation with r , so that the Grassberger-Procaccia algorithm provides an ambiguous determination of ν_s . However, as shown in Figure 2(a), the correlation integral $C(r)$ does obey a simple power-law scaling relation with r in the adiabatic regime. Consequently, one can at least examine ν_s as a function of η in this regime of dynamics.

Figure 3 shows the variation of ν_s with η in the adiabatic regime of the atomic dynamics. {Error bars are statistical in nature and reflect the ability to fit a straight line through the $\log[C(r)]$ versus $\log[r]$ data at the 95% confidence level.} Near the transition region from nonadiabatic to adiabatic dynamics ($\eta < 4$), the correlation dimension is integer: $\nu_s = 3$. However, for values of η greater than about 4, Figure 3 indicates that the geometry of the hypersurface changes, becoming noninteger with $\nu_s \approx 2.65$. Under the assumption of a uniformly covered

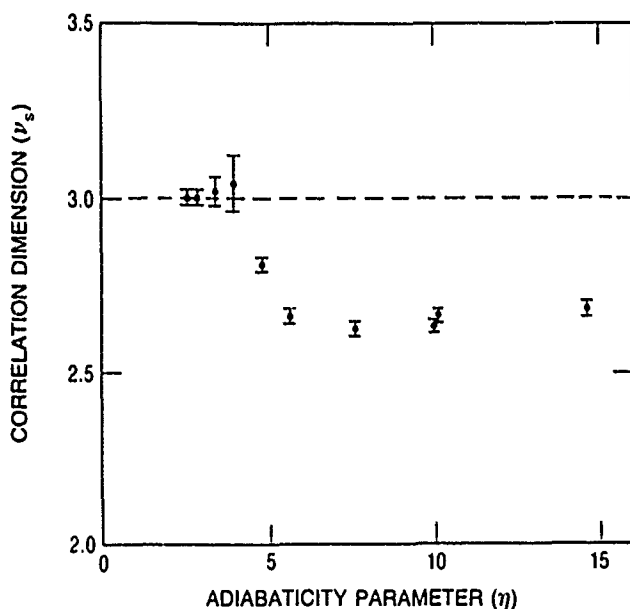


Figure 3 Correlation dimension of hypersurface portion of attractor ν_s vs the adiabaticity parameter η . These values were obtained by least-squares fits of $\log[C(r)]$ vs $\log[r]$. Close to the transition from nonadiabatic to adiabatic, $\nu_s = 3$. However, in the regime where the dynamics are clearly adiabatic (i.e., $\eta > 4$), $\nu_s \approx 2.65$.

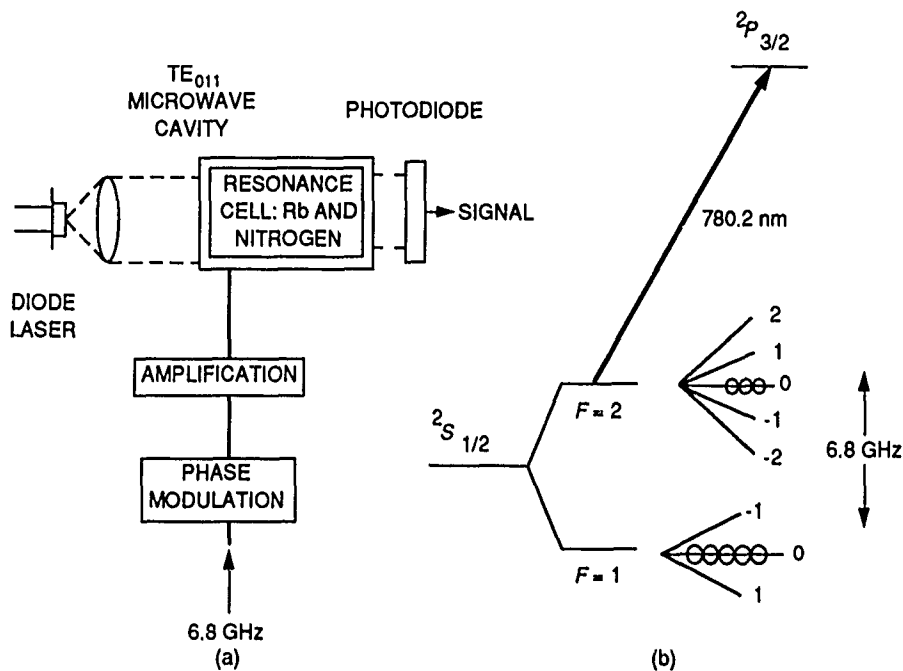


Figure 4. Schematic diagram of experimental apparatus. This apparatus is similar in design to the rubidium atomic clocks that are used on both GPS and Milstar satellites.

attractor, this implies that the actual attractor dimension is noninteger, and that the atomic dynamics have given rise to a strange attractor. To our knowledge, this is the first indication that linear dynamical systems may give rise to strange attractors.

At present, we are performing experiments on an atomic clock system to verify these results on a real multi-level atom. The experimental apparatus is shown schematically in Figure 4. A diode laser optically pumps a vapor of rubidium atoms contained in a glass resonance cell, creating a population imbalance between the ground-state hyperfine levels labeled by the quantum number F . As a result of the optical pumping process, the number density of atoms in the absorbing state ($F = 2$) is low, hence the intensity of laser light transmitted through the resonance cell is high. The resonance cell is placed in a microwave cavity whose TE_{011} mode is resonant with the ($F = 2, m_F = 0$) - ($1, 0$) hyperfine transition at 6.8 GHz. This is the clock transition of the gas-cell rubidium clock, the kind used on both GPS and Milstar satellites. As in our calculations, the phase of the microwave field is made to vary quasiperiodically, and this induces fluctuations in the population density of the $F = 2$ state. The population fluctuations then cause intensity fluctuations of the transmitted laser light, and these are recorded as a function of time.

An example of the data generated in the experiment is given in Figure 5. At time $t = 0$, the quasiperiodic phase modulation of the microwave field begins, and there is a corresponding rapid change in the level of transmitted laser light intensity. 10 ms later, erratic light intensity fluctuations are clearly apparent, indicating that the

quasiperiodic phase modulation of the microwave field has induced very complicated atomic population oscillations. The time series can be analyzed for the correlation dimension ν , using a variant of the Grassberger-Procaccia technique previously discussed [9]. At present, we are investigating the ability of this experimental analysis technique to yield unambiguous values of the correlation dimension.

We have shown that a careful study of attractor geometry can be quite useful for elucidating the dynamics of quantum systems interacting with rapidly fluctuating electromagnetic fields. In the specific case of a field whose phase varies quasiperiodically, we have found computationally that, even though the atomic dynamics appear quite complicated, they nonetheless give rise to only two limiting attractor geometries. Although in both cases the attractor is relatively simple, consisting of a hypersurface portion and a curvilinear portion, our results indicate that the geometrical characteristics of the attractor's hypersurface portion depend on the perturbation's degree of adiabaticity. Furthermore, the results suggest that in the adiabatic regime the hypersurface portion becomes fractal. The atomic dynamics would therefore exist on a strange attractor, even though the dynamics result from a system of linear differential equations. Experiments are now in progress to confirm these results in an atomic clock type system. In addition, analyses are in progress to test for chaotic dynamics in the frequency output of an atomic clock, similar to the type used on GPS satellites. This test will use the analytical tools of chaos developed in this project.

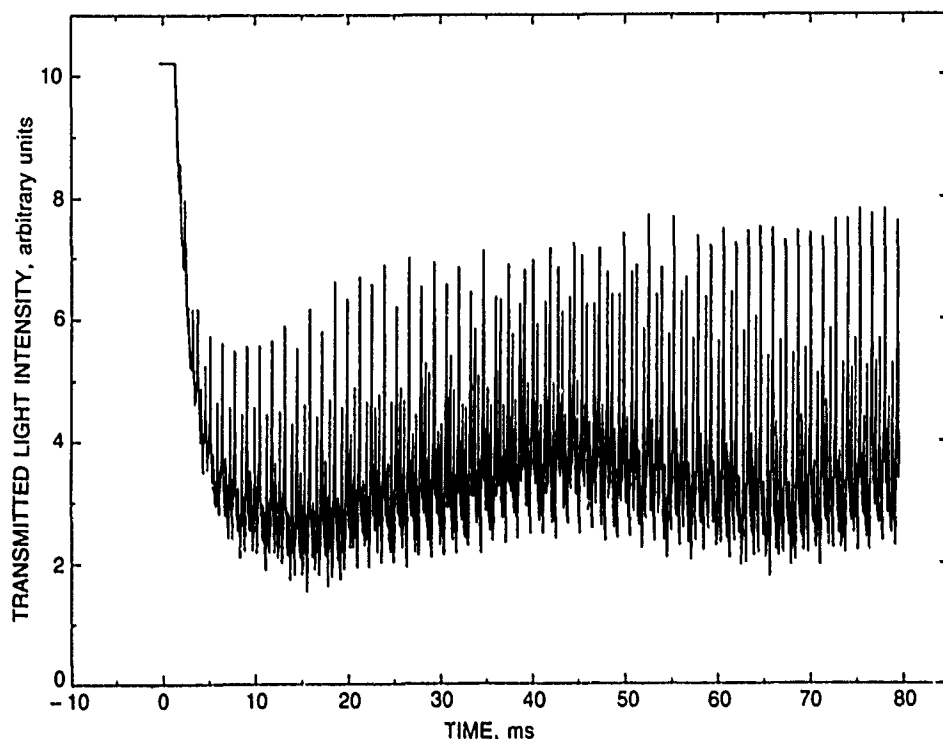


Figure 5. Example of experimental data. The change in transmitted laser light intensity is shown as a function of time. The origin of time corresponds to the instant when the phase of the microwave field at 6.8 GHz is made to vary quasiperiodically.

* * * * *

1. E. Ott, "Strange Attractors and Chaotic Motions of Dynamical Systems," *Rev. Mod. Phys.* **53**, 655 (1981).
2. R. G. Harrison and D. J. Biswas, "Chaos in Light," *Nature* **321**, 394 (1986).
3. K. A. Shore, "Nonlinear Dynamics and Chaos in Semiconductor Laser Devices," *Solid-State Electron.* **30**, 59 (1987).
4. P. Berge, Y. Pomeau, and C. Vidal, *Order Within Chaos*, John Wiley and Sons, New York (1984).
5. B. B. Mandelbrot, *The Fractal Geometry of Nature*, W. H. Freeman and Co., San Francisco (1983).
6. J. C. Camparo and R. P. Frucholz, "Observation of the Rabi-Resonance Spectrum," *Phys. Rev. A* **38**, 6143 (1988).
7. R. Loudon, *The Quantum Theory of Light*, Clarendon Press, Oxford (1983).
8. P. Grassberger and I. Procaccia, "Measuring the Strangeness of Strange Attractors," *Physica* **9D**, 189 (1983).
9. C. W. Simm et al., "On the Analysis of Experimental Signals for Evidence of Deterministic Chaos," *Helv. Phys. Acta* **60**, 510 (1987).

Camparo, J. C., and R. P. Frucholz, "Attractor Geometry of a Quasiperiodically Perturbed Two-Level Atom," *Phys. Rev. A* **43**, 338 (1991).

Semiclassical Analysis of Two-Electron Atoms

B. R. Johnson,
Chemistry and Physics Laboratory

The traditional model of atomic structure is based on the independent particle approximation. This model assumes that, to first order, an atom contains a collection of independent electrons, and the motion of each electron is determined by an average potential due to the nucleus

and the other electrons. These independent electrons are then assumed to be only slightly perturbed from their states of energy and angular momentum. About 10 years ago, this independent particle model was challenged, first for a set of rather exotic doubly excited states of helium

and then for the ground state and ordinary excited states of the alkaline earth atoms Be, Mg, Ca, Sr, and Ba. Evidence now indicates that the quantization of these two-electron and quasi two-electron atoms corresponds to the collective motion normally associated with the vibration-rotation states of a linear triatomic molecule rather than to independent-particle-like behavior [1,2]. Much effort has been directed in recent years toward understanding this problem; however, no semiclassical analysis has ever been attempted. Semiclassical analysis offers insights into the physics of a problem that is not easily available with a quantum mechanical solution [3]. In addition, quantum mechanical calculations become impractical to carry out in the regime of high quantum numbers, whereas the semiclassical calculations are much easier to carry out and, in accordance with the correspondence principle, are quite accurate in this limit.

Recently, we developed a new and very efficient semiclassical method for calculating the quantized energy levels of multidimensional, nonseparable systems [4]. This technique, which is now called the *adiabatic switching method (ASM)*, was applied with great success to several problems [4-6]. In particular, specialized procedures were developed for applying this method to three particle systems and successfully applied to calculating the vibrational energy levels of several triatomic molecules [5,6]. The basic objective of the present research is to apply these same semiclassical ASM procedures to two-electron atoms in order to gain more insight into the dynamics of these systems.

During the past year, our work focused on two major efforts:

- Test calculations were carried out to evaluate a proposed *semiclassical correction rule* for three-body systems. The test showed that the proposed rule is not generally valid for linear systems.
- Semiclassical calculations were undertaken to study the quasi two-electron magnesium atom.

In previous work on triatomic molecules, a technique was proposed for improving the accuracy of three-body semiclassical calculations [6]. This method, called the *three body semiclassical correction rule*, is based on an analogy to the Langer rule [7] of WKB theory. [The WKB (Wentzel-Kramers-Brillouin) theory is a semiclassical method for solving the one-dimensional Schrodinger equation. A discussion of this method can be found in most quantum mechanics text books.] The Langer rule and its implications are most easily explained by showing how it is applied to the hydrogen atom problem. The one-dimensional radial Schrodinger equation for the hydrogen atom is

$$\left(-\frac{1}{2} \frac{d^2}{dr^2} - \frac{1}{r} + \frac{\ell(\ell+1)}{2r^2} - E\right) \psi = 0. \quad (1)$$

The Langer rule basically states that the factor $\ell(\ell+1)$, which appears in the centrifugal potential term, should be replaced by the factor $(\ell+1/2)^2$. This is equivalent to the statement that one should add a *centrifugal* correction potential of the form $V(r) = 1/(8r^2)$ to the radial equation. If this correction potential is added to the potential in Eq. (1), then the WKB solution to the hydrogen atom problem is exact. In addition, the correction potential is repulsive and tends to keep the electron away from the nucleus, even for the zero angular momentum ($\ell = 0$) case.

The proposed three-body semiclassical correction rule is similar to the Langer rule. A *generalized centrifugal* correction potential is added to the potential for the three-body system. The details are given in [6]. This potential has the property that any two particles of the three-particle system are repelled if they approach too close to each other. For the case of the helium atom, this means that the correction potential prevents the electrons from coming too close to the nucleus. This property, or something similar, is needed if one is to calculate classical electron trajectories in the helium atom. Without this additional repulsive potential, the classical electron motion in the helium atom inevitably carries one of the electrons very close to the nucleus, where the potential and kinetic energies approach infinity. This causes severe numerical problems when calculating the classical trajectories, which terminate the calculation.

The proposed correction rule worked extremely well in improving the accuracy of the semiclassical vibrational energy levels of several nonlinear triatomic molecules [6]. However, at the time that this rule was proposed it was stated that more testing was required, especially for linear systems. We have carried out these test calculations on a simple model linear system [8]. Unfortunately, it must be reported that the proposed correction rule, which worked so well for nonlinear systems, did not improve the accuracy of the semiclassical eigenvalues of the linear model test system. Rather than continue to search for a good form for the correction rule, we decided to halt any further attempt to carry out semiclassical calculations on the helium atom. Instead, we will concentrate on the quasi two-electron alkaline earth atoms, where no additional correction potential is needed to prevent the electrons from coming too close to the nucleus.

The alkaline earth atoms have two outer valence electrons and a tightly bound inner electronic core. The important physical properties are determined by the valence electrons. The quantum mechanical treatment of these atoms is greatly simplified by a technique in which the action of the nucleus and the core electrons on the valence electrons is replaced by a nonclassical potential, which is now called the *psuedopotential*. This reduces the problem to that of solving a two-electron system. The

pseudopotential accounts for both the electronic repulsion of the core electrons and also the Pauli exclusion principle. We have chosen to work with a very simple form of pseudopotential due to Hellman [9]. The Hellman pseudopotential for a single electron that is outside the core is given by

$$U(r) = (Ae^{-br} - 2)/r. \quad (2)$$

The parameters in this potential for the Mg^+ ion have been determined by Szaz [10] to be $A = 4.656$ and $b = 1.688$, where both parameters are given in atomic units. At short distances, this potential has a positive barrier that simulates the action of the Pauli exclusion principle and repels the electron away from the nucleus. At long distances, it is an attractive Coulomb potential. Both of the valence electrons in the Mg atom are assumed to experience this same potential. Thus, the total potential for the quasi two-electron system is

$$V(r_1, r_2, r_{12}) = U(r_1) + U(r_2) + 1/r_{12}, \quad (3)$$

where r_1 and r_2 are the distances of valence electrons 1 and 2 from the nucleus and r_{12} is the distance between the two electrons.

Semiclassical calculations of the electronic states of this two-electron system will be carried out by the adiabatic switching method by the same techniques that were used to solve the triatomic molecule vibrational motion problem [5,6]. Hyperspherical coordinates ρ, θ, ϕ are the most convenient for this calculation. They are related to the interparticle distances r_1, r_2 , and r_{12} by:

$$\begin{aligned} r_1 &= \rho \sin(\theta/2), \\ r_2 &= \rho \cos(\theta/2), \\ r_{12} &= \rho [1 - \sin(\theta)\cos(\phi)]^{1/2}. \end{aligned} \quad (4)$$

The hyperspherical coordinates can be interpreted as ordinary spherical coordinates in a three-dimensional space called *configuration space* [11]. Thus, the motion of the two electrons defines a trajectory in this space.

Sometimes it is useful to use Cartesian coordinates in configuration space. These are related to the spherical coordinates in the usual way; i.e., $x = \rho \sin(\theta)\cos(\phi)$, $y = \rho \sin(\theta)\sin(\phi)$, and $z = \rho \cos(\theta)$. Each point in configuration space represents a definite set of values for the three distances r_1, r_2 , and r_{12} . Thus, the potential that is defined by Eqs. (2) and (3) can be mapped onto this space. Figure 1 shows the contours of the potential in configuration space. The contours are shown in two orthogonal planes: the $z = 0$ (or xy) plane and the $y = 0$ (or xz) plane. By merging these two images, one can obtain a good picture of the overall form of the potential in configuration space. The potential is almost cylindrically symmetric with respect to the z axis except in the regions near the positive half of the x axis. Points that fall on the positive x axis represent

configurations in which the electron-electron distance $r_{12} = 0$. Points that lie on the positive z axis represent configurations in which $r_1 = 0$, and points on the negative z axis represent configurations in which $r_2 = 0$. The potential is infinite at these points on the axes and is large and positive in the regions nearby, as is evident from the contour plots. Points that are on the negative x axis represent collinear configurations in which the electrons are at

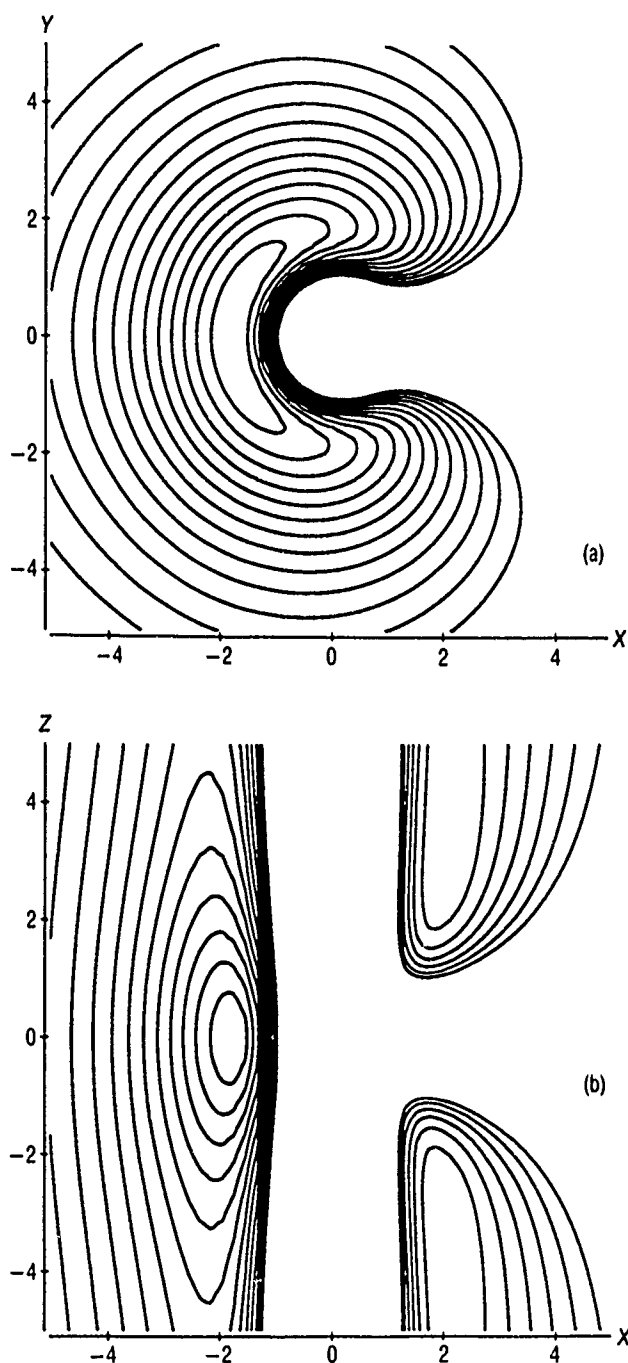


Figure 1. Contour plots of the potential energy surface for the two valence electrons of Mg in hyperspherical configuration space. Lengths are measured in atomic units. Contours are shown on two perpendicular planes, the $z = 0$ plane and the $y = 0$ plane.

equal distance and on opposite sides of the nucleus. It is evident from the contour plots that a stable equilibrium potential minimum exists at a point on this axis. The location of this point is calculated to be $x = -1.77167$, $y = 0$, $z = 0$. The system will execute a stable, bound motion in the region around this potential minimum. Motion in the x direction represents a symmetric stretch, motion in the y direction is an asymmetric stretch, and motion in the z direction represents bending. Thus, we see, even before we carry out any calculations, that the motion will resemble the motion we normally associate with a linear triatomic molecule.

Adiabatic switching calculations are carried out most efficiently in a coordinate system in which the potential contours are most nearly matched to the coordinate surfaces. It is evident from the contour plots that cylindrical coordinates are the most nearly matched to the potential contours. Thus, we define cylindrical coordinates r, ϕ, z , where r and z are defined by the relations $r = \rho \sin(\theta)$ and $z = \rho \cos(\theta)$, and the coordinate ϕ is unchanged from spherical coordinates. In order to carry out dynamical calculations, it is necessary to express the classical Hamiltonian function in these coordinates. We have derived this expression to be

$$H = \frac{1}{2} [4(P_r^2 + \frac{1}{r^2} P_\phi^2 + P_z^2) - 3 \frac{(rP_r + zP_z)^2}{r^2 + z^2}] + V(r, \phi, z), \quad (5)$$

where P_r, P_ϕ, P_z are the momenta conjugate to the coordinates r, ϕ, z . $V(r, \phi, z)$ is the potential energy function expressed in cylindrical coordinates. Heisenberg's equations of motion in these coordinates are then easily derived using this Hamiltonian. A computer program is now being written to carry out the classical trajectory adiabatic switching calculations in the cylindrical coordinate system.

In summary, test calculations were carried out to evaluate a proposed semiclassical correction rule. The tests showed that this rule is not valid for linear systems and therefore cannot be applied to the helium atom, where it is needed to stabilize the classical electron orbits. Rather than continue to search for a good form for the

correction rule for linear systems, it was decided to halt any further attempt to carry out calculations on helium. Instead, effort was concentrated on the quasi two-electron alkaline earth atoms, where no additional correction potential is needed to stabilize the electron orbits. Semiclassical calculations to analyze the magnesium atom are now under way.

* * * * *

1. R. Stephen Berry and Jeffery L. Krause, "Independent and Collective Behavior within Atoms and Molecules," *Adv. Chem. Phys.* **70**, 35 (1988).
2. C. D. Lin, "Doubly Excited States Including New Classification Schemes," *Adv. At. Mol. Phys.* **22**, 77 (1986).
3. Ian C. Percival, "Semiclassical Theory of Bound States," *Adv. Chem. Phys.* **36**, 1 (1977).
4. B. R. Johnson, "On the Adiabatic Invariance Method of Calculating Semiclassical Eigenvalues," *J. Chem. Phys.* **83**, 1204 (1985).
5. B. R. Johnson, "Semiclassical Vibrational Eigenvalues of H_3^+ , D_3^+ , and T_3^+ by the Adiabatic Switching Method," *J. Chem. Phys.* **86**, 1445 (1987).
6. B. R. Johnson, "Semiclassical Vibrational Eigenvalues of H_2O and SO_2 by the Adiabatic Switching Method," *Comput. Phys. Commun.* **51**, 1 (1988).
7. R. E. Langer, "On Connection Formulas and the Solutions of the Wave Equation," *Phys. Rev.* **51**, 669 (1937).
8. R. Crandall, R. Whitnell, and R. Bettega, "Exactly Soluble Two-Electron Atomic Model," *Am. J. Phys.* **52**, 438 (1984).
9. L. Szasz, *Pseudopotential Theory of Atoms and Molecules*, Wiley, New York (1985).
10. L. Szasz, *Pseudopotential Theory of Atoms and Molecules*, Wiley, New York (1985), p. 88.
11. B. R. Johnson, "On Hyperspherical Coordinates and Mapping the Internal Configurations of a Three Body System," *J. Chem. Phys.* **73**, 5051 (1980).

Physics and Chemistry of Metal-Semiconductor Clusters

S. M. Beck,
Chemistry and Physics Laboratory

Over the last 10 years, the interest in small clusters of atoms has increased dramatically. One factor for this increased interest is experimental technology. Superson-

ic molecular beam techniques have provided an effective method for preparing small, cold, atomic and molecular clusters [1]. However, a more comprehensive reason lies

in the broad range of scientific and technological disciplines to which clusters are relevant. From solid-state physics and materials science to solution chemistry and catalysis, clusters play a vital role. By studying clusters, basic scientific questions associated with the formation and properties of the condensed phase can be investigated on an atomic or molecular scale. The ability to define and study clusters as a function of their size and composition provides insight into the condensed phase at an unprecedented level of detail.

Associated with the many purely scientific questions regarding clusters are issues relevant to several important technological areas. Much of the interest in small metal clusters finds its roots in chemical catalysis. The high surface-to-volume ratio of the cluster, as well as its size-dependent chemical reactivity, promises new and more effective catalysts. For instance, a recently developed form of an iron oxide catalyst used in composite solid propellents for rocket motors consists of small particles with diameters on the order of 30 Å [2]. Although this would be considered a huge cluster, the small particles have much larger surface-to-volume ratios than the conventional catalyst and thus a higher efficiency.

Just as catalysis has driven the study of metal-containing clusters, solid-state electronics and optics technologies have motivated the study of semiconductor clusters. Our work on semiconductor and mixed metal/semiconductor clusters was conceived from this viewpoint. The objective of our work is to gain a better understanding of the chemical bonding interactions within a semiconductor and between a metal and a semiconductor by studying small semiconductor-metal clusters. The cluster, which is amenable to detailed experimental and theoretical study, provides a well-defined model for the bulk interactions. In the past, we have developed techniques for producing and studying the bonding interactions in small clusters of silicon and silicon mixed with a single transition metal atom [3,4]. It was discovered that the addition of a single metal atom to the silicon fundamentally changed the chemical bonding in the entire cluster. Close analogies were discovered between the structure of the mixed metal-silicon cluster and metal impurities in bulk silicon. Also, the first observation of a phase transition in a covalently bonded cluster was made in small silicon clusters [5]. It was determined that this transition occurred at a temperature below the bulk melting temperature but near the temperature where a specific surface reconstruction of silicon melts.

During this past year, we focused on developing experimental techniques for spectroscopic observation of small cluster ions. Spectroscopy is the primary tool for understanding geometric and electronic structure of small molecules. Despite the importance of obtaining spectra, only a small number of metal dimer [6] and trimer [7] structures have been determined. No experimentally determined spectrum from a semiconductor cluster has

been reported. Therefore, as a step toward understanding metal-semiconductor cluster structures, we have been applying the experimental technique of mass-selected photofragmentation spectroscopy to small semiconductor cluster ions.

The technique relies on the principle of multiphoton fragmentation as a means of detecting photon absorption. A mass-selected cluster ion beam is crossed with a tunable dye laser beam. When the dye laser wavelength is resonant with a rovibronic transition of the cluster, energy is absorbed by the cluster, causing it to dissociate. The charged fragments of the cluster are collected and detected. A spectrum is generated by monitoring the fragment signal as a function of the dye laser wavelength. Only recently have we completed upgrades to our experimental apparatus that allow for efficient signal averaging. This is crucial because the signal strengths are weak and the cluster source is inherently unstable. We have scanned wavelength regions in the visible and ultraviolet, looking for sharp structure from Si_2^+ and Si_3^+ . No assignable structure has been observed, but an increase in the fragmentation cross section of more than a factor of 2 was observed in changing from visible to ultraviolet fragmentation wavelengths. This is in accord with recent theoretical calculations, which indicate that Si_2^+ has an allowed, but broad, transition in the ultraviolet [8]. As these studies continue we plan to search for spectra of small silicon clusters containing single transition metal atoms.

We have also studied the production and fragmentation behavior of the technologically important III-V semiconductor material, indium phosphide (InP). This semiconductor holds promise for space applications in solar cell and microelectronic technology. Our interest has been in comparing the bonding characteristics in this ionic compound semiconductor with those we have measured for silicon.

Figure 1 shows the mass-spectra obtained from laser vaporization of InP in the supersonic nozzle. The upper spectrum was obtained by directly extracting the positive ion clusters produced in the source. The lower spectrum was obtained by 193-nm photoionization of the neutral clusters produced in the source. Both spectra show that the most common ion and neutral constituents in the source are indium clusters containing from zero to three phosphorus atoms. Apparently, there is no preference for formation of clusters with the same stoichiometry as the bulk semiconductor, which contains equal numbers of indium and phosphorus atoms. Interestingly, the mass distributions are also different from those observed for GaAs [9], another III-V semiconductor material. GaAs clusters were formed with a statistical (binomial) distribution of compositions, with no preferential bonding for As or Ga. The low phosphorus content observed in the InP clusters is attributed to a generally weak In-P bonding interaction. This is consistent with bulk InP, which evapo-

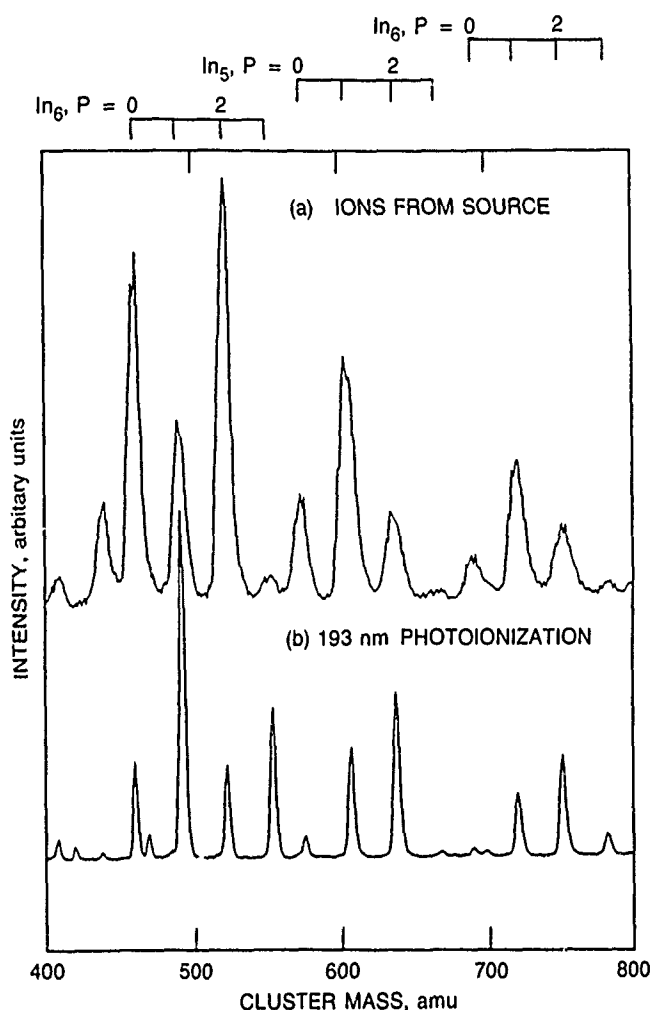


Figure 1. Mass spectra obtained by laser vaporization of an InP target wafer in the throat of a supersonic nozzle. The assignment of each cluster mass peak for both spectra is indicated above the upper spectrum. (a) Spectrum of ions extracted directly from the source; (b) mass spectrum obtained by 193-nm photoionization of the neutral clusters emitted by the source.

rates noncongruently, evolving P_2 at temperatures well below those where In atoms evaporate. However, the photofragmentation results of InP clusters discussed here show that the one or two phosphorus atoms attached to the clusters are strongly bound.

The $In_x P_{1,2}$ cluster distributions shown in Figure 1 present an interesting anticorrelation with respect to each other. The distribution of ions from the jet shows higher intensities for clusters containing even numbers of atoms (e.g., $In_4 P_2^+$, $In_5 P^+$), whereas the neutral clusters show higher intensities for the odd atom clusters; e.g., $In_4 P$, $In_5 P_2$. The origin of this relationship is not certain but likely derives from electronic considerations. The cluster ions and neutrals have the same anticorrelation between the even/odd parity of number of atoms and electrons in the cluster. Regardless of whether the cluster is neutral or charged, clusters with a total odd number of electrons

appear as more intense peaks in the mass spectra. This intensity alteration is dependent only on the electron number and not the identity of the atoms. Electron number dependencies of cluster stability have been observed previously for mixed clusters of main group metals [10]. However, the exact formula invoked in the case of the main group metal clusters relating electron number to increased stability does not fit our observed spectra.

Bonding in the small indium phosphide clusters was probed in greater detail by mass-selected photofragmentation experiments. The cluster ion $In_4 P_2^+$ was selected to be fragmented using photons in the visible (532 nm) and the near ultraviolet (355 nm). Figure 2 shows the resulting fragmentation difference spectra, obtained by subtracting the ion signal with the fragmentation laser on from the signal with the laser off. Negative peaks show a depletion of the parent ion, and positive peaks show production of daughter ions due to the presence of the fragmentation laser. The upper spectrum shows that the fragmentation pathway of $In_4 P_2^+$ at 532 nm is loss of In^+ and not loss of a phosphorus-containing component. The lower spectrum shows the results of using more energetic

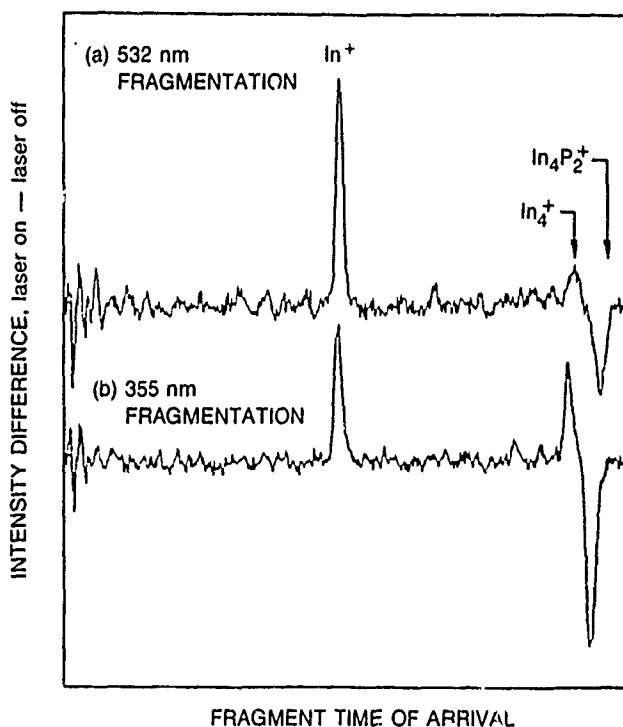


Figure 2. Fragmentation difference spectra of mass-selected $In_4 P_2^+$ clusters at two different fragmentation photon energies. The cluster ion is extracted directly from the source. The negative-going peaks result from parent ion depletion due to photofragmentation. The positive-going peaks are due to the production of daughter ions by the fragmentation process (a) Spectrum resulting from 532 nm fragmentation with almost exclusive production of In^+ daughter ion shown; (b) spectrum resulting from 355 nm photofragmentation. Two fragmentation channels are apparent: loss of In^+ and loss of neutral P_2 .

ultraviolet photons for fragmentation. The higher-energy photons allow access to a higher-energy dissociation channel, loss of neutral P_2 . These results appear to contradict the arguments of weak In-P bonds previously presented to explain the observed In-rich cluster distribution. Apparently, more than a single type of In-P interaction is present in these small clusters. Further work is under way to clarify this issue.

In summary, we have developed the hardware and software to carry out spectroscopic studies of bare semiconductor and mixed metal-semiconductor cluster ions. These techniques were applied to the study of small silicon cluster ions, which showed a broad increase in absorption cross section in the ultraviolet. We have also investigated the bonding interactions in small clusters of the III-V compound semiconductor InP using techniques of mass spectroscopy and mass-selected photofragmentation. Next year we plan to exploit our spectroscopic capabilities in pursuit of the spectra of small cluster ions. Also, we will continue our studies of III-V compound clusters, including GaAs, InP, GaP, and InAs, in order to gain insight into the relative importance of electronic configuration, ionic size, polarizability, and electronegativity effects in the bonding of these species.

* * * * *

1. T. G. Dietz, M. A. Duncan, and R. E. Smalley, "Laser Production of Supersonic Metal Cluster Beams," *J. Chem. Phys.* **74**, 6511 (1981).
2. T. P. Rudy, F. R. Goodson, and E. J. Shanabrook, *Superfine Iron Oxide Burning Rate Catalyst*, CPIA Publication No. 515, Vol II, p. 231.
3. S. M. Beck, "Studies of Silicon Cluster-Metal Atom Compound Formation in a Supersonic Molecular Beam," *J. Chem. Phys.* **87**, 4233 (1987).

4. S. M. Beck, "Mixed Metal-Silicon Clusters Formed by Chemical Reaction in a Supersonic Molecular Beam: Implications for Reactions at the Metal/Silicon Interface," *J. Chem. Phys.* **90**, 6306 (1989).
5. S. M. Beck and J. M. Andrews, "Phase Transition Behavior Observed in Small Silicon Cluster Ions," *J. Chem. Phys.* **91**, 4420 (1989).
6. D. E. Powers et al., "Supersonic Metal Cluster Beams: Laser Photoionization Studies of Cu_2 ," *J. Phys. Chem.* **86**, 2556 (1982).
7. M. Broyer et al., "Spectroscopy of Vibrational Ground-State Levels of Na_3 ," *J. Phys. Chem.* **91**, 2626 (1987).
8. P. J. Bruna et al., "Theoretical Prediction of the Potential Curves for the Lowest-Lying States of the CSi^+ and Si_2^+ Molecular Ions," *J. Chem. Phys.* **74**, 4611 (1981).
9. S. C. O'Brian et al., "Supersonic Cluster Beams of III-V Semiconductors: Ga_xAs_y ," *J. Phys. Chem.* **84**, 4074 (1986).
10. M. B. Bishop et al., "Growth Patterns and Photoionization Dynamics of In/Sb and In/Bi Intermetallic Clusters," *J. Phys. Chem.* **93**, 1966 (1989).

Beck, S. M., "Photophysics of Bare and Metal Containing Semiconductor Clusters," *Advances in Metal and Semiconductor Clusters*, M. A. Duncan, ed., JAI Press, Inc., Greenwich, Conn. (in press).

Spin Effects In Electron-Atom Collisions

B. Jaduszliwer and Y. C. Chan,
Chemistry and Physics Laboratory

A multiyear project is under way to study electron scattering on cesium atoms under conditions in which the spin states of both particles are known before and after the collision. The project will focus on collision processes in which spin exchange and spin-orbit coupling are both significant. In this way, new knowledge will be gained about the role of spin in electron-atom collisions. This project requires the development of new technologies to prepare an atomic cesium beam in a well-defined spin

state, and to detect the spin state of the atom after a collision with an electron. Technology development and hardware construction and testing for this project have been substantially completed.

In conventional scattering experiments, performed without measurement of the spins of the collision partners, effects depending on the relative orientation of electronic and atomic angular momentum and spin are washed out by averaging over all the possible initial states

of the system and summing over all the allowed final states. In order to obtain all the information that an electron-atom collision experiment can yield about the dynamics of atomic interactions, the spin states of electron and atom must be determined before and after the collision, in the manner known as the *perfect scattering experiment* [1].

Pauli's exclusion principle may introduce a dependence of the collision cross section on the electron and atom spins even in the absence of explicit spin-dependent interactions. This phenomenon has been investigated by performing experimental studies of electron collisions with sodium and potassium atoms [2], which have a tight closed-shell electronic core and a single *s*-state valence electron. In this case, exclusion will cause the effective electron-atom interaction to depend on whether the valence and projectile electrons are in a triplet or a singlet state, thus leading to different scattering cross sections. The total spin of the system is conserved by these spin exchange processes.

Magnetic (relativistic) interactions couple orbital and spin angular momenta, introducing interactions that depend explicitly on the atomic and electron spins, and opening up scattering channels that may not conserve total system spin. The strength of these interactions is proportional to Z^4 (the nuclear charge is $+Ze$), and so these processes become important for high- Z atoms. For the foregoing collisions, with sodium and potassium as target atoms, such processes are essentially negligible. They can be isolated from exchange effects by using atomic targets with no unpaired electrons; electron collisions with mercury atoms have been studied extensively [3] in this context.

Let us consider now electron scattering by a high- Z atom with unpaired valence electrons. Exchange and

magnetic interactions may both play significant roles in this case, and a wealth of unexplored, new physics will be present in such a collision system. For the types of atomic targets discussed before, two independent scattering amplitudes suffice to describe completely an elastic collision, but it has been shown [4] that, for this system, six independent scattering amplitudes may be required to describe that process. We have chosen cesium as the atomic target in a program to investigate this type of collision system. Cesium has a sufficiently high atomic number Z for relativistic effects to be significant in collisions with electrons; it also has the electronic configuration of an alkali metal atom, thus simplifying the study of the exchange aspects of spin effects.

Performing perfect scattering experiments involving electron collisions with cesium atoms involves the use of spin-polarized electron and atomic beams, as well as substantial post-collisional spin-polarization measurements. However, unpolarized substantial advances can be made with polarized atoms and unpolarized electrons. In our early experiments, we use an unpolarized electron source.

The experimental arrangement is shown schematically in Figure 1. It is based on the atomic recoil technique [5], in which post-collisional observations are made on the recoiled atom rather than on the scattered electron. During the first 3 years of this project, we built the atomic beam apparatus required to carry out these investigations, and developed and demonstrated the novel optical techniques (Figure 2) required to spin-polarize the cesium atomic beam and perform spin-state selective detection of the recoiled cesium atoms. Using these techniques, last year we produced and spin-analyzed a cesium atomic beam with an electron spin polarization of better than 80% (Figure 3). This experimental apparatus was also

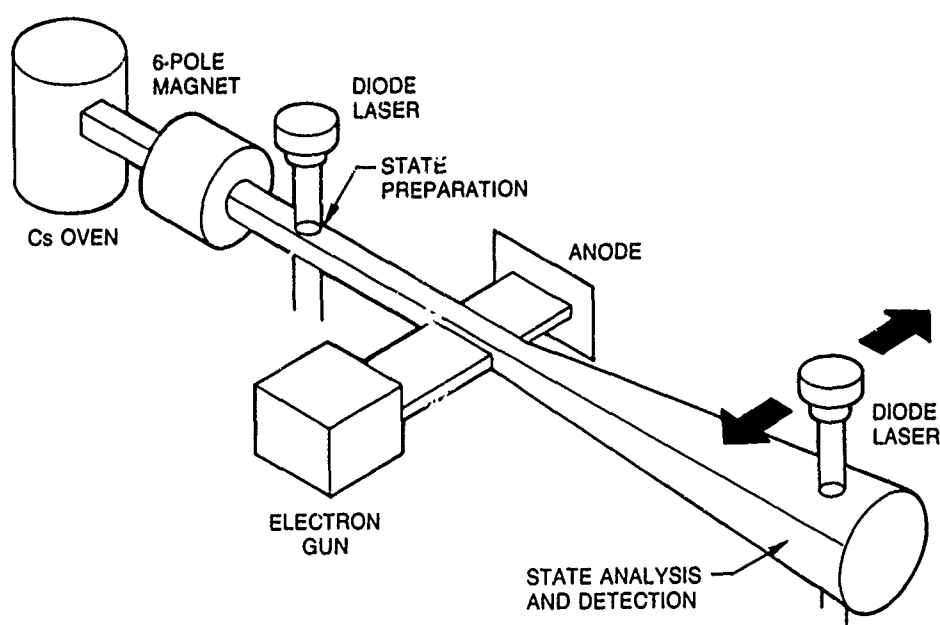


Figure 1. Experimental arrangement. The cesium atomic beam source is an effusive oven. A hexapole magnet provides focusing and velocity-selects the beam. After optical state preparation, the cesium atoms collide with electrons in the collision region. The recoiled cesium atoms are state-analyzed and detected by laser-induced fluorescence.

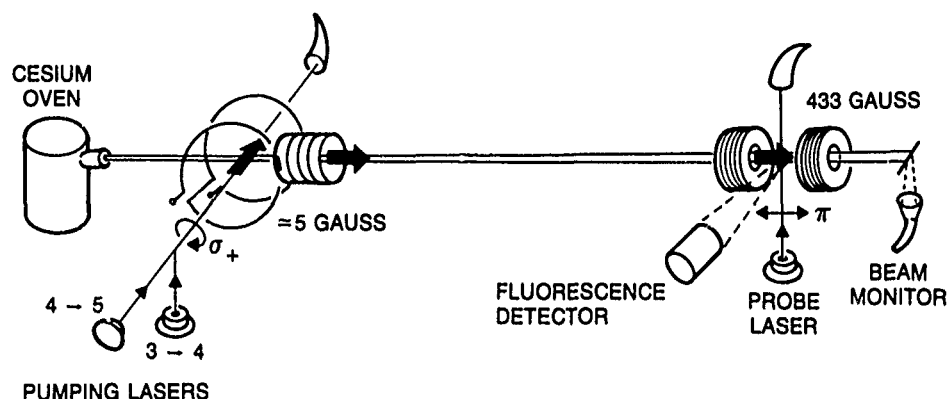


Figure 2. Optical state preparation and state-sensitive detection. Two circularly polarized diode lasers transfer essentially all the cesium atoms in the beam to the $F = 4$, $M = 4$ hyperfine state (with 100% valence electron spin polarization) by optical pumping. The two coils provide the quantization axis, transverse to the beam in the

optical pumping region and axial downstream. A 433 gauss field in the detection region allows for separate detection of atoms in each azimuthal state by providing enough Zeeman splitting of the hyperfine transitions.

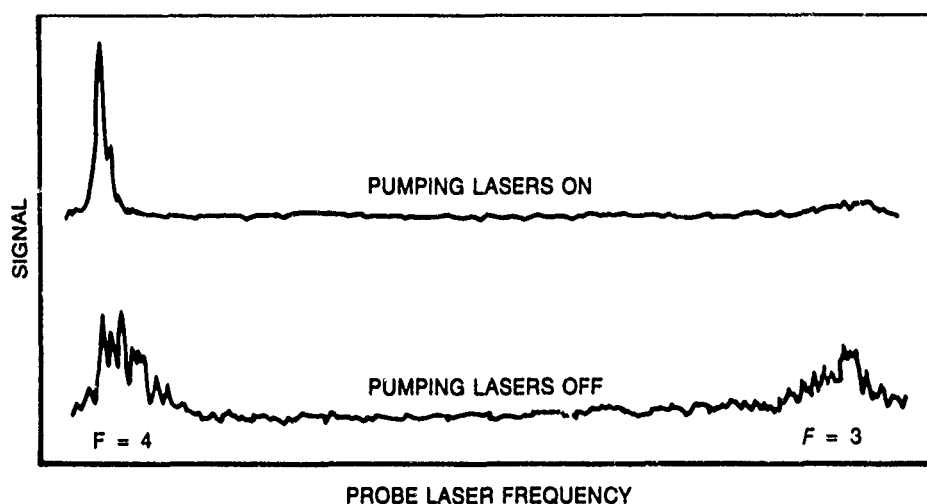


Figure 3. Atomic beam fluorescence signal (arbitrary units) vs detector laser frequency; the full frequency scan is approximately 10 GHz wide. Lower trace: state-preparation lasers off. Many emission peaks in both the $F = 3$ and $F = 4$ manifolds signal that all the hyperfine sublevels of the ground state are populated. Upper trace:

state-preparation lasers on. All peaks have been essentially quenched, except for one that has been greatly enhanced; this peak is the signature of the $F = 4$, $M = 4$ sublevel. The area under this peak indicates that at least 90% of the atoms in the beam are in that state, corresponding to an atomic spin polarization greater than 80%.

used to investigate optical state preparation and analysis techniques being considered for advanced cesium beam atomic frequency standards, of interest for satellite systems such as Global Positioning System (GPS) or Milstar.

This past year we installed in the collision chamber of our apparatus a planar geometry electron beam system, designed in this laboratory, that uses an alkaline-earth oxide cathode to provide an unpolarized electron beam with the required intensity and momentum-spread characteristics to perform scattering experiments at low energies. This system is shown schematically in Figure 4. It incorporates a retarding-field analyzer at its back end which, together with auxiliary electronics, can be used to

measure the electron energy distribution. A typical electron beam energy distribution measured using this technique is shown in Figure 5.

In our apparatus, the electron and atomic beams are orthogonal to each other (Figure 6). After a collision occurs, the electron motion is conventionally described in terms of the polar scattering angle θ and azimuthal scattering angle ϕ , where the polar axis z is given by the direction of the electron beam. The atom is recoiled by angles ψ , measured in the plane of the incident beams, and χ , measured in the orthogonal plane. These angles are usually very small, since at the energies these experiments are performed the atomic momentum in the laboratory

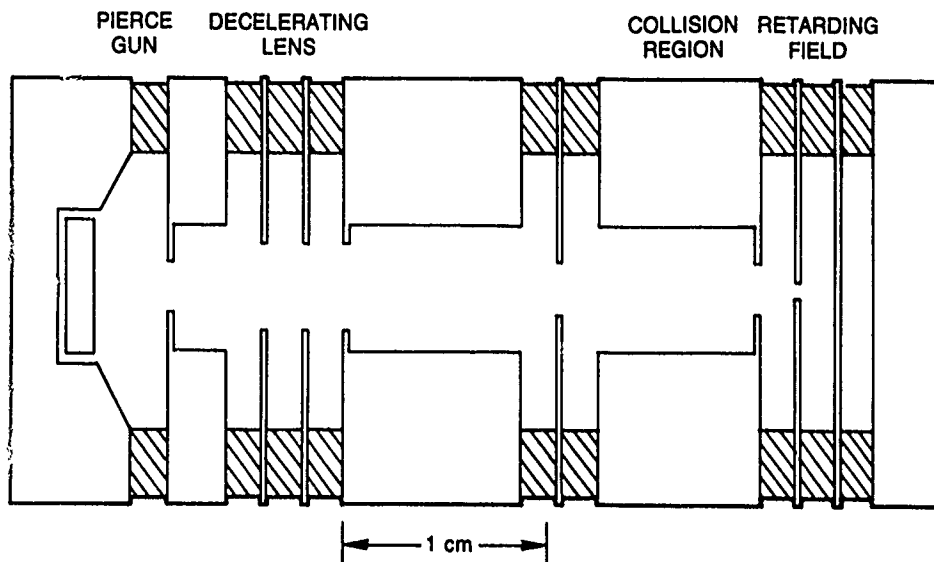


Figure 4. Schematic view of the planar geometry electron beam system, consisting of a Pierce gun using an alkaline-earth oxide cathode, a decelerating lens, an equipotential collision region, and a retarding-field electron energy analyzer. Hatched regions are ceramic spacers.

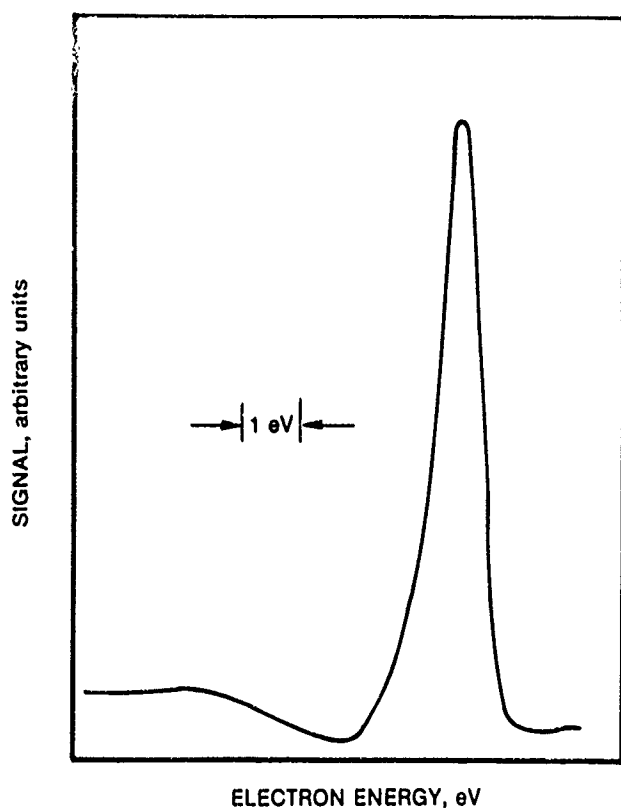


Figure 5. Typical electron beam energy distribution, measured by the retarding field technique. The energy spread is 500 meV full width at half maximum.

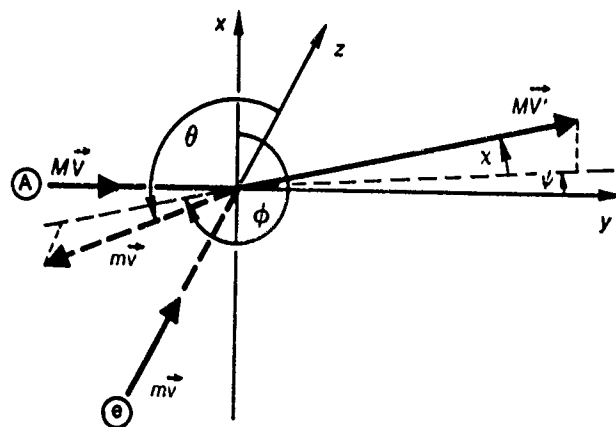


Figure 6. Collision kinematics. The atomic beam is incident along the y-axis, with momentum of magnitude MV . The electron beam is incident along the polar axis z , with momentum of magnitude mv . After the collision, the electron is scattered by polar angle θ and azimuthal angle ϕ ; the atom is recoiled by angles ψ (in the plane of the beams) and χ (in the orthogonal plane).

frame is much larger than the electron momentum. The electron scattering and atomic recoil angles are illustrated in Figure 6. Due to the energy and momentum conservation laws, it is easy to show that atomic recoil angles and electron scattering angles are related by

$$\psi \approx \frac{mv}{MV} - \frac{mv'}{MV} \cos \theta \quad (1)$$

and

$$\chi \approx \frac{mv'}{MV} - \sin \theta \sin \phi, \quad (2)$$

where mv and MV are the magnitudes of the electron and atom momenta before the collision, and mv' is the magnitude of the electron momentum after the collision. Interpretation of our scattering data thus requires the determination of these quantities. The magnitude of the electron momentum is of course related to the electron kinetic energy E ; the determination of the magnitude of the atomic momentum requires the measurement of the atomic speed.

Since the electron gun cathode is held at ground potential, when the target electrode is held at V_T the kinetic energy of the electrons in the collision region is $E = e(V_T - \Delta\Phi)$, where $\Delta\Phi$ is the contact potential difference between cathode and target electrode. This contact potential difference is not known *a priori* and, furthermore, it may change slowly with time. Thus, determination of the electron kinetic energy requires the periodic measurement of $\Delta\Phi$. This past year we developed a technique that allows us to do that.

In our scattering apparatus, the detection chamber and the drift tube connecting it to the collision chamber can be rotated about the region where the collisions occur, allowing us to measure the angular distribution of recoiled atoms in the plane of the intersecting beams. In addition to the state-sensitive optical detector mentioned previously, the detection chamber also contains a high-efficiency surface ionization atomic detector, which can be used to measure those angular distributions without spin-state discrimination. Figure 7 shows such an angular distribution, obtained at 6.15 eV electron energy and measured by chopping the electron beam at 17 Hz and performing phase-sensitive detection of the atomic beam signal from the surface ionization detector. Detector position z and atomic recoil angle ψ are related by $z = \psi L$, where L is the distance between the collision region and the detector. The prominent positive peak is the signature of forward electron scattering after resonant impact excitation of a cesium atom [6]. The position of the peak z_0 can be obtained by setting $\theta = 0$ in Eq. (1):

$$z_0 \approx \frac{mv}{MV} - \frac{mv'}{MV} = \frac{(2m)^{1/2}}{MV} [E^{1/2} - (E - E^*)^{1/2}], \quad (3)$$

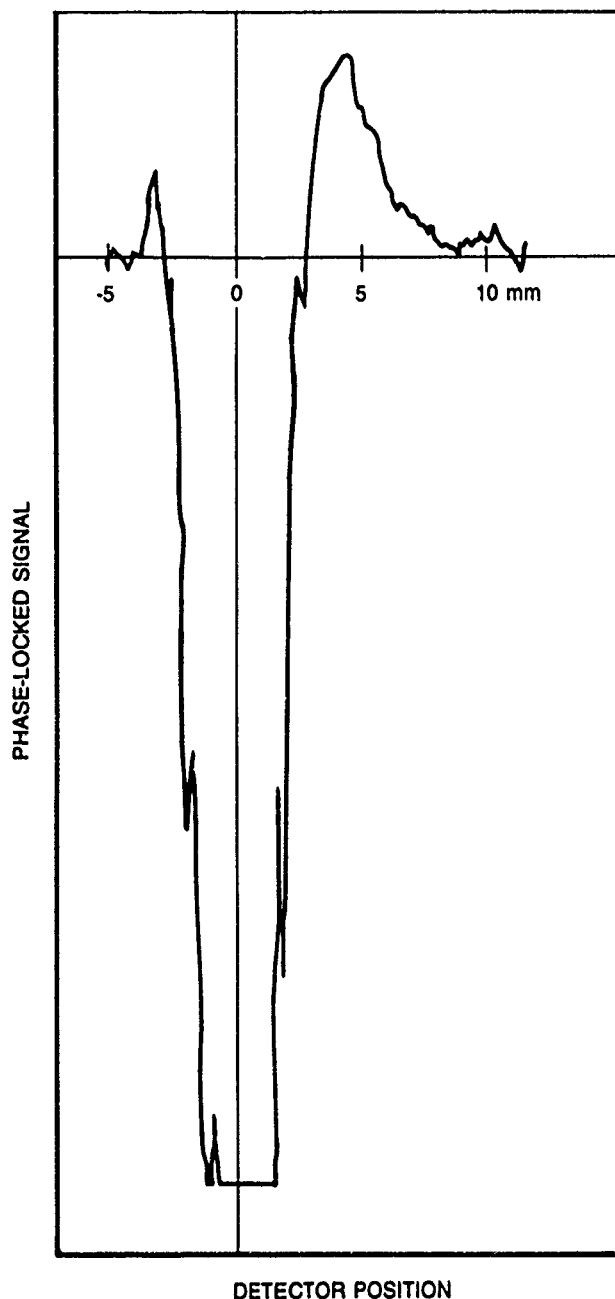


Figure 7. Atomic beam signal, phase-locked to the chopped electron beam (arbitrary units) vs surface ionization detector position. The large negative signal near the origin indicates that when the detector is in the direct path of the atomic beam, fewer atoms reach the detector as the electron beam is turned on, showing that atoms are being recoiled away from the detector. When the detector is moved outside the atomic beam, the phase-locked signal becomes positive, showing that atoms are being recoiled into the detector. The prominent peak at $z = 4.3$ mm is the signature of forward inelastic electron scattering. These data were taken at 6.15 eV electron energy.

where E^* is the resonant excitation energy; $E^* = 1.45$ eV for cesium. Equation (3) can then be used to determine the atomic speed V . We have shown that this technique obtains consistent results for V when varying the incident electron energy. Thus, this technique also provides a consistency check on our determination of the electron kinetic energy E .

We are now using our scattering apparatus to measure total scattering cross sections between 6 and 20 eV. Total electron-cesium scattering cross sections have been previously measured by Visconti and co-workers [7] at lower energies, so our experiments will expand the known cross-section range into the so-called intermediate energies, where the few-states close-coupling approximations used to calculate accurate cross sections at low energies become very poor, whereas high-energy calculational techniques like the Born approximation or its variants can not yet be used. In addition, by overlapping existing measurements we will also verify our apparatus and technique against possible systematic errors. Figure 8 shows some preliminary results, which are in reasonable agreement with existing measurements.

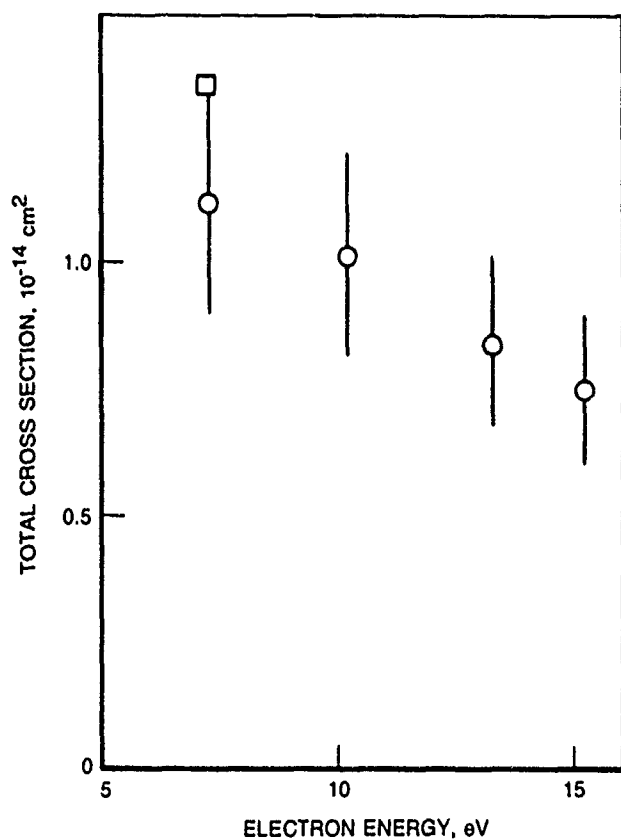


Figure 8. The open data points give our preliminary total cross section results for electron collisions with cesium atoms in the energy range of 7 to 15 eV. The error bars give only rough estimates of the actual errors in these measurements. The rectangular point gives a

result of Visconti and co-workers [7], included for comparison purposes.

After these total cross-section measurements are completed, we will be well positioned to start our first measurements of electron-cesium atom spin-selected cross sections to elucidate the role of spin in this very interesting collision system.

* * * * *

1. B. Bederson, "The Perfect Scattering Experiment," *Comments At. Mol. Phys.* **1**, 41 (1969).
2. B. Bederson and T. M. Miller, "Electron Scattering on Alkali Atoms," *Electron and Photon Interactions with Atoms*, H. Kleinpoppen and M. R. C. McDowell, eds., Plenum Press, New York (1976), p. 191.
3. J. Kessler, "Electron Spin Polarization by Low Energy Scattering from Unpolarized Targets," *Rev. Mod. Phys.* **41**, 3 (1969).
4. P. G. Burke and J. B. Mitchell, "Spin Polarization in the Elastic Scattering of Electrons by One-Electron Atoms," *J. Phys. B* **7**, 214 (1979).
5. R. Collins, B. Bederson, and M. Goldstein, "Differential Spin Exchange and the Elastic Scattering of Low Energy Electrons by Potassium," *Phys. Rev. A* **3**, 1976 (1971).
6. B. Jaduszliwer et al., "Small Angle (e^- , Na) Scattering in the 6-25 eV Range," *Phys. Rev. B* **30**, 1255 (1984).
7. P. J. Visconti, J. A. Slevin, and K. Rubin, "Absolute Total Cross Sections for the Scattering of Low-Energy Electrons by Rubidium, Cesium, and Potassium," *Phys. Rev. A* **3**, 1310 (1971).

Camparo, J. C., et al., "Injection Current Calibration of Diode Laser Wavelengths," *Opt. Commun.* **70**, 416 (1989).

Jaduszliwer, B., "Optical Hyperfine State Preparation and Analysis," *Bull. Am. Phys. Soc.* **31**, 1259 (1987).

_____, "Optical State Preparation and Analysis for Spin Effects Studies in Electron-Cesium Collisions," *Electronic and Atomic Collisions*, J. Geddes et al., eds., International Conference on the Physics of Electronic and Atomic Collisions, United Kingdom (1987), p. 811.

Atmospheric
Physics
and
Astronomy

ATMOSPHERIC PHYSICS AND ASTRONOMY

High-Resolution Infrared Technology and Applications

R. W. Russell, J. A. Hackwell, D. K. Lynch, G. S. Rossano, and R. J. Rudy,
Space Sciences Laboratory

Both productive research programs and the development of the high level of technical expertise necessary to support system applications in the areas of advanced infrared sensors and remote measurement programs from space and airborne platforms are exemplified in the accomplishments under this project during the past year. The successful field use of new sensors is the proof of the performance promised by state-of-the-art design: new Aerospace-developed sensors provided high-quality measurements of a variety of celestial sources, which led to a number of significant discoveries. At the same time, the experience necessary to constructively contribute to spacecraft and space-based systems and sensor designs was acquired. Techniques, methodologies, and requirements for calibration were all developed through this active research program with direct application to several Space Defense Initiative Organization and Space Systems Division programs.

Significant accomplishments this past year included:

- Five successful observing runs with the new Broad-band Array Spectrograph System (BASS).
- High-quality thermal infrared spectroscopy of four comets.
- Studies of several type-Ia supernovae.
- Studies of a variety of other celestial sources at wavelengths from the visible through the long-wavelength infrared (LWIR).

The BASS was completed at the end of last year. Its unique design permits covering the entire 2.9- to 13.5- μ m region simultaneously without moving parts by using 116 detectors in two linear arrays of 58 elements each. The instrument is described in detail in two published papers [1,2], but we note here that the design is optimal for use in

an airborne program, where there is very limited time for measurements or the source may be varying in time (or both). Because of atmospheric absorption in many regions of the infrared, certain types of observations can only be carried out by airborne or spaceborne sensors. Our proposal for BASS observing time next year on NASA's Kuiper Airborne Observatory (KAO) received an excellent rating and was approved for four flights. Prior to conducting such a program, or even being approved for one, the successful operation of the instrument on a ground-based telescope was essential. During the past year, four trips were made to the 1.5-m (60-in.) infrared telescope on Mt. Lemmon, which is partially supported by the Air Force through the Space Surveillance and Tracking System Program Office, and one trip was made to the 3-m NASA Infrared Telescope Facility (IRTF) on Mauna Kea in Hawaii.

The first two runs at Mt. Lemmon were essentially engineering tests during which the performance of the instrument was delineated and system problems addressed. Significant improvements were made in our understanding of techniques for the optical alignment of the cooled fore-optics module in the dewar that allows us to change from one f-ratio to another in order to adapt to a variety of telescopes. The system noise was shown to be background-limited, and a scattered light problem was identified on the shorter-wavelength array. A new baffle has been designed and will be installed next year. Some electrical problems were solved by redesigning and implementing an improved grounding scheme. As a result, the observing runs in the latter part of the year produced excellent long-wave spectroscopy of a wide variety of celestial sources, including Comet Levy, Neptune, Saturn's disk and rings, variable stars, calibration stars, and circumstellar shells around supergiants. Because the

BASS acquires the entire spectrum at one time, we were also able to step the beam across two extended, ionized nebular regions. This permitted the characterization of dust temperature and spectral structure as a function of position in the nebula. Analysis of the spectra of all these different sources has begun.

Not the least of the many important features of the BASS is its efficiency. Spectra that previously would have taken 20 min to 3 h have been acquired in only 4 to 20 min. Entire classes of sources can now be studied, where previously only the brightest few members could be investigated. The new ease with which cometary studies can now be made illustrates this point well.

Comets have been shown to provide a source, probably ultimately the major source, of the zodiacal dust cloud that pervades interplanetary space. Emission by this dust provides the fundamental background limit against which all space-based sensors must operate. Furthermore, because comets are believed to represent frozen material from the protosolar nebula, studies of the composition and physical nature of cometary dust can improve our understanding of solar system evolution and the possible link between interstellar and solar system dust. For these reasons, we have made an effort to study most of the comets that have appeared in the last 5 years.

The only comet with a periodic orbit similar to that of Halley's Comet is Comet Brorsen-Metcalf (CBM), which reappeared this past year. Observations of CBM have provided a test of our model for comet properties based on orbit type; i.e., periodic versus first-time solar encounters. In addition, three other comets with orbits resulting in only one apparition (*one-time comets*) or at least exhibiting very long periods were investigated through their thermal infrared spectral shapes: Okazaki-Levy-Rudenko (OLR), Austin, and Levy. Based on our earlier studies of periodic Comet Halley and such first-time comets as Bradfield and Wilson, we had developed a picture of comets that attempted to qualitatively predict their temporal behavior and spectral shape. We predicted that the periodic comets would have lost most of the volatile surface material because of their frequent passages near the sun, leaving behind a sticky, crusty layer of dark, probably carbonaceous material that might well be organic in nature. As the solar insolation increased during the progress of an apparition, heat would cause volatile material below the surface to build up pressure in pockets that would burst periodically, resulting in dramatic time variability. Silicate materials on or near the surface would be heated during each of the periodic apparitions by the close passage by the sun, and some of the amorphous silicate material would undergo a phase change to a more crystalline material. Crystalline silicate grains can be identified because they produce a much more structured infrared signature than amorphous material. In contrast, first-time comets would tend to brighten more regularly as the surface outgassing steadily increased with rising tempera-

ture during the approach to the sun. As the surface material was not envisioned as having been heated previously, the grains were expected to be amorphous and the resulting infrared spectra to be smooth. Contrary to this model, however, periodic comet CBM exhibited no silicate emission, much less structured silicate emission. Instead, we measured a smooth blackbody continuum typical of graphite or amorphous carbon grains. There was no significant variability in the light curve, either, a distinct contrast with the extremely variable behavior previously exhibited by Halley. In contrast, our observations of first-time comets Levy (Figure 1) and OLR showed that silicate emission was definitely present from beyond 1 AU (i.e., outside of the earth's orbit) to very close to the sun. Further, comet Levy exhibited the two slope changes in its spectrum, also seen in Halley's Comet, which have been attributed to partially crystalline olivine. The accumulation of observational data thus shows that the composition of comets and the nature of their temporal behavior is quite variable and does not exhibit a simple dependence on orbital period or solar processing. This points up the need for studies of a broad sample of comets, not just the few brightest ones. The capability to do this is now in place, as demonstrated with the BASS instrument during the August observing run at the IRTF when the bright Comet Levy (1990c) was measured in 4 min with signal to noise as good as any published cometary spectrum (Figure 1). The spectra on Comet Levy all showed the double-peaked structure seen in Figure 1, which is very similar to the spectra we obtained of comet Bradfield and other investigators obtained on Halley. It is indicative of partially crystalline grains basically of olivine composition. A comet about 50 times fainter than Levy was measured with fair signal to noise in only 20 min; analysis of this source will be carried out next year. Our group is now responsible for more than half of the existing thermal infrared spectra of comets, and our use of laboratory data on cosmic dust analogs to supplement our cometary spectral analysis puts us in a unique position to make further significant contributions in this field as we acquire spectroscopy of a more complete sample of comets.

The near infrared ($\sim 0.7\text{--}1.35\text{ }\mu\text{m}$) Ge grating system is maturing; significant improvements in the precision and repeatability of the grating drive, coupled with improved installation and alignment techniques at the telescope, resulted in greater sensitivity and an enhanced productivity. One example of the sources studied this past year is MWC 560, a peculiar emission line object believed to be a symbiotic binary star system that episodically ejects material at velocities from 500 to 5000 km/s. Symbiotic variables are believed to consist of an older, giant star that is losing mass and a smaller, hotter star that contributes ultraviolet flux, powers emission lines, and may be accreting some of the material ejected by the companion. The precise nature of the stars involved is not well understood, not even their spectral types are known well. Moderate to

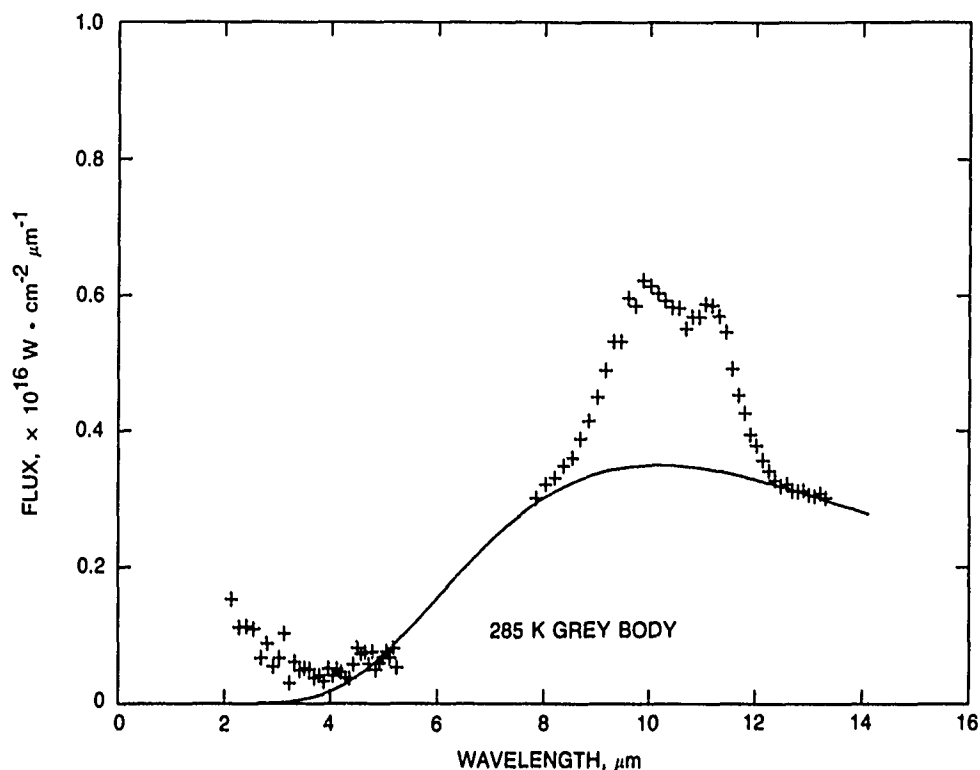


Figure 1. One of several spectra of a bright new comet, Comet Levy (1990c), obtained with the Broadband Array Spectrometer System (BASS) from the NASA Infrared Telescope Facility (IRTF) on Mauna Kea in August 1990. The gaps and noisy data between 5 and 7 μm are due to strong atmospheric absorptions produced by water vapor and methane in this spectral region. The rising tail at short wavelengths is solar light scattered by the dust grains in the coma, or

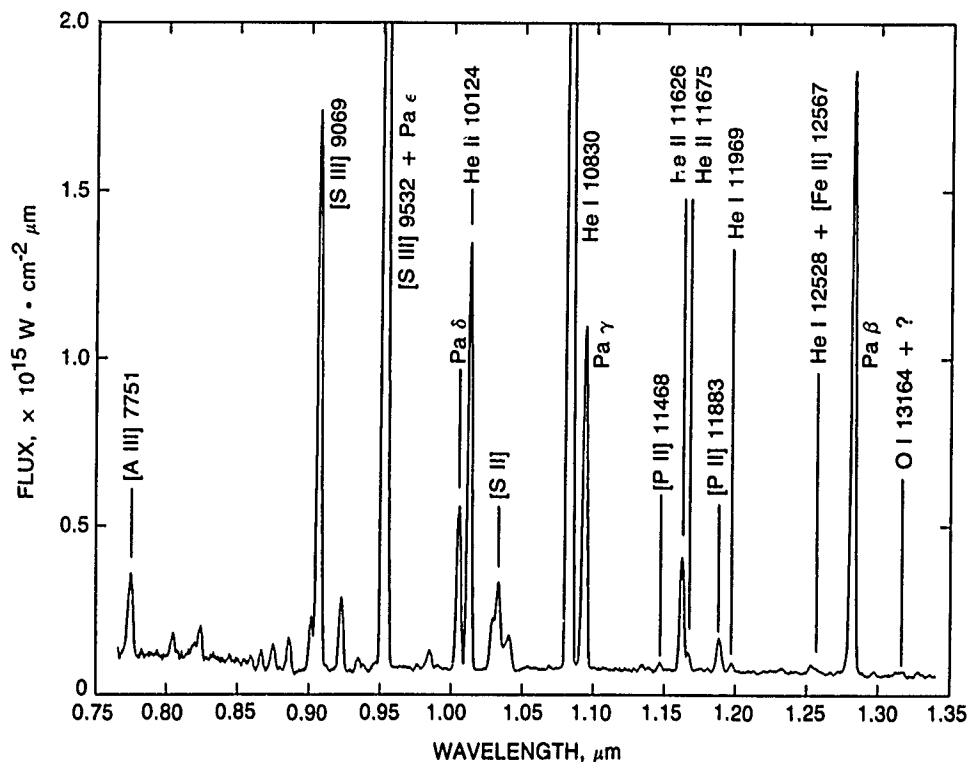
head, of the comet. The pronounced double-peaked feature between 9 and 12 μm is due to thermal emission by small silicate grains being lifted from the nucleus by the sublimation of the icy surface. The double-peaked shape and the wavelengths of the peaks, very similar to those seen in Comet Halley and Comet Bradfield, indicate partially crystalline grains of roughly the same composition as the mineral olivine.

high spectral resolution studies, such as those reported here, are used to identify spectral features that are characteristic of a particular stellar spectral type or that delineate temperature, radiation field, and density conditions of the gas in the system and thus the energy requirements for the hotter star. The source MWC 560 has recently drawn much attention because of its unusually violent outbursts. We obtained 0.8 to 1.35- μm spectra of MWC 560 using the 3-m Shane telescope at Lick Observatory. The spectrum shows TiO absorption bands near 8470, 8880 and 9350 \AA , characteristic of an M0-M5 giant. In addition, the absorption line due to neutral helium at 10830 \AA is seen blue-shifted by 1550 km/s with a full width at half maximum of 1800 km/s, which suggests rapid motion of a significant mass of gas. The continuum between 1.09 and 1.2 μm is irregular and suggests that other important sources of broadband emission or absorption are also present in the region. The absence of Paschen lines and other emission features suggests a low excitation or hydrogen-deficient mass of gas (or both). These data will improve our understanding of the physical conditions in this particular binary, which we plan to continue to monitor as the source evolves.

Another of our ongoing programs is near-infrared observations of planetary nebulae. Planetary nebulae represent a late stage in the evolution of many single stars. Such a nebula forms when a star throws off its outer gas layers, revealing its hot, collapsed inner core. The expelled gas is then photoionized and heated by the intense radiation from this stellar core, producing a characteristic emission line spectrum. In addition to other parameters, these strong emission features provide much of the information about elemental abundances throughout the Milky Way and in nearby galaxies.

NGC 7027 is the brightest and best studied of all planetary nebulae. Part of a spectrum obtained with our near-infrared grating spectrometer is shown in Figure 2. Although NGC 7027 has been observed in the near-infrared by three separate groups previously, those studies focused on the strong emission lines. Of the 12 features we have now been able to identify between 1.1 and 1.34 μm , only 3 were detected previously. The importance of these lines stems from their diagnostic qualities, which provide insights into the conditions and ongoing physical processes within the nebula. For example, the strength of the forbidden [Fe II] line at 1.2567 μm relative to an opti-

Figure 2. Part of a spectrum of the planetary nebula NGC 7027 obtained at Lick Observatory with the near-infrared grating spectrometer. Twelve features have now been identified between 1.1 and 1.34 μm (not all of which are denoted in this figure), of which only three of the brightest lines had been detected previously. The presence and relative strengths of these lines are diagnostic of conditions and physical process within the nebula and in some cases can be used to derive elemental abundances in this object, which represents a late stage of stellar evolution.



cal counterpart implies a density for the Fe^+ region of $\sim 50,000 \text{ cm}^{-3}$, very high compared to the majority of such nebulae. The detection of the [P II] line at 1.1468 μm confirms the earlier association of the feature at 1.1883 μm with phosphorous, a relatively rare element in such nebulae.

Moreover, the relative strengths of the features can be used to check the ratio of their calculated Einstein A values, since both lines arise from the same upper level. The calculated values are consistent with the observed ratio for these line intensities, but are not in agreement with the ratio for two additional transitions of this ion, both of which are weak features in the visible. The importance of observing these lines and correcting the atomic parameters is that these four features are the only transitions of phosphorus observable throughout the optical and near-infrared and thus our only means of determining phosphorus abundances.

During the past year, we continued our new program to study supernovae in the near-infrared. As part of our continuing collaboration with R. Puetter of the University of California, San Diego, we obtained the spectroscopy shown in Figure 3 of two type-Ia supernovae located in other galaxies: SN 1990M in the galaxy NGC 5493 and SN 1990N in NGC 4639. A type-Ia supernova is believed to result from an accreting white dwarf in a binary system whose carbon-rich core collapses, leading to a nuclear deflagration (a subsonic wave of nuclear burning) and an intense explosion. In conjunction with spectra taken last year of SN 1989B [3] and SN 1989M, we now have near infrared spectroscopy covering periods in the evolution of type Ia supernovae ranging from maximum light to a

month after maximum. These measurements, which represent four of the five spectra ever obtained of type-Ia SN in this wavelength regime, show the spectrum evolving from a near-blackbody with minor absorption and emission features to one displaying full-scale (and still-unidentified) broad absorption features, the primary interest in this wavelength region. Although our efforts to identify these features have so far been stymied, our new measurements extend the wavelength coverage down to 0.85 μm (versus $\sim 0.95 \mu\text{m}$ last year) and allow us to examine the known P Cygni emission/absorption feature that results from the mixing of velocity-broadened Ca II infrared triplet lines. We believe this may provide us with new clues to the unidentified absorption features. Expanded studies of these spectra and others like them should improve our understanding of the ejecta from such supernovae, and of the molecular formation and dust condensation processes that occur in the expanding shell and associated shock front.

We have also been studying the near-infrared spectra of slow novae, which result from the nuclear burning of hydrogen-rich material accreted on the surface of a white dwarf in a binary system. A swift and dramatic rise to maximum brightness is followed by a gradual decline back to a dim quiescence, a process that can take weeks for fast novae or years for slow novae. Unlike supernovae, singular catastrophes that destroy the star in question, novae are believed to be very long-term cyclical events, in which the star remains mostly unchanged in the millennia between outbursts. Our near-infrared spectra, the first ever taken of a slow nova, show Nova Ophiuchi 1988 in September 1988 and July 1989, 6 months and 16 months,

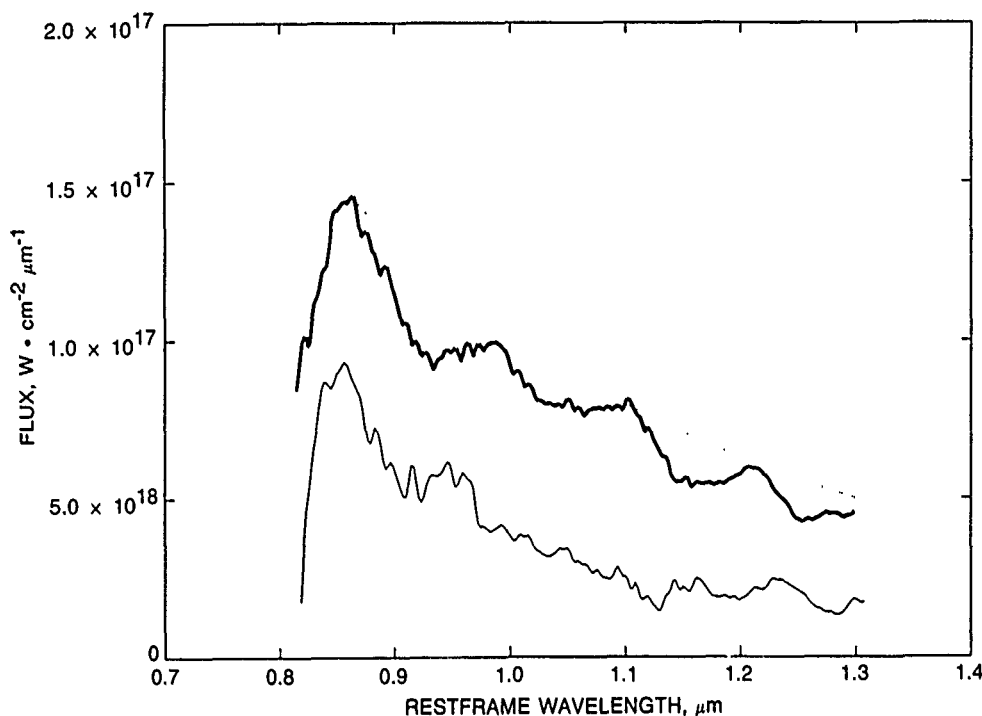


Figure 3. Spectra of two type-Ia supernovae, SN 1990M in the galaxy NGC 5493 (heavy solid curve) and SN 1990N in NGC 4639 (light solid curve). The high spectral resolution data have been smoothed to enhance the visibility of the broad features. The drop shortward of 0.85 μm is believed to be due to blue-shifted absorption by the Ca II triplet. Only five examples of this type of supernova have ever been spectroscopically measured in this wavelength range; our group has been responsible for four. All exhibit the very interesting, unidentified absorption features that appear characteristic of this type of evolved, exploded stellar object. The 6500 K grey body (dotted curve) is arbitrarily normalized to schematically show what the shape of the absorption features could be.

* * * * *

respectively, after its discovery. Both spectra exhibit strong hydrogen Paschen lines and the 10830 Å line of neutral helium in emission, superimposed on a weak continuum. A notable change occurred between the two spectra as the nova evolved from a low-excitation, prenebular state into what we believe is its early nebular phase: the continuum and most of the emission lines decreased in strength, and three emission lines of He II appeared. The latter are evidence of the hardening of the radiation field of the central star, which is now capable of doubly ionizing helium in the expanding shell. The absence of forbidden emission lines, such as those of doubly- and triply-ionized sulfur, indicates that the nova is still much denser than other more common nebular systems such as planetary nebulae or H II regions. Analysis of these data is continuing.

In conclusion, the completion of the BASS instrument and continuing improvements in our other instrumentation have permitted us to gather a wealth of valuable data. The unique capabilities of BASS, in particular, have aroused the interest of other investigators with the result that a number of productive new collaborations have been initiated. It has also led to NASA support for an airborne program. In addition to the scientific observations emphasized earlier, programs are under way to accurately measure and repeatedly monitor a number of celestial objects of interest to several program offices. Thus, this work continues to provide a productive research effort that acts also as the core for maintaining state-of-the-art expertise to be able to respond to the design and application needs of Air Force programs.

1. J. A. Hackwell et al., "A Low Resolution Array Spectrograph for the 2.9–13.5 μm Spectral Region," *Proc. SPIE* **1235**, 171 (1990); also, ATR-90(8531)-2, The Aerospace Corp. (15 April 1991).
2. D. W. Warren and J. A. Hackwell, "A Compact Prism Spectrograph Suitable for Broadband Infrared Spectral Surveys with Array Detectors," *Proc. SPIE* **115**, 314 (1989); also, ATR-89(8431)-4, The Aerospace Corp. (17 October 1989).
3. D. K. Lynch et al., "An Early 1.0–1.35 μm Spectrum of Type Ia Supernova 1989B and the J-band Absorption," *Astron. J.* **100**, 223 (1990); also, ATR-90(8531)-1, The Aerospace Corp. (19 November 1990).

Cohen, R. D., et al., "Helium I /10830 Observations of Seyfert 2 Galaxies," *Active Galactic Nuclei*, D. E. Osterbrock and J. S. Miller, eds., Kluwer Academic Press (1989), p. 126; also, ATR-88(8331)-9, The Aerospace Corp. (to be published).

Greenhouse, M. A., et al., *Near-Infrared [Fe II] Emission of M82 Supernovae Remnants: Implications for Tracing the Supernova Content of Galaxies*, ATR-90(8531)-5, The Aerospace Corp. (to be published).

- Lynch, D. K., "Comet Wilson World-Wide Data Log," *Proceedings of the NASA Cornell Workshop on Infrared Observations of Comets Halley and Wilson and Properties of the Grain*, NASA CP-3004 (1988), p. 19; also, ATR-88(8331)-14, The Aerospace Corp. (to be published).
- Lynch, D. K., and R. W. Russell, "Comet Halley's Colorful Outbursts," *Proceedings of the NASA/Cornell Workshop on Infrared Observations of Comets Halley and Wilson and Properties of the Grain*, NASA CP-3004 (1988); also, ATR-88(8331)-15, The Aerospace Corp. (to be published).
- _____, "5-13 μm Airborne Observations of Comet Wilson 1986I: Preliminary Results," *Proceedings of the NASA/Cornell Workshop on Infrared Observations of Comets Halley and Wilson and Properties of the Grain*, NASA CP-3004 (1988); also, ATR-88(8331)-16, The Aerospace Corp. (1 February 1990).
- _____, "The Sudden Appearance of Comet Halley's Tail," *Publ. Astron. Soc. Pac.* **100**, 1122 (1988); also, ATR-86(8438)-4, The Aerospace Corp. (24 January 1989).
- Lynch, D. K., R. W. Russell, and H. Campins, "10 μm Spectral Structure in Comets," *Proceedings of IAU Symposium No. 135*, NASA CP 3036 (1988), p. 417; also, ATR-88(8331)-8, The Aerospace Corp. (to be published).
- Lynch, D. K., P. F. Bowers, and J. B. Whiteoak, "A Deep Search for 21 cm Neutral Hydrogen Emission in the Tightly Bound Globular Cluster NGC 6388," *Astron. J.* **97** (1989); also, ATR-89(8431)-1, The Aerospace Corp. (19 February 1991).
- Lynch, D. K., et al., "5-13 μm Airborne Observations of Comet Wilson 1986I," *Icarus* **82**, 379 (1989); also, ATR-88(8331)-16, The Aerospace Corp. (1 February 1990).
- Lynch, D. K., et al., "Nova Ophiuchi 1988: 0.9-1.35 μm Spectroscopy 6 Months After Discovery," *Astron. J.* **98**, 1682 (1989); also, ATR-89(8431)-5, The Aerospace Corp. (4 January 1990).
- Lynch, D. K., and G. S. Rossano, "An IRAS Survey of Globular Clusters," *Astron. J.* **100**, 717 (1990); also, ATR-86A(8531)-4, The Aerospace Corp. (to be published).
- Lynch, D. K., et al., "Nova Ophiuchi 1988: 0.9-1.35 μm Spectroscopy," *Proceedings of IAU Colloquium No. 122*, "Physics of Classical Novae," A. Cassatella, ed., Springer-Verlag, Berlin (1990), p. 201.
- Nuth, J. A., III, and J. H. Hecht, "Signatures of Aging Silicate Dust," *Astrophys. Space Sci.* **163**, 79 (1990); also, ATR-89(8431)-6, The Aerospace Corp. (25 April 1990).
- Rank, D. M., et al., "Infrared Observations of SN 1987A from 5.3 to 12.6 Microns: Evidence for an Early Dust Echo," *Astrophys. J. Lett.* **325**, L1-L4 (1988); also, ATR-88(8331)-1, The Aerospace Corp. (20 May 1988).
- Rodriguez-Espinosa, J. M., R. J. Rudy, and B. Jones, "Star Formation in Seyfert Galaxies," *Star Formation in Galaxies*, G. Neugebauer and N. Scoville, eds., NASA Publication No. 2466 (1987), p. 669; also, ATR-86(8431)-10, The Aerospace Corp. (1 March 1987).
- Rossano, G. S., "Microcomputer Control of Infrared Detector Arrays Used in Direct Imaging and in Fabry-Perot Spectroscopy," *IEEE Trans. Nucl. Sci.* (in press).
- _____, "Remotely Operated Imaging Systems," *Proceedings of the 102nd Meeting of the Astronomical Society of the Pacific* (in press); also, ATR-90(8531)-6, The Aerospace Corp. (to be published).
- _____, *Microcomputer Control of Infrared Detector Arrays II: Data Acquisition with a High Speed Coaddier*, ATR-90(8531)-4, The Aerospace Corp. (to be published).
- Rudy, R. J., R. D. Cohen, and T. B. Ake, "Ultraviolet and Optical Spectrophotometry of the Seyfert 1.8 Galaxy Markarian 609," *Astrophys. J.* **332**, 172 (1988); also, ATR-86(8431)-1, The Aerospace Corp. (30 October 1988).
- Rudy, R. J., and G. D. Schmidt, "The Nature of the Strong Static Polarization of the Quasar OI 287," *Astrophys. J.* **331**, 325 (1988); also, ATR-88(8331)-10, The Aerospace Corp. (15 September 1988).
- Rudy, R. J., G. S. Rossano, and R. C. Puetter, "The Near-Infrared Oxygen I Lines of the Planetary Nebula IC 4997," *Astrophys. J.* **346**, 799 (1989); also, ATR-88(8331)-11, The Aerospace Corp. (15 January 1990).
- _____, "He I /10830 Observations of Seyfert 2 Galaxies," *Astrophys. J.* **341**, 120 (1989); also, ATR-88(8331)-7, The Aerospace Corp. (24 July 1989).
- _____, "Detection of the OI /11287 A Line in the Seyfert 1 Galaxy I Zwicky 1," *Astrophys. J.* **342**, 235 (1989); also, ATR-88(8331)-12, The Aerospace Corp. (15 September 1989).
- Rudy, R. J., et al., "Near-Infrared Spectrophotometry of the Symbiotic System V1016 Cygni," *Astrophys. J.* (in press); also, ATR-89(8431)-7, The Aerospace Corp. (12 November 1990).
- Rudy, R. J., et al., "Near-Infrared Spectroscopy of the Planetary Nebula NGC 6572," *Astrophys. J.* (in press); also, ATR-90(8531)-3, The Aerospace Corp. (to be published).

- Russell, R. W., "Chapter 4—Laboratory Investigations," *Infrared Observations of Comets Halley and Wilson and Properties of the Grains*, NASA CP-3004, (1988), p. 91; also, ATR-88(8331)-3, The Aerospace Corp. (15 April 1988).
- Russell, R. W., et al., " Si_3N_4 Grain Emissivity and the Unidentified Infrared Bands," *Proceedings of IAU Symposium No. 135*, NASA CP-3036 (1988); also, *Contributions to IAU Symposium No. 135 on Interstellar Dust*, ATR-88(8331)-2, The Aerospace Corp. (1 November 1988).
- Russell, R. W., and H. P. Erwin, "Airborne IR Spectroscopy of the Atmosphere," *Optical Remote Sensing of the Atmosphere*, Tech. Dig. 4, 541 (1990).
- Russell, R. W., D. K. Lynch, and M. Chatelain, *Properties of the Dust in Comet Bradfield Based on Thermal IR Data*, ATR-88(8331)-6, The Aerospace Corp. (to be published).
- Simons, D. A., et al., "Small-Aperture Infrared Photometry of Seyfert I Galactic Nuclei," *Astron. J.* **96**, 481 (1988); also, ATR-88(8331)-2, The Aerospace Corp. (August 1988).
- West, S. C., et al., "A Computer-Controlled Near Infrared Polarimeter Featuring a New Type of Stress-Birefringent Modulator," *Publ. Astron. Soc. Pac.* **100**, 861 (1988); also, ATR-86A(8531)-3, The Aerospace Corp. (15 November 1988).
- Williams, T. C., et al., "An Eight-Element Bolometer Array Camera for the WIRO 92-Inch Telescope," *Publ. Astron. Soc. Pac.* **100**, 124 (1988); also, ATR-86(8431)-15, The Aerospace Corp. (12 August 1988).

Atmosphere Dynamics and Coupling

R. L. Walterscheid, L. R. Lyons, M. N. Ross, and G. Schubert,
Space Sciences Laboratory

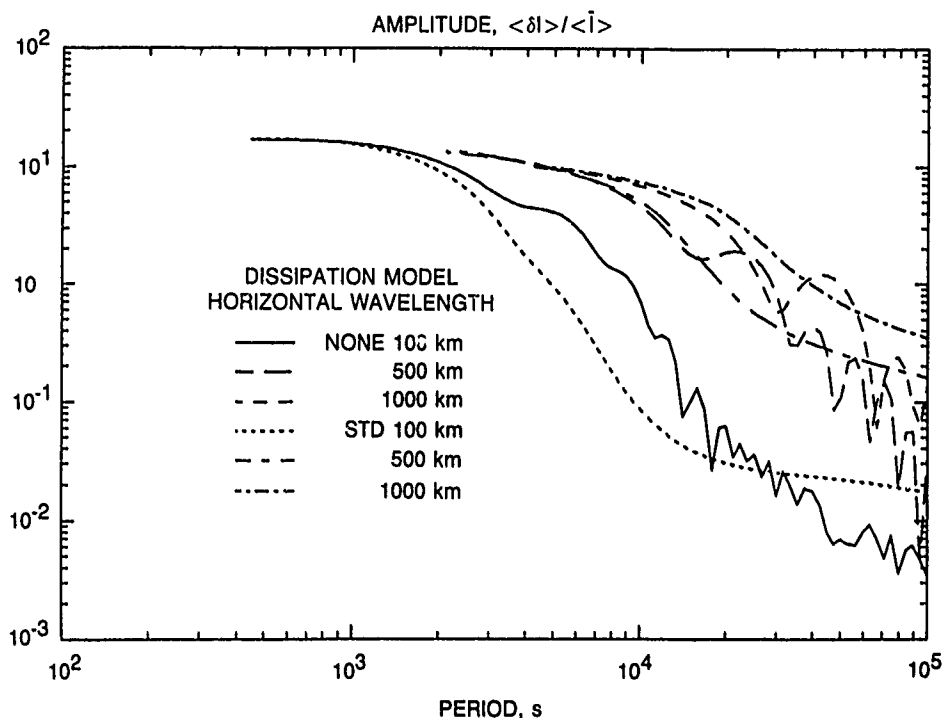
The overall objective of this research is to increase our understanding of dynamical processes in the upper atmosphere and mechanisms that couple the upper and lower atmospheres and couple the ionosphere and atmosphere. We seek to improve our understanding of phenomena and processes that are relevant to the natural environment that affects satellite systems. For example, a source of clutter against which space-based surveillance systems have to identify and track targets is the spatial variation in emitting species due to atmospheric gravity waves (AGWs). These waves change the rate at which constituents react chemically to produce molecules in excited states [1]. In this regard we have continued development of several computer models used to simulate dynamical and chemical processes in the upper atmosphere. These models, together with other models and data analysis, were applied to the following specific topics during this past year:

- Wave-driven fluctuations in OH nightglow.
- Vertical temperature gradients derived from OH nightglow.
- Diffusion by Stokes drift.
- Atmosphere-ionosphere coupling in the auroral region.
- Transient development of atmospheric tides.
- Development of a two-component high-resolution dynamical model.

A major effort has been the development of a theoretical model that calculates the steady-state response of airglow intensity to an AGW varying sinusoidally in space and time. Our model includes line-of-sight integrations through an emitting layer of finite thickness to simulate the natural airglow intensities and temperature near 85-km altitude [2]. Recently, we performed simulations with a model that includes the viscous damping of waves. Our calculations indicated that viscosity has a large effect on waves that have vertical wavelength comparable to or smaller than the depth of the emission layer. Rapid variations of the phase and amplitude of observed intensity and temperature fluctuations with wave frequency are suppressed by viscous damping (Figure 1).

Because airglow intensity is a nonlinear function of temperature, the temperature inferred from OH airglow varies from line pair to line pair. We have developed a model that predicts this variation in terms of temperature lapse rate. We have run the model for various estimates of transition probabilities and have applied the results to airglow data obtained from G. G. Sivjee of Embry-Riddle University. The temperature lapse rates that we have inferred are consistent with a highly structured mesopause. We conclude that airglow is a useful diagnostic for inferring the state of the region of the atmosphere that is strongly perturbed by vigorous gravity wave activity and that might affect space systems, such as the Space Shuttle and the proposed Aero-assisted Orbital Transfer Vehicle, as they reenter the sensible atmosphere.

Figure 1. Variation of OH airglow intensity fluctuations driven by atmospheric gravity waves vs wave period for three choices of wave horizontal wavelength. Results are shown for waves that are subject to damping by eddy viscosity and thermal diffusion and for those that are not subject to damping. The latter are denoted "none" and the former are denoted "std," indicating that nominal values of the coefficients of viscosity and thermal diffusivity are used. The quantity \bar{I} is the intensity averaged over a wave period; $\delta \bar{I}$ is the wave-driven departure therefrom. Angle brackets refer to line-of-sight integrations through the emission layer. Note that the low-frequency fluctuations (period $\geq 10^4$ s) exhibit rapid variations as a function of wave frequency in the undamped case, but not in the damped case.

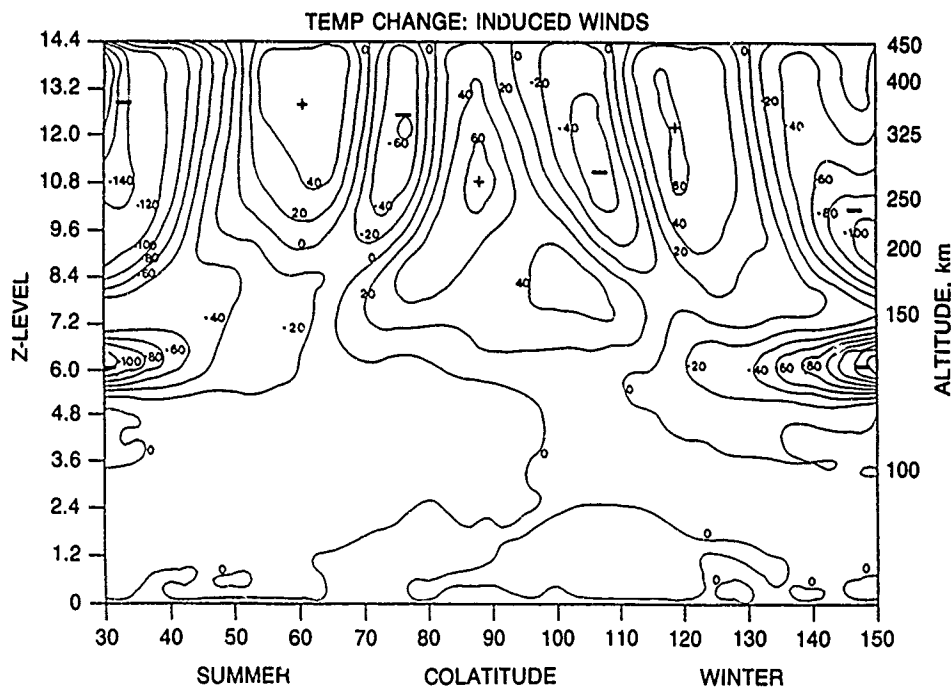


The second area of interest involves the energy deposited in the auroral region and the associated dynamical effects on the atmosphere. Auroral energy sources may cause substantial variations in density, neutral composition, temperature, and winds [3-6]. The most profound disturbances of the neutral thermosphere are caused by magnetic storms [7]. We have studied the redistribution of energy by waves and large-scale convection in an ongoing collaboration with S. V. Venkateswaran and Captain D. Brinkman of the University of California, Los Angeles. Numerical simulations have indicated that

warming at low latitudes is caused in large part by gravity wave-induced convection, and that the heating is due to a local redistribution of heat rather than the transport of heat from high to low latitudes (Figure 2). This explains how the observed low-altitude warming can occur within ~ 3 h of the onset of high-latitude heating.

We obtained another important result by considering internal gravity waves and the associated nonzero mean parcel displacement induced by them (Figure 3) [8]. The theoretical framework for the diffusive action of this drift has been expanded. A spectrum of waves can induce

Figure 2. Contours of temperature change (K) resulting from winds induced nonlinearly by gravity waves during a magnetic storm. The temperature change is over a 12-h period commencing with the onset of the storm. The vertical coordinate is the number of pressure scale heights from the bottom of the model, located at 90-km altitude. The corresponding altitude is given on the right-hand vertical axis. The horizontal axis is colatitude (90° minus latitude). Near the equator (90° colatitude) the warming due to wave-induced winds is approximately a third of the warming due to large-scale convection driven by auroral heating.



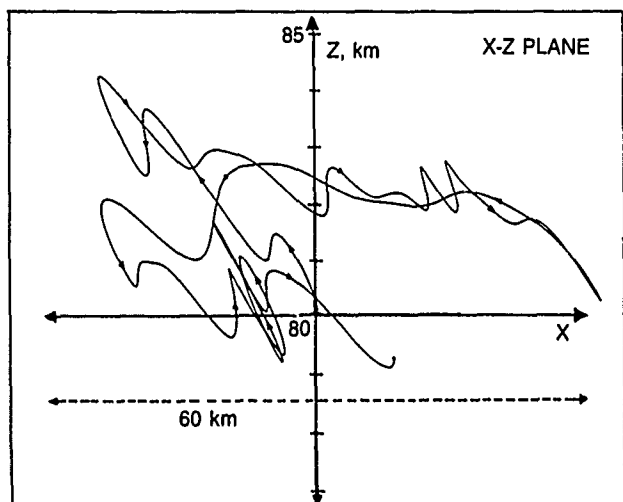


Figure 3. Trajectory of an air parcel moving under the influence of a spectrum of atmospheric gravity waves. The motion at each point in the horizontal-vertical (X - Z) plane is periodic with zero mean velocity. The trajectory simulation was performed over one complete cycle. Despite the fact that the velocity at each point averaged over the cycle was zero, there is a nonzero displacement of the parcel at the end of a cycle. This nonzero displacement is Stokes drift. The drift of parcels moving independently under the influence of a wave field can result in the stochastic diffusion of air parcels. Trajectory calculations for a large number of parcels indicate that Stokes diffusion can be as large as the diffusion usually attributed to small-scale turbulence.

drift because of superposition effects. A broad spectrum of waves can give the spatial variation in drift required to give dispersion of parcels. Theoretical limits have been established on the dispersion caused by conservative waves. We have continued to perform simulations in collaboration with W. Hocking of the University of Adelaide, Australia, for a collection of parcels for various wave models and have found diffusion coefficients comparable to values usually attributed to small-scale turbulence. We have also calculated the rate of change of atmospheric quantities due to Stokes diffusion. It appears that Stokes diffusion might be an important, hitherto overlooked, source of diffusion for atmospheric constituents.

A complement of simple models has been used to study the transient excitation of atmospheric tides and the separation of the disturbance into modes [9]. The response to changed tidal forcing consists of a continuum of free waves, a discrete spectrum of normal modes, and a discrete spectrum of forced tidal modes. These add up to yield a traveling disturbance that propagates away from the region of changed forcing and consists of a steady-state signal that has tidal frequency but no modal structure, preceded by a transient forerunner that has neither tidal frequency nor modal structure. We have elucidated the characteristics of the steady-state signal and have studied the evolution of the steady-state signal into a standing oscillation with modal structure. The steady-state sig-

nal spreads outward and upward away from the energy source with the group velocity of the fastest moving waves of the system. At a fixed position, the wavelength increases with time; at a fixed time the wavelength decreases with altitude. These results should help identify transient effects in tidal observations. It has also been shown that the time required to establish an observable modal structure is largely a question of how long it takes for the steady-state tide to emerge from the background consisting of the continuum and normal modes.

Work continued to test and improve our recently developed sophisticated high-resolution two-gas model (O and N_2-O_2) of thermospheric dynamics in order to increase the stability and speed of the numerical scheme. Also, work was undertaken to develop a three-component model (O , O_2 , and N_2), which we plan to use to support the Atmospheric Response In Aurora (ARIA) rocket program.

The zonal neutral wind within an auroral arc is driven into motion primarily by ion drag. The ion drag force is proportional to the difference $u - u_i$, where u is the neutral zonal wind speed and u_i is the zonal ion drift speed. Previous simulations of the neutral response to auroral arcs with sophisticated dynamical models have ignored the feedback effects of current driven by $u \times B$ electric fields on u_i [4, 10], where u and B are, respectively, the neutral wind and magnetic field vectors. Conventionally, u_i is a prescribed function of the impressed electric field E_o . For constant E_o , u approaches u_i , and the ion drag force is reduced. However, results of an earlier study with a simple model for coupled auroral and neutral dynamics indicated that, because of arc-neutral feedback, E_o increases with u such that u_i remains approximately constant in discrete arcs, and the ion drag force is not diminished [11]. We have performed simulations of the response to discrete arcs with a sophisticated high-resolution dynamical model with and without feedback. Over a 1-h simulation, feedback effects increased the zonal wind velocity within the arc by ~ 20 to 30% . The rate of divergence between results with and without feedback accelerates as time goes on. This acceleration was illustrated by extending the simulations to 2 h, although this period is unreasonably long for an auroral arc to remain stable. Over the 2-h simulation, feedback effects increased zonal wind speed within the arc by a factor of ~ 2 .

In summary, substantial progress has been made in all areas of this project. This progress will contribute to improved specification of the atmosphere for a number of space programs. We plan next year to complete work in some areas started this past year and to place continued focus on dynamical processes that occur in the high-latitude thermosphere, that couple the lower and upper atmosphere, and that cause variations in airglow emissions (clutter).

1. R. L. Walterscheid, G. Schubert, and J. M. Straus, "A Dynamical-Chemical Model of Wave Driven Fluctuations in the OH Nightglow," *J. Geophys. Res.* **92**, 1241 (1986).
2. G. Schubert and R. L. Walterscheid, "Wave-Driven Fluctuations in OH Nightglow from an Extended Source Region," *J. Geophys. Res.* **93**, 9903 (1988); also, ATR-86A(8533)-3, The Aerospace Corp. (31 October 1988).
3. T. S. Mikkelsen et al., "Neutral Winds and Electric Fields in the Dusk Auroral Oval 1. Measurements," *J. Geophys. Res.* **86**, 1513 (1981).
4. J. P. St.-Maurice and R. W. Schunk, "Ion-Neutral Momentum Coupling Near Discrete High-Latitude Ionospheric Features," *J. Geophys. Res.* **86**, 11,299 (1981).
5. T. J. Fuller-Rowell and D. Rees, "A Three Dimensional, Time-Dependent Simulation of the Global Dynamical Response of the Thermosphere to a Geomagnetic Substorm," *J. Atmos. Terr. Phys.* **43**, 701 (1981).
6. J. M. Straus, R. L. Walterscheid, and K. E. Taylor, "On the Local Response of the High Latitude Thermosphere to Geomagnetic Substorms," *Adv. Space Res.* **5**, 289 (1985).
7. A. D. Richmond, "Thermospheric Heating in a Magnetic Storm: Dynamic Transport of Energy from High to Low Latitudes," *J. Geophys. Res.* **84**, 5259 (1979).
8. L. Coy, D. C. Fritts, and J. Weinstock, "The Stokes Drift Due to Vertically Propagating Gravity Waves in a Compressible Atmosphere," *J. Atmos. Sci.* **43**, 2636 (1986).
9. R. Bernard, "Variability of the Semidiurnal Tide in the Upper Atmosphere," *J. Atmos. Terr. Phys.* **43**, 663 (1981).
10. R. L. Walterscheid, L. R. Lyons, and K. E. Taylor, "The Perturbed Neutral Circulation in the Vicinity of a Symmetrical Stable Auroral Arc," *J. Geophys. Res.* **90**, 12,235 (1985).
11. L. R. Lyons and R. L. Walterscheid, "Feedback Between Neutral Winds and Auroral Arc Electrodynamics," *J. Geophys. Res.* **91**, 13,500 (1986).

Schubert, G., and R. L. Walterscheid, "Temperature Gradients at Mesopause Heights Inferred from OH Nightglow Data," *J. Geophys. Res.* (in press).

Schubert, G., R. L. Walterscheid, and M. P. Hickey, "Gravity Wave-Driven Fluctuations from an Extended, Dissipative Emission Region," *J. Geophys. Res.* (August 1991).

Walterscheid, R. L., and L. R. Lyons, "The Neutral E-Region Winds During Intense Postmidnight Diffuse Aurora: Response to Observed Particle Fluxes," *J. Geophys. Res.* **94**, 3703 (1988); also, ATR-88(7162)-8, The Aerospace Corp. (15 June 1989).

Walterscheid, R. L., "Solar Cycle Effects on the Upper Atmosphere: Implications for Satellite Drag," *J. Spacecraft Rockets* **26**, 439 (1989); also, ATR-89(8433)-2, The Aerospace Corp. (15 January 1990).

Walterscheid, R. L., and G. Schubert, "Gravity Wave Fluxes of O₃ and OH at the Nightside Mesopause," *Geophys. Res. Lett.* **16**, 719 (1989); also, ATR-89(8433)-1, The Aerospace Corp. (30 October 1989).

_____, "Nonlinear Evolution of an Upward Propagating Gravity Wave: Overturning, Convection, Transience and Turbulence," *J. Atmos. Sci.* **47**, 101 (1989); also, ATR-88(7128)-1, The Aerospace Corp. (30 March 1990).

Aeronomy of Auroral/Airglow Emission

J. H. Hecht and A. B. Christensen,
Space Sciences Laboratory

The objective of this research is to establish a quantitative understanding of basic aeronomic processes, including particle precipitation, gravity wave propagation, and resonance scattering of solar photons. In particular, the research focuses on gaining an understanding of the following topics:

- The relationship between energy input into the atmosphere and composition changes in the lower thermosphere (100–150 km).
- The adequacy of current models to predict compositional changes, in species such as atomic and molecular oxygen, in the lower thermosphere (100–200 km) and in the upper thermosphere (above 400 km).
- The passage of atmospheric gravity waves through the mesopause (80–95 km) and their effects on the intensity of the OH Meinel and O₂ atmospheric band emissions.

Understanding these topics is important to a number of space programs for the following reasons:

- Understanding atmospheric composition is necessary for determining the orbits of low-altitude spacecraft.
- Species such as atomic oxygen can have a corrosive effect on some spacecraft surfaces.
- Atmospheric gravity-wave-induced composition changes can result in increased background and clutter in ultraviolet and infrared space-based surveillance systems.
- Understanding atmospheric gravity-wave phenomenology is important for the development of satellite weather systems.

In previous company-sponsored work, we have developed a number of remote sensing techniques that permit us to address these problems. We developed a Fabry-Perot interferometer system that is capable of measuring weak auroral and airglow emissions [1]. Using this system, we showed how, by measuring auroral emissions, one could determine the adequacy of an atmospheric model in its prediction of the atomic oxygen density [2–6]. We also measured weak OH Meinel airglow emissions and showed how these can be used to study the propagation of gravity waves through the mesopause region [7]. We improved on this technique by developing a charge-coupled device (CCD) camera system that could be used to take pictures of both the OH Meinel emission, which occurs near 85 km, and the O₂ atmospheric band emission, which arises near 94 km [8]. Measurements of both emissions simultaneously will permit determination of

the characteristics of the vertical propagation of atmospheric gravity waves. During the past year, we used these techniques to address our objectives.

During 8 to 10 February 1986, we obtained observations of auroral emissions during a great magnetic storm. During the most intense period of 8 to 9 February, the A_p index, a measure of geomagnetic activity, reached 202. This was one of the 10 largest storms since 1932 [9]. Figure 1 shows the predictions of various model atmospheres for the atomic oxygen density at 150 km during this storm period ratioed to the atomic oxygen density at the same

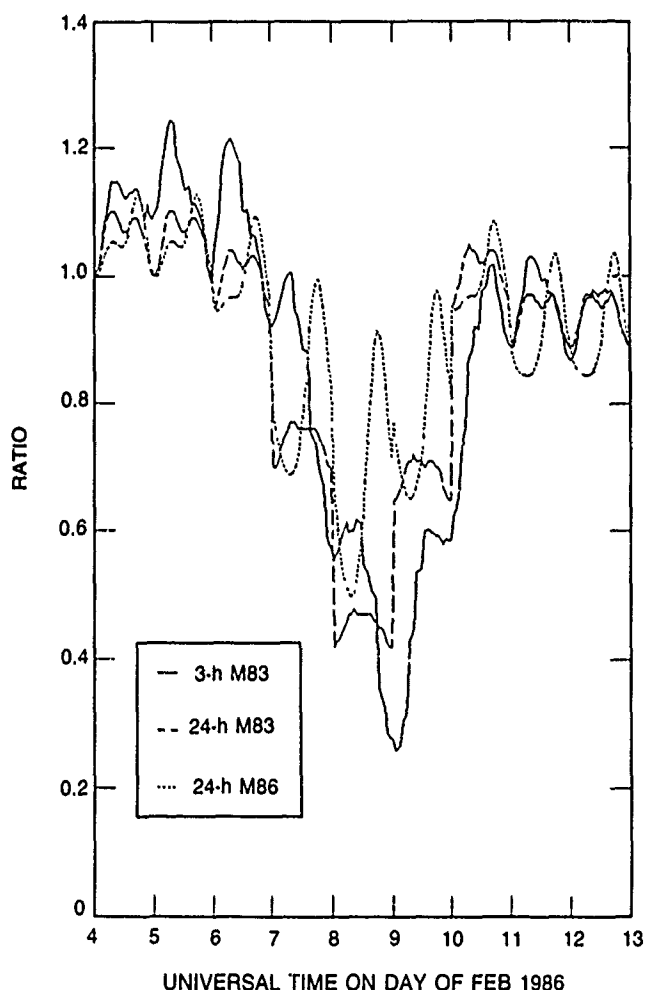


Figure 1. Model predictions for the ratio of atomic oxygen density at 150 km during the great magnetic storm in February 1986 to the oxygen density at 150 km on 4 February 1986 at 0000 UT, a period of low geomagnetic activity. The long-dashed curve represents the prediction of MSIS-83 using 24-h A_p indices. The short-dashed curve represents the prediction of MSIS-86 using 24-h A_p indices. The solid curve represents the predictions of MSIS-83 using 3-h A_p indices.

altitude but for 4 February 1986, a period of low geomagnetic activity. There is a factor of 2 difference for the predicted decrease at the peak of the storm. The models also predict different time responses for the changes in the atomic oxygen density during the course of the storm. Figure 2 shows the predictions of one of the models, the 3-h A_p mode of MSIS-83 [10], compared with our data. This model accounts for most but not all of the measured decrease. However, the predicted time response of the change in composition is faster than indicated by our data. Figure 3 shows the same comparison using the MSIS-86 model [11]. It does a noticeably poorer job than does MSIS-83 both in regards to the magnitude of the decrease of the oxygen density and to the time response for composition change. Thus, it appears at least regarding atomic oxygen density, that the older MSIS-83 model is better than the newer MSIS-86 model [12,13].

Data were also obtained on the O_2 density observed during the storm. Our measurements indicate that the

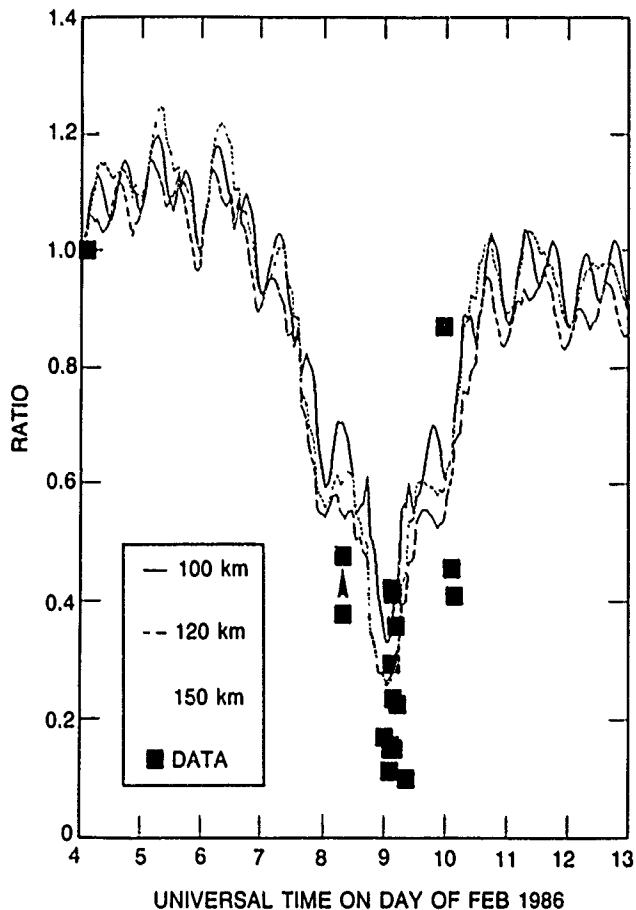


Figure 2. Observations and model predictions for the ratio of atomic oxygen density vs time to the oxygen density at 0000 UT on 4 February 1986, a period of low geomagnetic activity. The thin curves represent the predictions of MSIS-83 using 3-h A_p indices for three different altitudes. The solid squares represent our data. The arrow between the two data points near 0700 UT on daylight indicates that these points represent oxygen densities derived from the same measurement but using two different model atmospheres.

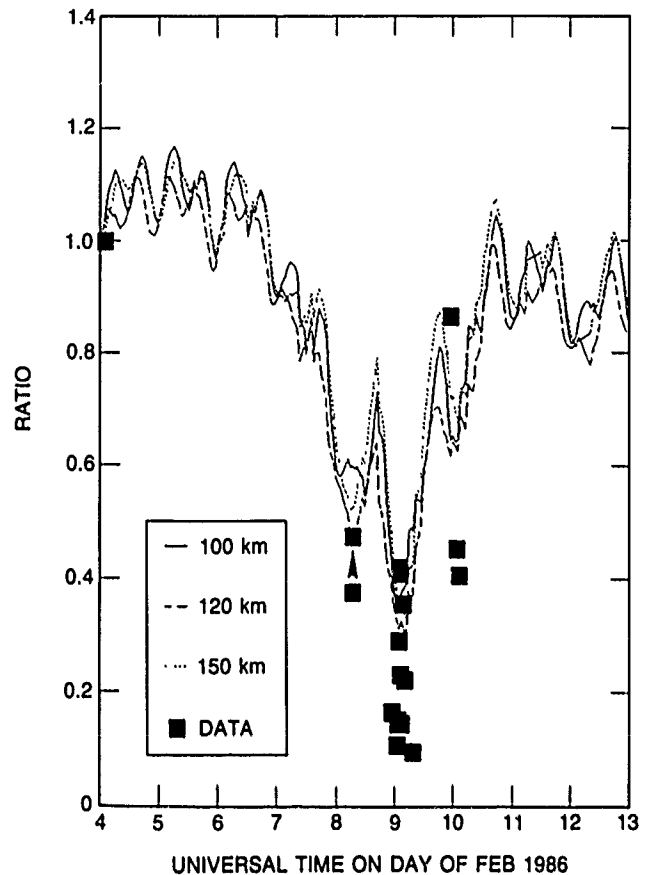


Figure 3. Observations and model predictions for the ratio of atomic oxygen density vs time to the oxygen density at 0000 UT on 4 February 1986, a period of low geomagnetic activity. The thin curves represent the predictions of MSIS-86 using 3-h A_p indices for three different altitudes. The solid squares represent our data. The arrow between the two data points near 0700 UT on daylight indicates that these points represent oxygen densities derived from the same measurement but using two different model atmospheres.

increase in O_2 was about half of that predicted by either MSIS model. That is, the data measured at the peak of the storm on 8 to 9 February 1986 are consistent with increases in the O_2/N_2 ratio, from geomagnetically quiet periods, of between 10 and 50%. Using the model from Kayser and Potter [14], which is based on diffusive equilibrium, and taking into account simply the temperature change at a nominal altitude of 130 km, there would be expected to be about a 10 to 20% change in the ratio during the peak of the storm. Because the masses of these two molecules are close to the mean molecular mass, dynamical effects should not significantly change the ratio. Thus, although these data are consistent with simple model expectations, it is not clear at present why MSIS model predictions are so much higher. It may be related to the extreme nature of this geomagnetic storm and to the fact that little of the data on which MSIS is based was obtained during such conditions. This is the only time that the MSIS models have been checked regarding their pre-

dictions for composition change during such an extreme storm. Thus, our data can be used to constrain and eventually improve empirical models such as MSIS.

There were other results from this data set that indicated the inadequacy of the MSIS model for predicting the detailed response of the atmosphere during geomagnetic activity. From the data shown in Figure 2, it can be seen that just after 0000 universal time (UT) on 9 February, there was an increase in the oxygen density. This occurred at an altitude of 130 to 140 km. In Figure 4, which shows this period at a higher time resolution, the f_O scaling factor used in our analysis is plotted versus time. As discussed previously [2-6], the f_O scaling factor is the amount one has to scale a model atmosphere, in this case MSIS-83, in order to match observations. It is proportional to the O/N_2 density ratio. The increase in oxygen, in Figure 2, corresponds to the increase in f_O , shown in Figure 4, between the times 0200 and 0300 UT. Figure 5 shows the results, during the same time period, for the f_{O_2} scaling factor, which is proportional to the O_2/N_2 density ratio. No corresponding increase is seen in that ratio from 0200 to 0300 UT. A large change in the O/N_2 density ratio without a corresponding change in the O_2/N_2 density ratio is the signature of an atmospheric gravity-wave-induced composition variation. Such dynamical effects are not included in the MSIS models. However, gravity waves, if they have a large horizontal wavelength, can be reproduced in the thermospheric global circulation model (TGCM) developed at the National Center for Atmospheric Research (NCAR). We are currently working with scientists at NCAR to see if these effects are reproduced when this storm is modeled using the TGCM.

The CCD camera system developed under previous company-sponsored work [8] was used to investigate gravity-wave effects at lower altitudes (80-95 km). The cam

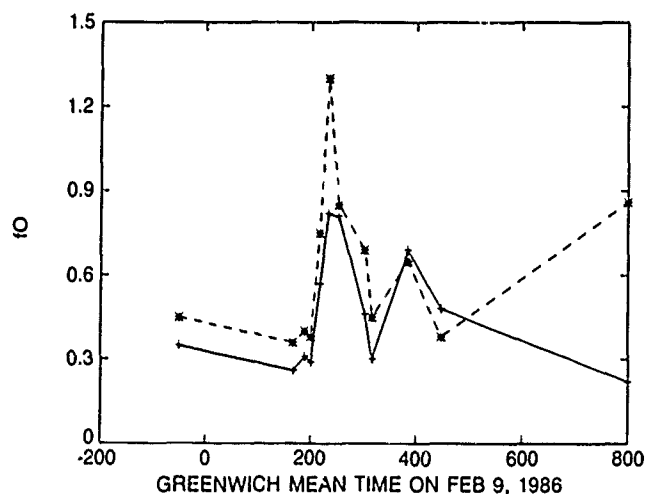


Figure 4. f_O for the night of 8 to 9 February 1986. The plus signs and the asterisks are the results using measurements from two different instruments.

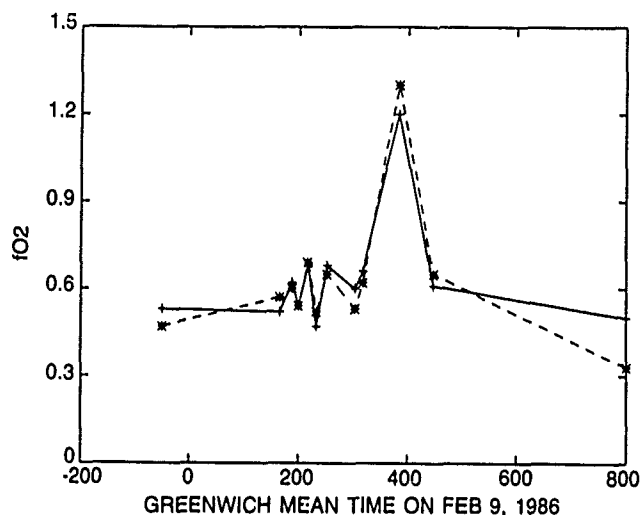


Figure 5. f_{O_2} for the night of 8 to 9 February 1986. The plus signs and the asterisks are the results using measurements from two different instruments.

era system was deployed in March and April at Mt. Haleakala as part of the ALOHA 90 campaign, which included scientists from the United States, United Kingdom, Canada, and Australia. This campaign was designed to study gravity waves over the Pacific Ocean. Although the data for this campaign are still being analyzed, preliminary results do not show evidence of good correlation between the intensity of the OH Meinel emission and the O_2 atmospheric band emission. In contrast, we have analyzed most of our data from the 1989 NSF-sponsored AIDA campaign, which was designed to study gravity-wave effects from Puerto Rico. On one day, 9 May 1989, we observed that the OH Meinel intensity and the O_2 atmospheric band intensity were almost 180 deg out of phase for most of the evening (Figure 6). Such a relationship is characteristic of a standing wave with a wavelength of greater than 6 km [15]. Although such waves have been seen in Na lidar data [16], they have not previously been reported from airglow data.

We have made some progress in gaining an understanding of the interpretation of OH Meinel data. We have shown, for the first time, that by using the intensities of several OH Meinel rotational lines, it is possible to determine not only the temperature of the region near 85 km, but also the temperature gradient throughout the emission layer [17]. It is anticipated that this technique will be used in the interpretation of some of the data obtained by our colleagues during the ALOHA campaign.

In summary, we have shown that our observations obtained during extreme geomagnetic activity can be used to put some constraints on the validity of various atmospheric models. In particular, we have shown that MSIS-83 appears to be a better predictor of the atomic

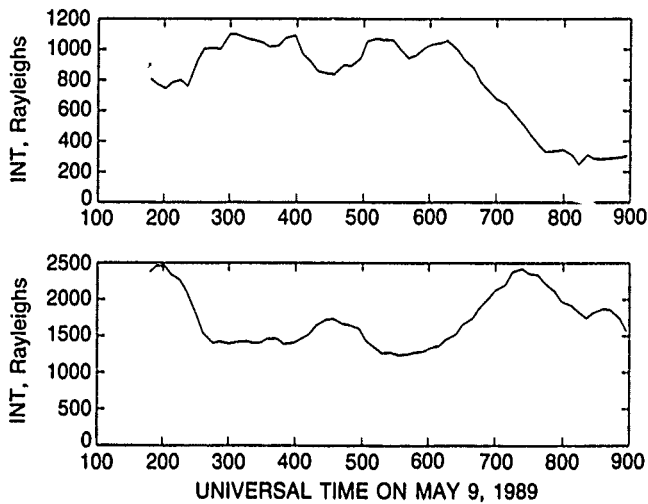


Figure 6. Intensity of the O₂ atmospheric band intensity, in Rayleighs (upper), vs UT on the morning of 9 May 1989 and the OH Meinel (6,2) band intensity, in Rayleighs (lower), vs UT on the morning of 9 May 1989. These data were obtained at Arecibo, Puerto Rico.

oxygen density than does the more recent MSIS-86. However, neither model correctly predicts the change in O₂. Our data also show that gravity-wave-induced composition changes can be significant. This is important since some models that attempt to predict geomagnetically induced atmospheric composition changes do not account for the effects of gravity waves. Currently under investigation are models developed at NCAR that may correctly account for the effects of gravity waves. We also hope that, due to the current historically large solar activity, during the next winter observing season we will obtain additional data that can be used to further validate or constrain these models. We obtained airglow data during an international campaign designed to study gravity waves over the Pacific Ocean. These data are currently being analyzed. Our data of the airglow obtained in Puerto Rico revealed the presence of a standing wave at approximately 85 to 95 km. Such a wave had not previously been observed in the nightglow.

* * * * *

1. J. H. Hecht et al., "Auroral and Airglow Fabry-Perot Spectrometer," *Rev. Sci. Instrum.* **57**, 240 (1986).
2. J. H. Hecht and A. B. Christensen, "Ground-Based Optical Aeronomy," *Aerospace Sponsored Research Summary Report, Scientific and Engineering Research*, ATR-89(8498)-1, The Aerospace Corp. (1 December 1989), p. 148.
3. J. H. Hecht et al., "Deducing Composition and Incident Electron Spectra from Ground-Based Auroral Optical Measurements: Variations in Oxygen Density," *J. Geophys. Res.* **94**, 13,553 (1989).

4. R. R. Meier et al., "Deducing Composition and Incident Electron Spectra from Ground-Based Auroral Optical Measurements: A Study of Auroral Red Line Processes," *J. Geophys. Res.* **94**, 13,541 (1989).
5. D. J. Strickland et al., "Deducing Composition and Incident Electron Spectra from Ground Based Auroral Optical Measurements," *J. Geophys. Res.* **94**, 13,527 (1989).
6. R. J. Niciejewski et al., "Coordinated Satellite and Ground-Based Measurements of the Energy Characteristics of a Bright Sun-Aligned Arc Over Søndreström," *J. Geophys. Res.* **94**, 17,201 (1989).
7. J. H. Hecht et al., "Observations of Wave-Driven Fluctuations of OH Nightglow Emission from Søndreström Fjord, Greenland," *J. Geophys. Res.* **92**, 6091 (1987).
8. J. H. Hecht and A. B. Christensen, "Prototype Space-Based OH Imager," *Aerospace Sponsored Research Summary Report, Scientific and Engineering Research*, ATR-89(8498)-1, The Aerospace Corp. (1 December 1989), p. 155.
9. J. H. Allen, "Major Magnetic Storm Effects Noted," *EOS* **67**, 537 (1986).
10. A. E. Hedin, "A Revised Thermospheric Model Based on Mass Spectrometer and Incoherent Scatter Data: MSIS-83," *J. Geophys. Res.* **88**, 10,176 (1983).
11. A. E. Hedin, "MSIS-86 Thermospheric Model," *J. Geophys. Res.* **92**, 4549 (1987).
12. D. C. Kayser and J. H. Hecht, "Anomalies and Other Phenomena in the MSIS-86 Atmospheric Model," *EOS* **71**, 575 (1990).
13. J. H. Hecht et al., "Ground Based Observations of Changes in E Region Atomic O. II. Data," *28th Plenary Meeting of the Committee on Space Research, 25 June-6 July 1990, Abstracts, COSPAR (1990)*, p. 165.
14. D. C. Kayser and W. E. Potter, "Molecular Oxygen Measurements at 200 km from AE-D Near Winter Solstice," *Geophys. Res. Lett.* **3**, 455 (1976).
15. J. H. Hecht and R. L. Walterscheid, "CCD Observations of the O₂ and OH Nightglow Taken During the AIDA Campaign," *EOS* **71**, 579 (1990).
16. C. S. Gardner et al., "Lidar Studies of the Nighttime Sodium Layer Over Urbana, Illinois 1. Seasonal and Nocturnal Variations," *J. Geophys. Res.* **91**, 13,659 (1986).
17. G. Schubert, R. L. Walterscheid, and G. G. Sivjee, "Temperature Gradients at Mesopause Heights Inferred from OH Nightglow Data," *J. Geophys. Res.* **95**, 19,061 (1990).

Ionospheric Processes

F. T. Djuth,
Space Sciences Laboratory

The natural ionosphere plays an important role in several space programs that are either currently operational or in various stages of development. This includes space-based receiver systems and radars and a variety of ground-based activities involving detection and tracking. Our project is designed to provide a better overall description of the earth's ionosphere through observations of the natural environment and through experiments involving artificial ionospheric modifications [1]. The response of the ionosphere to large externally generated perturbations (both natural and man-made) is also addressed as part of this work. Particular attention is given to gaining an understanding of the thermal balance of the upper atmosphere because it is crucial to first-principles modeling of the ionosphere. Moreover, this type of investigation also permits the measurement of fundamental ionospheric quantities, which facilitates simulations of the auroral and equatorial ionospheres. Additional investigations focusing on ionospheric turbulence are motivated by the need for a better description of auroral irregularity formation. Our current objectives are

- To validate models of thermal balance in the ionosphere.
- To use artificially produced changes in electron and ion temperature to examine cross sections and reaction rates of importance to the physics of the upper atmosphere.
- To characterize the development of resonant plasma phenomena in the upper regions of the ionosphere.

Studies of thermal balance in the ionosphere address several unresolved issues in atmospheric plasma physics, including heating and cooling rates in the upper ionosphere and the rate at which photoelectrons are produced by solar extreme ultraviolet radiation. In the past, we have shown that the ionospheric thermal balance can be greatly altered with high-power radio waves transmitted from the ground provided that ionospheric conditions are carefully selected for the modification process [2-5]. This experiment requires that observations be made at nighttime, when the electron density at the F layer peak is relatively low ($\sim 1 \times 10^5 \text{ cm}^{-3}$), and the height of the F layer is greater than about 270 km. Moreover, the overall temperature imbalance becomes more pronounced when background plasma temperatures are low (600-700 K). The essential physics is determined by the fact that locally deposited heat is not readily dissipated in this ionospheric environment. Energy deposited in the ionosphere by a high-power radio wave is channeled into electron temperature enhancements that continue to

build until thermal conduction (dependent on electron temperature gradients) is large enough to spread the heat to lower and higher altitudes along the geomagnetic field. Large electron temperature enhancements are achievable under these circumstances. However, the temperature of the background O^+ gas increases by only a small amount because of its larger unit mass (16 u).

The temporal development of electron temperature measured with the incoherent scatter radar at Arecibo Observatory, Puerto Rico, is shown in Figure 1 as the HF beam is turned on and then subsequently switched off. Measurements made at three different altitudes are shown. After about 1 min of HF heating, the electron temperature increases from a background value of 700 K to about 1800 K. During 1 to 3 min following turn-on, the electron temperature begins to fluctuate because of thermal instabilities that give rise to hot spots in the plasma [4]. After 3 to 4 min of HF modifications, the electron temperature rapidly decreases, particularly at higher altitudes. This is a geometrical effect brought about by the fact that the HF-modified volume drifts outside the field of view of the diagnostic radar. An ionospheric electron density depletion is created near the reflection point of the HF beam in the ionosphere, and this locks the HF beam into the drifting ionospheric plasma [5]. It is not unusual for the center of the HF beam to move laterally by as much as 100 km from its initial position directly above the HF facility. When the HF beam can no longer the vertical position in a manner similar to that of a relaxation oscillator. The snap back phenomenon is responsible for the return of the electron temperature enhancements in Figure 1 shortly before 8 min relative time. Immediately thereafter, the HF beam is turned off. The electron temperature quickly decreases until it equilibrates with the ion temperature; subsequently, the electron and ion temperatures slowly relax back to the ambient neutral temperature.

A detailed understanding of thermal balance in the ionosphere requires that complex numerical models be applied to the observations [3]. In these numerical studies, many reaction rates and cross sections essential to first-principles modeling of the natural ionosphere are used. In certain cases, our observations are used to provide information about the chemistry of the upper atmosphere that is difficult to obtain by other means. For example, the rate at which the electron and ion temperatures relax back to the neutral temperature after the HF beam is turned off is determined in part by the $\text{O}-\text{O}^+$ charge exchange rate. By focusing on measurements made near 375-km altitude, we obtain an analytical solu-

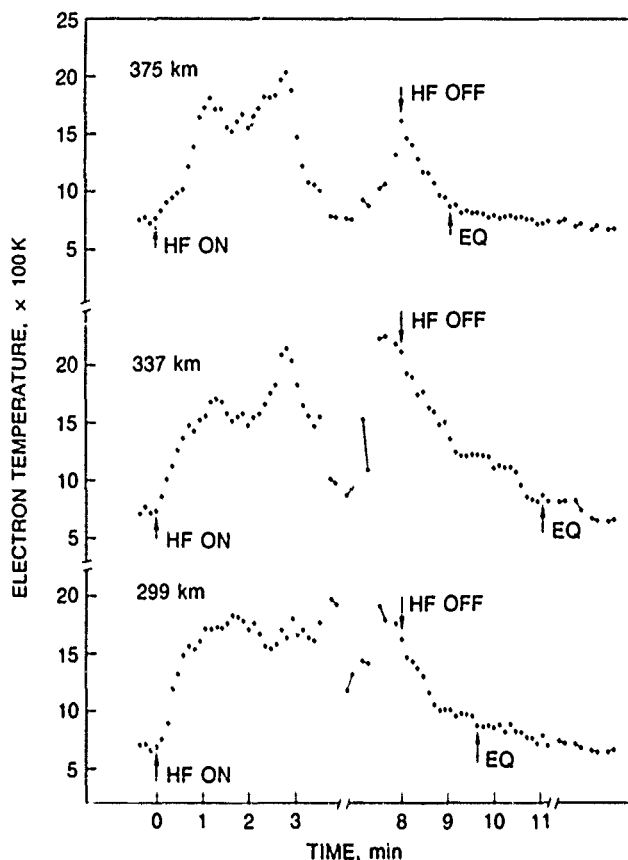


Figure 1. Temporal development of electron temperature as the ionospheric thermal balance is upset by a powerful HF radio wave. Temperatures are shown for three altitudes (299, 337, and 375 km). The HF beam is turned on at 0 min relative time and off at 8 min relative time. Three stages of plasma development are illustrated, initial temperature growth (0–1 min), thermal instability (1–3 min), and movement of the modification region outside of the diagnostic radar field of view (3–8 min). The HF beam is turned off when the modification region reenters the radar beam. The electron temperature subsequently equilibrates with the ion temperature at the point labeled EQ. After this, the electron temperature slowly approaches the neutral temperature. These measurements were made on 12 March 1990.

tion to ion and electron heat equations and thereby deduce the charge exchange rate. On the basis of our extensive database, it appears that the charge exchange cross section should be increased by a factor of 1.5 ± 0.1 beyond the currently accepted value. In general, O-O⁺ charge exchange determines the extent to which the earth's upper ionosphere couples to the principal neutral gas in the thermosphere. An understanding of this coupling is particularly important in the auroral region, where there are dynamical interactions between neutral gas and the ionosphere.

In addition to the charge exchange interaction, it should be possible to determine the temperature dependence of recombination rates responsible for the creation of electron density depletions observed in the experiment. However, this study requires that a comprehensive

numerical analysis of ionospheric thermal balance be performed with plasma transport included. Efforts are under way to perform such an analysis.

A second investigation that has yielded important results involves studies of resonantly excited turbulence in the ionosphere. Our examination of resonant processes in the ionospheric F region represents a somewhat unique area of research directed toward gaining an understanding of wave-plasma interactions in the ionosphere, the fundamental processes responsible for the excitation of plasma turbulence, and the ways in which ionospheric turbulence interacts with electron density irregularities. In these experiments, high-power radio waves are also used to modify the ionospheric plasma; but, in this case, background conditions are selected to suppress the temperature enhancements previously described. Our initial work in this area involved high-resolution radar techniques, which were used to characterize the development of ionospheric plasma turbulence in space and in time [6]. These observations revealed an unexpected richness in complex plasma structure and provided the first evidence that strong states of Langmuir turbulence, as described by the Zakharov equations, are excited in the ionosphere. Generally, there are clear distinctions between the excitation of weak turbulence and strong turbulence in a plasma. Weak turbulence theory implies that plasma nonlinearities are small, that the coupling of one plasma wave to another occurs weakly through the background ion gas, and that all waves have random phases. On the other hand, strong turbulence is characterized by large nonlinearities, chaotic behavior, and temporal and spatial coherence. Moreover, strong Langmuir turbulence entails the formation of highly localized plasma states (often called cavitons), which consist of high-frequency plasma waves trapped in self-consistent density cavities; i.e., an electron density depletion. Numerical simulations show that cavitons sustain the state of strong plasma turbulence through repetitive cycles of nucleation, collapse, and burnout [7]. The physics of strong turbulence in the ionosphere is similar to that used extensively in laser fusion studies. However, when one scales the essential plasma parameters from the laser fusion experiment to the ionosphere, it becomes apparent that development times in the plasma slow down considerably. For example, processes that occur within 1 ns in laser fusion occur over time scales of tens of milliseconds in the ionosphere. The ionospheric experiment has a great advantage in that it permits better diagnostic measurements to be made during the slow development period.

To clarify the roles played by strong turbulence and weak turbulence in the ionosphere, we have implemented a new data-taking procedure at Arecibo involving pseudorandom phase coded radar pulses, where the phase code is changed on a pulse by pulse basis. This technique permits high-range resolution measurements to be made in the plasma while preserving wideband spectral informa-

tion. Moreover, data taken in this manner use the full average power of the radar klystron at Arecibo and thereby represent the limit of Arecibo's measurement sensitivity. An example of data obtained with this technique is shown in Figure 2. The spectrum of 35-cm Langmuir turbulence is shown versus time relative to HF turn-on for three adjacent radar ranges separated by 300 m. The top panel corresponds to the altitude of HF radio wave reflection; the lowest height corresponds to the altitude where weak turbulence processes are expected to take place. At early times following HF turn-on, broad diffuse spectra

are seen in the reflection region. This is precisely what one would expect for strong Langmuir turbulence. However, at late times in the top panel and at virtually all times in the lower two panels, peaked spectral structure is evident as intense horizontal bands. These cascade sidebands are separated by twice the ion-acoustic frequency; they are the signature of weak turbulence processes in a plasma. Thus, strong and weak turbulence seemingly coexists in the ionosphere. This result and other related developments are discussed in greater detail in [8].

The manner in which weak turbulence simultaneously resides in a plasma with strong turbulence is currently being explored theoretically [9]. The greatest difficulty from the theoretical perspective is understanding how strong turbulence in the radio wave reflection region evolves into weak turbulence. Current models provide no mechanisms by which the caviton formation cycle can be interrupted. Part of the solution to this problem may lie in the formation of geomagnetic field-aligned irregularities, which are not accounted for in the current theory because of the neglect of cross-field diffusion. Results of a recent experimental study performed as part of this project [10] indicate that Langmuir turbulence can initiate the growth of geomagnetic field-aligned irregularities. Moreover, it appears that these irregularities, once formed, can have a significant impact on the development of Langmuir turbulence. Similar processes are believed to occur in the natural ionosphere, particularly at auroral and equatorial latitudes.

It is worth noting that the strong turbulence investigation is very demanding from a radar diagnostics standpoint. This type of experiment has traditionally led to the development of innovative data-taking techniques. In particular, the phase-coding technique mentioned earlier has found immediate application in the measurement of neutral temperatures and neutral mass densities in the atmosphere at altitudes near 100 km. In this region, the scale heights of the ionosphere and neutral atmosphere are very small, which necessitates the use of spectral methods that preserve good range resolution.

In summary, we have completed the first stage of a study designed to examine the thermal response of the ionosphere to an artificial heat source. In so doing, we have validated our thermal response model and succeeded in obtaining estimates of the $O-O^+$ charge exchange rate in the ionosphere. A more comprehensive model of heat and plasma transport in the ionosphere is currently being developed using the existing database as a guideline. This effort is expected to provide information about the temperature dependence of recombination rates in the ionosphere. Our studies of resonant processes in the upper ionosphere have led to the discovery of coexisting states of strong and weak turbulence in the ionosphere. These observations provide a way of validating new theoretical concepts that are applicable to laser fusion research. Moreover, there is experimental evidence that

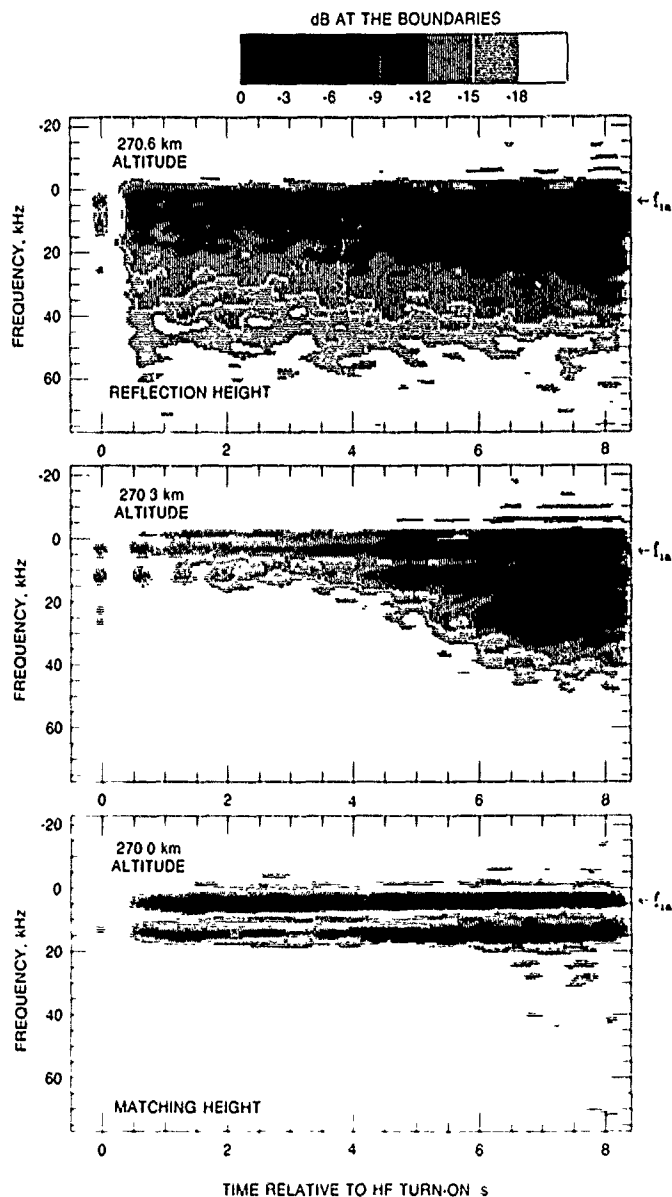


Figure 2. Frequency content of Langmuir turbulence vs time following turn-on of a high-power radio beam in the ionosphere. Spectral results are shown as gray scale spectrograms. The three panels contain measurements from three adjacent altitudes separated by 300 m, absolute altitudes are shown to the right of each panel. A frequency displacement of one ion-acoustic frequency relative to the origin is labeled as f_{ia} . These observations were made on 2 May 1990.

ionospheric turbulence gives rise to field-aligned electron-density structures as part of a step-wise evolution of plasma states. Such processes may greatly promote irregularity formation in the auroral ionosphere. Many of the new observing techniques developed for studies of ionospheric turbulence have broad applications in the natural ionosphere, particularly in situations where good altitude resolution is essential. The radar technique implemented for spectral observations of ionospheric turbulence now serves as a standard method for investigating the ionosphere and neutral atmosphere near 100-km altitude.

* * * * *

1. F. T. Djuth, "HF Ionospheric Modification," *Micro-waves and RF* **24**, 75 (1985); also, ATR-85(8332)-2, The Aerospace Corporation (25 August 1985).
2. F. T. Djuth et al., "Large F-Region Electron-Temperature Enhancements Generated by High-Power HF Radio Waves," *Geophys. Res. Lett.* **14**, 953 (1987); also, ATR-86A(8532)-2, The Aerospace Corp. (15 November 1987).
3. A. L. Newman et al., "Thermal Response of the F-Region Ionosphere for Conditions of Large HF-Induced Electron Temperature Enhancements," *Geophys. Res. Lett.* **311** (1988); also, ATR-88(8332)-1, The Aerospace Corp. (15 October 1988).
4. S. P. Kuo and F. T. Djuth, "A Thermal Instability for the Spread-F Echoes from HF-Heated Ionosphere," *Geophys. Res. Lett.* **15**, 1345 (1988); also, ATR-88(8332)-3, The Aerospace Corp. (15 September 1989).
5. F. T. Djuth, "Response of the Arecibo Ionosphere to Large HF-Induced Electron Temperature Enhancements," *Adv. Space Res.* **9**, 123 (1989); also, ATR-89(8432)-1, The Aerospace Corp. (15 September 1989).
6. F. T. Djuth, M. P. Sulzer, and J. H. Elder, "High Resolution Observations of HF-induced Plasma Waves in the Ionosphere," *Geophys. Res. Lett.* (in press).
7. D. F. DuBois, H. A. Rose, and D. Russell, "Excitation of Strong Langmuir Turbulence in Plasmas Near Critical Density: Application to HF Heating of the Ionosphere," *J. Geophys. Res.* (in press).
8. J. A. Fejer et al., "Height Dependence of the Observed Spectrum of Radar Backscatter from HF-Induced Ionospheric Langmuir Turbulence," *J. Geophys. Res.* (in press).
9. D. F. DuBois, H. A. Rose, and D. Russell, "Coexistence of Parametric Decay Cascades and Caviton Collapse at Subcritical Densities in HF modification of the Ionosphere," *J. Geophys. Res.* (in press).
10. S. T. Noble and F. T. Djuth, "Simultaneous Measurements of HF-Enhanced Plasma Waves and

Artificial Field-Aligned Irregularities at Arecibo," *J. Geophys. Res.* (in press).

-
- Bernhardt, P. A., S. T. Zalezak, and F. T. Djuth, "Comment on 'Interaction of Electromagnetic Waves in the Ionosphere' by V. N. Laxmi and A. K. Saha," *Radio Sci.* **25**, 85 (1990); also, ATR-89(8432)-3 (15 August 1990).
- Cheron, T., and F. T. Djuth, *Effect of High Power Radio Waves on Ionosphere, 1925-1986, Bibliography. Translation from Russian*, ATR-88(8332)-2, The Aerospace Corp. (15 February 1988).
- Djuth, F. T., "U. S. Contributions to Ionospheric Modification Research, October 1983-September 1986," *Review of Radio Science 1984-1986*, G. Hyde, ed., International Union of Radio Science, Brussels, Belgium (1987), p. G:H-12; also, ATR-86(8432)-5, The Aerospace Corp. (30 June 1987).
-
- _____, *Soviet Research in the Area of Ionospheric Modification by High-Power Radio Waves—An Assessment of Experimental Investigations of Plasma Instabilities*, ATR-86A(8532)-4, The Aerospace Corp. (1 December 1987).
- Djuth, F. T., et al., "Observations of HF-Enhanced Ion Waves in the Ionosphere," *Geophys. Res. Lett.* **14**, 194 (1987); also, ATR-86(8432)-2, The Aerospace Corp. (28 August 1987).
- Djuth, F. T., and C. A. Gonzales, "Temporal Evolution of the HF-Enhance Plasma Line in Sporadic-E," *J. Geophys. Res.* **93**, 196 (1988); also, ATR-86(8432)-6, The Aerospace Corp. (15 February 1988).
- Fejer, J. A., et al., "Simultaneous Observations of the Enhanced Plasma Line and of the Reflected HF wave at Arecibo," *J. Atm. Terr. Phys.* **51**, 721 (1989); also, ATR-89(8432)-2, The Aerospace Corp. (1 March 1990).
- Kuo, S. P., M. C. Lee, and F. T. Djuth, "A New Interpretation of the Plasma-Line Overshoot Phenomenon," *Geophys. Res. Lett.* **14**, 961 (1987); also, ATR-86A(8532)-1, The Aerospace Corp. (15 February 1988).
- Noble, S. T., et al., "Multiple Frequency Radar Observations of High Latitude E-Region Irregularities in the HF-Modified Ionosphere," *J. Geophys. Res.* **92**, 13,613 (1987); also, ATR-86(8432)-7, The Aerospace Corp. (15 February 1987).
- Providakes, J., et al., "Radar Observations of Ion Cyclotron Waves Associated with Two Barium Shaped Charge Releases," *J. Geophys. Res.* (in press); also, ATR-89(8432)-4, The Aerospace Corp. (to be published).

Infrared Studies of Star-Forming Regions

J. A. Hackwell, R. W. Cantera, D. J. Edelson, L. M. Friesen, J. H. Hecht,
J. Kepner, D. K. Lynch, R. W. Russell, and E. A. Walkup,
Space Sciences Laboratory

This research combines the analysis of data from the Infrared Astronomical Satellite (IRAS) with ground-based infrared observations to study the structure of the infrared sky over a wide range of spatial scales. Unlike visible light, infrared radiation can penetrate the dense clouds of gas and dust that pervade the galactic plane (Milky Way). Thus, infrared measurements can reveal regions of star formation and other heavily obscured regions of the Galaxy that were previously inaccessible to scientific study. One consequence of the ability of infrared radiation to penetrate interstellar space is that the appearance of the infrared sky cannot be predicted from measurements at shorter wavelengths. Thus, space surveillance programs that need to understand the infrared celestial background require direct infrared measurements of the sky at the wavelengths of interest.

During the past year, we continued to exploit techniques that we developed in previous years for recovering high-resolution images directly from raw, unevenly spaced IRAS data. Significant effort was directed toward a detailed analysis of infrared sources in the plane of the Galaxy at a galactic longitude of 30 deg. This region, like many on the galactic equator, is particularly difficult to study because of *confusion* introduced by the high density of stars and other sources. Source confusion results when

two or more sources illuminate an IRAS detector simultaneously. This, coupled with the emphasis placed on having no false detections in the IRAS Point Source Catalog (PSC), makes the PSC very unreliable in crowded regions. In particular, the limiting flux to which sources are detected can vary greatly over small distances, so that a relatively bright source may be omitted from the PSC, whereas a nearby faint star will be included in the catalog. These inconsistencies distort the star count statistics to the point where it is impossible to derive meaningful information about the distribution of infrared sources. We have used our image recovery techniques to overcome the effects of the confusion and to make a catalog of infrared sources at 30-deg galactic longitude that is complete to a limiting flux of $1.4 \times 10^{-18} \text{ W cm}^{-2} \mu\text{m}^{-1}$. Our study results reveal two new populations of infrared objects that are closely confined to the galactic plane and dominate the surface density of infrared objects within 2 deg of the plane (Figures 1 and 2). The first: newly discovered population consists of objects with very low 12- to 25- μm color temperatures ($T < 250 \text{ K}$) whose surface density falls off with a characteristic *exponential scale height* of 0.4 deg (i.e., the surface density of these objects falls by $1/e$ for every 0.4 deg away from the galactic plane). About 30% of these cool objects are associated with

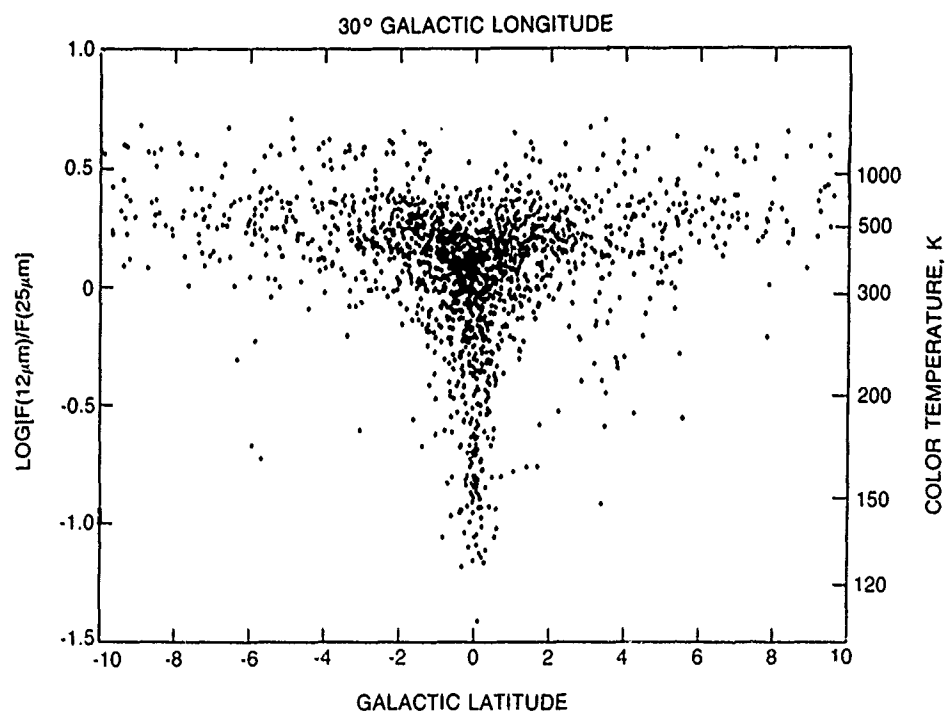


Figure 1. The ratio of the 12- to 25- μm flux plotted vs galactic latitude for each of the IRAS sources recovered around 30 ± 5 deg galactic longitude. This ratio can be interpreted as a color temperature. Note the high concentration of sources with color temperatures below 250 K within 2 deg of the galactic plane. These represent a hitherto undiscovered component of the infrared sky.

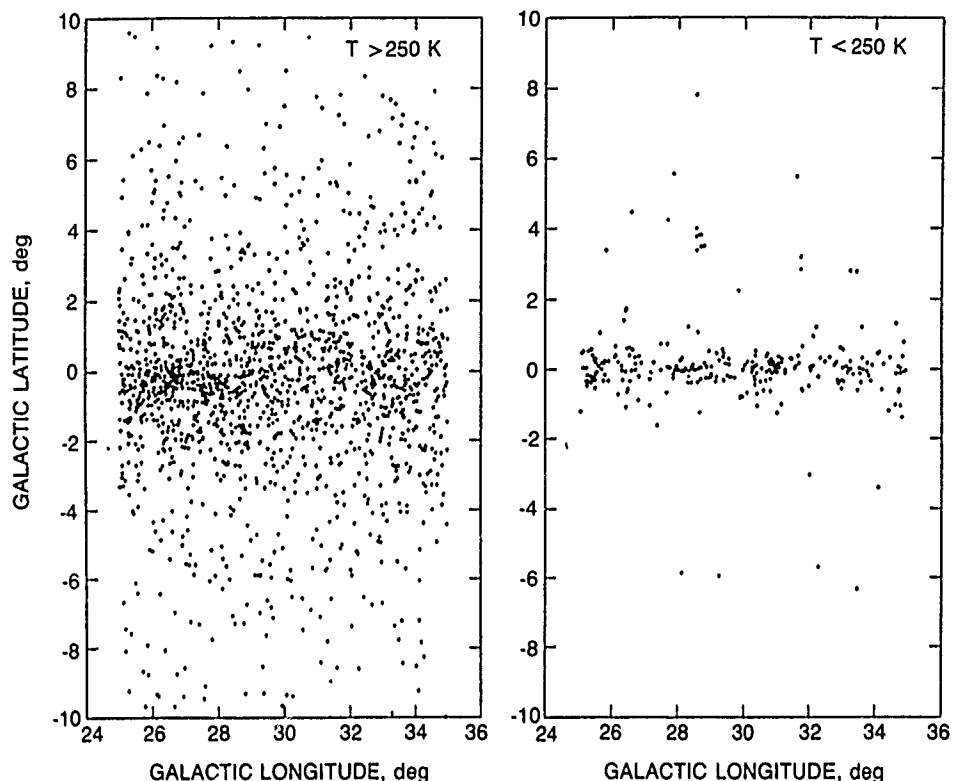


Figure 2. The distribution of sources around 30-deg galactic longitude that have color temperatures above 250 K (left) and sources in the same region that have color temperatures below 250 K (right). Note how strongly concentrated in the galactic plane are the low-temperature sources. About 30% of the low-temperature sources are HII (ionized) regions. The remainder are probably young stars that are too cool to ionize their surroundings.

known HII (ionized) regions from radio studies. The remainder are probably very young high-mass stars that are too cool to ionize the gas that surrounds them. The second population has a 12- to 25- μ m color temperature > 250 K and an exponential scale height of 1.1 deg. This population is probably a mixture of newly forming low-mass stars and evolved objects. Previous studies, which ignore sources that are in the crowded regions within 2 to 5 deg of the plane, have completely overlooked these newly discovered classes of infrared objects. Results of our new work show that the surface density of infrared objects in the galactic plane is a factor of 3 times higher than is predicted by current models of the infrared celestial background.

Another study that has sprung from the high-resolution enhancement of IRAS data concerns the infrared structure of galaxies. Photographs of many spiral galaxies show the presence of a *bar*, a linear structure that crosses the nucleus. Spiral arms appear to spring from the ends of the bar. We have recovered an infrared image of one of the closest such barred spiral galaxies, NGC 1365. Our data show that the bar seen at visible wavelengths is at a different position angle from the infrared bar. The infrared bar appears to align with an obscuring dust lane in the visible light photograph (Figure 3). Because the orientation of the IRAS spacecraft was known very accurately, it is unlikely that apparent rotation of the visible light and infrared images results from a misalignment error. This result has implications for the distribution of stars in the bar and for the flow of mass into the bar.

Because IRAS was in a sun-synchronous orbit and was also constrained to point away from the earth, it made many scans over the ecliptic poles. The most sensitive infrared celestial survey to date was made by co-adding hundreds of North Ecliptic Pole scans made by IRAS. Unfortunately, the ultimate sensitivity of this deep survey was limited by emission from diffuse *infrared cirrus* that could not be distinguished from unresolved sources such as distant galaxies. We are currently using our high-resolution techniques to reanalyze about 140 scans of the North Ecliptic Pole. Our objective is to improve the resolution of the old survey by a factor of 2 to 3 and thereby improve the survey sensitivity by a factor of 4 or more. During the past year, we modified our computer code to handle multiple scans of the same field that were taken at different angles. We also developed a method for modeling and removing the effects of diffraction around bright objects in the field.

One drawback of applying nonlinear image recovery techniques to multiband data is that the angular resolution achieved depends both on the size of the diffraction blur and on the signal-to-noise ratio of the data; high signal-to-noise ratios tend to give high final resolution. Both of these effects generally give a different position-dependent resolution for the final images in the two bands. This is a problem if it becomes necessary to compare, for example, the images of a galaxy recovered in two different wavelength bands. Thus, a researcher will be seriously misled by interpreting the point by-point ratio of the two images as a color temperature because the differ-

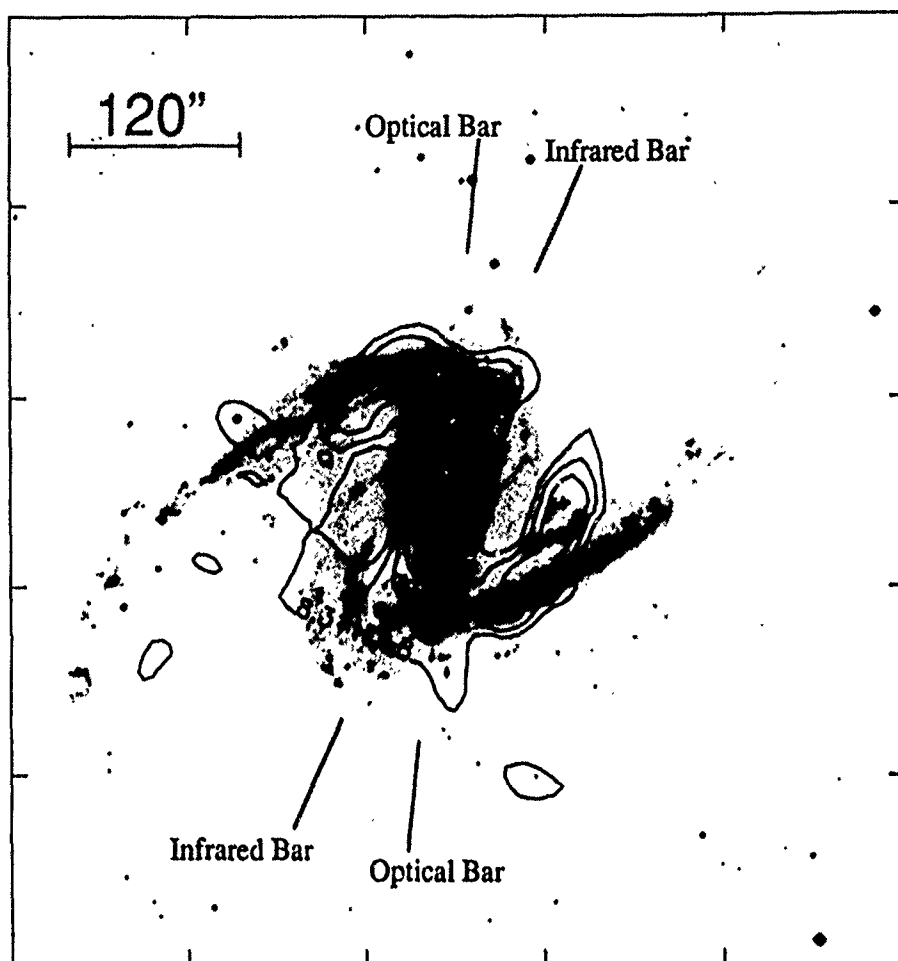


Figure 3. 60- μ m image of the barred spiral galaxy NGC 1365 recovered from IRAS data compared with a visible-light (blue) picture of the same object. Note that the infrared bar does not line up with the brightest part of the visible image. Rather, the infrared emission appears to come from a dark dust lane in the bar. This discovery has implications for the distribution of luminosity and mass transport in the bar.

ent spatial resolution of the two images will produce *color fringe* artifacts around the sources. We have been investigating methods of *data fusion* that combine the raw data from two different wavelengths to produce a high-resolution color ratio map that is free of such artifacts. Preliminary results are encouraging. The major stumbling block is in obtaining a measure of the color ratio that does not diverge when the intensity at both wavelengths is small compared to the noise.

A companion study to the image recovery project involves deriving infrared spectra from IRAS low-resolution spectrometer (LRS) data of slightly extended sources. The IRAS LRS is a slitless spectrometer designed to study point sources. Spectra of extended objects are blurred because the spectral information from the source is convolved with its spatial structure. We use our image recovery techniques to deconvolve the spectrum from the spatial structure in a two-step process. First, we use data from the array of broad-band survey detectors to recover an image of the extended source. From this image, we derive the spatial structure that the LRS detector would see as it scanned over the object if it did not also disperse the light to produce a spectrum. Second, we deconvolve this derived model of the spatial structure from the LRS data to recover a spectrum of the

object. During the past year, we developed a method for calibrating the results so that the final spectra are in absolute units. This has been crucial in understanding how to join the 7- to 13- μ m portion of the spectrum to the 13- to 23- μ m portion. These two portions are sensed by different detectors and must be overlapped accurately to make a complete spectrum. Although these IRAS spectra are difficult to recover, they provide a unique opportunity to study the infrared emission from sources that are too extended to be observed by ground-based telescopes. In addition, extended objects such as this are expected to have spectra that are similar to those produced by the *infrared cirrus*. This ropy, diffuse structure that permeates the Galaxy is believed to originate from interstellar grains that are heated by diffuse starlight. It is quite probable that the diffuse infrared emission from the Galaxy is not a blackbody continuum but a series of broad spectral features. We are currently deconvolving the LRS spectra of bright, slightly extended objects chosen both from Air Force rocket measurements summarized in the Geophysics Laboratory Infrared Catalog and from the IRAS Small-Scale Structure Catalog.

In related work, we have found the first observational link between the small dust grains that emit in the infrared to produce the ubiquitous infrared cirrus and the

particles that absorb starlight in the ultraviolet. We used the International Ultraviolet Explorer (IUE) satellite to observe the ultraviolet extinction along the line of sight to stars in two clusters. These clusters were chosen to be away from the plane of the Galaxy so that they lie behind the bulk of the cirrus emission. Thus, light from the stars passes through the same dust that is emitting in the infrared. We use a number of stars in the same cluster to avoid systematic errors and to characterize the properties of the dust over a relatively large area. The infrared data were taken from IRAS. We found that the dust that is associated with regions of star formation is deficient in small silicate grains that produce one portion of the ultraviolet extinction. These silicate grains have a relatively low color temperature and emit most strongly at 100 μm . When these small silicate grains are absent, the infrared cirrus emission is dominated by carbonaceous particles that are relatively hot and thus increase the observed color temperature of the cirrus emission. We suggest that the absence of small silicate particles near regions of star formation results from their accretion into larger particles inside protostellar nebulae.

Although our reprocessing of the IRAS data has allowed us to study relatively large areas of the infrared sky (> 1 deg or 20 μrad), it appears that it will be impossible to push the IRAS data beyond the resolution of 20 to 40 arcsec (100–200 μrad) that we currently achieve. Thus, as part of this project, we are in the last stages of developing an infrared camera system (called the *Aerospace Infrared Camera* or *AIRCam*) that will work in the long-wave infrared (LWIR) from 4 to 25 μm wavelength. This camera will achieve an angular resolution of 0.5 to 2.0 arcsec (2.5–10 μrad) and cover a field 0.5 to 2.0 arcmin across (.50–600 μrad). The camera is an ideal complement to the IRAS studies because it will provide us with the capability to make detailed observations of particularly interesting regions identified by the IRAS data.

Our experience with the Kuiper Infrared Technology (KITE) program and our collaboration with the Naval Research Laboratory on their LWIR array have shown us that one of the major problems with existing infrared arrays is that the large background photon flux seen by ground-based systems can overwhelm the small integration capacitors in the hybrid multiplexers. We are overcoming this in AIRCam by keeping the field of view of individual detectors small (to reduce the total background flux) and by keeping the integration time short (to reduce the total charge collected by the integration capacitors). Because short integration times yield a high data rate, we have designed and built a digital co-adder that adds together the digital data from several frames before sending it to the data processing computer. With this system, we can efficiently handle frame times as short as 150 μs with a 10×50 -element array without losing any data. The optical system, which was designed with D. W. War-

ren of the Electronics and Optics Division, uses a modified Offner relay. Its principal advantage is that the image scale does not change with telescope focus position. Thus, images taken through different filters will have the same scale and can be readily compared to one another. To minimize the thermal background, the filter wheel is operated at 4 K and is driven by a cryogenic motor. AIRCam is almost complete, and we are planning to use it for observations next year.

In summary, we are pursuing a multifaceted research effort with the objective to gain an understanding of the structure of the infrared sky on a variety of spatial scales. The ability of infrared radiation to penetrate interstellar dust is being used to study star-forming regions and to examine the structure of the Galaxy as revealed by distant infrared stars. We plan to continue to apply the techniques and instruments that we have developed to study the interaction between stars and the interstellar medium both in our own and in other galaxies.

-
- Canterna, R., and J. A. Hackwell, "High Spatial Resolution IRAS Images of M51," Second Wyoming Conference on The Interstellar Medium in External Galaxies, Kluwer, Dordrecht (in press).
- Canterna, R. W., et al., "Infrared Studies of the Galactic Plane I: The IRAS Disk Population at $l = 30^\circ$," *Astrophys. J.* (in press).
- Dietz, R. D., et al., "Infrared Imaging and Polarimetry of M82: Evidence for a Ring of Warm Dust," *Astronom. J.* **98**, 1260 (1989).
- Gehrz, R. D., et al., "PW Vulpeculae: A Dust-Poor DQ Herculis?," *Astrophys. J.* **329**, 894 (1988); also, ATR-86A(8523)-2, The Aerospace Corp. (15 April 1989).
- Hackwell, J. A., and J. H. Hecht, "IR Emission and UV Extinction in Two Open Clusters," *Proceedings of IAU Symposium 135 on Interstellar Dust*, NASA (1988), p. 131; also, ATR-88(8323)-2, The Aerospace Corp. (1 November 1988).
- Hackwell, J. A., J. H. Hecht, and M. Tapia, "Observations that Link Infrared Cirrus and Ultraviolet Extinction," *Astrophys. J.* (in press).
- Hayward, T. L., et al., "Infrared Imaging of W3 A," *Astrophys. J.* **345**, 894 (1989).
- Hecht, J. H., J. A. Hackwell, and R. W. Russell, "Observational Constraints on Interstellar Dust Models," *Proceedings of IAU Symposium 135 on Interstellar Dust*, NASA 1988, p. 391; also, ATR-88(8323)-6, The Aerospace Corp. (15 April 1989).
- Johnson, J. J., et al., "An Infrared Study of the Orion Molecular Cloud-2," *Astrophys. J.* (in press).

Little, S. J., et al., "High Resolution H and K Maps of W51," *Astronom. J.* **97**, 1716 (1989); also, ATR-88 (8323)-3, The Aerospace Corp. (17 October 1989).

Lynch, D. K., et al., "IRAS Spectra of Extended Objects: The Crab Nebula," *Proceedings of the 22nd ESLAB Symposium on Infrared Spectroscopy in Astronomy*, M. Kessler, ed., European Space Agency Special Publication 290 (1989), p. 193; also, ATR-88 (8323)-1, The Aerospace Corp. (15 December 1989).

Rossano, G. S., *Aerospace Infrared Camera (AIRCAM) Data Acquisition System User's Guide*, ATR-90 (8523)-1, The Aerospace Corp. (30 March 1990).

Smith, J., et al., "Near-Infrared Light and the Morphology of Arp 220," *Astrophys. J.* **329**, 107 (1989); also, ATR-86A(8523)-1, The Aerospace Corp. (15 June 1989).

_____, "Starlight Morphology of the Interacting Galaxy NGC 5195," *Astrophys. J.* (in press).

Auroral Energization and Geomagnetic Disturbances

L. R. Lyons and J. F. Fennell,
Space Sciences Laboratory

Energetic (1–10 keV) particles from high altitudes in the magnetosphere precipitate into the atmosphere in auroral regions. These energetic particles have two important effects on operational space systems. First, they are the major cause of satellite surface charging at both high and low altitudes. Surface charging has resulted in damaging electrostatic discharges on several satellites in geosynchronous and low-earth orbits. Second, the precipitating particles are a major energy source for the ionosphere and upper atmosphere and can significantly affect over-the-horizon radar performance and satellite drag. Understanding the dynamics of this energetic particle population is a key step in developing mitigating or avoidance procedures for future operational systems. The auroral particle intensity increases significantly during geomagnetic disturbances, called *substorms*, and its effect on space systems maximizes during these disturbances. Substorms involve the violent release of energy derived from the solar wind that becomes stored in the magnetospheric tail. As well as being important to the understanding of environmental effects on space systems, the topics of auroral particle precipitation, the energy release during substorms, and the transfer of solar wind energy to the magnetosphere are in the forefront of magnetospheric research throughout the international scientific community.

Significant progress was made during the past year in gaining an understanding of the physics of the transfer of solar wind energy to the magnetosphere and the substorm evolution of auroral phenomena and their connection to the geomagnetic tail. For solar wind energy to be stored in the magnetosphere, it must be transferred across the boundary between open and closed magnetic field lines. The earth's magnetic field consists of two distinct regions, a polar cap region, where the geomagnetic field is connected directly to the solar magnetic field

(region of open magnetic field lines), and a lower latitude region, where the geomagnetic field is confined to the earth's magnetosphere (closed field line region). Auroral precipitation occurs in an approximately circular region near the boundary between open and closed magnetic field lines. This region lies at about 70° geomagnetic latitude and, to a good approximation, the poleward boundary of the precipitation lies at the boundary between open and closed field lines.

The transfer of energy across the open-closed field line boundary involves an electric field along the boundary, which maps to a magnetic *X*-line in the distant magnetosphere. The *X*-line is a unique location where the magnetic field normal to the plasma flow becomes zero. A critical problem in understanding the energy transfer is determining the balance of forces near the *X*-line, and we have performed a theoretical study of this problem. Well away from an *X*-line, the condition $E = -V \times B$ is generally satisfied, where E is electric field, V is plasma velocity, and B is magnetic field. Obviously, this relation yields $E = 0$, where $V \times B = 0$, a condition that would prohibit a transfer of energy across the open-closed field line boundary.

A resolution to this problem was suggested by Dungey [1], who considered the effects of the plasma kinetic tensor K . The kinetic tensor is basically a pressure tensor, but it includes contributions from both the ordinary pressure (in the frame of reference of the moving plasma) and the dynamic pressure associated with the plasma flow. If we include K , then

$$E = V \times B - (1/en)\nabla \cdot K, \quad (1)$$

where e is the electronic charge and n is plasma density. Dungey noted that only the divergence of the off-diagonal elements of K were important near an *X*-line. These off-diagonal element of the pressure tensor act as an effective

viscosity, carrying momentum directed along an X -line in the direction normal to the X -line.

We have performed a two-dimensional analysis of the terms in Eq. (1) by following particle trajectories near an X -line [2]. In our model, the X -line lies in the y -direction at $x = z = 0$, and we confine attention to the $z = 0$ plane. We also define normalized coordinates (denoted here by a superscript prime), where $E' = 1$, $e' = 1$, and $B' = 1$ at $x' = 1$. B is assumed to vary linearly with x' and is equal to zero at $x' = 0$. In normalized, two-dimensional units, Eq. (1) becomes

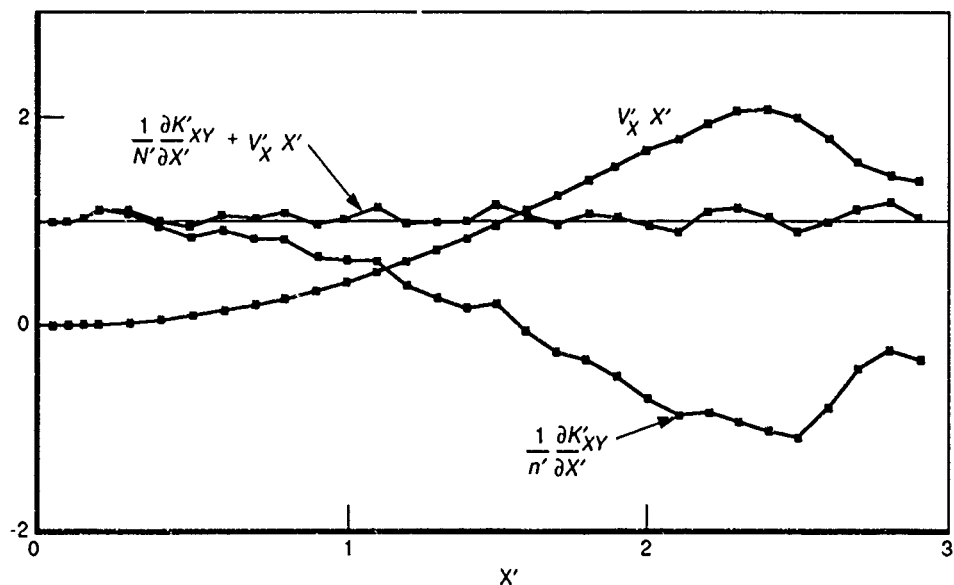
$$(1/n')[(\partial/\partial x')K_{xy}] + V_x' x' = 1, \quad (2)$$

where K_{xy}' is the off-diagonal element of the kinetic tensor that gives the viscous effect, $V_x' x'$ is the magnetic force, and the 1 on the right-hand side is the normalized electric field force.

By following the trajectories of a large number of particles, we evaluated the two terms on the left-hand side of Eq. (2) and compared their sum to 1. The results are shown in Figure 1 over the range $0 \leq x' \leq 3$. It can be seen that the sum of the two terms balances the electric field force (given by the thin line at the value of 1) to within numerical errors. In particular, the viscous effect, $(1/n')(\partial/\partial x')K_{xy}'$, precisely balances the electric field at the X -line ($x' = 0$).

On this basis, we concluded that the viscous effect proposed by Dungey [1] can indeed balance the electric field at an X -line and thus allow the transfer of energy across the boundary between open and closed magnetic field lines. This result offers an explanation for an important, previously unsolved, aspect of the transfer of solar wind energy to the magnetosphere. The result should also be applicable to collisionless plasmas in general and to other astrophysical situations in particular.

Figure 1. Balance of forces near a magnetic X -line located at $x' = 0$. The normalized viscous force $(1/n')(\partial/\partial x')K_{xy}'$, the normalized magnetic force $V_x' x'$, and their sum are shown vs x' . The normalized electric field force is shown by the thin line that has a value of 1.



A second significant accomplishment this past year was an evaluation of auroral changes and connections to the tail during substorms [3], which is important for understanding substorm dynamics and associated energy release processes. Prior to the onset of a substorm, during the substorm growth phase, the poleward boundary of the aurora is approximately circular, as illustrated in Figure 2. After the substorm onset, the poleward boundary of the aurora is distorted by the formation of an auroral surge. The striking evolution of the poleward boundary as determined from VIKING satellite images during the development of an auroral surge on 24 September 1986 is shown in Figure 3. The boundary of the aurora was obtained by displaying VIKING images, obtained approximately once per minute, in geographic coordinates and drawing smooth curves along the poleward boundary of identifiable aurora. For spatial reference, each panel in Figure 3 contains geographical coordinates, a bar identifying the magnetic meridian of the Søndreström radar in Greenland, a dot along the bar giving the location of the radar, and the poleward boundary of the aurora from an initial image for comparison with the later curves.

Figure 3 shows that, as the surge developed, the poleward boundary of the aurora moved poleward east of the head of the surge and equatorward west of the head of the surge. (The head of the surge is the region just to the west of the Søndreström meridian where the poleward boundary of the aurora assumes an approximately north-south orientation.) Such a distortion of the poleward boundary, which develops after substorm onset during the period called the *expansion phase*, is shown in Figure 2.

Under the assumption that the poleward boundary of the aurora lies along, or adjacent to, the boundary between open and closed magnetic field lines, the devel-

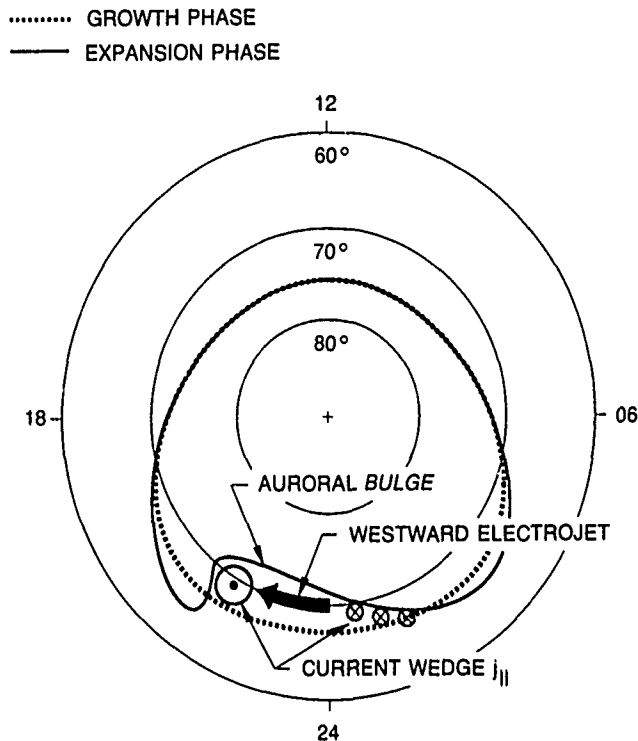


Figure 2. The poleward boundary of the auroral oval for times during the growth phase of a substorm and during the expansion phase after substorm onset. The auroral surge, also referred to as a bulge, is illustrated, along with the magnetic field-aligned currents and ionospheric electrojet that make up the expansion phase current wedge.

opment of an auroral surge must be associated with a distortion of the boundary. It is not necessary that the poleward boundary of the aurora lie precisely at the open-closed field line boundary, but we do require that the poleward boundary lie near the open-closed field line boundary and have approximately the same shape.

As shown in Figure 2, the distortion of the poleward boundary of the aurora at the edges of the auroral bulge occurs in the region of a pair of oppositely directed magnetic field-aligned currents. These currents are connected in the ionosphere by an intense current called the *westward electrojet*. The field-aligned currents map along magnetic field lines into the magnetosphere, where their magnetic effects are readily observable [4].

The field-aligned currents are associated with major magnetic field changes in the tail. During a substorm growth phase, magnetic field lines in the tail become stretched in the tailward direction. At substorm onset, the magnetic field returns to a more dipolar configuration. This reconfiguration is observed to begin in a relatively narrow longitude sector near midnight, and to then expand both eastward and westward [6]. Major particle injections in the magnetosphere are observed to accompany the dipolarization of the magnetic field.

As illustrated in Figure 4, the magnetic field perturbations associated with the substorm field-aligned current

should cross the midplane of the tail. This would give rise to an increase in closed magnetic flux at longitudes within the pair of field-aligned currents and a decrease in closed magnetic flux at longitudes outside the currents. Such a change in the closed flux should develop together with the formation of the field-aligned currents during the substorm expansion phase (the period after substorm onset). It requires a net closing of tail lobe field lines at longitudes within the currents and a net opening of tail-lobe field lines outside the current wedge. This should cause a distortion of the boundary between open and closed magnetic field lines as shown schematically in Figure 4. In Figure 4, the boundary between open and closed field lines is referred to as the *separatrix*.

In summary, significant progress was made during the past year on the physics of the transfer of solar wind energy to the magnetosphere and on substorm phenomena. The results have suggested future theoretical and observational studies that we intend to pursue concerning the energy transfer across the boundary between open and closed magnetic field lines and substorm electrodynamics. These studies will involve theoretical analysis and modeling, as well as analysis of data from satellites and from ground-based radars.

We therefore conclude that the currents that form during substorms are associated with a distortion of the separatrix between open and closed field lines, which extends from the ionosphere to well out into the magnetospheric tail. We suggest that the distortion forms the auroral bulge observed in the ionosphere during the expansion phase of substorms and that it causes other important effects observed in the tail during substorms. These effects include distortions of the hot plasma region that lies within the two boundaries (separatrices) between open and closed field lines in Figure 4, changes in B after substorm onset, and tailward plasma flows associated with the magnetic perturbation just outside the pair of field-aligned currents.

A distortion of the separatrix in the tail will map along field lines to the ionosphere in the region of the auroral bulge. In order to account for the bulge, it is necessary that the additional closed magnetic flux associated with the current wedge equal the magnetic flux that threads the bulge in the ionosphere. Let us assume that the ΔB crossing the midplane of the tail is 10 nT within the current wedge, and that this ΔB extends over an area given by $\Delta y = 2.5 R_e$ and $\Delta x = 20 R_e$. This gives an additional closed magnetic flux $\Delta \Phi = 500 \text{ nT} R_e^2$. Taking the vertical component of B in the auroral ionosphere to be $5 \times 10^{-5} \text{ T}$ and the longitudinal extent of the surge to be 750 km, $500 \text{ nT} R_e^2$ corresponds to a latitudinal distance of 540 km, or ~ 5 deg, which is reasonable for an auroral bulge.

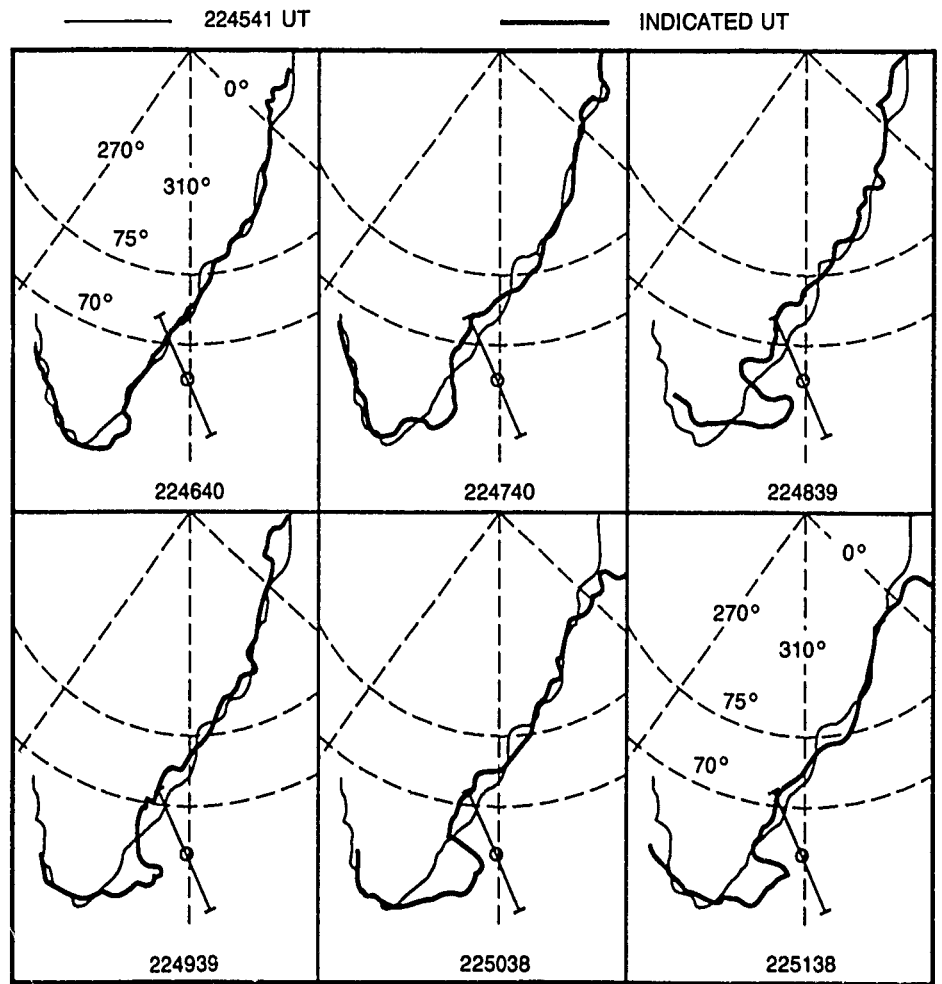
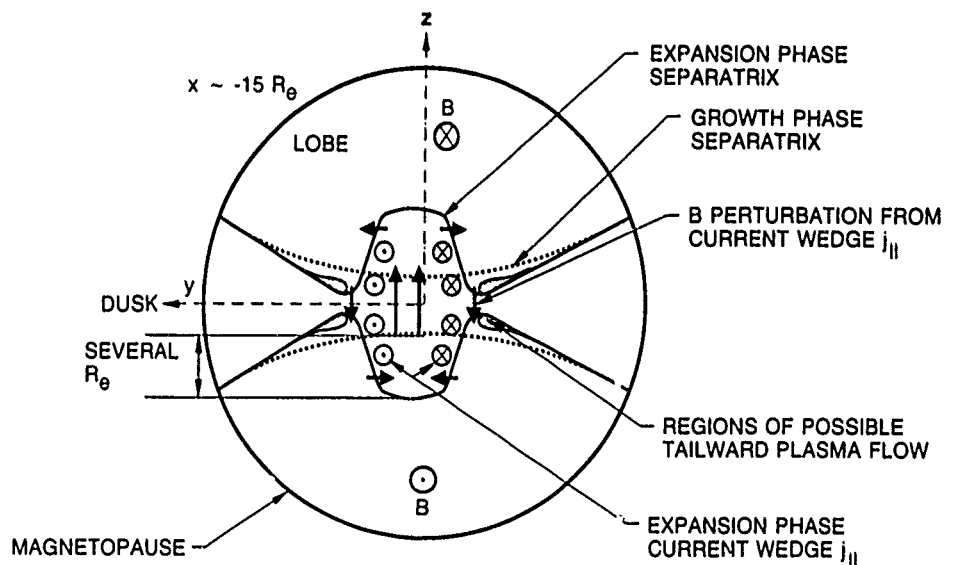


Figure 3. Poleward boundary of aurora identified from a sequence of images from the VIKING satellite on 24 September 1896 during a period of rapid development of an auroral surge near Søndreström, Greenland. The boundaries are displayed in geographical coordinates, and the lighter curve in each panel gives the poleward boundary from an initial image for comparison with the boundary from the UT indicated in the panel. The bar identifies the field of view of the Søndreström radar along its magnetic meridian; the open circle gives the radar location.

Figure 4. Phenomena predicted to occur in the geomagnetic tail, $-15 R_E$ from the earth, during a substorm expansion phase. The distortion of the boundary between open and closed magnetic field lines is shown by the curves labeled separatrix, heavy arrows give the magnetic perturbations resulting from the substorm field-aligned currents, and shading gives the location where plasma trapped between the upper and lower portion of the separatrix may escape by flowing tailward away from the earth. The region of open field lines that is devoid of trapped plasma is identified as the lobes.



1. J. W. Dungey, "Noise-Free Neutral Sheet," *Proceedings of an International Workshop in Space Plasma Physics*, ESA SP-285, Vol. II (1988), p. 15.
2. L. R. Lyons and D. C. Pridmore-Brown, "Force Balance Near an X-Line in a Collisionless plasma," *J. Geophys. Res.* (in press).
3. L. R. Lyons et al., "Analysis of Substorm Expansion and Surge Development," *J. Geophys. Res.* **95**, 10,575 (1990).
4. Nagai, T., "Field-Aligned Currents Associated with Substorms in the Vicinity of Synchronous Orbit, 2, Geos 2 and Geos 3 Observations," *J. Geophys. Res.* **92**, 2432 (1987).
6. R. L. Arnoldy, and T. E. Moore, "Longitudinal Structure of Substorm Injections at Synchronous Orbit," *J. Geophys. Res.* **88**, 6220 (1983).

de la Beaujardiere, O., and L. R. Lyons, "Instantaneous Measurements of the Global High Latitude Convection Pattern," *Outstanding Problems in Solar System Plasma Physics: Theory and Instrumentation*, American Geophysics Union (1989), p. 405; also, ATR-88(7162)-13, The Aerospace Corp. (15 December 1989).

Lyons, L. R., "Processes Associated with the Plasma Sheet Boundary Layer," *Physica Scripta* **718**, 103 (1987); also, ATR-86(7165)-2, The Aerospace Corp. (1 May 1988).

Lyons, L. R., A. L. Vampola, and T. W. Speiser, "Ion Precipitation from the Magnetopause Current Sheet,"

J. Geophys. Res. **92**, 6147 (1987); also, ATR-86A (7165)-3, The Aerospace Corp. (15 March 1988).

Lyons, L. R., and A. Nishida, "Description of Substorm Onset Incorporating Boundary Layer and Neutral Line Effects," *Geophys. Res. Lett.* **15**, 1337 (1988); also, ATR-88(7162)-5, The Aerospace Corp. (1 February 1989).

Lyons, L. R., J. F. Fennell, and A. L. Vampola, "A General Association between Discrete Auroras and Ion Precipitation from the Tail," *J. Geophys. Res.* **93**, 12,932 (1988); also, ATR-88(8319)-1, The Aerospace Corp. (24 July 1989).

Lyons, L. R., M. Schulz, and J. F. Fennell, "Trapped Particle Evacuation: Source of Magnetotail Bursts and Tailward Flows?," *Geophys. Res. Lett.* **16**, 353 (1989); also, ATR-89(7162)-2, The Aerospace Corp. (10 August 1989).

Lyons, L. R., and M. Schulz, "Access of Energetic Particles to Stormtime Ring Current through Enhanced Radial "Diffusion," *J. Geophys. Res.* **94**, 5491 (1989); also, ATR-88(7162)-11, The Aerospace Corp. (21 September 1989).

Lyons, L. R., and O. de la Beaujardiere, "Critical Problems Requiring Coordinated Measurements of Large-Scale Electric Field and Auroral Distribution," *Outstanding Problems in Solar System Plasma Physics: Theory and Instrumentation*, American Geophysics Union (1989), p. 399; also, ATR-88(7162)-6, The Aerospace Corp. (15 December 1989).

Lyons, L. R., "Discrete Auroras and Magnetospheric Processes," *Auroral Physics*, Cambridge University Press (in press).

Trends in Middle Atmosphere Ozone

M. N. Ross,
Space Sciences Laboratory

The primary objective of this research is to study how stratospheric trace gas pollution affects the atmospheric tides and the impact this modification has on models of middle and upper atmospheric dynamics. We have performed theoretical and data analysis concerning the consequences of the gradual depletion of middle-atmospheric ozone caused by anthropogenic trace gasses, principally chlorofluorocarbons. Since the atmospheric tides are driven by ozone absorption of solar ultraviolet radi-

ation, changes in stratospheric ozone cause changes in the tides. In addition, we maintained an active program in comparative planetary physics by examining several topics involving the atmospheric and orbital dynamics of the outer planet satellites Titan and Triton. The primary and secondary research objectives for the past year were:

- To predict changes in the amplitudes of the solar driven atmospheric tides caused by trace gas induced ozone depletion.

- To model the coupled thermal-dynamical evolution of Triton's interior and orbit.
- To study the propagation of gravity waves in the atmosphere of Titan.

A vast body of evidence supports the view that the accumulation of man-made trace gasses in the middle atmosphere, mainly chlorofluorocarbons, has reduced the amount of ozone there [1,2]. Measurements of ozone trends from ground- and space-based instruments generally agree with middle atmosphere chemistry models that predict that the greatest ozone loss occurs during winter and the loss increases with latitude. The details of the distribution and magnitude of the depletion remain poorly understood, however.

Since the absorption of solar ultraviolet radiation by middle-atmosphere ozone provides the thermal excitation mechanism for the major atmospheric tides, significant depletion of ozone will affect the amplitudes and latitudinal distribution of the tides. We wish to understand the dynamical consequences of ozone depletion on the tides because the upward propagating tides represent a significant component of the coupling between the middle and upper atmosphere, exerting considerable influence on the mean circulation of the upper atmosphere [3]. In addition, the semidiurnal surface pressure oscillation $S_{22}(p)$, a measure of the amplitude of the main semidiurnal tide, has been accurately measured over the past two decades and may offer important information on tropical ozone trends since the onset of significant depletion.

A classical atmospheric tide model was used to estimate the amount by which the solar-driven tides have decreased in amplitude since the onset of ozone depletion, circa 1960. The adopted model of present-day ozone depletion, based on observations and model predictions, is not likely in error by more than about 50%. The predicted change in amplitudes for the most important tide modes is given in Table 1. The decrease varies according

Table 1. Changes in Surface Pressure Oscillation $S_{nm}(p)$ and Upper Atmospheric Tidal Winds f_{nm} for Present-Day Ozone Depletion

Mode	$S(p)_{nm}$	f_{nm}
(2,2)	-2.0	-3.0
(2,3)	-8.0	-4.0
(2,4)	-4.0	-5.0
(2,5)	-11.0	-11.0
(1,1)	-1.0	-1.0
(1,-2)	0.0	-2.0
(1,-4)	-1.5	-0.5
(1,-1)	-1.0	-3.5

to how the latitude distribution of each tide mode interacts with the latitude dependent ozone loss model. We predict that the amplitude of $S_{22}(p)$ has decreased by about 2% over the past 30 years, an amount that should be detectable in suitable barometric records. In the upper atmosphere, decreases of horizontal winds are generally about 5%. Tidal momentum fluxes, proportional to the square of the wind amplitudes, have generally declined by about 10%. These changes may be large enough to modify waves in a realistic Titan atmosphere and evaluate the upper-atmospheric circulation and influence the upper-atmosphere dynamical and compositional model inputs represented by the tides.

Since ground-based ozone measurements are sparse in the equatorial regions, our knowledge of ozone loss there is limited. Tropical surface barometric data could provide a measure of low-latitude ozone trends unobtainable from direct measurements. We examined barometric records from six equatorial weather stations to characterize trends in $S_{22}(p)$ that might be indicative of tropical ozone loss. From 1973 to 1988, the six-station average of $S_{22}(p)$ declined by $9 \pm 7\%$; of the six stations, four showed declines, two showed increases. Although it is consistent with the decrease associated with typical ozone loss models, we can not conclusively attribute the recent behavior of $S_{22}(p)$ to stratospheric ozone loss. The uncertainty will be resolved by significantly increasing the weather station database.

Regarding the secondary research objectives, the recent Voyager flyby of Neptune provided the first reconnaissance of the icy satellite Triton. Measurements obtained during the flyby include estimates of satellite composition, size, and geologic history [4]. Triton is interesting because it was almost certainly captured by Neptune from heliocentric orbit shortly after or during the formation of the solar system. Consequently, the satellite's thermal evolution has been dominated by energy removed from the orbit and dissipated in the satellite during the orbital evolution to the current state. Previous Triton models that do not include the influence of dissipation predict that the dynamical and internal evolution would have been completed only a few hundred million years after Neptune capture and lead to the prediction that Triton's surface should be over 4 billion years old and heavily cratered, similar to that of the Moon. Voyager images, however, reveal that some regions on Triton are relatively free of craters, implying a surface no more than about 1 billion years old.

We developed a model to investigate the coupled orbital and thermal evolution of Triton. In the model, the rate of orbital evolution is a function of the internal temperature of Triton, which in turn is controlled by the energy deposited in the satellite by dissipation during the orbital evolution. In our model, the important free parameter

plausible choices of initial temperature, the resulting evolution is consistent with the history inferred from the geology. Figure 1 shows the semimajor axis of Triton's orbit and its internal temperature for a model with initial temperature of 220 K. Internal activity capable of smoothing the surface and erasing craters is expected only when the internal temperature nears 273 K, the melting temperature of ice; Figure 1 shows surface activity occurring at about 4 billion years after formation, less than a billion years ago. We conclude that the bulk of Triton's tidal heating did not occur soon after Neptune capture, as previously assumed.

The Saturnian satellite Titan has the only substantial satellite atmosphere in the solar system. Voyager measurements during flyby suggest that the atmosphere is in a state of superrotation, where middle- and upper-atmosphere zonal horizontal wind speeds significantly exceed the rotation rate of the solid body [5]. Earth and Venus have similar winds. Without a constant source of momentum, the superrotation will decay. The momentum source on Titan has not been identified but is assumed to be upward propagating gravity wave. Radio occultation measurements show signal scintillations that could represent density perturbations associated with upward propagating gravity waves [6]. The inferred waves decrease in amplitude from near the surface to about 20 km, maintain constant amplitude from about 20 to 60 km, and have vertical wavelengths of a few kilometers.

In summary, we have pursued a diversified research effort in several areas of planetary and atmospheric dynamics. The results of our work suggest the possible consequences ozone depletion may have on the upper atmosphere. The work also contributes to our understanding of the evolution and dynamics of the satellites of the outer planets.

Atmospheric gravity wave propagation is strongly affected by variations in atmospheric static stability and

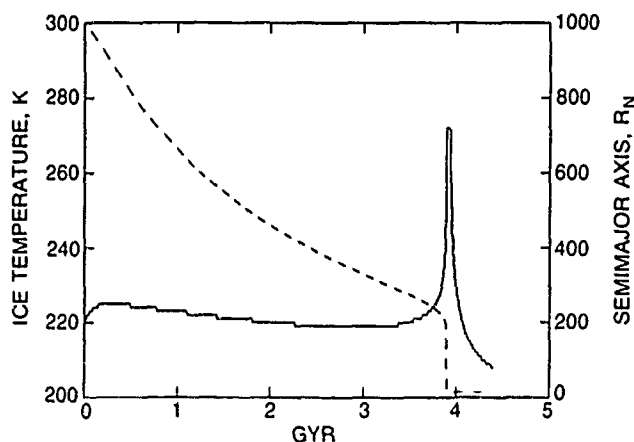


Figure 1 Coupled evolution of Triton from the time of capture by Neptune, in billions of years. The solid curve shows the satellite's internal temperature, the dashed curve shows the orbit semimajor axis in Neptune radii.

horizontal winds. Waves have difficulty moving through stably stratified atmospheric regions and can be absorbed at critical layers, where the horizontal phase speed equals the horizontal wind speed. We constructed a model to investigate the propagation characteristics of gravity plausibility of the putative gravity wave observations. We conclude that the radio scintillation observations are consistent with a gravity wave interpretation for only a narrow range of wave parameters. Waves with short horizontal wavelength do not propagate very high into the Titan stratosphere, whereas the vertical wavelength of significantly longer waves exceeds the observed value (Figure 2). The narrow range of *allowed* wave parameters will help us to infer the nature of the wave forcing mechanism.

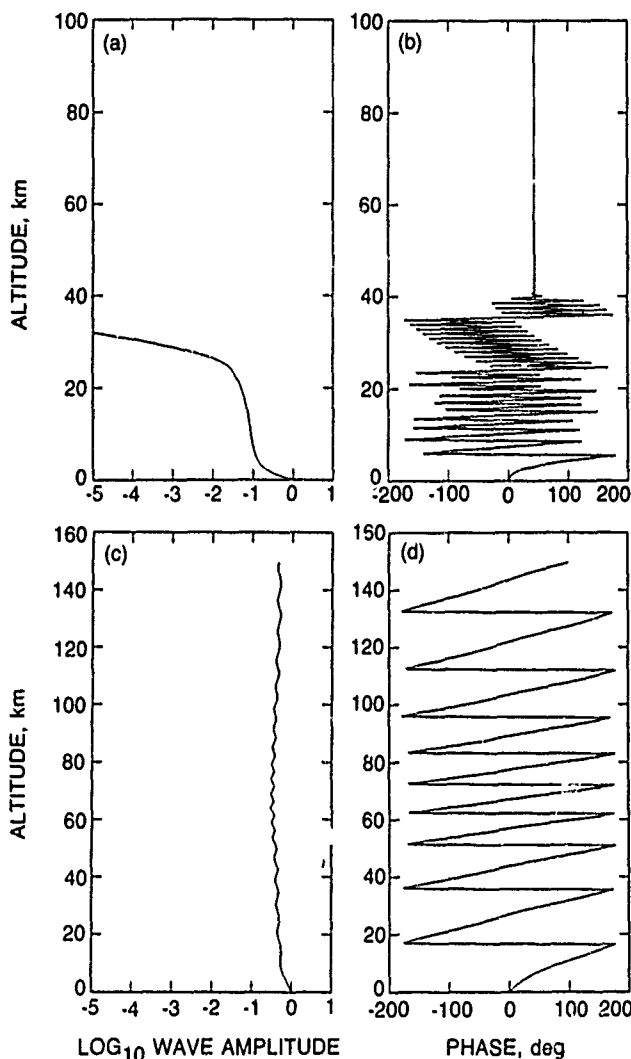


Figure 2. Propagation characteristics of surface forced gravity waves in Titan's atmosphere. The variation of wave amplitude (a) and phase (b) is shown for 2-h waves with 5-km horizontal wavelength; these waves attenuate before reaching 30-km altitude. The propagation of 2-h waves with 100-km horizontal wavelength is also shown in (c) and (d), these waves have vertical wavelength of about 20 km, an order of magnitude greater than the waves inferred from the radio data.

1. G. Megie et al., "Global Trends," *Scientific Assessment of Stratospheric Ozone*, World Meteorological Organization (1989), p. 163.
2. R. T. Watson and Ozone Trends Panel, *Present State of Knowledge of the Upper Atmosphere 1988: An Assessment Report*, NASA Ref. Pub. 1208 (1988).
3. R. S. Lindzen, "Turbulence and Stress Due to Gravity Wave and Tidal Breakdown," *J. Geophys. Res.* **86**, 9707 (1981).
4. B. L. Smith and Voyager Imaging Team, "Voyager 2 at Neptune: Imaging Science Results," *Science* **246**, 1422 (1989).

5. D. M. Hunten et al., "Titan," *Saturn*, T. Gehrels and M. S. Matthews, eds., University of Arizona Press 1984, p. 243.
6. D. P. Hinson and L. Tyler, "Internal Gravity Waves in Titan's Atmosphere Observed by Voyager Radio Occultation," *Icarus* **54**, 337 (1983).

Ross, M. N., G. Schubert, and R. L. Walterscheid, "Propagation of Gravity Waves in Titan's Atmosphere," *Bull. Am. Astron. Soc.* **21**, 233 (1989).

_____, "The Coupled Orbital and Thermal Evolution of Triton," *Geophys. Res. Lett.* **17**, 1749 (1990).

Solar-Terrestrial Physics and Astrophysics

R. J. Rudy, J. B. Blake, M. C. McNab, M. Schulz, and J. H. Hecht,
Space Sciences Laboratory

The major objective of this research is to gain an understanding of the space environment. The focus is on the ambient background of particle and electromagnetic radiation that influences space observation and experimentation, but the work encompasses all of astrophysics, which is the study of the conditions, constituents, and physical processes found in space, and solar-terrestrial physics, which concentrates on the influence of the sun on the earth and near-earth environment.

The project consists of a series of small-scale data-analysis or theoretical studies on topics of current interest and is sufficiently flexible that the investigators can take advantage of unexpected research opportunities within the overall framework of studies of the space environment. The following research tasks were addressed during the past year:

- Study cosmic rays.
- Model planetary magnetic fields.
- Model the galactic magnetosphere.
- Study the infrared emission from active and starburst galaxies.
- Delineate the ultraviolet extinction properties of circumstellar and interstellar dust.
- Understand the emission line formation processes in certain celestial sources.

Terrestrial radiation belts consisting of oxygen and similar ions from the anomalous component of the cos-

mic-ray spectrum have attracted both observational and theoretical attention in recent years. Such ions tend to be singly charged in the heliosphere, but can become trapped in the geomagnetic field when they are stripped of their remaining electrons by the terrestrial atmosphere. The resulting radiation belts are thus characterized by a pitch-angle distribution that peaks near the edge of the loss cone, and so energy degradation of the constituent ions in the vicinity of their mirror points is an immediately important dynamical process for such radiation belts. Calculation of the bounce-averaged atmospheric densities encountered by such ions is complicated by the fact that their gyro-radii are not necessarily small compared with the atmospheric scale height. However, we have devised a good analytical approximation for the gyration-averaged atmospheric density through the generating function for modified Bessel functions of order zero, and we are in the process of testing similarly motivated analytical approximations for bounce averages and drift averages of quantities that vary quasi-exponentially with altitude. We have found, for example, that the gyration-averaged atmospheric density can easily exceed twice the guiding-center value for geomagnetically mirroring ions of interest. This means that gyration-averaging is essential for the accurate estimation of the lifetimes of trapped anomalous cosmic rays in the magnetosphere. Our ability to estimate such lifetimes semianalytically rather than by purely numerical integration should greatly reduce the comput-

ing time expended in modeling the intensity and spatial distribution of this component of the earth's radiation environment.

In pursuit of our previously described idea of modeling galactic cosmic rays as the constituent particles of galactic radiation belts, we have begun, in collaboration with J. G. Luhmann of The University of California at Los Angeles, to compute the bounce and drift periods for energetic particles trapped in a model magnetic field that becomes dipolar at large distances from the galaxy but remains tangential to the galactic disk at distances 2 to 16 kpc from the galactic center (Figure. 1). The objective of this work is to develop a transport theory, based on radiation-belt methods, for the phase-space distribution of cosmic rays in the galactic magnetosphere. As a prerequisite to this, we are computing bounce and drift periods of representative particles in order to ascertain that they do not exceed the age of the universe, and to discern the nature of galactic magnetospheric disturbances that might lead to the further energization of such particles by virtue of radial transport. Our model yields bounce periods of order 10^5 years for relativistic particles trapped in the inner part of the galactic magnetosphere and thus imposes a lower bound of at least 10 GeV on particle energies for which a radiation-belt formulation is appropriate.

Solar and planetary magnetic fields show clear evidence of quadrupole, octupole, and higher moments in addition to dipole moments. We have previously demonstrated an equipartition of global magnetic-energy content among degrees of freedom (including the axial dipole for Uranus and Neptune; excluding the axial dipole for

Earth and Jupiter) for various planetary magnetic fields and are proceeding, in collaboration with J. T. Hoeksema of Stanford University, to test the solar magnetic field for global energy equipartition at various phases of the solar cycle. Preliminary results for the sun appear to show a greater variability of magnetic-energy content among degrees of freedom than we have found previously for planets. However, it is not clear that these results imply a breakdown of equipartition rather than, for example, an aliasing of the multipole decomposition caused by temporal evolution of the solar magnetic field during the 27-day period necessary for a complete observation. Further tests are being devised to answer this question.

M. Schultz of this laboratory recently completed a major article entitled *The Magnetosphere* [1]. Although it is partially a review chapter, this work contains at least six original calculations that help to elucidate magnetospheric phenomena. Topics treated in the original calculations include:

- Locus of minima in $|B|$ along field lines in a compressed magnetosphere.
- Azimuthal drift rates of trapped particles in such a magnetosphere.
- Partial penetration of interplanetary electric field into the magnetosphere.
- Shape of the plasmasphere and of tail plasma trajectories when the plasmopause grazes the magnetopause.
- Transition between strong and weak limits of pitch-angle diffusion caused by unstable whistler-mode waves.
- Resonance broadening in a turbulent plasma.

The four-volume set that includes this treatise is expected to become the standard reference work on geomagnetism, aeronomy, and space research for the next 10 years.

The principal constituents of the infrared sky outside the plane of the Milky Way at wavelengths greater than $25 \mu\text{m}$ are galaxies. Because of their high luminosities, active galaxies (galaxies whose nuclei contain compact, intense sources of radiation that may extend from the x-ray through the radio) and star-burst galaxies can be seen to great distances and are thus over-represented in a flux-limited survey. Thus, any sensor observing the sky at mid- or long-wave infrared wavelengths will see a disproportionate number of these sources. Our objective is to better understand the infrared emission of these sources by determining the relative contributions to their infrared luminosity from synchrotron emission, thermal dust emission, and active star formation. During the past year, we developed a computer program to calculate the bulk luminosity and infrared spectrum from dust grains residing in a galactic nucleus. The model calculates the emission from

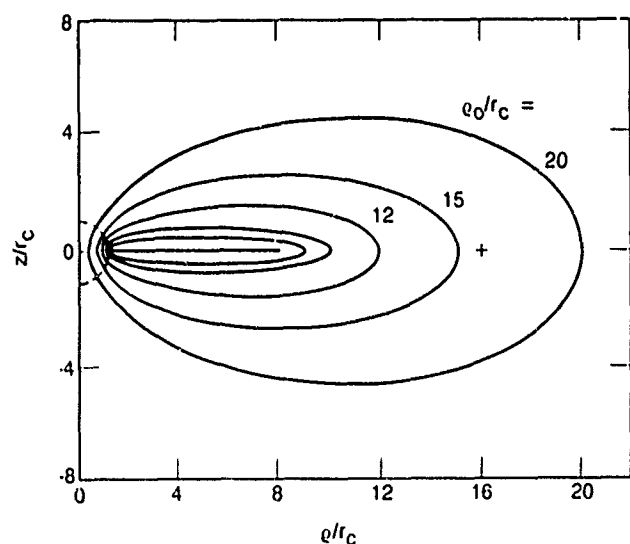


Figure 1 Field line model of the galactic magnetosphere. Field lines are shown that cross the plane of the disk ($z = 0$) at selected distances $\rho = \rho_0$ ($= 9, 10, 12, 15$, and 20 times the radius $r_c \sim 2$ kpc of the central region) from the magnetic axis ($=$ rotational axis) of the Galaxy. This model is used to calculate bounce and drift periods for cosmic rays (see text for additional details).

a series of concentric spherically symmetric dust shells warmed by a centrally positioned source of ultraviolet/visible radiation. The calculations incorporate a radial dependence for the particle density of the dust grains, the wavelength dependence of the grain emissivity, and the albedo and scattering function of the grains, and account for, in an approximate manner, the transfer of radiation through the dusty region. The results are displayed in a manner that provides a direct comparison with the IRAS data so that the user, in obtaining a best match to the observations, can derive such parameters as the dust type and optical depth, luminosity of the central source, and spatial distribution of the dust. Figure 2 shows results from a model of the infrared emission from the Seyfert galaxy NGC 2992. The model incorporates silicate grains with emissivities drawn from the tabulation of Draine [2]. The measured fluxes in each of the four IRAS passbands are shown for comparison. Although the match is fair, the spatial extent of the 100 μm flux exceeds the limit set by IRAS, indicating that grains that are more efficient radiators than the small silicates are needed.

The nature of the dust grains present throughout the interstellar medium is relevant for studies of our Galaxy as well. Not only do dust grains account for the

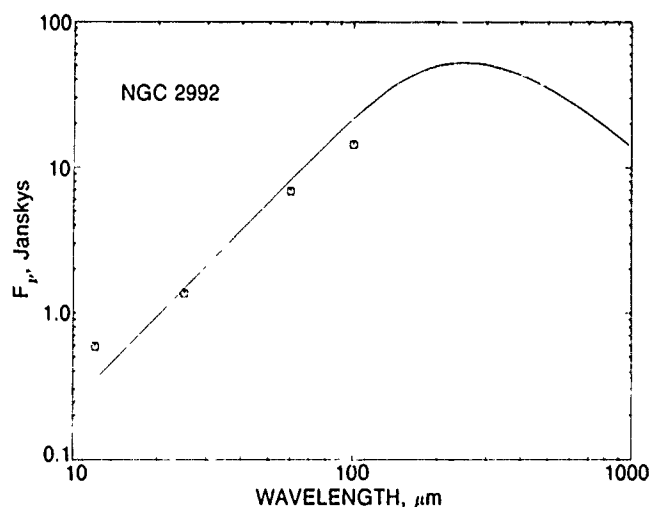


Figure 2. A synthetic spectrum of the infrared emission from the Seyfert galaxy NGC 2992 with the IRAS measurements overplotted for comparison. The spectrum shown was computed for silicate grains of 0.1 μm radius. The grains are assumed to be spherically distributed about a point source of ultraviolet radiation (the Seyfert nucleus) that they absorb and reradiate in the infrared. The density of dust particles falls as r^{-1} , where r is the radial distance from the nucleus. By matching the computed spectrum to the observed fluxes and the spatial extent of the emission, the free parameters allowed by the model can be constrained.

diffuse infrared emission in the galactic plane, but at optical and ultraviolet wavelengths extinction by these same grains modifies and restricts our view of the Galaxy. As part of our research on the properties of interstellar dust, we have studied the nature of the carbon grains associated with R Coronae Borealis stars [3]. These variable stars form carbon particles in the outer layers of their atmospheres and disperse them into the interstellar medium, where they make a significant contribution to the population of carbon grains. As such, their extinction properties have implications for the extinction properties at ultraviolet and visible wavelengths of the interstellar medium as a whole. Based on observations obtained with the International Ultraviolet Explorer satellite, we find that the extinction properties of grains formed by the R Coronae Borealis star are better described by small amorphous carbon spheres than by fractal aggregates of graphite grains. Moreover, such fractal grains are unlikely to form under the conditions present in the atmospheres of these stars.

Another task involving the analysis of observations of astrophysical sources has been our investigation of the emission lines of carbon from the planetary nebula BD + 30° 3639. Planetary nebulae represent one of the final stages of stellar evolution. They occur when a star ejects outer layers of its atmosphere, uncovering the hot core. Ultraviolet photons from this core then photoionize the expelled gas. This typically results in an emission line spectrum characterized by strong permitted lines of hydrogen and helium and forbidden lines of the heavier elements. In BD + 30° 3639, however, a rich spectrum of permitted carbon lines is observed as well (Figure 3). The unusual strength of these features is due to an anomalous over-abundance of carbon. Carbon was a by-product of the helium burning that generated much of the energy expended by the star while it was in its giant phase. This excess carbon was then mixed from the core to outer layers of the star, where it was revealed by the shell ejection. What is of interest about the excess carbon in BD + 30° 3639 is that it increases the optical depths of the lines, permitting us to study the effect of optical thickness in certain transitions on the observed line spectrum. Indeed, our analysis shows that the spectrum is not adequately described by recombination, but is optically thick in the resonance transitions. Moreover, certain other low-lying levels that do not connect directly to the ground state also give rise to optically thick transitions. The cumulative effect of this is to not only enhance certain emission lines in the ultraviolet, but to greatly increase specific features in the optical and near-infrared parts of the spectrum as well.

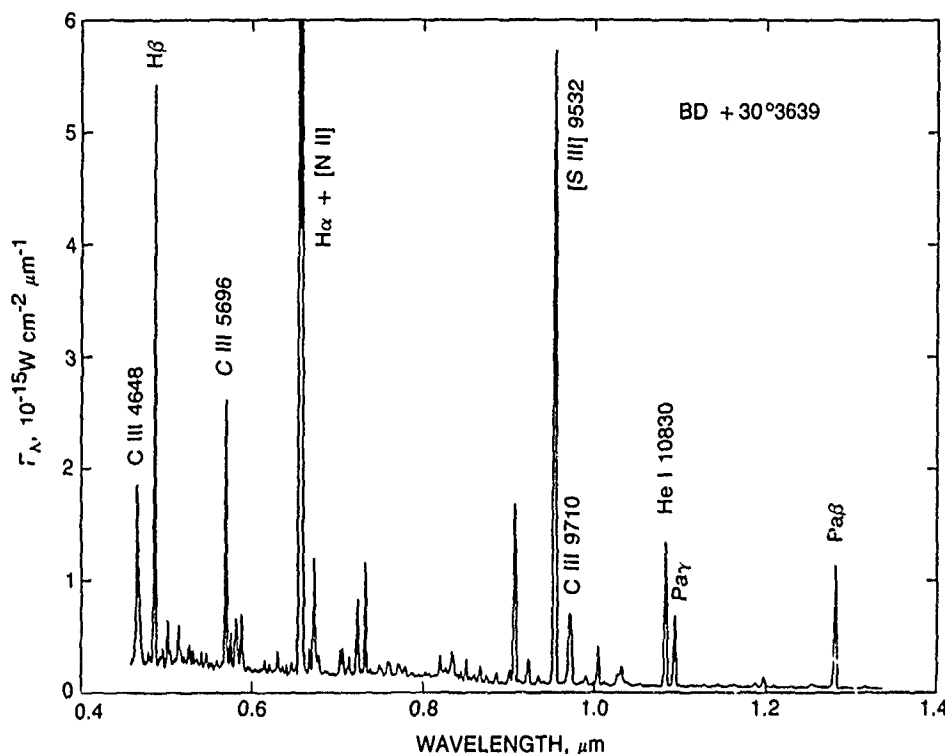


Figure 3. The optical and near-infrared spectrum of the planetary nebula BD + 30° 3639. Selected emission lines are identified. Most of the weak features in the spectrum are lines of C^{+2} . Because of a gross overabundance of carbon, these features are approximately 50 times stronger than in planetary nebulae with solar abundances. However, two of the lines, C III $\lambda 5696$ and $\lambda 9710$ are 1000 times greater than their typical values. This is because the resonant, and certain low-lying subordinate, transitions are optically thick. These transitions include alternate paths out of the upper levels of $\lambda 5696$ and $\lambda 9710$, which are favored at low optical depths. When these alternate transitions become optically thick, the electrons eventually make the transitions that give rise to $\lambda 5696$ and $\lambda 9710$, greatly increasing their strength.

* * * * *

1. M. Schulz, "The Magnetosphere," *Geomagnetism and Aeronomy*, Vol. 4, J. A. Jacobs, ed., Academic Press, London (1991), p. 87.
2. B. T. Draine, *Astrophys. J. (Suppl.)* **57**, 587 (1985).
3. J. H. Hecht, "The Nature of the Dust Around R CrB Stars: Isolated Amorphous Carbon or Graphite Fractals?," *Astrophys. J.* **367**, 635 (1991).

Blake, J. B., and D. S. P. Dearborn, "On the Possible Contribution of WC Stars to Isotopic Anomalies in Cosmic Rays and Meteorites," *Genesis and Propagation of Cosmic Rays*, M. M. Shapiro and J. Wefel, eds., D. Reidel (1988), p. 153.

_____, "A Local Source of ^{26}Al Gamma Rays," *Astrophys. J. Lett.* **338**, L17 (1989); also, ATR-88 (9558)-3, The Aerospace Corp. (in press).

Blake, J. B., "Geomagnetically Trapped Heavy Ions form Anomalous Cosmic Rays," *Proceedings of the 21st International Cosmic Ray Conference*, Adelaide, Australia (1990).

Bruner, M. E., et al., "Dynamic Evolution of the Source Volumes of Gradual and Impulsive Solar Flare Emissions," *Astrophys. J.* **322**, 494 (1988); also, ATR-86A(9558)-3, The Aerospace Corp. (1 April 1989).

Dearborn, D. S. P., and J. B. Blake, "Possible Contributions by Wolf-Rayet Stars to the Proto-Solar Nebula: Extinct Radioactivities, or, Grains of Truth from Wolf-Rayet Stars?," *Astrophys. J.* **332**, 305 (1988).

Doschek, G. A., et al., "High-Resolution X-Ray Spectra of Solar Flares. IX. Mass Upflow in the Long-Duration Flare of 1979 June 5," *Astrophys. J.* **345**, 1079 (1989); also, ATR-89(9558)-5, The Aerospace Corp. (15 December 1989).

McKenzie, D. L., "X-ray Line-Ratio Plasma Diagnostics Applied to Solar Active Regions," *J. Phys. (Paris)* **49**, C1-55 (1988).

Ness, N. F., et al., "The Magnetic Field and Magnetospheric Configuration of Uranus," *Uranus*, E. Miner and J. T. Bergstralh, eds., University of Arizona Press (in press).

Rice, C. J., "Contributions of The Aerospace Corporation to the 1989 Report of the Observatories of the AAS," *Bull. Am. Astron. Soc.* **21**, 7 (1989); also, ATR-89(9558)-1, The Aerospace Corp. (15 September 1989).

_____, "Contributions of The Aerospace Corporation to the 1990 Report of the Observatories of the AAS," *Bull. Am. Astron. Soc.* **22**, 1 (1990); also, ATR-90(9558)-1, The Aerospace Corp. (1 April 1990).

Rudy, R. J., et al., "The 0.46-1.3 μm Spectrum of the Planetary Nebula BD + 30/3639," *Astrophys. J.* **380** (1991).

Schulz, M., and G. T. Davidson, "Limiting Energy Spectrum of a Saturated Radiation Belt," *J. Geophys. Res.* **93**, 59 (1988).

Schulz, M., and G. A. Paulikas, "Planetary Magnetic Fields: A Comparative View," *Adv. Space Res.* **10** (1), 55 (1990).

Information Science

INFORMATION SCIENCE

Applications of Logic to Computer Verification

L. G. Marcus, J. V. Cook, J. E. Doner, I. V. Filippenko, and T. K. Menas,
Computer Systems Division

Computer verification refers to the mathematical proof that a program or machine description satisfies a given formal specification. Although it is not yet common in production software and hardware projects, computer verification has the potential, as a supplement to testing, for greatly increasing confidence in the correctness of a program or a machine design. Such an increase is particularly critical to Space Systems Division applications, where an incorrect implementation can cause the loss or degradation of a mission.

The State Delta Verification System (SDVS) is a prototype system being developed in the Computer Systems Division to assist in writing and checking proofs of computer correctness. This is part of a long-term effort to make computer verification a more usable technology for application to large projects in the design and development phases.

Numerous approaches and prototype verification systems are being developed at research facilities and universities throughout the world. Although their goals of mathematically proving the correctness of computer programs or hardware descriptions are similar, the approaches differ in the strength of expressibility and provability, the degree and ease of user interaction, the target computer program or machine description language, and the kind of specification to be verified. SDVS has a unique combination of strong foundations, usability, and wide applicability.

The objective of this project is to provide theoretical foundations for future extensions of SDVS in order to facilitate verification at all levels of the computer hierarchy, from low-level hardware design to high-level programming. Since the concept of formal proof is fundamental to verification, the necessary foundations for a system such as SDVS involve methods and results from mathematical logic.

Areas studied this past year included the expressibility of specifications, computer security, the offline characterization of procedures, recursion, and program composition. Among other applications, the results achieved will help extend SDVS to handle significant subsets of the Department of Defense standard programming language Ada [1] and the IEEE standard hardware description language VHDL [2], both of which efforts are funded by the Enhancements to Computer Verification Mission-Oriented Investigation and Experimentation (MOIE) task and the National Computer Security Center (NCSC) SDVS Verification Project. (MOIE is an Aerospace program supported by Space Systems Division to develop new scientific and engineering techniques applicable to Air Force space programs.)

A general problem dealt with in much of this research project is how to take a property one wishes to specify or prove, a property formulated in intuitive (and therefore imprecise) language, and find for it a formal analog. This analog can be either in the language of the underlying logic of the verification system (the State Delta logic as it currently exists), or in some extension of that language. Since the verification system is used to model real computer software and hardware, it is very important that the choice of the formal analog be as faithful as possible. It is also important, however, to make modifications to SDVS as compatible with the existing system as possible, consistent with the faithfulness of the representation, so that those modifications can be carried out in extensions to the current SDVS system without the need to rewrite large portions of SDVS. For example, the incorporation of invariants into SDVS, a company-sponsored research topic last year, was implemented this past year by adding several new proof commands and making some minor modifications to the existing commands, the design and implementation, supported by the NCSC, successful.

ly used the basic research results from the company-sponsored project, and the new version of SDVS was compatible with older versions.

A good example of the preceding principle of finding formal analogs to intuitive computational concepts is to be found in the first topic studied this past year, the specification of transmission. It is easy in English to state that the output stream of some system equals the input to that system. (We refer to this here as OEI.) However, to be of use in verification, specifications must be written in some formal language with rigorous semantics and proof theory. We studied the nuances of trying to express OEI in a class of logics (*temporal logic*) relevant to SDVS and discovered that it is impossible to express OEI in full generality. In other words, any formal specification either will allow some implementations in which output is not exactly equal to input or will not allow some implementations in which output is equal to input. Thus, we have a choice of using a stronger logic or using the same logic to specify as many of the admissible implementations as possible, albeit not all. We examined this second alternative.

We discovered that a minor, but useful, restriction on the set of implementations is to assume the existence of a clock; the formal analog of a real clock is a device that can be used to compare the value of the input with the value of the output at given times. The use of such a device allows the formal specification of OEI. It also turns out that a *necessary* condition for this expressibility is the existence (in the specification) of a device that is almost like a formal clock. The specifier *must* include this clock in the specification, even if the specifier was not interested in the clock per se. These results appear in [3].

Computer security is an ill-defined term that has been used to include just about any good property that a computer system can be purported to have. It is usually broken down into protection of information, protection of data, and protection of access. Short definitions of these concepts are, in order, guarding against the unauthorized release of information from the system, guarding against the unauthorized alteration of system data, and guarding against the unauthorized restriction of use of the system. Obviously, these are all important characteristics for critical computer systems.

Our research in computer security focused on two main aspects of the protection of information: information flow and probabilistic information security [4,5]. Building on our framework from previous years for formulating varieties of information in computations (viz., a model-theoretic formalization to capture the interaction of an adversary V and a protected variable X), we developed a formal definition of these two aspects because of their importance in *real-life* security considerations. We defined a framework that allows a fine-tuning of exactly what kinds of information flow are to be considered admissible. In particular, we want to prevent information flowing from X to V only if that information was not *caused*

by V in the first place. This formulation is based on two observations:

- Causality is *intensional* rather than *extensional*; the behavior of the values of variables in two computations can be identical, but one may reflect causal relationship, whereas the other does not.
- Causality is subjective; it is up to the specifier to decide which kinds of interactions he wants to consider as causal.

Thus, we take the view that the causality factor is as independent a part of the specification as any other correctness or security issue. We add a causality relation to the specification language and describe the semantics and possible proof methods for information security modulo that causality. We believe that it will be possible, although difficult, to prove claims of information-flow security in an extension of SDVS.

The case for probabilistic information-low security (PIF) is becoming more clear as computer systems become more complex. The adjective *probabilistic* refers to the fact that the adversary may not learn anything at all about X for sure, but only that the probabilities of the possible behaviors of X have changed, so at least one outcome has become more probable. This can be a very important consideration for an adversary able to sample the behavior of a system statistically. We developed a formal definition of PIF that is compatible with the logical framework of our other definitions of information, and we are studying possible methods of proof.

Perhaps the most immediately applicable topic studied this past year was how to incorporate offline characterizations of procedures into SDVS [6]. This problem arises when a program, say in Ada, contains a procedure that is called several (or many) times with different arguments. To prove some property about this program, we need to account for the effect this procedure has, whenever it is called, and with whatever arguments. We developed a method that allows one, instead of dealing with each procedure call separately, to treat the procedure as a module (offline) and to find a general characterization of it; this characterization can then be "plugged in" to the proof at the appropriate times. As part of the MOIE task mentioned earlier, an experimental version of this facility has now been implemented in SDVS.

Another topic of immediate application was recursion. In our context, recursion refers to the common programming technique of having a procedure call itself. This technique is sometimes very useful in writing efficient and understandable programs, but it can also cause problems. Incorrect recursive code, in addition to giving wrong answers, can easily lead to nontermination. In temporal logic in general (and in the logic of SDVS in particular) it is natural to represent recursion in a mathematically precise manner by means of circular formulas - formulas that contain occurrences of their own names. We devel-

oped a criterion and algorithm for determining the soundness of such circular definitions, i.e., for determining if a given circular definition actually defines a computation or if its circularity *prevents* one from computing anything. We anticipate that a successful implementation based on this research will be carried out under the aforementioned NCSC project [7,8].

The last topic studied this past year was composition. Last year, we continued our research on a notion of composition over sequential program fragments, giving a semantics to sequential computations in which the intermediate states are abstracted away, leaving only a specification of the input-output behavior of the computation. This past year, we worked out a very precise mathematical development of this idea and continued studies of a possible algorithm, as applicable to the formal verification of VHDL descriptions.

* * * * *

1. U. S. Department of Defense, *Reference Manual for the Ada Programming Language (ANSI/MIL-STD-1815A)* (22 January 1983).
2. *IEEE Standard VHDL Language Reference Manual*, IEEE Std. 1076-1987, IEEE (1988).
3. L. Marcus and T. Menas, *Expressing Transmission* ATR-90(8590)-4, The Aerospace Corp. (30 September 1990).
4. L. Marcus, *Generalized Probabilistic Information Flow*, ATR-90(8590)-2, The Aerospace Corp. (30 September 1990).
5. L. Marcus, *Proving Varieties of Information Flow Security*, ATR-90(5778)-3, The Aerospace Corp. (30 September 1990).
6. J. E. Doner and J. V. Cook, *Offline Characterization of Procedures in the State Delta Verification System (SDVS)*, ATR-90(8590)-5, The Aerospace Corp. (30 September 1990).
7. L. Marcus, *An Algorithm for Checking Soundness of Circular State Delta Definitions*, ATR-90(8590)-1, The Aerospace Corp. (30 September 1990).
8. L. Marcus, *Proving Claims about Recursive Procedures in SDVS*, ATR-90(5778)-2, The Aerospace Corp. (30 September 1990).

Marcus, L., and T. Redmond, "A Model-Theoretic Approach to Specifying Verifying and Hooking Up Security Policies," *Proceedings of the Computer Security Foundations Workshop*, J. Millen, ed., p. 127; also, ATR-89(8490)-1, The Aerospace Corp. (27 March 1989).

Marcus, L., "The Search for a Unifying Framework for Computer Security," *Cipher IEEE* (Fall 1989), p. 55; also, ATR-89(8490)-2, The Aerospace Corp. (30 September 1989).

_____, *The Semantics of Concurrency in SDVS*, ATR-89(8490)-4, The Aerospace Corp. (30 November 1990).

Menas, T., *Variants of Invariance*, ATR-89(8490)-5, The Aerospace Corp. (31 January 1990).

Redmond, T., L. Marcus, and I. Filippenko, "Composition of Sequential Program Fragments," ATR-89(8490)-3, The Aerospace Corp. (30 November 1990).

Neural Network Architectures

M. P. Plonski, W. K. Peter, and R. P. Ma,
Computer Systems Division

Neural computing is based on the use of a large connected network of simple processing elements, or nodes, that function on a massively parallel scale. The simultaneous combination of many simple operations, typically multiply-accumulate and thresholding, gives neural networks their power and fault-tolerant nature. Much of the research to date has been performed using software simulations of these massively parallel architectures. Special-purpose very-large-scale integrated (VLSI) neural network chips promise several orders of magnitude in speed

improvement, and the initial commercial versions of these chips with digital, analog, and stochastic pulse-train arithmetic became available this past year.

Current software simulations of neural networks assume ideal computing devices, which is not realistic for these VLSI devices. The computations performed by these devices can deviate from the ideal with respect to the number of bits of precision, bias and gain offsets, noise, and stochastic arithmetic errors. The objectives of this project are to explore the performance of feed-

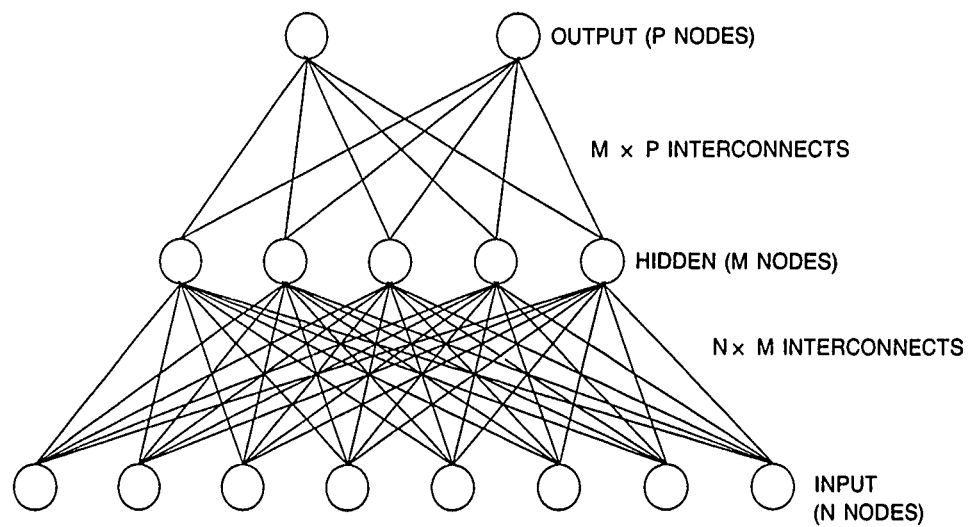


Figure 1. Feed-forward neural network.

forward neural networks, when the effects of these non-ideal computations are included in the software simulation, and to identify algorithms that work well under these conditions. Our primary focus has been on analyzing the effects of limited precision and other errors in numeric computations when analog devices are used.

A schematic of a simple feed-forward neural network is shown in Figure 1. Each circle represents a processing element or node, and each line represents a connection with a weighting factor between nodes. The data processing propagates from one layer to the next using the following computations for each node in a layer:

0z.

$$O_i = f(\text{net}_i) = 1/(1 + e^{-\text{net}_i}) \quad (1)$$

$$\text{net}_i = \text{bias}_i + \sum_j W_{ij} O_j,$$

where net_i is the net input to node i and is equal to a bias term plus the sum of the products of the outputs of all nodes that feed node i times their weight W_{ij} . O_i is the output of node i that results when a nonlinear transfer function f is applied to the input net_i . Feed-forward neural networks typically operate in two modes: a testing or forward mode, where the preceding computations are performed, and a training or backward mode, where the values for the connection weights and biases are modified in order to reduce some measure of the network error. The network error is usually defined as the mean-square error computed from the difference between the desired values at the output nodes and the actual values at the output nodes that were computed during the forward pass.

Equation (1) represents the ideal computations performed by a node. The actual computations performed by VLSI devices can be significantly different. In Figure 2, an ideal transfer function f , is compared with an actual transfer function from an analog VLSI chip (courtesy of

Jet Propulsion Laboratory). The deviations from the ideal can be either deterministic and known, deterministic and unknown, or random. The example with the transfer function in Figure 2 would be deterministic and could be either known or unknown depending on whether or not the actual transfer function was used in the training algorithm. One could argue that known deterministic errors are not really errors, since the errors can be incorporated into the training algorithm. The net effect of these known errors, then, becomes equivalent to simply choosing a different set of design parameters whose output under ideal assumptions will match that of the original nonideal design. For example, backpropagation (BP) [1] does not

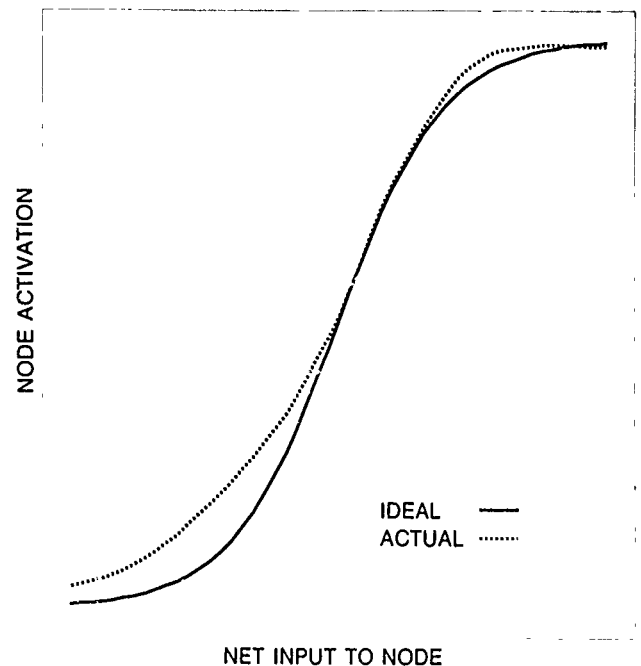


Figure 2 Node transfer function

require that one use a specific transfer function, but only that the transfer function f be differentiable and that its derivative f' be computed *a priori* in order to determine the magnitude of the error to backpropagate to the previous layer. We developed models for backpropagation training that incorporated effects of finite precision, bias and gain offsets, and noise into the network computations. Using simulated data, we then tested these models on a pattern recognition problem.

We found that more precision was required for the training phase than for the testing phase, a finding that is in agreement with results of other researchers. It appeared that the network performance did not decrease gradually with reduced precision, but rather appeared to drop suddenly at some minimum number of bits of precision. This sudden drop in performance appeared to occur when the computed weight modification dropped below the weight quantization level and the network was no longer able to modify the weight at each iteration. This effect was very dependent on the momentum and learning-rate terms used in the training.

Simulations indicated that BP training was able to compensate for certain types of unknown errors, but that the training failed to converge for other types. Backpropagation training is based on a gradient descent of the error surface in the solution space in order to find the values for the bias and weight terms that minimize the error. If the training is based on correct assumptions about the forward computations, then the gradients are correctly computed and the training descends the error surface efficiently. However, if the training is based on incorrect assumptions about the forward computations, the gradients are incorrectly computed and the training attempts to descend the error surface incorrectly; this can result in either increased training time or a failure to converge.

A simple example of this effect was to introduce an error offset term into the net computation. In theory, this offset could be easily compensated for by simply adjusting the bias, computed using ideal assumptions, by an amount equal to the offset. Although BP did not find this solution (because of the complex way in which the solution space is searched), it was able to find an equivalent solution in terms of the network performance on the classification task. In this case, the training was able to compensate for incorrect assumptions.

If the desired output for a node is set on the tails of the transfer function f (i.e., near the minimum or maximum output value), the node will be somewhat insensitive to errors in the computation of net , since f is relatively flat ($f' \approx 0$) in these regions (Figure 2). Although we found that operating on the tails of f made the network more robust with respect to errors in net , we also found that this made the network extremely sensitive to errors in f . This is to be expected, since a small error in f when operating on the tails requires the network to learn a large compensation in net in order to achieve the desired output. By

introducing errors in f , it was very easy to cause a lack of convergence in the training. Some researchers have advocated using error criteria other than minimum mean-square error to create more robust boundaries for pattern recognition applications. One such proposed definition for the error requires only that the output node exceed some specific value, rather than obtain some specific value, in order to achieve a correct classification and not produce any output error. Such an error definition may also prove more robust with respect to errors in the transfer function, but time did not allow us to explore this possibility.

With the advent of analog VLSI neural network chips, researchers have been searching for a hardware-based learning algorithm that does not require *a priori* knowledge of the network computations. One such algorithm is the Madaline III (MRIII) algorithm [2], which is functionally equivalent to BP, except that the gradient of the error surface is estimated at each weight change by *diddling* each weight ($\delta_j \approx \Delta \text{mean-square-error} / \Delta W_{ij}$). Backpropagation uses *a priori* knowledge or assumptions about the forward computations to compute δ_j analytically at each node in a recursive fashion, starting with the output nodes (hence the name *backpropagation*). MRIII is much more computationally expensive than backpropagation, since it requires a separate forward computation for each δ_j ; however, if the forward computations can be computed very rapidly by VLSI chips, then the cost of this computational expense can be mitigated.

We implemented the MRIII algorithm and confirmed that it precisely matched BP learning at each training step when a sufficiently small ΔW_{ij} was used and the BP training used correct assumptions about the computations. We also verified that MRIII was insensitive to unknown deterministic errors, since it does not require *a priori* knowledge. In effect, MRIII has the same performance on unknown deterministic errors as BP does when those errors are known and incorporated into the learning algorithm.

Intel Corporation recently released experimental versions of their analog VLSI chip, the Electrically Trainable Analog Neural Network (ETANN) [3]. This chip is capable of implementing the MRIII algorithm and can operate in the forward mode at an astounding 2 billion operations per second. The chip is designed for embedded systems that do not require real-time learning, so that although the weights are electrically modifiable, it is very time-consuming to do so. The chip is designed such that the weights can be initially estimated using BP software simulation, downloaded into the chip, and then modified using MRIII learning to compensate for chip-to-chip variations. We verified this combination method of training with software simulation, and it appears that BP training can be used to *seed* the network for MRIII training. The MRIII training will then compensate for any errors in the assumptions used for BP training.

In conclusion, backpropagation can compensate for certain errors in assumptions about the network computations. Some errors would simply cause the solution space to be searched less efficiently, whereas others could cause the network training to fail to converge. It was demonstrated that the Madaline III algorithm was insensitive to assumptions about the network computations, since it does not require *a priori* assumptions about the network computations. However, MRIII learning can be slow. One remedy is to use BP training followed by MRIII training, and we verified that this approach will work. Numer-

ous analog VLSI neural network chips are currently under development at various research facilities, and the results of this effort indicate that the minor inaccuracies associated with analog computing devices can be tolerated without a significant loss of performance for pattern recognition applications. The knowledge gained during this effort has also contributed to the development of an Aerospace training course in neural networks. This work will continue next year under the title *Artificial Neural Network Simulator*.

* * * * *

1. D. E. Rumelhart, J. L. McClelland, and the PDP Research Group, *Parallel Distributed Processing*, MIT Press (1986), Chap. 8.
2. M. Holler et al., "An Electrically Trainable Artificial Neural Network (ETANN) with 10240 Floating

Gate Synapses," *International Joint Conference on Neural Networks*, Vol. II (18-22 June 1989), p. 191.

3. D. Andes et al., "MRIII: A Robust Algorithm for Training Analog Neural Networks," *International Joint Conference on Neural Networks*, Vol. I (15-19 January 1990), p. 533.

Software Application Generators

R. R. Razouk,
Computer Systems Division

Improving the productivity of software development is an ongoing problem in the construction of large computer systems. Compared to the design and test phases, the mechanical task of producing code continues to occupy a large fraction of software development time. Application generation is an approach to automated software production that capitalizes on domain-specific knowledge in two ways: it reuses well-defined design approaches for some range of problems in a narrow domain, and it reuses software building blocks to implement designs [1]. Application generators are programs that transform specifications, written in a domain-specific language, into executable code [2,3]. Last year, we produced a prototype application generator for user interfaces that demonstrated the feasibility of applying application generation technology to that domain. The prototype supported a simple application language and produced applications that executed in the SunView or X-Windows windowing environments. The objective this past year was to evaluate the efficacy of this approach in improving software productivity. Work proceeded on three parallel tasks:

- Investigation of the application of standard code-generation techniques to application generators.
- Improvement of the capabilities of the prototype to make it a usable tool.
- Assessment of the effectiveness of application generators by applying the prototype to a sizable software development activity.

An application generator is similar in structure to a compiler. Both are responsible for processing high-level descriptions of applications, both must construct implementations of the applications, and both must transform the implementations into executable software targeted to a variety of execution environments. This final phase is called *code generation*. The code-generation phase encodes knowledge of the target execution environments, whereas the first two phases encode knowledge of the application domain.

The prototype completed last year contained code generators for each target windowing environment (SunView and X-Windows). During this past year, the code-generation phase was reimplemented to apply the

application ag

panel is a control panel with width 5.5 inches, height 5.5 inches.

panel contains a message named p1 with text "Phase I"

panel contains a toggle switch named pseudo with

label "Generate Pseudo-Code?"

value off

notifier pseudo-proc

panel contains a message named file with text "File name:"

panel contains a text entry named file-name with length 32

state disabled.

place top left of p1 down 0.25 inches right, 0.25 inches from top left of panel.

place bottom left of pseudo right 0.25 inches from bottom right of p1.

place top left of file down 0.25 inches from bottom left of pseudo.

place left of file-name right 0.125 inches from right of file.

panel contains a message name p2 with text "Phase I."

panel contains a toggle switch named code with

label "Generate Code?"

value off

notifier code-proc.

panel contains a radio button named C

with label "C Code"

value on

state disabled

notifier c-proc.

...

panel contains a button named quit

with label "Quit"

notifier quit-proc.

...

end application.

Figure 1. Sample application specification.

concept of *pseudo code*, which is used in many compilers. Pseudo code is a software specification that is at a sufficiently high level to span the range of target environments. In our prototype, the pseudo code consists of simple commands that describe the structure of the code to be generated. A simple customizable translator (a macro processor), customized for each target environment, transforms the pseudo code into code that will operate in a particular windowing system. The advantage of this more general approach is that the customizations can be readily changed to optimize the generated code, add new primitives, and correct errors.

A thorough evaluation of the effectiveness of application generators required that a usable tool be constructed. Consequently, we enhanced last year's prototype in three ways:

- By adding new constructs to the application language that spanned a broader range of applications.
- By producing a usable front end for the application generator.

- By implementing mechanisms that facilitate the development of applications.

Two capabilities were added to the prototype: a rich set of primitive objects for inclusion in applications (frames, radio buttons, check boxes, editable text fields, messages, and composite objects), and placement commands for performing screen-layout functions. The placement commands permit alignment of arbitrary points on an object to arbitrary points on other objects. The addition of frames and composite objects revealed fundamental limitations of the SunView windowing environment. Both of these objects permit nesting (the inclusion of objects within other objects). Whereas X-Windows supports such nesting, SunView does not. Consequently, the further development of the tool was limited to the X-Windows windowing system. Figure 1 shows a specification of a simple application screen; Figure 2 shows the resulting screen.

The usability of the application generator was significantly enhanced by adding a simple front end that was itself constructed using the application generator. This front end can be used to interactively control the execution of the various phases of the application generator. Figure 2 shows one of the windows of the application generator's front end. This window was generated from the specification in Figure 1. The usability of the tool was further enhanced by the construction of a *previewer*, which can be used to provide immediate feedback to the user by processing the application specification and displaying the

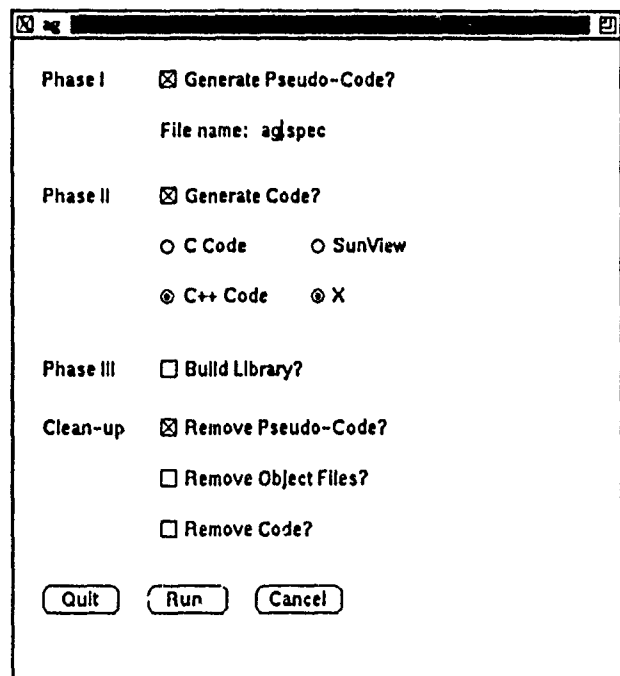


Figure 2. Application generator front end.

was to evaluate the effectiveness of application generators rather than to produce a general tool for user interface software development.

corresponding windows. The previewer was easily constructed by substituting a screen builder for the code generation phase of the application generator. The enhancements made the application generator a practical tool, albeit one with limited functionality. Additional enhancements were deferred, since the objective of the project

The primary objective this past year was to evaluate the effectiveness of using application generators. An ideal evaluation requires two parallel developments of a software system, one development proceeding with the application generator, the other without it. In such a study, the true impact of the application generator on productivity could be measured. Unfortunately, this experimental procedure is extremely costly. As an alternative, a less meaningful measure of productivity was used: lines of code. Comparing the number of lines of code produced by

the application generator to the number of lines in the application description is a loose measure of the savings achieved. The measure is inaccurate because it favors *inefficient* application generators; i.e., those that produce superfluous code. However, analysis of the code produced by the generator can reveal such anomalies.

The study involved developing an X-Windows user interface to the Vehicles system. The user interface now includes 13 interactive screens. Each screen contains a static and a dynamic component. A static screen component is one that is always displayed, such as a button or a prompt message. A dynamic screen component is one whose contents are determined during the execution of the program, such as a scrollable list of names. The application generator was used to describe the static component of 10 screens. Three screens were completely dynamic. The dynamic components of all 13 screens were coded manually. Figure 3 shows a screen that is partially generated by the application generator and partially man-

Figure 3. Example of vehicle screen.

The screenshot shows a window titled "testvkl" with a "Parametric Study Window" dialog. The dialog is split into two main panels. The top panel, "Independent Variable", has a "Subsystem" list with "comm" selected and a "Parameter" list with "wt_payload" selected. To the right of these lists are controls: a "> Select >" button, a "Clear" button, and input fields for "Minimum Value" (20), "Maximum Value" (30), "Step Size" (1), and "Units" (lbs). The bottom panel, "Dependent Variable(s)", also has "Subsystem" and "Parameter" lists with "comm" and "wt_payload" selected. To the right is a "DeSelect" button, a "Clear" button, and a large text area containing "comm.wt_payload". At the bottom of the window are three buttons: "Display Options ...", "Perform Parametric Study", and "Cancel".

aged by custom-crafted software. In the figure, the contents of the scrollable lists are generated manually. The remaining parts of the screen are generated automatically. The successful integration of automatically generated code with manually generated code was an important test of the applicability of our approach.

The results of the study are given in Table 1. The accounting for lines of code is broken down into several categories. The number of lines of graphics code that is automatically generated is shown in the first row. The number of lines of graphics code that is manually generated is shown in the second row; this code interfaces to the automatically generated code and enhances its functionality. The number of lines of nongraphics code that is manually generated is shown in the third row; this code interfaces to the Vehicles system and implements the internal storage of objects. The rows are further divided into columns. Lines of executable code are shown in the first column. Nonexecutable declarations in header files are shown in the second column; this code is essential to the correct functioning of the software, but is not directly executable. The data in the table show that 44% of the code was generated automatically. This is a loose measure of the range of the application generator. Although the tool is of limited functionality, it can be used to implement a significant portion of a large application. The measure of productivity gains is that the 5561 lines of automatically generated code were produced from 386 lines of application specification - a ratio of 14 to 1. An audit of the generated code revealed that it was comparable in most cases to equivalent manually generated code. As we expected, the application generator sometimes produced redundant code.

In conclusion, this project has demonstrated the utility of application generators. A general architecture for application generators was developed, and a prototype generator for user-interfaces was built. Although limited effort was spent on building a general tool, this tool proved useful when applied to a significant software-development activity. The improvements in productivity were demonstrated and measured. Although an ideal parallel development could not be done, the results of the evaluation show that application generators can yield important productivity gains.

Table 1. Study Results

Study Results			
Code Type	Lines of Code	Lines of Headers	Total Lines
Auto graphics	4395	1166	5,561
Manual graphics	3475	895	4,370
Manual nongraphics	1964	685	2,649
Total lines	9834	2746	12,580

* * * * *

1. R. Abbott, A Position Paper on Software Reuse, *3rd International Workshop on Computer-Aided Software Engineering, CASE '89 (July 1989)*.
2. J. Craig Cleaveland, "Building Application Generators," *IEEE Software* (July 1988), p. 25.
3. J. Craig Cleaveland and Chandra M. R. Kintala, "Tools for Building Application Generators," *AT&T Tech. J.* **46** (July/August 1988).

Razouk, R., *An Application Generator for User-Interfaces: User Manual*, ATR-90(8256)-1, The Aerospace Corp. (to be published).

_____, *An Application Generator for User-Interfaces: Design and Empirical Evaluation*, ATR-90(8256)-2, The Aerospace Corp. (to be published).

Classification Tree Optimization by Simulated Annealing

R. S. Bucy and R. S. Di Esposti,
Systems Engineering Division

In this research, we are investigating a new approach to the design of classification trees. The classification problem is described as follows. A set of classes is described by some common set of attributes. For example, the attributes may be based on the outcome of a number of tests or answers to questions. Then, given some unknown object, it is desired to identify which class it belongs to, based on the outcome of the tests as applied to that object.

For example, a binary identification problem uses only binary tests: tests with only two outcomes (yes/no). A finite set of objects $O = \{O_1, O_2, \dots, O_N\}$ is described by the answers to a finite set of tests (or questions), $T = \{T_1, T_2, \dots, T_M\}$. Each question can be thought of as a function $T_i : O \rightarrow \{\text{yes}, \text{no}\}$ from the set of objects to the set $\{\text{yes}, \text{no}\}$. This information provides the *a priori* knowledge for classification and can be represented by a diagnostic table (or incidence matrix).

Consider the four-object, three-question example with diagnostic table shown in Figure 1. Given some unknown object x , it can then be identified as belonging to one of the object classes. For example, suppose x has the attributes $T_1 = \text{no}$, $T_2 = \text{yes}$, $T_3 = \text{yes}$. Then, x belongs to class O_2 .

A classification tree corresponds to a sequential ordering of the tests in such a way that the current test depends on the outcome of the previous tests (a testing procedure). For example, the diagram in Figure 2 represents a tree in which the tests are always performed in the order T_1, T_2, T_3 . The terminal nodes of the tree are assigned objects in accordance with the incidence matrix.

		TESTS		
		T1	T2	T3
OBJECTS	01	YES	YES	YES
	02	NO	YES	YES
	03	NO	NO	YES
	04	NO	NO	NO

Figure 1. Diagnostic table.

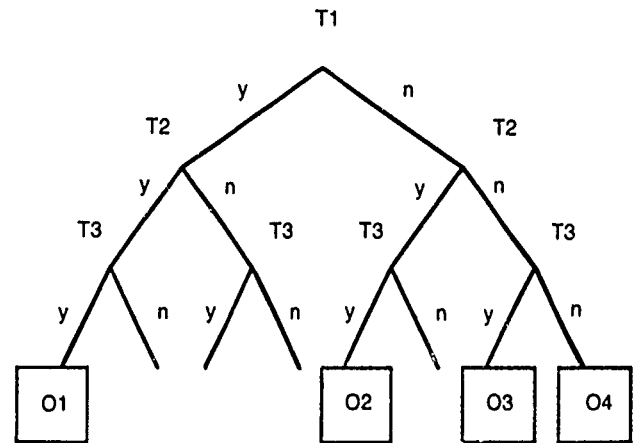


Figure 2. Complete binary tree.

Notice that if the answer to T_1 is yes, an object can be uniquely classified as belonging to class O_1 . Also, the answers $T_1 = \text{no}$, $T_2 = \text{yes}$ identifies x as belonging to O_2 . Thus, the tree can be simplified as shown in Figure 3. We call this procedure *pruning*. Assuming equal object probabilities, the average number of questions to identify some unknown object x is $1/4(1 + 2 + 3 + 3) = 9/4$.

Now consider the alternative tree shown in Figure 4. After pruning, this tree simplifies as in Figure 5. This classification tree has an average number of questions of $1/4(2 + 2 + 2 + 2) = 8/4 = 2$, which is minimal for this simple example.

The objective of this research is to find the classification tree that minimizes some cost function, such as the *average number of questions*, the average central processing unit (CPU) time to identify an object, or the storage to code a testing procedure in computer memory. For real-time applications, such as an expert system for target recognition, the importance of CPU time minimization is evident. Although algorithms exist for the design of classification trees, no practical one guarantees optimality for problems of significant size.

The tree design problem is called a *NP-hard* combinatorial problem. This means that the computational effort required to do an exhaustive search over all combinations grows superpolynomially with n , the size of the problem. For a problem with n questions, the number of distinct binary trees (trees with a unique, consistent assignment of questions to its nodes) is [1]:

$$N(n) = \prod_{i=0}^{n-1} (n-i)^{2^i}.$$

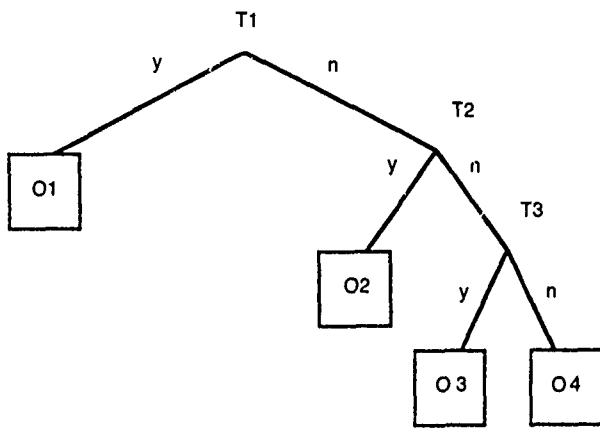


Figure 3. Simplified (pruned) tree.

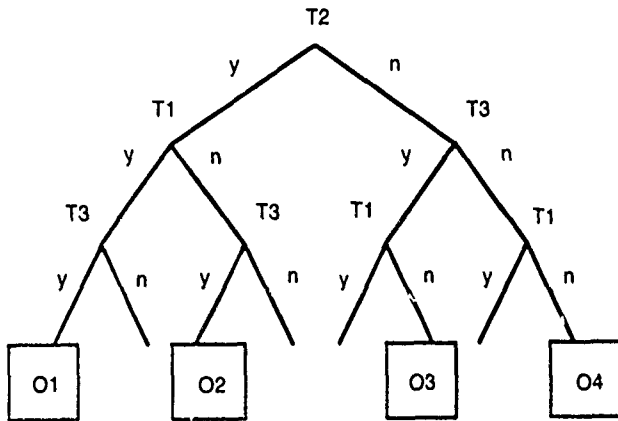


Figure 4. Alternative binary tree.

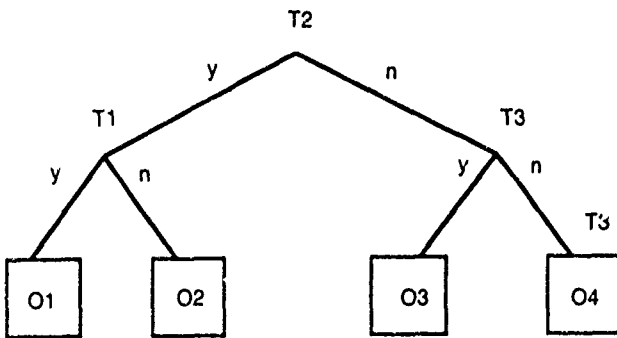


Figure 5. Pruned alternative tree.

For 7 questions, this amounts to $\approx 2 \times 10^{27}$ distinct trees, and for 10 questions, $\approx 6 \times 10^{24}$ distinct trees. For a given problem of size n , one approach to finding the optimal tree is to evaluate the cost for every question combination in the set. However, considering the size of the set, this is not practical even for relatively small n . Other algorithms that guarantee optimality, such as a dynamic programming approach, require storage and execution times that grow exponentially with n [2].

The simulated annealing algorithm is applied to find a classification tree with optimal or near-optimal cost. Simulated annealing is a numerical optimization algorithm that has been effectively applied to such *NP-hard* combinatorial problems as the traveling salesman problem [3], communication code design [4], and integrated circuit design [5]. It has the quality of escaping local minima at the expense of CPU run time [5, 6].

In metallurgy, annealing is the process whereby a metal is first liquified then slowly cooled. As the metal cools, the atoms form a lattice, a minimum energy configuration. In 1953, Metropolis and co-workers [7] defined and implemented this algorithm, called *simulated annealing*, based on the physical phenomenon of annealing. The process associates the objective function to be minimized with the energy of an artificial statistical mechanics problem. With the use of a computer, random walk over the states of the artificial problem is simulated and the temperature lowered. In particular, the random walk is constructed such that $\exp[-E(x)/kT]$ is proportional to the probability that the state is at x . As the temperature is lowered, this latter probability density approaches a delta function concentrated at x_0 , the global minimum of $E(x)$.

Classification trees can be applied directly in such areas as medical diagnosis, trouble-shooting systems, species identification, the evaluation of Boolean functions, and pattern recognition [1, 8]. Other mathematically similar problems, such as expert systems design and the design of logical data processing algorithms [2], can often be transformed to classification problems.

Several project milestones were completed during the past year. A computer program that implements the simulated annealing algorithm, was developed to generate random trees. As in the previous example, objects are assigned to terminal nodes, and the tree is simplified in agreement with the incidence matrix. In accordance with simulated annealing, the change in cost with respect to a randomly perturbed tree is evaluated, and a decision is made whether to keep the old tree or take the perturbed tree as the current *best* design. This process must be repeated many times in order to converge to a tree whose cost closely approximates that of a minimal cost tree. Since a configuration with higher cost is occasionally accepted, there is a tendency to escape local minima. In contrast, the method of iterative improvement [5] is more likely to converge to a local minimum, since only a rearrangement that lowers the cost is accepted.

The computer program was applied to the seven-segment digit recognition problem [3, 8, 9]. Seven diodes are shown in Figure 6. By turning on selected diodes, the decimal digits 0 to 9 can be represented. In this case, the objects are the 10 digits $\{0, 1, 2, \dots, 9\}$, and the tests are the 7 questions *Is diode number j lit?*, $j = 1, 2, \dots, 7$. The incidence matrix is shown in Figure 7. As an example, the digit 1 is represented by turning on diodes 3 and 6, while

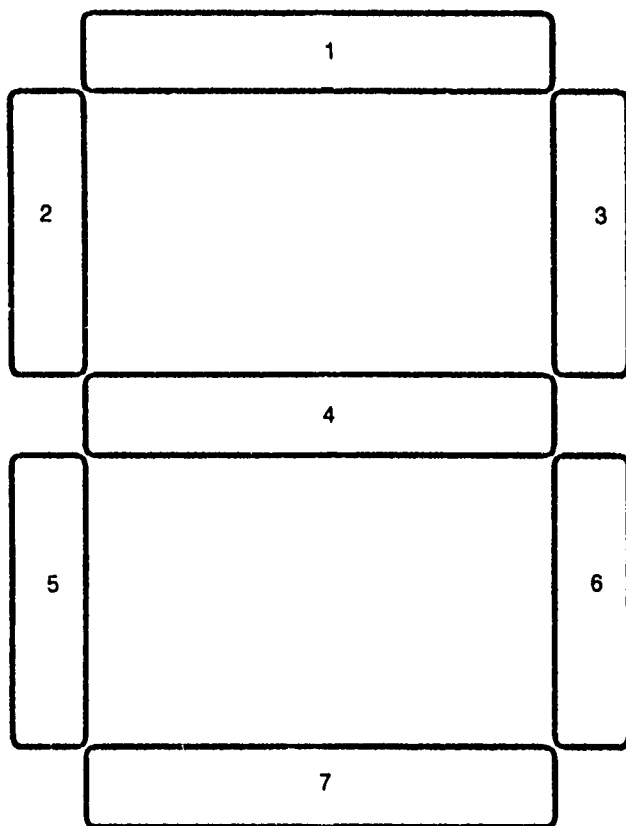


Figure 6. Diode configuration for seven-segment digit recognition problem.

QUESTION j : IS DIODE NUMBER j LIT?
OBJECTS i : THE DIGITS 0, ..., 9

	QUESTIONS, j							0 = NO 1 = YES
	1	2	3	4	5	6	7	
0	1	1	1	0	1	1	1	
1	0	0	1	0	0	1	0	
2	1	0	1	1	1	0	1	
3	1	0	1	1	0	1	1	
4	0	1	1	1	0	1	0	
5	1	1	0	1	0	1	1	
6	1	1	0	1	1	1	1	
7	1	0	1	0	0	1	0	
8	1	1	1	1	1	1	1	
9	1	1	1	1	0	1	1	

Figure 7. Incidence matrix for seven-segment digit problem.

turning off the remaining diodes. Hence, the row corresponding to digit 1 has a 1 (on) in the third and sixth columns and a 0 (off) in the remaining columns.

The average number of questions cost function is given by

$$Q = \sum_{i=1}^{NO} PR(i)IL(i),$$

where NO is the number of objects, $PR(i)$ is the prior probability of object i , and $IL(i)$ is the number of questions on the tree used to classify object i .

For the case of equal prior probabilities, the optimal tree has a cost of 3.4 [9]. The simulated annealing program was applied to this problem. Shown in Figure 8 are three temperature histories of the cost function for three different implementations of the algorithm. As the temperature lowers, the cost tends to approach the minimum. The second and third runs, which converged to the minimal solution of 3.4, correspond to improvements in the original version of the algorithm. The corresponding optimal tree is shown in Figure 9.

Errors and robustness considerations can be factored into the design by the inclusion of the probability of classification error in the cost function. For example, the cost function can be modified to

$$Cost = \sum_{i=1}^{NO} PR(i)IL(i) + \beta P_e,$$

where β represents the relative weighting factor and P_e is the probability of classification error. For $\beta = 0$, the cost reduces to average number of questions. As β increases, the error probability has a larger effect and the algorithm tends to produce a design that reduces the error probability at the expense of average number of questions.

As an example, consider again the equal prior probability digit problem. Diode 2 is assumed to be flickering

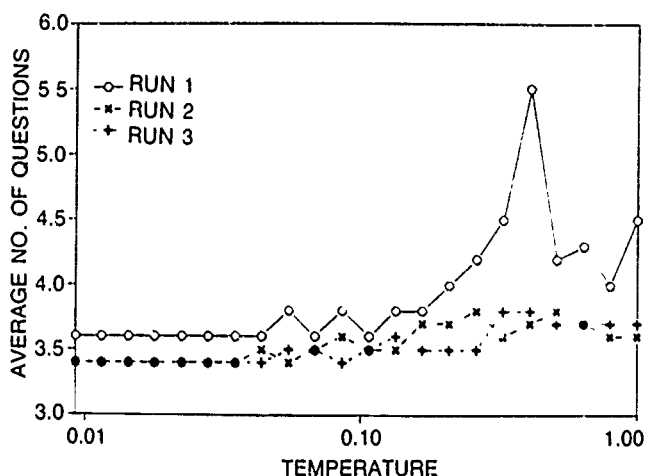
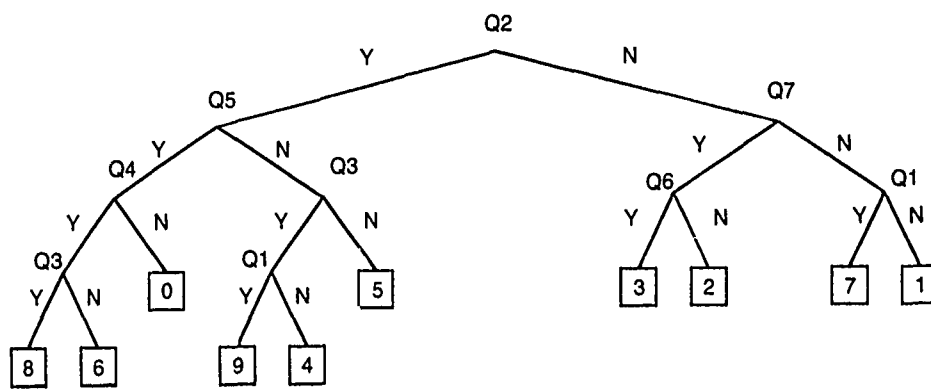


Figure 8. Simulated annealing temperature histories for the seven segment digit problem.



AVERAGE No. OF QUESTIONS = 3.4

Figure 9. Classification tree designed by simulated annealing for the seven-segment digit problem.

and thus unreliable in the on state. To simulate this effect, take $Pr(Q_2 \text{ in error/object } O_i) = 0.10, i = 1, 5, 6, 7, 9, 10$. The program is then run using the previous cost function as β is varied parametrically. For small values of β , the optimal tree is a Huffman tree [9] that applies question Q_2 first. (The Huffman algorithm is primarily used to construct minimal length code words for communication applications. Its use for tree design is limited in that it may not be possible to find a Huffman tree that satisfies the constraints imposed by the incidence matrix.) As β increases, the algorithm tends to converge to a tree that uses question Q_2 as few times as possible to classify the objects in the set $\{O_1, O_5, O_6, O_7, O_9, O_{10}\}$. An evolution of the optimal cost as β varies is shown in Figure 10. At $\beta = 2$, the optimal tree transits from a Huffman tree to a non-Huffman tree that uses question Q_2 only to classify object O_4 (no error contribution since $Q_2 = 0$ for object O_4) and object O_{10} . Since all six objects in the set $\{O_1, O_5, O_6, O_7, O_9, O_{10}\}$ contribute an error for the Huffman tree, and since only O_{10} contributes an error for the non-Huffman tree, the slope of the optimal cost versus β is six times greater for $\beta < 2$ than for $\beta > 2$. A Huffman tree and a non-Huffman tree are shown in Figure 11.

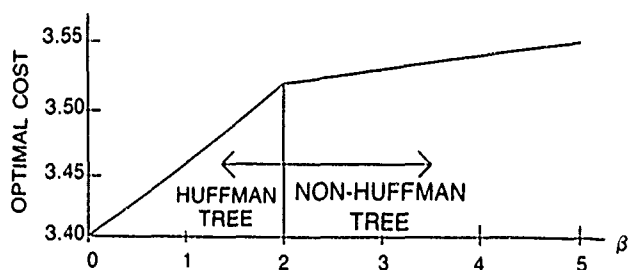


Figure 10. Transition from Huffman tree to non-Huffman tree for flickering diode problem as weighting factor varies.

An absolute lower bound for the average number of questions cost is found, by the Huffman algorithm, to be 4.1849. This bound is guaranteed to be tight, however, only if a Huffman tree consistent with the incidence matrix exists. For this problem, it can be shown that a consistent Huffman tree does not exist.

The performance of the simulated annealing algorithm can be gauged by comparison to the design obtained using the Information Theory Heuristic Rule [1, 2, 11]. This rule usually gives good designs for the average number of questions cost but is not guaranteed to be optimal [11], and in some cases produces poor designs. For this problem, the Information Theory Rule produced a tree with cost 4.3989. Using the simulated annealing algorithm, we obtained a tree with cost of 4.3879.

In conclusion, the simulated annealing algorithm was successfully applied to find an optimal classification tree for the seven-segment digit recognition problem. Good designs were also demonstrated for this problem when classification errors were included. For the larger 5×5 pixel problem, the simulated annealing algorithm gave a design with smaller cost than the Information Theory design. However, additional progress to speed up the algorithm must be achieved before it can be effectively applied to generate minimal cost designs for larger problems.

A long-term objective is to investigate applications to decision systems. It is anticipated that considerations inherent to decision systems such as constraints on question sequencing, costs due to asking a question (CPU time and memory), and penalties for erroneous decisions, can be successfully integrated into the algorithm.

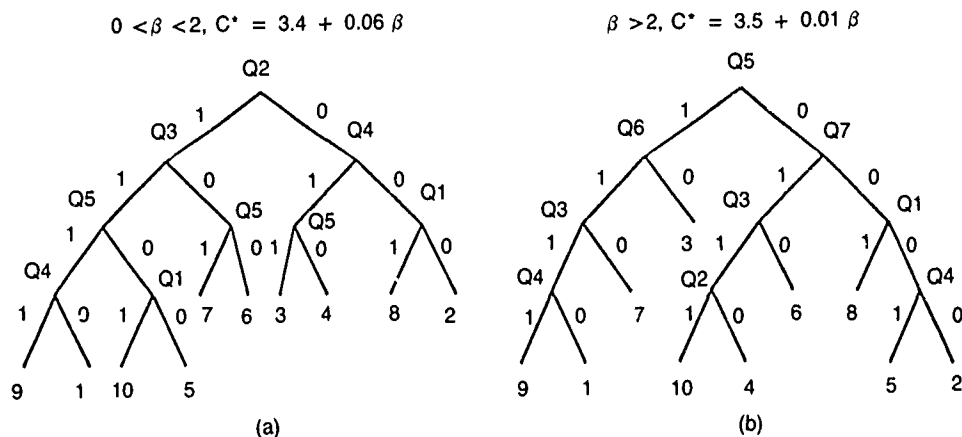


Figure 11. Huffman tree (a) and non-Huffman tree (b) for the flickering diode problem.

* * * * *

1. B. Moret, "Decision Trees and Diagrams," *Comput. Surv.* **14** (4), 593 (1982).
2. C. R. P. Hartmann et al., "Application of Information Theory to the Construction of Efficient Decision Trees," *IEEE Trans. Info. Theory* **IT-28** (4), 565 (1982).
3. E. Aarts and J. Korst, *Simulated Annealing and Boltzmann Machines*, John Wiley and Sons (1989).
4. A. El Gamal et al., "Using Simulated Annealing to Design Good Codes," *IEEE Trans. Info. Theory* **IT-33** (1), 116 (1987).
5. S. Kirkpatrick et al., "Optimization by Simulated Annealing," *Science* **220** (4598), 671 (1983).
6. W. Press et al., *Numerical Recipes in C. The Art of Scientific Computing*, Cambridge University Press (1989).
7. N. Metropolis et al., "Equation of State Calculations by Fast Computing Machines," *J. Chem. Phys.* **21** (6), 1087 (1953).
8. L. Breiman et al., *Classification and Regression Trees*, Wadsworth International Group (1984).
9. R. S. Bucy and M. R. Chernick, *Tree Based Expert Systems: Algorithm Comparison and Optimization*, The Aerospace Corp. (April 1987). Available from the author.
10. G. Dewey, *Relative Frequency of English Speech Sounds*, Harvard University Press (1950).
11. R. S. Bucy, *The Greedy Information Theoretic Tree Design is Suboptimal*, The Aerospace Corp. (July 1990). Available from the author.

Fractals and Image Processing

D J Evans,
Laboratory Operations,
L A Campbell and M Jankins,
Computer Systems Division

Fractals are patterns with a recursive self-similarity at a variety of scales. The Sierpinski triangle (Figure 1) is a deterministic fractal because it can be reassembled precisely from scaled-down versions of itself that have been rotated and translated to the proper positions. Random fractals have statistically repeating patterns that can be seen, for instance, in the kinks of coastlines and the water vapor distribution in clouds. Random fractals are most

familiar from their use in generating artificial landscapes on computers. Deterministic fractals have been used in compression algorithms for which ratios of up to 10,000:1 were claimed. Our primary interest in fractals lies in their use in imagery for compression, detection, and classification, particularly in the context of real-world multispectral images. Our research objectives this past year were to clarify the mathematical basis of the fractal approach to

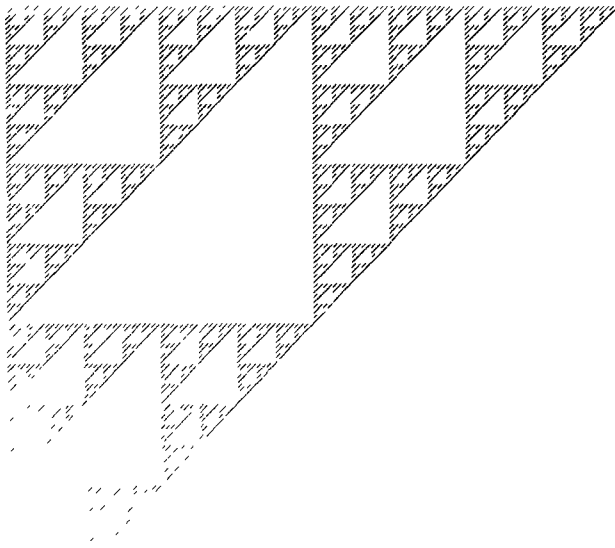


Figure 1. Sierpinski triangle.

image representation and modeling, and to investigate the reciprocal relationship between image processing operations and the fractal representation of images.

The original motivation for the research that led to this project was the desire to improve compression algorithms for multispectral data from satellite sensors such as the Landsat Thematic Mapper imaging system. Algorithms involving fractals offer large compression ratios in special cases, and, in contrast to compression algorithms that treat an image simply as a linear string of values obtained from a raster scan, they do not destroy planar geometric relationships. This latter fact means that fractal representations are appropriate for use in detection and classification as well as in compression.

Last year, we studied Iterated Function System (IFS) encodings of deterministic fractal images in detail. An IFS code consists of a small number of affine (scaling + translation + rotation) transformations, with attached probabilities. By choosing an arbitrary initial point and repeatedly selecting a transformation to apply to it, according to the given probabilities, and then plotting the sequence of points obtained, one can recreate the represented image. This *random iteration* algorithm illustrates the connection between the IFS code and the image. The inverse problem—computing an IFS code from an image—is what must be solved for applications to real-world images. We built a testbed for experimenting with IFS codes on a Sun workstation (using Sun's object-oriented NEWS extensions to PostScript). We also tracked progress reported by Iterated Systems, Inc. (ISI), a pioneer company in this research. We concluded that public inverse-problem algorithms are not suitable for efficient automation. (ISI works with improvements on the basic

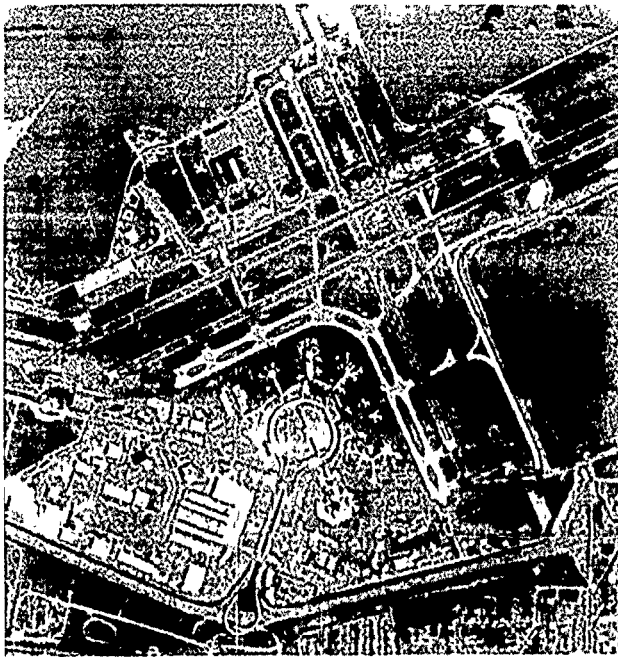
algorithms, but keeps them as trade secrets to which we had no access.)

Our objective this past year was to examine more closely the basic relationships between image processing operations and fractal modeling of images. Indeed, for application purposes, one wants a mathematical calculus that relates the two. We proceeded on two fronts, theoretical and practical.

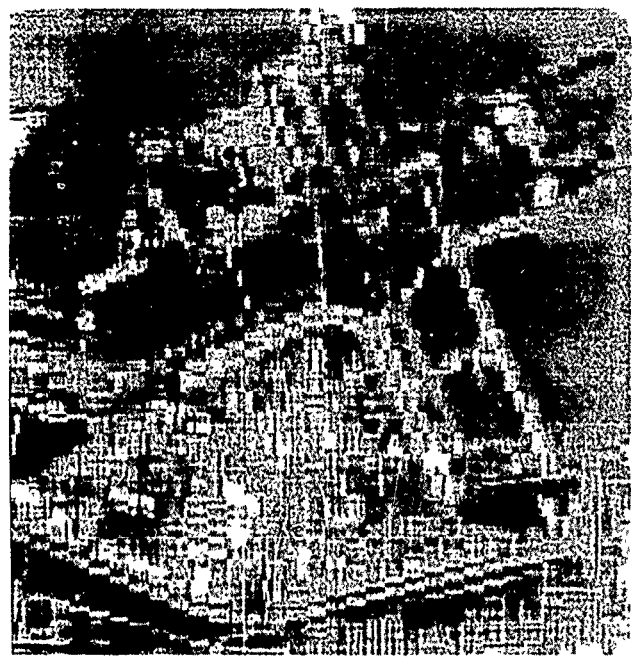
The theoretical investigation pursued the connection between an IFS code and the *ideal image* it represents (a continuous gray-level image with perfect resolution). This abstracts from the details of the digital representation of the image and its actual reproduction as a print. It still allows for the consideration of image processing operations, introducing discretization in additional steps where necessary. We defined an abstract IFS as a space X , together with a probability distribution on the set of maps of X to itself (the semigroup of endomorphisms of X). This notion unifies a number of different examples, in which the precise nature of the space X varies. The appropriate context for this general definition is Category Theory [1]. X is taken to be an object of a category C , and the category C is Cartesian-closed and equipped with a (natural) functor to the category of sigma-algebras [2]. We defined the ideal image of an abstract IFS as the stationary distribution for an associated Markov process, as in [3], but in our more general context. Image processing operations became transformations of one abstract IFS to another, and we demonstrated useful sufficient conditions under which ideal image formation is preserved [4].

On the practical side, we examined the effect that two image transforms have on the fractal dimension of images. The two transforms used were the discrete cosine transform (DCT) and the singular value decomposition (SVD). The DCT is analogous to the Fourier transform in that it measures the (spatial) frequency content of an image. The SVD transforms an $n \times n$ image into n new images, called the *singular planes*. The SVD is computed using small blocks that tile the original image area (16×16 for a 512×512 image in our examples). The sum of the first k planes gives the best least-squares approximation to a rank- k matrix within each block. The first singular plane looks most like the original image, since it captures most of the energy, and the remaining planes fill in the details (Figure 2).

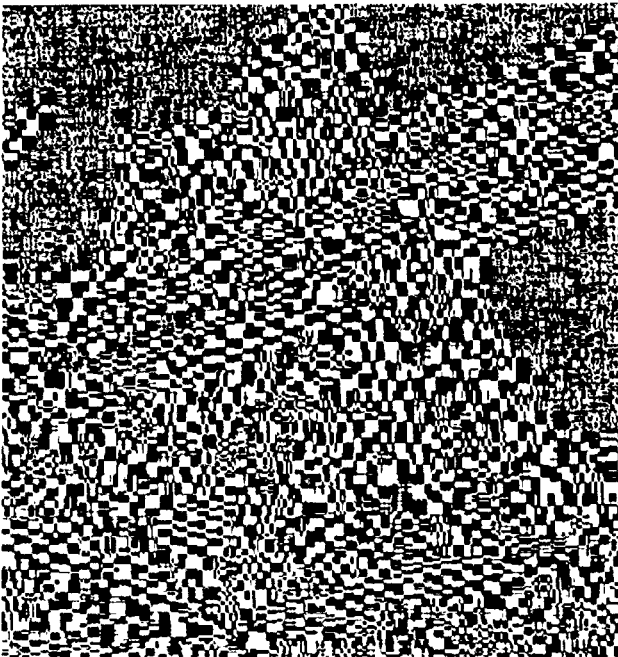
The fractal dimension of an ideal (infinite resolution) gray-level image should be between 2 and 3, with numbers closer to 3 indicating more jaggedness in the intensity as a function of position. There are a number of methods used for determining analogs of the fractal dimension for discrete quantized images. We used code contributed by S. H. Margolis of the Computer Systems Division, based on an established technique [5] that starts by computing a power spectral density (PSD) for the image and then fits an exponential to the PSD curve to



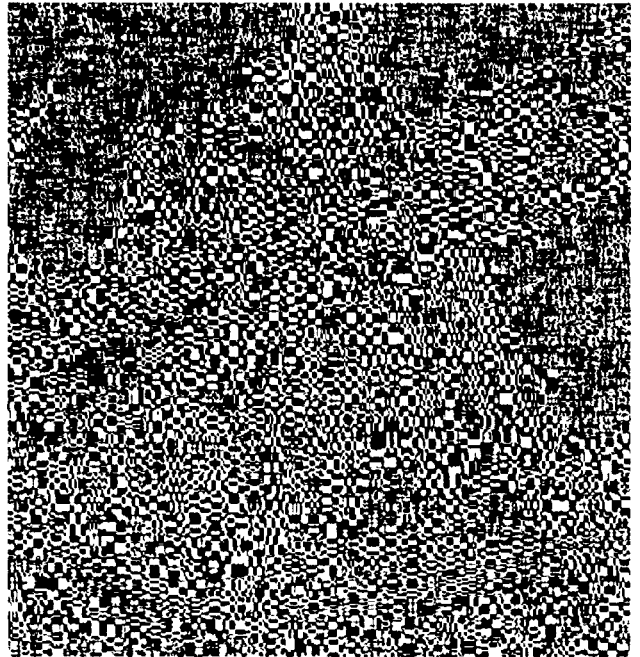
(a)



(b)



(c)



(d)

Figure 2. SVD transform plane fractal dimensions. (a) Original image, fractal dimension 2.60; (b) plane 1, fractal dimension 2.69,

(c) plane 2, fractal dimension 2.63, (d) plane 3, fractal dimension 2.69.

compute the fractal dimension. The method assumes that the image exhibits the self-similarity characteristic of fractals, and one must occasionally reject anomalous values that result from small sample size or lack of fractal character.

For our experiments, we used both real-world images (such as the aerial view of an airport shown in Figure 2) and computer-generated fractal images of known

fractal dimension. Using the DCT, we removed much of the high-frequency content of the images, then calculated the fractal dimension of both the original and the smoothed (low pass) images. For the SVD, we calculated the fractal dimensions of the first few SVD planes.

The results basically supported our expectations. Smoothed images (either low-pass transforms from the DCT or the first SVD plane) tended to have a slightly low-

er fractal dimension than the original, and the fractal dimension climbed for higher-order SVD planes.

Both theory and practice have thus provided support for the proposition that the fractal modeling of images and image processing operations can be combined in meaningful ways that preserve essential characteristics of both components, while remaining consistent with the contiguity relations that result from the planar spatial geometry of the images.

* * * * *

1. Saunders MacLane, "Categories for the Working Mathematician," *Graduate Texts in Mathematics*, Springer-Verlag, New York (1971).

2. Walter Rudin, "Real and Complex Analysis," *McGraw-Hill Series in Higher Education*, McGraw-Hill, New York (1966).
3. M. F. Barnsley and S. Demko, "Iterated Function Systems and the Global Construction of Fractals," *Proc. Royal Soc. London, Series A* **399**, 243 (1985).
4. L. A. Campbell, *The Effect of Image Processing Operations on Iterated System Function Representations for Fractal Images*, ATR-90(8242)-1, The Aerospace Corp. (30 November 1990).
5. Richard F. Voss, "Fractals in Nature: from Characterization to Simulation," Heinz-Otto Peitgen and Dietmar Saupe, eds., *The Science of Fractal Images*, Springer-Verlag, New York (1988).

Linear Algebra with Symbolic Interface

D. M. Nystrom,
Computer Systems Division;
R. S. Beezley, H. E. Kim, B. H. Sako, and W. K. Yeung,
Vehicle and Control Systems Division

Matrix computation software is essential to a variety of engineering functions performed by Aerospace in the fields of structural dynamics, structural mechanics, and controls. In particular, it is used extensively to create, validate, and couple vehicle spacecraft and launch vehicle dynamic models for use in flight loads analyses. This project has addressed the development of matrix computation software capable of manipulating the large matrices often used in these analyses. Specifically, the objectives are to demonstrate the feasibility of developing an efficient, robust, easily portable and maintainable user-friendly matrix computation program and to provide a framework that can be readily expanded to a full implementation of the system.

A prototype computational linear algebra system with symbolic interface (CLASSI) has been developed. The prototype permits users to specify matrix computations in a symbolic, algebraic language similar to that used to express engineering analyses. The language may be freely intermixed with FORTRAN to provide a very powerful computation tool. The CLASSI precompiler translates this language to FORTRAN subroutine calls that are executed by the numerical program.

The CLASSI language essentially provides an extension to FORTRAN that permits matrices to be manipulated as entities in equations and input/output operations. Matrix names must be identified for the precompiler in the declaration section of the FORTRAN program. They may then be used with operators defined by

the CLASSI language and intermixed in equations with FORTRAN variables and operators (Figure 1). The matrix declaration statement does not specify matrix size. Size and compatibility are determined at run time. This feature permits the size of input matrices to change without the need to modify the user's code.

The CLASSI language defines three types of operators: basic, elementary mnemonic, and compound mnemonic. The basic operators are represented by a nonalphanumeric character and generally perform simple operations for which there is a scalar counterpart; e.g., addition and subtraction. Elementary mnemonic operators are represented by a name composed of several alphanumeric characters and return only one result; e.g., transpose and inverse. Their usage parallels that of FORTRAN functions in that they can be referenced within equations. The compound mnemonic operators are also represented by a name composed of several alphanumeric characters. However, they return multiple results; e.g., eigensolution and matrix decomposition. Consequently, references to these operators are equations in themselves.

The CLASSI language also provides keyword-driven read, write, and print operations for matrices. These operations permit the user to easily input and output data in CLASSI's internal format or that of another analysis code by simply selecting the appropriate value for the format keyword.

Figure 1. A common procedure in which massless nodes are statically condensed using a Guyan reduction and a generalized eigenvalue problem is solved to determine a structure's natural modes. The CLASSI code to perform this procedure is shown on the left; the corresponding algebraic equations are on the right.

PROGRAM GUYAN

INTEGER IN, OUT, RC
MATRIX K, M, KRED, LAMBDA, PHI

CALL UNALL (IN, RC)
OPEN (UNIT = IN, FILE = 'INFILE')
READ (UNIT = IN, FMT = MATRIX) K, M

K11 = K (1:200, 1:200)
K12 = K (1:200, 201:500)
K22 = K (201:500, 201:500)
KRED = K22 - TRANS (K12) // INV (K11) * K12
KRED = 0.5 * (TRANS (KRED) + KRED)

(LAMBDA, PHI) = SGE (KRED M (201:500, 201:500))

CALL UNALL (OUT, RC)
OPEN (UNIT = OUT, FILE = 'OUTFILE')
WRITE (UNIT = OUT, FMT = CLASSI) LAMBDA, PHI

STOP
END

$$[K] = \begin{bmatrix} K_{11} & K_{12} \\ K_{21} & K_{22} \end{bmatrix} \quad [M] = \begin{bmatrix} 0 & 0 \\ 0 & M_{22} \end{bmatrix}$$

$$[K^*] = [K_{22}] - [K_{12}]^T [K_{11}]^{-1} [K_{12}]$$

$$[K_{RED}] = \frac{1}{2} ([K^*]^T + [K^*])$$

$$[M_{RED}] = [M_{22}]$$

$$[K_{RED}] (\phi) = [M_{RED}] (\phi) \lambda$$

The CLASSI precompiler translates the CLASSI language to FORTRAN and was developed in C using the UNIX tools Lex and Yacc. These tools generate a lexical analyzer and parser based on descriptions of the character strings that occur in the language, the language grammar, and code fragments that perform appropriate processing when individual grammar rules are recognized. Lex and Yacc significantly reduced the time required to develop the precompiler and are expected to reduce maintenance time by allowing enhancements to be made by means of changes to the grammar description rather than to the precompiler code itself.

The CLASSI precompiler uses two types of grammar rules for operators. Since the basic operators must be available in every installation, they are tied to grammar rules that contain the characters representing them. The mnemonic operators, however, are stored in a table that is read by the precompiler at run time and are associated with a generalized grammar rule. Thus, when the precompiler recognizes the syntax associated with a mnemonic operator, a table look-up is performed to verify the operator, verify the type and number of arguments, and determine the subroutine that must be called to perform the operation. This has yielded a very flexible precompiler that allows CLASSI to be tuned to the power of a platform by adding or subtracting operators in the table. In addition, this scheme allows operators to be added without having to regenerate the precompiler executable. This will significantly simplify the maintenance of multiple installations.

Grammar rules for CLASSI's input/output operations are currently specified individually for each format. It is expected that this will become unwieldy as the number of formats increases. Consequently, a future enhancement will use a generalized grammar rule and a table much like that described for the mnemonic operators.

The CLASSI numerical program executes the subroutine calls generated by the precompiler. It is written in

FORTRAN and is composed of numerical computation routines, a memory manager, and a file manager. Since interfaces between programming languages are generally machine-dependent, the precompiler was isolated from the computation software and communicates with it through external files. This approach has the added advantage of permitting the precompiler and numerical program to run on separate platforms. For example, the precompiler could be run on a personal computer or workstation while the numerical program runs on a mainframe. This would permit the user to debug CLASSI code locally and submit the FORTRAN program output by the precompiler to the mainframe for execution.

Each numerical computation routine is interfaced to CLASSI by a controller routine. The controller isolates the CLASSI specific code and allows the numerical program to take advantage of the highly vectorized routines available on the Cray and existing math libraries; e.g., EISPACK, LINPACK. Thus, new operations can be easily added by developing a controller routine, supplying the underlying calculation software, and adding the mnemonic to the previously described operator table. As with the precompiler, operations can be added or subtracted without recompiling.

CLASSI's internal memory management system is based on a heap. Controller routines call the memory manager to allocate and release the space associated with matrices declared by the user and work matrices needed for computation. The memory manager automatically merges adjacent empty blocks and compacts the heap when necessary. Currently, all matrices must reside in the heap. A future extension to the memory management system will allow matrices to be swapped to disk. This extension is easily accommodated by the current design and will increase the maximum allowable matrix size for most computation runs.

CLASSI's file management system allocates and releases FORTRAN units for input and output. Both the user and the controller routines must allocate and release

all files through this system. This system will be essential for implementing the extension that allows matrices to be swapped to disk, as it will ensure that neither the user nor the controller routines overwrite the other's files.

In conclusion, the CLASSI prototype has proven the feasibility of developing an efficient, robust, easily portable and maintainable user-friendly matrix computation system and provides a framework that can be readily

expanded to a full implementation of the system. The CLASSI prototype permits users to express matrix computations in a symbolic algebraic language that is easy to debug and validate. It is composed of expandable, maintainable modules that have ported to multiple platforms without modification. Documentation of the prototype is under way. The system will be released for user evaluation when the documentation is completed.

On-Line Parameter Estimation

L. A. Campbell,
Computer Systems Division

The research objectives of this project were to investigate some fundamental unresolved issues related to techniques for on-line system parameter identification. Stochastic systems in state-space form typically accept inputs, alter their internal state, and produce outputs. Both the system dynamics and the observed outputs are perturbed by noise processes, and time can be continuous (*differential* system equations) or discrete. The on-line state estimation problem, in which estimates are developed as soon as possible after observations become available, is particularly important for controlling systems by feedback. For linear state-space systems, the Kalman filter produces optimal estimates. It has an extension to nonlinear systems, the extended Kalman filter (EKF), with desirable properties, but no guarantee of optimality. Both these estimators can be used only in the *white box* case, where the system equations and noise statistics are fully known. In system parameter estimation, also known as *system identification* [1], one attacks the *black box* problem of determining not only the system state, but also the system itself (e.g. some of the coefficients of the governing equations), from knowledge of the inputs and observed outputs. System identification is a problem of considerable practical importance [2]. For example, it has applications to the control of flexible, coupled space structures [3-5] and to target discrimination in real-time tracking [6].

Two on-line parameter estimation techniques were central to the study. In the extended Kalman filter used as a parameter estimator (EKFPE), one enlarges the state vector of a (usually linear) system model to include parameters of the model. Even though the system to be identified is linear, the resulting expanded problem is nonlinear except in trivial cases. The Wiberg estimator (WE) [7] is a novel higher-order approximation to the continuous-time optimal nonlinear filter. That is, in addition to means and covariances, it computes and propagates approximations to certain higher-order statistical

moments. Except in certain degenerate cases, the WE is known to generate parameter estimates that converge, with probability 1, to the true parameter values [8]. Furthermore, it appears to have a fast transient response, like the EKFPE.

We investigated the convergence behavior of the continuous-time EKFPE experimentally. As our underlying linear system, we took a two-dimensional system with two distinct stable poles, which we treated as parameters to be determined. No global convergence results are known for this case. We used Ljung's ordinary differential equation (ODE) method [1, 2] to search for possible points of convergence. The ODE method has only recently been shown to apply to continuous-time systems [9].

In the ODE method, an ordinary, noise-free differential equation (in the parameters and some additional variables) is produced using averaging theory. With probability 1, convergent realizations of the EKFPE will produce parameter estimates that approach the parameter values at a stationary point of the ODE. Thus, one can calculate *algebraically* the possible convergence points of the EKFPE, as the zeros of an *indicator vector field* that defines the parameter part of the ODE. The calculation of that vector field is practical only point by point (not in closed form). Using MATLAB (matrix manipulation and display software), and a partitioned computational technique we developed, we could compute and plot the indicator vector field. A sample plot is shown in Figure 1. The true pole values were $(-1, -2)$ and correspond to the center point of the grid, where the vector field has a zero. The negative of the norm of the vector field is the actual quantity plotted, so that the zero appears as a maximum. The spatial axes are semilog, with parameters ranging from 2^{-7} times the true value to 2^7 times the true value. Based on our experimental results, we conjecture that the true parameter values define the only possible convergence

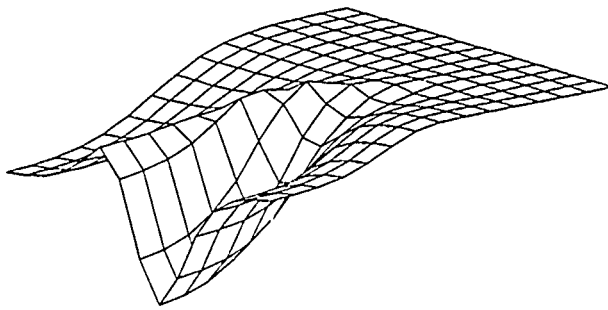


Figure 1. Indicator vector field for the EKFPE.

point in cases such as this (with divergence remaining a possibility).

Figure 2 shows the negative of the log likelihood function. The likelihood function is the (Gaussian) probability of asymptotically matching the observed output by the output of a Kalman filter that assumes that it knows the pole parameters. The fact that the negative of the log likelihood, and therefore the likelihood, has a (difficult to discern, but verified) maximum at the grid center corresponds to the fact that the true system is necessarily a maximum likelihood solution.

Our investigation of the WE was somewhat diverted from its planned course. We ported FORTRAN code for the one-dimensional WE to our Sun workstation and reproduced results that can be found in [10]. We originally planned to extend this code to higher-dimensional cases and to perform experimental comparisons of the continuous-time EKFPE and the WE, using stochastic simulations. However, an unanticipated theoretical result caused us to redirect our efforts. The WE, hitherto developed for continuous time only, was shown by D. M. Wiberg to have a discrete-time analog in certain cases. As discrete-time estimation procedures are (although often more complex) significantly more useful in applications, we concentrated on developing the discrete-time WE and comparing its convergence to that of several standard discrete-time system identification tools. We are using MATLAB again as a development tool, and so far have

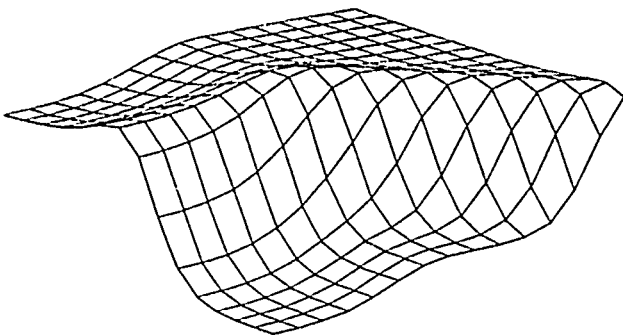


Figure 2. Negative of log likelihood-maximum at center.

worked only with a simple one-dimensional system and a limited set of cases. Some results for this case will appear soon [11]. The theory of the discrete-time WE can be confidently expected to extend to additional situations, although the complexity of the calculations can be daunting. However, a considerable amount of work remains to be done, to verify the theory experimentally.

In summary, we have tested experimentally a global convergence property of the continuous-time EKFPE, for which there is no proof in the literature. We are also developing and testing a discrete-time WE, for which we anticipate both a proof of global convergence and a fast transient response.

* * * * *

1. L. Ljung and T. Söderström, *Theory and Practice of Recursive Identification*, MIT Press (1983, 3rd edition 1986).
2. L. Ljung, *System Identification: Theory for the User*, Prentice-Hall (1987).
3. A. Y. Lee et al., "System Identification for Space Applications," *Aerospace Sponsored Research Summary Report, Exploratory Technology*, ATR-85(8498)-2, The Aerospace Corp. (1 December 1986), p. 117.
4. A. Y. Lee et al., "Adaptive Control for Space Applications," *Aerospace Sponsored Research Summary Report, Exploratory Technology*, ATR-87(8498)-2, The Aerospace Corp. (1 December 1987), p. 168.
5. P. H. Mak et al., "Adaptive Control for Space Applications," *Aerospace Sponsored Research Summary Report, Exploratory Technology*, ATR-88(8498)-2, The Aerospace Corp. (1 December 1988), p. 199.
6. Yaakov Bar-Shalom and Thomas E. Fortman, *Tracking and Data Association*, Academic Press (1988).
7. Donald M. Wiberg, "Another Approach to On-Line Parameter Estimation," *Proceedings of the 1987 American Automatic Control Conference* (1987), p. 199.
8. Donald M. Wiberg, "Towards a Globally Convergent Approximation of Optimal On-Line Parameter Estimation," *Proceedings of the Eighth IFAC Symposium on Identification and System Parameter Estimation* (1988), p. 1165.
9. D. G. DeWolf and D. M. Wiberg, "An Ordinary Differential Equation Technique for Continuous Time Parameter Estimation," *Proceedings of the 1991 American Conference on Automatic Control* (1991), Volume 2.

10. Douglas G. DeWoll, *An Ordinary Differential Equation Limit Technique for the Analysis of Continuous Time Stochastic Parameter Estimators*, Ph.D. Thesis, University of California, Los Angeles (1989).
11. D. M. Wiberg and L. A. Campbell, "A Discrete-Time Convergent Approximation of the Optimal Recursive Parameter Estimator," *Proceedings of the Ninth IFAC Symposium on Identification and System Parameter Estimation* (1991), p. 140.

Bibliography of Journal Publications

A summary listing of publications during the 1988-1990 period resulting from Aerospace Sponsored Research (ASR) and related projects and published in scientific and technical journals is included here to provide a measure of Aerospace contributions to the national scientific and engineering research community. More detailed reporting of ASR work is, in many cases, presented in Aerospace Technical Reports (ATRs), most of which are available in the Aerospace Library.

- Adams, P. M., J. F. Knudsen, R. C. Bowman, Jr., A. D. Campaan, and H. D. Yau, "Double-Crystal X-Ray Diffraction Studies of Si Ion-Implanted and Pulsed Laser Annealed GaAs," *Adv. X-Ray Anal.* **34**, 531 (1991).
- Arnold, G. S., and D. J. Coleman, "Surface Mediated Radical Recombination Luminescence: O + NO + Ni," *J. Chem. Phys.* **88**, 7147 (1988).
- Arnold, S., T. R. O'Keefe, K. M. Leung, L. M. Folan, T. Scalese, and A. Pluchino, "Optical Bistability of an Aqueous Aerosol Particle Detected Through Light Scattering: Theory and Experiment," *Appl. Opt.* **29**, 3473 (1990).
- Arnold, G. S., and D. J. Coleman, "Surface-Mediated Chemiluminescent Reaction of O and NO," *Chem. Phys. Lett.* **177** (3), 279 (1991).
- Beck, S. M., "Mixed Metal-Silicon Clusters Formed by Chemical Reaction in a Supersonic Molecular Beam: Implications for Reactions at the Metal/Silicon Interface," *J. Chem. Phys.* **90**, 6306 (1989).
- Beck, S. M., and J. E. Wessel, *Appl. Phys. Lett.* **50**, 149 (1989).
- Beck, S. M., and J. M. Andrews, "Phase Transition Behavior Observed in Small Silicon Cluster Ions," *J. Chem. Phys.* **91**, 4420 (1989).
- Beck, S. M., "Photophysics of Bore and Metal Containing Semiconductor Clusters," *Advances in Metal and Semiconductor Clusters*, M. A. Duncan, ed., JAI Press, Inc., Greenwich, Conn. (in press).
- Bernhardt, P. A., S. T. Zalezak, and F. T. Djuth, "Comment on 'Interaction of Electromagnetic Waves in the Ionosphere' by V. N. Laxmi and A. K. Saha," *Radio Sci.* **25**, 85 (1990).
- Bhaskar, N. D., R. P. Frueholz, C. M. Klimcak, and R. A. Cook, "Production of Mass-Selected Neutral Clusters of Rubidium," *Chem. Phys. Lett.* **154**, 175 (1989).
- Bhaskar, N. D., C. M. Klimcak, and R. P. Frueholz, "Liquid Metal Ion Source for Cluster Ions of Metals and Alloys: Design and Characteristics," *Rev. Sci. Instrum.* **61**, 336 (1990).
- Bhaskar, N. D., C. M. Klimcak, and R. A. Cook, "Electronic Shell Structures Effects in $s\text{Cs}_n^+$," *Phys. Rev. B* **42** (14), 9147 (1990).
- Blake, J. B., and D. S. P. Dearborn, "On the Possible Contribution of WC Stars to Isotopic Anomalies in Cosmic Rays and Meteorites," *Genesis and Propagation of Cosmic Rays*, M. M. Shapiro and J. Wefel, eds., D. Reidel (1988), p. 153.
- _____, "A Local Source of ^{26}Al Gamma Rays," *Astrophys. J. Lett.* **338**, L17 (1989).
- Blake, J. B., "Geomagnetically Trapped Heavy Ions form Anomalous Cosmic Rays," *Proceedings of the 21st International Cosmic Ray Conference*, Adelaide, Australia (1990).
- Bloss, W. L., "Electric Field Dependence of Quantum Well Eigenstates," *J. Appl. Phys.* **65**, 4789 (1989).
- _____, "Density of States and Linewidths of Quantum Wells with Applied Electric Fields," *J. Appl. Phys.* **66**, 1240 (1989).
- _____, "Resonant Enhancement of Quantum Well Linewidths by Pseudo-Barrier Energy Levels," *J. Appl. Phys.* **66**, 2481 (1989).

- _____, "Energy Resonances of a Single Quantum Barrier," *Superlattices Microstruct.* **6**, 129 (1989).
- _____, "Effects of Hartree, Exchange, and Correlation Energy on Intersubband Transitions," *J. Appl. Phys.* **66**, 3639 (1989).
- _____, "Linewidths of Quantum Wells with Finite Barriers," *Superlattices Microstruct.* **7**, 63 (1990).
- _____, "Electric Field Dependence of the Eigenstates of Coupled Quantum Wells," *J. Appl. Phys.* **67**, 1421 (1990).
- _____, "Local Plasma Modes of a Semiconductor Superlattice," *J. Appl. Phys.* **69**, 3068 (1991).
- _____, "Coupled Interface-Plasma Modes of a Superlattice and Doped Overlayer," *Phys. Rev. B* **45**, 4034 (in press).
- Bowman, R. C., Jr., P. M. Adams, J. F. Knudsen, S. C. Moss, P. A. Dafesh, D. D. Smith, M. H. Herman, and I. D. Ward, "Effects of Helium Ion Implantation on the Optical and Crystal Properties of GaAs," *Proc. Mater. Res. Soc. Symp.* **147**, 303 (1989).
- Bowman, R. C., P. M. Adams, C. C. Ahn, S. P. Chang, V. Arbet, and K. L. Wang, "Structural Characterization of Symmetrically Strained Si_mGe_n Superlattices," *Proc. Mater. Res. Soc. Symp.* **160**, 101 (1990).
- Bowman, R. C., Jr., P. M. Adams, M. A. Englehardt, and H. Hochst, "Structural Characterization of $\alpha\text{-Sn}$ and $\alpha\text{-Sn}_{1-x}\text{Ge}_x$ Alloys Grown by Molecular Beam Epitaxy on CdTe and InSb," *J. Vac. Sci. Technol. A* **8**, 1577 (1990).
- Bowman, R. C., Jr., J. F. Knudsen, P. M. Adams, H. D. Yau, and A. D. Campaan, "X-Ray and Topographic Studies of GaAs Implanted with $^{28}\text{Si}^+$ and Pulsed Laser Annealed," *Proc. Mater. Res. Soc. Symp.* **157**, 157 (1990).
- Bowman, R. C., Jr., J. F. Knudsen, and R. G. Downing, "Neutron Depth Profiles of Boron Implanted Semiconductors," *Proc. Mater. Res. Soc. Symp.* **166**, 331 (1990).
- Bruner, M. E., C. J. Crannell, F. Goetz, A. Magun, and D. L. McKenzie, "Dynamic Evolution of the Source Volumes of Gradual and Impulsive Solar Flare Emissions," *Astrophys. J.* **322**, 494 (1988).
- Campaan, A., R. C. Bowman, Jr., and D. E. Cooper, "Raman Studies of Composition and Structural Ordering in $\text{Hg}_{1-x}\text{Cd}_x\text{Te}$," *Semicond. Sci. Technol.* **5**, S73 (1990).
- Camparo, J. C., and R. P. Frueholz, "Observation of the Rabi-Resonance Spectrum," *Phys. Rev. A* **38**, 6143 (1988).
- Camparo, J. C., Y. C. Chan, B. Jatuszliwer, and J. Malenfant, "Injection Current Calibration of Diode Laser Wavelengths," *Opt. Commun.* **70**, 416 (1989).
- Camparo, J. C., and R. P. Frueholz, "Attractor Geometry of a Quasiperiodically Perturbed Two-Level Atom," *Phys. Rev. A* **43**, 338 (1991).
- Canterna, R., J. A. Hackwell, R. Hermann, and G. L. Grasdalen, "Infrared Studies of the Galactic Plane I: The IRAS Disk Population at $l=30^\circ$," *Astrophys.* (in press).
- Canterna, R., and J. A. Hackwell, *High Spatial Resolution IRAS Images of M51*, Second Wyoming Conference on the Interstellar Medium in External Galaxies, (Kluwer, Dordrecht) (in press).
- Chan, Y. C., M. D. Tabat, and J. A. Gelbwachs, "Experimental Demonstration of Internal Conversion in the Magnesium Atomic Filter," *Opt. Lett.* **14**, 722 (1989).
- Chang, S. J., V. Arbet, K. L. Wang, R. C. Bowman, Jr., P. M. Adams, D. Nayak, and J. C. S. Woo, "Study of Ultra-Thin Ge/Si Strained Superlattices," *J. Cryst. Growth* **95**, 451 (1989).
- Chang, S. J., C. Huang, M. Kalil, K. Wang, R. C. Bowman, Jr., and P. M. Adams, "Studies of Interdiffusion in Ge_mSi_n Strained Layer Superlattices," *J. Electron. Mater.* **19**, 125 (1990).
- Cohen, N., "Predicting the Preexponential Temperature Dependence of Bimolecular Metathesis Reaction Rate Coefficients using Transition State Theory," *Int. J. Chem. Kinet.* **21**, 909 (1989).

- Cohen, R. D., R. J. Rudy, G. S. Rossano, R. C. Puetter, and S. D. Chapman, "Helium I/10830 Observations of Seyfert 2 Galaxies," *Active Galactic Nuclei*, O. E. Osterbrock and J. S. Miller, eds., Kluwer Academic Press (1989), p. 126.
- Dafesh, P. A., V. Arbet, and K. L. Wang, "Electronic Transitions in A Si_mGe_n Strained Monolayer Superlattice Measured by Photoreflectance," *Appl. Phys. Lett.* **56**, 1498 (1990).
- Dafesh, P. A., "Characterization of GaAs/Al_xGa_{1-x}As Multiple Well IR Detector Structures Using Photoreflectance," *J. Appl. Phys.* (in press).
- Dafesh, P. A., V. Arbet, and K. L. Wang, "Electronic Transitions in a Ge-Rich Strain-Symmetrized Si₈Ge₃₂ Strained Monolayer Superlattice Measured by Photoreflectance Spectroscopy," *Proceedings of the International Conference on Modulation Spectroscopy, Proc. SPIE* **1286**, 308 (1990).
- de la Beaujardiere, O., and L. R. Lyons, "Instantaneous Measurements of the Global High Latitude Convection Pattern," *Outstanding Problems in Solar System Plasma Physics: Theory and Instrumentation*, American Geophysics Union (1989), p. 405.
- Dearborn, D. S. P., and J. B. Blake, "Possible Contributions by Wolf-Rayet Stars to the Proto-Solar Nebula: Extinct Radioactivities, or, Grains of Truth from Wolf-Rayet Stars?," *Astrophys. J.* **332**, 305 (1988).
- Dietz, R. D., R. D. Gehrz, T. J. Jones, G. L. Grasdalen, J. Smith, C. Gullixson, and J. A. Hackwell, "Infrared Imaging and Polarimetry of M82: Evidence for a Ring of Warm Dust," *Astron. J.* **98**, 1260 (1989).
- Djuth, F. T., and C. A. Gonzales, "Temporal Evolution of the HF-Enhanced Plasma Line in Sporadic-E," *J. Geophys. Res.* **93**, 196 (1988).
- Djuth, F. T., "Response of the Arecibo Ionosphere to Large HF-Induced Electron Temperature Enhancements," *Adv. Space Res.* **9**, 123 (1989).
- Djuth, F. T., M. P. Sulzer, and J. H. Elder, "High Resolution Observations of HF-Induced Plasma Waves in the Ionosphere," *Geophys. Res. Lett.* (in press).
- Doschek, G. A., U. Feldman, J. F. Selly, and D. L. McKenzie, "High-Resolution X-Ray Spectra of Solar Flares. IX. Mass Upflow in the Long-Duration Flare of 1979 June 5," *Astrophys. J.* **345**, 1079 (1989).
- DuBois, D. F., H. A. Rose, and D. Russell, "Coexistence of Parametric Decay Cascades and Cavity Collapse at Subcritical Densities in HF Modification of the Ionosphere," *J. Geophys. Res.* (in press).
- _____, "Excitation of Strong Langmuir Turbulence in Plasmas Near Critical Density: Application to HF Heating of the Ionosphere," *J. Geophys.* (in press).
- Fejer, J. A., F. T. Djuth, H. M. Ierkie, and M. P. Sulzer, "Simultaneous Observations of the Enhanced Plasma Line and of the Reflected HF Wave at Arecibo," *J. Atmos. Terr. Phys.* **51**, 721 (1989).
- Fejer, J. A., M. P. Sulzer, F. T. Djuth, and J. H. Elder, "Height Dependence of the Observed Spectrum of Radar Backscatter from HF-Induced Ionospheric Langmuir Turbulence," *J. Geophys. Res.* (in press).
- Fleischauer, P. D., J. R. Lince, P. A. Bertrand, and R. Bauer, "Electronic Structure and Lubrication Properties of MoS₂: A Qualitative Molecular Orbital Approach," *Langmuir* **5**, 1009 (1989).
- Fleischauer, P. D., M. R. Hilton, and R. Bauer, "Effects of Microstructure and Adhesion on Performance of Sputter-Deposited MoS₂ Solid Lubricant Coatings," *Proceedings of the 16th Leeds-Lyon Conference on Mechanics of Coatings, Tribology Series*, Vol. 17, D. Downson, C. M. Taylor, and M. Godet, eds., Elsevier, London (1990), p. 121.
- Gehrz, R. D., T. E. Harrison, E. P. Ney, K. Matthews, G. Neugebauer, J. Elias, G. L. Grasdalen, and J. A. Hackwell, "PW Vulpeculae: A Dust-Poor DQ Herculis?," *Astrophys. J.* **329**, 894 (1988).
- Gelbwachs, J. A., "Atomic Resonance Filters," *IEEE J. Quantum Electron.* **24**, 1266 (1988).
- _____, "Recent Developments in the Fraunhofer-Wavelength Atomic Filter," *Proceedings of the 1988 Lasers and Electro-Optics Society*, IEEE (1988), p. 240.

- _____, "Broadening and Shift of the Mg Intercombination Line and First Triplet Line due to the Presence of Noble Gases," *Phys. Rev. A* **39**, 3343 (1989).
- Gelbwachs, J. A., and M. D. Tabat, "Solar Background Rejection in the Pressure Broadened Fraunhofer Wavelength Atomic Resonance Filter," *Opt. Lett.* **14**, 211 (1989).
- Gelbwachs, J. A., and Y. C. Chan, "CW Laser Spectroscopy of the Triplet Manifold of Magnesium," *Laser Spectroscopy IX*, Academic Press, Boston (1989), p. 113.
- Gelbwachs, J. A., "A 422.7 nm Atomic Filter with Superior Solar Background Rejection," *Opt. Lett.* **15**, 236 (1990).
- _____, "Sunlight Suppression by Fraunhofer-Wavelength Atomic Resonance Filters," *Proceedings of the International Conference on Lasers '90*, D. G. Hanes and T. M. Shay, eds., STS Press, McClean, Virginia (1990), p. 928.
- _____, "Active Wavelength-Shifting in Atomic Resonance Filters," *IEEE J. Quantum Electron.* **26**, 1140 (1990).
- _____, "A Proposed Fraunhofer-Wavelength Atomic Filter at 534.9 nm," *Opt. Lett.* **15**, 1165, (1990).
- Gelbwachs, J. A., and Y. C. Chan, "Passive Fraunhofer-Wavelength Atomic Filter at 422.7 nm," *Opt. Lett.* **16**, 336 (1 March 1991).
- Hackwell, J. A., and J. H. Hecht, "IR Emission and UV Extinction in Two Open Clusters," *Proceedings of IAU Symposium 135 on Interstellar Dust*, NASA (1988), p. 131.
- Hackwell, J. A., et al., "A Low Resolution Array Spectrograph for the 2.9–13.5 μm Spectral Region," *Proc. SPIE* **1235**, 171 (1990).
- Hackwell, J. A., J. H. Hecht, and M. Tapia "Observations that Link Infrared Cirrus and Ultraviolet Extinction," *Astrophys. J.* (in press).
- Harris, S. J., and L. R. Martin, "Methyl vs. Acetylene as Diamond Growth Species," *J. Mater. Res.* **5**, 2313 (1990).
- Hayward, T. L., G. L. Grasdalen, C. E. Woodward, J. A. Hackwell, R. D. Gehrz, and J. L. Pipher, "Infrared Imaging of W3 A," *Astrophys. J.* **345**, 894 (1989).
- Hecht, J. H., J. A. Hackwell, and R. W. Russell, "Observational Constraints on Interstellar Dust Models," *Proceedings of IAU Symposium 135 on Interstellar Dust*, NASA (1988), p. 391.
- Hecht, J. H., A. B. Christensen, D. J. Strickland, and R. R. Meier, "Deducing Composition and Incident Electron Spectra from Ground-Based Auroral Optical Measurements: Variations in Oxygen Density," *J. Geophys. Res.* **94**, 13,553 (1989).
- Hecht, J. H., and R. L. Walterscheid, "CCD Observations of the O₂ and OH Nightglow Taken During the AIDA Campaign," *EOS* **71**, 579 (1990).
- Hecht, J. H., D. J. Strickland, R. L. Gattinger, and A. Vallence Jones, "Ground Based Observations of Changes in E Region Atomic O.II. Data," *28th Planetary Meeting of the Committee on Space Research, 25 June–6 July 1990, Abstracts*, COSPAR (1990), p. 165.
- Hecht, J. H., "The Nature of the Dust Around R CrB Stars: Isolated Amorphous Carbon or Graphite Fractals?," *Astrophys. J.* **367**, 635 (1991).
- Helvajian, H., and R. P. Welle, "Threshold Level Laser Photoablation of Crystalline Silver: Ejected Ion Translational Energy Distributions," *J. Chem. Phys.* **91**, 2616 (1989).
- _____, "Ejected Product Energy Distributions from Laser Ablated Solids," *Proc. Mater. Res. Soc. Symp.* **129**, 359 (1989).
- Herbelin, J. M., "Short-Wavelength Chemical Laser Development," *Proceedings of the International Conference on Lasers '89*, STS Press (1989), p. 241.
- _____, "High-Power Gas Lasers," *Proc. SPIE* **1225** (1990).
- Hochst, H., M. A. Engelhardt, and R. C. Bowman, Jr., "Characterization of MBE-grown α -Sn Films α -Sn_{1-x}Gex Alloys," *Semicond. Sci. Technol.* **5**, S240 (1990).

- Holloway, J. S., "Kinetics of the $\text{Bi}(^2\text{D})$ and $\text{BiF}(\text{XO}^+)$ in the $\text{NF}(a'\Delta)/\text{BiF}$ Laser System," *Proceedings of the International Conference on Lasers '90*, STS Press (1991).
- Janousek, B. K., M. J. Daugherty, W. L. Bloss, M. L. Rosenbluth, M. J. O'Laughlin, H. Kanter, F. J. DeLucca, and L. E. Perry, "High Detectivity GaAs Quantum Well IR Detectors with Peak Responsivity at $8.2\text{ }\mu\text{m}$," *J. Appl. Phys.* **67**, 7608 (1990).
- Johnson, B. R., "Semiclassical Vibrational Eigenvalues of H_2O and SO_2 by the Adiabatic Switching Method," *Comput. Phys. Commun.* **51**, 1 (1988).
- Johnson, J. J., R. D. Gehrz, T. J. Jones, J. A. Hackwell, J. Smith, and G. L. Grasdalen, "An Infrared Study of the Orion Molecular Cloud-2," *Astrophys. J.* (in press).
- Kayser, D. C., and J. H. Hecht, "Anomalies and Other Phenomena in the MSIS-86 Atmospheric Model," *EOS* **71**, 575 (1990).
- Kuo, S. P., and F. T. Djuth, "A Thermal Instability for the Spread-F Echoes from HF-Heated Ionosphere," *Geophys. Res. Lett.* **15**, 1345 (1988).
- Lacoe, R. C., J. P. Hurrell, S. E. Kohn, C. B. Mombourquette, K. Springer, R. A. Lemons, and I. D. Raistrick, "Flicker $1/f$ Noise in $\text{YBa}_2\text{Cu}_3\text{O}_7$ Thin Films," *Bull. Am. Phys. Soc.* **35**, 425 (1990).
- Lacoe, R. C., J. P. Hurrell, K. Springer, I. D. Raistrick, R. Hu, J. Birch, and R. S. Simon, "Low Frequency $1/f$ Noise Measurements in $\text{YBa}_2\text{Cu}_3\text{O}_7$ Thin Films and the Implications for HTS IR Detectors," *IEEE Trans. Magn.* **27**, 2832 (1991).
- Lince, J. R., " $\text{MOS}_{2-x}\text{O}_x$ Solid Solutions in Thin Films produced by RF-Sputtering," *J. Mater. Res.* **5**, 218 (1990).
- Lince, J. R., M. R. Hilton, and A. S. Bommannavar, "Oxygen Substitution in Sputter-Deposited MoS_2 Films Studied by EXAFS, XPS, and X-Ray Diffraction," *Surf. Coat. Techn.* **43/44**, 640 (1990).
- Lipeles, R. A., D. A. Thiede, and M. S. Leung, "Barium Diffusion in Metallo-Organic Solution Deposited Barrier Layers and $\text{Y}_1\text{Ba}_2\text{Cu}_3\text{O}_{7-x}$ Films," *Proc. SPIE* **1287**, 206 (1990).
- Lipeles, R. A., D. J. Coleman, M. B. Tueling, and M. S. Leung, "Hydrolysis of Methoxyethoxide Coating Solutions for $\text{Y}_1\text{Ba}_2\text{Cu}_3\text{O}_{7-x}$ Films," *J. Non-Cryst. Mater.* (in press).
- Little, S. J., C. Gullixson, R. D. Dietz, J. A. Hackwell, D. R. Gehrz, and G. L. Grasdalen, "High Resolution H and K Maps of W51," *Astron. J.* **97**, 1719 (1989).
- Lynch, D. K., "Comet Wilson World-Wide Data Log," *Proceedings of the NASA Cornell Workshop on Infrared Observations of Comets Halley and Wilson and Properties of the Grain*, NASA CP-3004 (1988), p. 19.
- Lynch, D. K., and R. W. Russell, "Comet Halley's Colorful Outbursts," *Proceedings of the NASA/Cornell Workshop on Infrared Observations of Comets Halley and Wilson and Properties of the Grain*, NASA CP-3004 (1988).
- _____, "5-13 μm Airborne Observations of Comet Wilson 1986 ℓ : Preliminary Results," *Proceedings of the NASA/Cornell Workshop on Infrared Observations of Comets Halley and Wilson and Properties of the Grain*, NASA CP-3004 (1988).
- _____, "The Sudden Appearance of Comet Halley's Tail," *Publ. Astron. Soc. Pac.* **100**, 1122 (1988).
- Lynch, D. K., R. W. Russell, and H. Campins, "10 μm Spectral Structure in Comets," *Proceedings of IAU Symposium No. 135*, NASA CP 3036 (1988), p. 417.
- Lynch, D. K., P. F. Bowers, and J. B. Whiteoak, "A Deep Search for 21 cm Neutral Hydrogen Emission in the Tightly Bound Globular Cluster NGC 6388," *Astron. J.* **97** (1989).
- Lynch, D. K., R. W. Russell, F. C. Witteborn, J. M. Bregman, D. M. Rank, M. C. Cohen and H. Campins, "5-13 μm Airborne Observations of Comet Wilson 1986 ℓ ," *Icarus* **82**, 379 (1989).
- Lynch, D. K., R. J. Rudy, G. S. Rossano, H. P. Erwin, and R. C. Puetter, "Nova Ophiuchi 1988: 0.9-1.35 μm Spectroscopy 6 Months After Discovery," *Astron. J.* **98**, 1682 (1989).

- Lynch, D. K., "IRAS Spectra of Extended Objects: The Crab Nebula," *Proceedings of the 22nd ESLAB Symposium on Infrared Spectroscopy in Astronomy*, M. Kessler, ed., European Space Agency Special Publication 290 (1989), p. 193.
- Lynch, D. K., and G. S. Rossano, "An IRAS Survey of Globular Clusters," *Astron. J.* **100**, 717 (1990).
- Lynch, D. K., R. J. Rudy, G. S. Rossano, P. Erwin, R. C. Puetter, and D. Branch, "An Early 1.0–1.35 μm Spectrum of Type Ia Supernova 1989B and the J-Band Absorption," *Astron. J.* **100**, 223 (1990).
- Lynch, D. K., R. J. Rudy, G. S. Rossano, H. P. Erwin, and R. C. Puetter, "Nova Ophiuchi 1988: 0.9–1.35 μm Spectroscopy," *Proceedings of IAU Colloquium No. 122*, "Physics of Classical Novae," A. Cassatella, ed. Springer-Verlag, Berlin (1990), p. 201.
- Lyons, L. R., and A. Nishida, "Description of Substorm Onset Incorporating Boundary Layer and Neutral Line Effects," *Geophys. Res. Lett.* **15**, 1337 (1988).
- Lyons, L. R., J. F. Fennell, and A. L. Vampola, "A General Association between Discrete Auroras and Ion Precipitation from the Tail," *J. Geophys. Res.* **93**, 12,932 (1988).
- Lyons, L. R., M. Schulz, and J. F. Fennel, "Trapped Particle Evacuation: Source of Magnetotail Bursts and Tailward Flows?," *Geophys. Res. Lett.* **16**, 353 (1989).
- Lyons, L. R., and M. Schulz, "Access of Energetic Particles to Stormtime Ring Current through Enhanced Radial Diffusion," *J. Geophys. Res.* **94**, 5491 (1989).
- Lyons, L. R., and O. de la Beaujardiere, "Critical Problems Requiring Coordinated Measurements of Large-Scale Electric Field and Auroral Distribution," *Outstanding Problems in Solar System Plasma Physics: Theory and Instrumentation*, American Geophysics Union (1989), p. 399.
- Lyons, L. R., et al., "Analysis of Substorm Expansion and Surge Development," *J. Geophys. Res.* **95**, 10,575 (1990).
- Lyons, L. R., O. de la Beaujardiere, G. Rostoker, S. Murphree, and E. Friis-Christensen, "Analysis of Substorm Expansion and Surge Development," *J. Geophys. Res.* **95**, 10,575 (1990).
- Lyons, L. R., "Discrete Auroras and Magnetospheric Processes," *Auroral Physics*, Cambridge University Press (1991), p. 195.
- Lyons, L. R., and D. C. Pridmore-Brown, "Force Balance Near an X-Line in a Collisionless Plasma," *J. Geophys. Res.* **92**, 20,903 (1990).
- Marcus, L., "The Search for a Unifying Framework for Computer Security," *Cipher, IEEE* (Fall 1989), p. 55.
- Martin, L. R., and A. R. Calloway, "Some Experiments on the Mechanism of Diamond Film Growth," *Proceedings of the 197th ACS National Meeting*, Vol. 34, No. 2 (1989), p. 535.
- Martin, L. R., and M. W. Hill, "Methyl Regeneration: An Important Role for Hydrogen Atoms in Diamond Film Synthesis," *Proceedings of the First International Symposium on Diamond and Diamond-Like Films*, J. P. Dismukes et al., eds., Electrochemical Society (1989).
- _____, "Diamond Film Synthesis in a Chemically Simplified System," *Appl. Phys. Lett.* **55**, 2248 (1989).
- _____, "A Flowtube Study of Diamond Film Growth: Methane versus Acetylene," *J. Mater. Sci. Lett.* **9**, 621 (1990).
- McKenzie, D. L., "X-Ray Line-Ratio Plasma Diagnostics Applied to Solar Active Regions," *J. Phys. (Paris)* **49**, C1-55 (1988).
- Meier, R. R., D. J. Strickland, J. H. Hecht, and A. B. Christensen, "Deducing Composition and Incident Electron Spectra from Ground-Based Auroral Optical Measurements: A Study of Auroral Red Line Processes," *J. Geophys. Res.* **94**, 13,541 (1989).
- Ness, N. F., J. E. P. Connerney, R. P. Lepping, M. Schulz, and G. H. Voigt, "The Magnetic Field and Magnetospheric Configuration of Uranus," *Uranus*, E. Miner and J. T. Bergstahl, ed., University of Arizona Press (in press).

- Newman, A. L., H. C. Carlson, G. P. Mantas, and F. T. Djuth, "Thermal Response of the F-Region Ionosphere for Conditions of Large HF-Induced Electron Temperature Enhancements," *Geophys. Res. Lett.* **311** (1988).
- Niciejewski, R. J., J. W. Meriweather, Jr., J. H. Hecht, A. B. Christensen, D. J. Strickland, G. Swenson, S. B. Mende, A. Vallence Jones, and H. C. Carlson, "Coordinated Satellite and Ground-Based Measurements of the Energy Characteristics of a Right Sun-Aligned Arc Over Sondrestrom," *J. Geophys. Res.* **94**, 17,201 (1989).
- Noble, S. T., and F. T. Djuth, "Simultaneous Measurements of HF-Enhanced Plasma Waves and Artificial Field-Aligned Irregularities at Arecibo," *J. Geophys. Res.* (in press).
- Nuth, J. A., III, and J. H. Hecht, "Signatures of Aging Silicate Dust," *Astrophys. Space Sci.* **163**, 79 (1990).
- Pluchino, A., "Nonlinear Optical Properties of CDS Microspheres," *J. Aerosol Sci.* **20**, 1083 (1989).
- Pollard, J. E., et al., "Time-Resolved Mass and Energy Analysis by Position-Sensitive Time-Of-Flight Detection," *Rev. Sci. Instrum.* **60** (10), 3171 (1989).
- Providakes, J., W. E. Swartz, M. C. Kelley, F. T. Djuth, S. T. Noble, and R. J. Jost, "Radar Observations of Ion Cyclotron Waves Associated with Two Barium Shaped Charge Releases," *J. Geophys. Res.* (in press).
- Rank, D. M., J. Bregman, F. C. Witteborn, M. Cohen, D. K. Lynch, and R. W. Russell, "Infrared Observations of SN 1987A from 5.3 to 12.6 Microns: Evidence for an Early Dust Echo," *Astrophys. J. Lett.* **325**, L1-L4 (1988).
- Rice, C. J., "Contributions of The Aerospace Corporation to the 1989 Report of the Observatories of the AAS," *Bull. Am. Astron. Soc.* **21**, 7 (1989).
- _____, "Contributions of The Aerospace Corporation to the 1990 Report of the Observatories of the AAS," *Bull. Am. Astron. Soc.* **22**, 1 (1990).
- Rodriguez Espinosa, J. M., R. J. Rudy, and B. Jones, "Star Formation in Seyfert Galaxies," *Star Formation in Galaxies*, G. Neugebauer and N. Scoville, eds., NASA Publications (in press).
- Ross, M. N., G. Schubert, and R. L. Walterscheid, "Propagation of Gravity Waves in Titan's Atmosphere," *Bull. Am. Astron. Soc.* **21**, 233 (1989).
- _____, "The Coupled Orbital and Thermal Evolution of Triton," *Geophys. Res. Lett.* **17**, 1749 (1990).
- Rossano, G. S., "Microcomputer Control of Infrared Detector Arrays Used in Direct Imaging and in Fabry-Perot Spectroscopy," *IEEE Trans. Nucl. Sci.* (in press).
- _____, "Remotely Operated Imaging Systems," *Proceedings of the 102nd Meeting of the Astronomical Society of the Pacific* (in press).
- Rudy, R. J., R. D. Cohen, and T. B. Ake, "Ultraviolet and Optical Spectrophotometry of the Seyfert 1.8 Galaxy Markarian 609," *Astrophys. J.* **332**, 172 (1988).
- Rudy, R. J., and G. D. Schmidt, "The Nature of the Strong Static Polarization of the Quasar OI 287," *Astrophys. J.* **331**, 325 (1988).
- Rudy, R. J., G. S. Rossano, and R. C. Puetter, "The Near-Infrared Oxygen I Lines of the Planetary Nebula IC 4997," *Astrophys. J.* **346**, 799 (1989).
- _____, "He I/10830 Observations of Seyfert 2 Galaxies," *Astrophys. J.* **341**, 120 (1989).
- _____, "Detection of the OI/11287 A Line in the Seyfert 1 Galaxy I Zwicky 1," *Astrophys. J.* **342**, 235 (1989).
- Rudy, R. J., R. D. Cohen, G. S. Rossano, P. Erwin, R. C. Puetter, and D. K. Lynch, "The 0.46-1.3 μ m Spectrum of the Planetary Nebula BD + 30/3639," *Astrophys. J.* **380** (1991).
- Rudy, R. J., et al., "Near-Infrared Spectrophotometry of the Symbiotic System V1016 Cygni," *Astrophys. J.* **362**, 346 (1990).

- Rudy, R. J., et al., "Near-Infrared Spectroscopy of the Planetary Nebula NCC 6572," *Astr. J.* **268**, 468 (1991).
- Russell, R. W., "Chapter 4—Laboratory Investigations," *Infrared Observations of Comets Halley and Wilson and Properties of the Grains*, NASA CP 3004, (1988), p. 91.
- Russell, R. W., M. A. Chatelain, J. H. Hecht, and J. R. Stephens, "Si₃N₄ Grain Emissivity and the Unidentified Infrared Bands," *Proceedings of IAU Symposium No. 135*, NASA CP 3036 (1988).
- Russell, R. W., and H. P. Erwin, "Airborne IR Spectroscopy of the Atmosphere," *Optical Remote Sensing of the Atmosphere, Tech. Dig.* **4**, 541 (1990).
- Schubert, G., and R. L. Walterscheid, "Wave-Driven Fluctuations in OH Nightglow from an Extended Source Region," *J. Geophys. Res.* **93**, 9903 (1988).
- Schubert, G., R. L. Walterscheid, and M. P. Hickey, "Gravity Wave-Driven Fluctuations from an Extended, Dissipative Emission Region," *J. Geophys. Res.* (August 1991).
- Schubert, G., R. L. Walterscheid, and G. G. Sivjee, "Temperature Gradients at Mesopause Heights Inferred from OH Nightglow Data," *J. Geophys. Res.* **95**, 19,601 (1990).
- Schulz, M., and G. T. Davidson, "Limiting Energy Spectrum of a Saturated Radiation Belt," *J. Geophys. Res.* **93**, 59 (1988).
- Schulz, M., and G. A. Paulikas, "Planetary Magnetic Fields: A Comparative View," *Adv. Space Res.* **10** (1), 55 (1990).
- Schulz, M., "The Magnetosphere," *Geomagnetism and Aeronomy*, Vol. 4, J. A. Jacobs, ed., Academic Press, London (1991), p. 87.
- Simons, D. A., A. T. Tokunaga, R. J. Rudy, and W. A. Stein, "Small-Aperture Infrared Photometry of Seyfert I Galactic Nuclei," *Astron. J.* **96**, 481 (1988).
- Smith, J., R. D. Gehrz, G. L. Grasdalen, J. A. Hackwell, and R. D. Dietz, "Near-Infrared Light and the Morphology of Arp 220," *Astrophys. J.* **329**, 107 (1989).
- Smith, J., R. D. Gehrz, G. L. Grasdalen, J. A. Hackwell, R. D. Dietz, and S. D. Friedman, "Starlight Morphology of the Interacting Galaxy NGC 5195," *Astrophys. J.* (in press).
- Speckman, D. M., and J. P. Wendt, "Atmospheric Pressure OMCVD Growth of GaAs Using Triethylarsenic and Alkylgallium Organometallic Precursors," *Proc. Mater. Res. Soc. Symp.* **102**, 187 (1988).
- _____, "Triethylarsine and Arsine as Co-Reagents: The Novel Manipulation of in-situ GaAs OMCVD Growth Chemistry to Improve Growth Efficiency and Safety," *J. Cryst. Growth* **93**, 29 (1988).
- _____, "The Role of Arsine in Reducing Carbon in Triethylarsenic Grown GaAs Films," *Proc. Mater. Res. Soc. Symp.* **145**, 145 (1989).
- _____, "Vapor Deposition of High Purity GaAs Epilayers Using Monoethylarsine," *Appl. Phys. Lett.* **56**, 1134 (1990).
- _____, "Carbon Reduction in Triethylarsenic-Grown GaAs Films Using Chemically Activated Arsine as a Co-Reagent," *J. Electron. Mater.* **19**, 495 (1990).
- _____, "Monoethylarsine as a Novel Replacement for Arsine in the Vapor Deposition of GaAs," *J. Cryst. Growth* **105**, 275 (1990).
- Steadman, J., and J. A. Syage, "Picosecond Mass-Selective Measurements of Phenol-(NH₃)_n Acid-Base Chemistry in Clusters," *J. Chem. Phys.* **92**, 4630 (1990).
- Steadman, J., E. W. Fournier, and J. A. Syage, "Detection of Neutral and Ionic Reaction Mechanisms in Molecular Clusters," *Appl. Opt.* **29**, 4962 (1990).
- Strickland, D. J., R. R. Meier, J. H. Hecht, and A. B. Christensen, "Deducing Composition and Incident Electron Spectra from Ground Based Auroral Optical Measurements," *J. Geophys. Res.* **94**, 13,527 (1989).

- Syage, J. A., "Measurements of Electron-Impact Ionization and Dissociation Cross Sections in a Crossed Electron-Supersonic Molecular Beam," *Chem. Phys. Lett.* **143**, 19 (1988).
- Syage, J. A., E. W. Fournier, R. Rianda, and R. B. Cohen, "Dynamics of Flame Propagation Using Laser-Induced Spark Initiation: Ignition Energy Measurements," *J. Appl. Phys.* **64**, 1499 (1988).
- _____, "Minimum Ignition Energy Measurements Using Laser-Induced Spark Initiation," *Proceedings of the JANNAF Combustion Meeting*, CPIA Press, Baltimore (1988).
- Syage, J. A., "Reactivity of Aniline Cation to Stepwise Solvation in Hydrogen-Bonded Molecular Clusters," *J. Phys. Chem.* **93**, 170 (1989).
- _____, "On the Direct Vibrational Spectroscopy of Transition States," *Chem. Phys. Lett.* **158**, 122 (1989).
- _____, "Radiative Trapping of a Direct Photodissociation," *Bull. Am. Phys. Soc.* **34**, 1534 (1989).
- Syage, J. A., J. E. Pollard, and J. Steadman, "Resonance Ion Dissociation Spectroscopy of CH_3I^+ Produced by Molecular Beam Electron-Impact Ionization," *Chem. Phys. Lett.* **161**, 103 (1989).
- Syage, J. A., "Photodissociation and Metastable Decay of Solvated Cluster Ions," *J. Chem. Phys.* **92**, 1804 (1990).
- _____, "Picosecond Photochemistry in Molecular Clusters," *Proc. SPIE* **1209**, 64 (1990).
- _____, "New Developments in Molecular Detection by Supersonic Molecular Beam Laser Mass Spectrometry," *Lasers and Mass Spectrometry*, D. M. Lubman, ed., Oxford University Press (1990), p. 468.
- Syage, J. A., and J. Steadman, "Photodissociation Spectroscopy of Cold Molecular Ions and Cluster Ions," *Laser Spectroscopy IX*, M. S. Feld, J. E. Thomas, and A. Mooradian, eds., Academic Press, New York (1989), p. 418.
- _____, "Strong Field Effects in the Spectroscopy of the B State of CF_3I ," *J. Phys. Chem.* **94**, 7343 (1990).
- _____, "Picosecond Mass-Selective Measurements of Molecular Cluster Reactions: $(\text{CH}_3\text{I})_n$ A State Excitation," *Chem. Phys. Lett.* **166**, 159 (1990).
- _____, "A Time-of-Flight Mass Filter for Ion and Cluster Ions Photodissociation Studies," *Rev. Sci. Instrum.* **61**, 1204 (1990).
- Vaghjiani, G. L., A. R. Ravishankara, and N. Cohen, "Reactions of OH and OD with H_2O_2 and D_2O_2 ," *J. Phys. Chem.* **93**, 7833 (1989).
- Walterscheid, R. L., and L. R. Lyons, "The Neutral E-Region Winds During Intense Postmidnight Diffuse Aurora: Response to Observed Particle Fluxes," *J. Geophys. Res.* **94**, 3703 (1988).
- Walterscheid, R. L., "Solar Cycle Effects on the Upper Atmosphere: Implications for Satellite Drag," *J. Spacecraft Rockets* **26**, 439 (1989).
- Walterscheid, R. L., and G. Schubert, "Gravity Wave Fluxes of O_3 and OH at the Nightside Mesopause," *Geophys. Res. Lett.* **16**, 719 (1989).
- _____, "Nonlinear Evolution of an Upward Propagating Gravity Wave: Overturning, Convection, Transience and Turbulence," *J. Atmos. Sci.* **47**, 101 (1989).
- Wang, J. C. T., and G. F. Widhopf, "A High Resolution TVD Finite Volume Scheme for the Euler Equations in Conservation Form," *J. Comput. Phys.* **84**, 145 (1989).
- _____, "Numerical Simulation of Blast Flowfields Using a High Resolution TVD Finite Volume Scheme," *Int. J. Comput. Fluids* **18**, 103 (1990).
- Warren, D. W., and J. A. Hackwell, "A Compact Prism Spectrograph Suitable for Broadband Infrared Spectral Surveys with Array Detectors," *Proc. SPIE* **115**, 314 (1989).
- West, S. C., G. D. Schmidt, R. Paulicki, G. H. Rieke, J. R. P. Angel, and R. J. Rudy, "A Computer-Controlled Near Infrared Polarimeter Featuring a New Type of Stress-Birefringent Modulator," *Publ. Astron. Soc. Pac.* **100**, 861 (1988).

- Wiberg, D. M., and L. A. Campbell, "A Discrete-Time Convergent Approximation of the Optimal Recursive Parameter Estimator," *Proceedings of the Ninth IFAC Symposium on Identification and System Parameter Estimation* (1991), p. 140.
- Wiedeman, L., and H. Helvajian, "Threshold Level Laser Ablation of $Y_1Ba_2Cu_3O_{x+6}$ at 351 nm, 248 nm and 193 nm, Ejected Product Population and Kinetic Energy Distributions," *Proc. Mater. Res. Soc. Symp.* **191** (1990).
- _____, "UV Tunable Laser Ablation of $Y_1Ba_2Cu_3O_{x+6}$: Changes in the Product Population and Kinetic Energy Distributions as a Function of the Laser Wavelength and Target Bulk Temperature," *Proc. Mater. Res. Soc. Symp.* **191** (1990).
- Williams, T. C., G. L. Grasdalen, J. A. Hackwell, and R. D. Gehrz, "An Eight-Element Bolometer Array Camera for the WIRO 92-Inch Telescope," *Publ. Astron. Soc. Pac.* **100**, 124 (1988).
- Young, S. J., and R. R. Herm, "Model for Radiation Contamination by Outgassing from Space Platforms," *J. Spacecraft Rockets* **25**, 413 (1988).

Author Index

Adams, P. M., see C. J. Selvey	35
Amimoto, S. T., and R. F. W. Gross: Stimulated Brillouin Scattering Phase Conjugation ..	50
Arnold, G. S., and D. J. Coleman: Vibrational Chemiluminescence in Gas-Solid Reactions	113
Beck, S. M. : Physics and Chemistry of Metal-Semiconductor Clusters	123
Beezley, R. S., see D. M. Nystrom	187
Bhasker, N. D., and C. M. Klimcak: Metallic Clusters Ions—Electronic Structure and Stability	110
Blake, J. B., see R. J. Rudy	164
Bloss, W. L., and B. K. Janousek: Superlattice Plasmon Excitations for EHF Devices	13
Bott, J. F., see R. F. Heidner	72
(see also N. Cohen)	94
Bucy, R., and R. S. Di Esposti: Classification Tree Optimization by Simulated Annealing	180
Camparo, J. C.: Chaotic Dynamics of Atoms	116
Campbell, L. A.: On-Line Parameter Estimation	189
(see also D. J. Evans)	184
Canterna, R. W., see J. A. Hackwell	153
Chan, see J. A. Gelbwachs	31
(see also B. Jaduszliwer)	126
Childs, J. L., see J. R. Lince	99
Christensen, A. B., see J. H. Hecht	145
Cohen, N., and J. F. Bott: Reacting Flow Field Kinetics	94
Cohen, R. B., see R. F. Heidner	72
(see also T. A. Spiglanin)	74
(see also J. E. Pollard)	79
(see also S. W. Janson)	89
Coleman, D. J., see M. S. Leung	20
(see also G. S. Arnold)	113
Cook, J. V., see L. G. Marcus	171
Dafesh, P. A., see C. J. Selvey	35
Di Esposti, R. S., see R. S. Bucy	180
Djuth, F. T.: Ionospheric Processes	149
Doner, J. E., see L. G. Marcus	171
Edelsohn, D. J., see J. A. Hackwell	153
Evans, D. J., L. A. Campbell, and M. Jenkins: Fractals and Image Processing	184
Fennell, J. F., see L. R. Lyons	157
Fields, R. A.: Characterization of Radiation Damage in Solids	23

Filippenko, I. V., see L. G. Marcus	171
Friesen, L. M., see J. A. Hackwell	153
Gelbwachs, J. A., and Y. C. Chan: Magnesium Atomic Filters for Submarine Laser Communications	31
Gross, R. F. W., see S. T. Amimoto	50
Hackwell, J. A., R. W. Cantera, D. J. Edelson, L. M. Friesen, J. H. Hecht, J. Kepner, D. K. Lynch, R. W. Russell, and E. A. Walkup: Infrared Studies of Star-Forming Regions	153
(see also R. W. Russell)	135
Halle, L. F., and D. C. Marvin: Indium Phosphide Photovoltaic Technology	26
Hecht, J. H., and A. B. Christensen: Aeronomy of Auroral/Airglow Emissions	145
(see also J. A. Hackwell)	153
(see also R. J. Rudy)	164
Heidner, R. F., D. G. Sutton, R. B. Cohen, J. F. Bott, J. Steadman, J. B. Koffend, and J. A. Syage: Ultraviolet-Visible Plume Chemistry and Spectroscopy	72
Helvajian, H., H. -S. Kim, and L. M. Wir Jeman: Laser Surface Photolyzed Chemistry ...	67
Herbelin, J. M.: Novel Short-Wavelength Lasers	45
Hilton, M. R., see J. R. Lince	99
Hurrell, J. P., see R. C. Lacoe	5
Ives, N. A., see A. H. Zimmerman	106
Jaduszliwer, B., and Y. C. Chan: Spin Effects in Electron-Atom Collisions	126
Jankins, M., see D. J. Evans	184
Janousek, B. K., see W. L. Bloss	13
Janson, S. W., R. P. Welle, T. A. Spiglanin, and R. B. Cohen: Propulsion Diagnostics Program	89
Johnson, B. R.: Semiclassical Analysis of Two-Electron Atoms	120
Johnson, L. K., see J. E. Pollard	79
Kepner, J., see J. A. Hackwell	153
Kim, H. E., see D. M. Nystrom	187
Kim, H. -S., see H. Helvajian	67
Kirshman, J. F., see M. S. Leung	20
Klimcak, C. M., see N. D. Bhaskar	110
Koffend, J. B., see R. F. Heidner	72
Lacoe, R. C., J. P. Hurrell, and J. P. Wendt: High Temperature Superconducting Electronics	5
(see also M. S. Leung)	20
Lake, D. E., see D. W. Pack	59
Leung, M. S., R. A. Lipeles, D. J. Coleman, J. F. Kirschman, and R. C. Lacoe: Deposition of High-T _c Superconducting Oxides	20
Lichtin, D. A., see J. E. Pollard	79
Lince, J. R., M. R. Hilton, and J. L. Childs: Extended X-ray Absorption Fine Structure of Metal Dichalcogenides	99
Lipeles, R. A., see M. S. Leung	20

Lynch, D. K., see R. W. Russell	135
(see also J. A. Hackwell)	153
Lyons, L. R., and J. F. Fennell: Auroral Energization and Geomagnetic Disturbances	157
(see also R. L. Walterscheid)	141
Ma, R. P., see M. P. Plonski	173
Marcus, L. G., J. V. Cook, J. E. Doner, I. V. Filippenko, and T. K. Menas: Applications of Logic to Computer Verification	171
Martin, L. R.: Mechanism of Diamond Film Growth	86
Marvin, D. C., see L. F. Halle	26
Masturzo, D. E., and A. Pluchino: Microparticle Linear and Nonlinear Optics	54
McNab, M. C., see R. J. Rudy	164
Menas, T. K., see L. G. Marcus	171
Moss, S. C.: Picosecond Studies of Space Optical Materials	39
Nystrom, D. M., R. S. Beezley, H. E. Kim, B. H. Sako, and W. K. Yeung: Linear Algebra with Symbolic Interface	187
Pack, D. W., A. Pluchino, and D. E. Lake: High-Energy Laser Particle Interaction	59
Peter, W. K., see M. P. Plonski	173
Plonski, M. P., W. K. Peter, and R. P. Ma: Neural Network Architectures	173
Pluchino, A., see D. E. Masturzo	54
(see also D. W. Pack)	59
Pollard, J. E., L. K. Johnson, D. A. Lichtin, and R. B. Cohen: High-Resolution Chemical Dynamics	79
Quinzio, M. V., see A. H. Zimmerman	106
Razouk, R. R.: Software Application Generators	176
Rose, T. S.: Transition Dynamics and Guest-Host Interactions in Laser Materials	17
Ross, M. N.: Trends in Middle Atmosphere Ozone	161
(see also R. L. Walterscheid)	141
Rossano, G. S., see R. W. Russell	135
Rudy, R. J., J. B. Blake, M. C. McNab, M. Schulz, and J. H. Hecht: Solar-Terrestrial Physics and Astrophysics	164
(see also R. W. Russell)	135
Russell, R. W., J. A. Hackwell, D. K. Lynch, G. S. Rossano, and R. J. Rudy: High Resolution Infrared Technology and Applications	135
(see also J. A. Hackwell)	153
Sako, B. H., see D. M. Nystrom	187
Schubert, G., see R. L. Walterscheid	141
Schulz, M., see R. J. Rudy	164
Selvey, C. J., P. A. Dafesh, R. P. Wright, and P. M. Adams: Analysis of Infrared Detector Materials	35
Speckman, D. M., and J. P. Wendt: Novel Approaches to GaAs Growth	9
Spiglanin, T. A., J. A. Syage, and R. B. Cohen: Flame Front Kinetics	74
(see also S. W. Janson)	89

Steadman, J., see R. F. Heidner	72
(see also J. A. Syage)	82
Stewart, T. B., <i>Ab Initio</i> Calculations of Solid Lubricants	102
Sutton, D. G, see R. F. Heidner	72
Syage, J. A., and J. Steadman: Picosecond State-Specific Reaction Dynamics	82
(see also R. F. Heidner)	72
(see also T. A. Spiglanin)	74
Walkup, E. A., see J. A. Hackwell	153
Walterscheid, R. L., L. R. Lyons, M. N. Ross, and G. Schubert: Atmosphere Dynamics and Coupling	141
Wang, J. C. T., and G. F. Widhopf: Chemically Reacting Flows	96
Wendt, J. P., see R. C. Lacoe	5
(see also D. M. Speckman)	9
Welle, R. P., see S. W. Janson	89
Widhopf, G. F., see J. C. T. Wang	96
Wiedeman, L. H., see H. Helvajian	67
Wright, R. P., see C. J. Selvey	35
Yeung, W. K., see D. M. Nystrom	187
Zimmerman, A. H., M. V. Quinzio, and N. A. Ives: Scanning Tunneling Microscope Studies of Nickel Oxyhydroxides	106